Assessment of Corrosion Defects in Pipelines

By

Duane S. Cronin

A thesis
presented to the University of Waterloo
in the fulfillment of the
thesis requirement for the degree of

Doctor in Philosophy
In
Mechanical Engineering

Waterloo, Ontario, Canada, 2000

© Duane S. Cronin, 2000

National Library of Canada
Acquisitions and Bibliographic Services
395 Wellington Street
Ottawa ON K1A 0N4
Canada

Bibliothèque nationale du Canada
Acquisitions et services bibliographiques
395, rue Wellington
Ottawa ON K1A 0N4
Canada

Your file Votre référence

Our file Notre référence

The author has granted a non-exclusive licence allowing the National Library of Canada to reproduce, loan, distribute or sell copies of this thesis in microform, paper or electronic formats.

L'auteur a accordé une licence non exclusive permettant à la Bibliothèque nationale du Canada de reproduire, prêter, distribuer ou vendre des copies de cette thèse sous la forme de microfiche/film, de reproduction sur papier ou sur format électronique.

The author retains ownership of the copyright in this thesis. Neither the thesis nor substantial extracts from it may be printed or otherwise reproduced without the author's permission.

L'auteur conserve la propriété du droit d'auteur qui protège cette thèse. Ni la thèse ni des extraits substantiels de celle-ci ne doivent être imprimés ou autrement reproduits sans son autorisation.

0-612-51187-1

Canada

The University of Waterloo requires the signatures of all persons using or photocopying this thesis. Please sign below, and provide address and date.

Abstract

Pipelines are a safe and economic means for transporting oil and natural gas with the number of failures, defined as a loss of product, being relatively low compared to other means of transportation. However, it should be pointed out that even a single major failure, such as a rupture, will have a significant financial and environmental impact.

The focus of this thesis is the assessment of corrosion defects in pipelines with the goal of providing a more complete understanding of the failure of these defects and addressing the conservatism in the currently accepted assessment procedures. At present, these procedures do not take advantage of the detailed corrosion measurements available from high-resolution inspection devices and the plastic material behaviour, which has a significant effect on the failure of corrosion defects, is characterized with a simple flow stress. The currently accepted procedures were developed from experimental burst tests on machined defects with simple geometries but have not been investigated with complex natural corrosion defects.

Two forms of simply shaped defects, long grooves and single pits, were investigated in detail to develop a fundamental understanding of corrosion defect failure. A solution to predict the failure pressure of a long groove was developed and agrees with Finite Element analyses and experimental test results. In addition, a solution to predict the failure pressure of uncorroded pipe was developed since this is an upper bound for the failure pressure of a corrosion defect. Single pit defects were investigated in detail using the Finite Element method. The effect of element mesh density, defect circumferential dimension, varying material properties and defect interaction on the defect failure pressure were considered. In addition, the validity of the Folias factor used in RSTRENG was investigated and found to be inconsistent with the Finite Element results.

Burst test results of 40 pipe sections removed from operating pipelines due to the presence of corrosion defects are presented in an experimental database. This database was used to investigate the accuracy of the currently accepted assessment procedures. The RSTRENG procedure was found to be the most accurate due to the consideration of the

actual corrosion geometry. Other proposed methods based on the total defect length and maximum depth were also considered but were not as accurate as RSTRENG. Twenty-five of the defects in the experimental database were analyzed using three-dimensional elastic-plastic Finite Element analysis. When accurate material properties and defect measurements are available this is the most accurate method of assessment. However, use of the Finite Element method requires expertise in interpretting the results and inaccurate corrosion measurements can significantly reduce the accuracy of the failure pressure predictions.

A new model for predicting the failure pressure of corrosion defects is proposed. This model uses the elastic-plastic material properties, as determined from uniaxial tensile tests, and corrosion measurements in the same form as the currently accepted RSTRENG procedure to predict the defect failure pressure. This procedure is based on a Weighted Depth Difference model and uses the long groove and plain pipe failure pressures as lower and upper bounds respectively for the defect failure pressure. The actual defect failure pressure is then determined by considering each point within the corrosion defect and evaluating the effect of the adjacent material loss through the proposed weighting scheme. This method is iterative in nature and applied with a computer program called Corroded Pipe Strength (CPS). When used to evaluate the corrosion defects in the experimental database, this method provided the most accurate failure pressure predictions. This solution was developed from fundamentals and utilizes the actual material properties so that it is applicable to other materials not considered in the experimental database. In addition the Weighted Depth Difference model identifies the predicted failure location.

A statistical model, based on the experimental database, is presented for the various assessment procedures considered and a three-level assessment procedure is proposed when detailed material properties are available. This procedure consists of the solution for a long groove, the Weighted Depth Difference model and three-dimensional Finite Element analysis. When detailed material properties are not available, an alternate two-level assessment procedure, which makes use of the currently accepted assessment procedures, is proposed.

Acknowledgements

I would sincerely like to thank my supervisor, Dr. Roy Pick, for his professional support, excellent guidance and the many learning opportunities offered during my studies. Most importantly I would like to thank him for his friendship, patience and encouragement throughout my degree.

Development of the experimental database would not have been possible without a great deal of hard work from a number of co-op students, which included Rob Marshman and Bill Leonard. I would also like to thank my fellow students for their advice and encouragement. In particular, I would like to thank Roger Chen for many helpful conversations. Steve Hitchman and Peter Rutledge have provided indispensable computer support through this entire project and are greatly appreciated.

I would especially like to thank Ernst Huber and Andy Barber for all of their support, advice and hard work above and beyond the call of duty.

The first two years of my work were supported by a PGS B Natural Sciences and Engineering Research Council of Canada scholarship. The remainder of my work was supported in part by Enbridge Pipelines Inc. and Transcanada Pipelines Inc. I would also like to thank British Gas for the use of their Cray supercomputer during the initial finite element work.

I would like to thank my parents, Robert and Shirley Cronin, for their unconditional support and encouragement. Finally, I am indebted to my wife Leah, who believed in me and supported me throughout this project.

Table of Contents

Chapter 1

Introduction 1

1.1 Causes of corrosion 3

1.2 Current assessment techniques 5

1.3 Thesis outline 6

Chapter 2

Literature Review 8

2.1 B31G/CSA Z662/RSTRENG 8

Calculation of projected area 12

Folias Factor 13

Flow Stress 16

Projected area 17

2.2 Finite Element Method 18

2.2.1 Failure criteria 20

2.2.2 Material model 21

2.3 Alternative models to predict the failure of corrosion defects 23

2.3.1 PCORR 23

2.3.2 British Gas proposed corrosion defect assessment guidance 24

2.3.3 Modified B31G model 25

2.3.4 Analytical shell analysis 26

2.3.5 Fracture mechanics approach 28

2.4 Important parameters in corrosion defects 30

2.5 Defect interaction and limits 31

2.6 Corrosion measurement 34

2.6.1 Intelligent pigs 35

2.6.2 Corrosion measurement methods for excavated pipe sections 38

2.6.3 Automated measurement of external corrosion 40
2.7 Evaluation of RSTRENG/B31G 40

Chapter 3

Failure pressure prediction of simple corrosion defects 43
3.1 Failure mode of corrosion defects 43
3.2 Failure of plain pipe 46
3.3 Longitudinal groove analysis 49
3.3.1 Defect length 49
3.3.2 Finite Element Analysis 50
3.3.3 Material model: incremental vs. deformation plasticity 52
3.3.4 Circumferential corrosion dimension 55
3.3.5 Prediction of the failure pressure of long, longitudinally oriented grooves 55
3.4 Analysis of single pits 64
3.4.1 Finite Element Analysis 64
Mesh convergence 65
Element type and material model 66
Typical single pit behaviour 67
Effect of circumferential extent 68
Assessment of the Folias factor 70
Flow Stress investigation / Material Properties 71
Reduced wall thickness analysis 73
Simplified defect interaction analysis 74

Chapter 4

Experimental testing and modeling of corrosion defects 76
4.1 Background 76
4.2 Experimental database of complex corrosion defects 79

4.2.1 Research program at the University of Waterloo 79
4.2.2 Corrosion measurement 80
4.2.3 Material properties 85
4.2.4 Burst test procedure 87
4.2.5 Test results 88
4.2.6 Sources of experimental error 88
4.3 Current state of evaluation procedures 90
4.4 Complex corrosion defect assessment – B31G and RSTRENG 92
4.4.1 Plain pipe analysis 95
4.4.2 Long groove model 96
4.4.3 Proposed methods of assessment 97
4.5 Finite Element modeling of complex corrosion defects 99
4.5.1 Finite Element Analysis 99
4.5.2 Mesh generation 101
4.5.3 Model size / mesh refinement 103
4.5.4 Material model: incremental vs. deformation plasticity 106
4.5.5 Finite element analyses 106
4.5.6 Internal vs. external corrosion 111

Chapter 5

Prediction of failure pressure for complex corrosion defects 112
5.1 Weighted Depth Difference model to predict
the failure pressure of corrosion defects 113
5.1.1 Weighted Depth Difference (WDD) model 114
5.1.2 Corrosion extent and defect interaction 119
5.2 Statistical analysis of the failure pressure prediction models 122
5.2.1 Operating pressure 125

Chapter 6

Multi-level defect assessment 129

6.1 Assessment procedure 129

6.2 Assessment philosophy 131

6.3 Proposed three-level assessment procedure 132

6.4 Alternate two-level assessment procedure 135

6.5 Proposed assessment procedure – sample calculation 136

Chapter 7

Closure 143

Prediction of corrosion defect failure pressures using CPS 144

Finite Element modeling of complex corrosion defects 146

Statistical model of failure predictions 146

Multi-level assessment of corrosion defects 147

Chapter 8

Recommendations 148

References 150

List of Tables

Table 2.7.1 Failure ratios for RSTRENG and B31G 157
Table 2.7.2 Failure ratios for RSTRENG and B31G for long corrosion defects 157
Table 4.2.1 Experimental database material summary – average values 158
Table 4.2.2 Burst test summary 159
Table 4.2.3 Failure prediction summary 160
Table 4.4.1 Failure pressure prediction statistics for B31G and RSTRENG 161
Table 4.4.2 Plain pipe failure pressure predictions 162
Table 4.4.3 Failure pressure prediction statistics for PCORRC, Ritchie and Last, and Modified RSTRENG models 163
Table 4.5.1 Finite element failure predictions 164
Table 5.1.1 Failure pressure statistics for CPS 165
Table 5.2.1 Summary statistics for the percent error in various evaluation procedures 166
Table 5.2.2 Probability of defect failure based on operating pressure and raw residuals 166
Table 5.2.3 Allowable operating pressure for various probabilities of failure 167
Table 6.5.1 Long Groove solution – defect failure pressure as a function of defect depth 168
Table 6.5.2 Defect depths and predicted failure pressure for selected defects on pipe section TCP-02 168
Table 6.5.3 Defect reliability for defects on pipe section TCP-02 at an operating pressure of 1032 psi (100 SMYS) 169
Table 6.5.4 Allowable operating pressures for defects on pipe section TCP-02 at a 99% defect reliability 169

List of Figures

Figure 2.1.1 Corrosion defect profiles 170
Figure 2.1.2 RSTRENG River bottom projection 171
Figure 2.2.1 Shell analysis of corrosion defects 172
Figure 2.3.1 Membrane-arch model 172
Figure 2.5.1 CSA defect interaction rules 173
Figure 2.6.1 Internal inspection device (intelligent pig) 174
Figure 2.6.2 Schematic of magnetic flux leakage technology 175
Figure 2.6.3 Schematic of ultrasonic technology 176
Figure 3.1.1a Ductile tearing of a pit ligament 177
Figure 3.1.1b Ductile tearing of a pit ligament resulting in a leak 177
Figure 3.1.2a Partial ductile tearing of a pit ligament 178
Figure 3.1.2b Partial ductile tearing of a pit ligament
(magnified view of crack tip) 178
Figure 3.2.1 Circumferential strain in pressurized plain pipe 179
Figure 3.2.2 True von Mises stress for pressurized plain pipe 180
Figure 3.2.3: Failure pressure of plain pipe for 6 burst tests 181
Figure 3.3.1a Long, longitudinally oriented natural corrosion defect 182
Figure 3.3.1b Long, longitudinally oriented natural corrosion defect (Magnified). 182
Figure 3.3.2 Failure Pressure of 40% depth grooves with varying length 183
Figure 3.3.3 Failure pressures of infinitely long, longitudinally oriented grooves .. 184
Figure 3.3.4 Variation in failure pressure with mesh density for a
65% depth longitudinal groove 185
Figure 3.3.5: True stress-strain curve for grade API-5L-X42 steel 186
Figure 3.3.6: von Mises stress at the outside of the ligament for a
65% depth longitudinal groove 187
Figure 3.3.7 Ratio of hoop stress / longitudinal stress for a 65% depth
longitudinal groove analyzed using incremental plasticity 188

Figure 3.3.8 Variation in failure pressure for a 65% depth
longitudinal groove with varying width 189
Figure 3.3.9 Long groove free body diagram 190
Figure 3.3.10 Infinitesimal element from the ligament of a long groove 191
Figure 3.3.11 Failure pressures of infinitely long, longitudinally oriented machined
grooves -Experimental data and predictions from equation 3.3.24 . 192
Figure 3.3.12 Failure pressures of long, longitudinally oriented defects
Experimental data and predictions from equation 3.3.24 193
Figure 3.3.13 Failure pressures of infinitely long, longitudinally oriented grooves
FE vs. analytical solution failure pressure predictions 194
Figure 3.4.1 Single pit finite element mesh (1/4 model) 195
Figure 3.4.2a Failure pressure for varying number of elements
through the thickness 196
Figure 3.4.2b Equivalent stress at the critical point for varying number
of elements through the thickness 196
Figure 3.4.3a Single pit finite element mesh – full model 197
Figure 3.4.3b Single pit finite element mesh – full model – mesh at pit location 198
Figure 3.4.4 Failure pressure of single pits for varying element type 199
Figure 3.4.5 Failure pressure of single pits for two material models 200
Figure 3.4.6 Single spherical pit 65% WT deep - von Mises stress
at the deepest point in the defect 201
Figure 3.4.7 Single spherical pit 65% WT deep – hoop and longitudinal
stresses at the deepest point in the defect 202
Figure 3.4.8 Single pit finite element mesh – varying the
circumferential dimension 203
Figure 3.4.9 Predicted failure pressure for varying circumferential dimension 204
Figure 3.4.10 Axisymmetric groove 65% WT deep - von Mises stress
at the deepest point in the defect 205

Figure 3.4.11 Axisymmetric groove 65% WT deep
- Hoop and longitudinal stresses at the deepest point 206
Figure 3.4.12 Single pit failure pressure as a function of % Depth
- Corrosion factor = 0.938 207
Figure 3.4.13 Single pit failure pressure as a function of % Depth
- Corrosion factor = 0.82 208
Figure 3.4.14 Single pit failure pressure as a function of % Depth
- Corrosion factor = 0.938, thick-walled pipe 209
Figure 3.4.15 Stress-strain curves with varying material yield strength 210
Figure 3.4.16 Stress-strain curves with varying stress at necking 211
Figure 3.4.17 Stress-strain curves with varying strain at necking 212
Figure 3.4.18 von Mises stress as a function of internal pressure with
varying material yield stress. Single spherical pit, 65% depth 213
Figure 3.4.19 Failure pressure as a function of yield stress
- Single spherical pit, 65% depth 214
Figure 3.4.20 von Mises stress as a function of internal pressure with
varying material Critical Stress. Single spherical pit, 65% depth ... 215
Figure 3.4.21 Failure pressure as a function of Critical Stress
- Single spherical pit, 65% depth 216
Figure 3.4.22 von Mises stress as a function of internal pressure with varying
strain at the Critical Stress. Single spherical pit, 65% depth 217
Figure 3.4.23 Failure pressure as a function of the strain at the Critical Stress
- Single spherical pit, 65% depth 218
Figure 3.4.24 Failure pressure as a function of defect separation
- 65% Depth spherical corrosion pit 219
Figure 4.1.1a Typical fracture path for a flat-bottomed defect 220
Figure 4.1.1b Fracture path for a large flat-bottomed defect 220
Figure 4.1.1c Fracture path for a flat-bottomed defect with a
small circumferential dimension 221

Figure 4.1.2a Failure location and fracture path for test NOV06 222
Figure 4.1.2b Test NOV06 at failure location 222
Figure 4.2.1 Surface scanning from a flat plane 223
Figure 4.2.2 Surface scanning from a cylindrical plane 223
Figure 4.2.3a University of Waterloo 3-D Laser Scanner 224
Figure 4.2.3b University of Waterloo 3-D Scanner and System 224
Figure 4.2.4 University of Waterloo Compact Scanner 225
Figure 4.2.5 University of Waterloo Long Scanner 225
Figure 4.2.6 3-D scanner surface and image plots for a complex corrosion defect (TCP01-AB) 226
Figure 4.2.7 Transformation of a longitudinal line of scanned data 227
Figure 4.2.8 Scanner image with corrosion defects identified by the program (circles) 228
Figure 4.2.9 Original and transformed scanned surface data 229
Figure 4.2.10 Scanner image of the corrosion defect with the corrosion profile (crosses) identified using the projection method . 230
Figure 4.2.11 Projection method applied to a simply shaped corrosion defect 231
Figure 4.2.12 Typical Engineering and true stress-strain curves 232
Figure 4.2.13 True stress-strain curve and corresponding Ramberg-Osgood curve fit 233
Figure 4.3.1 Failure ratio for pipe sections operating at 72% SMYS 234
Figure 4.3.2 Failure ratio for pipe sections operating at 100% SMYS 235
Figure 4.4.1 B31G and RSTRENG failure pressure predictions for the experimental database- % Error 236
Figure 4.4.2 Normal probability plot for the % error in the RSTRENG predictions 237
Figure 4.4.3 Normal probability plot for the % error in the B31G predictions 238
Figure 4.4.4 B31G and RSTRENG failure predictions for the experimental database – failure ratio 239

Figure 4.4.5 B31G and Long Groove failure pressure predictions for the experimental database - % Error 240
Figure 4.4.6 PCORRC and B31G failure pressure predictions for the experimental database - % Error 241
Figure 4.4.7 Ritchie and Last and B31G failure pressure predictions for the experimental database - % Error 242
Figure 4.4.8 Modified RSTRENG and B31G failure pressure predictions for the experimental database - % Error 243
Figure 4.5.1a Scanned surface data 244
Figure 4.5.1b Surface grid file data 244
Figure 4.5.1c Local finite element mesh at defect 245
Figure 4.5.1d Global finite element mesh showing model extent 246
Figure 4.5.2 von Mises stress history for a varying number of elements through the thickness 247
Figure 4.5.3 Percent error in failure prediction as a function of elements through the thickness 248
Figure 4.5.4 Analysis of defect BCG-08E using incremental and deformation plasticity material models 249
Figure 4.5.5a Burst test SOL02 (scanner image, corrosion profile) 250
Figure 4.5.5b Burst test SOL02 (surface plot, stress history) 251
Figure 4.5.6a Burst test SOL04 (scanner image, corrosion profile) 252
Figure 4.5.6b Burst test SOL04 (surface plot, stress history) 253
Figure 4.5.7a Burst test SOL06 (scanner image, corrosion profile) 254
Figure 4.5.7b Burst test SOL06 (surface plot, stress history) 255
Figure 4.5.8a Burst test SOL10 (scanner image, corrosion profile) 256
Figure 4.5.8b Burst test SOL10 (surface plot, stress history) 257
Figure 4.5.9a Burst test SOL11 (scanner image, corrosion profile) 258
Figure 4.5.9b Burst test SOL11 (surface plot, stress history) 259
Figure 4.5.10a Burst test SOL12 (scanner image, corrosion profile) 260

Figure 4.5.10b Burst test SOL12 (surface plot, stress history) 261
Figure 4.5.11a Burst test ESS01 (scanner image, corrosion profile) 262
Figure 4.5.11b Burst test ESS01 (surface plot, stress history) 263
Figure 4.5.12a Burst test NOR02-4A (scanner image, corrosion profile) 264
Figure 4.5.12b Burst test NOR02-4A (surface plot, stress history) 265
Figure 4.5.13a Burst test RLK01 (scanner image, corrosion profile) 266
Figure 4.5.13b Burst test RLK01 (surface plot, stress history) 267
Figure 4.5.14a Burst test RLK01 (scanner image, corrosion profile) 268
Figure 4.5.14b Burst test RLK01 (surface plot, stress history) 269
Figure 4.5.15a Burst test RLK01 (scanner image, corrosion profile) 270
Figure 4.5.15b Burst test RLK01 (surface plot, stress history) 271
Figure 4.5.16a Burst test BCG02 (scanner image, corrosion profile) 272
Figure 4.5.16b Burst test BCG02 (surface plot, stress history) 273
Figure 4.5.17a Burst test BCG03 (scanner image, corrosion profile) 274
Figure 4.5.17b Burst test BCG03 (surface plot, stress history) 275
Figure 4.5.18a Burst test BCG04 (scanner image, corrosion profile) 276
Figure 4.5.18b Burst test BCG04 (surface plot, stress history) 277
Figure 4.5.19a Burst test BCG05 (scanner image, corrosion profile) 278
Figure 4.5.19b Burst test BCG05 (surface plot, stress history) 279
Figure 4.5.20a Burst test BCG06 (scanner image, corrosion profile) 280
Figure 4.5.20b Burst test BCG06 (surface plot, stress history) 281
Figure 4.5.21a Burst test BCG07 (scanner image, corrosion profile) 282
Figure 4.5.21b Burst test BCG07 (surface plot, stress history) 283
Figure 4.5.22a Burst test BCG08 (scanner image, corrosion profile) 284
Figure 4.5.22b Burst test BCG08 (surface plot, stress history) 285
Figure 4.5.23a Burst test BCG09 (scanner image, corrosion profile) 286
Figure 4.5.23b Burst test BCG09 (surface plot, stress history) 287
Figure 4.5.24a Burst test NOV01 (scanner image, corrosion profile) 288
Figure 4.5.24b Burst test NOV01 (surface plot, stress history) 289

Figure 4.5.25a Burst test NOV04 (scanner image, corrosion profile) 290
Figure 4.5.25b Burst test NOV04 (surface plot, stress history) 291
Figure 4.5.26a Burst test NOV06 (scanner image, corrosion profile) 292
Figure 4.5.26b Burst test NOV06 (surface plot, stress history) 293
Figure 4.5.27a Burst test TCP01 (scanner image, corrosion profile) 294
Figure 4.5.27b Burst test TCP01 (surface plot, stress history) 295
Figure 4.5.28a Burst test TCP02 (scanner image, corrosion profile) 296
Figure 4.5.28b Burst test TCP02 (surface plot, stress history) 297
Figure 4.5.29a Burst test TCP03 (scanner image, corrosion profile) 298
Figure 4.5.29b Burst test TCP03 (surface plot, stress history) 299
Figure 4.5.30 Error in the Finite Element prediction plotted with the RSTRENG and B31G results 300
Figure 4.5.31 Error in the Finite Element prediction plotted as a function of time.. 301
Figure 4.5.32 Error in the Finite Element predictions for defects mapped with the 3-D surface scanner 302
Figure 5.1.1 Corrosion evaluation parameters 303
Figure 5.1.2 Actual and CPS corrosion profiles 303
Figure 5.1.3 The hyperbolic secant function 304
Figure 5.1.4 Integral of the hyperbolic secant function 305
Figure 5.1.5 Percent error in failure pressure prediction versus plain pipe extension length (expressed as a normalized length) -65% depth, 0.80" length single pit 306
Figure 5.1.6 Failure pressure as a function of % Depth Single pits, WT=0.195", Constant Corrosion factor = 0.938 307
Figure 5.1.7 Error in failure pressure prediction for the weighted depth difference method(Calculated using the CPS program) 308
Figure 5.1.8 Variation in % error and standard deviation for different values of the plain pipe failure pressure scale factor 309

Figure 5.1.9 Normal probability plot for the % error in the CPS predicted failure pressures 310
Figure 5.2.1 Defect reliability as a function of operating pressure 311
Figure 5.2.2 Probability of failure as a function of operating pressure for defect BCG02 312
Figure 5.2.2 Operating pressure as a function of probability of failure for defect BCG02 313
Figure 6.2.1 Three-level assessment procedure 314
Figure 6.5.1 Pipe section TCP02 – corrosion defects 315
Figure 6.5.2 Pipe section TCP02 – corrosion defects 315
Figure 6.5.3 Long Groove solution failure pressure as a function of defect depth - allowable defect depths for selected operating pressures (based on the SMYS) are indicated. 316
Figure 6.5.4 Pipe section TCP02 – defect TCP02-1A-1F 317
Figure 6.5.5 Pipe section TCP02 – defect TCP02-1G 317
Figure 6.5.6 Pipe section TCP02 – defects TCP02-1G and TCP02-1H 318
Figure 6.5.7 Pipe section TCP02 – failure at defect TCP02-1G 318
Figure 6.5.8 TCP02-1A-1F scanner image plot 319
Figure 6.5.9 TCP02-1G scanner image and surface plots 320
Figure 6.5.10 TCP02-1H scanner image and surface plots 321
Figure 6.5.11 Individual and combined defect profiles for defect TCP02-1A-1F .. 322
Figure 6.5.12 Defect profile for defect TCP02-1G 323
Figure 6.5.13 Defect profile for defect TCP02-1H 323

List of Symbols

α	Material coefficient for the Ramberg-Osgood relationship
α_{BG}, β_{BG}	Constants for the British Gas corrosion length factor
a	Long groove radial bulge displacement
A	Longitudinally projected area of a corrosion defect
A_0	Longitudinally projected area of the pipe wall
a_f, b_f	Constants in the Folias factor expression
b	Plain pipe radial displacement
B	Defect geometry factor used in CSA Z662 and B31G
c	Through-wall crack ½ length
C_1, C_2, C_3	Material constants for a critical strain definition
CVP	Charpy v-notch upper plateau energy
C_L	Material coefficient for Ludwick's equation
CF	Corrosion Factor from RSTRENG and B31G
CPS	Corroded pipe strength
ds	Infinitesimal circumferential dimension at ligament (Long Groove solution)
$d_{Evaluation}$	The corrosion depth at the evaluation point for the WDD model
$d\varepsilon_{ij}$	i, j component of plastic strain increment
d_{Max}	Maximum depth within a corrosion defect
D_o	Nominal pipe diameter
E	Young's modulus of elasticity
ε	Equivalent true strain
e	Engineering strain
ε_f	Material failure strain
ε_{UTS}	Strain corresponding to the material ultimate tensile strength
ε_{YS}	Strain corresponding to the material yield strength
ε_p	Plastic strain

ε_{Equiv}	Equivalent plastic strain
FP	Failure pressure
$FP_{Experimental}$	Database – Experimentally measured burst pressure
$FP_{Predicted}$	Database – Predicted burst pressure
F_L	Ligament hoop force
F_H	Plain pipe hoop force
F,L,J,T	Design, location, joint and temperature factors respectively
ϕ_{MA}	Non-dimensional circumferential corrosion extent (Shell membrane arch model
$G(\ell, r, t, d_{Max})$	B31G geometry factor
G	Modulus of rigidity
g	corrosion/pipe geometry function for the WDD model
$\gamma^{\bullet}$	Surface energy
H'	Slope of the equivalent plastic strain versus true equivalent stress curve
K_c	Fracture toughness
ℓ	Defect length
$L_{Evaluation}$	The location of the evaluation point for the WDD model
L	The longitudinal separation between the current location and the evaluation point for the WDD model
M	Original Folias factor
M_R	RSTRENG Folias factor
M_{B31G}	B31G Folias factor
M_T	Modified definition of the Folias factor
M_{BG}	British Gas corrosion length factor
M_{RL}	Ritchie and Last corrosion length factor
$MAWP_R$	Maximum allowable working pressure
MaxWDD	Maximum weighted depth difference sum for the defect with respect to the current evaluation point
n_{MA}	Material strain hardening coefficient (Shell membrane arch model)

n	Material coefficient for the Ramberg-Osgood relationship
n_L	Strain hardening exponent for Ludwick's equation
$N:(\mu,s^2)$	Normal distribution with a mean (μ) and variance (s)
ν	Poisson's ratio
$\hat{p}_{Ref}$	Reference failure pressure for the Shell membrane arch model
p_f	Corrosion defect failure pressure
$p_{f\,Calc}$	Calculated / predicted failure pressure corrosion defect failure pressure
$p_{f\,Actual}$	True corrosion defect failure pressure
p_0, $p_{Plain\ Pipe}$	Plain pipe failure pressure
$p_{Long\ Groove}$	Long groove failure pressure
$p_{Operating}$	Pipeline operating pressure
p_L	Hydrostatic stress
r	Current pipe radius
r_o	Original inside pipe radius
r_i	Inside pipe radius
R_f	Defect failure ratio
R_S	Defect remaining strength ratio
RSF	Residual strength factor
SMYS	Material specified minimum yield strength
SumWDD	Weighted depth difference sum for the defect with respect to the current evaluation point
S_{ij}	i, j component of deviatoric stress
σ_e	Equivalent stress
σ_{Mises}	von Mises equivalent stress
σ_{11}, σ_{Hoop}	Hoop / circumferential stress
σ_{22}, σ_{Long}	Longitudinal stress
σ_{33}, σ_{Rad}	Radial stress
σ^*	Critical stress in the Griffith criterion

$\overline{\sigma_e}$	Extensional stress
σ	Equivalent true von Mises stress
σ_{Flow}	Material flow stress
σ_{Shell}	Membrane stress in a shell
σ_{Plate}	Tensile stress in a plate
$\sigma_{Hoop\ at\ Failure}$	Hoop / circumferential stress at failure
$\sigma_{Fracture}$	Material fracture strength
σ_{UTS}	Material ultimate tensile strength
σ_{YS}	Material yield strength
t	Pipe wall thickness
t_o	Original pipe wall thickness
t_L	Current ligament thickness (Long Groove solution)
t_{Lo}	Original ligament thickness (Long Groove solution)
t_H	Plain pipe thickness (Long Groove solution, at the location of F_H)
U	Energy
w	Width
WDD	Weighted depth difference
Z	Normalized longitudinal separation between the current location and the evaluation point for the WDD model
z	The current location

Chapter 1
Introduction

Pipelines have the highest capacity, and are the safest and least environmentally disruptive form of transportation for oil and gas (Jones, 1995). Although the performance of pipelines has been exceptional, their increasing age has raised concerns among pipeline operators, particularly with respect to corrosion. Currently, the most significant cause of failure in gas and oil pipelines is external interference or third party damage. However, failures due to internal and external corrosion defects are approaching a similar rate of incidence worldwide (Hopkins, 1995).

Pipelines in Canada are regulated under the National Energy Board (NEB) and incidents are investigated by the Transportation Safety Board (TSB). An incident is defined as any failure or malfunction of the pipeline, a fire or explosion, a liquid spill, pipeline rupture, fatality or an injury requiring hospitalization (NEB, 1998). Pipeline operators are required to report any incident to the NEB for investigation. The rules and regulations for installing, operating, and maintaining a pipeline are specified by the Canadian Standards Association (CSA). The current version of the code, CSA-Z662-99 (CSA, 1999) was revised specifically to include an increased emphasis on pipeline maintenance and to address new issues and technology. However, the corrosion assessment

procedures have remained essentially unchanged since the development of the original assessment criterion proposed in the 1970's. This code is discussed briefly in section 1.2 and in detail in Chapter 2.

In Canada, 78 pipeline incidents were reported to the NEB in 1998 (NEB, 1999) with thirty-one resulting in product release and only one of these being a rupture. Only 3% of the reported incidents were due to corrosion defects with the highest rate (32%) related to operator error. Although the rate of corrosion failures appears to be small, the environmental and financial impact of a corrosion failure is generally higher than contained failures at compressor stations due to the significant release of product. In 1998, nine of the reported pipeline incidents were investigated by the TSB, compared to the five-year average of 24 investigations per year. Most of these investigations were related to the release of product resulting from corrosion or cracking damage (TSB, 1999). Amongst other causes, external corrosion problems experienced in Canadian pipelines can be attributed to a lack of corrosion protection, incorrect application of coatings to the pipe, or disbondment of the coating due to soil forces acting on the pipe (Dovico and Montero, 1996, Yen and Tofani, 1985, Davis and Thomas, 1985).

At present, many post-world war II pipelines containing corrosion damage are still in operation worldwide. The fact that these lines are still in operation suggests that many of the defects are not critical, although the actual factor of safety is unknown. In the past, operators could only ascertain the current state of their line by selectively excavating sections of the pipeline and inspecting for damage or investigating a section of the line after a failure occurred. However, with the advent of high-resolution inspection devices operators are now aware of the state of their entire line. It has been shown that regular inspection of lines with high-resolution tools and repair of significant defects is much more economical than not inspecting and bearing the cost of a future line failure (Grimes, 1996). However, a large portion of the savings are not realized as currently accepted methods of assessing corrosion defects are overly conservative and result in costly and unnecessary removal or repair of defects.

The goal of this work is to investigate the current defect assessment methods and provide a more accurate means of predicting the failure pressure of corrosion defects. The

unique aspect of this work is that it is based on experimental burst tests conducted on pipe sections with natural, complex corrosion defects removed from service. Prior to this, the available experimental data included detailed information on simple, machined defects and incomplete data on burst tests and failures of natural corrosion defects. The incomplete data is due, in part, to the currently accepted assessment procedures which require only limited information on the defect geometry and material properties. Although the simple machined defects have been accurately modeled using the Finite Element Method, and failure prediction equations have been developed from these analyses, the application to natural corrosion with a complex geometry has not been investigated. The experimental database developed at the University of Waterloo is used to study the accuracy of the current assessment procedures, provide guidance on their application to complex corrosion defects, and to validate a proposed new method of assessment.

It should be noted that, in terms of unit systems, the Canadian pipeline industry is still in a transition and primarily uses the English system of units. In addition, the experimental work is dominated by the United States which use the English system of units. The information presented in this thesis is meant to be used directly by the industry and is presented in the English system of units, with SI values quoted in brackets.

1.1 CAUSES OF CORROSION

Many pipelines in Canada have been in operation for nearly 5 decades and some of these lines were originally installed without protective coating. For example, the author is aware of one line operated for 20 years unprotected until it was excavated and coated in the 1970's to protect against further corrosion. It is expected that an unprotected, buried pipeline will experience external corrosion. However, the failure of corrosion protection systems can also lead to extensive corrosion in pipelines. The corrosion process occurs naturally on unprotected steel exposed to the environment. Buried pipelines are typically protected from external corrosion using coatings and cathodic protection. However, improper coating installation, coating failure due to mechanical damage or improper use of

cathodic protection can lead to significant external corrosion. Corrosion can also occur on the internal surface of the pipe from contaminants in the product. This type of corrosion is typically controlled using inhibitors (Papavinasam and Revie 1998) and can be assessed in the same manner as external corrosion (CSA 1999).

Polyethylene tape was introduced in the 1960's as a protective coating for pipelines. It was installed by spirally wrapping a continuous sheet of polyethylene around the pipe in the field. Unfortunately, this coating tends to disbond from the pipe during service due to soil stresses and/or improper installation. In many cases, the disbonded coating wrinkles and fills with water and the pipe is preferentially corroded in this area. The resulting defects tend to be relatively long and groove-like with a nearly uniform depth. In other instances, the spiral joint between adjacent wraps of the coating fails resulting in spirally oriented corrosion grooves in the pipe. Disbondment of the coating can also occur at the weld reinforcement over the longitudinal and/or girth welds which results in 'tenting' of the coating. As with wrinkling, tenting creates a gap between the coating and pipe surface which can fill with water and result in localized corrosion at or near the weld.

Asphalt-based coatings are also commonly used to protect pipelines from external corrosion. Although this coating has not had the problems of polyethylene tape, placement of the pipe in the trench while the coating is still soft, or in the presence of certain types of gravel can result in piercing of the coating. This generally creates small, deep corrosion pits where the coating is pierced while the rest of the pipe remains uncorroded. This coating may also be susceptible to disbondment leading to corrosion.

Today, plant applied coatings such as fusion bonded epoxy are more common and are of higher quality than previous coatings which were installed in the field. However, the girth welds must still be coated in the field after the pipe sections are welded together. Various forms of tape wrap and heat-shrink sleeves are used in these areas.

Cathodic protection utilizes an imposed electric current and sacrificial anode to impede corrosion in pipelines (Parker and Peattie, 1984). Although this is a proven method of protection, incorrect adjustment of the current to the pipe can allow corrosion to occur and may result coating disbondment (Payer et al. 1996).

1.2 CURRENT ASSESSMENT TECHNIQUES

The first and most well known research in the assessment of corrosion defects was conducted by Kiefner and Vieth and resulted in what is now known as the AMSE B31G (ASME 1991) criterion for the evaluation of part-wall defects. The corrosion assessment codes in Canada, the United States and Europe are based on this criterion (ASME 1991, CSA 1999). In the late 1980's, a major improvement to B31G was introduced by Kiefner. This method was iterative and evaluated the failure pressure of corrosion defects using a program known as RSTRENG (Kiefner and Vieth 1989). New definitions for a bulging factor and the material flow stress were introduced and a more detailed consideration of the shape of the corrosion was used to reduce the conservatism in the B31G criterion.

In 1991, researchers at the University of Waterloo (Mok et al. 1991) published one of the first applications of the Finite Element Method (FEM) to the analysis of corrosion defects in line pipe. This work was continued at the University of Waterloo (Chouchaoui 1993) with experimental burst tests on pipe with single pits and groups of interacting single pits. Natural corrosion defects of simple geometry were also considered. Finite element analysis (FEA) was successfully applied to these three-dimensional defects and various failure criteria were evaluated. Defect interaction rules were also proposed based on the experimental results. More detailed Finite Element results of simply shaped defect behavior and failure criteria were published by British Gas (Fu and Kirkwood 1995). To date, extensive numerical analysis of these defects has been carried out at British Gas with the goal of using the results to develop a less conservative method of assessment. Many other researchers (Stephens 1997, Klever 1995, Popelar 1993) have proposed new methods of assessment based on analytical analysis of simple two-dimensional defects, or the numerical analysis of simple, three-dimensional defects.

At present, both the original B31G and RSTRENG criteria are used by pipeline operators for defect assessment. Unfortunately, the factors of safety associated with these criteria are not well understood due to the lack of appropriate experimental data. Further, their application to complex defects is not well defined. The Finite Element Method has also been proposed as a less conservative method of assessment (Chouchaoui 1993, Fu and

Kirkwood 1995) yet it has only been validated for simple corrosion geometries. Further, the cost and expertise necessary to conduct such analyses prohibit their general use. As a result, a less conservative method of assessment which is not as expensive or difficult to apply as three-dimensional elastic plastic finite element analysis is required.

1.3 THESIS OUTLINE

An accurate assessment procedure to predict the failure pressure of corroded pipelines is required. This will allow operators to identify critical defects for repair or removal while reducing the costly removal of defects which are still fit for service. For this purpose, the failure of corrosion defects has been investigated using the Finite Element Method, analytical analysis and an experimental database developed by the author. The goals of this work have been:

- To provide guidance on the application of the currently accepted assessment procedures and determine the accuracy of these procedures.
- To propose a new method of failure pressure assessment based on numerical and analytical analyses of corrosion defects, and validate it with the experimental database.

In this thesis, Chapter 2 discusses the current state of corrosion assessment and the available experimental and numerical data used to develop and evaluate these techniques.

The deformation and failure behaviour of plain pipe is examined in detail in Chapter 3 since this is often used as an upper limit in evaluation procedures, or to define the factor of safety relative to the burst pressure of plain pipe. A long, longitudinally oriented groove of uniform depth is then considered since this can generally be used as a lower bound for the failure pressure of complex corrosion defects. Complex defects have a finite length and variable depth. Both the analytical and finite element results for these two cases are compared to experimental work. The simplest three-dimensional defect, a single

pit, is then analyzed using the Finite Element Method. These analyses are not used to develop an assessment method, since the number of variables is large, but are used to investigate specific aspects and assumptions in the current code. This includes the flow stress assumption, stress concentration (Folias) factor and defect geometry representation.

Chapter 4 presents a detailed investigation into the behaviour of complex, natural corrosion defects. The experimental database developed by the author is presented and the application of assessment procedures to complex defects is discussed. Guidance on the application of RSTRENG to complex corrosion defects is also presented. The use of three-dimensional elastic-plastic finite element analysis to predict the failure pressure of complex corrosion defects is investigated using examples from the experimental database. Lastly, a new evaluation procedure, which utilizes the actual material properties and corrosion geometry, is developed and compared to the experimental database. This is known as the weighted depth difference model and is implemented using a computer program called Corroded Pipe Strength (CPS).

A three-level evaluation procedure is proposed in Chapter 5 based on the solution for a long, longitudinally oriented, uniform depth groove, the CPS program and elastic-plastic finite element analysis. In particular, methods of corrosion measurement and the necessary material properties for corrosion evaluation are discussed.

Conclusions regarding the assessment of corrosion defects are presented in Chapter 6 along with recommendations for future work.

Chapter 2
Literature Review

2.1 B31G / CSA Z662 / RSTRENG

To date, the most significant body of work related to the assessment of corrosion defects are the pipeline safety codes and the many years of research associated with the development of these codes. The original work in this area was conducted at Battelle Memorial Institute in Columbus, Ohio and the result was a section of the American code known as B31G (ASME 1991). For simplicity, B31G will be referenced as the original source of this procedure as described in the ASME B31G-1991 code. The Canadian code (CSA Z662-99 1999) and many other codes around the world use the same assessment procedure as defined in B31G.

The B31G criterion is based on the assumption that the circumferential or hoop stress which is the maximum principal stress in defect free pipe, controls the failure. The failure pressure of a corrosion defect is related to the material flow stress through a bulging

factor (M), known as the Folias factor, and the amount of material lost due to corrosion (equation 2.1.1).

$$p_f = \left(\frac{t}{r}\right)\sigma_{Flow}\left[\frac{1-\frac{2}{3}\left(\frac{d_{Max}}{t}\right)}{1-\frac{2}{3}\left(\frac{d_{Max}}{t}\right)M^{-1}}\right]$$

$$\text{where } M = \sqrt{\left[1+\frac{0.8\,\ell^2}{2rt}\right]} \qquad (2.1.1)$$

$$\text{and } \sigma_{Flow} = 1.1(SMYS)$$

Equation (2.1.1) can also be written as:

$$\sigma_{Hoop\,at\,failure} = \sigma_{Flow}\left[\frac{1-\frac{2}{3}\left(\frac{d_{Max}}{t}\right)}{1-\frac{2}{3}\left(\frac{d_{Max}}{t}\right)M^{-1}}\right] \qquad (2.1.2)$$

If we assume that the maximum stress level ($\sigma_{Hoop\ at\ failure}$) is limited to 100% of the specified minimum yield stress equation (2.1.2) can be rearranged in terms of the defect length so that:

$$\ell = 1.12\left[\sqrt{\left(\frac{\frac{d_{Max}}{t}}{1.1\frac{d_{Max}}{t}-0.15}\right)^2}-1\right]\sqrt{2rt}$$

$$or \qquad (2.1.3)$$

$$\ell \le 1.12B\sqrt{2rt}$$

Equation (2.1.3) describes the allowable defect length for a given pipe diameter, thickness and maximum defect depth so that the maximum stress does not exceed the specified

minimum yield stress. This is the form of B31G used in many codes including the Canadian CSA Z662 code. The value of B is generally available from a graph with a limit that B cannot be greater than 4.0. This maximum value results in a discontinuity in the failure pressure as a function of defect length and is related to the assumption that a defect has a finite length or behaves as an infinite length defect (B>4.0). Corrosion defects with a d/t > 0.8 are not permitted and when d/t <0.125 the length of the defect is not limited.

Rewriting equation (2.1.1) in the more familiar form for the hoop stress in a thin-walled pressure vessel, the stress at failure (σ_{Flow}) is equal to the hoop stress modified by the geometry of the defect.

$$\sigma_{Flow} = \frac{p_f r}{t} G(\ell, r, t, d_{Max})$$

where

$$\sigma_{Flow} = 1.1(SMYS)$$

$$G(\ell, r, t, d_{Max}) = \left[\frac{1 - \frac{2}{3}\left(\frac{d_{Max}}{t}\right)}{1 - \frac{2}{3}\left(\frac{d_{Max}}{t}\right) M^{-1}} \right]^{-1} \qquad (2.1.4)$$

recall that

$$\sigma_{Hoop} = \frac{pr}{t}$$

This assumes the material is elastic perfectly plastic with a flow stress 10% higher than the specified minimum yield strength. The most important component of this equation is the geometry factor which includes the Folias or bulging factor.

In terms of the geometry of the defect it is assumed that the increase in stress is inversely proportional to the remaining cross sectional area of the material within the defect. Given d_{Max} and ℓ, B31G assumes that the cross section of a complex shaped corrosion defect can be approximated by a parabola (Figure 2.1.1) (Kiefner 1973, 1990a, 1990b). In this case the area of the defect is expressed as $\frac{2}{3} d_{Max} \ell$ so that the remaining area

is $t\ell - \frac{2}{3} d_{Max} \ell$ or $\ell t(1 - \frac{2}{3}\frac{d_{Max}}{t})$ which appears in the geometry term of equation (2.1.4).

All corroded areas are considered to be projected onto a longitudinal plane. The geometry term consists of the remaining cross sectional area modified by the factor M^{-1} in the denominator. This factor is known as the Folias or bulging factor and was originally developed as a scale factor for the elastic stress concentration of a through-wall crack in a cylindrical shell with respect to a flat plate.

As shown in equation (2.1.1), the Folias factor is a function of the defect length and the pipe geometry. As the defect length increases the Folias factor increases and becomes very large for large defects. In terms of equation (2.1.1) this implies that the inverted Folias factor tends to zero and the equation simplifies to equation (2.1.5) which essentially describes a section of defect free pipe with a reduced wall thickness. This limit is reasonable and the linear dependency of long defects on the defect depth has been shown experimentally (Mok et al. 1991).

$$p_f = \left(\frac{t}{r}\right) 1.1(SMYS)\left[\ell - \left(\frac{d_{Max}}{t}\right)\right] \text{ when } \ell \to \infty \qquad (2.1.5)$$

As the length of the defect tends to zero, the Folias factor tends to 1.0 so that, as expected, the failure pressure is that of plain pipe as shown in equation (2.1.6).

$$p_f = \left(\frac{t}{r}\right) 1.1(SMYS) \text{ when } \ell \to 0 \qquad (2.1.6)$$

These equations assume that the failure is stress based and that it occurs at a stress level equal to the flow stress. This aspect will be discussed further when the failure of plain pipe is considered.

The last two equations indicate that the Folias factor, at least at the limits, provides reasonable results. However, it is important to realize that any factor which varies from 1 to ∞ for defect lengths from 0 to ∞ respectively will provide the same results.

Although pipeline operators realize that the B31G approach is conservative (Stephens et al. 1997b), it is widely accepted because it has been successfully used for many years. In addition it is easily applied, particularly in the field, since B31G requires only the maximum depth and length to characterize a corrosion defect. With the advent of high resolution inspection tools and other techniques, accurate measurement of corrosion geometries for many kilometers of line are readily available. Unfortunately B31G does not take advantage of the accuracy of this information since it approximates the corrosion geometry and may conservatively suggest repair or removal of pipe which is still fit for service.

To reduce the conservatism, B31G was modified to what is known as the '0.85dl B31G' criterion. Specifically the parabolic area approximation was changed from $2/3 d_{Max} \ell$ to $0.85\ d_{Max} \ell$.

Subsequently, a major improvement to B31G was introduced and has become known as the modified B31G criterion. This method is applied through the use of a computer program known as RSTRENG. This improvement involved identifying and revising three sources of conservatism in B31G: calculation of the projected area, the Folias factor and the flow stress.

Calculation of Projected Area

Both B31G and RSTRENG assume that the circumferential stress controls failure. Therefore, the corrosion geometry is projected onto a longitudinal axis of the pipe (perpendicular to the maximum principal stress) and the stress concentration is assumed proportional to the cross sectional area of the remaining material. In B31G, the corrosion geometry is assumed parabolic in shape with dimensions given by the length and maximum depth of the defect. This representation is overly conservative when only a small portion of the corrosion is at the maximum depth and the defect size is overestimated. Alternatively, the defect size could be underestimated if the defect is flat bottomed so that the profile approaches a rectangular shape.

RSTRENG utilizes a more accurate measure of the corrosion geometry by projecting a river bottom path through the corrosion onto the longitudinal axis as shown in

Figure 2.1.2. The area is calculated using a trapezoidal rule integration with the accuracy of the area calculation depending on the number of points used to represent the defect profile. Figure 2.1.1 shows a comparison between the RSTRENG and B31G representations of the projected area.

Folias Factor

As mentioned above, the Folias or bulging factor is used to account for the stress concentration related to the longitudinal dimension of the corrosion defect. This factor was originally developed to relate the elastic stress concentration of a through-wall flaw in a spherical shell to the stress concentration of a through-wall flaw in a flat plate (Folias, 1965a). It was assumed that the flaw was in a shell of isotropic homogeneous material, loaded in tension. Subsequently Folias (1965b, 1969) extended the elastic analysis to a cylindrical shell with a through-wall flaw. These analyses consider the stretching and bending of thin shallow shells of constant thickness which are subject to small deformations and strains. The equilibrium and compatibility conditions can be described by a set of coupled differential equations which Folias solved to determine the change in stress concentration due to the curvature of the shell. The solution includes both bending and extensional stresses which result from the applied stress. It can also accommodate applied bending stress but this quantity is assumed to be zero in the case of defects in pipe.

The solution generally takes the form shown in equation (2.1.7) in which $O\frac{1}{r^2}$ represents higher order terms in the series solution which are neglected. The half-length of the flaw is represented by the variable c.

$$\frac{\sigma_{Shell}}{\sigma_{Plate}} \approx 1 + \left(a_f + b_f \ln\left(\frac{c}{\sqrt{rt}}\right)\right)\left(\frac{c^2}{rt}\right) + O\left(\frac{1}{r^2}\right) \qquad (2.1.7)$$

A fracture criterion based on the Griffith stress (2.1.8a) was combined with equation (2.1.7) and, after a great deal of manipulation, resulted in equation (2.1.8b).

$$\frac{\partial(U)}{\partial c} = 0$$

where (2.1.8a)

$$U = \text{System Energy} = U_{Loading} + U_{Strain} + U_{Surface}$$

$$(1 + 0.49\lambda^2)\left(\frac{\bar{\sigma}_e}{\sigma^*}\right)^2 + O(\lambda^4 \ln \lambda) = 1$$

where

$$\sigma^* = \left(\frac{16G\gamma^*}{\pi c}\right)^{1/2} \qquad (2.1.8b)$$

$$\lambda = \sqrt[4]{\frac{12(1-\nu^2)c^4}{r^2t^2}}$$

This excludes applied bending stresses and neglects the higher order terms of λ which leads to the more common form of the Folias factor. It should be noted that embedded in this solution are limits on the value of λ. The limit on the original solution was $\lambda<1.0$ implying that the defect dimension had to be small relative to the pipe geometry. Numerical techniques were later applied to the equations resulting in solution coefficients which were valid for $\lambda<8.0$ (Erdogan, 1969). For a poisson's ratio of 0.3, and $c = \ell/2$, this equation reduces to:

$$\left(\frac{\sigma^*}{\bar{\sigma}_e}\right) = \sqrt{1 + 0.49\lambda^2}$$

$$= \sqrt{1 + 0.8\frac{\ell^2}{2rt}} \qquad (2.1.8c)$$

$$= M$$

which is the two term approximation used in the original B31G equation (2.1.1). Equation (2.1.8c) can be interpreted as the ratio between the failure stress and the applied extensional (hoop) stress due to the geometry of the pipe and size of the defect. As the pipe radius tends towards infinity, M_T tends to 1.0. The Griffith failure stress is approximated by the material flow stress.

The Folias factor was originally used in equation (2.1.9) to describe the failure of through-wall defects in pipes (Eiber et al. 1971).

$$\frac{K_c^2 \pi}{8c\sigma_{Flow}^2} = \ln \sec \frac{\pi}{2} \frac{M_T \sigma_{hoop}}{\sigma_{Flow}}$$

where (2.1.9)

$$M_T = \sqrt{1 + 1.255\frac{c^2}{rt} - 0.0135\frac{c^4}{(rt)^2}}$$

This equation used both fracture mechanics and a Dugdale flow stress criterion to predict failure and was compared to full-scale tests by Eiber et al. It was found that when typical values for pipeline materials and defects were considered, the left side of equation (2.1.9) reached a constant value (≈4.0) and the material became flow stress dependant so that the failure of through-wall defects could be described by equation (2.1.10).

$$M_T \sigma_{hoop} = \sigma_{Flow} \qquad (2.1.10)$$

An equation for a surface flaw, first suggested by Kiefner (1969), is given in equation (2.1.11). It was assumed that the behavior of a surface flaw could be described by equation (2.1.10) with an equivalent surface flaw length used in place of the length of the through-wall flaw (Kiefner, 1973). The equivalent surface flaw half-length is defined as $2c_{eq} = A / d_{Max}$ where A is the projected area of the defect and d_{Max} is the flaw depth.

$$\sigma = \sigma_{Flow}\left[\frac{1-\frac{d_{Max}}{t}}{1-\frac{d_{Max}}{M_T t}}\right] \qquad (2.1.11)$$

B31G uses the first two terms in a series approximation for the Folias factor as shown in equation (2.1.8c). RSTRENG considers the first 3 terms of the series to provide a more accurate, less conservative approximation to the series solution but is also inaccurate for values of $\ell^2/(2rt)$ greater than 50. Therefore RSTRENG assumes a second linear relation to model the region where $\ell^2/(2rt)$ >50 as shown in equation (2.1.12). Note that the three-term form used in RSTRENG is the same as that shown in equation (2.1.9) with the equivalent crack length for a surface flaw used in place of the through-wall crack half-length.

Flow Stress

B31G and RSTRENG use the same relation between the failure pressure and the material flow stress and corrosion dimensions. To define the flow stress, B31G uses 1.1 times the specified minimum yield stress (SMYS) while RSTRENG uses the SMYS + 10000 psi (69 MPa) as a better approximation (Maxey, 1971, Kiefner 1973).

The purpose of the flow stress is to represent ductile material behaviour and predict failure loads when a material exhibits a significant degree of plastic deformation. This approach is common and is most appropriate in cases where the entire section undergoes collapse at the same instant. An example of this is a beam subject to bending which fails when the stress through the thickness exceeds the flow stress (a fully plastic moment is reached). The analogous situation is a pressurized pipe with an infinitely long, longitudinally oriented, uniform depth groove. Theoretically, failure occurs by the simultaneous collapse of the defect along its entire length when the critical stress is reached. In contrast, real defects, which can be of finite length and typically vary in depth, will experience this critical stress state at only one point along their length. The material surrounding this critical location is at a lower stress depending on the stress-strain relationship for the material and the wall thickness of the adjacent material. The effect of

this adjacent material is to constrain the defect leading to an increased burst pressure. This constraint explains the significant dependence of the failure pressure on the defect length which has been recognized in many studies (Chouchaoui and Pick, 1993, Batte et al. 1997, Stephens and Leis 1997c). The defect length is included in B31G and RSTRENG through the projected area of the defect and the Folias factor. However the location of the initial failure point is not defined and it can only be said that it falls somewhere between the ends of the corrosion defect.

Projected Area

The equation for predicting failure pressure used in RSTRENG (2.1.12) has a form similar to B31G (equation 2.1.1).

$$p_f = \left(\frac{t}{r}\right)(SMYS + 10000)\left[\frac{1-\left(\frac{A}{A_0}\right)}{1-\left(\frac{A_0}{A}\right)M_R^{-1}}\right]$$

$$M_R = \sqrt{\left[1 + 0.6275\frac{\ell^2}{2rt} - 0.003375\frac{\ell^4}{4r^2t^2}\right]} \quad \text{for} \quad \frac{\ell^2}{2rt} \le 50 \qquad (2.1.12)$$

$$M_R = \left(0.032\frac{\ell^2}{2rt} + 3.3\right) \quad \text{for} \quad \frac{\ell^2}{2rt} > 50$$

However, RSTRENG has a more accurate definition of the defect area. As shown in Figure 2.1.1 the defect is characterized in RSTRENG by a number of evenly spaced depth measurements along the length of the defect in contrast to the parabolic profile assumed in B31G. As mentioned earlier, the area of the defect (A) is calculated by summing the area of the series of trapezoids defining the corrosion geometry. An interesting result is that a lower failure pressure may be predicted if only a portion of the defect is considered. This is because a larger ratio of A/A_0 can result when considering a shorter section of the corrosion where the average corrosion depth is higher than for the whole defect. This led

to the development of an iterative method which considers all combinations of the defect measurements to find the lowest predicted burst pressure. This is known as the effective area technique. Due to the iterative nature of the calculations, the effective area technique is commonly applied using the computer program known as RSTRENG.

Application of B31G and RSTRENG to a database of burst tests of corroded pipe developed by Kiefner and Vieth (1994) has shown that RSTRENG is less conservative. B31G produces an average ratio of predicted to actual burst pressure of 1.37 with a standard deviation of 0.33 while the RSTRENG predictions have an average of 1.15 with a standard deviation of 0.18 (Bubenik et al. 1992).

2.2 FINITE ELEMENT METHOD

While showing promise, the Finite Element Method (FEM) is not commonly used to assess defects due to its cost, complexity and the lack of validation for more complex forms of natural corrosion. Accurate application of the FEM involves the use of a large number of 3-dimensional solid elements to correctly model the corrosion geometry, and the use of large displacement, elastic-plastic analysis to model the material response. Currently, the FEM is primarily used as a research tool to assess specific corrosion geometries since it provides detailed insight into the behavior of the defect.

One of the first uses of the FEM was for the analysis of longitudinally and spirally oriented grooves in line pipe (Mok et al., 1991) using simplified 2-D and 3-D models. With the use of actual material properties and groove geometry, the FEM predictions were found to be within 5% of experimental burst pressures. The material was modeled with incremental plasticity (Prandtl-Reuss) from tensile test data. Failure was predicted when the strains in the corrosion ligament began increasing in an asymptotic manner.

Chouchaoui et al. (1992) conducted a number of 3-D, elastic-plastic finite element analyses on single corrosion pits and more complex interacting groups electro-chemically machined flat-bottomed pits. Some natural corrosion defects of simple geometry were also analyzed. Isoparametric parabolic hybrid elements with reduced integration and large

deformation theory were used in the finite element model. It was found that the FEM predictions were within -6% to 7% of the actual burst pressure. The accuracy of the solution was dependent on the coarseness of the finite element mesh used. While coarser meshes were shown to be convergent, they tended to be inaccurate in representing the corrosion geometry and resulted in a conservative estimate of the burst pressure. The material was modeled using incremental plasticity and failure was predicted when the stress exceeded the ultimate tensile strength of the material through the full thickness of the corrosion ligament.

British Gas has undertaken a project which, in part, consists of the analysis of complex shaped corrosion defects using the FEM. Published data to date involves the analysis of single corrosion pits, longitudinally oriented grooves and larger flat-bottomed machined defects. The British Gas FEM model considered a much larger section of the pipe than Mok et al. and Chouchaoui (Fu and Kirkwood 1995) however the reported accuracy was not any greater. British Gas used the same failure criterion as Chouchaoui.

Stephens (1997) at Battelle Memorial Institute developed a dedicated finite element code based on shell elements for the analysis of corrosion defects. The use of shell elements assumes that the corrosion defect can be represented as an equivalent amount of material loss on the external and internal surfaces of the pipe as shown in Figure 2.2.1. The corrosion defect is assumed to be of uniform depth over each element, with discontinuous changes in depth between elements. This method is limited to blunt defects which have no stress concentrations within the defect. The failure criterion is based on the tensile properties as well as the Charpy upper plateau energy and is discussed in more detail below.

Researchers at Shell (Klever et al., 1995) have also investigated the use of shell elements in modelling the failure of corrosion defects. In their analysis it was assumed that membrane stresses dominated the behaviour of the defect so that a shell model could be used. These results have not been validated against experimental data.

2.2.1 Failure Criteria

Corrosion defects are relatively smooth and pipe materials are generally tough, therefore the failure of a corrosion defect is usually by plastic collapse of the defect ligament as opposed to low ductility fracture. FEM analysis of pipe with corrosion defects does not in itself predict the failure pressure of the pipe since the finite element models used to date do not predict local instabilities, such as necking, which usually leads to ultimate failure.

Two criteria have been proposed and are commonly used to assess the plastic collapse of a corrosion defect using the Finite Element Method. The first is a strain-based criterion which was proposed by Mok et al. (1991). This criterion predicts plastic collapse to occur when the gradient of plastic strain through the entire ligament becomes constant and the plastic strain increases asymptotically. It has been found that this occurs at the deepest point in the corrosion defect for simple corrosion geometries. Failure initiates on the outside surface of the pipe when the corrosion defect is located on the outside of the pipe (Chouchaoui 1993, Mok et al. 1991, Fu and Kirkwood 1995).

The second criterion for predicting plastic collapse and necking is actually a two-criterion approach which is stress-based or instability-based. Chouchaoui (1993) considered a critical strain-based approach and several critical stress-based approaches when comparing FEM results to experimentally determined burst pressures. These approaches involve the determination of a critical stress or strain value from the stress-strain curve of the material. Of the stress-based approaches, the use of the equivalent Tresca stress produced the most accurate result compared to experiments while use of the von Mises stress produced only slightly less accurate results. Plastic collapse was predicted to occur when the equivalent stress exceeded the critical stress through the entire thickness of the ligament. The critical stress is defined as the ultimate tensile strength from an engineering stress-strain curve expressed as a true stress. A similar approach was taken for the critical strain criterion which used the strain at necking. Chouchaoui found that a great deal of scatter existed for the strain-based approach. An investigation by British Gas concluded that the strain-based approach typically overestimates the failure pressure. A

critical stress state based on the true von Mises stress at the point of necking increased the accuracy of the results (Fu and Kirkwood 1995b).

Stephens et al. (1997) have suggested a third criterion based on the stress-strain and fracture behaviour of the material. They suggest that the material fails when the stress reaches the fracture stress as defined by equation 2.2.1 where C_1, C_2 and C_3 are constants.

$$\varepsilon_f = \frac{C_1(CVP)^{C_2}}{\sigma_{UTS}};\ \varepsilon_{UTS} = C_3\varepsilon_f$$
$$\sigma_{Fracture} = \sigma_{YS}\left(\frac{\sigma_{UTS}}{\sigma_{YS}}\right)^{\frac{\log(\varepsilon_f/\varepsilon_{YS})}{\log(\varepsilon_{UTS}/\varepsilon_{YS})}} \qquad (2.2.1)$$

It has been suggested by Leis (1997) that such a failure criterion is necessary if stable tearing in the ligament leads to the development of a flaw. In low toughness materials such a flaw could lead to brittle fracture prior to plastic collapse.

Valenta et al. (1995, 1996) have suggested a failure criterion based on accumulated plastic strain and the size of the plastic zone in the defect. The limit strain is defined as occurring between the yield and fracture points in a uniaxial stress-strain curve although a specific definition was not presented. Sims and DePadova (1996) also used a critical strain failure criterion in a parametric numerical analysis of locally thinned areas or corrosion defects. The limiting strain was defined as 2% equivalent plastic strain however these results were not verified with experimental testing.

2.2.2 Material Model

To accurately predict the behavior of a corrosion defect, the material behavior, in particular the plastic behaviour must be modeled appropriately. The Finite Element Method allows the material behavior to be modeled with a uniaxial true stress-strain curve. The use of true stress versus strain data allows an incremental plasticity scheme to be used which can account for strain hardening and subsequent unloading (Mendelson 1983), but

requires a significant increase in computing resources (Chouchaoui 1993). If the stresses increase monotonically and significant unloading does not occur, the stress-strain behavior of typical pipeline materials can be modeled with deformation plasticity theory using the Ramberg-Osgood equation to represent to true stress-strain curve (Equation 2.2.2).

$$\varepsilon = \frac{\sigma}{E} + \alpha \left(\frac{\sigma}{\sigma_{YS}} \right)^{n-1} \frac{\sigma}{E} \tag{2.2.2}$$

Although stress is uniquely related to strain when both increase monotonically in simple situations such as uniaxial loading, this relationship is not always valid in the more general three-dimensional case. A proportional increase in the deviatoric stress components with respect to the effective stress is also required for this material model to be equivalent to incremental plasticity (Anderson 1991, Mendelson 1983). Chouchaoui (1993) has shown that the deformation plasticity model is valid for simple defect shapes through experimental validation of the finite element results.

Pipeline steels typically display anisotropic yield behaviour as a result of the rolling process used to create the steel plate from which the pipe is manufactured. For the analysis of corroded pipe, Chouchaoui recommended using the material properties in the circumferential direction since this is the direction of maximum principal stress in plain pipe. It should be noted that at the location of failure, Chouchaoui found the stresses to be triaxial in nature and so the use of the circumferential properties may be questioned. However, the UTS of the material and hardening behavior are similar in both the longitudinal and circumferential directions and since a large degree of plasticity occurs within a corrosion defect near failure, the use of the circumferential properties is reasonable.

2.3 ALTERNATIVE MODELS TO PREDICT THE FAILURE OF CORROSION DEFECTS

The complexity and cost of applying the FEM, and the empirical nature of B31G and RSTRENG have prompted a number of researchers to investigate other prediction techniques. Many techniques involve modifications to the RSTRENG code to better fit the experimental and numerical data. Other methods are based on shell analyses of simplified corrosion geometries which model the corrosion defect as a two-dimensional problem. Purely elastic analysis is a further simplification.

2.3.1 PCORR

Stephens (1997c) has developed a dedicated finite element code which uses shell elements to model corrosion defects. This simplification allows a complex defect to be modeled with fewer elements than a full three-dimensional analysis but is only a good approximation in specific cases. Application of this method to large, flat-bottomed defects has produced reasonable results. This will not be the case for small, deep defects in which there are through-thickness stress variations and plasticity in the corrosion ligament. These phenomena are not adequately modeled using shell elements.

Stephens presented one case of an irregular shaped defect in 30-inch diameter pipe which failed at a pressure of 1775 psi (12.24 MPa). The PCORR program predicted a failure pressure of 1734 psi (11.96 MPa) using detailed corrosion geometry. This corrosion defect was 39% of the wall thickness deep with a length of 5" and width of 4". It is expected that shell elements should perform well in these cases since the defect is relatively shallow and long. Stephens has also used this method to study the effect of defect dimensions and material properties on the failure pressure of rectangular and elliptical shaped, flat-bottomed corrosion defects. These results (Stephens and Leis 1997c) were then used to develop a model (equation 2.2.3) for predicting the failure pressure of blunt

corrosion defects. This model, known as PCORRC, is a curve fit to the numerical data and uses a flow stress based failure criterion.

$$p_f = \sigma_{UTS}\frac{t}{r}\left(1-\frac{d_{Max}}{t}\left(1-\exp\left(-0.157\frac{\ell}{\sqrt{r(t-d_{Max})}}\right)\right)\right) \qquad (2.2.3)$$

When applied to the database used to develop and validate B31G and RSTRENG, PCORRC predicted failure pressures with an average failure ratio of 0.97 and standard deviation of 0.105. This is more accurate than the RSTRENG predictions to be discussed in section 2.6.

2.3.2 British Gas Proposed Corrosion Defect Assessment Guidance

Researchers at British Gas PLC (Batte et al. 1997) have undertaken a number of finite element analyses and experimental burst tests on machined defects in several grades and diameters of line pipe. An assessment method has been proposed which is based on the B31G criterion but includes modifications to the Folias factor and replacement of the flow stress with the failure pressure of plain pipe. This is shown in equation 2.2.4.

$$\frac{p_f}{p_o} = \frac{(1-\frac{d_{Max}}{t})}{(1-\frac{d_{Max}}{t}\frac{1}{M_{BG}})}$$

and (2.2.4)

$$M_{BG} = 1+\alpha_{BG}(\frac{\ell}{\sqrt{Dt}})^{\beta_{BG}}$$

The values of the constants α_{BG} and β_{BG} depend on the material properties. This method accounts for the projected area loss through the defect depth, length and the constants α_{BG} and β_{BG}. It is noted that this method does not have a discontinuity in

predicted failure pressure as a function of defect depth as seen in B31G as discussed in Section 2.1. Comparison of published experiments with the predicted burst pressures from equation (2.2.4) and those of B31G indicates slightly more scatter in the B31G predictions with higher conservatism at higher predicted failure pressures. This method does not appear to be an improvement over RSTRENG and it does not address the interaction of defects such as colonies of pits or the effects of complex geometry.

2.3.3 Modified B31G Model

Ritchie and Last (as described in Stephens et al. 1997b) have proposed a model with a form similar to that of B31G but using a flow stress equal to 90% of the ultimate tensile strength of the material. The model is expressed in equation (2.2.5).

$$p_f = 0.9\sigma_{UTS}\frac{t}{r}\left[\frac{1-\frac{d_{Max}}{t}}{1-\left(\frac{d_{Max}}{t}\right)M_{RL}^{-1}}\right]$$

where (2.2.5)

$$M_{RL} = \sqrt{1+0.8\frac{\ell^2}{2rt}}$$

This model assumes the defect is rectangular in shape as opposed to B31G (equation 2.1.1) which assumes a parabolic shape for the metal loss. This assumption will result in more conservative predictions, but the increase in flow stress will reduce the conservatism. The Ritchie and Last model does not address the defect shape in detail and will not produce results more accurate than the B31G analysis currently in use.

2.3.4 Analytical Shell Analysis

The Membrane Arch Model

Researchers at Shell (Klever et al. 1995) have proposed an analytical model based on a membrane arch concept. This involves modeling the corrosion as a cylindrical membrane within a section of pipe which is pinned at its edges so that it can rotate to accommodate deformation as shown in Figure 2.3.1a. The assumption embodied in this model is that the uncorroded area of the pipe remains elastic and the associated elastic deformations are negligible compared to the local deformation of the defect. This assumption produces the boundary conditions for the membrane arch model. Within the membrane arch a two-zone model was introduced (Figure 2.3.1b) to represent a smaller defect within a larger defect. Although this is a two-dimensional model, it is stated that treating a finite length defect as a plane strain membrane which is restrained at the boundary provides a conservative estimate of the burst pressure. This is due to the exclusion of the resistance of axial bulging to the deformation of the defect.

Equations were developed to describe a long corrosion patch with a constant depth and varying circumferential dimension. For a constant depth defect and material properties represented by a power hardening law, the model predicts a variation in the maximum pressure with the circumferential dimension according to equation 2.2.6.

$$p_f = \left(\frac{2}{1+\phi_{MA}}\right)^{n_{MA}} \hat{p}_{ref} \qquad (2.2.6)$$

The circumferential extent of the corrosion will cause $\left(\frac{2}{1+\phi_{MA}}\right)$ to vary between 2.0 and 1.0 as ϕ_{MA} varies between 0.0 and 1.0. For an example, if n_{MA}=0.15 and $\hat{p}_{ref}$ = 10 MPa, then the limit load failure pressure could vary between 11.1 MPa and 10.0 MPa depending on the circumferential extent of the corrosion. However, it has been shown experimentally that the circumferential dimension of the corrosion is not significant (Mok et al. 1991, Batte et al. 1997, Chouchaoui and Pick 1994). Two-dimensional plane strain

finite element analysis results indicate only a minor dependence of the failure pressure on the circumferential dimension when this dimension is less than 3 wall thicknesses (Fu et al. 1995).

The membrane arch model is useful in understanding the deformation processes associated with larger rectangular defects however the applicability to natural corrosion defects is questionable.

Plain Strain Analysis Model

Elastic shell theory was used by Popelar (1993) to assess the failure of long, longitudinally oriented grooves. The effect of the groove is considered as a stress concentration and limit load analysis is applied to determine the plastic collapse pressure.

One interesting feature of this model is that it can consider the corrosion as occurring on the inside or outside surface and not as a defect which is symmetric about the midwall of the pipe, a common assumption in shell analyses. It was found that the stress concentration factor for the same defect located on either the internal or external surface was similar. This is in agreement with analyses conducted at the University of Waterloo on single pit defects (Chouchaoui 1993) and is due to similar amounts of bending stress induced in the defect in both cases.

Popelar determined the failure pressure through the application of limit load analysis. The upper bound solution, in which a kinematically admissible deformation field is found, produces a similar result to the lower bound solution in which a statically admissible stress field, which does not violate the yield condition, is applied. In agreement with Mok et al. (1991), Popelar shows that the failure pressure of a long, longitudinally oriented groove of constant depth is a linear function of the groove depth. However, his failure pressure prediction was a complex function of the circumferential dimension. Plots of the stress concentration factors indicate they only tend to become independent of the circumferential dimension when the circumferential angle exceeds 25°.

Analysis of multiple, equally spaced grooves results in a stress concentration factor similar to that of a single groove. This is in agreement with Chouchaoui's (1993) results.

Although this model does not represent corrosion defects of finite length, the failure predictions are in agreement with published data for long defects.

2.3.5 Fracture Mechanics Approach

It has been argued that since the original B31G criterion is based on fracture mechanics and the failure predictions have been conservative other fracture mechanics based approaches can be proposed to predict the failure pressure of corroded pipe.

Fracture Mechanics Applied to Spirally Oriented Defects in Line Pipe

Early research at British Gas involved the fracture mechanics analysis of spirally oriented defects (Fu et al. 1994). Mode I and mode II stress intensity factors were developed for spiral defects based on elastic FE analyses. These factors were then applied using a strain energy density criterion to predict the failure pressure. Solutions were developed for through wall cracks and were extended to part-wall corrosion defects using the B31G equations. In the development of the B31G criterion it was shown empirically that the Folias bulging factor for through wall defects could also be used for part-wall defects when an appropriate flow stress was utilized (Kiefner and Vieth 1989).

The result of this work was a spiral angle correction factor $A(\alpha,\lambda)$ which was used to correct the Folias factor in B31G to account for the orientation of the defect.

The spiral angle correction factor varies from 1.0 for longitudinally aligned defects to $\approx$0.2 for long, nearly circumferentially aligned defects. The predictions are in good agreement with the experimental data for through-wall defects but produce conservative results for part-wall defects with a great deal of scatter associated with the spiral angle. Coulson and Worthingham (1990) have proposed a different spiral angle correction factor while Mok et al. (1991) proposed using the length projected along the longitudinal axis of the pipe in the B31G equations. Both of these methods were based on experimental testing of part-wall machined defects in line pipe and also produce conservative results.

Although the fracture mechanics based spiral angle correction factor produces the least conservative results for through thickness defects, application to part-wall corrosion defects is questionable for the same reasons that the Folias factor may not be applicable to corrosion defects. These methods are applicable to a specific type of corrosion; a uniform depth, continuous groove oriented at a constant angle. When applied to naturally occurring complex geometries, simplifications are necessary which will generally increase the conservatism of the prediction.

Other Fracture Mechanics Applications

Although fracture mechanics is not expected to be useful for predicting the failure of typical blunt corrosion defects, such an analysis method may be useful in the determination of leak versus rupture failures and is discussed briefly.

Fracture mechanics for defect assessment can utilize a failure assessment curve (FAC) to determine the mode of failure and maximum supported load. The curve is based on a two-mode failure model which includes linear elastic fracture and plastic collapse. Balsara (1996) focused on the failure prediction of pressurized rings with sharp, longitudinally aligned defects. It was found that the simplest approach using limit load analysis produced non-conservative results which exceeded the actual burst pressure by 5 to 8%. Also, the FAC predicted that failure was dominated by plastic collapse and no stable crack growth occurred prior to failure. This agrees with experimental findings for this type of defect and also indicates that, in general, even relatively sharp defects fail by plastic collapse. This is related to the high fracture toughness (170 $MN/m^{3/2}$) of the Grade X65 pipeline steel tested. Detailed FE analysis was also completed to produce more accurate estimates of the stresses and Stress Intensity Factors and resulted in conservative predictions of between 94 and 100% of the actual failure pressure.

This analysis indicated that only in cases where the material has low toughness and the stress intensity is very large will the failure mode be linear elastic fracture.

2.4 IMPORTANT PARAMETERS IN CORROSION DEFECTS

A number of important parameters such as defect depth and material strength have been recognized as significant in the remaining strength of corroded pipe but the relative importance of each parameter was difficult to quantify. With the development of numerical techniques, parametric studies have been carried out to determine the effect of different parameters. Stephens and Leis (1997c) reported the parameters in order of significance as:

- Internal pressure
- Pipe diameter
- Wall thickness / defect depth
- Ultimate strength
- Defect length
- Defect shape characteristics
- Yield strength / strain hardening characteristics
- Defect width
- Fracture (Charpy) toughness

British Gas has reported similar results (Fu and Kirkwood 1995b) although they indicate that the order of the above list is somewhat arbitrary. It is generally accepted that the circumferential width of the defect does not play a significant role in the failure of blunt corrosion defects and this parameter is neglected in B31G. The above also lists that the failure pressure is related to the ultimate tensile strength of the material while the fracture toughness is not considered important. This is expected for typical pipeline steel which generally exhibits good toughness but may not be true for low toughness steels such as older, lower grade material where fracture toughness was not a manufacturing requirement.

2.5 DEFECT INTERACTION AND LIMITS

Most accepted methods of defect assessment require complex-shaped natural corrosion to be represented by a simplified geometry often enveloping the corrosion defect. Accurate assessment of corroded pipe requires the interaction of defects to be considered since most complex corrosion consists of interacting and individual pits with varying geometry. In this case a comprehensive set of interaction and defect simplification rules are useful since failure initiation of corrosion defects is generally localized. The local initial failure may be followed by a rupture that is governed by the full corrosion geometry, however it is the initial failure that must be predicted.

The interaction of corrosion defects has been investigated by a number of authors and a number of different sets of rules have been suggested. It is well understood that the presence of adjacent defects may reduce the burst pressure of a particular defect. On the other hand, application of the B31G criterion based solely on the maximum length and depth of a group of defects neglects islands of thicker or full-thickness material which may reinforce the defect and result in a higher burst pressure. To simplify complex corrosion geometries and reduce the conservatism in the failure predictions, defect interaction has been investigated.

One of the problems associated with defect interaction is that the number of possible geometries is infinite. As a result, early studies focused on the interaction of simple defects such as adjacent longitudinally oriented grooves. The first work in this area (Coulson and Worthingham, 1990a and 1990b) focused on the interaction of machined grooves of various lengths. The corrosion defects were 40% of the wall thickness deep and 25.4 mm (1 inch) in width. They found that the defect interaction was very complex depending on the defect length, width, depth and separation. They proposed two criterion for longitudinally oriented defects:

- Defects separated by a longitudinal distance greater than the length of the shortest defect do not interact.
- Defects separated by a circumferential distance greater than the width of the narrowest defect do not interact.

Spirally oriented defects were also considered since they were a common problem due to the disbondment of spirally wrapped pipe coating. It was found that spiral defects did not interact when the separation of the defects (measured along the spiral) exceeded the spiral length of the shortest defect. Application of the B31G criterion resulted in burst pressure estimates which were consistently conservative by approximately 14%.

Kiefner et al. (1990) and O'Grady et al. (1992) also suggested some interaction and evaluation guidelines. They suggest that corrosion defects with a maximum depth less than 20% of the wall thickness are safe and corrosion defects that exceed 80% of the wall thickness must be removed from service or repaired. Their interaction guidelines are:

- Defects separated by more than 25.4 mm (1") of uncorroded material in the longitudinal direction do not interact.
- Defects separated by a distance of 6 times the wall thickness in the circumferential direction do not interact.
- Defects occurring within a region of general corrosion can be treated as defects within a reduced wall thickness pipe.

Limits on the circumferential extent of corrosion defects were also suggested by Kiefner based on the work of Wilkowski and Eiber (1979):

- Defects with a depth between 50% and 60% of the wall thickness shall not exceed 1/6 of the circumference of the pipe.
- Defects with a depth between 60% and 80% of the wall thickness shall not exceed 1/12 of the circumference of the pipe.
- Defects with a depth greater than 80% of the wall thickness must be removed or repaired.

Some early experimental work at British Gas (Hopkins and Jones, 1992) also determined that defect interaction was a complex phenomenon. They considered 4 cases of the interaction of long grooves, similar to the work by Coulson and Worthingham but also looked at the interaction of groups of single pits with various spacing. The long groove results showed that:

- Grooves aligned in the longitudinal direction do not interact if separated by a distance greater than 3 wall thicknesses.
- Longitudinally oriented grooves offset by 12.5 mm or 1 wall thickness in the circumferential direction showed only a small interaction.

Investigation of the groups of single pits oriented in the longitudinal and circumferential directions and at 45 degrees to the longitudinal axis showed that:

- Pits separated by a distance equal to one wall thickness of material do not interact in the longitudinal or circumferential directions.

Sims and DePadova (1996) suggested that defects separated by a minimum distance of D/10 do not interact. These results were based on a parametric numerical study and have not been validated experimentally.

Experimental and numerical analyses carried out at the University of Waterloo have indicated that groups of simple corrosion pits only interact if they touch in the circumferential direction or are within a distance equal to one wall thickness in the longitudinal direction (Chouchaoui and Pick, 1993). Numerical analysis of more complicated defects represented by a series of single pits within a longitudinally oriented groove generally showed similar results (Cronin, Roberts and Pick 1996). It was found that the interaction began at a longitudinal defect separation of 6 wall thicknesses and only became significant when the separation was below 2 wall thicknesses. These results imply that defect interaction varies in a non-linear manner with the distance of defect separation.

The Canadian CSA Z662-99 code states that corrosion defects do not interact if separated by a critical length of full thickness material. The critical length is defined as the length of the shorter defect and is applicable in both the longitudinal and circumferential directions (Figure 2.5.1). These rules are conservative compared to the literature. The code requires that defects which exceed 80% of the wall thickness in depth be removed and states that corrosion defects less than 10% of the wall thickness in depth do not need to be evaluated.

It should be noted that the B31G criterion does not itself contain interaction rules but with experience, various dimensions in complex geometries can be selected to minimize conservatism in the predicted failure pressure. The RSTRENG method is

somewhat more advanced in that it does consider defect interaction through the use of the projected area of the corrosion. RSTRENG uses an iterative procedure which chooses the most critical area and then uses this area to assess the defect. Thus, some parts of the corrosion defect are excluded from the analysis (Kiefner and Vieth 1989). The validity of this procedure and a comparison to experimental data requires further investigation with more complex, but typical, corrosion geometries.

Many authors have also focused on identifying types of corrosion as a means of simplifying the analysis procedure or providing separate analysis techniques for specific defects. In particular, single pits (Chouchaoui 1993) and long grooves (Mok et al. 1991) have been investigated.

Stephens (1993) has suggested that defects can be classed in terms of increasing scale as:

- Short and narrow (pits)
- Long and narrow (axial defects or long grooves)
- Short and wide (circumferential defects)
- Long and wide (general corrosion defects)

Kiefner and Vieth (1990b) have suggested that the defects can be classed according the defect interaction.

- Type I defects are those which interact in the circumferential direction.
- Type II defects lie in the same longitudinal plane and can interact in the longitudinal direction.
- Type III defects are those in which a corrosion defect is contained within another defect.

2.6 CORROSION MEASUREMENT

Accurate defect dimensions are required for the burst pressure prediction of a pipe with a corrosion defect. The defect depth must be measured accurately with a sufficient number of measurements taken to adequately characterize the shape of the defect. The

required level of measurement accuracy can be difficult to define except that it must be sufficiently fine to capture the important aspects of the defect. The easiest manner to completely measure a defect is using an equally spaced grid of measurement locations. This technique has been successfully used with the 3-D scanner at the University of Waterloo (discussed in Chapter 4) and in industry with intelligent pigs (internal inspection devices). Although evenly spaced grids provide a detailed map of the defect surface, very small increments may be required to ensure the deepest points in the defect are found. It has been found that, for measurements made on an evenly spaced grid, 0.1" measurement increments in the circumferential and longitudinal directions are sufficient for most defects. However, certain defects with rapid changes in depth require grids of 0.05". Unfortunately, the required grid size is dependent on the shape of the corrosion so that it is difficult to provide an optimum value for this increment size. It must be recognized that such detail may not be feasible in some circumstances. For example, manual measurement of defects to this accuracy is costly, tedious and often inefficient. In the following sections, the various corrosion measurement techniques commonly in use are discussed.

2.6.1 Intelligent Pigs

Internal inspection devices, often called intelligent pigs, move through the pipe recording the thickness and morphology of the pipe wall over distances of up to 100 km. At present, three technologies are commonly used in these devices: ultrasonic, magnetic flux leakage and eddy current. The choice of technology depends on the product (gas or liquid) and the required accuracy (Beller, 1995). Ultrasonic and magnetic flux leakage methods are the most common and are discussed in detail.

In general, these devices rely on sensors equally spaced around the circumference of the pig to measure variations in the wall thickness of the pipe. Data from the sensors is stored onboard and retrieved from the pig when it is removed from the line. A typical internal inspection device is shown in Figure 2.6.1. The accuracy of these devices is determined by three parameters:

- The circumferential resolution which is determined by the number of sensors.
- The longitudinal resolution which is determined by the tool speed, measurement frequency and position measurement accuracy.
- The accuracy of the wall thickness measurement.

The current industry terminology refers to 'high resolution inspection devices' however; each supplier has their own definition of high resolution since there are no industry standards at present. In addition, the actual resolution of the tools is not always fully defined by the manufacturers partly because the resolution depends on the type of defect being measured. One inspection company, Pipetronix (1999), has published device resolutions and these are quoted for comparison to the experimental database measurements.

Magnetic flux leakage tools

This technology makes use of strong permanent magnets to magnetize the pipe wall as the pig passes through the pipe. Variations in the pipe wall thickness and morphology result in flux leakage that is detected using Hall probes or induction coils located in the pig (Figure 2.6.2). Interpretation of these results to accurately size the detected corrosion defects requires a significant amount of expertise (Atherton, 1999). This is partially related to the fact that both residual and operating stresses in the pipe affect the flux leakage and consequently the measured defect depth (Hauge and Atherton 1996).

Magnetic flux leakage tools are available in various resolutions and can travel through the line at speeds up to 8 mph (12 kph) collecting wall thickness measurements. The maximum speed is generally lower for higher resolution devices. The specifications for the Standard Resolution Pipetronix Magnetic Flux Leakage tool are:

- Minimum detected flaw depth: 15% of the wall thickness.
- Minimum detected flaw size: 3 x wall thickness in length.
- Location accuracy of detected anomalies: ±1 inch from the nearest girth weld.

Defects detected during a scan are classified into 5 categories based on depth:

1. 20% - 29% of the wall thickness in depth

2. 30% - 39% of the wall thickness in depth
3. 40% - 49% of the wall thickness in depth
4. 50% - 59% of the wall thickness in depth
5. Greater than 60% of the wall thickness in depth

The Pipetronix extra-high resolution device has a reported minimum flaw depth of 5% of the wall thickness.

Ultrasonic inspection tools

These devices make use of ultrasonic sensors equally spaced around the circumference of the intelligent pig. The wall thickness is determined by measuring the time for the ultrasonic wave to leave the transmitter and reflect back to the receiver. This actually involves the measurement of two reflections, one from the internal surface of the pipe and one from the external surface of the pipe. The distance from the ultrasonic transducer to the internal pipe surface is known as the standoff distance (Figure 2.6.3). The advantages of this method are; it provides a direct measurement of the wall thickness and accurately identifies internal and external corrosion. The disadvantage of ultrasonics is that a couplant is required between the transducer and the pipe wall. This is not a problem in liquid lines where the product is used as a couplant, but makes inspection of gas lines difficult. Some remedies to this situation have been to embed the sensors in the hubs of rubber wheels or to run the inspection device in a slug of liquid (usually water) in the gas line.

The maximum speed of the Pipetronix Ultrascan device is similar to that of the magnetic flux leakage tool and the quoted specifications are:

- +/- 0.008 in (+/- 0.2 mm) accuracy on the wall thickness measurement
- +/- 0.020 in (+/- 0.5 mm) average accuracy on corrosion depth measurement
- Circumferential resolution: approx. 0.315 in (8 mm) (the distance between the sensors)
- Longitudinal resolution: 0.129 in (3.3 mm)
- Location accuracy: +/- 7.8 in (+/- 0.2 m) from nearest the girth weld

This technology provides wall thickness measurements that are more accurate than the magnetic flux leakage technique, with the longitudinal resolution being similar to that recommended for evenly spaced grid measurements. However, the circumferential spacing is much larger than recommended and the maximum defect depth will only be measured if it is beneath one of the transducers.

2.6.2 Corrosion Measurement Methods for Excavated Pipe Sections

Manual methods of defect measurement using pit gauges and ultrasonics are still common for the external mapping of defects. Manual methods are generally employed when significant defects are found on a pipe section, often initially identified by an internal inspection. In these cases the pipe is excavated and detailed corrosion measurements are made to confirm the internal inspection and provide more accurate measurement of the defects. For external corrosion, the general shape of the defect is commonly recorded with a rubbing and the pit depths are measured and marked on the rubbing. It is recommended that photographs be taken of the defects to record details not captured in the rubbing.

For internal corrosion or defects within the pipe wall, ultrasonic measurements are used to identify the defects. Although ultrasonic techniques are well established, it can be difficult to achieve accurate defect measurements for smaller pits or pits with rapid changes in depth. This is due to the sensor size and the fact that the ultrasonic sensor must be properly coupled and oriented perpendicular to the surface. Ultrasonic measurements are a fast and accurate means of determining the true wall thickness of the pipe when applied to a clean, relatively flat surface free of corrosion products.

Pit or depth gauges are also commonly used for the manual external measurement of defects and are suitable for all forms of corrosion as long as a reference surface is present. In the case of general corrosion surrounding a locally deep defect, the remaining wall thickness must be estimated using an ultrasonic method.

Automated corrosion measurement typically makes use of a uniformly spaced grid for consistency. However, the grid size required to capture the corrosion geometry tends to be small and is dependent on the geometry of the corrosion. In contrast, detailed manual measurements of external corrosion defects can be made in critical areas while adjacent areas can be characterized with fewer measurements. With the exception of the Finite Element Method, the assessment procedures described in Chapter 4 require that only the defect depth and longitudinal position be measured. The circumferential position of the measurement is not required.

Independent areas of corrosion should be identified using interaction rules. It is conservatively suggested that defects surrounded by a perimeter of uncorroded material greater than 6 wall thicknesses can be assessed individually and will not interact with other corrosion defects.

The CSA (1999) code defines the interaction distance as the length of the shorter defect when considering the interaction of two defects. However, this definition can be ambiguous for natural, complex corrosion defects. Both CPS and RSTRENG consider longitudinal interaction and as such, do not require detailed longitudinal interaction rules. The interaction rules are simply used to reduce the calculation time. Corrosion profiles for use in CPS or RSTRENG are generated using the projection method, which requires that all corrosion depths be projected onto the same longitudinal plane. If the defect is measured with a uniformly spaced grid, the maximum depth on each circumferential line of depth measurements is used in the profile. For manual measurements, the measurer can make detailed measurements of the corrosion, particularly in the deepest areas of the defect. This data can then be used to create the defect profile using the projection method.

For B31G, only the total defect length and maximum depth are required where the defect length is determined from all of the interacting defects. In this case, the interaction rules have a significant effect on the predicted failure pressure.

2.6.3 Automated Measurement of External Corrosion

Manual external measurement of corrosion defects is accurate but can be costly and time consuming. This has prompted the development of automated measuring devices.

A laser-based corrosion mapping system was developed by the Edison Welding Institute (Bruce et al. 1997) for the purpose of mapping external corrosion defects. This system utilizes a laser light source and digital camera detector to determine the profile of corrosion defects. The camera and laser are attached to a frame which is mounted on the pipe. The quoted accuracy is +/- 0.012" on the pit depth (Kania and Carroll 1998).

A number of automated and semi-automated external corrosion measurement systems have been developed by the author at the University of Waterloo. These devices have evolved from the need to accurately measure the defect geometry for research purposes, and the accurate measurement of defects in the field for evaluation purposes and are discussed in detail in Chapter 4.

2.7 EVALUATION OF RSTRENG/B31G

Any experimental or numerical work on the burst pressure of corrosion defects is inevitably compared to accepted assessment criteria. This comparison is important since it not only validates the accepted practice but also provides estimates of the error in these prediction methods. One common value used to quantify the accuracy of the evaluation methods is the failure pressure ratio (R_f). This is the ratio of the predicted failure pressure to the actual failure pressure as shown in equation (2.7.1). If this ratio is less than 1.0 the prediction is conservative.

$$R_f = \frac{p_{f\,Calculated}}{p_{f\,Actual}} \qquad (2.7.1)$$

Assessment of the failure pressure for 86 experimental tests (Kiefner and Vieth 1989) resulted in the failure pressure ratios summarized in Table 2.7.1. The test results have been separated based on the failure mode since the B31G criterion is stated to be better at predicting ruptures than leaks. The table indicates that RSTRENG is more accurate in terms of the average predicted failure pressure however, a non-conservative prediction is possible. If a normal distribution for the failure ratios is assumed, it can be seen that the mean RSTRENG failure ratios are 0.04 and 1.0 times the standard deviation away from a ratio of 1.0 (non-conservative prediction) for leaks and ruptures respectively. Thus, there is a probability that the prediction could be non-conservative. The mean B31G failure ratios are 1.77 and 2.60 times the standard deviation away from non-conservative predictions for leaks and ruptures respectively. Thus, although RSTRENG and B31G are conservative on average, there is a probability that the prediction could be non-conservative. Table 2.7.2 shows similar results when each model was applied to 22 corrosion defects in the form of long grooves (Cronin, Roberts and Pick 1996). In these results it was noted that the conservatism in RSTRENG decreased with increasing defect depth. Chouchaoui's results (1993) for 10 single pit defects result in an average failure ratio of 0.792 with a standard deviation of 0.087 for B31G. The average failure ratio for RSTRENG was 0.960 with a standard deviation of 0.077.

Another variable used to quantify accuracy was suggested by Stephens et al. (1997b) as the ratio of the actual failure pressure to the reduced maximum allowable working pressure as defined in equation (2.7.2). Using the plastic collapse load predicted by RSTRENG and B31G:

$$R_S = \frac{\text{Actual Failure Pressure}}{MAWP_R}$$

where

$$MAWP_R = MAWP \text{ when } RSF \geq 0.90$$

$$MAWP_R = MAWP\left(\frac{RSF}{0.9}\right) \text{ when } RSF < 0.90 \qquad (2.7.2)$$

$$MAWP = \frac{[\text{Lesser of}:(2/3\sigma_{YS}) \text{ or } (1/4\sigma_{UTS})]t}{R + 0.6t}$$

$$RSF = \frac{\text{Plastic collapse load of the damaged component}}{\text{Plastic collapse load of the undamaged component}}$$

The results indicate that B31G has an average ratio of 4.62 with a minimum of 2.29 while RSTRENG has an average ratio of 3.94 with a minimum of 2.28. This implies a minimum factor of safety of approximately 2 for the tests considered.

The proper application of any assessment procedure requires a statistical understanding of the prediction error in the procedure based on representative experimental data. Although RSTRENG is conservative and has been validated with a number of experiments, it is evident from the previous results that the degree of conservatism is related to the defect geometry. It appears to be accurate for single pit defects but the conservatism decreases with defect depth for long defects. Unfortunately, few of the tests used to validate B31G and RSTRENG considered real corrosion defects with accurate material properties and defect dimensions. This issue is addressed in Chapter 4 where the application of these methods to complex natural corrosion defects is considered so that a more accurate probability of defect failure can be defined.

Chapter 3

Failure pressure prediction of simple corrosion defects

3.1 FAILURE MODE OF CORROSION DEFECTS

Numerous pipes with machined pits and over 40 pipes containing corrosion defects created during service have been burst at the University of Waterloo. This has provided a unique opportunity to observe the failure of these defects and to examine the influence of the corrosion geometry on the failure pressure.

Observation of the corroded material in the vicinity of the failures show a significant amount of plastic deformation and localized necking indicating that the initial failure occurred by plastic collapse. Microscopic investigation of the material at the failure location confirms ductile shear failure as shown in Figure 3.1.1. The contours of the grain structure in the vicinity of the failure show a significant localization of the deformation at the failure location.

The failure mechanism for complex corrosion defects in pipelines made with typical modern pipeline steel is:

- Increasing pressure results in a localization of the stress (necking) at one of the deepest points in the corrosion.

- Shortly after necking begins, ductile tearing initiates at the outside surface of the pipe (for external corrosion) creating a crack. The outside surface of the pipe is the most highly stressed area in the defect due to the combination of membrane and bending stresses. This is also true for internal corrosion defects.
- Final failure occurs in two possible modes depending on the toughness of the material and geometry of the corrosion defect:
    1. The ductile tearing progresses through the ligament resulting in a leak. This occurs for high toughness material and shorter defects in which a great deal of constraint is imposed by the surrounding uncorroded material. In this case the tear is usually confined within the corrosion defect and arrests as it grows into thicker adjacent material. It is possible for this leak to reseal itself at lower pressures if significant plastic deformation has not occurred in the vicinity of the failure and the tear length is small. A ductile tear only part way through the ligament of a corrosion defect has been observed by the author during a burst test on corroded pipe at the University of Waterloo. The pipe contained two similar defects, one of which failed. A cross-section through the defect which did not fail (Figures 3.1.2a and 3.1.2b) shows the initiation of a tear. It is believed that the ductile tear arrested prior to failure as the presence of the tear and subsequent bulging of the defect allowed the stress to be shed to adjacent material.
    2. The crack grows to a critical size through ductile tearing within the corrosion defect. Final failure occurs by fast fracture creating a rupture. Once a rupture or running crack is initiated it may run for a very long distance depending on the type of product in the line, soil constraint and material properties (Maxey et al. 1971).

It should be noted that some older pipeline steels and steel which is subjected to temperatures below the ductile to brittle transition temperature may behave in a brittle manner, failing at relatively small defects at low strains.

Examination of two pipes with service corrosion showed that the corrosion defects had failed by fatigue. Such failures can produce leaks if a critical crack size is not reached. These failures can reseal at lower pressures since the fatigue mechanism does not result in significant plastic deformation in the vicinity of the crack.

During testing, it was also observed that most pipes experienced significant plastic deformation in the uncorroded region directly adjacent to the defect and many experienced global plasticity in which the entire pipe yielded. Observations of failures which have occurred in plain pipe indicate that failure is typically the result of a local inhomogeneity in the material which leads to localized deformation and failure.

Plastic deformation of corroded pipe can be described in 3 regions:

1. Global plastic deformation of the entire pipe. This deformation is symmetric and corresponds to yielding of the uncorroded pipe material due to internal pressure.
2. Permanent deformation in the material surrounding the defect. This is in the form of bulging and occurs in the area around the defect. In the case of a single pit this bulging occurs over a distance of approximately two defect lengths around the failure location.
3. Local plastic deformation at the failure location in the form of bulging and necking.

While the effect of each type of deformation is important in a failure model, the failure of a typical corrosion defect will primarily be due to local bulging at the failure location.

As discussed in section 2.2.1 an appropriate failure criterion is necessary for any model when predicting the failure of corrosion defects. The observations of failures in actual corrosion defects indicate a two-stage approach to failure. The onset of failure is indicated by localized plastic deformation similar to necking in a uniaxial tensile specimen. This similarity suggests that a critical value approach based on the true stress/strain state at necking in a uniaxial tensile specimen would be appropriate to describe the initial failure of a corrosion defect assuming the defect stresses can be predicted accurately.

A subsequent stage can involve ductile tearing of the defect ligament resulting in a stable leak, or unstable rupture which can result in a running crack. This stage is best predicted by fracture mechanics and the critical size of the tear can be evaluated using the equations developed by Maxey et al. (1971). This may also explain why B31G, which was derived from these equations, is better at predicting ruptures than leaks (Kiefner and Vieth 1989).

Although different critical values have been proposed (Section 2.2.1) most agree that the failure of a corrosion defect can be related to the instability in a tensile specimen by using the equivalent von Mises or Tresca stress. Chouchaoui (1993) proposed that failure would occur when the von Mises stress through the entire thickness of the defect ligament exceeded the true stress in a tensile specimen just prior to the onset of necking (the ultimate tensile strength). However, in this study the failure pressure will be defined as the pressure at which the stress at any point in the defect first exceeds a critical value. This criterion is discussed in more detail in the following sections where numerical and experimental results are compared.

3.2 FAILURE OF PLAIN PIPE

The failure pressure of plain pipe is commonly used as a limit in defect assessment procedures or to normalize the burst pressure of defects. For the latter, the remaining strength of the corrosion defect is expressed as a percentage of the plain pipe strength. It is frequently assumed that as the corrosion depth decreases, the failure pressure increases linearly until the pipe fails at the pressure of plain pipe. Although such a statement may seem intuitively obvious, it also includes the assumption that the failure mechanism for pipe containing corrosion defects and plain pipe is the same. Svensson (1959) showed that pipe made of high toughness material which exhibits hardening behavior will reach a point of geometric instability prior to reaching a critical stress level. His use of a deformation plasticity based analysis was justified by the fact that the principal axes of stress and strain remain coincident throughout the loading history. The failure pressure for a pressurized

cylinder was derived assuming the plastic behavior of the material could be described using Ludwick's equation (equation 3.2.1) and that the elastic strains could be neglected. The derived relationship between the failure pressure, material properties and geometry is shown in equation 3.2.2.

$$\varepsilon_p = C_L \sigma^{n_L} \tag{3.2.1}$$

$$p = (2)^{n+1} \frac{C_L t_o}{r_o} \frac{\left(\ln \frac{r}{r_o}\right)^n}{\left(\frac{r}{r_o}\right)^3} \tag{3.2.2}$$

This equation predicts increasing radius and decreasing wall thickness with increasing pressure up to geometric instability. The value of instability can be found by taking the derivative of equation (3.2.2) and setting it equal to zero.

Analysis of some typical pipeline material from tests at the University of Waterloo indicated that a Ramberg-Osgood material model provides a more accurate representation of the material behaviour than Ludwick's equation. Also, the Ramberg-Osgood model includes the elastic strain components which are important at the early stages of the loading history. Svensson's analysis was revised to incorporate the Ramberg-Osgood material model and the result is shown in equation (3.2.3).

$$p^n \left[\frac{\alpha}{E\sigma_{YS}^{n-1}} \left(\frac{\sqrt{3}}{2} \frac{r^2}{r_o t_o}\right)^n\right] + p\left[\frac{\sqrt{3}}{2} \frac{r^2}{r_o t_o E}\right] - \frac{2}{\sqrt{3}} \ln\left(\frac{r}{r_o}\right) = 0 \tag{3.2.3}$$

This equation is solved using a numerical algorithm since the derivative of pressure with respect to radius cannot be easily evaluated. It allows the geometry to be predicted as a function of pressure up to the point of geometric instability. In practice, it has been found that the equation is most easily solved by incrementing the radius and solving for the

pressure until the pressure reaches a maximum. This is due to the fact that the same pressure can correspond to two different radii (i.e. the equation has multiple roots).

The stresses and strains in plain pipe calculated using equation (3.2.3), the finite element method and measured experimentally on a pressurized pipe are shown in Figures 3.2.1 and 3.2.2. Collapse is indicated by global geometric instability of the model. At this point of instability the stresses and strains are below the critical values found in tensile tests. The instability is the result of decreasing wall thickness and increasing pipe radius which leads to increasing stress. When the increasing stress overcomes the strain hardening of the material, instability occurs. In the Finite Element Method this can be predicted numerically using Rik's method (Hibbit et al. 1998).

Six of the burst test experiments conducted at the University of Waterloo failed in uncorroded areas although these specimens contained corrosion defects up to 41% of the wall thickness in depth. The pipes were all removed from the same line and were manufactured in the early 1950's. When the failure pressure predicted by equation 3.2.3 was compared to the experimental data it was found that the failure pressure was overpredicted (Figure 3.2.3). It is believed that inhomogeneities (possibly in the form of inclusions) resulted in localized necking and failure prior to reaching the point of instability. In addition, this older pipe had variations in thickness which would have resulted in localization of the stresses and failure prior to the predicted instability. It was found that RSTRENG underestimated the failure pressure by an average of 10% and B31G underestimated the failure pressure by an average of 19%. The results are discussed in more detail in Chapter 4.

Depending on the service conditions, typical maximum pipeline operating pressures result in a nominal hoop stress of 72% of the SMYS (CSA, 1999). For these burst tests on plain pipe, the nominal hoop stress at failure exceeded the actual yield strength by 21% on average and the SMYS by 36% on average.

This experimental work, analytical analysis and other experimental work (Svensson 1959) show that the failure of plain pipe occurs by global geometric instability while analysis of the experimental database indicates that pipe with typical corrosion defects fails at a critical stress.

3.3 LONGITUDINAL GROOVE ANALYSIS

The simplest corrosion defect shape to consider is a very long, longitudinally aligned groove of uniform depth. Some of the initial studies into the failure of corrosion defects were focused on experimental and numerical analysis of such defects (Mok et al.). It should be noted that natural corrosion defects may appear to have this shape but, being formed by natural corrosion processes, have local variations in depth. Three examples of this type of corrosion (RLK1, RLK2 and RLK3) are discussed in Chapter 4. A photograph of RLK1 is shown in Figures 3.3.1a and 3.3.1b. The corrosion occurred due to wrinkling of a polyethylene tape coating. Although defects such as long grooves of uniform depth are idealizations, they provide an excellent starting point for understanding the failure behaviour of corrosion defects and in the development of a new assessment procedure. In particular, some of the important variables in the problem can be investigated through the use of two-dimensional numerical models.

3.3.1 Defect Length

It is useful to determine the critical length at which a groove behaves as an infinitely long groove. Mok et al. conducted tests on longitudinally oriented, machined grooves which were 40% of the wall thickness in depth. The pipe was API-5L-X60 (Grade 414) with a diameter of 20" (508 mm) and wall thickness of 0.25" (6.53 mm). British Gas (Hopkins and Jones, 1992) also conducted tests on longitudinally oriented grooves of various lengths in grade API-5L-X52 material. The grooves were 40% of the wall thickness deep and the pipe was 24" (610 mm) in diameter with a wall thickness of 0.486" (12.34 mm). The results are shown in Figure 3.3.2 with the groove length normalized by the pipe diameter.

Figure 3.3.2 shows that the defect behaviour is that of an infinite length groove for lengths greater than approximately 1 pipe diameter. This value has been suggested as the

critical length for treating a defect as an infinite length groove by Mok et al., Hopkins and Jones, and Coulson and Worthingham (1990b).

3.3.2 Finite Element Analysis

Mok et al. showed that the Finite Element Method could be used to predict the failure pressure of long uniform depth grooves using two-dimensional analysis. Analysis of typical defects using the Finite Element Method were undertaken to investigate their behaviour. Plane strain elements were used to model a cross-section of a pipe with a long groove. This corresponded to the pipe being restrained from expanding or contracting in the longitudinal direction (plane strain conditions). Second order (8-noded quadrilateral), reduced integration hybrid elements were used to model the curved surfaces in the corrosion defects. A hybrid formulation of the element was recommended for situations in which the material behavior is incompressible or nearly incompressible and a large amount of plastic deformation occurs. In this case very small changes in displacement produce large changes in hydrostatic pressure and the solution can become numerically unstable when it is based purely on displacements. Standard elements tend to 'lock' or become overconstrained as the material becomes more incompressible. The hybrid elements treat the pressure stress as an independent variable in the solution and are not susceptible to this instability. A reduced integration formulation was also used which results in a reduced analysis time since these elements use a lower order integration for the stiffness matrix (but full integration for distributed loads). In general, it has been found that reduced second-order elements are more accurate than their full integration counterparts (Hibbit et al. 1998b).

The material response was modelled using both incremental and deformation plasticity with the material properties measured from a tensile test of Grade X46 pipeline material. While incremental plasticity is a more general material model formulation, deformation plasticity results in reduced computing time for the analysis which is useful for larger analyses. This is discussed in more detail in section 3.3.3. The failure pressure

was defined as the point at which the equivalent critical stress at any point in the finite element model was equal to the ultimate tensile strength of the material expressed as a true stress as described in section 3.1.

Test cases using incremental plasticity indicated the same failure pressure for reduced integration and reduced integration hybrid elements. As expected, the regular elements did exhibit some 'locking' which was indicated by an increase in failure pressure. For the deformation plasticity material model, reduced hybrid elements exhibited instability before reaching the critical stress. The standard formulation was slightly stiffer while the reduced integration elements produced results similar to those of the incremental plasticity model. It should be noted that the variation in failure pressure for these test cases was approximately 1 psi (0.007 MPa) for a failure pressure of 997 psi (6.9 MPa) (i.e. approximately 0.1%).

Figure 3.3.3 shows the calculated burst pressure of long grooves as a function of defect depth. Defects with depths ranging from 0% to 90% of the wall thickness were analyzed using the finite element method. In general, the failure pressures are a linear function of the defect depth in agreement with previous analyses and experiments (Mok et al., Hopkins and Jones). However, this is only the case for defect depths greater than approximately 20%. For shallower defects, the failure pressure deviates from the linear curve plotted on the figure. At a depth of 0% (plane pipe) the pipe fails by geometric instability which occurs at stress levels below the critical stress level. The RSTRENG and B31G results (equations 2.1.12 and 2.1.1) are also shown in this Figure. Although these predictions are conservative, it is evident that the degree of conservatism decreases with increasing defect depth. A similar result was found by Cronin, Roberts and Pick (1996) when the experimental failure pressures of long, groove-like defects were compared to RSTRENG and B31G predictions.

The author investigated convergence of the finite element model by varying the mesh density. The failure pressure is plotted as a function of the number of elements through the thickness of the ligament in Figure 3.3.4. The figure shows that the mesh has converged when two or more elements are used through the ligament thickness. All

longitudinal groove meshes for the analyses described above had four elements through the thickness.

3.3.3 Material Model: Incremental vs. deformation plasticity

Incremental plasticity is a more general material response model than deformation plasticity and does not result in a significant increase in computing time for simple 2-dimensional analyses. However, as will be shown later, the use of a deformation plasticity model can greatly reduce computation time for more complex 3-dimensional analyses and is feasible since this model has no load history dependence. That is, the final load and deformation states can be determined without having to consider the increments of load up to the point of failure. Further, the material behavior can be characterized with only a few parameters.

Strictly speaking, use of the deformation plasticity model is restricted to cases in which the deviatoric stresses increase proportionally to one another and significant unloading does not occur. In cases where these conditions are not met incremental plasticity is the most accurate material model (Mendelson, 1983) for pipeline steels. Use of the deformation plasticity model assumes that the shape of the true stress-strain curve can be approximated by the model. It was found that the Ramberg-Osgood stress-strain curve representation was suitable for the grades of steel considered. Figure 3.3.5 shows an example of a stress-strain curve for grade API-5L-X42 material. The Ramberg-Osgood fit deviates near the yield stress but is accurate for strains greater than 0.008. The incremental plasticity model uses the experimental data, not a curve fit, and the stress-strain curve is properly represented.

Analysis of the long groove models using deformation plasticity did not result in any significant change in the predicted burst pressure. The stress history at the deepest point in a 65% depth groove is plotted in Figure 3.3.6 as von Mises equivalent stress versus internal pressure for both material response models. The yield behaviour is not properly

represented by the deformation plasticity model due to the lack of fit of the Ramberg-Osgood model at this point.

Since the defect ligament is subjected to biaxial (circumferential and longitudinal) stresses which remain proportional throughout the loading history once the yield stress has been exceeded the deformation plasticity model is expected to be accurate.

To support this point, consider the incremental plasticity flow rule associated with the von Mises yield criterion:

$$d\varepsilon_{ij}^{p} = \frac{3}{2}\frac{d\sigma_e}{H'\sigma_e}S_{ij}$$

where (3.3.1)

$$H' = \frac{d\sigma_e}{d\varepsilon_p}$$

Where H' is the slope of the equivalent plastic strain versus equivalent stress curve which can be determined from a uniaxial true stress-strain curve. If we chose to represent this curve with the Ramberg-Osgood relationship:

$$\varepsilon = \varepsilon_{Elastic} + \varepsilon_{Plastic}$$

$$\varepsilon = \frac{\sigma}{E} + \alpha\left(\frac{\sigma}{\sigma_{YS}}\right)^{n-1}\frac{\sigma}{E} \qquad (3.3.2)$$

we can evaluate the derivative of the plastic strain component with respect to stress to be:

$$d\varepsilon_p = \alpha n\left(\frac{\sigma}{\sigma_{YS}}\right)^{(n-2)}\frac{\sigma}{E}\frac{d\sigma}{\sigma_{YS}} \qquad (3.3.3)$$

so equation (3.3.1) becomes:

$$d\varepsilon_{ij}^{p} = \frac{3}{2}\alpha n\left(\frac{\sigma_e}{\sigma_{YS}}\right)^{(n-2)}\frac{S_{ij}}{E}\frac{d\sigma_e}{\sigma_{YS}} \tag{3.3.4}$$

The general three-dimensional form of the plastic strain (from equation 3.3.2) in the deformation plasticity equation is:

$$\varepsilon_{ij}^{p} = \frac{3}{2}\alpha\left(\frac{\sigma_e}{\sigma_{YS}}\right)^{n-1}\frac{S_{ij}}{E} \tag{3.3.5}$$

Thus, the deformation and incremental plasticity material models will be equivalent if equation (3.3.4) can be integrated to give equation (3.3.5). This will occur for the case where the deviatoric stresses are proportional to the equivalent stress so that:

$$S_{ij} = c_{ij}\sigma_e \tag{3.3.6}$$

where c_{ij} is a constant tensor that does not depend on strain. The von Mises equivalent stress for biaxial loading is given by:

$$\sigma_e = \sqrt{S_{11}^2 - S_{11}S_{22} + S_{22}^2} \tag{3.3.7}$$

This implies that the deviatoric stress components must also be proportional to each other. Figure 3.3.7 shows the ratio of the hoop stress (maximum principal stress) to longitudinal stress (intermediate principal stress) for an FE analysis of a groove 65% of the wall thickness in depth. The radial stress is neglected since it is small in comparison to the hoop and longitudinal stresses. The figure indicates that the stresses are proportional above yield (approximately 435 psi internal pressure) supporting the use of a deformation plasticity approach.

3.3.4 Circumferential Corrosion Dimension

One of the fundamental assumptions in corrosion assessment codes (CSA, 1999, ASME-B13G, 1991) is that the circumferential extent of the corrosion does not affect the burst pressure of the defect. This assumption is based on the assumption that corrosion defects are blunt with a defect width that is at least similar to the defect depth. It should be noted that this may not always be true. One example is preferential corrosion at longitudinal seam welds. In this case the defect can be relatively narrow and deep.

The effect of groove width was investigated for a defect 65% of the wall thickness in depth. The results are shown in Figure 3.3.8 and indicate that there is a slight variation in burst pressure with a peak occurring when the defect width is approximately twice the wall thickness. In any case, the burst pressure varies by less than 2% which is not significant. In general, the circumferential dimension of typical blunt long grooves does not affect the burst pressure. For narrow grooves, the burst pressure is expected to decrease. This is related to the increased stress concentration as the defect radius becomes smaller or, in the limit, as the defect tends towards a sharp crack. Part of this effect is due to the fact that a similar amount of bending deformation must be accommodated by the defects although they differ in circumferential extent. Thus, in the case of a narrow defect, larger bending stresses are induced, resulting in a reduced failure pressure.

3.3.5 Prediction of the failure pressure of long, longitudinally oriented grooves

In applying equilibrium to a structure, it is common to consider one section and replace the remainder with the appropriate boundary conditions. In the case of a long groove, one half of the defect can be analyzed (due to symmetry) with the remainder of the structure replaced by an equivalent bending moment, hoop force and shear force as shown in Figure 3.3.9a.

Finite element results indicate that the bending moment in the ligament tends to be very small as the defect approaches failure. This is expected due to the large degree of

plasticity at this point and so the moment (M_L) can be assumed to tend to zero. Also, for plain pipe M_H=0. Finite element analysis indicates that this is also a reasonable assumption for long grooves. Due to the symmetry of the problem, the shear forces (V_L, V_H) are also zero as shown in Figure 3.3.9b. The stress in the radial direction has a maximum value at the inside surface of the pipe equal to the internal pressure which is small compared to the hoop and longitudinal stresses and can be neglected. Consider a section of material in the corrosion ligament at the plane of symmetry with an infinitesimal circumferential dimension (ds) as shown in Figure 3.3.10. In this case the thickness is equal to the ligament thickness (t_L), the section has length w and is subjected only to longitudinal (F_{Long}) and hoop forces (F_{Hoop}) (i.e. biaxial stretching).

The purpose of this analysis is to determine the pressure required to create the critical stress in the ligament of the defect. A deformation plasticity material model is used so that this pressure can be found without considering the loading history of the defect. Both equilibrium and compatibility must be considered to solve this problem. Applying equilibrium to the deformed geometry shown in Figure 3.3.9b where 'b' refers to the radial deformation of the plain pipe and 'a' is the radial bulging of the groove:

$$F_L + F_H = pw\left[2(r_i + b) + a\right] \tag{3.3.8}$$

We assume that:

$$\begin{aligned} F_H &= pw(r_i + b) \\ &\quad and \\ F_L &= pw(r_i + b + a) \end{aligned} \tag{3.3.9}$$

Considering moment equilibrium about the pressure centre:

$$\left(r_i + b + \frac{t_H}{2}\right)F_H = \left(r_i + b + a + \frac{t_L}{2}\right)F_L$$

which can be combined with (3.3.9) and by neglecting second order terms, simplifies to 3.3.10

$$a = a_{Max} = \frac{(t_H - t_L)}{4}$$

This states that the maximum radial bulge is a function of the difference in thickness between the plain pipe and corrosion ligament and has been confirmed with finite element analysis. The bulging occurs to eliminate the bending moment at this point.

At failure, the average ligament strain is equal to the equivalent true strain corresponding to the ultimate tensile strength of the material. Due to the large degree of plasticity we can assume that the material is incompressible:

$$\begin{aligned} &0 = \varepsilon_{thick} + \varepsilon_{hoop} + \varepsilon_{long} \\ &and\ \varepsilon_{long} = 0\ for\ plane\ strain\ so \\ &-\varepsilon_{thick} = \varepsilon_{hoop} \end{aligned} \qquad 3.3.11$$

The equivalent plastic strain is:

$$\begin{aligned} \varepsilon_{equiv} &= \sqrt{\frac{2}{3}\left(\varepsilon_{thick}^2 + \varepsilon_{long}^2 + \varepsilon_{hoop}^2\right)} \\ &= \sqrt{\frac{4}{3}\varepsilon_{thick}^2} = \sqrt{\frac{4}{3}\left[\ln\left(\frac{t_L}{t_{Lo}}\right)\right]^2} \\ &= -\sqrt{\frac{4}{3}}\ln\left(\frac{t_L}{t_{Lo}}\right) \end{aligned} \qquad 3.3.12$$

Note that the negative sign in equation (3.3.12) is necessary to produce a positive equivalent strain since the thickness strain is negative. At failure, the stress and strain state

corresponds to that of the ultimate tensile strength and strain expressed as a true quantities. So:

$$\varepsilon_{UTS} = -\sqrt{\frac{4}{3}}\ln\left(\frac{t_L}{t_{Lo}}\right)$$
$$rearranging: \qquad 3.3.13$$
$$t_L = t_{Lo}\exp\left(-\sqrt{\frac{3}{4}}\varepsilon_{UTS}\right)$$

which is the ligament thickness at failure.

If we consider the element shown in Figure 3.3.10 we can define the stresses as:

$$\sigma_{hoop} = \sigma_{11} = \frac{F_{hoop}}{wt_L}$$
$$\sigma_{long} = \sigma_{22} = \frac{F_{long}}{ds\,t_L} \qquad 3.3.14$$
$$\sigma_{radial} = \sigma_{33} \approx 0 \quad (negligibly\ small)$$

The hydrostatic component of the stress is:

$$p_h = -\frac{1}{3}(\sigma_{11} + \sigma_{22} + \sigma_{33})$$
$$= -\frac{1}{3}\left(\frac{F_{hoop}}{wt_L} + \frac{F_{long}}{ds\,t_L} + 0\right) \qquad 3.3.15$$
$$= -\frac{1}{3}\left(\frac{F_{hoop}ds + F_{long}w}{wt_L ds}\right)$$

so the deviatoric components are:

$$
\begin{aligned}
S_{ii} &= \sigma_{ii} + p_h \\
S_{11} &= \frac{F_{hoop}}{wt_L} - \frac{1}{3}\left(\frac{F_{hoop}ds + F_{long}w}{wt_L ds}\right) \\
S_{22} &= \frac{F_{long}}{ds\,t_L} - \frac{1}{3}\left(\frac{F_{hoop}ds + F_{long}w}{wt_L ds}\right) \\
S_{33} &= -\frac{1}{3}\left(\frac{F_{hoop}ds + F_{long}w}{wt_L ds}\right)
\end{aligned}
\qquad 3.3.16
$$

where 1 indicates the hoop direction, 2 indicates the longitudinal direction and 3 indicates the through-thickness direction. The three-dimensional deformation plasticity constitutive relationship can be written as:

$$
E\underline{\varepsilon} = (1+\nu)\underline{S} - (1-2\nu)\underline{p_h} + \frac{3}{2}\alpha\left(\frac{\sigma_{mises}}{\sigma_{YS}}\right)^{n-1}\underline{S} \qquad 3.3.17
$$

where the underscored quantities are tensors. If we neglect shear and bending as shown in our free body diagram (Figure 3.3.10), and assume that the material is incompressible at failure (ν=0.5):

$$
\begin{aligned}
E\varepsilon_{11} &= (1+\nu)S_{11} + \frac{3}{2}\alpha\left(\frac{\sigma_{mises}}{\sigma_{YS}}\right)^{n-1} S_{11} \quad (a) \\
E\varepsilon_{22} &= (1+\nu)S_{22} + \frac{3}{2}\alpha\left(\frac{\sigma_{mises}}{\sigma_{YS}}\right)^{n-1} S_{22} \quad (b) \\
E\varepsilon_{33} &= (1+\nu)S_{33} + \frac{3}{2}\alpha\left(\frac{\sigma_{mises}}{\sigma_{YS}}\right)^{n-1} S_{33} \quad (c)
\end{aligned}
\qquad 3.3.18
$$

As mentioned above, ε_{22}=0 for plane strain, so equation (3.3.18b) becomes:

$$E\varepsilon_{22} = 0 = (1+\nu)S_{22} + \frac{3}{2}\alpha\left(\frac{\sigma_{mises}}{\sigma_{YS}}\right)^{n-1} S_{22}$$

or 3.3.19

$$0 = \left[(1+\nu) + \frac{3}{2}\alpha\left(\frac{\sigma_{mises}}{\sigma_{YS}}\right)^{n-1}\right] S_{22}$$

where the quantity in the square brackets will always be a positive value, or zero in the trivial case where no load is applied. This requires that:

$$S_{22} = 0$$

$$\left(\frac{F_{long}}{ds\,t_L} - \frac{1}{3}\left(\frac{F_{hoop}ds + F_{long}w}{wt_L ds}\right)\right) = 0$$

and finally

$$F_{long} = \frac{F_{hoop}}{2}\frac{ds}{w} \qquad 3.3.20$$

or in terms of stress

$$\sigma_{22} = \frac{1}{2}\sigma_{11}$$

This result matches that of Figure 3.3.7 for stresses above the yield stress. The deviatoric stresses can now be expressed as:

$$S_{11} = \frac{1}{2}\frac{F_{hoop}}{t_L w}$$

$$S_{22} = 0 \qquad 3.3.21$$

$$S_{33} = -\frac{1}{2}\frac{F_{hoop}}{t_L w}$$

The von Mises stress as a function of the hoop force is:

$$\begin{aligned}\sigma_{mises} &= \sqrt{\frac{3}{2}(S_{11}^2 + S_{33}^2)} \\ &= \sqrt{\frac{3}{2}\left(\left[\frac{1}{2}\frac{F_{hoop}}{t_L w}\right]^2 + \left[-\frac{1}{2}\frac{F_{hoop}}{t_L w}\right]^2\right)} \\ &= \sqrt{\frac{3}{4}}\frac{F_{hoop}}{t_L w}\end{aligned} \qquad 3.3.22$$

and at failure:

$$\sigma_{mises} = \sigma_{UTS} = \sqrt{\frac{3}{4}}\frac{F_{hoop}}{wt_L}$$

or, for a unit length (i.e. w=1) 3.3.23

$$\frac{F_{hoop}}{t_L} = \frac{\sigma_{UTS}}{\sqrt{\frac{3}{4}}}$$

From equations (3.3.9) and (3.3.23) and we can express the failure pressure of a long groove as:

$$p(r_i + b + \frac{t_H - t_L}{2}) - \frac{\sigma_{UTS}}{\sqrt{\frac{3}{4}}} t_L = 0 \qquad 3.3.24$$

Here b and t_H are found from the plain pipe solution for the given pressure. Equations 3.2.3 and 3.3.24 must be solved together in an iterative manner until equation 3.3.24 is satisfied.

The predictions of equation 3.3.24 have been compared to the experimental data of Mok as shown in Figure 3.3.11. The RSTRENG and B31G calculations are also shown for comparison. It can be seen that this method predicts the failure of these long, longitudinally oriented, machined defects with a maximum error of 10%. The RSTRENG and B31G predictions are on average 30% and 34% conservative respectively.

Three burst tests from the University of Waterloo database contained defects which could be approximated as long, longitudinally oriented grooves. The burst predictions and actual failure pressures are shown in Figure 3.3.12. It was assumed that the groove depth was equal to the maximum depth of the corrosion defect. The significant underprediction of the burst pressures is attributed to the fact that these defects were formed by natural corrosion processes and, as a result contain local variations in depth. The resulting defect which can be approximated as a single pit within a longitudinal groove has a higher burst pressure than a longitudinal groove with a depth equal to the maximum depth of the corrosion. Equation 3.3.24 underpredicted the failure pressures by an average of 23% while RSTRENG and B31G underpredicted the failure pressure by 48% and 52% respectively.

Figure 3.3.13 shows the failure predictions of equation 3.3.24 compared to finite element analysis of grade API-5L-X42, 10-inch nominal diameter pipe, 0.2-inch nominal wall thickness pipe. The analytical solution and finite element predictions agree within 2%. Some of the difference can be attributed to the interpolation of the failure pressure from the finite element results. The predictions of equation 3.3.24 are only applicable to defect depths greater than 5% of the wall thickness. At shallower depths geometric instability of the pipe begins to dominate the problem and equation 3.3.24 cannot be used to predict the failure pressure. Depths less than 5% can be assumed to fail at a pressure equal to the failure pressure of plain pipe. The prediction of equation 3.3.24 is also unstable for the trivial case where the corrosion depth is 100% of the wall thickness. It can be assumed that corrosion defects with depths in excess of 99% of the wall thickness have a failure pressure of 0 psi.

The solution of equation 3.3.24 is not trivial due to the nonlinear behaviour of the plain pipe solution as a function of pressure. However, if we assume that the plain pipe

deformation (b) and defect bulging (a) are negligible in comparison to the pipe radius, equation (3.3.24) can be expressed as:

$$pr_i - \frac{\sigma_{UTS}}{\sqrt{\frac{3}{4}}} t_L = 0 \tag{3.3.25}$$

Equation (3.3.25) can then be combined with equation (3.3.13) and rearranged to express the failure pressure as a function of the geometry and material properties as shown in equation (3.3.26).

$$p = \frac{\sigma_{UTS}}{r_i \sqrt{\frac{3}{4}}} t_{Lo} \exp\left(-\sqrt{\frac{3}{4}} \varepsilon_{UTS} \right) \qquad \frac{t_L}{t_{Lo}} \geq 0.2 \tag{3.3.26}$$

The failure pressure can be solved for directly in equation (3.3.26) and the results are plotted in Figure 3.3.13. The figure indicates that the assumptions in equation (3.3.26) are suitable for defect depths in excess of 20% of the wall thickness. Below this depth the non-linear behaviour of the plain pipe becomes significant and is not appropriately modeled by equation (3.3.26).

Both the experimental and finite element results indicate that the proposed analytical solution (equation 3.3.24) adequately models the failure behaviour of long, longitudinally aligned grooves in line pipe which fail by the stress-based criterion. The failure behaviour of these defects can also be accurately predicted by equation (3.3.26) when the defect depth exceeds 20% of the wall thickness.

3.4 ANALYSIS OF SINGLE PITS

The analysis of single pits is the next level of complexity beyond long, longitudinally oriented grooves. Chouchaoui and Pick (1993) have investigated the behaviour of single corrosion pits in detail both experimentally and using the FEM. After confirming the accuracy of the FEM, the method was used to investigate parameters associated with the failure of single pits and the interaction of groups of pits. Fu and Kirkwood (1995a,b) also investigated the behaviour of simply shaped defects and validated the finite element method with experimental burst tests. The stresses in a single pit are a complex three-dimensional function of the geometry and loading. The models of single pits provide insight into the behaviour of more complex corrosion defects which contain variations in the ligament thickness causing localized stresses. Failure initiates at one of these localized areas in a fashion similar to the behaviour of a single pit. This has led some authors to propose that the deepest point in a large corrosion defect can be treated as a single pit in a reduced wall thickness pipe. This is discussed in section 3.4.1.

A study of single pits was undertaken to provide a simple, three-dimensional model for which the effect of material properties, circumferential extent and applicability of evaluation procedures could be investigated. It should be noted that these results are not meant to provide rules for evaluation since the number of variables to be considered is nearly infinite. Instead, these analyses are meant to investigate assumptions in the current evaluation codes and identify important variables for the development of a new assessment procedure.

3.4.1 Finite Element Analysis

The behaviour of single pit defects was investigated using the finite element method. The defects were spherical in shape and only one quadrant of the defect was analyzed due to symmetry conditions. A typical finite element mesh is shown in Figure

3.4.1. Chouchaoui (1993) found that single pits could be modeled adequately by parabolic or spherical shaped defects with a similar length and depth.

The failure pressure was estimated by monitoring the peak von Mises stress in the defect. When this stress exceeded the critical stress, failure was considered to have initiated. For single pits located on the external surface of the pipe this maximum stress occurs on the outside surface of the pipe at the location of the maximum pit depth. Final failure of the defect may occur at this pressure or require a further small increase in pressure. The pressure and mode of final failure will depend on the defect geometry and material properties, including the fracture toughness of the steel.

Unless otherwise specified, all analyses used the incremental plasticity material model with four elements through the thickness of the pipe wall. The circumferential extent of the model was 180° of the pipe circumference as required by the symmetry conditions. The longitudinal length of the uncorroded material was six times the wall thickness. This is sufficient for the pit to behave as an isolated defect (Cronin, Roberts and Pick 1996) in a long section of pipe restrained from deforming in the longitudinal direction. The inside radius of the pipe was 10.436" (265 mm) and the wall thickness was 0.195" (4.95 mm). These dimensions were taken from a series of 10-inch nominal diameter, Grade API-5L-X42 pipes burst tests at the University of Waterloo.

The typical defect considered was a spherically shaped pit 65% of the wall thickness in depth with a total length of 0.784" (20 mm). The choice of dimensions was somewhat arbitrary, and meant only to demonstrate specific behaviour of this type of defect. Other researchers have considered flat-bottomed pits primarily because the experimental specimens are easier to manufacture. In any case the choice is arbitrary since there is no 'typical' pit shape within natural, complex corrosion defects.

Mesh convergence

Convergence of the finite element mesh was investigated for the typical defect geometry (65% depth spherical pit) using the finite element mesh shown in Figure 3.4.1. This is known as the ¼ model since symmetry allows for only one quadrant to be analyzed.

The predicted failure pressure varied less than 1% when the number of elements through the thickness was varied from 1 to 4 (Figure 3.4.2a). The equivalent von Mises stress is shown as a function of internal pressure in Figure 3.4.2b. The stress history for analyses with one element through the thickness deviates significantly from the other analyses, particularly between yield and final failure. This is related to the localized bending and plastic zone which is not adequately modeled by a single element through the thickness. However, the predicted failure pressures are similar. The analyses indicate the mesh has approximately converged with only two elements through the thickness. Differences between the 2 and 4 element cases are primarily due to differences in the pressure increments automatically chosen by the finite element code. Varying the density of elements on the surface of the pit indicated no change in failure pressure as long as there were sufficient elements to properly model the geometry.

To examine the effect of meshing and the boundary conditions for the ¼ model, the defect was fully modeled in a larger section of plain pipe as shown in Figure 3.4.3a and 3.4.3b. Two elements were used through the thickness as shown in the Figures. The predicted burst pressure was the same as for the ¼ model (Figure 3.4.1) indicating that the simplified ¼ model was appropriate.

For single pit defects, accurate finite element results require a mesh with at least 2 elements through the thickness and sufficient elements on the surface to adequately model the geometry of the defect.

Element type and material model

As discussed in the longitudinal groove modeling, the element type and material response used in modeling these defects is important since each type embodies specific assumptions. Chouchaoui (1993) suggested the use of reduced integration hybrid elements when modeling three-dimensional defects using incremental plasticity. As discussed with the long groove analysis, it is of benefit to also investigate a deformation plasticity material model since this allows the stress and strain state of the material to be determined without considering the loading history. Also, finite element analyses utilizing this material model require less computation time and this model will be beneficial in any analytical solution

developed to describe these defects since the failure pressure can be calculated without considering the load history.

The results of three analyses using the incremental plasticity model are shown in Figure 3.4.4. The element type has been varied and it can be seen that the stress histories are similar. The failure pressures differ by less than 1%. The results were similar when using the deformation plasticity model. As shown by Chouchaoui, the reduced integration, hybrid elements provide the most consistent results in terms of burst pressure. This is expected since the hydrostatic component of stress is eliminated from the constitutive equation (equation 3.3.17) after the material yields and Poison's ratio becomes 0.5.

Figure 3.4.5 shows a comparison between the incremental and deformation plasticity material responses using the reduced integration hybrid element type. Although the predicted burst pressures are the same, it is evident that the stress histories differ. This difference is related to possible unloading of parts of the model during the load history and the assumption that the deviatoric stresses remain proportional. It should be noted that many analyses conducted on various geometries using both material models have yielded the same burst pressure indicating that this difference may not be significant in terms of predicting the final failure. This aspect is discussed in more detail in Chapter 4 where the modeling of natural corrosion defects is considered.

Typical single pit behaviour

The typical behaviour for these spherically shaped pits is similar to that of the longitudinal grooves. This behaviour is shown in Figure 3.4.6 using the von Mises equivalent stress at the deepest point in the corrosion defect and the corresponding point on the inside surface of the pipe. The highest stresses occur at the outside surface of the corrosion pit due to the combined bending and membrane stresses. Yielding begins at this location and continues through the ligament until it reaches the inside surface of the pipe. With increasing pressure the stresses through the ligament increase in the same manner until failure occurs. The onset of failure occurs when the stress at any point in the model exceeds the critical stress which is 79971 psi (551 MPa) for this material. This occurs at an

internal pressure of 2134 psi (14.7 MPa) as shown in the figure. This failure criterion is validated with the experimental results discussed in Chapter 4.

The failure criterion of Chouchaoui, Pick and Yost (1992) requires that the equivalent stress in the entire ligament exceed this critical stress which results in the final failure pressure of 2229 psi (15.4 MPa). This failure criterion was developed from experimental tests and finite element modeling of single pits in a specific type of material. For different geometries and materials, this failure criterion may not be appropriate and so the onset of failure is quoted for all analyses.

The longitudinal and hoop stresses at the deepest point in the corrosion defect (on the external surface) are shown as a function of internal pressure in Figure 3.4.7. The onset of failure pressure is indicated by the vertical line. The ratio of these two stresses is also plotted on the figure indicating that the principal stresses are not proportional throughout the loading history as was the case for the long grooves. However, once the entire ligament has yielded the ratio of the stresses is relatively constant with a value of approximately 1.6. This value is less than the value of 2.0 for the long groove case since local bulging of the defect increases the longitudinal stress. The hoop stress corresponds to the maximum principal stress and the longitudinal stress corresponds to the intermediate principal stress. The axes of these principal stresses do not rotate significantly during the loading history.

Effect of circumferential extent

As with the long groove defects, the effect of the circumferential dimension on the failure pressure was investigated. This is important since neglecting the circumferential dimension is a fundamental assumption of the current assessment techniques. In addition, new assessment procedures can be simplified by incorporating this assumption.

The effect of circumferential extent was investigated with three finite element meshes of a single pit, 65% of the wall thickness in depth with a length of 0.784" (20 mm). The ratio of pit width to pit length was varied from 0.5 to 1.5 and the failure pressure was predicted using the Finite Element Method. Figure 3.4.8 shows the finite element mesh for a pit width to length ratio of 0.5. Figure 3.4.9 shows that the predicted failure pressure

only varies by approximately 6% for the three meshes considered. Similar results have been found by other authors (Chouchaoui 1993, Fu 1995a and Stephens 1997c) but it is important to note that this result cannot be generalized to the limit where the defect extends around the entire circumference of the pipe. In this case, the longitudinal stress becomes the maximum principal stress since the cross-sectional area in the longitudinal direction is reduced around the entire circumference (axisymmetric). This results in a higher failure pressure since there is no localization of the hoop stress and the stress concentration is actually reduced. An axisymmetric defect can be considered as a group of rings of varying thickness and of small length joined to one another with a common internal radius. Thus, the pipe material behaves as a number of small sections of plain pipe, with the sections near the defect restrained from expanding radially by the surrounding material. Burst tests by Chouchaoui (1993) indicate that pipes with machined circumferential grooves 60% of the wall thickness in depth tended to failed in defect free material away from the machined groove. These grooves had varying circumferential extents ranging from 25% to 100% around the circumference of the pipe.

A circumferential groove of uniform depth and with the same longitudinal profile as the single pit was analyzed using a two-dimensional axisymmetric model. The von Mises stress is plotted as a function of the internal pressure in Figure 3.4.10. The equivalent stresses at the inside and outside surfaces of the defect are approximately equal throughout the loading history. This is due to the full circumferential extent of the groove which doesn't allow for localization of the hoop stress due to a local change in wall thickness. In other words, localized bending does not occur in the hoop direction since there is no change in thickness in this direction. However, there is bending in the longitudinal direction which results in the slightly higher stress on the external surface of the pipe. The longitudinal stress is the maximum principal stress for this defect as shown in Figure 3.4.11 and is related to the reduction in wall thickness around the full circumference providing less material to carry the longitudinal load.

The onset of failure is predicted at a pressure of 2249 psi (15.5 MPa) which exceeds the single pit failure pressure by 5%. Although this error does not appear to be significant, the fundamental differences in the stress history, as compared to single pits, indicate that an

axisymmetric analysis is not appropriate for modeling three-dimensional corrosion defects. In particular, additional analyses have shown that the predicted defect behaviour is not consistent for different defects and is highly dependent on the defect length. In general the circumferential dimension of the defect does not significantly affect the failure pressure of corrosion defects, but a limit to the circumferential dimension is necessary for this to be the case. In terms of natural corrosion defects, this limited circumferential dimension is present due to variability in the corrosion depth which tends to localize the stresses. One specific instance where this effect may be observed is corrosion defects resulting from the tenting of polyethylene tape coating over a girth weld. This results in corrosion defects which are circumferentially oriented and may behave as full circumferential grooves. However, these defects can be conservatively analyzed as defects with a limited circumferential extent (Cronin and Pick, 1996b).

Assessment of the Folias factor

One of the fundamental assumptions in the current assessment procedures is that the defect behaviour can be described by the Folias factor. In order to investigate the applicability of this factor it is necessary to consider the corrosion geometry term from the RSTRENG formula (equation 2.1.12). The corrosion factor (CF) is defined as:

$$CF = \left[\frac{1 - \frac{A}{A_o}}{1 - \left(\frac{A}{A_o}\right) M^{-1}} \right] \qquad 3.4.1$$

The Folias factor cannot be considered separately since A, A_o and M are all dependent on the defect length. The analysis of the corrosion factor is meant to demonstrate that RSTRENG has some fundamental inconsistencies which are related to the Folias factor. The CF was investigated by analyzing single pit defects with varying length and depth selected so that the CF remained constant. This results in a constant failure pressure prediction by RSTRENG.

The failure pressures of single pits with varying lengths and depths but with a constant corrosion factor of 0.938 were predicted using the finite element method and are shown in Figure 3.4.12. The constant RSTRENG failure pressure and the plain pipe (0% depth) failure pressures are also plotted. Figure 3.4.12 indicates that the failure pressure predicted using the finite element method decreases with increasing depth. However, the predicted RSTRENG failure pressure at a constant corrosion factor remains constant. This is also the case for a corrosion factor of 0.82 as shown in Figure 3.4.13 indicating that RSTRENG is not only conservative, but does not accurately represent the corrosion behaviour.

For comparison, defects in a thicker walled pipe with the same inside radius and a corrosion factor of 0.938 were analyzed. The trend (Figure 3.4.14) is similar to that of Figure 3.4.12.

Flow Stress investigation / Material Properties

Many assessment methods, including the current codes, use flow stress to represent the behaviour of actual pipeline steel materials. The use of a flow stress implies that the material can be described by an elastic-perfectly plastic material model with a yield stress equal to the flow stress. To investigate the validity of a flow stress approach, three parameters in the incremental plasticity model were varied: yield stress, ultimate tensile strength and strain at the ultimate tensile strength. Note that although the ultimate tensile strength is generally referred to in engineering terms, it is expressed as a true stress for the purposes of finite element defect evaluation. Variations in the true stress-strain curve were achieved by scaling the appropriate variable in the true stress-strain curve for use in the incremental plasticity model. These true stress-strain curves are plotted in Figures 3.4.15, 3.4.16 and 3.4.17 where the yield stress, critical stress (true stress at necking) and critical strain (true strain at necking) were varied.

Figure 3.4.18 shows the von Mises stress at the deepest point in the defect as a function of internal pressure. Increasing the yield stress results in a non-linear increase in the onset of yielding as expected. More importantly, there is also a significant effect on the final failure pressure indicated by the intersection of the von Mises stress curve and critical

stress line. The variation of failure pressure with yield stress is shown in Figure 3.4.19. The effect of yield stress on burst pressure is also related to the longitudinal extent and geometry of the defect. Higher yield material and greater thickness adjacent to the corrosion defect will reduce the extent of the plasticity increasing the constraint on the defect resulting in a higher burst pressure.

The effect of varying the stress at necking or the critical stress is shown in Figure 3.4.20. The von Mises stress history is similar for the three critical stresses considered. The failure pressure as a function of critical stress is shown in Figure 3.4.21. Note that the critical strain was the same for each critical stress. Thus a percent change in the critical stress corresponds to the same percent change in the ultimate tensile strength of the material (expressed as an engineering stress). For the cases considered in Figure 3.4.20, the ratio of change in failure pressure to change in UTS is non-linear with values between 0.69 and 0.84 for the cases considered. In contrast, the assessment procedures proposed by Stephens and Ritchie suggest that changes in the failure pressure are directly related to the UTS.

Variation in the critical strain (strain at necking) was also investigated. The stress-strain curves are shown in Figure 3.4.17 and the von Mises stress histories are shown in Figure 3.4.22 as a function of internal pressure. The curves are plotted for different reductions in the critical strain where a 0% reduction corresponds to the typical material model. The Figure indicates that materials with varying reductions in the critical strain result in a similar failure pressure for the defect considered with the exception of a 100% reduction in the critical strain. The 100% reduction corresponds to an elastic-perfectly plastic analysis and the failure pressure can be predicted by an elastic analysis since the failure is assumed to initiate when the critical stress (the flow stress in this case) is first exceeded. These results are shown more clearly in Figure 3.4.23 and suggest that the shape of the plastic stress-strain curve is not important in terms of plastic strain, as long as some finite amount of plastic strain is present. It should be noted that the lower predicted failure pressure associated with the elastic-perfectly plastic analysis may be partially due to the failure criterion. Also, this analysis assumes a flow stress equal to the critical stress although elastic-perfectly plastic material models have not been considered in detail.

These results also indicate that the failure pressure of a defect is related to the critical stress and not to the ultimate strength of the material. Maintaining a constant critical stress while varying the critical strain, and thus the ultimate tensile strength of the material, resulted in no significant change in burst pressure.

These analyses show that the failure pressure of a defect is a function of yield stress and critical stress but is not dependent on the magnitude of the critical strain, and consequently on the shape of the stress-strain curve. However, the use of an elastic-perfectly plastic stress-strain curve is not appropriate.

Reduced wall thickness analysis

Many authors have considered the use of a reduced wall thickness analysis for cases in which local areas of metal loss are located within larger areas of general corrosion. A reduced wall analysis assumes that these defects can be considered as local areas of metal loss in a pipe with a wall thickness equal to the original wall thickness minus the depth of the general corrosion. If we consider the failure pressure of a long groove and plain pipe of equal wall thickness, the failure pressure of the long groove will always be higher. This is due to the adjacent full thickness material which acts to constrain the groove deformation resulting in a higher, stress-based failure pressure. In contrast, plain pipe of the same thickness as the long groove fails by geometric instability at lower stress levels.

Chouchaoui (1993) compared finite element analyses of single pits within general corrosion to experimental results. He was able to predict the burst pressure within 3% using a von Mises based failure criterion when the entire defect was considered. Chouchaoui also analyzed these defects as single pits within a reduced wall thickness pipe where the wall thickness reduction was equal to the depth of the surrounding general corrosion. He found that the predicted burst pressures were conservative by an average of 26%.

In terms of an RSTRENG or B31G analysis, the reduced wall approach is reasonable since a reduced wall thickness pipe and long groove of the same thickness are predicted to fail at the same pressure by these methods. However, it should be noted that this is an inconsistency in the RSTRENG and B31G methods when compared to

experiments and Finite Element analyses, and may introduce a significant conservative error in the predictions. From a practical point of view, the definition of a reduced wall thickness is somewhat arbitrary due to natural variations in the defect depth. Further, it should be expected that this area of general corrosion must be some minimum size to behave as reduced wall thickness pipe. Chouchaoui's results indicate that this size is large relative to the pipe dimensions and as a result there may be no increase in efficiency by including a reduced wall thickness provision in an assessment procedure.

Simplified defect interaction analysis

The interaction of a row of equally spaced single pits was considered using Finite Element analysis. One definition of interaction is: an appreciable reduction in failure pressure of a particular defect due to adjacent metal loss. Ideally, two regions of metal loss are separated by uncorroded material, and the degree of interaction is based on this distance. Even in this simple case, an appreciable reduction in failure pressure can be difficult to define since the failure pressure is a continuously varying quantity. In application, it is convenient to define independent regions of corrosion and consider their influence on one another. However, in practice it is difficult to define such boundaries for complex defects.

Consider the results plotted in Figure 3.4.24 for a row of evenly spaced single pits. The defect separation is normalized by the material wall thickness as suggested by Chouchaoui (1993) although this is an arbitrary choice. The maximum defect length (CSA, 1999) and other measures involving the pipe diameter and defect dimensions have been proposed. Determination of the point at which interaction begins is difficult since there is no distinct or abrupt change in the failure pressure. It can be said with confidence that very little interaction occurs with a defect separation exceeding 6 wall thicknesses. Chouchaoui has suggested that a distance of one wall thickness is more realistic. In any case, these results cannot be generalized to all corrosion defects since the possible geometric variations are infinite.

The purpose of this analysis is to show that even when the defect geometry is well defined, a complete definition of interaction is difficult. In general, the accuracy of an

assessment method should not rely on detailed interaction rules. However, it is recognized that the use of interaction is desirable to simplify the assessment of defects. Ideally, the interaction rules should be available to exclude non-interacting defects from a particular analysis, but should not result in a change in the predicted burst pressure. In other words, an assessment procedure should account for the interaction of adjacent defects and the only purpose of the interaction rules should be to reduce the calculation time. The latter may be desirable if a large number of defects must be analyzed such as in the case of high-resolution inspections.

Chapter 4
Experimental testing and modeling of corrosion defects

4.1 BACKGROUND

In order to evaluate the accuracy of the currently accepted corrosion assessment procedures and to develop a new method of assessment, an experimental database is necessary. Such a database is also necessary to validate models, particularly if they are to be the basis of any code or standard. In 1994, Vieth and Kiefner collected all of the available data for pipeline defect failures in a report sponsored by the American Gas Association (Vieth and Kiefner, 1994). Unfortunately, much of the published burst test data is incomplete with only nominal pipe dimensions and material properties, and inaccurate representations of the corrosion defects. In addition, many of the reported tests with detailed measurements involve artificial or machined defects with simple geometries such as grooves and notches. Although this type of test was an important stepping-stone in the development of numerical methods and understanding defect behavior, the complexity of real corrosion defects can often not be accurately represented with simpler shapes. More importantly, the behaviour of natural corrosion defects can be misrepresented by the use of machined defects.

The two most common methods used to create artificial defects are mechanical and electro-chemical machining. Mechanical machining is done on a mill with a mechanical cutter. Although accurate, it can be difficult to achieve uniform depth in the circumferential direction due to the curvature of the pipe. It has also been suggested that this process may introduce residual stresses into the defect. However, the author suspects this is not important due to the large degree of plasticity in the defect prior to failure. Electro-chemical machining utilizes an electrode in the shape of the defect to be machined. An electrolyte is continuously pumped between the electrode and pipe surface, while a power supply is used to provide the necessary current for the artificial corrosion process. Although this process is more representative of the natural corrosion process, it can be difficult to achieve a smooth surface due to the accumulation of debris and variations in the flow of the electrolyte. This process is used at the University of Waterloo to create artificial defects.

Testing artificial defects was an important first step in terms of quantifying important corrosion defect parameters and investigating defect interaction. Initial investigations at the University of Waterloo involved the chemical machining of single pits and their interaction (Chouchaoui, 1993). These smaller defects generally exhibited failure behaviour similar to natural corrosion defects. Failure initiated at a deep point in the corrosion defect, oriented in the longitudinal direction. Chouchaoui also showed that such machined defects were accurately modeled using the Finite Element Method.

Other researchers have attempted to simplify the experimental testing of complex corrosion defects by representing them with large flat-bottomed patches with a depth equal to the maximum defect depth and a length equal to the overall defect length. In terms of metal loss, this is a conservative representation of a complex corrosion defect and is appropriate for conservative assessment of a defect. However, experimental testing and numerical analysis of these defects has shown that the failure mode differs from that of natural corrosion defects. Large, flat-bottomed machined defects are created with smooth surfaces so that a significant localization of stress does not occur within the defect. Consequently, the patch behaves in a similar fashion to a curved plate subjected to pressure on one side and fixed around its edges. The abrupt change from the maximum defect depth

to full pipe wall thickness at the edges of the defect results in a large degree of restraint. The patch deforms by bulging such that the stresses are primarily membrane in nature within the defect and are dominated by localized bending at the restrained edges. This localized bending at the edges of the defect results in a higher equivalent stress so that failure initiates at this point and follows the edges of the defect, even in the circumferential direction. These defects fail by rupture with the fracture running around the circumference of the defect as shown in Figure 4.1.1a, 4.1.1b and 4.1.1c.

In contrast, natural corrosion defects have local variations in depth which result in stress localization and localized failure at one of these deeper points. If failure occurs by rupture the fracture generally propagates in the longitudinal direction although it may change circumferential position to follow the deepest path in the corrosion defect. A typical failure is shown in Figures 4.1.2a and 4.1.2b where the rupture path has followed the path of least resistance through adjacent defects, but is predominantly oriented in the longitudinal direction.

The use of artificial defects to represent natural corrosion is justified for smaller defect sizes. The maximum allowable size for a machined defect to behave as a complex corrosion defect has not been investigated. Nevertheless, it can be said that tests which fail by rupture around the edges of the machined defect are not representative of natural corrosion defects. These tests should not be used to represent natural corrosion defects or to validate failure prediction models. In some cases, such as preliminary investigations, it may be necessary to use large, flat-bottomed defects due to their simplicity in shape. In these cases the author suggests that a chemical machining method is more appropriate, and that the surface be prepared to create local variations in the defect depth to result in the required stress localization.

The experimental data available for the validation of current assessment procedures or the development of new procedures is incomplete in many respects and has led to the development of an experimental database at the University of Waterloo.

4.2 EXPERIMENTAL DATABASE OF COMPLEX CORROSION DEFECTS

4.2.1 Research Program at the University of Waterloo

A research program has been underway for several years at the University of Waterloo with the focus of improving corrosion assessment methods. Although early work (Chouchaoui, 1993) focused on electro-chemically machined pits and their interaction, later work has focused on testing and evaluation of real or natural corrosion defects. This was motivated by the lack of appropriate experimental data for validation of the current codes and their application to natural, complex corrosion defects.

The research program at the University of Waterloo has involved:

- Development of accurate corrosion defect measurement devices.
- Experimental burst testing of pipe removed from service containing natural corrosion defects.
- Validation of the currently accepted codes and their application to complex natural corrosion defects.

The burst tests are considered appropriate for validation of current assessment procedures since all pipe sections considered were removed from service due to the presence of critical corrosion defects (as determined by the operators of each pipeline).

The first database of the burst tests was reported by Cronin and Pick in 1996. This database included 30 pipe sections for which the pipe dimensions, material properties and corrosion geometry were accurately measured. Since 1996 ten additional tests have been conducted on larger diameter pipe. The complete database of 40 burst tests includes many different types of corrosion such as single pits, interacting pits, general corrosion, longitudinally aligned corrosion and corrosion adjacent to girth welds. The test procedure, corrosion defect measurement and material properties measurement are discussed in the following sections. Application of B31G and RSTRENG to the tests is then investigated.

4.2.2 Corrosion Measurement

Accurate measurement of the corrosion defects is the most important and most difficult stage of the test procedure. The corrosion measurement techniques at the University of Waterloo have been based on mapping or scanning the external surface of the pipe and determining the remaining wall thickness based on the original pipe wall thickness. A number of corrosion measurement systems have been developed at the University of Waterloo evolving from the need to accurately measure the defect geometry for research purposes, and the accurate measurement of defects in the field for evaluation purposes.

The first measurement device developed at the University of Waterloo used a contacting displacement transducer which moved in a flat plane above the pipe surface via computer controlled stepper motors. Although this planar scanner produced accurate results, there were several shortcomings. Movement in a flat plane above the cylindrical pipe surface limited the scan range in the circumferential direction for smaller diameter pipes due to the large range of transducer displacement required. As shown in Figure 4.2.1, the transducer displacement is a function of the distance from the centreline of the pipe. This results in a scanned image that includes the curvature of the pipe. In addition, a longitudinal slope may be introduced into the data (Figure 4.2.1) if the scanner plane is not parallel to the pipe. In order to determine the true corrosion depth, computer software was developed to correct the scanned image. This will be discussed below. The contacting sensor required a mechanism to lift it from the surface when in motion between measurement locations. When the transducer remained in contact with the surface during movement, the measurement tip could be caught in areas where the corrosion depth changed rapidly.

A second scanning device was constructed after 18 burst tests had been completed using the planar scanner for mapping. The remaining corroded pipes were measured with a new scanner, known as the 3-D scanner, which used a non-contacting infrared measurement system to map the surface. For this scanner, the movement mechanism was modified so that the laser transducer moved in a cylindrical path and remained a constant

distance from the pipe surface as shown in Figure 4.2.2. A photograph of the 3-D scanner is shown in Figure 4.2.3. Although this development improved the accuracy and repeatability of the measurements, it was found that most pipe surfaces were not cylindrical in shape resulting in curvature in the scanned image. In addition, the data commonly had a slope in the longitudinal direction due to positioning tolerance in placement of the scanner on the pipe surface. This was corrected using the software described above. Although this scanner provides complete and accurate defect data, it was not designed for use in the field.

A prototype of a field ready scanner was developed utilizing a contacting displacement transducer with 12" of longitudinal travel as shown in Figure 4.2.4. The device was designed to be light and compact with data recorded on a portable laptop computer via a standard interface card. This particular scanner was developed for areas which were generally corroded so that circumferential travel of the transducer was not necessary or could be accomplished manually.

The next development was prompted by the need to measure relatively long defects in the field in an automated manner. Known as the Long Scanner (Figure 4.2.5), it consisted of a longitudinally oriented beam mounted on machined, circumferentially oriented rails. The beam had approximately 160° travel in the circumferential direction. A non-contacting infrared transducer was mounted on the beam with linear bearings allowing for 36" of travel in the longitudinal direction. The transducer was used to accurately measure the distance from the beam to the surface of the pipe. Position was measured by means of optical encoders, accurate to the nearest 0.010" in both the longitudinal and circumferential directions. The primary goal of this device was to allow the user to move the measurement head to any location within the range of the scanner and record the surface depth. This allows the user to make only those measurements necessary to characterize the corrosion defect. The surface distance, longitudinal position and circumferential position were recorded by a computer when the user pushed a trigger button at the desired measurement location. Although the accuracy of the position measurements exceeded the required values and the laser depth measurement system was sufficiently accurate, deviations of the pipe surface from cylindrical led to errors in the depth measurement. In addition, if the pipe was out of round a longitudinal slope could

also be introduced into the data. These effects needed to be excluded from the data through computer processing which required a number of data points on the uncorroded pipe surface to define the reference surface. During development it was determined that the measurement head of this scanner was relatively heavy for field use. This could be improved with a counter-balancing mechanism, however this was abandoned as being too complex for field use. Further development of this scanner is required.

At the time of writing, a totally new scanner which makes use of a unique lightweight position measurement system is under development. The initial prototype has been developed and proven to be accurate in both position and depth measurement. As this scanner has commercial potential, further development will be pursued as a separate topic.

One of the major improvements in the accuracy of the planar and 3-D scanners was the development and improvement of a computer program to remove the curvature and longitudinal slope from the data. This program outputs the actual corrosion depths from the scanned surfaces by identifying the shape of the uncorroded surface and transforming the scanned surface to a flat plane containing the actual corrosion measurements. This is accomplished in three steps:

- Application of a corrosion identification algorithm. This identifies areas of corrosion and excludes them from the data so the uncorroded surface can be identified.
- Calculation and removal of any longitudinal slope in the data.
- Calculation and removal of the uncorroded surface curvature.

The most important step in this process is identifying the corroded areas in the scan. This is achieved by considering the longitudinal and circumferential slopes at each data point compared to the overall longitudinal and circumferential slope of the surface. The data is then considered as separate longitudinal lines where the corrosion defects are identified and removed to determine the shape of the uncorroded surface. Once determined, the uncorroded surface can be used to calculate the actual corrosion depth at each point.

As an example, surface and image plots of a corrosion defect from one of the burst tests are shown in Figure 4.2.6. Although the method considers both the longitudinal and circumferential directions, a single longitudinal line of data will be used to explain the method.

For a given longitudinal line of data, the average and standard deviation of the absolute value of the slope between adjacent data points is calculated. Slopes which exceed 3 standard deviations from the average are flagged as corrosion. A longitudinal line of data at a circumferential position of 1.4 inches (Figure 4.2.6) is shown in Figure 4.2.7a where these points are identified with circles. This identifies the edges of the corrosion defect where the slope between adjacent points is much larger than the longitudinal slope in the scanned data. The next step is to identify the bottoms of the corrosion pits. A linear regression is performed on the data, excluding the previously flagged points. The average and standard deviation of the distance of the points from the regression line is then calculated. Points which are below the linear regression line and exceed a distance of 0.5 standard deviations from this line are also flagged as corrosion (Figure 4.2.7b).

Linear regression is then applied to each longitudinal line of data with the flagged (corrosion) points removed. Regressions with a correlation coefficient greater than 0.95 are averaged to determine the longitudinal slope in the scanned surface. This value typically has a maximum magnitude of approximately 0.006 in./in. (mm/mm). This can be significant over scans with large longitudinal dimensions. As an example, a length of 9.0" corresponds to a change in depth of 0.054" over the length of the defect due to the longitudinal slope. The longitudinal slope for the line of data considered in Figure 4.2.7 was 0.002 in/in (mm/mm).

The curve representing the uncorroded surface in the circumferential direction is defined by the intercepts of the linear regression equations for each longitudinal line of data. A third order polynomial is fit to these points to define a smooth curve representing the curvature of the uncorroded surface in the scanned data.

As mentioned previously, the surface is actually analyzed in both the circumferential and longitudinal directions. Figure 4.2.8 shows an image plot of the corrosion defect from Figure 4.2.6 with the corrosion pits identified by the program

(plotted as open circles). It can be seen that the program has been successful in identifying the defects in this case.

The longitudinal slope and circumferential curvature are then removed from the original surface scan data to produce a flat surface containing the corrosion defects. In some instances, such as those where the uncorroded surface is defined by only a few points, multiple applications of the algorithm are required to transform the scanned data to a flat plane. To assist the user in this process, contour and surface plots of the data are displayed on a screen to indicate the current state of the data. The transformed data containing the actual corrosion defect measurements is then output to a file for use in assessing the corrosion defects. The original and transformed surfaces are shown in Figure 4.2.9.

Although accurate corrosion measurements are necessary for the evaluation of corrosion defects, they must be utilized in a manner that adequately quantifies the corrosion defect. For the case of three-dimensional finite element analysis, the data can simply be used directly to create an appropriate finite element mesh. A simplification is made for B31G where only the total length and maximum depth are used to quantify the defect. An intermediate approach is used with RSTRENG where a river bottom path through the corrosion defect is defined to represent the corrosion defect (refer to section 2.1). While this incorporates detailed measurements of the corrosion defect, the circumferential extent and position of adjacent metal loss regions is neglected since the river bottom path is projected onto a longitudinal axis. The use of this approach has been validated for simply shaped defects but applying the river bottom approach is difficult in practice for complex shaped defects. If the defect in Figure 4.2.6 is considered, it is evident that many different river bottom paths could be selected and the RSTRENG method does not provide adequate guidance for the selection of the correct profile in more complex corrosion defects. The only appropriate method of determining the correct profile would be to select the path that results in the minimum predicted burst pressure. Algorithms to accomplish this task are necessarily complicated and require additional computing time due to the iterative nature of the process.

To overcome this problem a simplified approach has been developed by the author to determine the effective corrosion defect profile. It has been found that the critical corrosion profile can be determined by considering isolated patches of corrosion using the interaction rules described in Section 2.5. The profile for this isolated patch can then be generated by selecting the deepest corrosion measurement on each circumferential line of data and projecting it to a longitudinal plane for the entire length of the defect. This is known as the projection method. Application of this method to the defect in Figure 4.2.6 is shown in Figure 4.2.10 where the crosses indicate the deepest point for each circumferential line of data. The resulting defect profile is also shown in Figure 4.2.10 where the depth is plotted as a percent of the total wall thickness.

The river bottom path is easily defined for simply shaped defects such as single pits or defects oriented in the longitudinal direction. For these simple defects, the projection method results in a river bottom path as specified in RSTRENG since this path tends to be the location of the deepest points in the defect. An example is shown in Figure 4.2.11.

For complex defects, such as the one shown in Figure 4.2.10, the profile generally includes points which do not necessarily follow a river bottom path. In other words, a significant circumferential separation exists between points selected on adjacent circumferential lines. It should also be noted that the profile may not return to a depth of zero at the ends of the defect as shown in Figure 4.2.10.

Application of the projection method will result in an accurate or conservative corrosion profile since the deepest points in the scanned area are considered.

4.2.3 Material Properties

Since most failure prediction methods are stress-based, accurate material properties are required for accurate prediction of the failure pressure. The presently accepted codes for failure assessment are based on the specified minimum yield stress of the material although proposed techniques require the actual yield strength or ultimate tensile strength to predict the failure pressure of a defect. Fracture toughness is another material property

that is generally quoted since earlier pipeline steels could experience brittle fracture. Today, minimum fracture toughness limits are placed on pipeline steels based on fracture initiation and propagation considerations (CSA, 1999). All pipes in the database failed in a ductile manner and all of the failure criteria considered are based on a critical stress so that only the plastic material properties were required. The fracture toughness was not measured for these materials.

The plastic material properties were determined with uniaxial tensile tests of specimens oriented in the longitudinal and circumferential directions. A minimum of four longitudinal and four circumferential specimens were tested for each pipe material. In most cases, 6 to 10 specimens were tested to characterize a particular material.

The specimens were tested at a strain rate of 0.08 in/ minute (2 mm/minute). The specimens had a thickness equal to the wall thickness of the pipe and a width of approximately 0.5 in. (12.7 mm). Several of the original tests were repeated when a significant non-linearity was found in the 2.0" gauge length extensometer used for the tests. For the repeated tests, deformation was measured with a 1.0" gauge length, high extension extensometer. An elastic modulus of 30×10^6 psi (207 GPa) was assumed. The yield strength was calculated using a 0.5% strain offset.

A summary of the properties for the materials considered in the database is given in Table 4.2.1.

The engineering and true stress-strain curves for a typical test are shown in Figure 4.2.12. The true strain can be calculated from the engineering strain as shown in equation (4.2.1). The true stress can be calculated from the engineering stress using equation (4.2.2) where constancy of volume (incompressibility) is assumed. This assumption is only valid up to the point of necking where the deformation becomes localized in the tensile specimen.

$$\varepsilon = \ln(1+e) \tag{4.2.1}$$

$$\sigma_{True} = \sigma_{Eng}(1+e) \tag{4.2.2}$$

The Ramberg-Osgood equation can express the total strain as the sum of the elastic and plastic strains in terms of three parameters: α, n and σ_{YS}. This is useful since it provides a simple means for describing the true material behaviour as shown in equation (4.2.3).

$$\varepsilon_{Total} = \varepsilon_{Elastic} + \varepsilon_{Plastic}$$
$$\varepsilon_{Total} = \frac{\sigma}{E} + \frac{\alpha}{E}\left(\frac{|\sigma|}{\sigma_{YS}}\right)^{n-1}\sigma \qquad (4.2.3)$$

The yield stress was determined from the engineering stress-strain curve using the 0.5% offset method. The constants α and n were then calculated from a non-linear regression on the true stress-strain tensile test data. Figure 4.2.13 shows a plot of the true stress-strain curve and the corresponding Ramberg-Osgood curve for one of the materials from the database. It has been found that this equation accurately represents the true stress-strain curve for the materials tested. Typically, there is a moderate lack of fit near the yield stress and the correlation coefficient is very near 1.0 (0.999 in this case) indicating a good fit.

4.2.4 Burst Test Procedure

The following procedure was used for the pipe burst tests:

- **Corrosion measurement.** All defects on the pipe surface were accurately mapped using the surface scanners developed at the University of Waterloo. Defects which were larger than the maximum scan size were mapped in sections with a suitable overlap where necessary to permit the scans to be joined together. The scanner data was then processed to determine the actual corrosion depths and create RSTRENG input files for analysis.
- **Material properties.** The material properties were measured with uniaxial tensile tests of specimens in the circumferential and longitudinal directions.

- **Pipe dimensions.** The pipe wall thickness and diameter were measured in four locations for each pipe tested.
- **Data analysis.** The RSTRENG files were analyzed using the RSTRENG software to calculate the approximate burst pressure of the pipe section.
- **Defect photographs.** All defects were photographed in colour. This included overall photographs of the pipe as well as photographs of each scanned area.
- **Burst testing.** All pipes were closed with endcaps and filled with water. The pipe was then pressurized to approximately 25% of the predicted burst pressure and inspected for leaks. The pressure was then increased at a rate of 6 cubic inches per minute to failure. The internal pressure in the pipe was measured using a pressure transducer and amplifier calibrated with a dead weight tester at the approximate burst pressure determined by the RSTRENG analysis. The transducer was found accurate within 1.0% of the dead weight test pressure for repeated pressurization. The pressure was also monitored with Bourdon tube pressure gauge with a lower accuracy.
- **Failure photographs.** The failure location was photographed and the initiation site was identified. The initiation site could be determined based on localized necking through the wall thickness, bulging of the pipe material and the fracture surface.

4.2.5 Test Results

The relevant properties and failure predictions are summarized for each test in Tables 4.2.2 and 4.2.3.

4.2.6 Sources of Experimental Error

As with all experimental testing, the test measurements made for the experimental database contain a degree of error. It is important to quantify the error so that the data can

be used confidently to evaluate existing models or validate new models. To consider the precision of the corrosion measurements, the variability in the measurements and the variability within the data processing must be considered.

Variability is introduced with the placement of the scanner on the pipe since the data is measured in a uniform grid. A slight movement of the scanner in the longitudinal direction corresponds to a shift in the measurement locations and can result in differences depending on the size of the measurement grid and morphology of the corrosion. One natural corrosion defect was measured independently six times with the University of Waterloo scanner. Analysis of the corrosion profiles generated from the scans indicated a maximum difference of 0.010" in depth for the 0.01" spaced grid used. Note that this precision includes the combined effects of data measurement and processing.

The accuracy of the scanner was determined using a calibration pipe with machined defects. The actual depth of the defects was measured with a dial gauge accurate to +/- 0.0005". The maximum error in the depth measurements was 0.003" which includes variability from the scanner placement, measurement grid size and data processing software. The quoted accuracy of the infrared measurement system is 0.00004" (1 μm), which is dependent on the colour and roughness of the surface being measured.

The material properties were determined with uniaxial tensile tests in the longitudinal and circumferential directions. The strains were measured using a high extension extensometer. In general, the longitudinal values differed from the circumferential values. The ratio of circumferential yield stress to longitudinal yield stress varied from 0.88 to 1.13. The ratio of circumferential UTS to longitudinal UTS varied from 0.97 to 1.02. In all cases, the variability in the UTS was smaller than that in the yield stress. The average standard deviation for the yield stress was 2053 psi while the average standard deviation for the ultimate tensile strength was 955 psi. The circumferential properties were used in all analyses.

The wall thickness was measured to the nearest 0.0005" using a micrometer and the pipe diameter was measured to the nearest 0.020". These measurements are sufficiently accurate however, significant variations in the wall thickness were noted for some of the

older pipe tested. In particular the SOL series of pipes showed the most significant variation in thickness between tests and within a test.

The burst pressure was measured with a pressure transducer and amplifier calibrated to the approximate burst pressure using a dead weight tester. Multiple tests with the dead weight tester indicated the pressure measurement was linear with and varied by 1.0% at the burst pressure.

4.3 CURRENT STATE OF EVALUATION PROCEDURES

To consider the accuracy of the current assessment procedures it is useful to compare the failure pressure of corroded pipe removed from service to the allowable operating pressure of the line. It should be noted that this comparison contains the safety factor adopted by the pipeline code in setting the allowable operating pressure of a defect-free pipeline and the reduction in strength of the line caused by the corrosion.

The comparison can be expressed as the ratio of nominal hoop stress at failure to the nominal hoop stress under the maximum allowable operating pressure. This provides a measure of the factor of safety against failure of the defects considered. The design or maximum allowable operating pressure for Canadian pipelines (CSA, 1999) is defined as:

$$p_{Operating} = \frac{2t}{D_o} SMYS \times F \times L \times J \times T \qquad (4.3.1)$$

where the design factor (F) is equal to 0.8. The location factor (L), joint factor (J) and temperature factor (T) are equal to 1.0 unless an additional factor of safety is required for the operating conditions where these values are less than 1.0. Consider equation (4.3.2):

$$p_{Operating} = \frac{2t}{D_o} SMYS \times 0.8 \qquad (4.3.2)$$

This equation states that the nominal operating hoop stress in the pipe wall is limited to 80% of the specified minimum yield stress (SMYS). In cases where the pipe is not manufactured to CSA Standard Z245.1 or API Specification 5L the nominal hoop stress in the pipe wall is limited to 72% of the specified minimum yield stress. It is important to note that these limits apply to defect-free pipe. Assessment of corrosion defects that have developed in service may require the defects to be repaired or the operating pressure of the line to be reduced to provide the same factor of safety as a defect free pipeline.

For a maximum operating pressure corresponding to 72% of the SMYS, a failure ratio can be defined by equations (4.3.3) and (4.3.4).

$$\sigma_{\text{Hoop Nominal at Failure}} = \frac{p_{Failure}\, r_i}{t} \tag{4.3.3}$$

$$R_{Failure} = \frac{\sigma_{\text{Nominal Hoop at Failure}}}{0.72 \times SMYS} \tag{4.3.4}$$

Note that a failure ratio greater than 1.0 indicates the pipe section would not have failed at a nominal hoop stress of 72% of the SMYS although it contained corrosion defects. The failure ratios for the 40 burst tests conducted at the University of Waterloo are plotted in Figure 4.3.1 as a function of maximum defect depth. The Figure indicates that all pipe sections failed at pressures exceeding the allowable operating pressure for defect-free pipe. That is, in all cases there remained a factor of safety against failure, which generally decreased with increasing defect depth. Note that the maximum depth is quoted for the failure location although deeper defects may have existed elsewhere on the pipe section. The average failure ratio was 1.75 with a maximum value of 2.075 and a minimum value of 1.285 indicating that current assessment techniques have resulted in the removal of many pipe sections which could be considered still fit for service. However, it should be noted that the factor of safety for continued service of this pipe which contains corrosion defects is lower than that for defect-free pipe.

The remaining factor of safety can be investigated by undertaking a hydrostatic pressure test on the pipeline. This would be conducted prior to the line being returned to service to determine the minimum factor of safety remaining in the pipeline. The maximum allowable hoop stress for a hydrostatic test is 100% of the SMYS. The failure ratios for a hoop stress equal to 100% of the SMYS are shown in Figure 4.3.2. This figure indicates that only four of the 40 pipe sections would have failed at this pressure level. The average failure ratio of 1.26 indicates that many sections of pipe would have passed a hydrostatic test but were conservatively removed from service. The trend in Figures 4.3.1 and 4.3.2 shows that the failure ratio decreases with increasing defect depth as would be expected. Operators remove pipe with deeper defects due to the reduced factor of safety and concerns regarding the effect of additional corrosion.

4.4 COMPLEX CORROSION DEFECT ASSESSMENT – B31G AND RSTRENG

B31G and RSTRENG have been applied to the database of burst tests to investigate the accuracy of each method and provide guidance on the application of these methods to complex corrosion defects.

As required in these assessment procedures, the specified minimum yield strength (SMYS) was used in the flow stress estimation. However, the actual pipe diameter and pipe wall thickness were used in the assessments rather than the nominal dimensions which are normally used. The assessment procedures were applied to the failure location although lower burst pressures may have been predicted elsewhere on the pipe. Knowing the failure location, the extent of the defect at this location was determined using interaction rules. Defects separated by more than 2 wall thicknesses of full thickness material in the longitudinal direction and 1 wall thickness of full thickness material in the circumferential direction were assumed to act independently. Although these rules appear simple they can be difficult and ambiguous to apply in real situations. The definition of full thickness pipe requires some interpretation since general, superficial corrosion is often present in the vicinity of larger defects. This may be in the form of a general reduction in

wall thickness or shallow pitting. The B31G criterion states that corrosion less than 10% of the wall thickness in depth may be left in place regardless of the defect length. The value was increased to 20% for RSTRENG. Although authors have interpreted this as the maximum depth of corrosion which does not affect the failure pressure of the pipe, these limits are more correctly related to conservatism in the assessment procedure itself. Investigation of the failure data for long grooves (Figure 3.3.13) indicated that the failure pressure is relatively constant for corrosion depths less than 10% of the wall thickness. Therefore, corrosion that was less than 10% of the wall thickness in depth was considered as uncorroded for the purpose of applying the interaction rules although this shallow corrosion was included in the defect analysis.

The maximum defect depth for the B31G assessment was determined from the transformed scanned surface data. The defect length was determined from the scanned surface data, defect photographs and pipe section. This required some care since the transition between corroded and uncorroded areas was indistinct in some cases.

The RSTRENG profile was determined using the projection method as discussed in section 4.2.2. These profiles generally had a length greater than the B31G assessment although the full profile was not always used in the RSTRENG analysis. The iterative nature of the RSTRENG method chose the most critical section of the corrosion defect so that adjacent plain pipe or shallow corrosion is not included in the failure pressure prediction. The form of longitudinal interaction embodied in RSTRENG is beneficial when assessing complex defects. For other assessments interaction rules require a great deal of interpretation when applied to complex defects.

The error in the B31G and RSTRENG predictions, calculated using equation (4.4.1), are shown in Figure 4.4.1 where:

$$\%\,Error = \frac{FP_{Experimental} - FP_{Predicted}}{FP_{Experimental}} \qquad (4.4.1)$$

The percent error is plotted as a function of maximum defect depth at the failure location although this may not have been the deepest defect on the pipe section. For example, several pipes failed in uncorroded regions although corrosion defects up to 39% of the wall thickness were present. All predictions were conservative with the RSTRENG predictions being less conservative and more consistent than the B31G predictions. Linear trend lines are plotted in Figure 4.4.1 indicating increased conservatism with increasing depth for the defects analyzed. This effect is more significant for the B31G predictions. Previous analysis of RSTRENG predictions for long, groove-like defects has indicated an opposite trend, decreasing conservatism with increasing depth (Cronin et al, 1996).

A statistical summary of the data in Figure 4.4.1 is shown in Table 4.4.1. Comparison of the standard deviations for each method indicates that the RSTRENG predictions are much more consistent. Normal probability plots of the percent error for the RSTRENG and B31G predictions are shown in Figures 4.4.2 and 4.4.3 respectively. These plots are a measure of the deviation from a normal distribution where a normal distribution would fall on the solid line plotted in the figures. Figure 4.4.2 indicates that the errors in the RSTRENG predictions are reasonably normal in distribution so that common statistical parameters can be used to describe the accuracy of the predictions. In contrast, Figure 4.4.3 shows that the errors in the B31G predictions are not normally distributed. The histogram plots for this data were also analyzed and showed that this distribution is skewed in the positive or conservative direction. Skewness can be calculated as shown in equation (4.4.2).

$$Skewness = S = \frac{n}{(n-1)(n-2)} \sum \left(\frac{x_j - \bar{x}}{s} \right)^3 \qquad (4.4.2)$$

The skewness for the RSTRENG percent error in prediction was 0.03 and for the B31G predictions is was 0.77. A skewness value of 0.0 indicates a symmetric distribution while positive values of skewness indicate the distribution is skewed towards values that are more positive. Another characterizing parameter is the kurtosis of the distribution which

describes the shape of a distribution (flat or peaked) relative to the normal distribution. A normal distribution has a kurtosis value of 0.0 while a flattened distribution has a negative kurtosis value. The kurtosis values calculated using equation (4.4.3) were –0.31 and -0.04 for the RSTRENG and B31G predictions respectively indicating the RSTRENG distribution is relatively flat.

$$Kurtosis = K = \left\{ \frac{n(n+1)}{(n-1)(n-2)(n-3)} \sum \left(\frac{x_j - \bar{x}}{s} \right)^4 \right\} - \frac{3(n-1)^2}{(n-2)(n-3)} \qquad (4.4.3)$$

These results are presented so that the standard deviation for each can be interpreted appropriately.

A more commonly quoted measure of the accuracy of the prediction is the failure ratio as defined in equation (4.4.4). The results are plotted in Figure 4.4.4 where ratios greater than 1.0 indicate a conservative prediction.

$$\text{Failure Ratio} = R_F = \frac{FP_{\text{Predicted}}}{FP_{\text{Experimental}}} \qquad (4.4.4)$$

Although this measure is commonly used, the failure ratio tends to have an increase in scatter for larger errors and decrease in scatter for smaller errors which may obscure trends in the data. In terms of statistical analysis, the residuals or difference between actual and predicted values is a more common means of verifying predictive methods. For further analysis purposes, the percent error in the prediction (normalized residual) will be considered.

4.4.1 Plain Pipe Analysis

It is useful to consider the application of the Plain Pipe solution (Section 3.2) to the tests in the database which failed in uncorroded areas. The plain pipe model assumes that failure in defect-free pipe occurs by geometric instability prior to reaching critical stress levels.

Table 4.4.2 shows the actual and predicted failure pressures for the plain pipe failures. The geometric instability method developed in Section 3.2 significantly overpredicts the failure pressure while other models generally underpredict the failure pressure. The use of a flow stress equal to 90% of the UTS as specified by Ritchie and Last produces good agreement. As discussed in Section 3.2, the failure of plain pipe is not expected to be stress-based. The failure of plain pipe involves large global plastic deformation which may not be adequately modeled by a flow stress, particularly for higher strength materials which are in common use today.

It is suggested that inhomogeneities in the material, or local variations in wall thickness led to failure of the pipe prior to the predicted instability pressure. It has been found through regression analysis that the use of 0.86 times the instability pressure produces good results for this grade of pipe.

4.4.2 Long Groove Model

Application of the Long Groove model (Section 3.3) to the database provides a lower bound estimate of the failure pressure by assuming that the defects can be considered as infinite length, uniform depth grooves, with a depth equal to the maximum defect depth. As discussed previously, this method will produce a conservative estimation of the failure pressure since all natural corrosion defects have some variation in depth so that the effective depth is less than the maximum defect depth. The percent error (equation 4.4.1) in the prediction is plotted as a function of defect depth in Figure 4.4.5. The B31G results are included for comparison. Trend lines plotted for both models have similar slopes while

the Long Groove model predictions are less conservative. It should be noted that the Long Groove solution is conservative for all defects considered, however it can be slightly non-conservative for plain pipe as indicated in Figure 4.4.5. This was discussed in section 4.4.1. The summary statistics (Tables 4.4.1 and 4.4.3) indicate that the Long Groove model has an average prediction error similar to RSTRENG while the scatter in the data is comparable to the B31G predictions. However, the failure pressure of these shallower defects significantly exceeds the maximum allowable operating pressure as shown in Figure 4.3.1.

4.4.3 Proposed Methods of Assessment

As discussed in Chapter 2, many other methods of corrosion assessment have been proposed. Two of these methods, PCORRC and the Ritchie and Last model (Stephens, 1997), were used to analyze the burst test database. The percent error as a function of maximum defect depth is plotted in Figures 4.4.6 and 4.4.7. The B31G results are plotted for reference and the data is summarized in Table 4.4.3.

Figure 4.4.6 indicates that PCORRC and B31G have similar trends with the PCORRC predictions being less conservative. However, there is an increase in the standard deviation of the data compared to B31G as shown in Tables 4.4.1 and 4.4.3.

The Ritchie and Last model (equation 2.2.5) includes an estimation of the flow stress based on the ultimate tensile strength of the material. This estimation leads to a higher flow stress than the original B31G approximation, producing higher predicted burst pressures than B31G. Although this modification produces less conservative results than B31G, Table 4.4.3 indicates that the standard deviation of the prediction errors is higher. The change in slope of the trend line in Figure 4.4.7 compared to B31G is due to the non-linear relationship between the material SMYS and ultimate tensile strength.

Both PCORRC and the Ritchie and Last model show a decrease in the average error in prediction due to the increased flow stress approximation, with PCORRC being the least conservative. Although this is an improvement in terms of the average prediction error,

both methods result in an increase in standard deviation of the prediction error. In addition, the trend shown in B31G of increasing conservatism with increasing depth is present in both methods. This trend may be considered reassuring from an assessment point of view since deeper defects present more of a concern. However, such a trend indicates these methods do not accurately model the corrosion defect behaviour. This effect is attributed to the representation of the corrosion defect in these models. PCORRC, the Ritchie and Last model and B31G all model corrosion defects based on the maximum defect depth and overall defect length. In comparison, the RSTRENG results (Figure 4.4.1) do not have a significant trend with defect depth and have less variance in the prediction error.

The consistency of the RSTRENG predictions suggests that it may be more appropriate to consider a modification to the flow strength approximation in RSTRENG. For example, the Ritchie and Last flow stress approximation of 90% of the ultimate tensile strength can be used as shown in equation (4.4.5) to create a Modified RSTRENG model.

$$p_f = \left(\frac{t}{r}\right)(0.9\times\sigma_{UTS})\left[\frac{1-\left(\frac{A}{A_0}\right)}{1-\left(\frac{A_0}{A}\right)M^{-1}}\right]$$

$$M = \sqrt{\left[1+0.6275\frac{l^2}{2rt}-0.003375\frac{l^4}{4r^2t^2}\right]} \quad \text{for} \quad \frac{l^2}{2rt} \le 50 \qquad (4.4.5)$$

$$M = \left(0.032\frac{l^2}{2rt}+3.3\right) \quad \text{for} \quad \frac{l^2}{2rt} > 50$$

The error in the failure pressure prediction using the Modified RSTRENG method is plotted as a function of maximum defect depth in Figure 4.4.8. The figure indicates that the lower variance of the RSTRENG method is maintained while reducing the average error. The original RSTRENG predictions are shown in Figure 4.4.1. A summary of the data is shown in Tables 4.4.1 and 4.4.3. Although the Modified RTSRENG method

produces more accurate results, the definition of the flow stress is somewhat arbitrary and may not be accurate when applied to higher grades of steel. In addition, some of the predictions are almost non-conservative.

The two-dimensional models proposed by Popelar (1993) and Klever (1995) are not discussed in detail since the Long Groove model developed in Section 3.3 has been shown to be an accurate two-dimensional model and has been applied to the database. The Long Groove model results in a variance and trend similar to B31G but can produce less conservative results. It should be noted that this model requires only the maximum defect depth and accurate material properties and as a result is easy to apply.

The British Gas Proposed Guidance model has not been assessed due to the unavailability of two constants used in the model. This model has a form similar to Stephen's model and quantifies the corrosion geometry with the maximum defect depth and length. The British Gas model is expected to produce results similar to the model proposed by Stephens.

RSTRENG was found to produce the most consistent results and only showed a slight trend towards increased conservatism for increasing defect depth. Predictions with the Modified RSTRENG method including a modification to the flow stress produced the most accurate results. However, this flow stress approximation may not be appropriate for higher strength materials not represented in this database.

4.5 FINITE ELEMENT MODELING OF COMPLEX CORROSION DEFECTS

As discussed in Chapter 2, many researchers have shown that two-dimensional and three-dimensional finite element analysis can be used to predict the failure pressure of simply shaped corrosion defects (Mok et al. Chouchaoui and Pick, Fu and Kirkwood). Application of three-dimensional finite element analysis using an incremental plasticity material model is considered in this section.

The defects analyzed by other authors to date have consisted of flat-bottomed machined defects and naturally occurring single pits. Although it seems intuitive that the

Finite Element method can be applied to complex shaped defects, this has not been validated. To assist in this validation the required model size, boundary conditions, mesh density, material properties and the failure criterion have been investigated for the complex corrosion geometries in the database.

4.5.1 Finite Element Analysis

To study the behavior of complex shaped corrosion defects and investigate the points listed above, corrosion patches on 25 different sections of pipe from the database described in section 4.2 have been analyzed using the Finite Element Method. Since the failure location was known prior to the analysis, only the corrosion in the vicinity of the failure was considered. The purpose of these analyses was to provide guidance on the application of the Finite Element Method, determine the accuracy of the method and to provide insight into the defect behaviour. In general, the group of defects was analyzed with the boundary defined by the interaction rules discussed in section 2.5. Fifteen of the tests were not analyzed using the Finite Element Method due to the size of the corrosion defects. Many were several pipe diameters in length so that the computation time for the analysis would have been unacceptably long. This is an important point since line pipe in service may contain a large number of defects making application of the Finite Element Method unrealistic due to the required computation time.

All models were analyzed using the commercial finite element code Abaqus (Hibbit et al., 1994). This code was chosen since it has been used successfully in the past to model simply shaped corrosion defects (Mok et al., Chouchaoui and Pick, Fu and Kirkwood). The non-linear geometry option was specified to accommodate the large deformations and three-dimensional, 20-noded brick elements with a reduced hybrid formulation were used as suggested by Chouchaoui (1993). The material was modeled as isotropic using the average material properties measured in the circumferential direction and an incremental plasticity model.

The pressure load was applied in increments using the Abaqus automatic incrementation procedure with a maximum allowable increment size of approximate 20% of the failure pressure. In general, large increments were only used during the early stages of loading where the response was primarily elastic. Manually specifying smaller increment sizes did not alter the results indicating the automatic incrementation procedure was appropriate.

Failure was predicted using a von Mises stress-based criterion as discussed in sections 2.2 and 3.1. As stated, initial failure is assumed to occur when the stress in the defect first exceeds the ultimate tensile strength of the material expressed as a true stress. Final failure of the defect occurs between the initial failure pressure and the pressure required for the critical stress to progress through the entire corrosion ligament. Initial failure occurs on the outside of the pipe, for external defects, and propagates through the thickness to the inside surface. Unlike simple defects, plasticity does not always progress radially due to the non-symmetric deformation in complex defects. To determine the initial failure pressure, the von Mises stress on the outside surface of the pipe was monitored until it exceeded the critical stress. Stress values for the finite element model were reported as averaged values extrapolated from the integration points to the nodes. Since Abaqus uses an automated incrementation procedure, the critical failure pressure generally occurred between two increments. In this case, the node with the highest stress was taken as the failure location, and the failure pressure was linearly interpolated between the two increments. Depending on the corrosion geometry, the von Mises stress can increase in an exponential manner near the failure pressure so that linear interpolation underpredicts the burst pressure for larger load increments. In these cases, the models were analyzed with smaller load increments near failure to provide a better approximation of the burst pressure. Final failure can occur by complete plastic collapse of the ligament (at the final failure pressure) or by fracture at some intermediate load level between the initial and final failure pressures. No attempt was made to calculate these values, however they may be approximated by the pressure where the critical stress is first exceeded on the inside surface of the defect.

4.5.2 Mesh Generation

One of the most difficult problems in the analysis of complex defects is creating the finite element mesh. Creation of the mesh in the corroded region is not suited to commercial modeling packages since the geometry is not easily defined. In contrast, it is necessary to reduce the mesh density away from the defect to reduce computing time and this is a common feature in commercial packages. A custom program was written to generate the mesh in the corroded region while a commercial package, MSC/Patran, was used to model and mesh the adjacent pipe. This led to a three-step procedure:

- A grid file was created from the original scanned surface data using the commercial software package Surfer (Golden Software, 1997). The grid file contains evenly spaced points representing the defect surface. The density of points in the longitudinal and circumferential directions can be varied by the user using triangulation with linear interpolation. The original data is used to create a patchwork surface of triangular faces where each face is defined by three of the original data points. The grid points are then determined from the triangular surfaces. This method was chosen since it preserves the original surface shape. Non-linear interpolation methods were also considered but found to result in unrealistic surface shapes in certain instances. If the chosen density of points in the grid file was the same as that in the original scanned data file, the original data points were used in the grid file. Creating the grid file also allowed only the corroded region of interest to be extracted from the original scanned surface data reducing the size of the finite element model. Image plots of the original scanned surface data and the grid file data for one defect are shown in Figures 4.5.1a and 4.5.1b.
- A custom program was written to read the corrosion surface data from the grid file and generate an input file for the Abaqus finite element program. Typically, the corrosion was scanned using a 0.1" (2.5 mm) grid in the longitudinal and circumferential directions. A 0.05" (1.2 mm) grid was used in some cases where the pit depth changed significantly over a small distance. The FE mesh was created with measured coordinates at the nodal points of 20-noded brick elements. Nodes around the outer perimeter of the corrosion patch were set to a depth of zero (full wall thickness pipe) so

that the corrosion patch surfaces and adjacent uncorroded pipe surfaces were matched. This intermediate input file was then pre-processed with Abaqus to create a neutral output file (Figure 4.5.1c) which the commercial meshing software, MSC/Patran, could read. The custom program also creates a MSC/Patran session file that is used to assist in the modeling of the uncorroded pipe surrounding the corrosion defect.

- The corrosion mesh was read into MSC/Patran and the session file was used to create the geometry of the plain pipe surrounding the defect (Figure 4.3.1d). The symmetry conditions that were assumed in the circumferential direction consider that an identical defect occurs at 180 degrees to the existing defect. In addition, the symmetry conditions assumed in the longitudinal direction consider that identical defects occur at a distance of one pipe diameter on either side of the defect. The effect of the model extent in the circumferential and longitudinal directions was investigated. It was found that the defect behaviour was not affected by the boundary conditions when the pipe was modeled with a circumferential extent of 180 degrees and a longitudinal length of ½ pipe diameter on either side of the defect (refer to section 4.3.3).

Unless otherwise stated, the above model dimensions were used with the ends of the pipe fixed in the longitudinal direction such that plain strain conditions would be created in plain pipe. The effect of the longitudinal conditions was investigated by modeling the end load produced by endcaps but no significant variation in the burst pressure was found compared to the assumed plain strain conditions. Roberts (1998) found that the burst pressure for simple chemically machined defects decreased only a small amount from closed end to plane strain conditions.

4.5.3 Model Size / Mesh Refinement

When modeling complex shaped corrosion it is important to accurately model the local geometry (corrosion patch) as well as the global geometry (surrounding plain pipe)

and boundary conditions. Mesh refinement was considered in two stages: the number of elements through the thickness of the corrosion patch and the surface element density. The effect of the global circumferential and longitudinal extent of the model was also investigated.

Several analyses were used to determine the effect of increasing the number of elements through the thickness of the corrosion patch. In general, it was found that increasing the number of elements through the thickness resulted in a small decrease in the predicted failure pressure. This is similar to the result for the single pit analysis; however, the magnitude of the change depends on the specific corrosion geometry. The von Mises stress at the critical location is plotted as a function of internal pressure in Figure 4.5.2. Comparing the results indicates very little difference in the predictions. The stress history is slightly different between the yield and critical stresses when only one element is used through the thickness. This is related to yielding through the thickness of the ligament and is convergent with two or more elements through the thickness. However as shown in Figure 4.5.3, the failure pressure predictions are all within approximately 1.0%. Two elements were used through the wall thickness for all complex corrosion analyses to better model the yielding phenomenon while minimizing the required computing time. This also resulted in an element aspect ratio close to 1.0 for the typical surface mesh densities used.

The number of elements on the surface of the mesh was both halved and doubled. It was found that halving the number of elements changed the results while doubling did not. This is explained by the fact that accurate representation of the corrosion geometry is reduced when the number of elements is reduced. When the number is increased, additional points are interpolated between the existing ones and the geometry is not changed. This implies that the mesh needs to be fine enough to model the real geometry but further reductions will not improve the FE result. It is important to note that mesh convergence refers to convergence of the finite element model and does not necessarily relate to the accuracy of the prediction. This can only be determined by comparison to experimental data. However, analysis of single pit defects has suggested that relatively few elements are needed to model the defect. In general, the accuracy of the model is

determined by the accuracy of the corrosion measurements and the mesh representing the corrosion defects.

To accurately simulate the experiments, a full 360° of the pipe and the full length of the test specimen, including endcaps, should be modeled. In practice, only enough of the pipe needs to be modeled so that the location of the boundary conditions does not influence the solution at the defect. Experimental and FE results have shown that defects only need to be separated by a few wall thicknesses of full thickness material to act independently (Chouchaoui, 1993, Cronin, Roberts and Pick, 1996, Fu and Kirkwood, 1995). However, through the symmetric boundary conditions all analyses of complex corrosion defects were effectively conducted conservatively with a length equal to one pipe diameter between adjacent defects.

Three different circumferential extents were considered: 85° (reduced), 180° (half pipe) and 360° (full pipe). Boundary conditions for the 85° model allowed only radial expansion, as would be the case in plain pipe. The results have shown that for the case of a symmetric, deep, small defect (such as a single pit) this is a reasonable assumption. This is primarily due to the symmetric deformation of the pipe in general, and the localized, symmetric deformation of the pit. When considering complex corrosion, large deformations may not be localized and will generally not be symmetric. The reduced model boundary conditions create excess restraint on the model and resulted in an increase in the predicted burst pressure that is dependent on the corrosion geometry. Modeling the full pipe resulted in a decrease in burst pressure of approximately 0.5% compared to the half pipe. Therefore, all complex corrosion finite element analyses were conducted with a circumferential extent of 180°. Modeling the endcaps produced an increase in burst pressure of approximately 2% compared to the assumption of plain strain in the longitudinal direction which was used in all analyses.

4.5.4 Material Model: Incremental vs. Deformation Plasticity

As discussed in section 3.3.2, use of the deformation plasticity model can greatly reduce computation time, particularly for models with a large number of elements. The results from one model (defect BCG-08E) are shown in Figure 4.5.4. It should be noted that standard formulation elements were used with the deformation plasticity model while reduced hybrid elements were used with the incremental plasticity model. It was found that the reduced hybrid formulation elements tended to be less stiff and underpredicted the burst pressure. The predicted failure pressures for the incremental and deformation plasticity models are consistent but the model response between yielding and final failure differs. This is related to the local deformation in the ligament that includes bending and non-uniform yielding.

In general it has been found that the deformation plasticity material model produces burst pressure predictions in agreement with the incremental plasticity material model, however, the calculated load history may differ due to the assumptions in each material model. The more general incremental plasticity model was used in all analyses.

4.5.5 Finite Element Analyses

The results of each finite element analysis are presented in two figures. The first shows an image plot of the defect with the corresponding defect profile determined using the Projection Method. The actual failure location is indicated by the intersection of the longitudinal and horizontal lines in the image plot. The predicted failure location is shown with a white 'X' on the plot. The second figure shows a surface plot of the defect, with the predicted and actual failure locations indicated. A plot of the von Mises stress history as a function of internal pressure is also shown in this second figure. The stress is plotted for the critical point in the defect which is the first location where the von Mises stress exceeds the critical stress for the material. The intersection of the von Mises stress history and horizontal critical stress line defines the failure pressure.

At least one defect from each type of pipe tested was modeled to obtain a representative set of results. Each test is listed below with references to the figures and notes on the model, where applicable.

- SOL-02 (failure pressure = 3535 psi, predicted failure pressure = 3832 psi)
  Figures 4.5.5a and 4.5.5b.
  This pipe section failed at a pressure similar to the experimentally measured plain pipe failure pressure for this material. The finite element method generally overpredicts the failure pressure as the failure approaches that of plain pipe.
- SOL-04 (failure pressure = 3351 psi, predicted failure pressure = 3419 psi)
  Figures 4.5.6a and 4.5.6b.
  This defect actually had a larger circumferential dimension than was modeled. This simplification led to an error in the predicted failure location.
- SOL-06 (failure pressure = 3659 psi, predicted failure pressure = 3365 psi)
  Figures 4.5.7a and 4.5.7b.
- SOL-10 (failure pressure = 3471 psi, predicted failure pressure = 3321 psi)
  Figures 4.5.8a and 4.5.8b.
- SOL-11 (failure pressure = 3154 psi, predicted failure pressure = 3408 psi)
  Figures 4.5.9a and 4.5.9b.
  This defect actually had a larger circumferential dimension than was modeled. This simplification led to an error in the predicted failure location.
- SOL-12 (failure pressure = 3127 psi, predicted failure pressure = 3690 psi)
  Figures 4.5.10a and 4.5.10b.
  The maximum defect depth at the failure location was relatively shallow so that this the failure mode was approaching that of plain pipe. The finite element method generally overpredicts the failure pressure as the failure approaches that of plain pipe.
- ESS-01 (failure pressure = 1412 psi, predicted failure pressure = 1370 psi)
  Figures 4.5.11a and 4.5.11b.
- NOR-02 (failure pressure = 2850 psi, predicted failure pressure = 2619 psi)

Figures 4.5.12a and 4.5.12b.

This defect was relatively shallow. Over prediction of the burst pressure by the finite element method may be related to the fact that the failure pressure is near that of plain pipe which is typically overestimated by the finite element method.

- RLK-01 (failure pressure = 1370 psi, predicted failure pressure = 1154 psi)

  Figures 4.5.13a and 4.5.13b.

  This defect had a length of 35.5 inches (total defect profile, Figure 4.5.13a). Only a 7-inch long section at the failure location was modeled as shown in the local defect profile in Figure 4.5.13a. For this defect, the model had a longitudinal length of 7 inches with symmetry conditions at ends of the defect. The full circumference of the pipe was modeled. This approximation is valid for a long, uniform depth groove but is conservative for a defect with varying depth as discussed in the Long Groove model.

- RLK-02 (failure pressure = 1143 psi, predicted failure pressure = 1262 psi)

  Figures 4.5.14a and 4.5.14b.

  This defect had a length of 56.4 inches (total defect profile, Figure 4.5.14a). Only a 7-inch long section at the failure location was modeled as shown in the local defect profile in Figure 4.5.14a. For this defect, the model had a longitudinal length of 7 inches with symmetry conditions at ends of the defect. Note that there is an uncorroded region on the left side of the profile (Figure 4.5.14a) which leads to a non-conservative calculation due to the assumption that the uncorroded material occurs at regular intervals along the corrosion profile. The total defect profile indicates that this is not the case for the actual defect. The full circumference of the pipe was modeled. This approximation is valid for a long, uniform depth groove but is non-conservative when addition full-thickness material is assumed to occur in the profile due to the symmetry conditions.

- RLK-03 (failure pressure = 1423 psi, predicted failure pressure = 1105 psi)

  Figures 4.5.15a and 4.5.15b.

This defect had a length of 54.0 inches (total defect profile, Figure 4.5.15a). Only a 6.4 inch long section at the failure location was modeled as shown in the local defect profile in Figure 4.5.15a. For this defect, the model had a longitudinal length of 6.4 inches with symmetry conditions at ends of the defect. The full circumference of the pipe was modeled. This approximation is valid for a long, uniform depth groove but is conservative for a defect with varying depth as discussed in the Long Groove model.

- BCG-02 (failure pressure = 2000 psi, predicted failure pressure = 1984 psi)
  Figures 4.5.16a and 4.5.16b.
- BCG-03 (failure pressure = 1988 psi, predicted failure pressure = 2050 psi)
  Figures 4.5.17a and 4.5.17b.
  This defect was scanned at a resolution of 0.1" but the grid file and Finite Element mesh was created with a 0.05" resolution to more accurately represent the size of the defect.
- BCG-04 (failure pressure = 2201 psi, predicted failure pressure = 2120 psi)
  Figures 4.5.18a and 4.5.18b.
  The Finite Element Method predicted failure to occur in an adjacent, deeper pit.
- BCG-05 (failure pressure = 2174 psi, predicted failure pressure = 2183 psi)
  Figures 4.5.19a and 4.5.19b.
- BCG-06 (failure pressure = 2078 psi, predicted failure pressure = 1936 psi)
  Figures 4.5.20a and 4.5.20b.
  This defect consisted of a number of interacting single pits. Failure was predicted in an adjacent pit with a depth similar to the actual failure location.
- BCG-07 (failure pressure = 1849 psi, predicted failure pressure = 1838 psi)
  Figures 4.5.21a and 4.5.21b.
- BCG-08 (failure pressure = 2040 psi, predicted failure pressure = 2147 psi)
  Figures 4.5.22a and 4.5.22b.
- BCG-09 (failure pressure = 1939 psi, predicted failure pressure = 1831 psi)

Figures 4.5.23a and 4.5.23b.

This defect consisted of a number of interacting single pits. Failure was predicted in an adjacent, deeper pit.

- NOV-01 (failure pressure = 1556 psi, predicted failure pressure = 1476 psi)
  Figures 4.5.24a and 4.5.24b.
- NOV-04 (failure pressure = 1582 psi, predicted failure pressure = 1632 psi)
  Figures 4.5.25a and 4.5.25b.
  The predicted and actual failure locations had similar behaviour and there was only a small difference in predicted burst pressure for the two locations.
- NOV-06 (failure pressure = 1669 psi, predicted failure pressure = 1566 psi)
  Figures 4.5.26a and 4.5.26b.
- TCP-01 (failure pressure = 1567 psi, predicted failure pressure = 1555 psi)
  Figures 4.5.27a and 4.5.27b.
  Failure was predicted to occur in a deeper single pit near the failure location.
- TCP-02 (failure pressure = 1531 psi, predicted failure pressure = 1521 psi)
  Figures 4.5.28a and 4.5.28b.
- TCP-03 (failure pressure = 1330 psi, predicted failure pressure = 1378 psi)
  Figures 4.5.29a and 4.5.29b.

As with other assessment methods, the finite element results were evaluated based on the percent error in the predicted failure pressure. The results are shown in Table 4.5.1 and plotted as a function of maximum pit depth in Figure 4.5.30. For all the results, the average error in prediction is –0.18% with a standard deviation of 8.45%. The standard deviation seems somewhat high in comparison to the other models. Most of the larger prediction errors are associated with relatively shallow defects (less than 30% depth). As discussed above, failure pressures for these shallow defects are similar to those for plain pipe. The finite element method has been shown to overpredict the failure pressure for plain pipe based on the instability pressure. In addition, plotting the prediction error as a function of test date yields some interesting results. Figure 4.5.31 shows the error in the finite element prediction arranged in chronological order. The new surface scanner was

implemented after analysis number 10 (RLK03). It can be seen that there is a significant reduction in the scatter of the data beyond this point. However, it must be pointed out that the tests using the planar scanner incorporate two types of pipe so that some of this scatter could be related to the pipe material.

Elimination of the data prior to the new surface scanner results in an average error of 0.1% with a standard deviation of 4.1%. These results are shown in Figure 4.5.32 with the corresponding RSTRENG and B31G analyses.

It has been found that the Finite Element method is much more sensitive to local changes in defect depth than RSTRENG. This is related to the fact that, in the Finite Element Model, the local stresses are primarily determined by the local geometry, with the surrounding geometry as a secondary effect. In contrast, RSTRENG tends to average the defect depths so that a small error in a deep measurement does not appear as critical.

4.5.6 Internal vs. External Corrosion

Past analyses have shown that an internal corrosion defect will fail at approximately the same pressure as an external corrosion defect of the same geometry in the same material (Chouchaoui, 1993, Batte et al., 1997). Although this has been shown for regularly shaped defects, it has not been proven for more complex shaped natural corrosion.

At present, one corrosion defect (BCG08E) has been analyzed as both an internal and an external defect. Both defects had the same dimensions, material properties and pipe dimensions. The predicted failure pressure based on the von Mises stress in the ligament differed by 1.2% based on the failure pressure of the external corrosion.

Chapter 5

Prediction of failure pressure for complex corrosion defects

The accurate prediction of the failure pressure of a corrosion defect requires accurate defect measurements and material properties. In this chapter, a new method of assessment is developed which makes use of detailed corrosion data and removes the conservatism embodied in the currently accepted evaluation procedures. This method has been called the Weighted Depth Difference Method and is implemented using a computer program called CPS (Corroded Pipe Strength). The experimental database presented in Chapter 4 is used to develop a statistical approach for this proposed model which is presented in a three-level assessment procedure in Chapter 6. For cases where detailed measurements or material properties are not available, it is suggested that the currently accepted codes be used in a two-level procedure with the defect reliability calculated using the proposed statistical model.

5.1 WEIGHTED DEPTH DIFFERENCE MODEL TO PREDICT THE FAILURE PRESSURE OF CORROSION DEFECTS

The most important advance in the assessment of corroded pipelines has been the introduction of the modified B31G or RSTRENG criterion. As discussed in Chapter 2, RSTRENG makes use of detailed defect measurements and an iterative process to select the most critical area in the corrosion defect. This can consider aspects of the interaction of defects in the longitudinal direction and is important since interaction rules in the circumferential direction are well defined while those in the longitudinal direction are still open to debate. In contrast, B31G (and its modifications) evaluate the defect as a whole and do not specifically identify the critical location within the corrosion defect. Although RSTRENG does not identify a specific failure location, it does select a specific region within the corrosion defect which is considered the most critical area. One common improvement to B31G quoted by many authors is the modification of the Folias factor from the 2-term approximation used in B31G to a 3-term approximation with a linear curve fit for larger values of $\frac{l^2}{2rt}$. This does not result in a significant change in the predicted burst pressure but does remove the length limit on the Folias factor imposed in B31G.

It must be pointed out that both RSTRENG and B31G contain the essential features of corrosion defect behaviour and have been used successfully for many years. Comparison with the authors' experimental database has shown the prediction error to vary with defect depth and length. In addition, the definition of flow stress as SMYS + 10000 psi (6.9 MPa) also provides a varying degree of conservatism, which is believed to decrease for higher strength steels. This is a concern since the use of higher strength steels is becoming common. Although RSTRENG has always proven to be conservative, the degree of conservatism has been unknown.

There is value in defining a new assessment method, which removes some of the conservatism and ensures equal conservatism for all corrosion geometries and materials. This section will describe such a development. Simplicity of application must be an

essential feature to provide an advantage over RSTRENG. In addition, the issue of automated assessment must be considered and is discussed in this Chapter.

In order to remain consistent with current evaluation methods, a new model has been developed which utilizes the RSTRENG defect profile but also includes the actual material properties. The development of a new model requires key features, such as the failure pressure limits, to be quantified. The proposed model also incorporates a weighting scheme to account for the behaviour of finite length, varying depth defects and the interaction effect of adjacent defects.

5.1.1 Weighted Depth Difference (WDD) Model

The failure pressure for any corrosion defect can be bounded by the failure pressure of plain pipe (upper bound) and the failure pressure of an infinite length, longitudinally oriented, uniform depth groove (lower bound). These bounds assume a defect of limited circumferential width, which is typical of natural corrosion for reasons discussed in section 4.1. Based on these limits, the failure pressure of a corrosion defect can be expressed as a function of the plain pipe and long groove failure pressures (equation 5.1.1),

$$p_{Failure} = p_{Long\,Groove} + \left[p_{Plain\,Pipe} - p_{Long\,Groove} \right] \times g \qquad (5.1.1)$$

where the parameter g varies from 0.0 to 1.0 and is a function of the corrosion and pipe geometry. Note that the material strength is included in the failure pressure predictions for the plain pipe and the pipe with a long groove. Observations and analysis of real corrosion defects suggest the function g should incorporate some specific features:

- The failure of a corrosion defect initiates at some point which is not necessarily the deepest point in the defect. The method should consider each point in the

defect to determine the failure location. The point at which the method is being applied will be known as the evaluation point.

- The effect of adjacent corrosion defects diminishes with increasing longitudinal separation. Since the pipe is a continuous body, it should be expected that the effect of adjacent wall loss would be weighted according to the longitudinal distance from the evaluation point.
- The corrosion defect can be considered as metal loss projected onto the longitudinal axis of the pipe. The profile can be restricted using circumferential and longitudinal interaction rules to reduce the area of the pipe to be considered. However, it should be noted that in the proposed method these rules are not necessary for defect evaluation since the proposed method incorporates longitudinal interaction. Since the defect is projected on to a plane, all calculations are based on area, not volume loss. The river bottom approach used in RSTRENG is similar and both incorporate the fact that the circumferential dimension does not affect the failure pressure of corrosion defects.

To model the behaviour of a corrosion defect it is necessary to consider the actual corrosion geometry. In RSTRENG and B31G, the geometry effect appears as the ratio of the remaining ligament area to the original area. This ratio is recognized as an appropriate means of quantifying the effect of the corrosion defect and is expressed in equation (5.1.2) where dz is an infinitesimal length in the longitudinal direction (Figure 5.1.1).

$$\frac{Ligament\ Area}{Original\ Area} = \frac{(t-d)\,dz}{t\,dz} = 1 - \frac{d}{t} \tag{5.1.2}$$

At an evaluation point (Figure 5.1.1) the failure pressure will be influenced by the adjacent corrosion weighted by the distance it is from the evaluation point. A hyperbolic secant function was chosen as a function to weight the effect of corrosion at a normalized

longitudinal distance H from the evaluation point. This function (equation 5.1.3) is appropriate since it has an exponential decay about the evaluation point as shown in Figure 5.1.2. Thus, increasing distance from the evaluation point results in a decreased weight for adjacent areas of corrosion. It should be noted that other functions with similar shape, such as the normal distribution, could have also been used. The hyperbolic secant was chosen for ease of evaluation.

$$\operatorname{sech}(H) = \frac{2}{e^{H} + e^{-H}}$$
$$\textit{where} \tag{5.1.3}$$
$$H = \frac{L}{\textit{Normalization Factor}}$$

In equation (5.1.3), H represents the normalized longitudinal separation of the corrosion from the evaluation point. The Folias factor (equation 2.1.1) suggests that length can be normalized by the factor $\sqrt{Dt}$. This factor was also used by Batte (1997). Stephen's (1997) (equation 2.2.3) uses a normalization factor of $\sqrt{r(t-d_{max})}$ which is based on the maximum defect depth. Analysis of finite element results indicated the latter is more appropriate when the pipe diameter, not the radius, is considered. Thus the assumed normalization factor is $\sqrt{D(t-d_{max})}$ which leads to the weighting function:

$$\text{sech(H)} = \text{sech}\left[\frac{L}{\sqrt{D(t-d_{Max})}}\right] \tag{5.1.4}$$

where L is the distance to the current depth measurement location (z) from the evaluation point ($z_{Evaluation}$-z) (Figure 5.1.1). As assumed in RSTRENG and B31G, the circumferential

extent of the defect is neglected and the corrosion profile is found by projecting the corrosion defects on to the longitudinal axis (Figures 4.2.10 and 4.2.11).

The effect of adjacent corrosion on the evaluation point can be described in terms of the difference in the remaining ligament ratio as shown in equation (5.1.5).

$$Depth\ Difference = \left[1-\frac{d}{t}\right]-\left[1-\frac{d_{Evaluation}}{t}\right] \tag{5.1.5}$$

A positive depth difference is due to shallower adjacent corrosion which provides a strengthening effect while a negative depth difference results in a reduction in strength. The effect of corrosion at a distance L from the evaluation point can be described by a weighted depth difference (WDD) evaluated by combining equations (5.1.4) and (5.1.5) into equation (5.1.6).

$$\begin{aligned} WDD &= \operatorname{sech}\left[\frac{L}{\sqrt{D(t-d_{Max})}}\right]\left[\left(1-\frac{d}{t}\right)-\left(1-\frac{d_{Evaluation}}{t}\right)\right] \\ &= \operatorname{sech}\left[\frac{z_{Evaluation}-z}{\sqrt{D(t-d_{Max})}}\right]\left[\left(1-\frac{d}{t}\right)-\left(1-\frac{d_{Evaluation}}{t}\right)\right] \end{aligned} \tag{5.1.6}$$

Here, z is the current position and $z_{Evaluation}$ is the location of the evaluation point (Figure 5.1.1) from an arbitrary origin for z.

The value of the **WDD** for the entire defect with respect to the evaluation point can be determined by integrating from -∞ to +∞ in the longitudinal direction.

$$Defect\ WDD = \int_{-\infty}^{+\infty}\left\{\operatorname{sech}\left[\frac{z_{Evaluation}-z}{\sqrt{D(t-d_{Max})}}\right]\left[\left(1-\frac{d(z)}{t}\right)-\left(1-\frac{d_{Evaluation}}{t}\right)\right]\right\}dz \tag{5.1.7}$$

where the defect depth can be described as a function of z.

In practice, a defect is characterized by a number of depth measurements which are normally made at uniform intervals along the length of the defect. The corrosion defect can then be approximated by stepwise changes in depth as shown in Figure 5.1.3 where Δz is the distance between adjacent measurements. This will be termed the CPS corrosion profile. Increased accuracy of the corrosion profile representation will depend on an increased number of measurements, similar to the RSTRENG method.

For a set of **n** measurements, the effect of the corrosion can be evaluated by approximating the integral as a summation and summing the **WDD** for the measurements as shown in equation (5.1.8).

$$SumWDD = \sum_{i=1}^{i=n} WDD = \sum_{i=1}^{i=n} \left\{ \operatorname{sech}\left[\frac{z_{Evaluation} - z_i}{\sqrt{D(t - d_{Max})}} \right] \left[\left(1 - \frac{d}{t}\right) - \left(1 - \frac{d_{Evaluation}}{t}\right) \right] \Delta z \right\} \qquad (5.1.8)$$

For defects with uniform depth, such as a long groove, equation (5.1.8) is equal to zero. Similarly, for defects with no depth (plain pipe) SumWDD is zero. For real corrosion defects, equation (5.1.8) can take on values between 0.0 and some maximum (MaxWDD) which corresponds to the weighted difference of plain pipe with respect to the current evaluation depth. This maximum weighted difference is determined from equation (5.1.9) where the depth is set to 0.0 corresponding to plain pipe, at all locations except the evaluation point.

$$MaxWDD = \sum_{i=1}^{i=n} \left\{ \operatorname{sech}\left[\frac{z_{Evaluation} - z_i}{\sqrt{D(t - d_{Max})}} \right] \left[\left(1 - \frac{0.0}{t}\right) - \left(1 - \frac{d_{Evaluation}}{t}\right) \right] \Delta z \right\} \qquad (5.1.9)$$

If the function g is defined as the ratio of the sum of weighted depth difference to the maximum sum of the weighted depth difference (equation 5.1.10), it can theoretically vary between 0.0 and 1.0 as required.

$$g = \frac{SumWDD}{MaxWDD} \tag{5.1.10}$$

A value of 1.0 for g is a theoretical limit, which is not achieved for real defects. As the defect depth decreases and the wall thickness approaches that of plain pipe, the long groove solution converges to the plain pipe solution. Substituting equation (5.1.10) into equation (5.1.1), the failure pressure of a corrosion defect, evaluated at a specific point, is:

$$p_{Failure} = p_{Long\,Groove} + \left[p_{Plain\,Pipe} - p_{Long\,Groove} \right] \times \frac{SumWDD}{MaxWDD} \tag{5.1.11}$$

Equation (5.1.11) must be evaluated at each point in the defect to determine the location with the minimum failure pressure. For the case of single pits, this will always occur at the deepest location in the pit. However, this may not be the case for natural corrosion defects where failure can initiate at locations other than the deepest point in the defect depending on the geometry of the surrounding corrosion.

5.1.2 Corrosion Extent and Defect Interaction

One of the important features of the weighted depth difference method is that it considers the entire defect so that the weighting method includes the interaction of adjacent defects. Recall that equation (5.1.7) was evaluated from $-\infty$ to $+\infty$ so that all defects in the pipe are considered as potentially interacting with the current evaluation point. In reality, the hyperbolic secant function decreases (approximately) to zero within a finite distance of the evaluation point as seen in Figure 5.1.2. This can be investigated by considering the integral of the hyperbolic secant term as shown in equation (5.1.12).

$$\int_{-\infty}^{+\infty} \operatorname{sech}(H)dz = 2\int_{0}^{+\infty} \operatorname{sech}(H)dz = 2\left[2\tan^{-1}\left(\exp(H)\right)\right]_{0}^{+\infty} \qquad (5.1.12)$$

$$where\ H = \frac{z}{\sqrt{D(t-d_{Max})}}$$

Since the function is symmetric about the point H=0, the value of the integral from -∞ to +∞ is equal to twice the value of the integral from 0 to +∞. The value of the integral is plotted in Figure 5.1.4 and varies from a value of π at H=0 to a value of 2π at H=+∞. Also plotted in the figure is the percent difference between the integral evaluated at the given distance and the integral value at infinity. At a normalized distance of H=10.0, the percent error is approximately 0.003%. Thus equation (5.1.7) can accurately be represented as:

$$Defect\ WDD = \int_{H=-10}^{H=+10} \left\{ \operatorname{sech}[H]\left[\left(\frac{1-d(z)}{t}\right) - \left(\frac{1-d_{Evaluation}}{t}\right)\right]\right\} dz \qquad (5.1.13)$$

To ensure that the sums of the weighted depth difference (equations 5.1.8 and 5.1.9) are consistent, a length of plain pipe (Figure 5.1.5) with length equal to $10\sqrt{D(t-d_{Max})}$ is added to each side of the corrosion defect. The extension of plain pipe is added to each end of the defect to ensure that the integral or sum of the weighted depth difference is not affected by the finite length of the defect. Figure 5.1.5 shows an example calculation for a single pit 65% of the wall thickness in depth and 20 mm (0.80") in length. The percent error in the predicted burst pressure, relative to a very long extension of plain pipe, is plotted as a function of shorter extensions of plain pipe on either side of the defect. For an extension length of $10\sqrt{D(t-d_{Max})}$ (H=10) the percent error is 0.0004 indicating the summation has converged in terms of the length of the defect and adjacent plain pipe.

To investigate the accuracy of the weighted depth difference model, single pit defects were analyzed. Due to the iterative nature of this method, it was implemented using a computer program called CPS (Corroded Pipe Strength). As in Chapter 3 the

corrosion factor of the pits, which relates to the defect geometry and Folias factor, was kept constant while the pit depth was varied. The results are plotted for a corrosion factor of 0.938 in Figure 5.1.6. As previously shown in Figure 3.4.12, RSTRENG predicts no change in the failure pressure while the Finite Element analyses show decreasing failure pressure with increasing depth. The CPS results are plotted as a solid line and are in agreement with the Finite Element results. This example indicates that the CPS method characterizes the behaviour of single pits better than RSTRENG.

Application of the CPS program to the experimental database resulted in an average error in prediction of 3.1% with a standard deviation of 6.5%. The results are shown in Table 5.1.1. The individual results are plotted as a function of maximum defect depth in Figure 5.1.7. This model utilizes the long groove failure pressure as predicted by the Long groove solution. However, the plain pipe failure pressure has been approximated as 0.86 times the predicted instability pressure as discussed in Section 4.2 for the pipes which failed in uncorroded areas. Investigation of this approximation is shown in Figure 5.1.8 where the plain pipe failure pressure scale factor was varied from 0.6 to 1.0. The figure shows that the average percent error is a linear function of this quantity and is approximately zero at a scale factor of 0.88. The standard deviation varies in a non-linear manner and is a minimum for a scale factor of 0.74.

Figure 5.1.9 shows a normal probability plot of the percent error in the CPS predictions which indicates the distribution is nearly normal. The Kurtosis was calculated to be –0.74 compared to a value of –0.31 for RSTRENG. This indicates that the CPS distribution is flatter than the RSTRENG distribution. The CPS skewness was found to be 0.13 indicating that the percent error distribution is skewed towards the positive or conservative direction. The skewness value for RSTRENG was 0.03 implying that this distribution was more symmetric.

5.2 STATISTICAL ANALYSIS OF THE FAILURE PRESSURE PREDICTION MODELS

It has been shown that the Finite Element, CPS and RSTRENG models provide the most accurate burst pressure predictions so these models are analyzed in detail. The B31G model is also included since it is the basis for currently accepted corrosion assessment procedures. Note that the Finite Element results are considered as two data sets. The first, referred to as FE-All, considers the results from all Finite Element analyses. The second set, FE-New Scanner, considers only those tests where the 3-D scanner was used to map the defects. It was shown in Section 4.3 that the precision of the Finite Element predictions improved significantly after the introduction of this new scanner. The following discussion is based on the tests reported in the University of Waterloo experimental database and should not be extended to different grades of pipe without further investigation.

It has long been recognized that B31G and RSTRENG contain 'built-in' factors of safety and result in conservative burst pressure predictions. This degree of conservatism can be investigated using the experimental database. One important statistical measure of the models is the probability of making a non-conservative burst pressure prediction since this provides insight into the conservatism embodied in the model. As shown with the normal probability plots in Figures 4.4.2 and 5.1.9 for the percent error (equation 5.2.1), the RSTRENG and CPS predictions are normally distributed. This is also true for the Finite Element results.

$$\%Error = \frac{FP_{\text{Experimental}} - FP_{\text{Predicted}}}{FP_{\text{Experimental}}} \tag{5.2.1}$$

Although Figure 4.4.3 indicates the B31G percent errors deviate from a normal distribution they will be assumed to follow a normal distribution for comparison to the other models. With a normal distribution for all models, the percent errors and the associated variability can be represented by a mean and standard deviation. A conservative prediction occurs for

cases in which the predicted failure pressure is lower than the actual failure pressure (i.e. the percent error is greater than or equal to zero). However, it is more appropriate to consider the probability of failure. The probability of this event occurring can be calculated with the integral of the normal density function shown in equation (5.2.2a) where **X** represents the percent error. Note that σ^2 is the variance of the distribution which we assume to be equal to the square of the sample standard deviation (s).

$$\text{Prob}(X<0) = \int_{-\infty}^{0} f(x,\mu,\sigma)dx = \int_{-\infty}^{0} \frac{1}{\sqrt{2\pi}\sigma} e^{-\left(\frac{(x-\mu)^2}{2\sigma^2}\right)} dx \qquad (5.2.2a)$$

$$= \text{Probability of Failure}$$

Recall X: $N(\mu,s^2)$

Define Q:N(0,1) → A standard normal distribution

then (5.2.2b)

$$Q = \frac{X-\mu}{\sigma}$$

$$\text{(Defect Reliability)} = \text{Prob}(X>0) \qquad (5.2.2c)$$

$$= 1.0 - [\text{Prob}(X<0)]$$

In general, equation (5.2.2a) is evaluated using statistical software or printed tables. The transformation shown in equation (5.2.2b) allows the normal distribution X to be defined in terms of the standard normal distribution Q. This is beneficial since evaluations of the integral shown in equation (5.2.2a) are available in tabular form for the standard normal distribution. An alternate means of expressing the variability in failure pressure is the defect reliability as shown in equation (5.2.2c). However, this value is not commonly used since typical values for the probability of failure are very small so that the defect reliability is approximately 1.0.

The mean and standard deviation of the percent errors for each method are summarized in table 5.2.1. The probability of a non-conservative prediction, determined from the integral of the normal density function, is also shown along with the probability of a conservative prediction for each evaluation method. It can be seen that both B31G and RSTRENG contain a large degree of conservatism since the probabilities of non-conservative predictions are 0.014 and 0.001 without considering any additional factor of safety. In contrast, the probability of a non-conservative prediction using the CPS method is 0.317 implying the CPS method is less conservative. The probability of a non-conservative prediction from the Long Groove solution is not quoted since this is a lower bound solution. Ideally, an accurate method should have a probability of 0.50, as is the case with the Finite Element results. It should be noted that minimizing the variability is also important.

As shown in Table 5.2.1, the variability for all of the Finite Element results is relatively high, while the variability for the Finite Element results obtained using the new scanner is the lowest of all methods considered. The lower variability results in a lower probability of failure (more accurate prediction) for a given operating pressure.

To this point, the failure pressure prediction model accuracy has been investigated using the percent error based on the actual failure pressure (equation 5.2.1). Although this is an effective measure of the model accuracy relative to the experimental database, it is difficult to include in a statistical analysis due to the incorporation of the actual failure pressure in both the numerator and denominator. It is beneficial to consider the data in a different manner for the purpose of probabilistic failure prediction. In addition, an error quantification that is normally distributed is necessary to simplify this analysis.

Several additional methods of error quantification were considered as shown in equations (5.2.3) to (5.2.5):

$$\%Error_{\text{Predicted}} = \frac{FP_{\text{Experimental}} - FP_{\text{Predicted}}}{FP_{\text{Predicted}}} \tag{5.2.3}$$

$$Failure\ Ratio = \frac{FP_{Experimental}}{FP_{Predicted}} \tag{5.2.4}$$

$$\text{Raw Residual} = FP_{Experimental} - FP_{Predicted} \tag{5.2.5}$$

Each of these methods was applied to the failure pressure predictions from the B31G, RSTRENG, CPS and Finite Element models. It was found that the error expressed in equation (5.2.1) was the most normally distributed and had the lowest variance in all cases. The raw residual (equation 5.2.5) also produced good results with equations (5.2.3) and (5.2.4) being the least normal in distribution. The raw residuals, as defined in equation (5.2.5) are used in the following section to determine the variability in the predicted failure pressures since they are normally distributed and can be straightforwardly included in a statistical model. It should be noted that the distributions of equations (5.2.3) and (5.2.4) are the same since equation (5.2.3) can be rearranged as shown in equation (5.2.6).

$$\begin{aligned} \%Error_{Predicted} &= \frac{FP_{Experimental} - FP_{Predicted}}{FP_{Predicted}} \\ &= \frac{FP_{Experimental}}{FP_{Predicted}} - 1 \end{aligned} \tag{5.2.6}$$

5.2.1 Operating Pressure

To incorporate a factor of safety in a pipeline, one must select an appropriate operating pressure. In principal, a line can be kept in service if the operating pressure is reduced with growing corrosion. Upon finding corrosion, an operator has three options: continued operation of the line at the current operating pressure, removal or repair of the corrosion defect and/or reduction of the operating pressure. This decision has economic consequences since removal or repair of defects, or operating at a reduced pressure can be

costly. However, the primary decision is to ensure that the pipeline retains a certain level of reliability, often termed integrity. Consider the pressure margin to be represented by the difference between the failure pressure and the operating pressure, as shown in equation (5.2.7):

$$\text{Pressure Margin} = \left[FP - P_{\text{Operating}} \right] \tag{5.2.7}$$

The operating pressure will be considered constant although in service it may fluctuate over time, in which case the peak operating pressure can be used. When this sum (equation 5.2.7) is positive, the defect will not fail. The failure pressure can be expressed as a variable quantity in terms of the predicted burst pressure as:

$$FP = FP_{\text{Predicted}} + \mu + N(0, s^2) \tag{5.2.8}$$

where μ is the mean error in the prediction and $N(0,s^2)$ is a normal distribution representing the variability in the prediction. This distribution has a mean of zero and a variance of s^2 (standard deviation of s). In our case, μ is equal to the mean of the raw residuals and N is a normal distribution with a standard deviation equal to that of the raw residuals. Substituting equation (5.2.8) into equation (5.2.7) we have:

$$\begin{aligned} \text{Pressure Margin} &= \left[FP - P_{\text{Operating}} \right] \\ &= \left[FP_{\text{Predicted}} + \mu + N(0, s^2) - P_{\text{Operating}} \right] \\ &= \left[FP_{\text{Predicted}} + \mu - P_{\text{Operating}} \right] + N(0, s^2) \\ &= N\left(FP_{\text{Predicted}} + \mu - P_{\text{Operating}}, s^2 \right) \end{aligned} \tag{5.2.9}$$

If the pressure margin is positive, the defect will not fail at the current operating pressure. The reliability of the defect with respect to the current operating pressure can be calculated as the probability of the pressure margin having a value greater than or equal to zero.

Alternatively, the probability of failure for the defect can be expressed as shown in equation (5.2.10).

$$\text{Defect Probability of Failure} = \text{Prob}(X < 0)$$
$$\textit{where} \qquad (5.2.10)$$
$$X : N\left(\left[FP_{\text{Predicted}} + \mu - P_{\text{Operating}}\right], s^2\right)$$

As an example, the defect from test BCG 02 was analyzed and an operating pressure was assumed as that which corresponds to a hoop stress of 72% of the SMYS. The raw residuals for each model are shown in Table 5.2.2. The probability of failure depends on the magnitude of the operating pressure and a particular failure pressure prediction. The Finite Element, CPS and RSTRENG predictions indicate a low probability of failure (Table 5.2.2). The B31G predictions have the highest probability of failure (7.49×10^{-5}) due to the increased variability in this model.

To further investigate this aspect, the defect reliability is plotted as a function of operating pressure in Figure 5.2.1. Note that these plots are specifically related to the assessment of the defect in test BCG 02, however other defects are expected to provide similar results. Note that the operating pressure is expressed in terms of the ratio of hoop stress to SMYS. It can be seen that the CPS model provides a slightly higher reliability than RSTRENG below an operating pressure of approximately 120% SMYS. This is due to a lower standard deviation. The FE-New Scanner results have the lowest variability and thus result in a higher reliability. Nevertheless, the FE-All reliabilities are between those of B31G and RSTRENG due to the increase in variability. This emphasizes the fact that although the Finite Element Method can produce very accurate predictions of the burst pressure, this accuracy is highly dependant on the material and geometry measurements used in the analysis. These effects are shown more clearly in Figure 5.2.2 where the probability of failure for each model is plotted on a logarithmic scale as a function of the operating pressures. The difference in probability of failure is primarily due to differences

in the variability of the model predictions. As expected, the probability of failure increases as the operating pressure increases.

Alternatively, an operator may want to specify a minimum reliability and calculate the corresponding maximum allowable operating pressure for consideration of a reduced operating pressure for the line. Rearranging equation (5.2.10):

$$\begin{aligned} P_{Operating} &\le (FP_{Predicted} + \mu) - N^{-1}[pf,0,s^2] \\ &\le N^{-1}[pf,(FP_{Predicted} + \mu),s^2] \end{aligned} \qquad (5.2.11)$$

where:

$N^{-1}[pf,(FP_{Predicted} + \mu),s^2]$ is the pressure corresponding to the specified probability of failure (pf).

Equation (5.2.11) was applied to the predicted failure pressures and the results are shown in Table 5.2.3 for two different probabilities of failure. Calculated operating pressures are shown as a function of the probability of failure in Figure 5.2.3. Since B31G is the most conservative and has the highest variability, the allowable operating pressures are expected to be the lowest.

Chapter 6
Multi-level defect assessment

6.1 ASSESSMENT PROCEDURE

A multi-level assessment philosophy has been accepted by the industry as an appropriate means of treating the large amounts of data available to pipeline operators from automated corrosion measurement methods, such as intelligent pigs. The goal of a multi-level approach is to apply a simple evaluation method to the data and identify critical defects. These defects can then be analyzed using a more accurate, and necessarily more complex, evaluation method. One disadvantage of the currently accepted evaluation procedures is that they depend on interaction rules which are relatively complicated to apply in an automated manner without introducing excess conservatism. For example B31G is simple to apply when the defect depth and length are known, however accurate definition of the length may require manual analysis. Thus, the level of complexity in the assessment should not be related to the complexity of calculations required, but to the complexity of the required corrosion measurements. The goal of the simplest analysis

(Level I) should be to identify those defects that are safe using a minimum amount of knowledge of the defect geometry and to identify defects which require further consideration. Once the defects requiring further consideration are identified, more detailed geometry measurements and a more detailed analysis can be considered.

Chouchaoui was the first to suggest a three-level approach for the assessment of line pipe with corrosion defects. He proposed that simple evaluation methods such as B31G and RSTRENG be used to exclude non-critical defects and that more accurate methods be applied to assess those defects which were not found to be acceptable by the simple techniques. Chouchaoui defined the three levels in order of increasing complexity as:

1. B31G or RSTRENG.
2. Simplified elastic or pseudo-elastic finite element analysis.
3. Full, three-dimensional elastic-plastic finite element analysis.

Chouchaoui's primary focus was the validation of three-dimensional, elastic-plastic finite element analysis (Level 3) for simply shaped defects. He also investigated the application of B31G and RSTRENG (Level 1) to these simple defects. Chouchaoui proposed simplified finite element methods for Level 2 but did not investigate these in detail. It is important to point out that Chouchaoui's level I included RSTRENG or B31G, based primarily on their accuracy. However, as shown in Chapter 4, RSTRENG requires a significant amount of detail in terms of the corrosion geometry, and provides a more accurate and consistent prediction of the burst pressure. Therefore, these techniques should be considered separately. The use of simplified finite element-based approaches, as suggested in Level 2, are not expected to produce more accurate results than the currently proposed CPS technique although they would require more detailed corrosion measurements.

6.2 ASSESSMENT PHILOSOPHY

It is has been shown that accurate prediction of the failure pressure of a corrosion defect requires both accurate geometry measurements and accurate material properties. In terms of the assessment procedure, it is that latter which is most important since the solutions developed by the author are based on a detailed knowledge of the material properties. The motivation for the use of detailed material properties was to remove the conservatism related to the flow stress approximation currently used by the accepted assessment procedures. In addition, this allows the proposed model to be used for the higher strength materials in common use today. In contrast, application of the current assessment procedures to higher strength steels will require a new definition of the flow stress.

When detailed material properties are available, as determined from tensile tests on the material, a 3-level assessment procedure can be used to evaluate corrosion defects occurring in the pipeline. Development of methods to determine the material properties without removing specimens from an operating line is a topic for future investigation. Alternately, operators could develop a long-term plan that would include determining the true material properties of their lines during maintenance, construction or repair procedures.

In the following sections the author assumes accurate material properties are known and proposes a 3 level assessment procedure based primarily on the level of knowledge of the corrosion geometry (procedure A). The Level IA analysis is based on the Long Groove solution from Chapter 3 with the intention of identifying critical defects using a minimum amount of information. Defects that exceed the allowable depth predicted by this Level IA analysis should then be analyzed using the Level IIA weighted depth difference method. This is described in detail in Chapter 4 and implemented using the CPS computer program. In special cases, a full 3-D Finite Element Analysis may be required as specified in Level IIIA.

If detailed material properties are not available (i.e. only the SMYS is known) then the defects should be evaluated using an alternate 2-level assessment procedure (procedure B). It is proposed that B31G be used as a Level IB and RSTRENG be used as a Level IIB.

For each level of assessment, the predicted failure pressure can be compared to the maximum operating pressure using equation (5.2.10) to determine the probability of failure of the defect. The mean and standard deviation of the raw residuals for each method applied to the experimental database can be found in Table 5.2.2. Alternatively, the maximum allowable pipeline operating pressure can be calculated for a given probability of failure (equation 5.2.11). If the probability of failure is sufficiently low, the defect may be considered safe and left in service although the potential for continued growth of the defect must be considered. If the probability of failure is not sufficient, remedial action must be taken. This can include repair of the defect with a sleeve, removal of a section of pipe containing the critical defect or a reduction in the operating pressure of the line to achieve a suitable probability of failure. This assessment philosophy is shown Figure 6.2.1.

6.3 PROPOSED THREE-LEVEL ASSESSMENT PROCEDURE

Level IA – Maximum defect depth (Long Groove Solution)

A Level-I approach should be simple to apply so that ideally, application could be undertaken in the field. However, to improve the prediction accuracy, this approach should make use of accurate material properties. The long groove solution developed in Section 3.3 meets these requirements. The application is simple since evaluation is based only on the maximum defect depth. However, accurate material properties and depth measurements are required for this technique to be useful. With accurate material properties the maximum allowable defect depth can be determined. Note that this solution predicts a lower bound failure pressure for natural corrosion defects. Defects with depths

that exceed the maximum allowable defect depth can be identified quickly and assessed with the recommended Level IIA procedure. It should be stressed that the foundation of this method is accurate material properties. If detailed properties are unavailable, and the material behaviour is represented by a flow stress based on the specified minimum yield strength many non-critical defects will be identified for detailed analysis and the Level IA assessment will be ineffective.

The recommended approach for the Level IA assessment procedure is:

- Determine the true stress-strain behaviour of the pipe material in the circumferential direction with uniaxial tensile tests or other methods.
- Calculate the predicted failure pressure as a function of depth using equations (3.2.3) and (3.3.24). A typical result is shown in Figure 3.3.13. Alternatively, equation (3.3.26) can be used with the condition that the defects must be greater than 20% of the wall thickness in depth.
- Specify the maximum operating pressure of the pipeline and determine the maximum allowable defect depth from the previous calculations. It should be noted that this method is a lower bound and inherently conservative as shown in Figure 4.4.5. When applied to the experimental database, it is found that the Long Groove solution is more conservative for deeper defects (Figure 4.4.5). This is due to the fact that deeper areas in natural corrosion defects are typically of limited length so that the infinite length assumption in the Long Groove solution results in conservative failure pressure predictions.
- Inspect all defects for depths exceeding the maximum allowable depth. Shallower defects are considered non-critical under the current operating conditions. However, provisions for changes in operating conditions or continued corrosion growth must be considered.
- Defects which exceed the maximum allowable defect depth must be considered for the more detailed Level IIA analysis as described in the next section.

Level IIA – Weighted depth difference method (CPS)

In cases where defects fail a Level IA evaluation, a more accurate approach which utilizes the defect length is required. The Weighted Depth Difference model (Section 4.4) has been shown to be accurate and easily applied when detailed corrosion measurements are available. It relies on a set of easily defined interaction rules meant to reduce computation time and considers the longitudinal interaction of adjacent defects.

The Weighted Depth Difference method is implemented in the CPS computer program. As an initial step, individual or non-interacting areas of corrosion may be identified for evaluation. Since this model includes longitudinal interaction, such an interaction rule is only meant to reduce the size of the analysis, but is not required to improve the accuracy of the analysis. However, circumferential interaction rules are necessary for all evaluation methods which exclude the circumferential dimension of the defect.

Areas of corrosion are considered independent if separated by more than 2 wall thicknesses of full thickness material in all directions. Although circumferential interaction is recognized to occur only when defects are touching in this direction, a variation of interaction distance with angular position makes assessment more complex. The 2-wall thickness criterion will be conservative in this direction. In terms of the longitudinal direction, conservative interaction rules do not affect the predicted burst pressure since the CPS evaluation procedure considers the longitudinal interaction of adjacent defects.

The recommended approach for the Level IIA assessment procedure is:

- Identify critical locations with the Level IA (Long Groove) assessment procedure.
- Determine the extent of the defects. Defects do not interact if separated by more than 2 wall thicknesses of full thickness material in any direction.

- Measure the maximum corrosion depth around the circumference as a function of longitudinal position for each defect. Measurement techniques are outlined in Section 4.2.2.
- Calculate the predicted burst pressure of each defect using the CPS program.
- Compare the predicted failure pressure to the maximum operating pressure using equation (5.2.10). Defects with an unacceptable probability of failure must be removed or repaired. Alternatively, the operating pressure of the pipeline may be reduced so that the predicted failure pressure exceeds the maximum operating pressure with an acceptable probability of failure (equation 5.2.11).

Level IIIA – Full Three-dimensional Finite Element Analysis

Full, three-dimensional finite element analysis has been shown to be the most accurate method of failure prediction when very detailed and accurate information regarding the pipe geometry and material properties is available. However, a significant level of expertise is required on the part of the user to accurately model the defect and interpret the results. Due to the required computing resources it can only be justified in very special circumstances. It should also be noted that in cases where accurate properties and measurements are not available, the Finite Element Method can produce less accurate results than the other proposed methods. The author considers that the finite element method is not feasible for the general evaluation of corrosion defects due to the required computing resources and accurate measurements. However, use of this method may be justified in specific instances. The application of this method is discussed in Chapter 4.

6.4 ALTERNATE TWO-LEVEL ASSESSMENT PROCEDURE

The proposed three-level assessment procedure in the previous section is dependent on detailed knowledge of the material properties. In cases where detailed material properties and corrosion measurements may not be available, an alternate two-level approach (procedure B) is suggested as outlined in Figure 6.2.1. The original B31G code is proposed as the Level IB assessment with the RSTRENG evaluation procedure to be used as Level IIB. Although application of these methods may seem simple, both B31G and RSTRENG require interaction rules to define the defect limits. Even with these rules, both methods are very conservative in the assessment of natural corrosion defects. This is related in part to the material characterization with the flow stress defined by the specified minimum yield stress.

It is recommended that B31G be applied as a Level IB assessment in the manner defined by the Canadian code CSA Z662-99 (CSA, 1999). The defect is quantified by the maximum depth and overall length. Interaction is said to occur if the distance between adjacent areas is less than the longitudinal length of the smallest defect. This applies in both the longitudinal and circumferential directions.

The Level IIB assessment procedure is applied using the RSTRENG program as outlined by Kiefner and Vieth (1989). However, it is recommended that the defect profile be determined using the Projection Method (Section 4.2) in place of the river bottom path suggested by Kiefner and Vieth. The Projection Method is straightforward in application and does not require interpretation of the defect by persons measuring the corrosion or analyzing inspection data. For consistency, the same interaction rules described above for B31G should be used in the RSTRENG assessment.

6.5 PROPOSED ASSESSMENT PROCEDURE – SAMPLE CALCULATION

To demonstrate the assessment of a pipe section, consider pipe section TCP-02 from the University of Waterloo database. Figures 6.5.1 and 6.5.2 show the corrosion defects on this section of pipe. Values marked on the pipe are approximate maximum defect depths in inches, used to identify areas for scanning. The pipe material was grade API-5L-X46 with a specified minimum yield stress of 46000 psi. The pipe wall thickness was 0.373" with an outside diameter of 34.0".

The true stress-strain behaviour for this material was determined from six uniaxial tensile tests on specimens oriented in the circumferential direction. The test that most closely approximated the average yield and UTS was chosen as the representative stress-strain curve. The average yield stress for this grade API-5L-X46 material was 59753 psi in the circumferential direction. The representative test had a yield stress of 58050 psi and an ultimate tensile strength of 73680 psi with a corresponding critical stress of 82351 psi. The Ramberg-Osgood material parameters (equation 2.2.2) were determined from a non-linear regression on the true stress-strain data. The strain hardening coefficient, α was found to be 3.007 and the strain hardening exponent, n was 8.345.

Level IA Assessment – Long Groove Solution

The failure pressure as a function of depth can be determined by solving equation (3.3.26). Note that this is only valid for defect depths exceeding 20% of the wall thickness. For shallower defects, equations (3.2.3) and (3.3.24) must be solved simultaneously to determine the burst pressure. The results are shown in Figure 6.5.3 where the predicted failure pressure from the Long Groove solution (equations 3.2.3 and 3.3.24) is plotted as a function of defect depth, expressed as a percentage of the wall thickness. The hoop stress for three operating pressures expressed as a percent of the SMYS, and the corresponding maximum allowable defect depths are shown in the Figure.

An often used operating pressure is that which creates a nominal hoop stress of 72% SMYS in the pipe wall. This results in an operating pressure of 743 psi as shown in equation (6.5.1).

$$\begin{aligned} p_{Operating} &= \frac{(72\%)(SMYS)(t)}{(r_i)} \\ &= \frac{(0.72)(46000)(.373)}{(16.627)} \\ &= 743\,psi \end{aligned} \qquad (6.5.1)$$

The corresponding maximum allowable defect depth is 61% of the wall thickness or 0.228". The data for the three operating pressures considered in Figure 6.5.3 is shown in Table 6.5.1. A conservative approximation of the maximum allowable operating pressure is that which creates a nominal hoop stress equal to 100% of the SMYS in the pipe wall. This magnitude of pressure can be reached during hydrostatic testing of the pipeline and is the maximum allowable pressure for a pipeline (CSA 1999). The corresponding maximum allowable depth (Figure 6.5.3) is 46% or 0.172". An approximate measurement of the maximum pit depths on this pipe section indicated that none of the corrosion defects exceeded this maximum allowable depth. The maximum defect depths, as measured by the University of Waterloo 3-D scanner, for selected defects are shown in Table 6.5.2. Thus, according to a conservative lower bound (Level IA) assessment, this pipe section will not fail at an operating pressure corresponding to 100% SMYS.

To emphasize the need for detailed material properties, consider the infinite length, uniform depth groove solution from RSTRENG in which the flow stress is based on the SMYS (equation 6.5.2). An operating pressure corresponding to 100% SMYS has been assumed.

$$
\begin{aligned}
p_{Operating\,100\%SMYS} &= p_{Max.Allowable} \\
&= 1032\,psi \\
&= (SMYS + 10000)\left(\frac{t}{r}\right)\left(1 - \frac{d_{Max.All.}}{t}\right) \\
&= (56000)\left(\frac{0.373}{16.627}\right)\left(1 - \frac{d_{Max.All.}}{0.373}\right) \qquad (6.5.2) \\
&\text{or} \\
d_{Max.All.} &= 0.067" \\
\frac{d_{Max.All.}}{t} &= 18\%
\end{aligned}
$$

The maximum allowable depth is 18% for the RSTRENG infinite length groove solution compared to 46% for the author's Long Groove solution. For this pipe section, the RSTRENG long groove solution would identify almost every defect as critical and require a Level II assessment. This example indicates the need for detailed material properties for a Level I assessment procedure to be effective.

Level IIA Assessment – CPS Program

The long groove solution used in the Level IA assessment did not identify any defects on the pipe section for detailed analysis. As an example, to undertake a Level IIA assessment, assume that the desired maximum allowable operating pressure is 1393 psi, corresponding to 135% of the SMYS. Then the maximum allowable defect depth predicted by the Long Groove solution is 27% or 0.100". Several of the defects on this pipe section exceed this depth limit and should be investigated using the Level IIA assessment (the CPS procedure as described in Chapter 4). For brevity, only defects TCP02-1A-1F, TCP02-1G and TCP02-1H are considered although approximately 18 defects on this section exceeded 0.100" in depth. Note that a Level IIA assessment would also be required to obtain the defect reliability for risk analysis.

To begin, isolated defects must be identified according to the chosen interaction rules. It has been suggested that adjacent defects do not interact if separated by a distance equal to 2 wall thicknesses of full thickness material. The identified defects are indicated with square boxes in Figures 6.5.1 and 6.5.2. Note that the limited range of the scanner required one defect, TCP02-1A-1F, to be scanned in six blocks as seen in Figure 6.5.4. Defects TCP02-1G and TCP02-1H are shown in Figures 6.5.5 and 6.5.6 respectively. The failure location, defect TCP02-1G, is indicated in Figure 6.5.7.

Each defect was measured using the three-dimensional scanner developed at the University of Waterloo. The actual depths were then determined using the data processing technique described in Chapter 4. The scanner image and surface data for defects TCP02-1A-1F, TCP02-1G and TCP02-1H are shown in figures 6.5.8, 6.5.9 and 6.5.10 respectively. The corrosion profiles were calculated from this data using the projection technique (Chapter 4) and then analyzed with the appropriate pipe dimensions and material properties using the CPS program which incorporates the Weighted Depth Difference Model. The corrosion profiles are shown in Figures 6.5.11, 6.5.12 and 6.5.13. The predicted failure location identified in the Figures was calculated by the CPS program. The statistical model (equation 5.4.10) was applied to the predicted failure pressures assuming an operating pressure of 1032 psi (100% SMYS). The results are shown in Table 6.5.3 indicating that the defect reliability exceeds 99% in all cases.

Figure 6.5.12 shows that the predicted failure location corresponds to the actual failure location in defect TCP02-1G as determined from the fracture surface after the burst test (Figure 6.5.7). The failure pressure was 1531 psi. The analysis results are shown in Table 6.5.2 where the CPS predictions are the least conservative. Interestingly, the minimum predicted failure pressure is for defect TCP02-1A-1F although the actual failure occurred at defect TCP02-1G. This is true for the predictions from all three of the assessment procedures shown in Table 6.5.2. Such a result is not uncommon and occurred in a number of the burst tests in the database. Despite this anomaly, the spread in failure pressure between the three locations is within the expected variability of the method. This includes variability in the material properties and measured defect geometry. In addition,

the projection method used to characterize the defects has not considered the defect orientation so that if the defect had a spiral or circumferential orientation they would be treated conservatively.

The failure of this pipe section initiated at defect TCP02-1G as shown in Figure 6.5.7. Local necking and bulging of the material identified the initiation site within this defect.

Level III – 3-D Finite element analysis

The finite element analysis of defect TCP02-1G is discussed in detail in section 4.3. The results of the analysis are shown in Table 4.5.1 and Figures 4.5.28a and 4.5.28b. The predicted burst pressure using the finite element method was 1521 psi which was within 0.6% of the actual failure pressure. Note that the predicted and actual failure locations correspond.

Application of the statistical model to the data (Table 6.5.3) indicates that the defect has a probability of failure of 5.03×10^{-7} at an operating pressure of 1032 psi (100% of the SMYS). The maximum allowable operating pressure for this defect with a probability of failure of 1×10^{-6} was calculated to be 1169 psi.

Level IB and IIB Analysis

If detailed material properties are not available, an alternate two-level assessment procedure can be used to predict defect failure pressures.

The B31G (Level IB) failure pressure predictions are shown in Table 6.5.2 for the selected defects from test TCP-02. If we consider the maximum operating pressure to be 743 psi, corresponding to a stress level of 72% SMYS, it is found that defect TCP02-1A-1F is identified for detailed analysis. Defects TCP02-1G and TCP02-1H are predicted to be safe at this operating pressure. Table 6.5.3 shows that the probability of failure of defects TCP02-1G and TCP02-1H are 0.00501 and 0.00116 respectively at an operating pressure

of 1032 psi (100% SMYS). Defect TCP02-1A-F has a probability of failure of 0.112 and would be selected for a Level IIB assessment if this probability of failure were not acceptable. The relatively high probability of failure and maximum allowable operating pressure predicted by this method are related to the higher degree of scatter for the B31G predictions. Table 6.5.4 indicates that this defect has a maximum allowable operating pressure of 117 psi for a probability of failure of one in one million ($1x10^{-6}$).

The RSTRENG failure predictions for the defects on pipe section TCP-02 are shown in Table 6.5.2. Table 6.5.3 indicates that all defects have a probability of failure less than 0.0116 for the RSTRENG predictions when an operating pressure of 1032 psi (100% SMYS) is considered. The maximum allowable operating pressure, with a defect reliability of one in one million, was calculated to be 552 psi.

Chapter 7
Closure

Pipelines are a safe and economic means for transporting oil and natural gas with the number of failures, defined as a loss of product, being relatively low compared to other means of transportation. However, it should be pointed out that even a single major failure, such as a rupture, will have a significant financial and environmental impact. It is well known that the currently accepted assessment procedures contain a large degree of conservatism and that much of the pipe removed from service due to corrosion is still safe at the current pipeline operating pressure. Until now, the degree of conservatism in the prediction methods could not be quantified due to the lack of complete experimental data. Thus the reliability of the pipeline or the risk of failure of the pipeline could not be quantified.

The focus of this thesis has been the assessment of corrosion defects in pipelines with the goal of providing a more complete understanding of the failure of these defects and addressing the conservatism in the currently accepted assessment procedures. This has been achieved through the development of a comprehensive experimental database which has not only provided a means of validating the currently accepted and proposed

assessment criteria, but has also allowed for consideration of the defect reliability. This is an important aspect when evaluating the integrity of a pipeline.

All forty pipe sections included in the experimental database were removed from operating pipelines due to the presence of natural corrosion defects. The material properties were measured, the defects mapped and the pipe sections were then burst to determine the remaining strength of the corroded pipe section.

RSTRENG and B13G were applied to the experimental database. The percent error, based on the experimentally measured burst pressure was found to be 20% conservative on average for RSTRENG with a standard deviation of 6.6% while B31G was 34% conservative on average with a standard deviation of 15%.

Other proposed models were applied to the database but were found to have a high degree of scatter that varied with defect depth. The Modified RSTRENG solution, with a modification to the flow stress, produced the best results. This flow stress is somewhat arbitrary and has not been validated for higher strength materials.

Prediction of corrosion defect failure pressures using CPS

A new model for predicting the failure pressure of corrosion defects, based on the Weighted Depth Difference model, has been proposed. This model uses the elastic-plastic material properties and corrosion measurements in the same form as the currently accepted RSTRENG procedure, with the corrosion profile determined using the projection method. The Long Groove and Plain Pipe solutions are used as lower and upper bounds respectively for the defect failure pressure.

The failure of plain, defect-free pipe occurs by geometric instability before the stress in the pipe wall exceeds a critical value and provides an upper bound for the failure pressure of a corrosion defect. This upper bound was investigated with finite element analyses and modifications to a solution proposed by Svensson. Both solutions produced similar burst pressure predictions, however comparison to the experimental database indicated that the predicted failure pressure exceeded the experimental values by an average of 14%. It should be noted that the burst test results for plain pipe were from a single operating pipeline. Failure of these pipe sections occurred in uncorroded areas even

though corrosion defects up to 40% of the wall thickness were present. Use of a burst pressure equal to 86% of the geometric instability pressure was recommended. However this recommendation requires further investigation since it appears that inhomogeneities in the material and variations in the wall thickness may have lead to premature failure.

The failure behaviour of infinite length, uniform depth grooves was investigated using the Finite Element method. It was found that the failure pressure was a linear function of the defect depth, when the depth exceeded 20% of the wall thickness. Shallower defects fail at pressures near the failure pressure of plain pipe. The Long Groove solution was developed from an equilibrium analysis and makes use of the actual material properties to predict the failure pressure. This solution agrees with the finite element results within 2% and is 4% non-conservative, on average, for the experimental data for long grooves. The Long Groove solution provides a lower bound for the failure pressure of a typical natural corrosion defect with varying depth. Application of the Long Groove model to the experimental database resulted in an average error similar to RSTRENG with a variability similar to B31G. This is expected since the Long Groove solution does not consider the defect length but does use the actual material properties.

The failure pressure of a typical corrosion defect can be determined using the Weighted Depth Difference Method by considering each point within the corrosion defect and evaluating the effect of the adjacent material loss through a weighting scheme which incorporates longitudinal defect interaction. Application of this method is iterative and is implemented using the computer program called CPS. This method utilizes the actual material properties and so is applicable to materials not considered in the database such as higher strength steel. In addition it identifies the predicted failure location.

Simple, single pit defects were analyzed in detail by the author using the finite element method. The CPS program accurately predicted the failure pressure and failure location of the single pits without requiring any adjustment or scaling factors. However, it was necessary to scale the plain pipe failure pressure for the failure prediction of natural corrosion defects. In contrast, RSTRENG and B31G did not predict the failure pressure of the single pits with the same accuracy and the error varied in a nonlinear manner.

When applied to the experimental database, the CPS program predicted the failure pressures with an average error of 3.1% and a standard deviation of 6.5%.

Finite element modeling of complex corrosion defects

The Finite Element method has been successfully applied to complex natural corrosion defects with limited longitudinal and circumferential extents. The corrosion geometry was modeled using the scanner data processed with software developed by the author and a commercially available solid modeling program. Failure was predicted using a critical stress criterion. The burst pressure for twenty-five of the pipe sections from the experimental database were predicted using the Finite Element method. The average error in prediction was –0.18% with a standard deviation of 8.45%. However, when the defects which had been mapped with the more accurate 3-D scanner were considered, the average error in prediction was 0.1% with a standard deviation of 4.1%.

It has been found that the Finite Element method is very sensitive to local changes in defect depth and requires very accurate geometry measurements. This is related to the fact that, in the Finite Element Model, the local stresses are primarily determined by the local geometry, with the surrounding geometry as a secondary effect. Detailed material properties are also required for accurate burst pressure predictions

Statistical model of failure predictions

One of the most important uses for the database is to gain an understanding of the prediction error and variability for the various assessment methods considered. However, it should be noted that the reliability of these predictions is based solely on the application of a particular assessment procedure to the database and may not be appropriate for materials or geometries not considered in the database.

The raw residuals (actual minus predicted failure pressure) were found to be normally distributed and were used to predict the average and variability of the prediction error for each procedure considered. The defect reliability was calculated by considering the probability that the failure pressure prediction (including the mean error and variability)

did not exceed the operating pressure. Alternatively, the defect reliability can be specified and the maximum allowable operating pressure can be calculated.

Multi-Level assessment of corrosion defects

A three-level assessment procedure is proposed which makes use of the assessment techniques described in this thesis. This procedure assumes that detailed material properties are available. Increasing levels require more detailed corrosion measurements and produce more accurate failure pressure predictions. The proposed levels are:

- Level IA – Long Groove solution
- Level IIA – CPS (Weighted Depth Difference solution)
- Level IIIA – Finite Element Analysis

In cases where detailed material properties are not available, an alternate two-level assessment utilizing B31G and RSTRENG is proposed. B31G and RSTRENG should be applied as specified in the appropriate code. However, the RSTRENG defect profile should be determined using the projection method. The alternate two-level assessment procedure is:

- Level IB – B31G
- Level IIB – RSTRENG

Chapter 8
Recommendations

The material properties of the pipe sections included in the database have been accurately determined with uniaxial tensile tests. These properties are sufficient for the proposed analysis techniques but the material fracture toughness is also commonly quoted in material specifications and should be determined for these pipeline steels.

Although the elastic-plastic material properties can accurately be characterized with uniaxial tensile tests, it would be beneficial to have a means for characterizing the material without removing specimens from the line. This would allow for a more efficient assessment of in-service pipelines.

The mode of defect failure (rupture or leak) is an important quantity when considering the risk of a failure and should be investigated using the experimental database. The material fracture toughness will be necessary for this work.

The experimental database includes pipe materials and sizes which have been in common use for many years and may have corroded while in service. Although the database addresses the current needs of the industry, larger diameter and higher strength pipe materials are becoming more common and may eventually require evaluation. Thus, the database should be expanded to include additional grades of material and diameters of pipe.

The failure pressure of plain pipe is a fundamental component of the Weighted Depth Difference solution. It has been shown that the proposed solution agrees with the Finite Element results but overpredicts the burst pressure of the experimental tests. The experiment data for the burst pressure of plain pipe considered only one grade of pipe material. The failure pressure of plain pipe requires further investigation.

It has been found that the conservatism in RSTRENG can be reduced by modifications to the flow stress approximation. It is recommended that this modification not be used without further validation since it may not be applicable to other grades of pipe.

At present, the Weighted Depth Difference model has only been validated using the experimental database developed at the University of Waterloo. Additional experimental data would be desirable to continue the validation of this assessment procedure. It should be noted that much of the currently published experimental data is incomplete and not useful for validation purposes. The Weighted Depth Difference method predicts the failure location within a given defect and has been shown to accurately predict this location for simple defects. This aspect requires further investigation for complex defects.

REFERENCES

Ahmmed, M., "Prediction of remaining strength of corroded pressurized pipelines", International journal of pressure vessels and piping, Volume 71, 1997, pp. 213-217.

American Society for Metals, "Metals Handbook, Volume 8, Mechanical Testing", ASM, Ninth Edition, 1985.

American Society for Metals, "Metals Handbook, Volume 7, Mechanical Testing", ASM, Ninth Edition, 1985.

Anderson, T.L. (1991) Fracture Mechanics Fundamentals and Applications. CRC Press Inc., 1991.

ASME B31G (1991), "Manual for Determining the Remaining Strength of Corroded Pipelines", ASME B31G-1991, New York, 1991.

Atherton, David, http://phy-server.phy.queensu.ca/wwwhome/atherton/applied_magnetics.html, 1999.

Balsara, M.N. (1996), "Application of advanced fracture mechanics to the assessment of linepipe defects", OMAE, Vol. V., pp. 569-585, 1996.

Batte, A.D., Fu, B., Kirkwood, M.G. and Vu, D. (1997), "New methods for determining the remaining strength of corroded pipelines", OMAE, Vol. V, pp. 221-228, 1997.

Beller, M., "Integrity assessment of pipelines: what information can intelligent pigs provide?", 2nd International Pipeline Technology Conference, Ostend, Belgium, September 11-14, 1995, V I, pp. 211-222.

Bubenik, Olson, Stephens and Fracini (1992), "Analyzing the pressure strength of corroded line pipe", OMAE - Volume V-A, Pipeline Technology, pp 225-231. 1992

Bruce, W.A., Yapp, D. Barborak, D., Fingerhut, M., Kania, R.,"Simple laser-based pipeline corrosion assessment system", Pipeline and Gas Journal, March 1997.

Chouchaoui, B.A. (1993), "Evaluating the remaining strength of corroded pipelines", Ph.D. Thesis, Department of Mechanical Engineering, University of Waterloo, Canada, 1993.

Chouchaoui, B.A. and Pick, R.J. (1994), "Behavior of circumferentially aligned corrosion pits", International Journal of Pressure Vessels and Piping, pp. 187-200, Vol. 57, 1994.

Chouchaoui, B.A., and Pick, R.J. (1993), "Interaction of closely spaced corrosion pits in line pipe", ASME OMAE, Vol. V, Pipeline Technology, pp. 203-214, 1993.

Chouchaoui, B.A., Pick, R.J. and Yost, D.B. (1992), "Burst pressure predictions of line pipe containing single corrosion pits using the finite element method", OMAE, Vol. V-A, pp. 203-210.

Coulson, K. and Worthingham, R. (1990a), "New guidelines promise more accurate damage assessment", Oil and Gas Journal, April 16, 1990a, pp. 41-45.

Coulson, K. and Worthingham, R. (1990b), "Standard damage-assessment approach is overly conservative", Oil and Gas Journal, April 9, 1990b, pp. 54-58.

CSA, "CSA Z662-99, Oil and gas pipeline systems", CSA, Toronto, 1999.

Cronin, D.S., Roberts, K.A. and Pick, R.J. (1996), "Assessment of long corrosion grooves in line pipe", ASME International Pipeline Conference, Vol. 1, pp. 401-408, 1996a.

Cronin, D.S., and Pick, R.J., "Database: Burst pressure of corroded line pipe", Report to British Gas, Nova and Inter Provincial Pipelines, 1996b.

Cronin, D.S., "Analysis of defects in line pipe: Analysis of corrosion defects in line pipe and finite element modeling of pressurized delaminations in line pipe", M.A.Sc. Thesis, University of Waterloo, 1996c.

Davis, J.A. and Thomas, S.J., "Properties and Application Procedures for Polyethylene Tape Coating Systems", Pipeline Engineering Symposium - 1985, Dallas Texas, AMSE, Feb. 17, 1985, pp 11-16.

Dovico, D. and Montero, E., "The Evaluation and Restoration of a Deteriorated Buried Gas Pipeline", Proceedings of the 1st International Pipeline Conference, Calgary, Canada, July 9, 1996, Vol. I, pp. 435-441.

Eiber, R.J., Maxey, W.A., Duffy, A.R., McClure, G.M. (1971), "Further work on flaw behaviour in pressure vessels", Institution of Mechanical Engineers, C88/71, pp. 232-238.

Erdogan, F. and Kibler, J. (1969), International journal of Fracture Mechanics, 53, September 1969.

Folias, E.S. (1965a), "A finite line crack in a pressurized spherical shell", International Journal of Fracture Mechanics, Vol. 1, 1, pp . 20-46, March, 1965.

Folias, E.S. (1965b), "An axial crack in a pressurized cylindrical shell", International Journal of Fracture Mechanics, Vol. 1., pp . 104-113, June, 1965.

Folias, E.S. (1969), "On the effect of initial curvature on cracked flat sheets", International Journal of Fracture Mechanics, Vol. 5., pp . 327-346, 1969.

Fu, B. and Kirkwood, M. (1995b), "Predicting failure pressure of internally corroded linepipe using the finite element method", OMAE, Vol. V, pp. 175-184, 1995.

Fu, B. and Kirkwood, M.G. (1995a), "Determination of failure pressure of corroded linepipes using the nonlinear finite element method", Pipeline Technology Conference, Belgium, Vol. II, pp. 1-9, 1995.

Fu, B., Jones, D.G. (1994), "Failure of spiral corrosion in linepipe", OMAE, Vol. V, pp. 1-8, 1994.

Golden Software Inc., "Surfer for Windows User Manual", Surfer Version 6.04, Golden Software Inc., Colorado, 1997.

Grimes, K. and Jones, D., "Life after inspection", Proceedings of the 1st International Pipeline Conference, Calgary, Canada, July 9, 1996, Vol. I, pp417-433.

Hauge C., Atherton D.,"TECHNOLOGY Line pressure stress affects MFL signals",Oil&Gas Journal, Volume 94, Issue 12, March 18, 1996.

Hibbit et al, "Abaqus: Theory Manual", HKS Inc. CA, Ver 5.4, 1998.

Hibbit et al, "Abaqus: Users Volume I", HKS Inc. CA, Ver 5.4, 1998.

Hopkins, P. and Jones, D.G., "A study of the behaviour of long and complex-shaped corrosion in transmission pipelines", OMAE, Pipeline Technology Volume V-A, ASME, 1992.

Hopkins, P., "Transmission Pipelines: How to improve their integrity and prevent failures", Proceedings of the 2nd International Pipeline Conference, Ostend, Belgium, Sept 11, 1995, Vol. I, pp 683-706.

Jones, E.G., "Pipelines in the 1990's... And Beyond", Proceedings of the 2nd International Pipeline Conference, Ostend, Belgium, Sept 11, 1995, Vol. I, pp 1-9.

Kania, R., Carroll, L., "Non-destructive techniques for measurement and assessment of corrosion damage on pipelines", International pipeline conference, Volume I, ASME 1998, pp. 309-313.

Kiefner, J. and Vieth, P. (1990), "PC program speeds new criterion for evaluating corroded pipe", Oil and Gas Journal, August 20, 1990, pp. 91-93.

Kiefner, J. F. and Vieth, P. H. (1989), "A Modified Criterion for Evaluating the Remaining Strength of Corroded Pipe", Final Report on Project PR 3-805, Battelle Memorial Institute, Columbus.

Kiefner, J.F. (1969), Fourth Symposium on Line Pipe Research, American Gas Association, Catalog No. L30075, Nov. 1969.

Kiefner, J.F. (1973), "Failure Stress Levels of Flaws in Pressurized Cylinders." ASTM STP 536, American Society for Testing and Materials, 1973, pp. 461-481.

Kiefner, J.F. (1990a), "Evaluating Pipe -1: New Method Corrects." OGJ Special, Oil and Gas Journal, August 6, 1990.

Kiefner, J.F. and Vieth, P.H. (1990b), "Evaluating Pipe - Conclusion: PC program speeds new Criterion for Evaluating Corroded Pipe." OGJ Special, Oil and Gas Journal, August 20, 1990.

Klever, F.J., Stewart, G. and Clemens, A.C. van der Valk (1995), "New developments in burst strength predictions for locally corroded pipelines", OMAE, Vol. V, pp. 161-173,1995.

Leis, B.N. and Stephens, D.R. (1997), "An alternative approach to assess the integrity of corroded line pipe – Part I: Current Status", Seventh International Offshore and Polar Engineering Conference, May 1997.

Jackenstein, P. and Schmidt, W., "Evaluating the strength of defective pipes: methods and assessment criteria", Pipes and Pipelines International, September-October, 1996, pp. 23-30.

Maxey, W.A., Kiefner, J.F., Eiber, R.J. and Duffy, A.R., "Ductile fracture initiation, propagation, and arrest in cylindrical vessels", Proceedings of the 1971 National Symposium on Fracture Mechanics, Part II, 31 Aug. – 2 Sept., 1971, pp. 71-81.

Mendelson, A. (1983), Plasticity: Theory and Application. Krieger Publishing Co., Malabar, Florida, 1983.

Mok, D. H. B., Pick, R. J., Glover, A. J., and Hoff, R. (1991), "Bursting of Line Pipe with Long External Corrosion", Int. J. Pres. Ves & Piping, 46, pp. 195-215.

NEB (National Energy Board), "1998 – Annual report", http://www.neb.gc.ca, 1999.

O'Grady, T., Hisey, D. and Kiefner, J. (1992), "A systematic method for the evaluations of corroded pipelines", Pipeline Engineering, ASME 1992, PD-Vol. 46, pp. 27-35.

Papavinasam, S. Revie, R.W., "Inhibitor selection for internal corrosion control of pipelines", Proceedings of the International Pipeline Conference, V. 1 Jun 7-11, 1998 ASME pp. 225-230.

Parker, M. and Peattie, E., Pipe Line Corrosion and Cathodic Protection Gulf Publ. Co., Houston, Third Edition, 1984.

Payer, Fink, Perdomo, Rodriquez, Song, Trautman, "Corrosion and cathodic protection at disbonded coatings", Proceedings of the 1st International Pipeline Conference, Calgary, Canada, July 9, 1996, Vol. I, pp471-483.

Pipetronix, http://www.pipetronix.de/, 1999.

Popelar, C.H. (1993), "A plane strain analysis model for corroded pipelines", OMAE, Vol. V, pp. 281-288, 1993.

Roberts, K.A., (1998) "Correction for longitudinal stress in corroded line pipe", M.A.Sc. Thesis, University of Waterloo, Waterloo, Canada.

Sims, J.R., Hantz, B.F., and Kuehn, K.E. (1992), "A basis for the fitness for service evaluation of thin areas in pressure vessels and storage tanks," PVP-Vol. 233, Pressure Vessel Fracture, Fatigue, and Life Management, ASME 1992, pp. 51-5

Sims, J.R., and DePadova, T.A., (1996) "Fitness for continued service: local thin areas", International conference on pressure vessel technology, Volume 2, ASME 1996, pp. 175-181.

Stephens, D.R. (1993), "Decision criteria for acceptance or repair of corrosion defects in pipelines", Pipeline Risk Assessment, Rehabilitation and Repair Conference, September 1993, Houston.

Stephens, D.R., Krishnaswamy, P., Mohan, R., Osage, D. and Wilkowski, G. (1997b), "A review of analysis methods and acceptance criteria for local thinned areas in piping and piping components", PVP-Vol. 359, Fitness for Adverse Environments

Stephens, D.R., Leis, B.N. (1997c), "Material and geometry factors controlling the failure of corrosion defects in piping", PVP, 1997.

Stephens, D.R., Leis, B.N. and Rudland, D.L. (1997a), "Influence of mechanical properties and irregular geometry on pipeline corrosion defect behaviour", 1997. FINISH REF

Svensson, N.L., "The bursting pressure of cylindrical and spherical vessels", ASME Pressure Vessel and Piping Design, 1959.

TSB (Transportation Safety Board), "1998 preliminary transportation occurrence statistics", http:www.bst-tsb.ca, 1999.

Valenta, F., Sochor, M., Spaniel, M., Michalec, J., "Remaining load carrying capacity of gas pipelines damaged by surface corrosion", International Journal of Pressure Vessels and Piping, Vol. 59, 1995, pp. 217-226.

Valenta, F., Sochor, M., Spaniel, M., Michalec, J., Ruzicka, M., Halamika, V., "Theoretical and experimental evaluation of the limit state of transit gas pipelines having corrosion defects", International Journal of Pressure Vessels and Piping, Vol. 66, 1996, pp. 187-198.

Vieth, P. H. and Kiefner, J. F. (1994), "Database of Corroded Pipe Tests", Final Report on Contract No. PR 218-9206, Kiefner and Associates, Inc., Worthington, Ohio.

Wilkowski, G.M., and Eiber, R.J. (1979), "Determination of the maximum size of girth weld repair on offshore pipelines", American Gas Association, 1979.

Yen, B.C., and Tofani, G.D. "A Geotechnical Assessment of Soil Stresses on Pipeline Coating", Pipeline Engineering Symposium - 1985, Dallas Texas, AMSE, Feb. 17, 1985, pp 17-35.

Yong, B., Moe, E. Mork, K., "Probabilistic assessment of dented and corroded pipeline", Fourth international offshore and polar engineering confrerence, Osaka, Japan, 1994, pp. 93-101.

	Ruptures	
	RSTRENG	B31G
Mean Failure Ratio	0.850	0.537
Standard Deviation	0.150	0.178
	Leaks	
	RSTRENG	B31G
Mean Failure Ratio	0.992	0.630
Standard Deviation	0.180	0.209

Table 2.7.1 Failure ratios for RSTRENG and B31G

	RSTRENG	B31G
Mean Failure Ratio	0.824	0.490
Standard Deviation	0.112	0.131

Table 2.7.2 Failure ratios for RSTRENG and B31G
for long corrosion defects

Material Type	Material Grade	Circumferential Direction					Longitudinal Direction				
		YS (MPa)	YS (psi)	UTS (MPa)	UTS (psi)	ε_{UTS} (-)	YS (MPa)	YS (psi)	UTS (MPa)	UTS (psi)	ε_{UTS} (-)
BCG	X42	345.2	50063	452.6	65649	0.125	366.7	53181	455.9	66123	0.104
SOL	X46	360.6	52301	471.2	68338	0.148	407.8	59146	485.9	70481	0.150
NOR	X52	391.6	56798	496.4	72001	0.136	403.7	58548	504.4	73157	0.139
TCP	X46	412.0	59753	527.3	76480	0.111	365.1	52955	518.2	75164	0.115
NOV	X55	388.1	54729	498.3	72273	0.132	385.8	55957	491.1	71231	0.127
RLK	X52	421.4	61121	568.2	82404	0.114	367.2	53264	549.8	79738	0.116
ESS	X46	(Chouchaoui, 1993)									

Material Type	Ramberg-Osgood Material Parameters				Critical Stress	
	YS (MPa)	YS (psi)	alpha	n	(MPa)	(psi)
BCG	350.9	50852	3.143	8.07	506.2	73367
SOL	356.7	51689	3.741	7.45	542.0	78557
NOR	389.0	56376	3.493	7.74	575.8	83450
TCP	400.5	58050	3.007	8.34	568.2	82351
NOV	462.7	67055	2.254	8.65	648.6	93997
RLK	433.6	62841	1.198	10.97	603.7	87497

Table 4.2.1 Experimental database material summary (average values) and Ramberg-Osgood model parameters

Test ID	Outside Diameter (in)	Wall Thickness (in)	SMYS (psi)	YS (psi)	UTS (psi)	Failure Pressure (psi)	Max. Defec Depth (mil)	Defect Length (in)
SOL-1	12.740	0.335	46000	51689	68062	3635	0	0.0
SOL-2	12.730	0.340	46000	51689	68062	3535	85	2.5
SOL-3	12.740	0.340	46000	51689	68062	3545	0	0.0
SOL-4	12.720	0.338	46000	51689	68062	3351	117	8.0
SOL-5	12.760	0.336	46000	51689	68062	3627	0	0.0
SOL-6	12.720	0.340	46000	51689	68062	3659	106	2.4
SOL-7	12.660	0.328	46000	51689	68062	3258	0	0.0
SOL-8	12.740	0.344	46000	51689	68062	3469	0	0.0
SOL-9	12.760	0.332	46000	51689	68062	3375	0	0.0
SOL-10	12.740	0.339	46000	51689	68062	3471	130	5.7
SOL-11	12.740	0.340	46000	51689	68062	3154	105	5.0
SOL-12	12.720	0.336	46000	51689	68062	3127	86	2.0
SOL-14	12.750	0.340	46000	51689	68062	3556	0	0.0
NOR-1	10.750	0.206	52000	56376	72845	2423	73	16.1
NOR-2	10.750	0.207	52000	56376	72845	2619	68	5.5
NOR-3	10.750	0.208	52000	56376	72845	2501	0	0.0
TNG-01	10.750	0.325	46000	59364	69780	3076	156	9.5
RLK-1	24.069	0.258	52000	58381	77524	1370	130	35.5
RLK-2	24.116	0.253	52000	58381	77524	1143	140	56.4
RLK-3	24.075	0.252	52000	58381	77524	1423	101	54.0
BCG-1	10.760	0.195	42000	50852	65825	1994	130	7.2
BCG-2	10.747	0.184	42000	50852	65825	2000	103	1.9
BCG-3	10.769	0.188	42000	50852	65825	1988	64	1.2
BCG-4	10.752	0.192	42000	50852	65825	2201	86	4.0
BCG-5	10.783	0.194	42000	50852	65825	2174	63	1.8
BCG-6	10.793	0.197	42000	50852	65825	1936	85	4.9
BCG-7	10.805	0.180	42000	50852	65825	1838	108	2.6
BCG-8	10.792	0.196	42000	50852	65825	2147	107	1.5
BCG-9	10.808	0.190	42000	50852	65825	1831	83	6.2
ESS-01	12.750	0.200	46000	54058	68512	1412	144	3.9
NOV01	19.950	0.226	55000	67055	85184	1556	119	5.2
NOV02-2	19.880	0.223	55000	67055	85184	1168	128	18.2
NOV03-2	20.000	0.224	55000	67055	85184	1244	148	24.4
NOV04	20.000	0.226	55000	67055	85184	1434	151	21.0
NOV04-2	20.000	0.226	55000	67055	85184	1582	120	16.4
NOV05	20.010	0.221	55000	67055	85184	1167	132	23.5
NOV06	20.000	0.222	55000	67055	85184	1669	97	6.7
TCP01	34.000	0.379	46000	58050	73680	1567	143	8.4
TCP02	34.000	0.373	46000	58050	73680	1531	118	7.3
TCP03	34.000	0.369	46000	58050	73680	1330	182	3.6

Table 4.2.2 Burst test summary

Test ID	Fail. Press. (psi)	RSTRENG Calc'd (psi)	RSTRENG Error (%)	B31G Calc'd (psi)	B31G Error (%)	PCORRC Calc'd (psi)	PCORRC Error (%)	Ritchie and Last Calc'd (psi)	Ritchie and Last Error (%)
SOL-1	3635	2945	19.0	2809	22.7	3778	-3.9	3400	6.5
SOL-2	3535	2831	19.9	2684	24.1	3580	-1.3	3115	11.9
SOL-3	3545	2989	15.7	2853	19.5	3838	-8.3	3454	2.6
SOL-4	3351	2562	23.5	2331	30.5	2943	12.2	2481	26.0
SOL-5	3627	2949	18.7	2813	22.4	3784	-4.3	3405	6.1
SOL-6	3659	2793	23.7	2639	27.9	3517	3.9	3027	17.3
SOL-7	3258	2902	10.9	2765	15.1	3719	-14.2	3348	-2.7
SOL-8	3469	3024	12.8	2889	16.7	3885	-12.0	3497	-0.8
SOL-9	3375	2914	13.7	2778	17.7	3736	-10.7	3363	0.4
SOL-10	3471	2529	27.1	2339	32.6	3024	12.9	2475	28.7
SOL-11	3154	2710	14.1	2476	21.5	3265	-3.5	2736	13.3
SOL-12	3127	2788	10.8	2683	14.2	3577	-14.4	3143	-0.5
SOL-14	3556	2987	16.0	2851	19.8	3834	-7.8	3451	3.0
NOR-1	2423	1912	21.1	1472	39.3	1923	20.6	1749	27.8
NOR-2	2619	2048	21.8	1908	27.1	2305	12.0	1945	25.7
NOR-3	2501	2399	4.1	2303	7.9	2932	-17.2	2639	-5.5
TNG-01	3076	2312	24.8	1693	44.9	2764	10.1	2335	24.1
RLK-1	1370	908	33.7	622	54.6	852	37.8	789	42.4
RLK-2	1143	814	28.7	548	52.1	743	35.0	686	40.0
RLK-3	1423	992	30.3	733	48.5	994	30.1	912	35.9
BCG-1	1994	1567	21.4	579	71.0	1061	46.8	867	56.5
BCG-2	2000	1655	17.3	1350	32.5	1862	6.9	1442	27.9
BCG-3	1988	1727	13.1	1576	20.7	2212	-11.3	1937	2.6
BCG-4	2201	1626	26.1	1348	38.8	1814	17.6	1450	34.1
BCG-5	2174	1750	19.5	1577	27.5	2226	-2.4	1902	12.5
BCG-6	1936	1630	15.8	1369	29.3	1811	6.5	1473	23.9
BCG-7	1838	1531	16.7	1199	34.8	1607	12.6	1175	36.1
BCG-8	2147	1734	19.3	1507	29.8	2085	2.9	1684	21.6
BCG-9	1831	1569	14.3	1285	29.8	1635	10.7	1362	25.6
ESS-01	1412	1234	12.6	1062	24.8	1185	16.1	794	43.8
NOV01	1556	1187	23.7	1064	31.6	1402	9.9	1074	31.0
NOV02-2	1168	963	17.5	591	49.4	890	23.8	808	30.8
NOV03-2	1244	969	22.1	470	62.2	677	45.5	636	48.9
NOV04	1434	988	31.1	464	67.6	682	52.5	636	55.7
NOV04-2	1582	1169	26.1	656	58.5	1007	36.3	899	43.2
NOV05	1167	973	16.6	550	52.8	797	31.7	741	36.5
NOV06	1669	1202	28.0	1076	35.5	1415	15.2	1144	31.4
TCP01	1567	1086	30.7	968	38.2	1373	12.4	1123	28.3
TCP02	1531	1128	26.3	995	35.0	1440	6.0	1215	20.7
TCP03	1330	1091	18.0	995	25.2	1414	-6.3	1172	11.9

Table 4.2.3 Failure prediction summary

	% Error		* Failure Ratio	
	RSTRENG	B31G	RSTRENG	B31G
Average	20.2	33.8	1.261	1.624
Standard Deviation	6.6	15.3	0.106	0.523
Minimum	4.1	7.9	1.043	1.086
Maximum	33.7	71.0	1.508	3.443

Table 4.4.1 Failure pressure prediction statistics for B31G and RSTRENG

* Failure Ratio = (Predicted Failure Pressure) / (Actual Failure Pressure)

	Failure Pressure	* Predicted Geometric Instability		** RSTRENG		*** B31G		**** Ritchie and Last		***** Modified Geometric Instability	
	(psi)	(psi)	% Error	(psi)	% Error	(psi)	% Error	(psi)	% Error	(psi)	% Error
SOL-1	3635	4096	-12.7	3109	14.5	2809	22.7	3400	6.5	3522	3.1
SOL-3	3545	4099	-15.6	3158	10.9	2853	19.5	3454	2.6	3525	0.6
SOL-5	3627	4092	-12.8	3113	14.2	2813	22.4	3405	6.1	3519	3.0
SOL-7	3258	4089	-25.5	3060	6.1	2765	15.1	3348	-2.7	3516	-7.9
SOL-8	3469	4029	-16.1	3197	7.8	2889	16.7	3497	-0.8	3465	0.1
SOL-9	3375	4092	-21.3	3074	8.9	2778	17.7	3363	0.4	3519	-4.3
SOL-14	3556	3984	-12.0	3155	11.3	2851	19.8	3451	3.0	3426	3.6
Average->			-16.6		10.5		19.2		2.1		-0.3
Std. Dev.->			5.04		3.14		2.84		3.44		4.34

* Plain Pipe solution from Section 3.2
** RSTRENG Flow Stress = (SMYS+10000)
*** B31G Flow Stress = (1.1xSMYS)
**** Ritchie and Last Flow Stress = (0.9xUTS)
***** Modified Geometric Instability = 0.86x(Geometric Instability Pressure)

Table 4.4.2 Plain Pipe Failure Pressure Predictions

	% Error			
	PCORRC*	Ritchie**	Mod. RSTRENG***	Long Groove****
Average	10.3	23.1	10.2	19.3
Standard Deviation	18.28	16.59	6.72	15.48
Minimum	-17	-6	-1	-7.9
Maximum	52	57	25	51

	Failure Ratio			
	PCORRC*	Ritchie**	Mod. RSTRENG***	Long Groove****
Average	1.17	1.37	1.12	1.29
Standard Deviation	0.297	0.330	0.086	0.283
Minimum	0.85	0.95	0.99	0.93
Maximum	2.10	2.30	1.34	2.05

Table 4.4.3 Failure pressure prediction statistics for PCORRC
Ritchie and Last and Modified RSTRENG models

* Equation (2.2.3)
** Equation (2.2.5) - B31G with modified flow stress
*** Equation (4.4.5)
****Equation (3.3.24)

Test	Maximum % Depth	Length (in)	Failure Pressure (psi)	FE Prediction (psi)	% Error
SOL-2	25	2.5	3535	3832	-8.4
SOL-4	35	8.0	3351	3419	-2.0
SOL-6	31	2.4	3659	3365	8.0
SOL-10	38	5.7	3471	3321	4.3
SOL-11	31	5.0	3154	3408	-8.0
SOL-12	26	2.0	3127	3690	-18.0
NOR-2	33	5.5	2619	2850	-8.8
RLK-1	50	35.5	1370	1154	15.7
RLK-2	55	56.4	1143	1262	-10.4
RLK-3	40	54.0	1423	1105	22.4
BCG-2	56	1.9	2000	1984	0.8
BCG-3	34	1.2	1988	2048	-3.0
BCG-4	45	4.0	2201	2124	3.5
BCG-5	32	1.8	2174	2183	-0.4
BCG-6	43	4.9	1936	2078	-7.3
BCG-7	60	2.6	1838	1849	-0.6
BCG-8	55	1.5	2147	2040	5.0
BCG-9	44	6.2	1831	1939	-5.9
ESS-01	72	3.9	1412	1370	3.0
NOV01	53	5.2	1556	1476	5.1
NOV04	53	16.4	1582	1633	-3.2
NOV06	44	6.7	1669	1566	6.2
TCP01	38	8.4	1567	1555	0.8
TCP02	29	8.0	1531	1521	0.6
TCP03	49	3.6	1330	1378	-3.6
				Average->	-0.18
				Standard Deviation ->	8.45

Table 4.5.1 Finite Element Failure Predictions

	% Error CPS	Failure Ratio CPS
Average	3.1	1.04
Standard Deviation	6.5	0.070
Minimum	-8	0.93
Maximum	17	1.20

Table 5.1.1 Failure pressure prediction statistics for CPS

	Percent Error *		Probability of a Non-conservative Prediction	Probability of a Conservative Prediction
	Mean	Standard Deviation		
	(%)	(%)	(-)	(-)
B31G	33.6	15.3	1.39E-02	9.86E-01
RSTRENG	20.2	6.6	1.08E-03	9.99E-01
CPS	3.1	6.5	3.17E-01	6.83E-01
FE-All	-0.2	8.4	5.08E-01	4.92E-01
FE-New Scanner	0.1	4.1	4.94E-01	5.06E-01

Table 5.2.1 Summary statistics for the percent error in various evaluation procedures

* Percent Error = $(FP_{Actual}-FP_{Predicted})/FP_{Actual}*100\%$

Example: BCG 02	FP = 2000 psi SMYS = 42000 psi t = 0.184" OD = 10.747"						
	Raw Residual **			Predicted Failure Pressure	Operating Pressure ***	Failure Function		Probability of Failure
	Mean	Standard Deviation				Mean	Standard Deviation	
	(psi)	(psi)		(psi)	(psi)	(psi)	(psi)	(-)
B31G	702	258		1350	1072	979	258	7.49E-05
RSTRENG	450	192		1655	1072	1033	192	3.53E-08
CPS	57	146		1969	1072	954	146	2.93E-11
FE-All	-21	190		1984	1072	890	190	1.36E-06
FE-New Scanner	1	74		1984	1072	913	74	0.00E+00

Table 5.2.2 Probability of defect failure based on operating pressure and the raw residuals

** Raw Residual = $(FP_{Experimental}-FP_{Predicted})$

*** Operating Pressure Stress Level = 72% SMYS

Example: BCG 02		FP = 2000 psi SMYS = 42000 psi t = 0.184" OD = 10.747"						
	Raw Residual **		**Predicted Failure Pressure**	**Probability of Failure**		**Failure Function Mean**	**Allowable Operating Pressure**	
	Mean (psi)	Standard Deviation (psi)	(psi)	(-)		(psi)	(psi)	(% SMYS)
B31G	702	258	1350	1.00E-06		2051	820	57
RSTRENG	450	192	1655	1.00E-06		2105	1191	83
CPS	57	146	1969	1.00E-06		2026	1331	93
FE-All	-21	190	1984	1.00E-06		1962	1058	74
FE-New Scanner	1	74	1984	1.00E-06		1985	1632	113
B31G	702	258	1350	1.00E-03		2051	1253	87
RSTRENG	450	192	1655	1.00E-03		2105	1513	105
CPS	57	146	1969	1.00E-03		2026	1576	110
FE-All	-21	190	1984	1.00E-03		1962	1376	96
FE-New Scanner	1	74	1984	1.00E-03		1985	1756	122

Table 5.2.3 Allowable operating pressure for various probabilities of failure

** Raw Residual = ($FP_{Experimental}$-$FP_{Predicted}$)

Operation Pressure (%SMYS)	Operation Pressure (psi)	Allowable Defect Depth (%)	Allowable Defect Depth (inches)
72	743	61	0.228
100	1032	46	0.172
135	1393	27	0.100

Table 6.5.1 Long Groove solution - defect failure pressure as a function of defect depth

Defect	Maximum Defect Depth (%)	Maximum Defect Depth (inches)	Defect Length (inches)	Predicted Failure Pressure CPS (psi)	RSTRENG (psi)	B31G (psi)
TCP02-1A-F	43	0.161	25.2	1349	1018	645
TCP02-1G	32	0.118	7.3	1463	1128	995
TCP02-1H	41	0.153	1.8	1454	1162	1117

Actual Failure Pressure: 1531 psi

Table 6.5.2 Defect depths and predicted failure pressure for selected defects on pipe section TCP-02

Defect	CPS		FE		RSTRENG		B31G	
	Calc'd Failure Pressure (psi)	Prob. of Failure (-)	Calc'd Failure Pressure (psi)	Prob. of Failure (-)	Calc'd Failure Pressure (psi)	Prob. of Failure (-)	Calc'd Failure Pressure (psi)	Prob. of Failure (-)
TCP02-1AF	1349	5.16E-03	-	-	1018	1.16E-02	645	1.12E-01
TCP02-1G	1463	4.12E-04	1521	5.03E-07	1128	2.23E-03	995	5.01E-03
TCP02-1H	1454	5.14E-04	-	-	1162	1.27E-03	1117	1.16E-03

Table 6.5.3 Defect reliability for defects in section TCP-02 an operating pressure of 1032 psi (100% SMYS)

Defect	CPS		FE		RSTRENG		B31G	
	Calc'd Failure Pressure (psi)	Maximum Operating Pressure (psi)	Calc'd Failure Pressure (psi)	Maximum Operating Pressure (psi)	Calc'd Failure Pressure (psi)	Maximum Operating Pressure (psi)	Calc'd Failure Pressure (psi)	Maximum Operating Pressure (psi)
TCP02-1AF	1349	710	-	-	1018	552	645	117
TCP02-1G	1463	824	1521	1169	1128	662	995	467
TCP02-1H	1454	815	-	-	1162	696	1117	589

Table 6.5.4 Allowable operating pressures for defects in pipe section TCP-02 for a 1x10^-6 probability of failure.

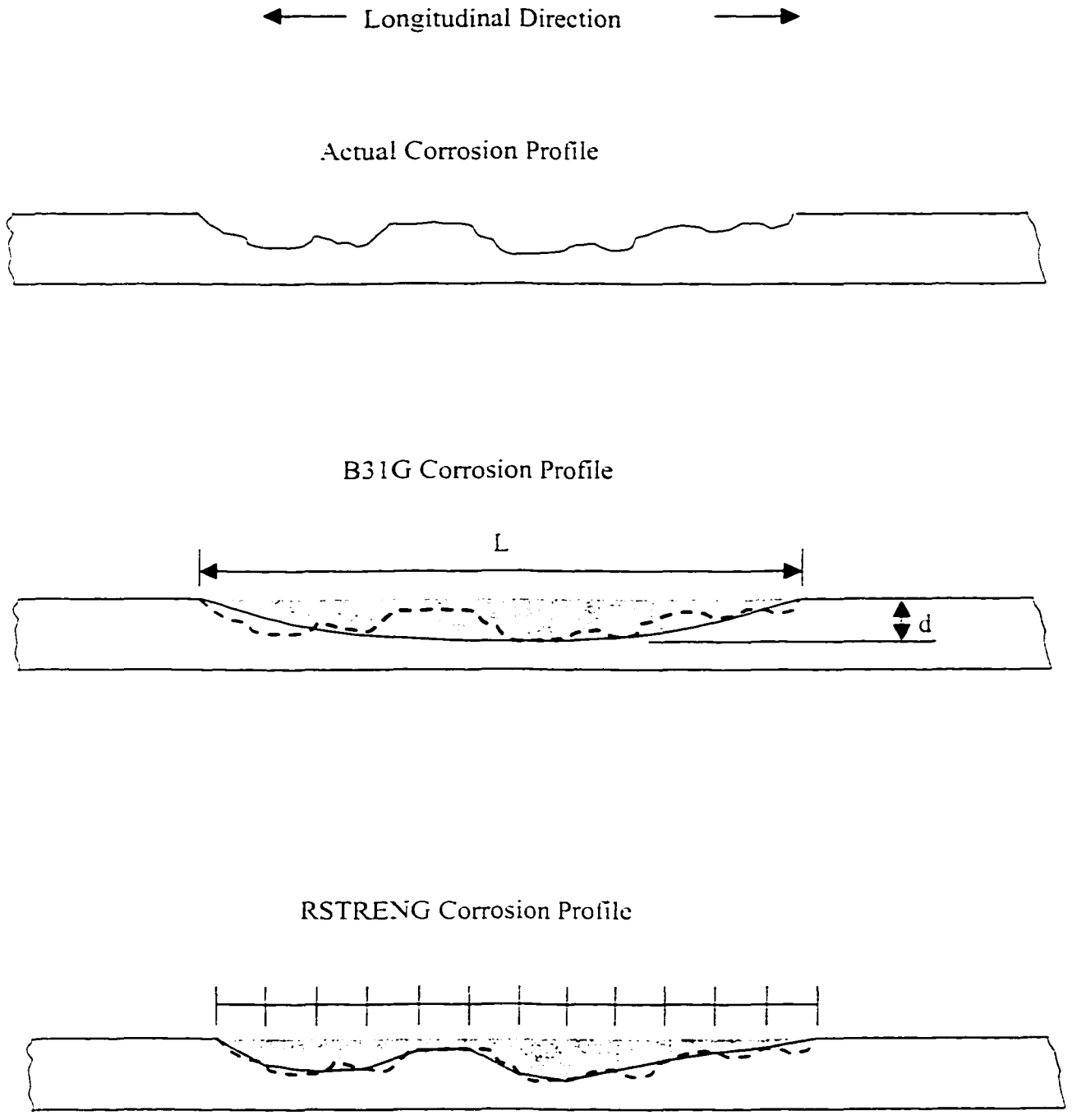


Figure 2.1.1 Corrosion defect profiles

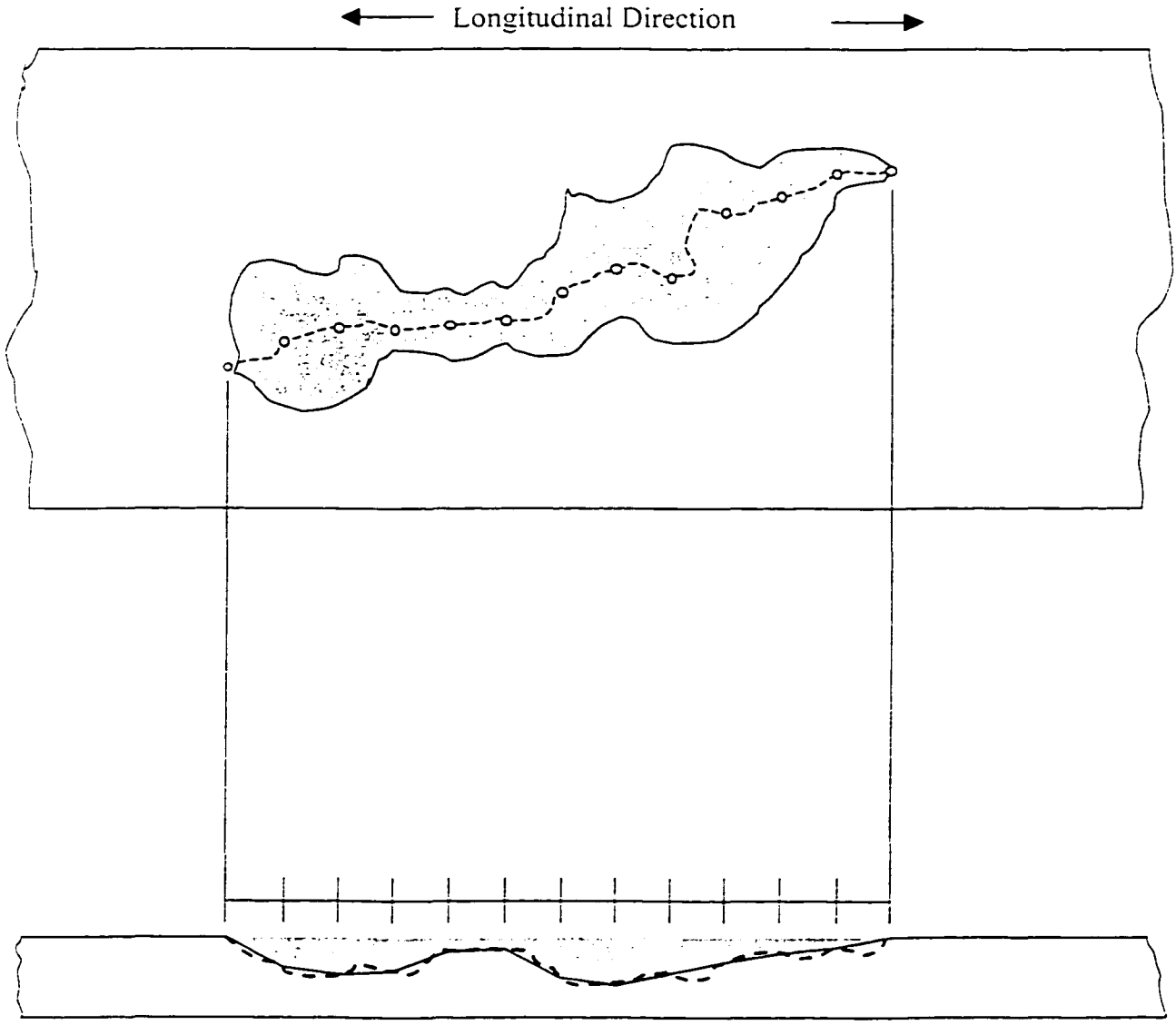


Figure 2.1.2 RSTRENG River bottom projection

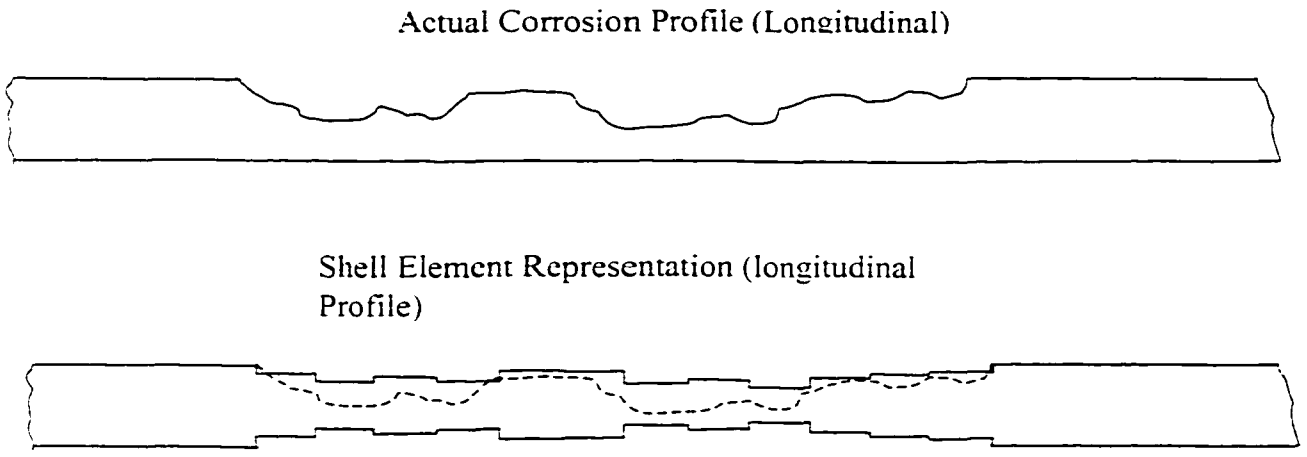


Figure 2.2.1 Shell analysis of corrosion defects

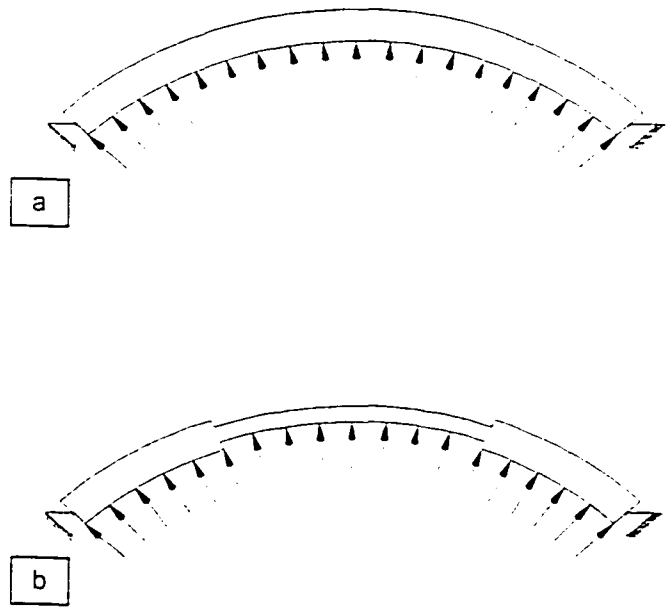


Figure 2.3.1 Membrane-arch model

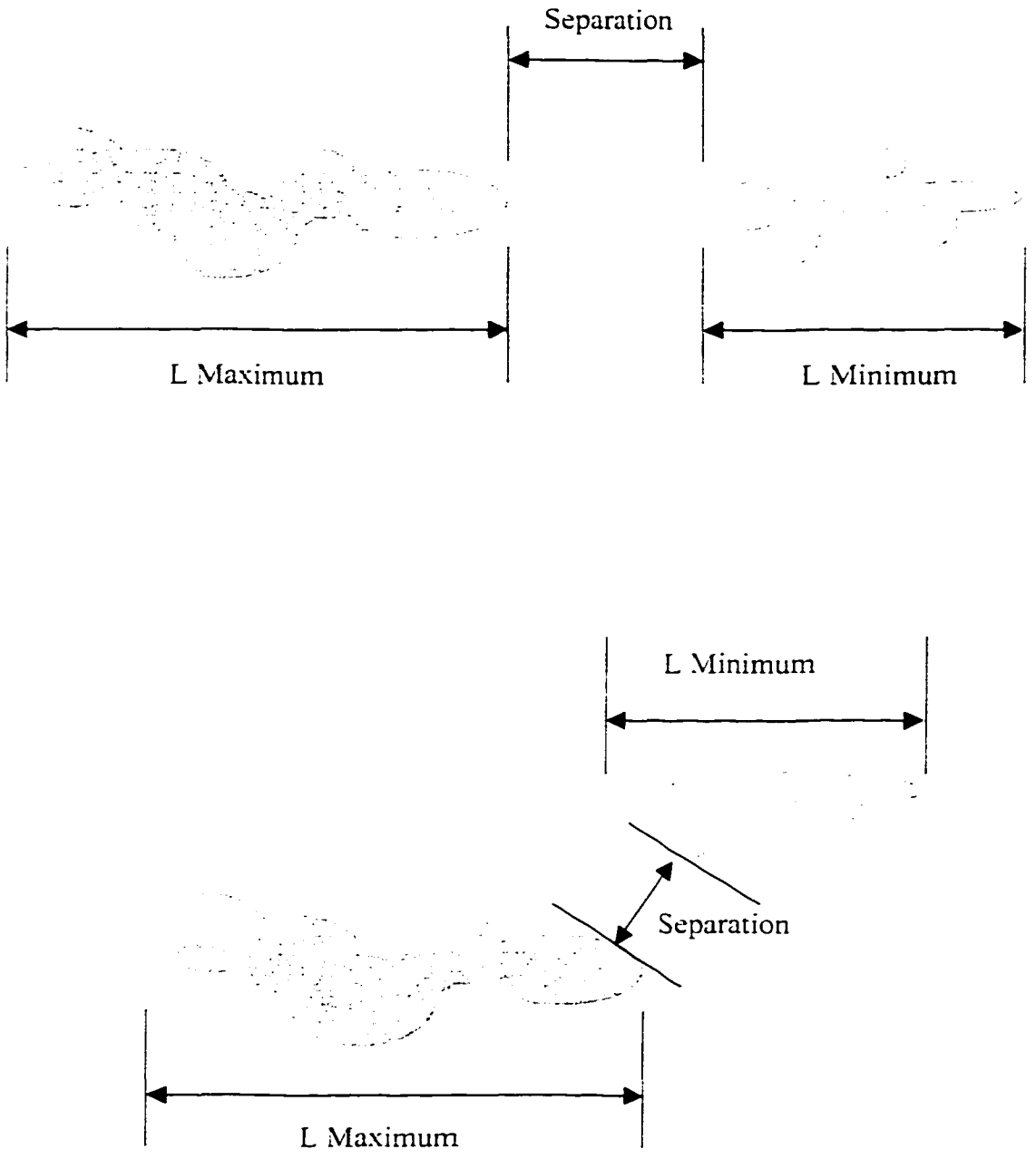


Figure 2.5.1 CSA defect interaction rules

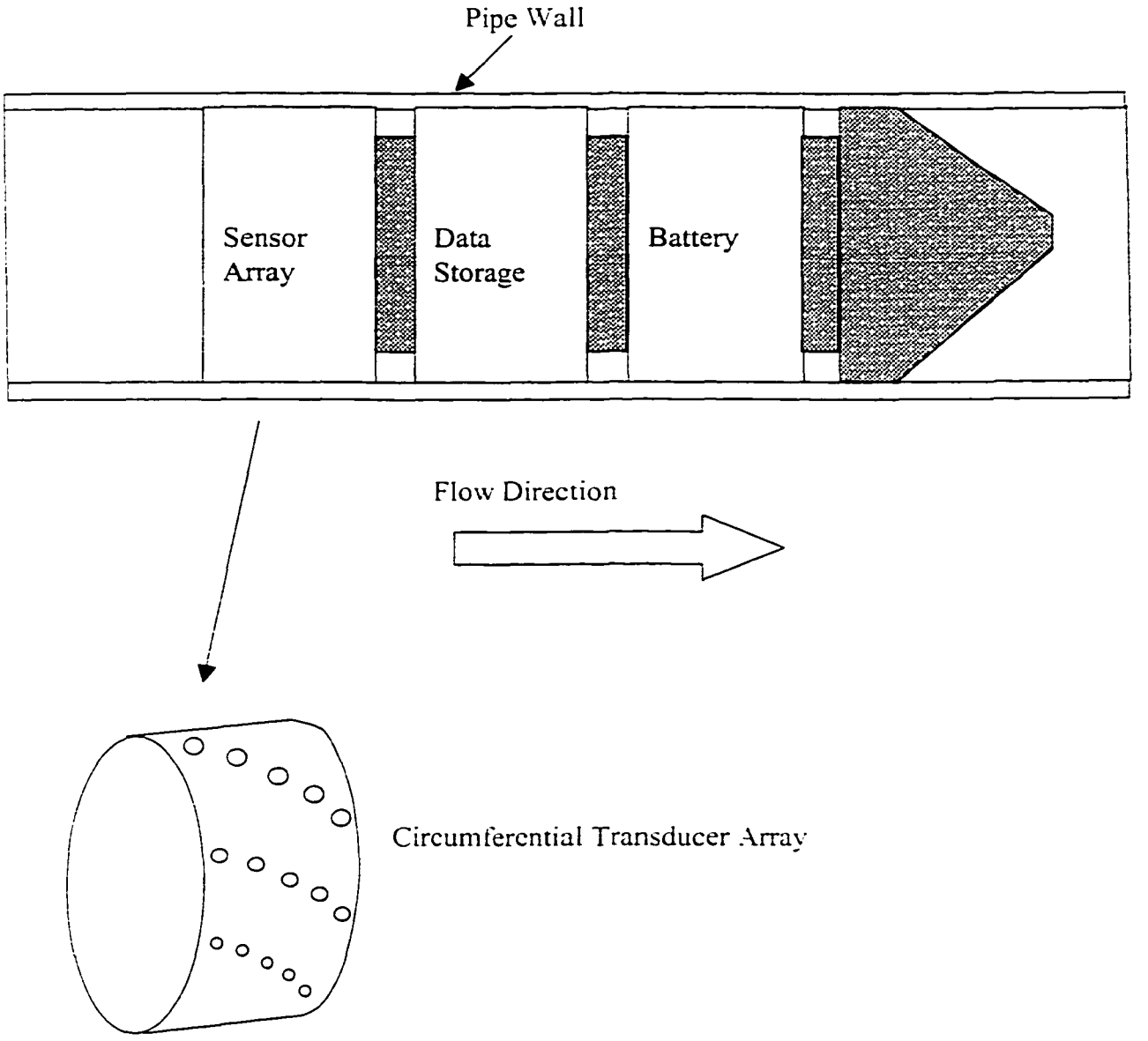


Figure 2.6.1 Internal inspection device (intelligent pig)

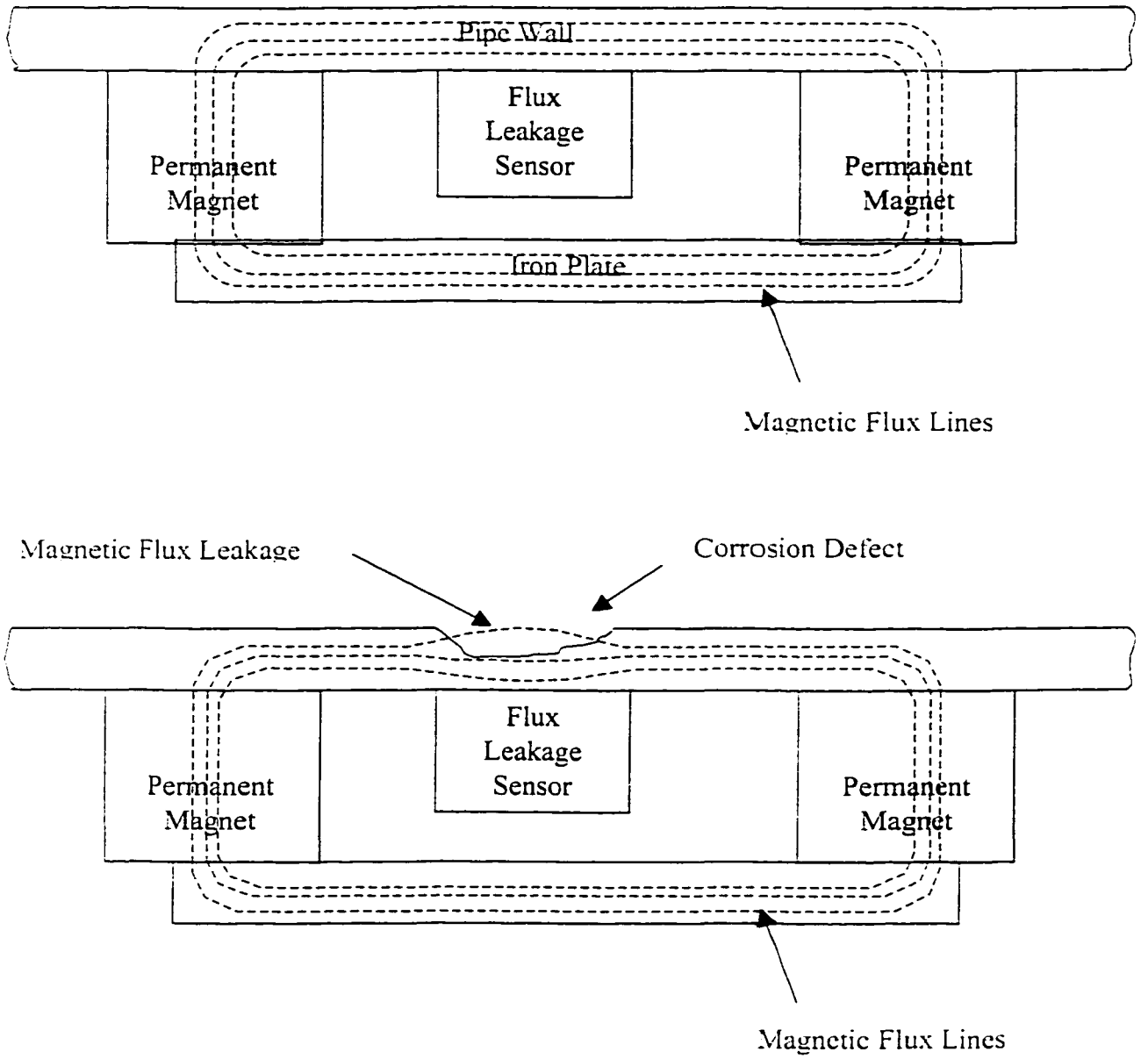


Figure 2.6.2 Schematic of magnetic flux leakage technology

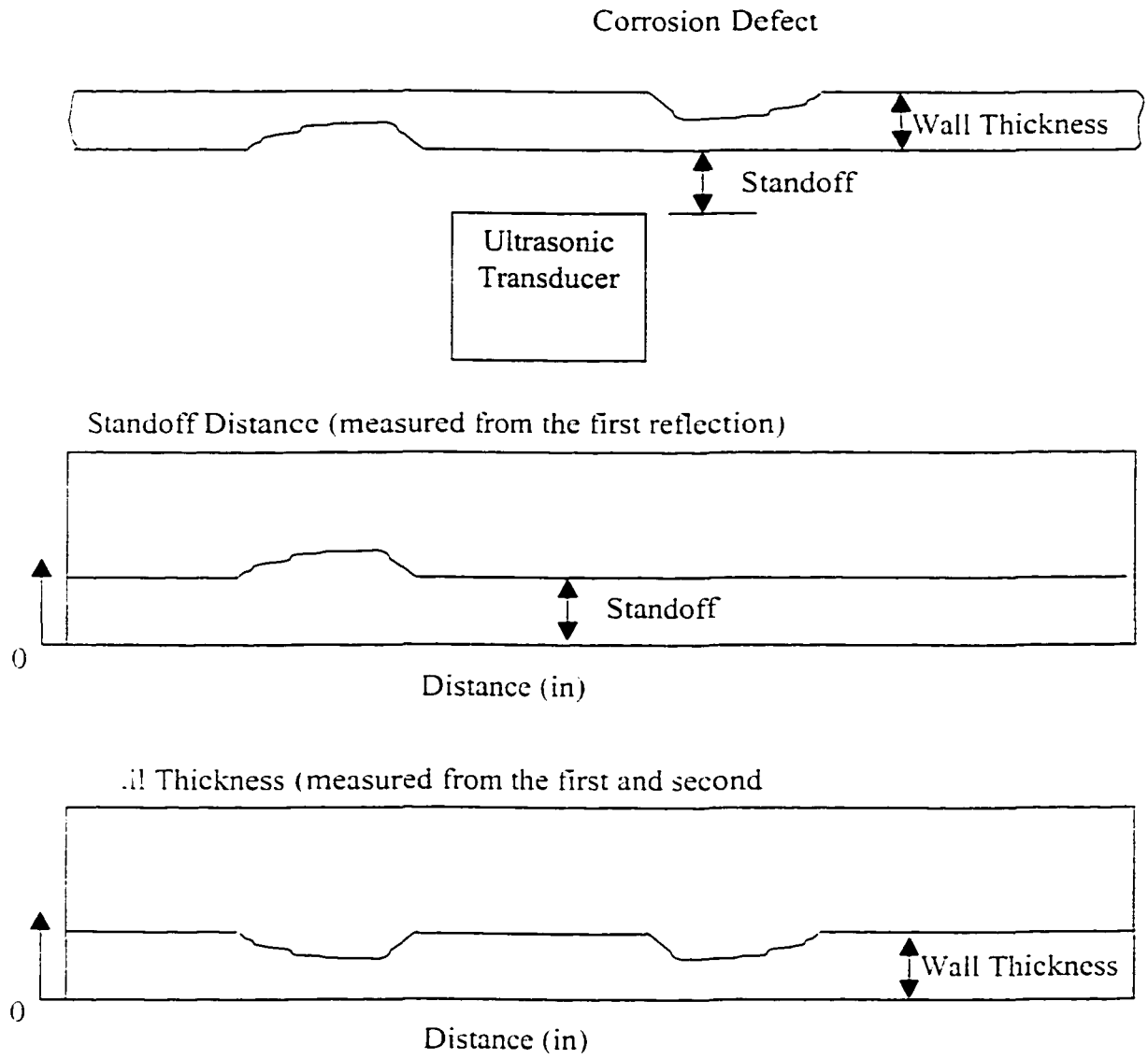


Figure 2.6.3 Schematic of ultrasonic technology

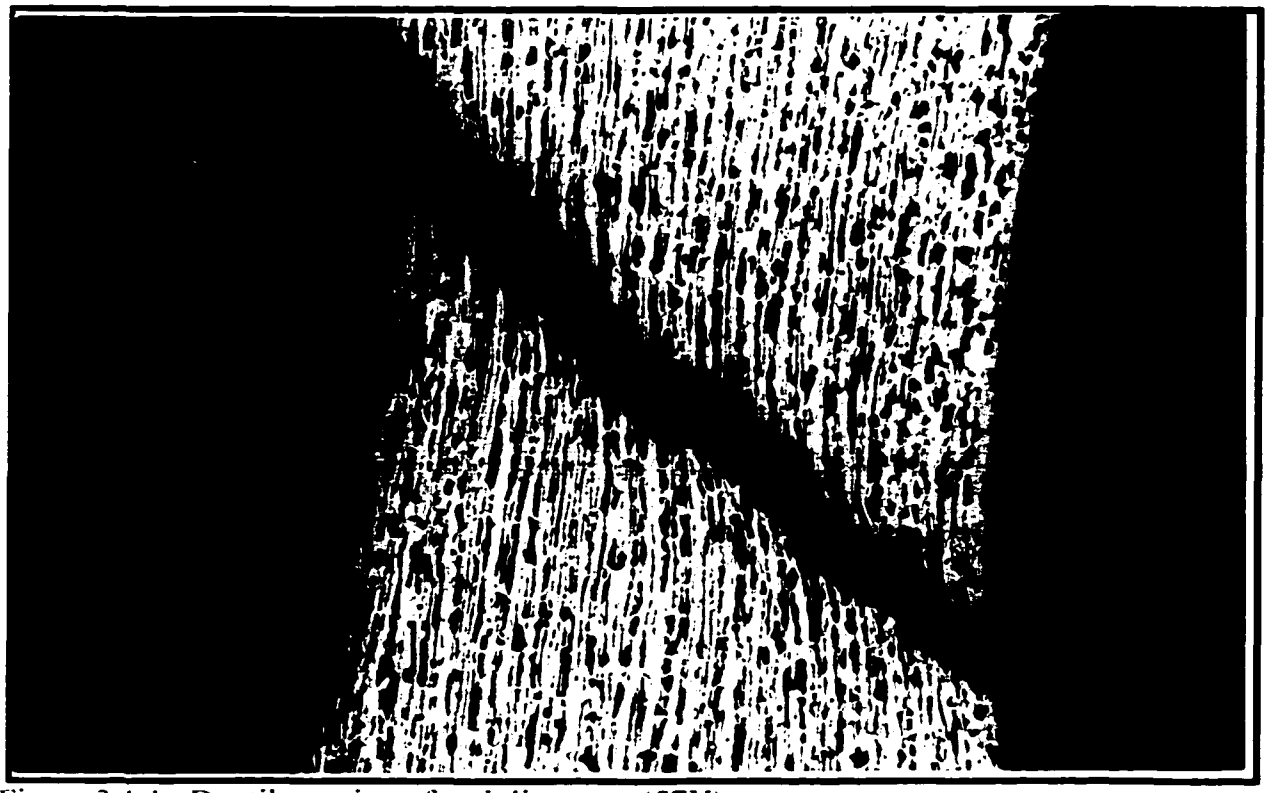


Figure 3.1.1a Ductile tearing of a pit ligament (57X)

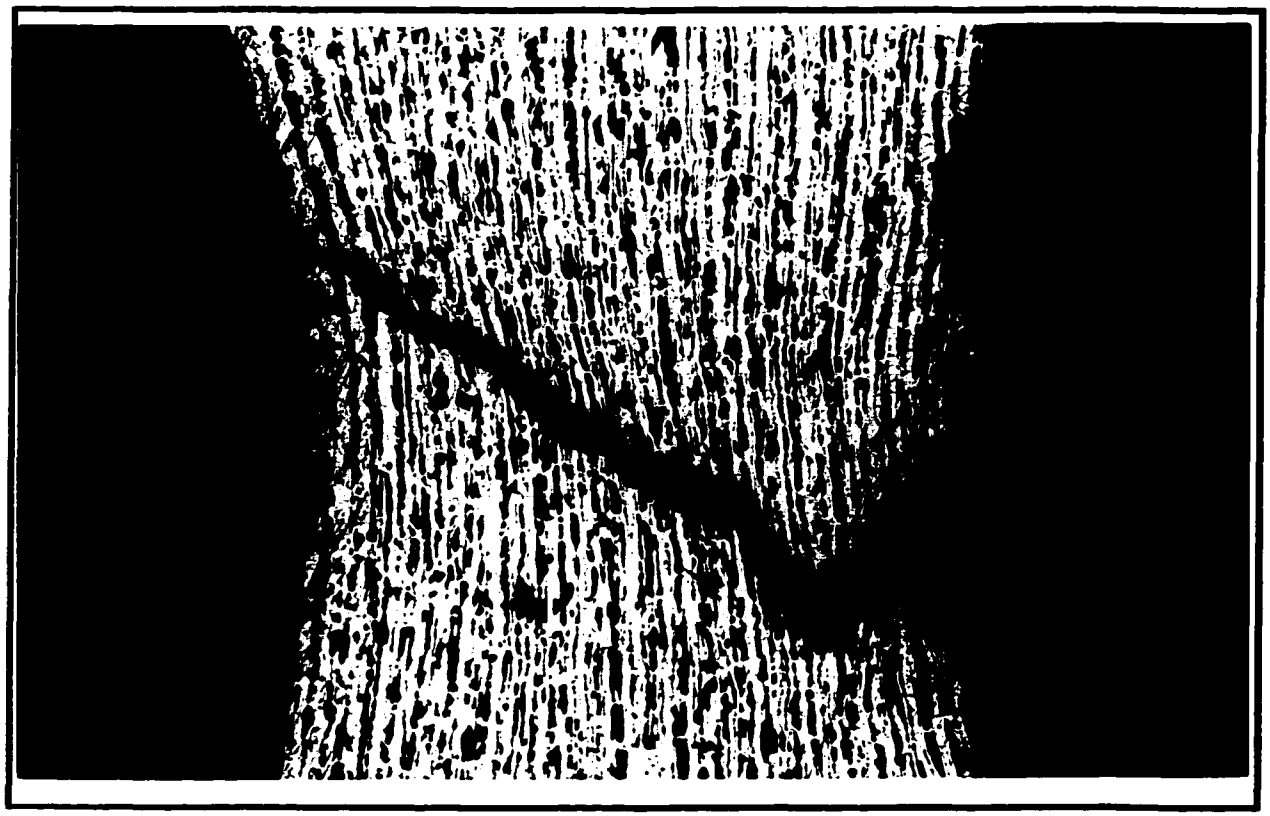


Figure 3.1.1b Ductile tearing of a pit ligament resulting in a leak (57X)



Figure 3.1.2a Partial ductile tearing of a pit ligament (57X)

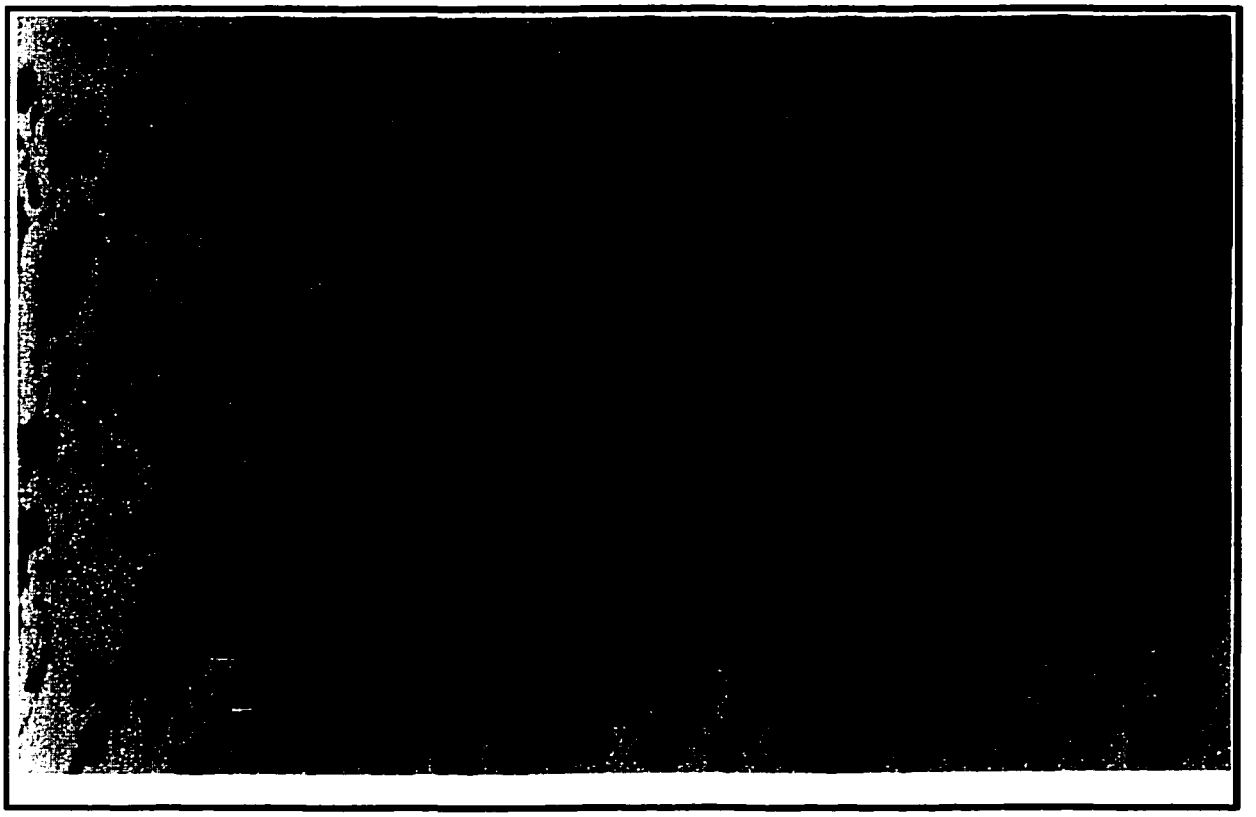


Figure 3.1.2b Partial ductile tearing of a pit ligament (230X)

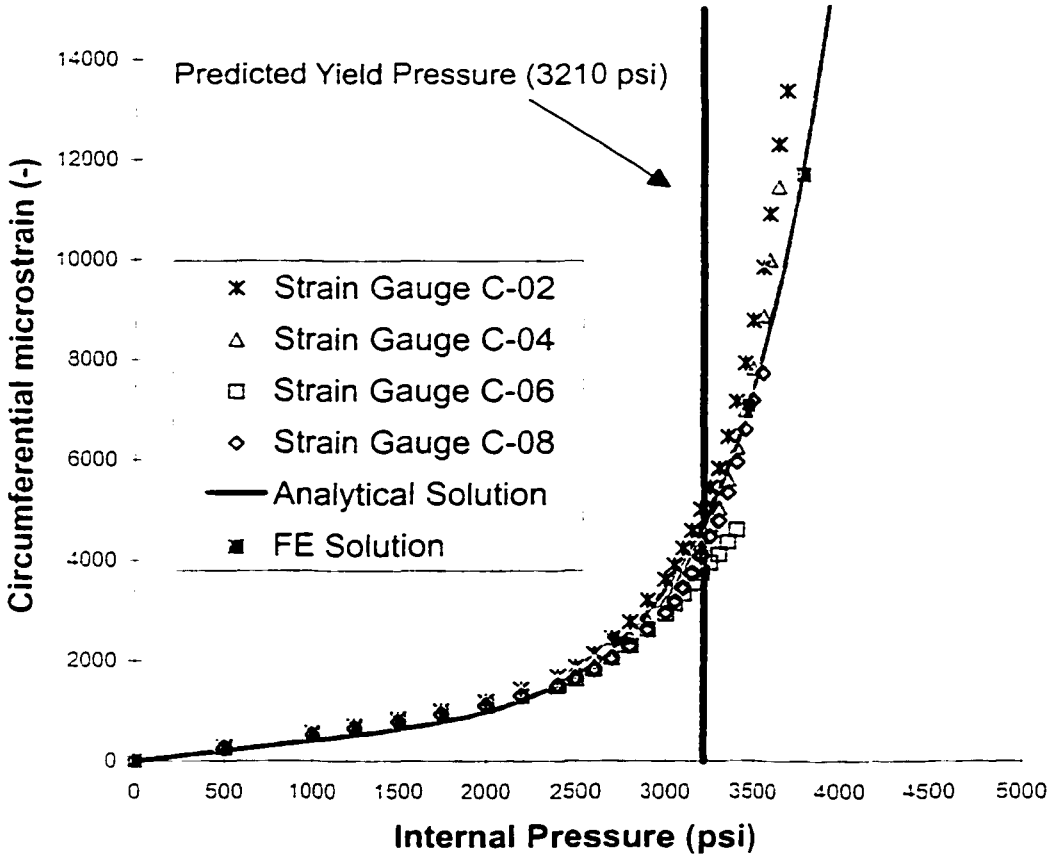
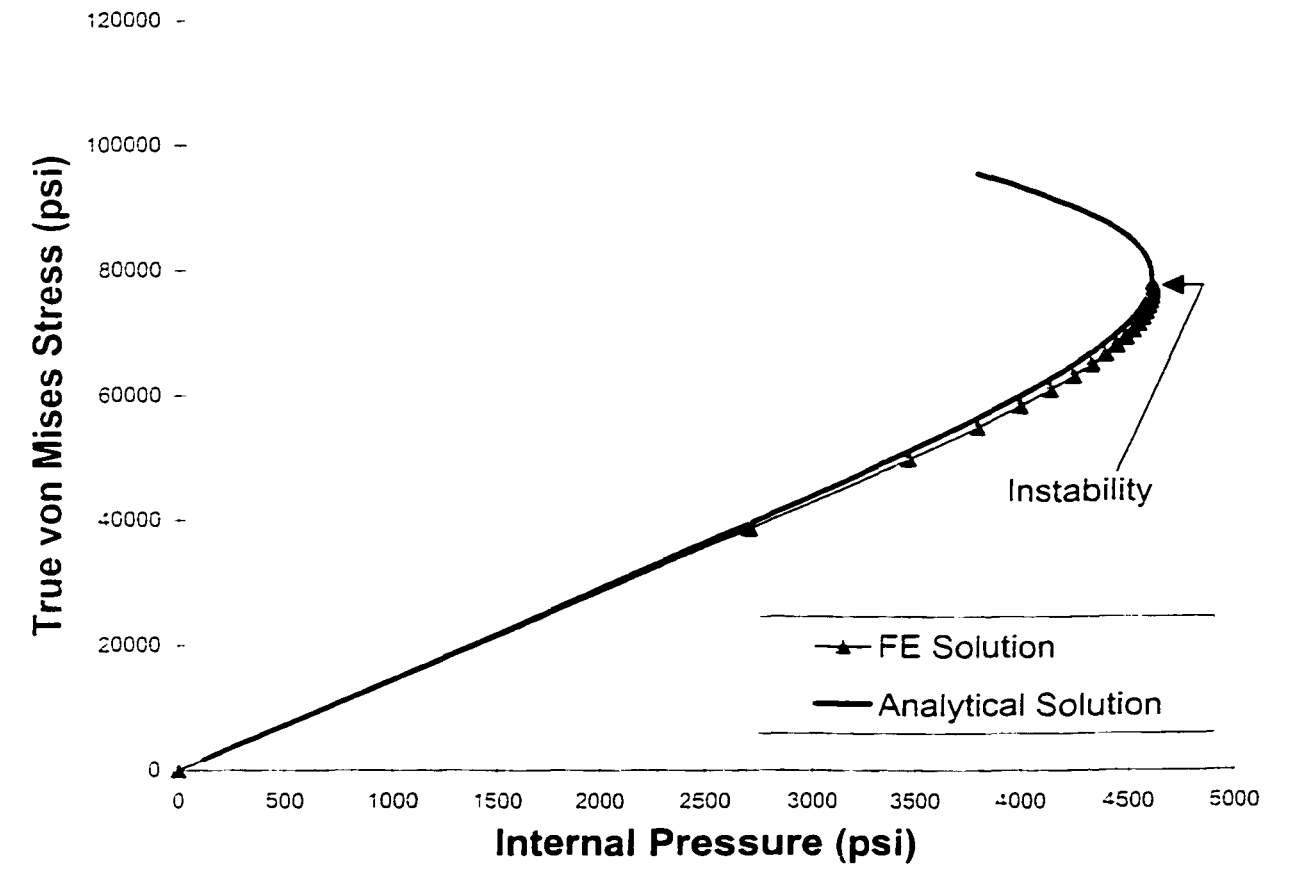


Figure 3.2.1 Circumferential strain in pressurized plain pipe



Instability	Pressure	True von Mises Stress
FE Solution	4608 psi	77107 psi
Analytical Solution	4605 psi	78641 psi

Figure 3.2.2 True von Mises stress for pressurized plain pipe

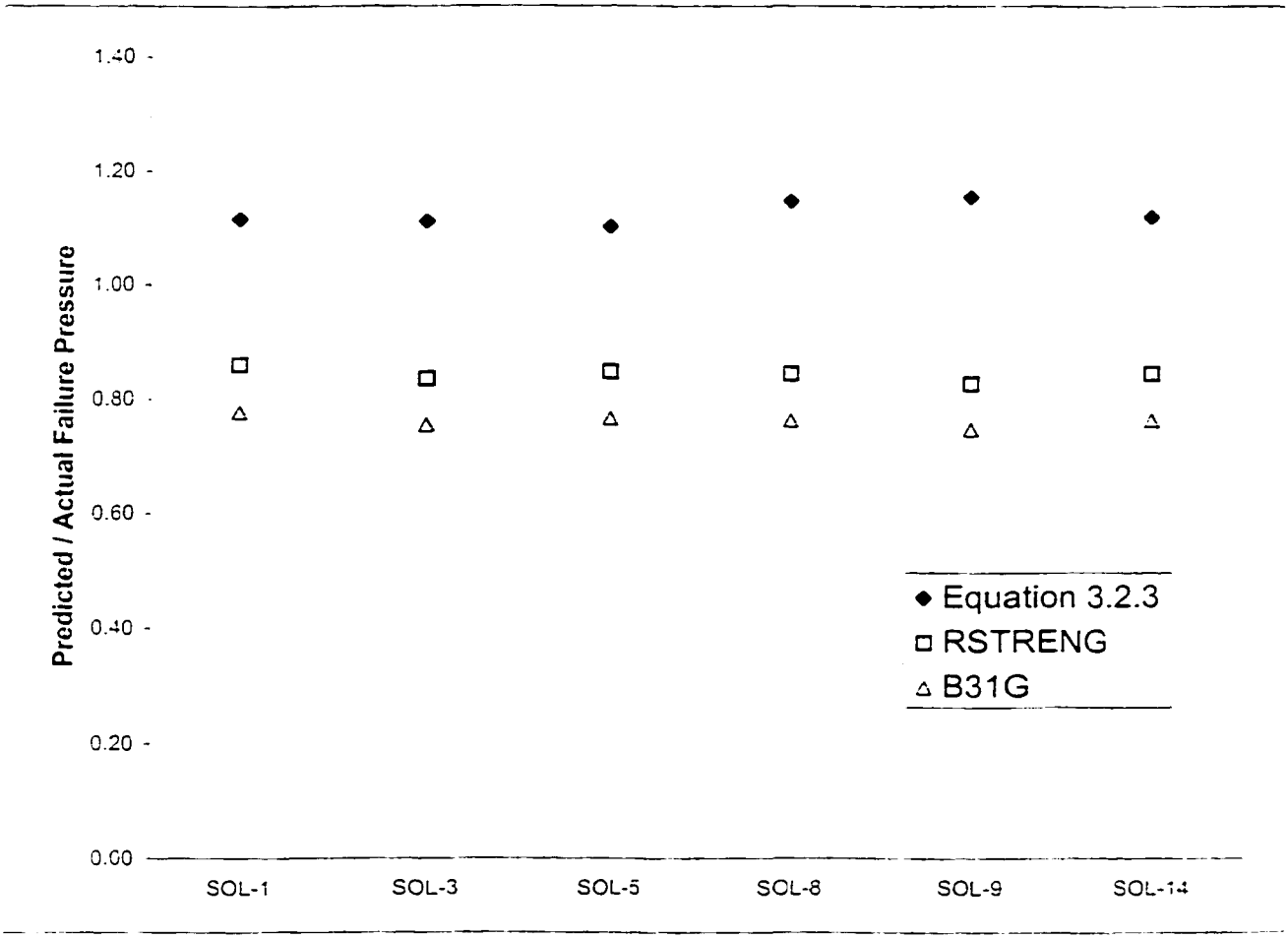


Figure 3.2.3: Failure pressure of plain pipe for 6 burst tests

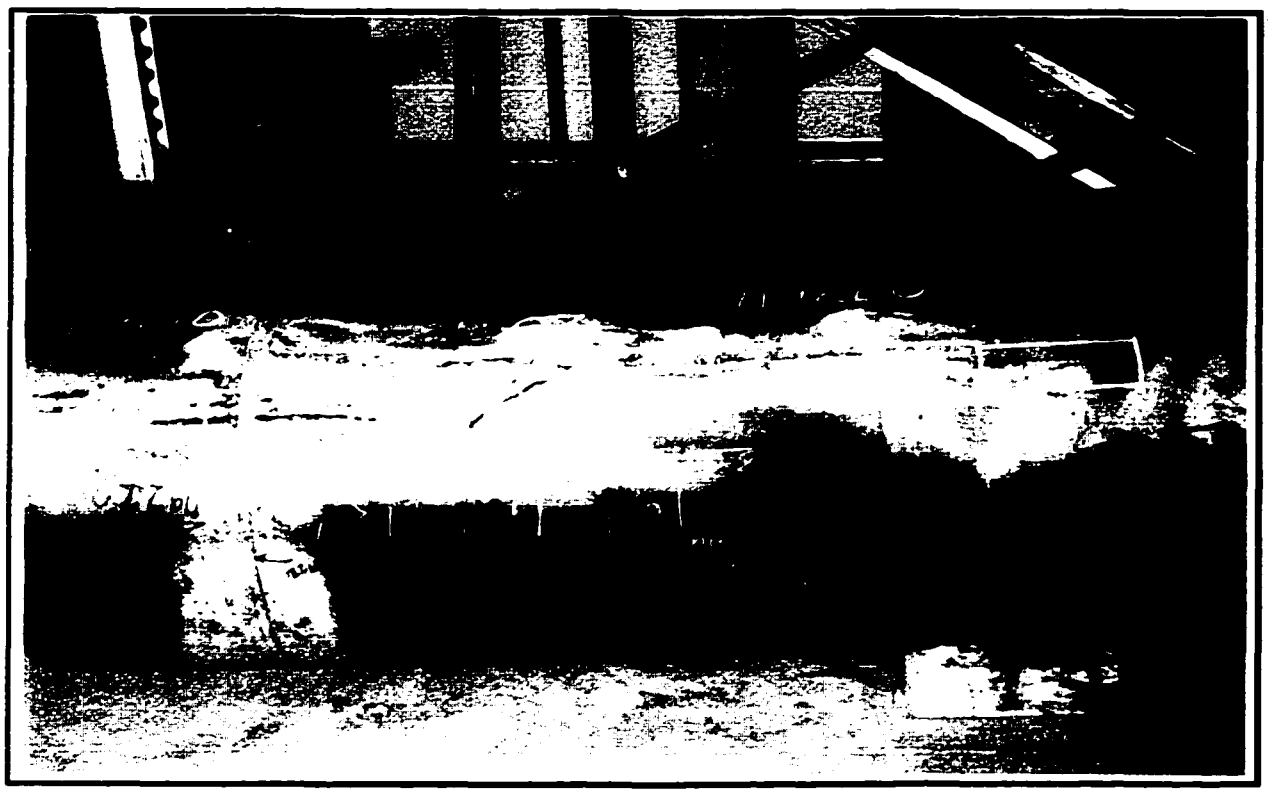


Figure 3.3.1a: Long, longitudinally oriented natural corrosion defect

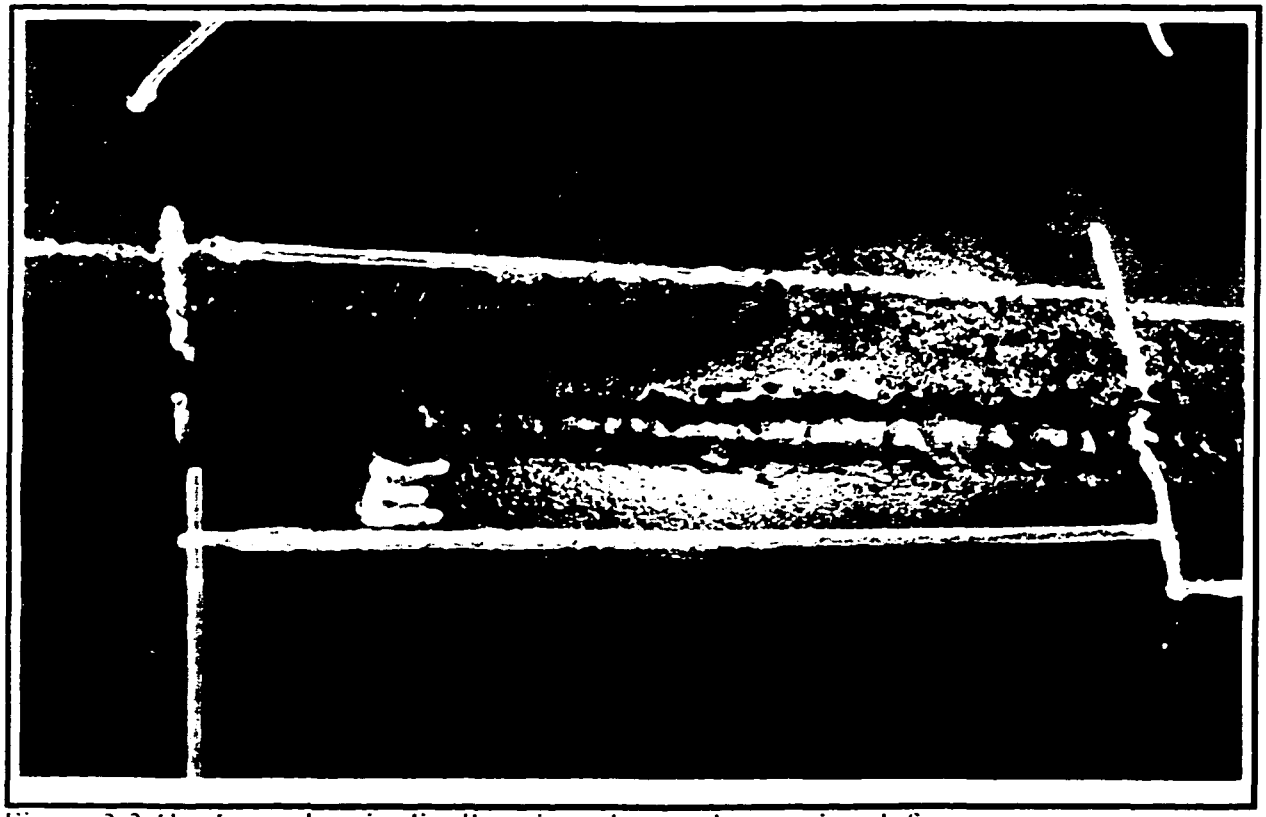


Figure 3.3.1b: Long, longitudinally oriented natural corrosion defect

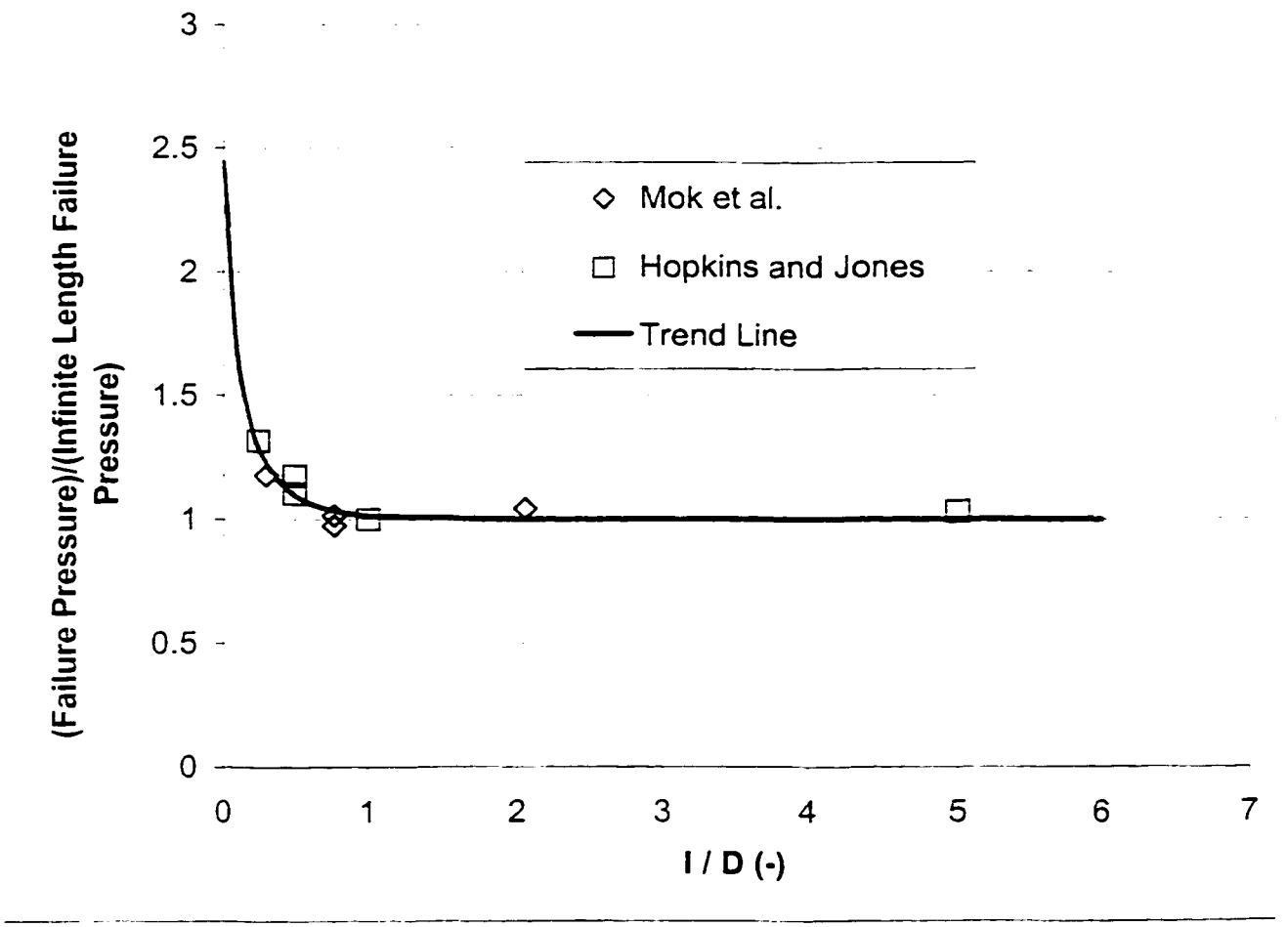


Figure 3.3.2: Failure Pressure of 40% depth grooves with varying length

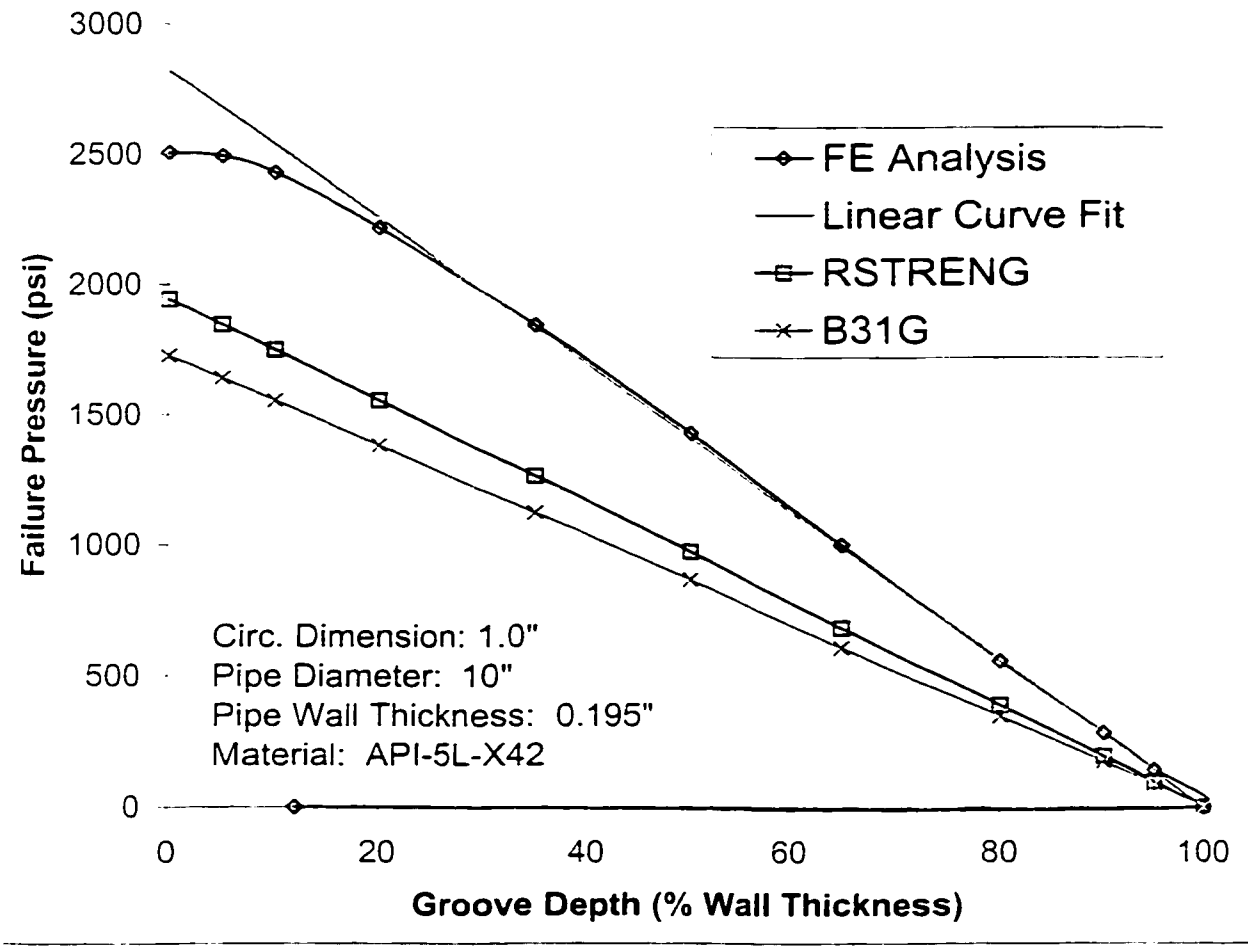


Figure 3.3.3: Failure pressures of infinitely long, longitudinally oriented grooves

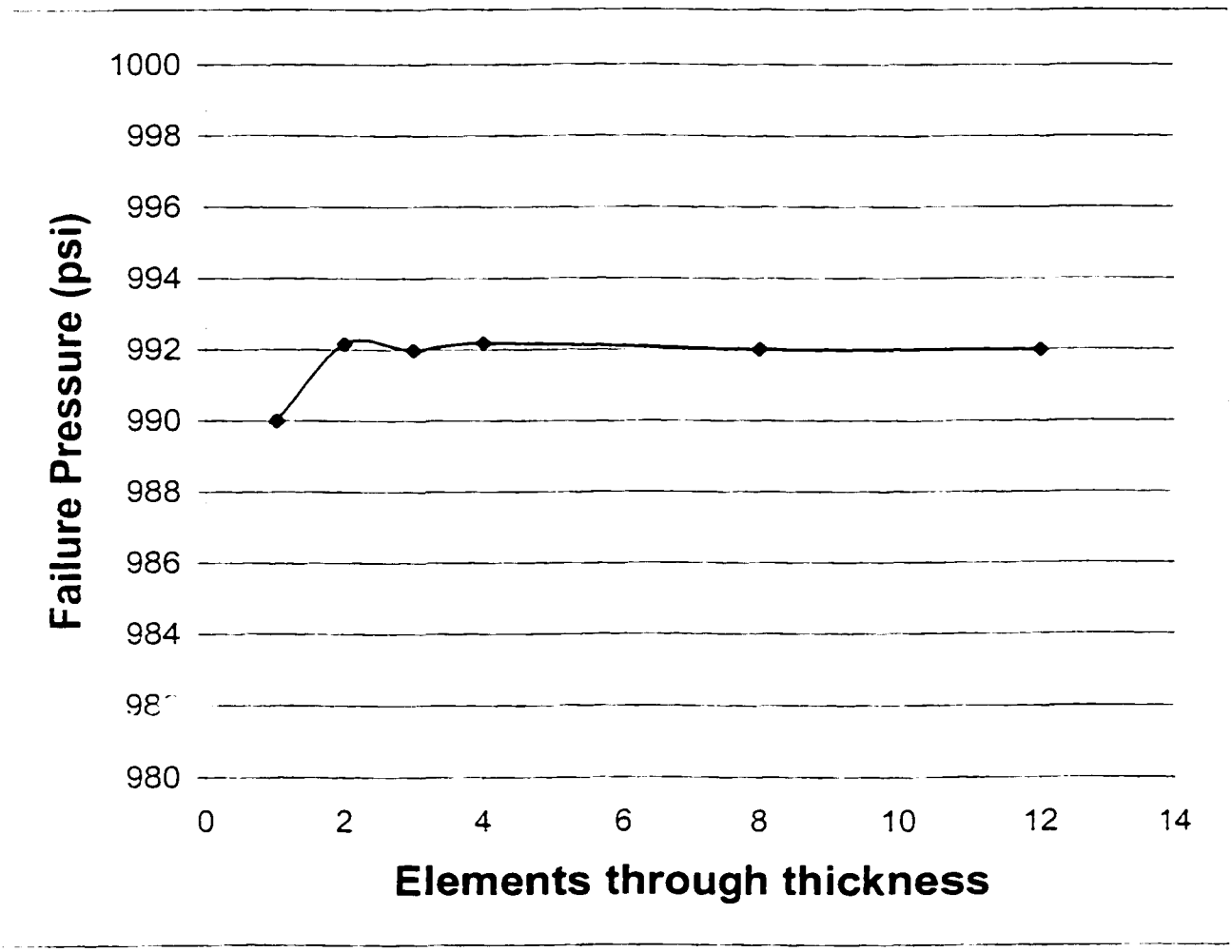


Figure 3.3.4: Variation in failure pressure with mesh density
for a 65% depth longitudinal groove

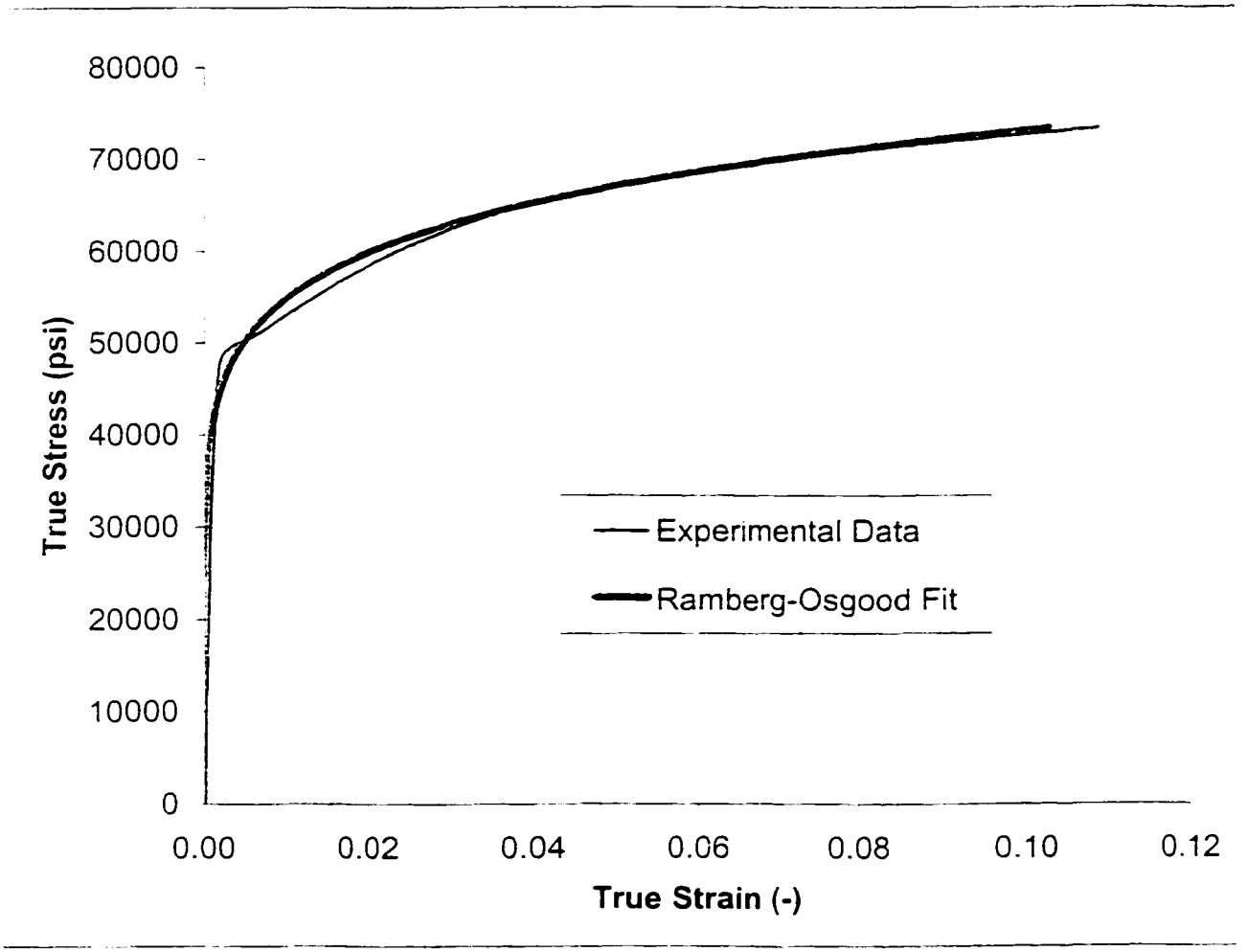


Figure 3.3.5: True stress-strain curve for grade API-5L-X42 steel

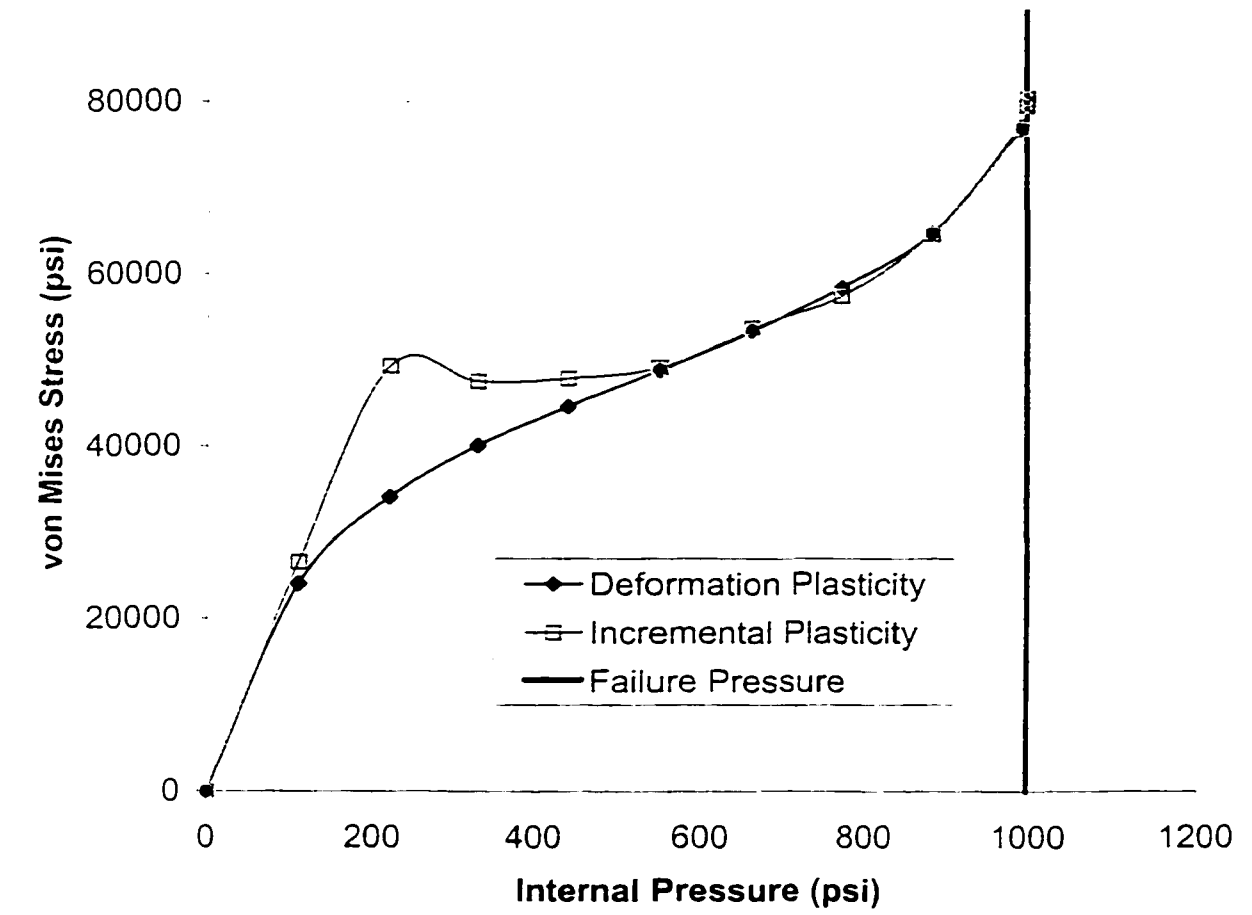


Figure 3.3.6: von Mises stress at the outside of the ligament
for a 65% depth longitudinal groove

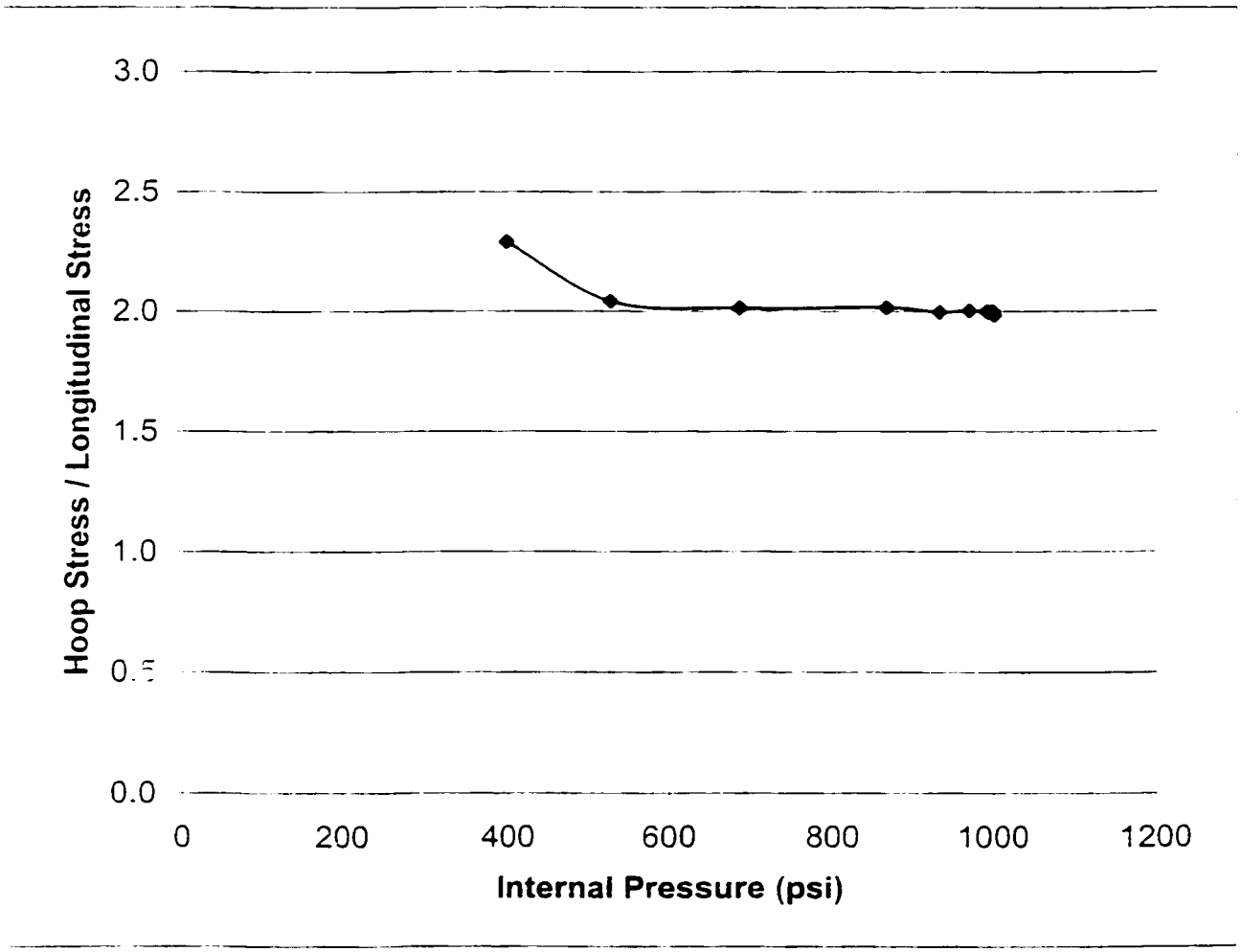


Figure 3.3.7: Ratio of hoop stress / longitudinal stress for a 65% depth longitudinal groove analysed using incremental plasticity

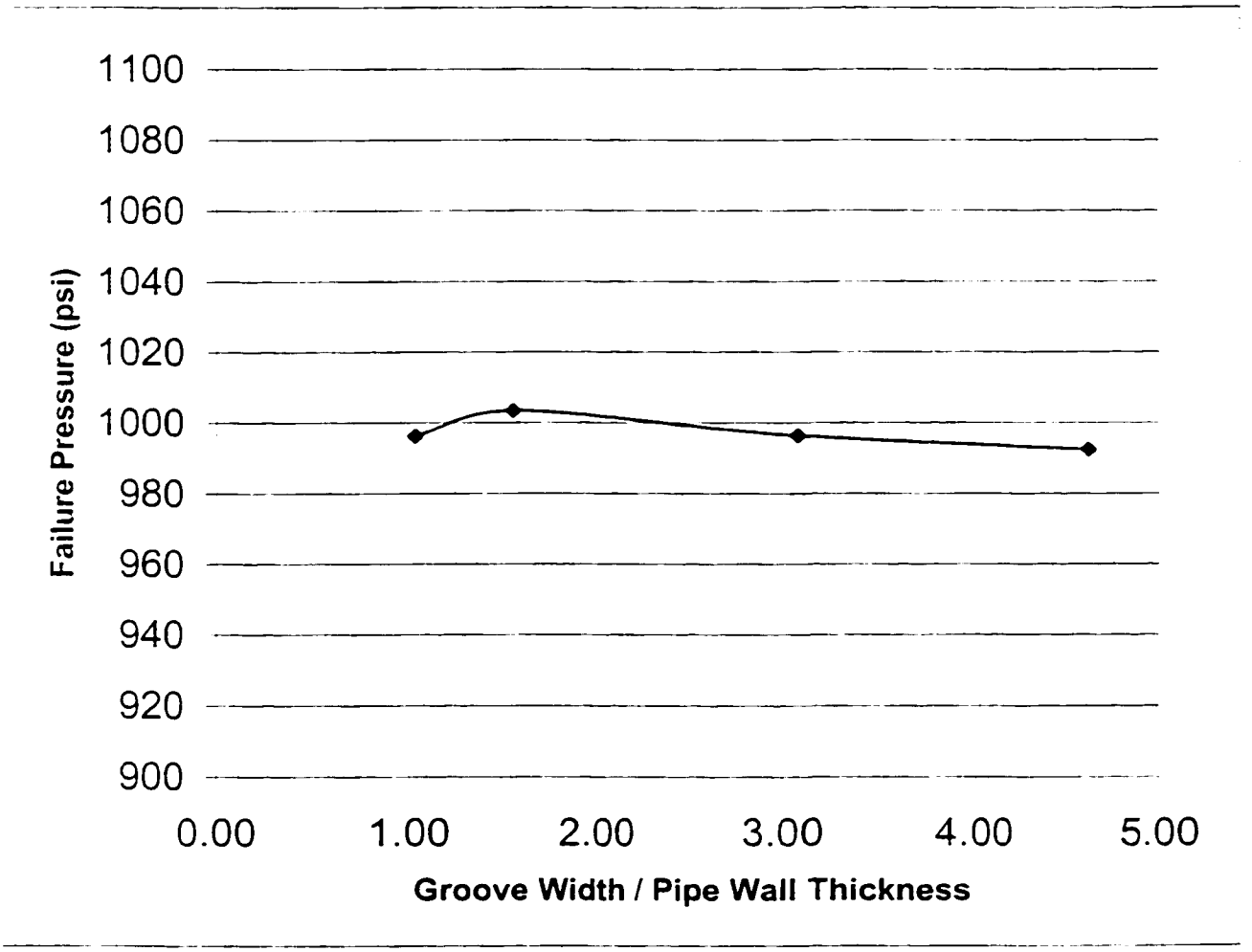
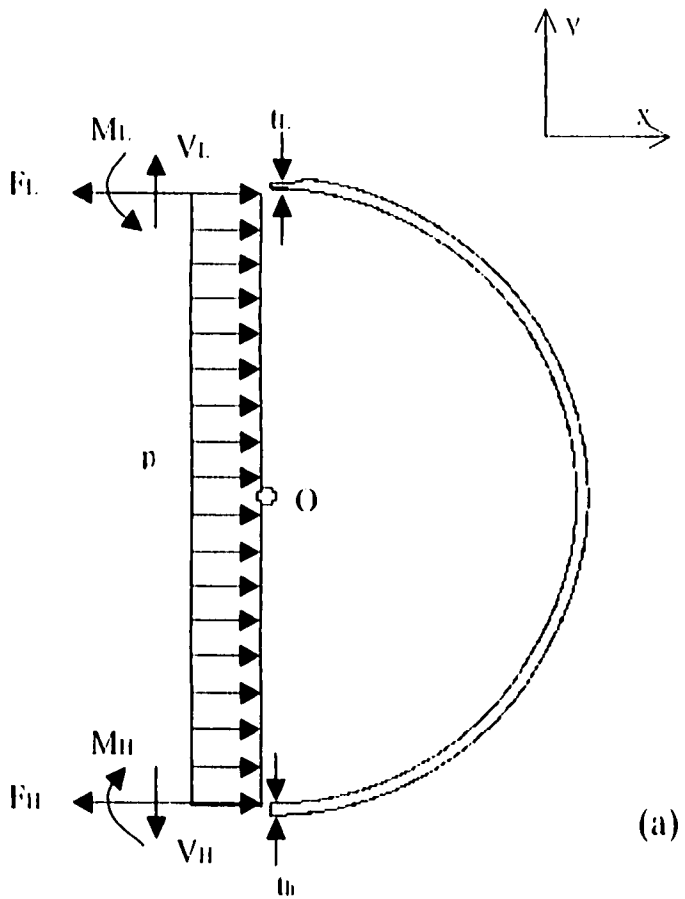


Figure 3.3.8: Variation in failure pressure for a 65% depth longitudinal groove with varying width



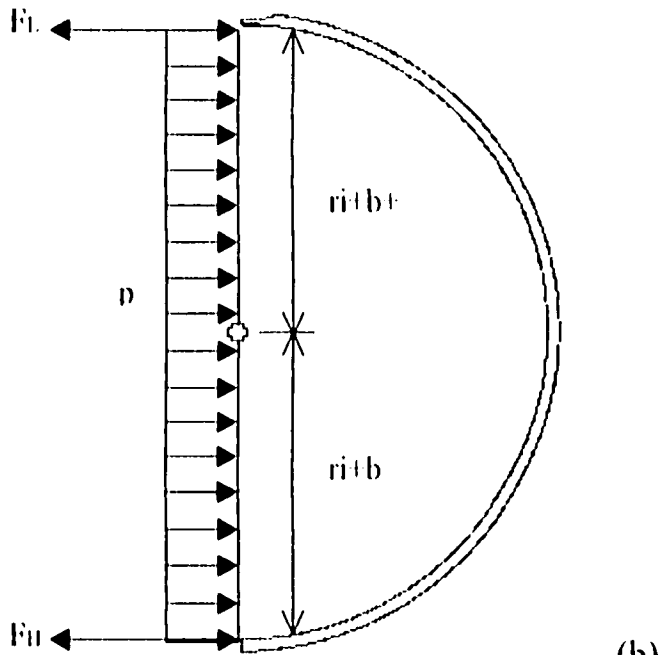


Figure 3.3.9: Long groove free body diagram

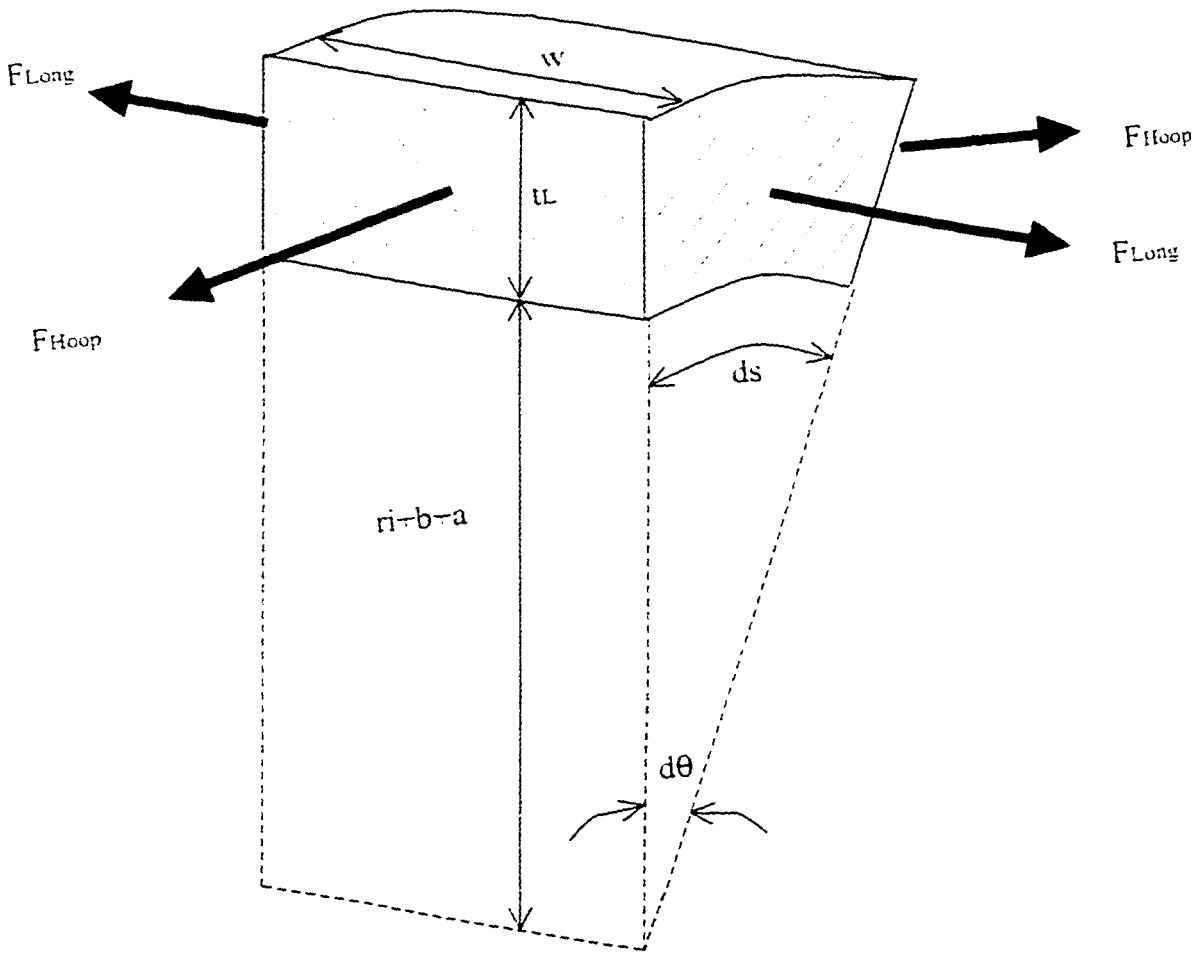


Figure 3.3.10: Infinitesimal element from the ligament of a longitudinal groove

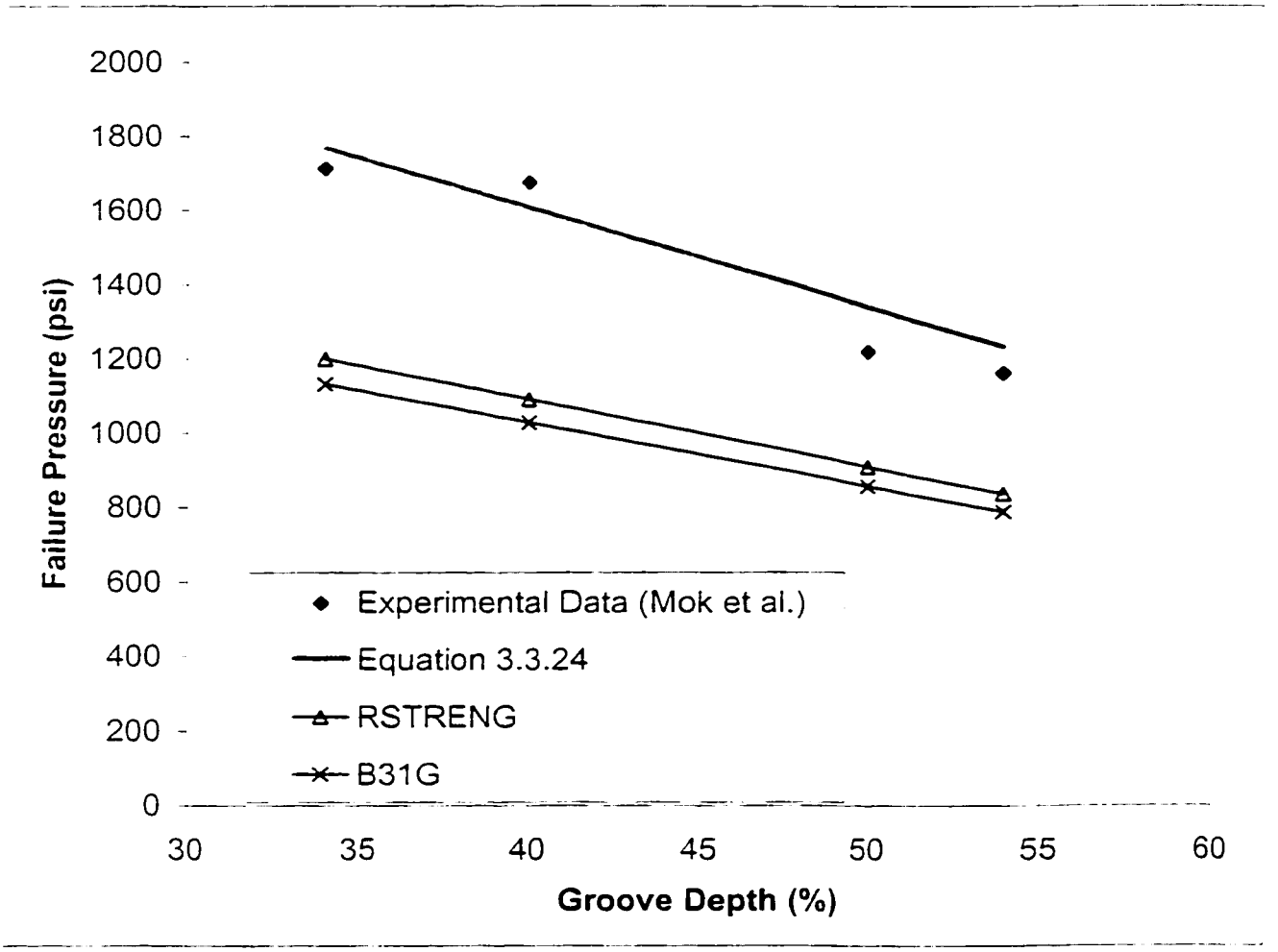


Figure 3.3.11: Failure pressures of infinitely long, longitudinally oriented grooves
Experimental data and predictions from equation 3.3.24

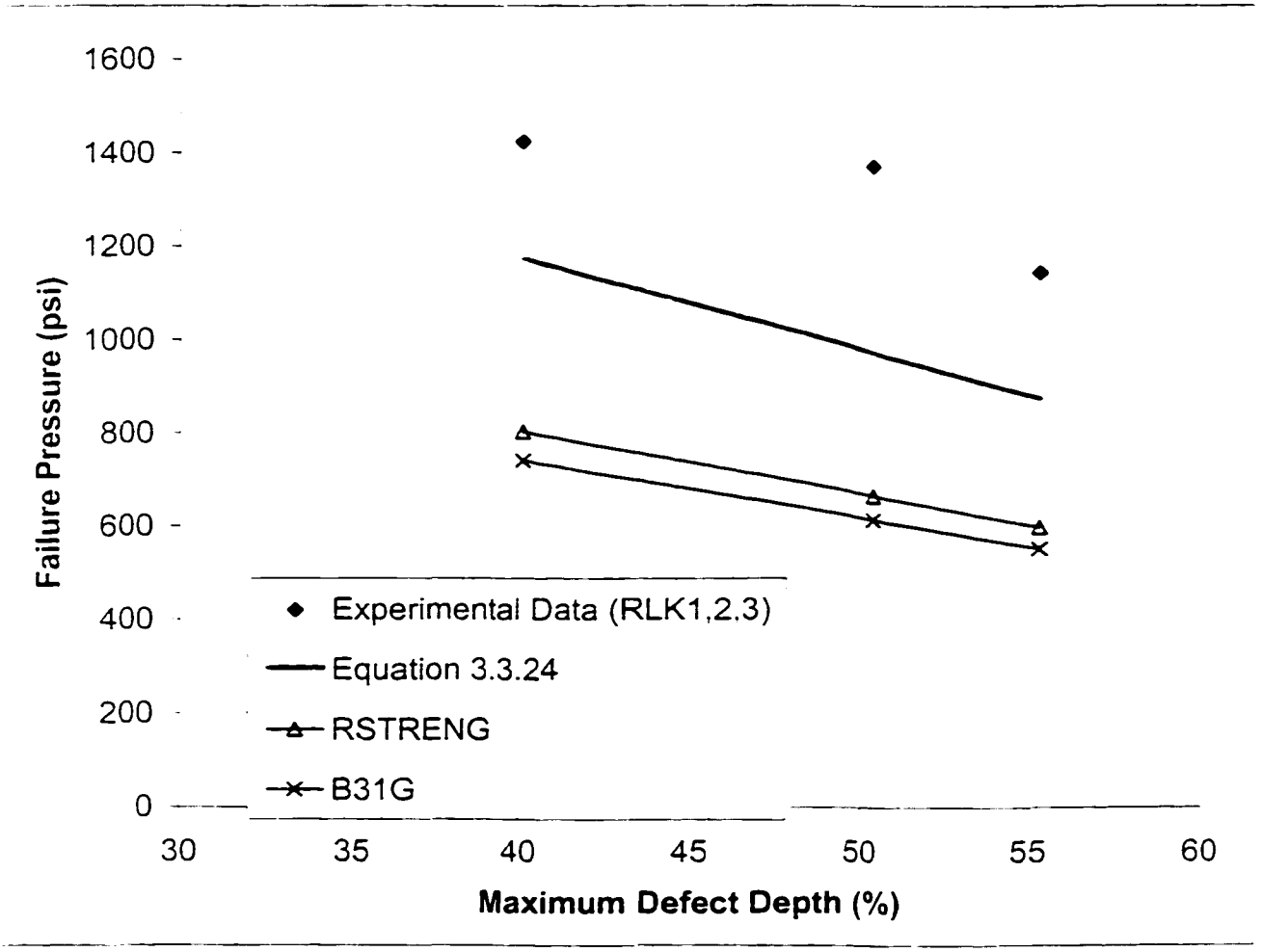
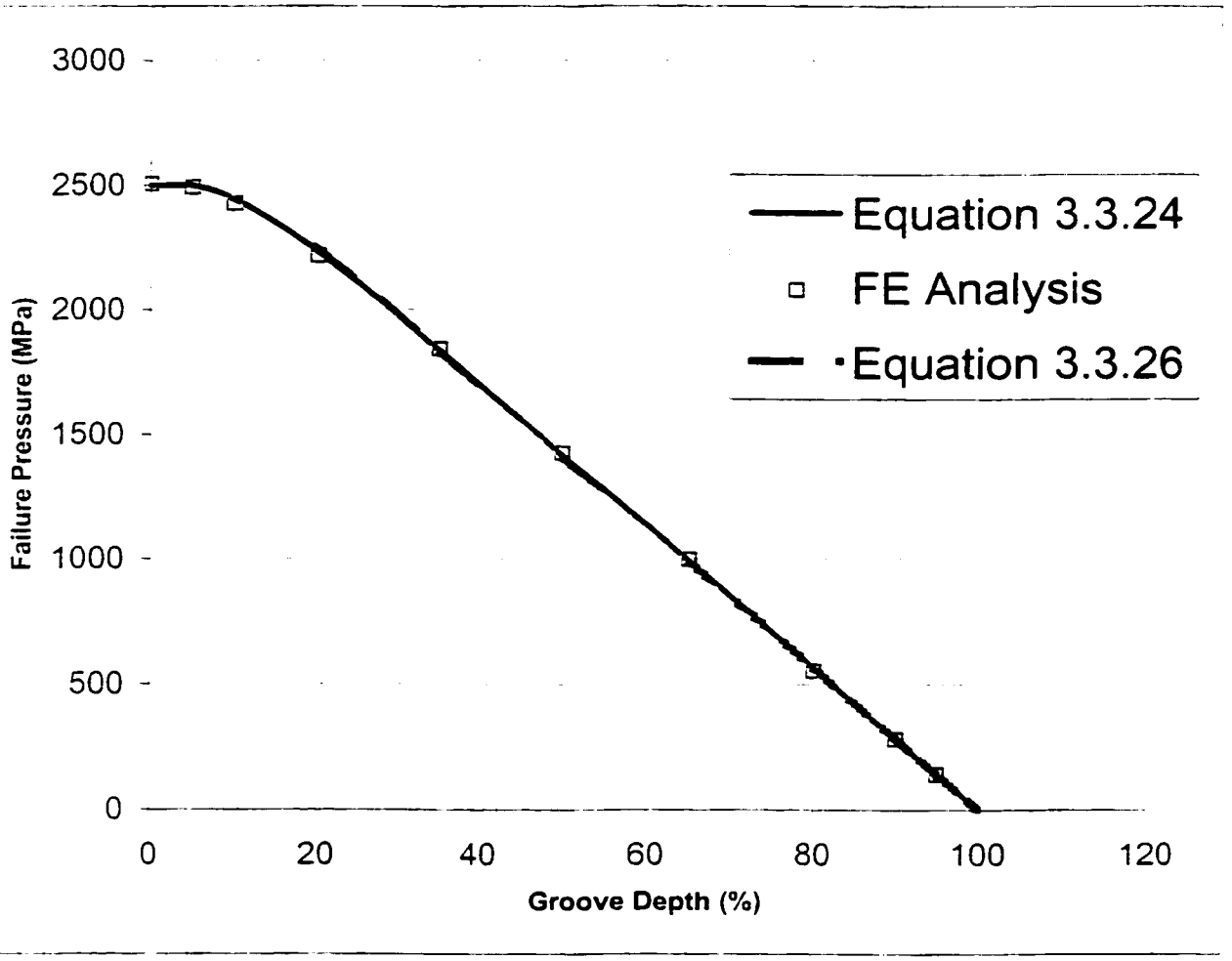


Figure 3.3.12: Failure pressures of long, longitudinally oriented defects
Experimental data and predictions from equation 3.3.24



Groove width: 1.0"
Grade X42 material
Inside Diameter: 10.436"
Wall thickness: 0.195"

Figure 3.3.13: Failure pressures of infinitely long, longitudinally oriented grooves
FE vs. analytical solution failure pressure predictions

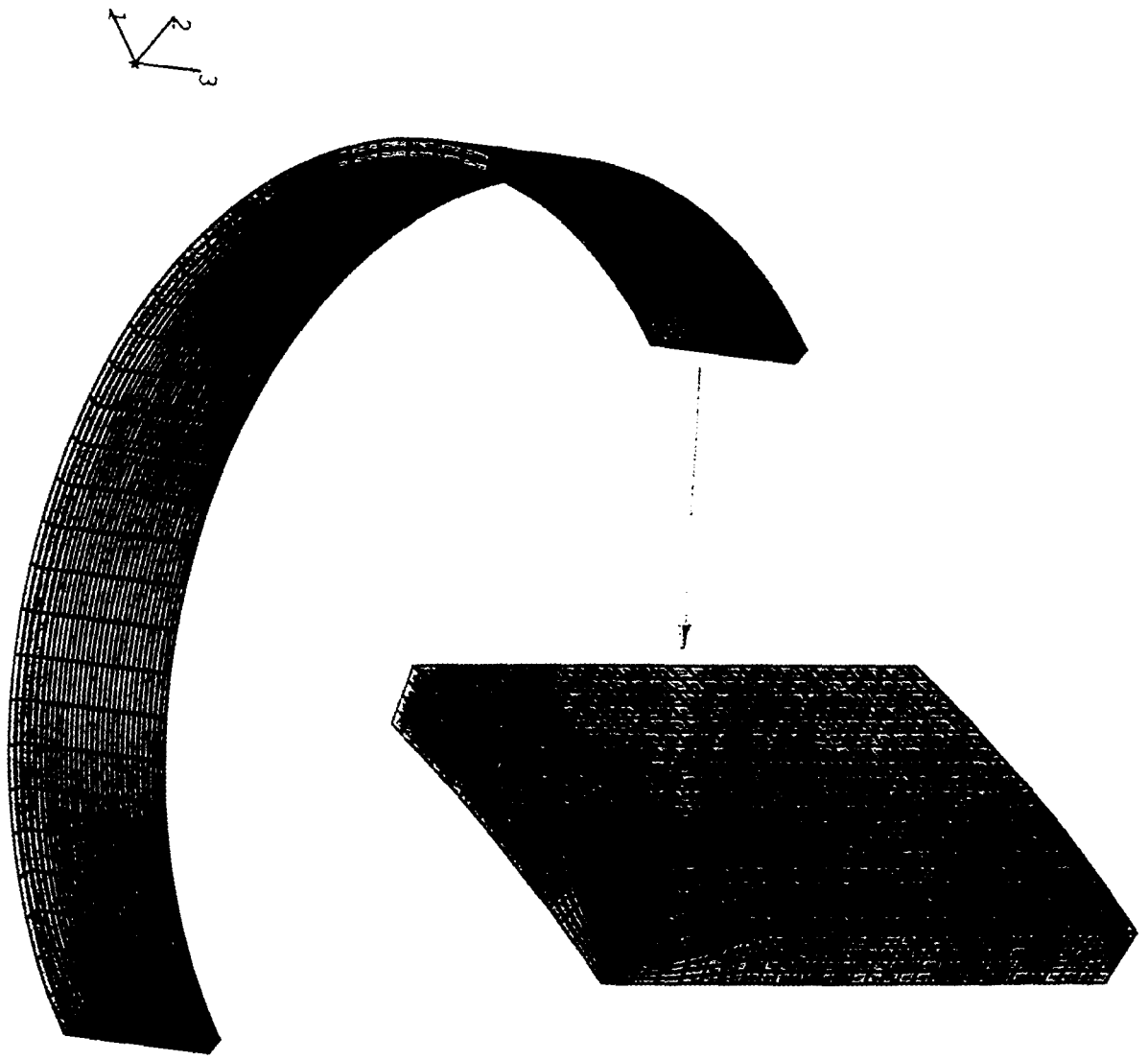


Figure 3.4.1: Single pit finite element mesh (1/4 model)

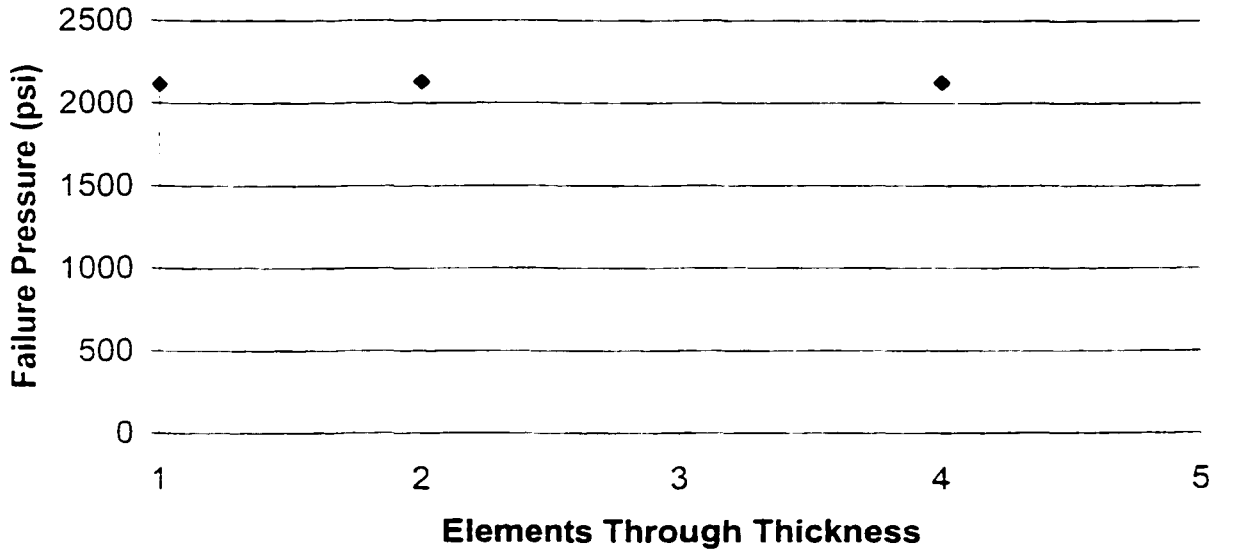


Figure 3.4.2a Failure pressure for varying number of elements through the thickness

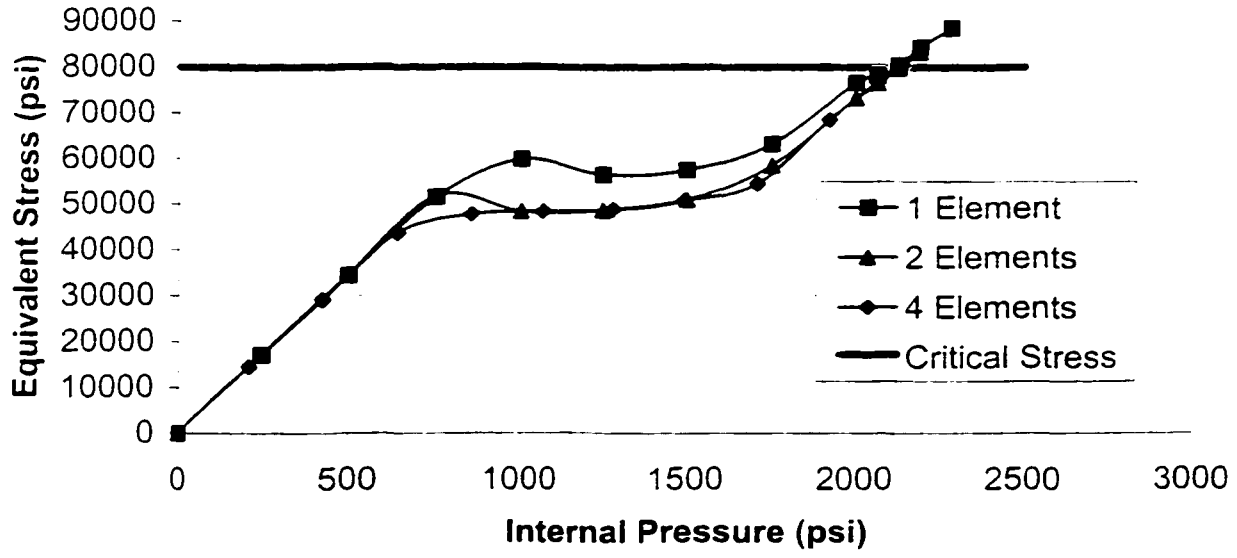


Figure 3.4.2b Equivalent stress at the critical point for varying number of elements through the thickness

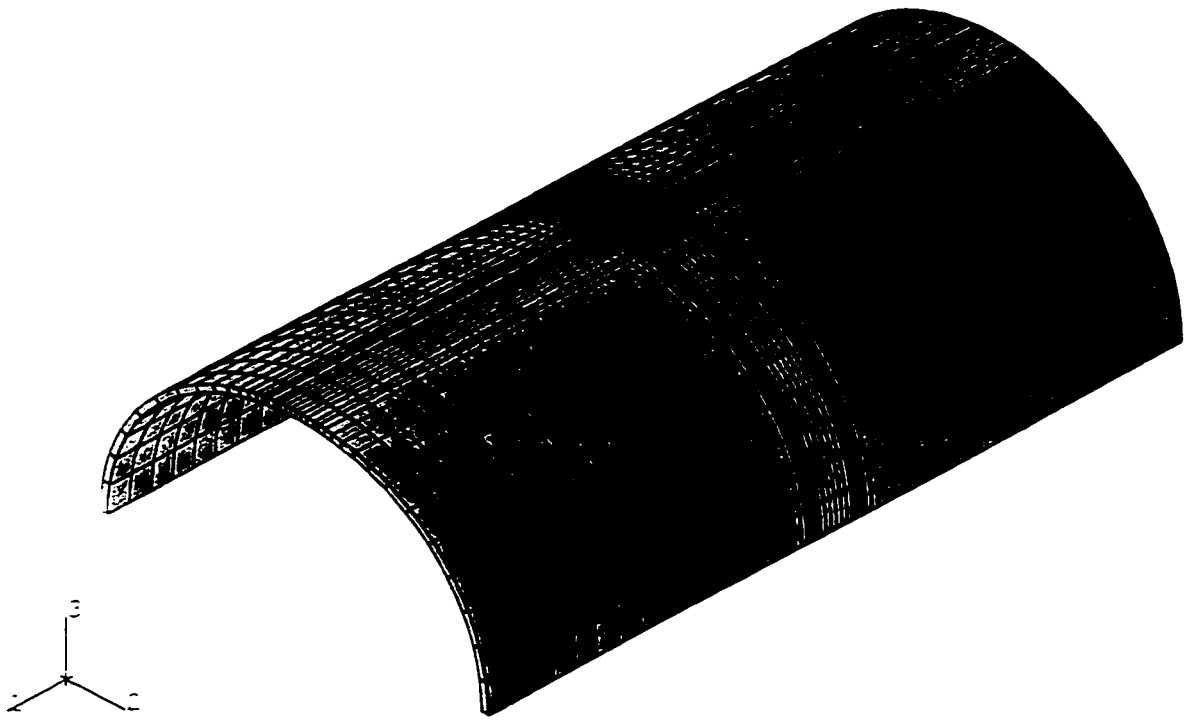


Figure 3.4.3a: Single pit finite element mesh - full model

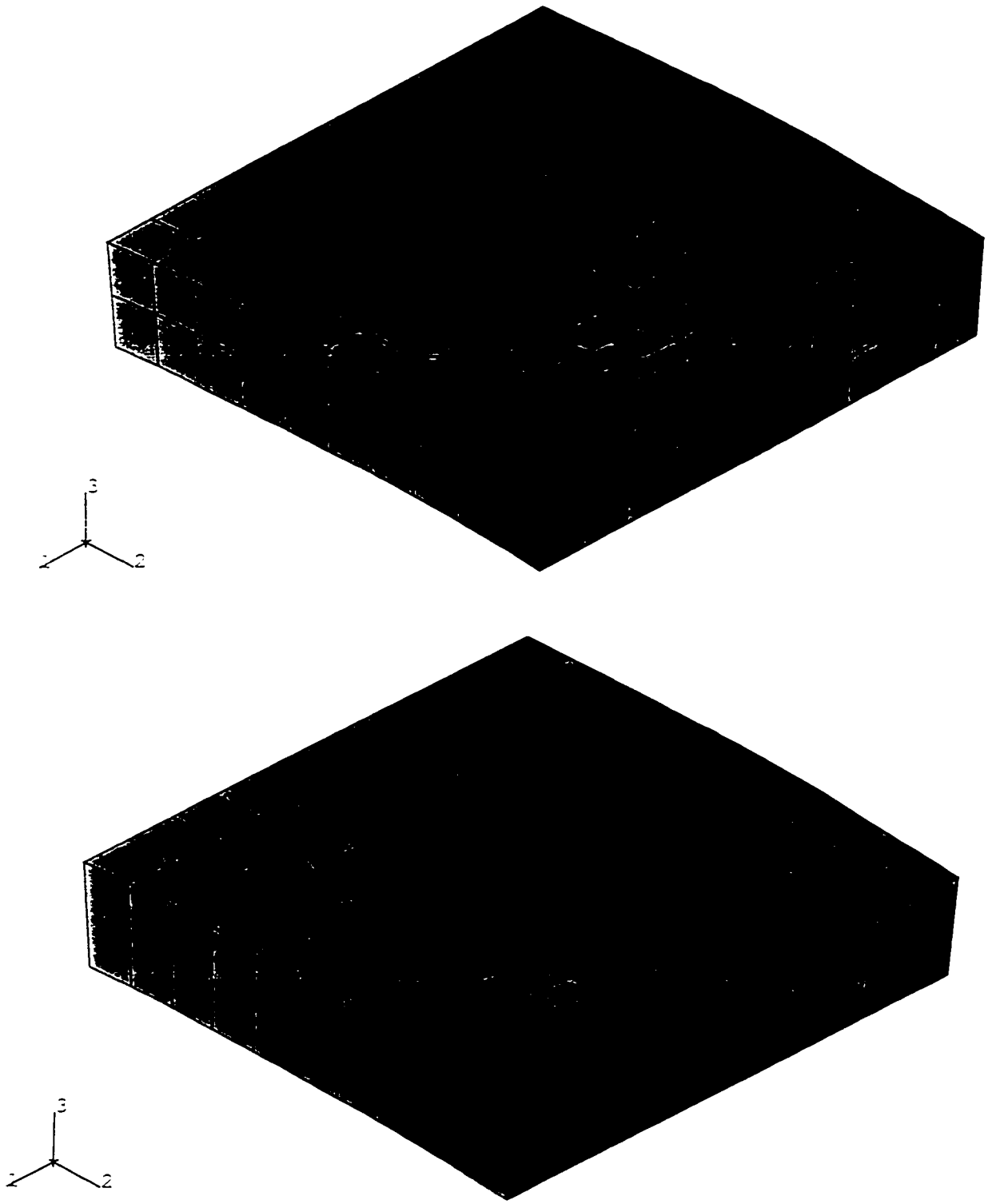


Figure 3.4.3b: Single pit finite element mesh - full model - mesh at pit location

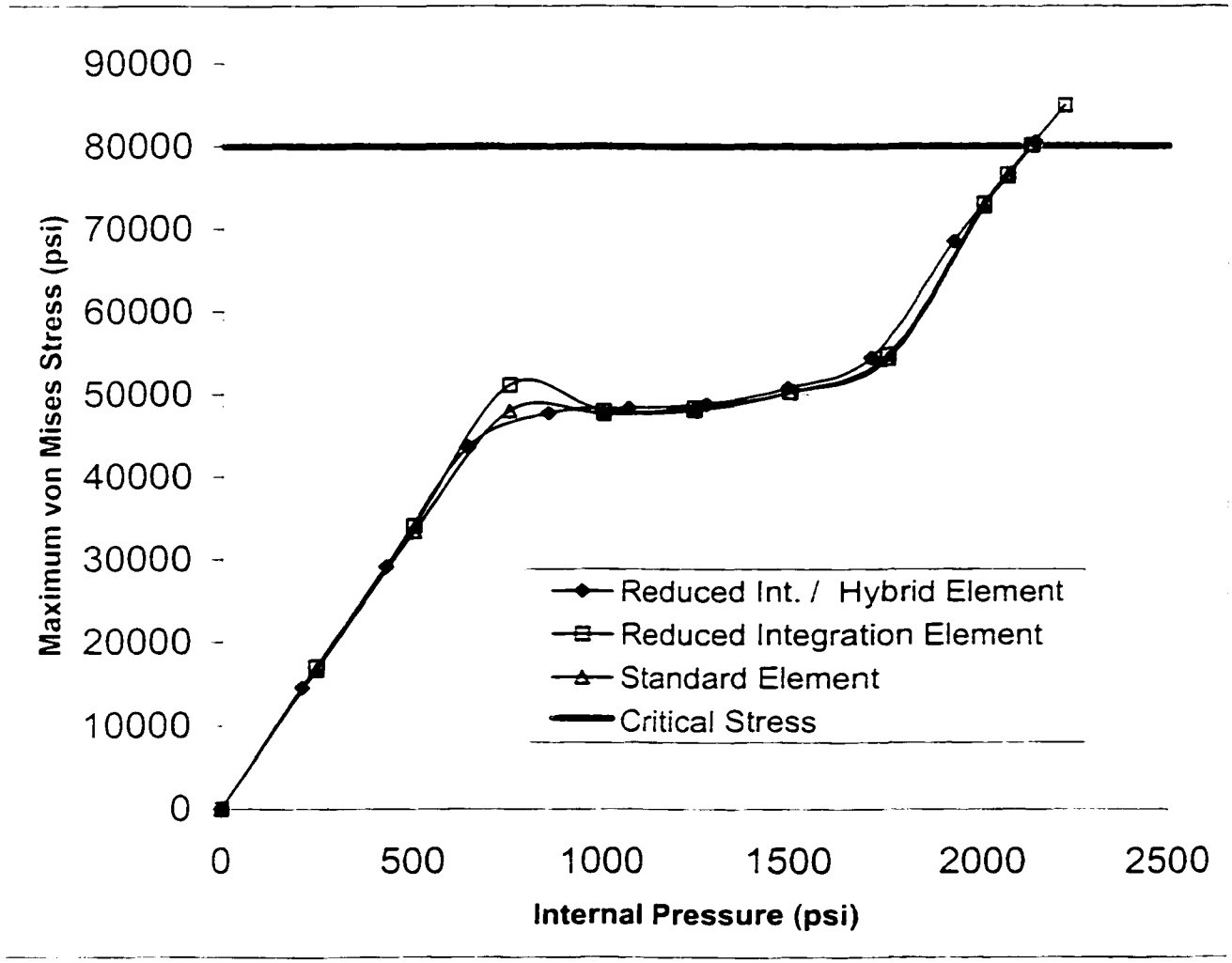


Figure 3.4.4 Failure pressure of single pits for varying element type

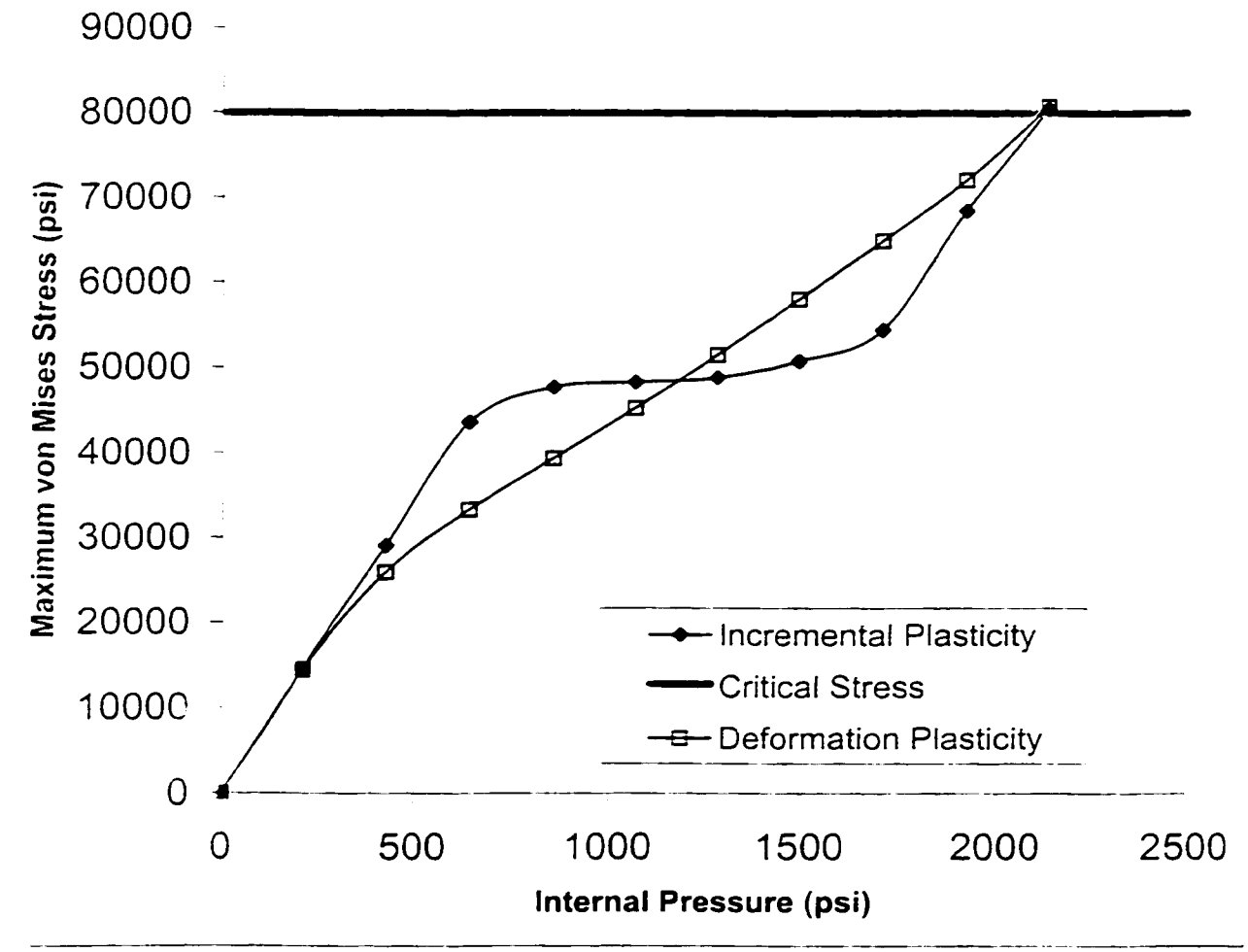


Figure 3.4.5 Failure pressure of single pits for two material models

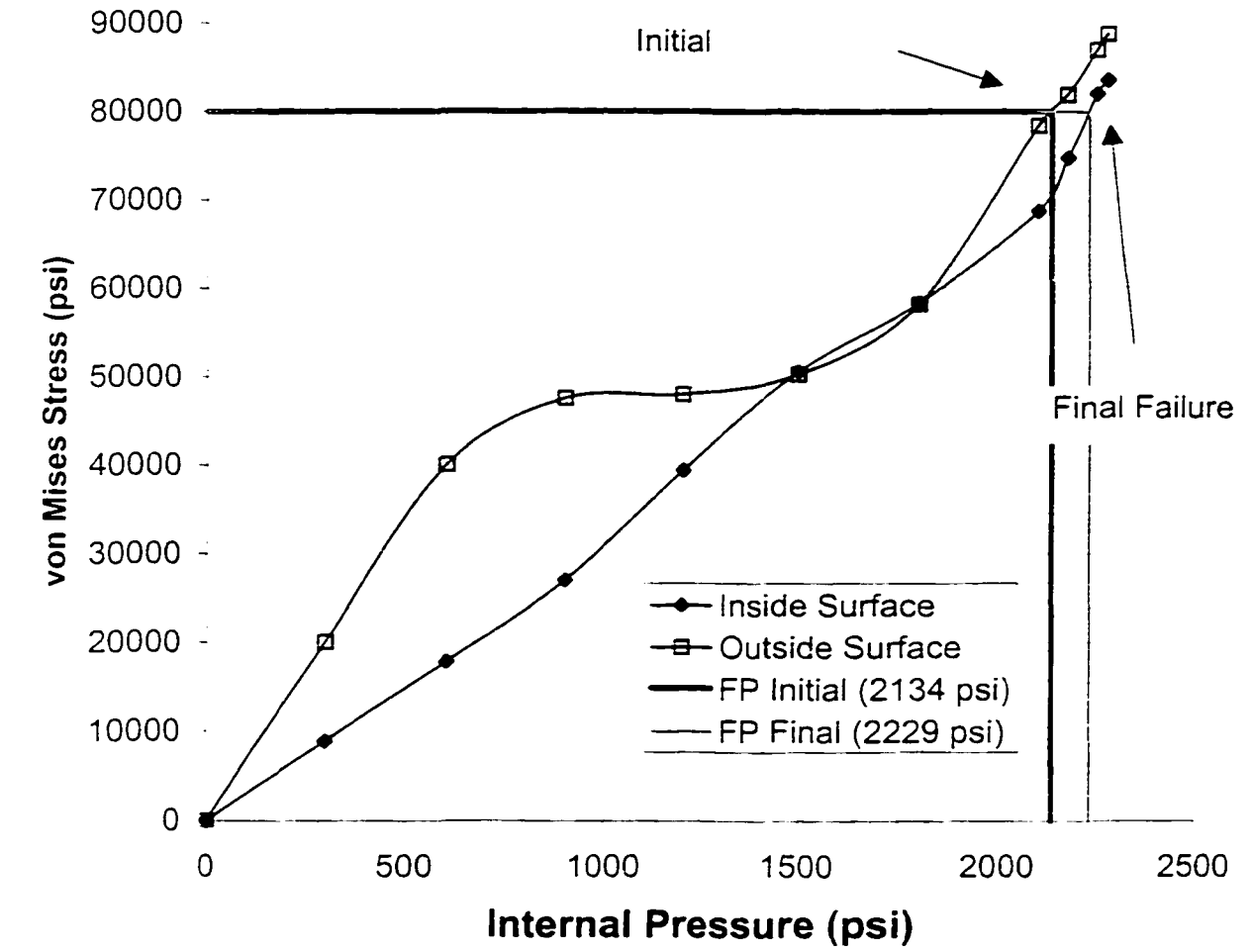


Figure 3.4.6: Single spherical pit 65% WT deep
von Mises stress at the deepest point in the defect

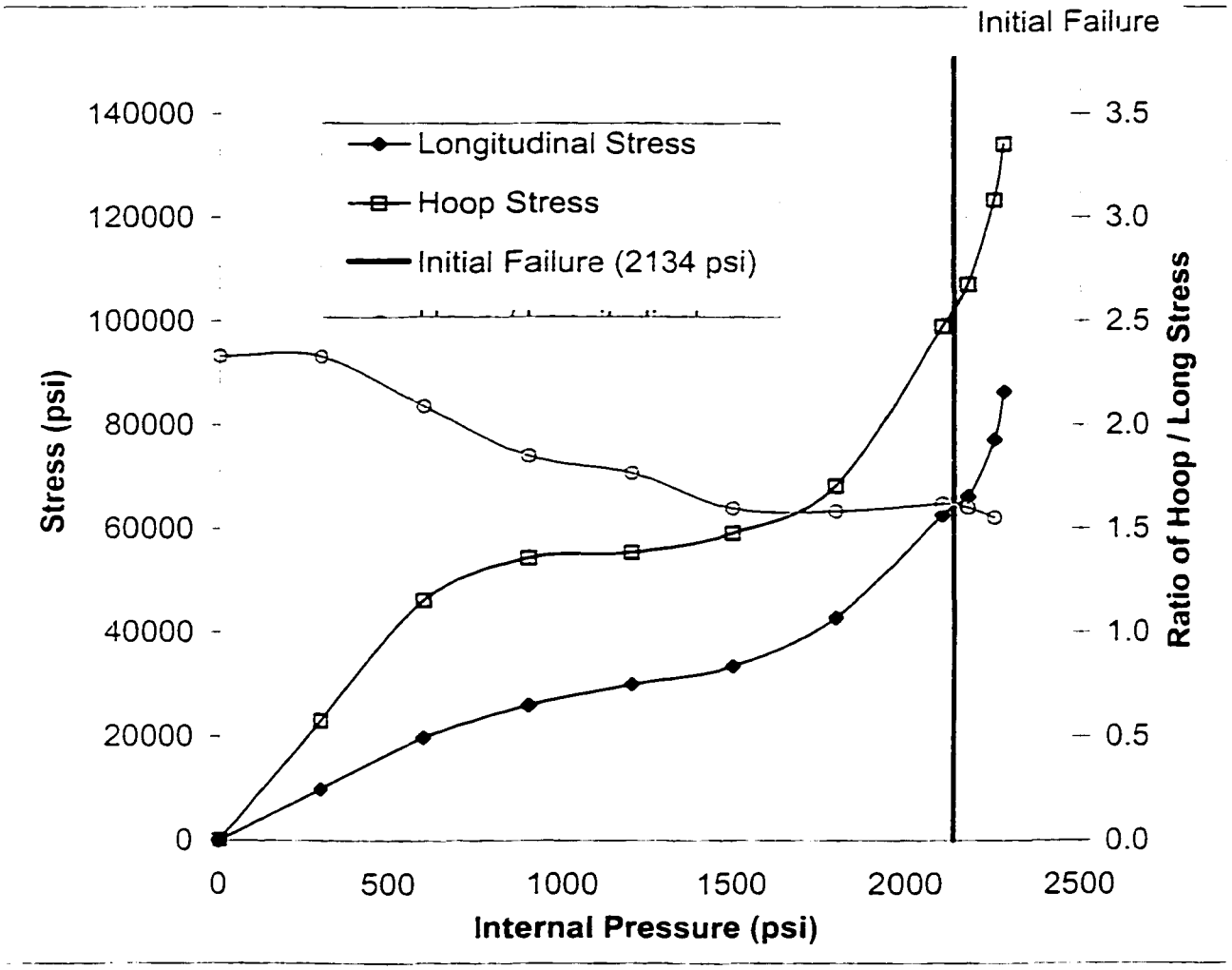


Figure 3.4.7: Single spherical pit 65% WT deep
Hoop and longitudinal stresses at the deepest point in the defect.
Outside surface

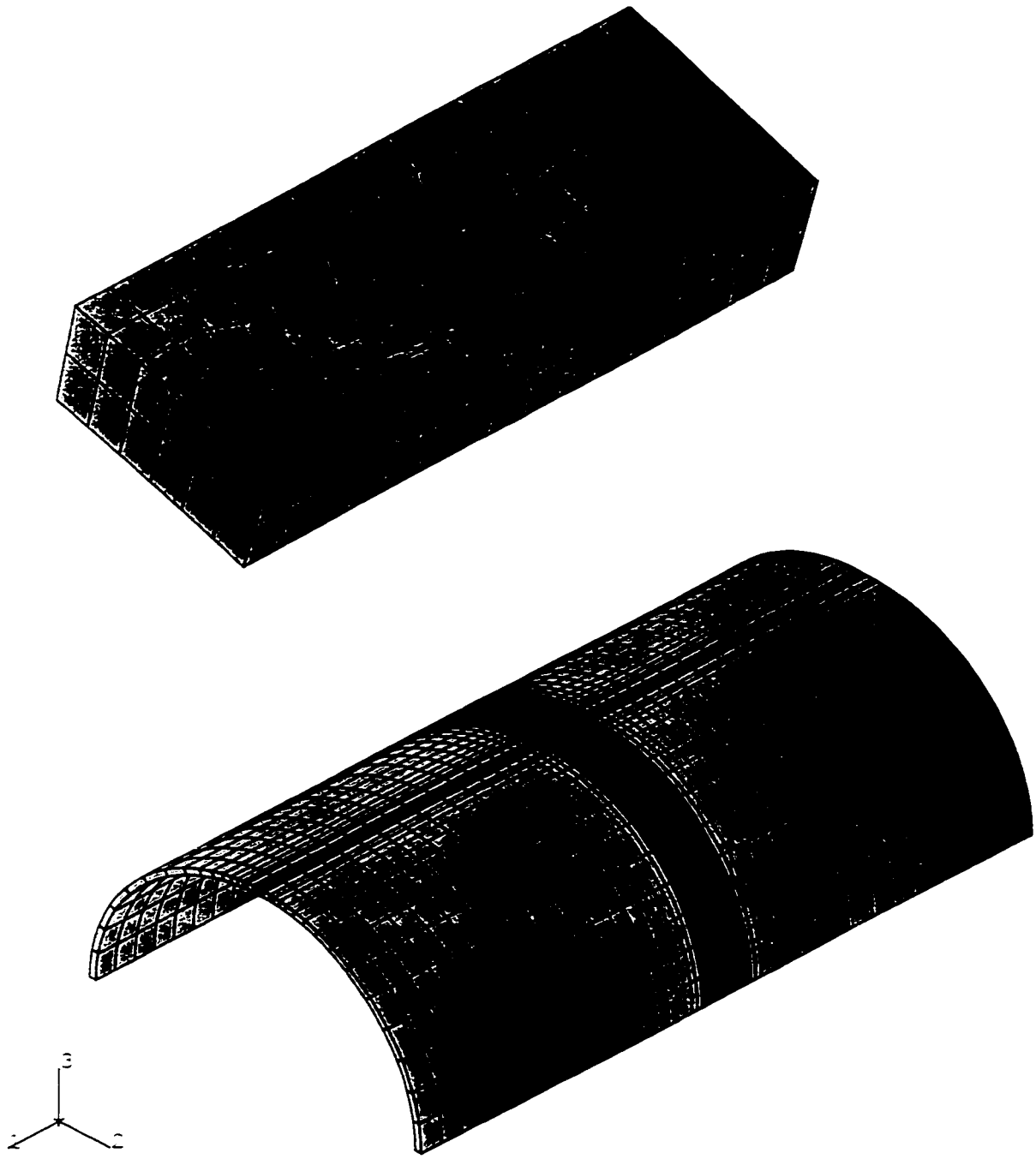


Figure 3.4.8: Single pit finite element mesh
- varying the circumferential dimension

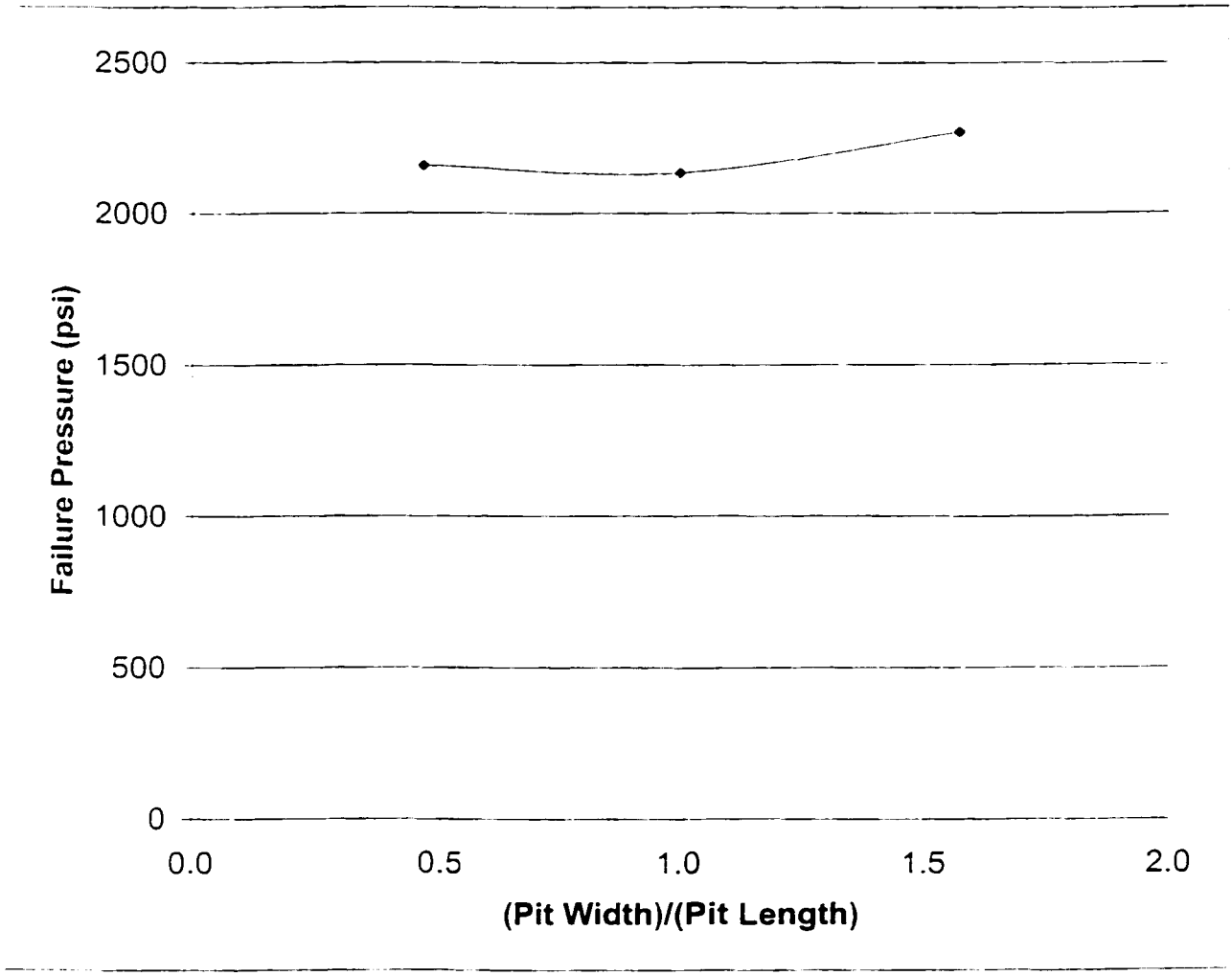


Figure 3.4.9 Predicted failure pressure of single pits for varying circumferential dimension

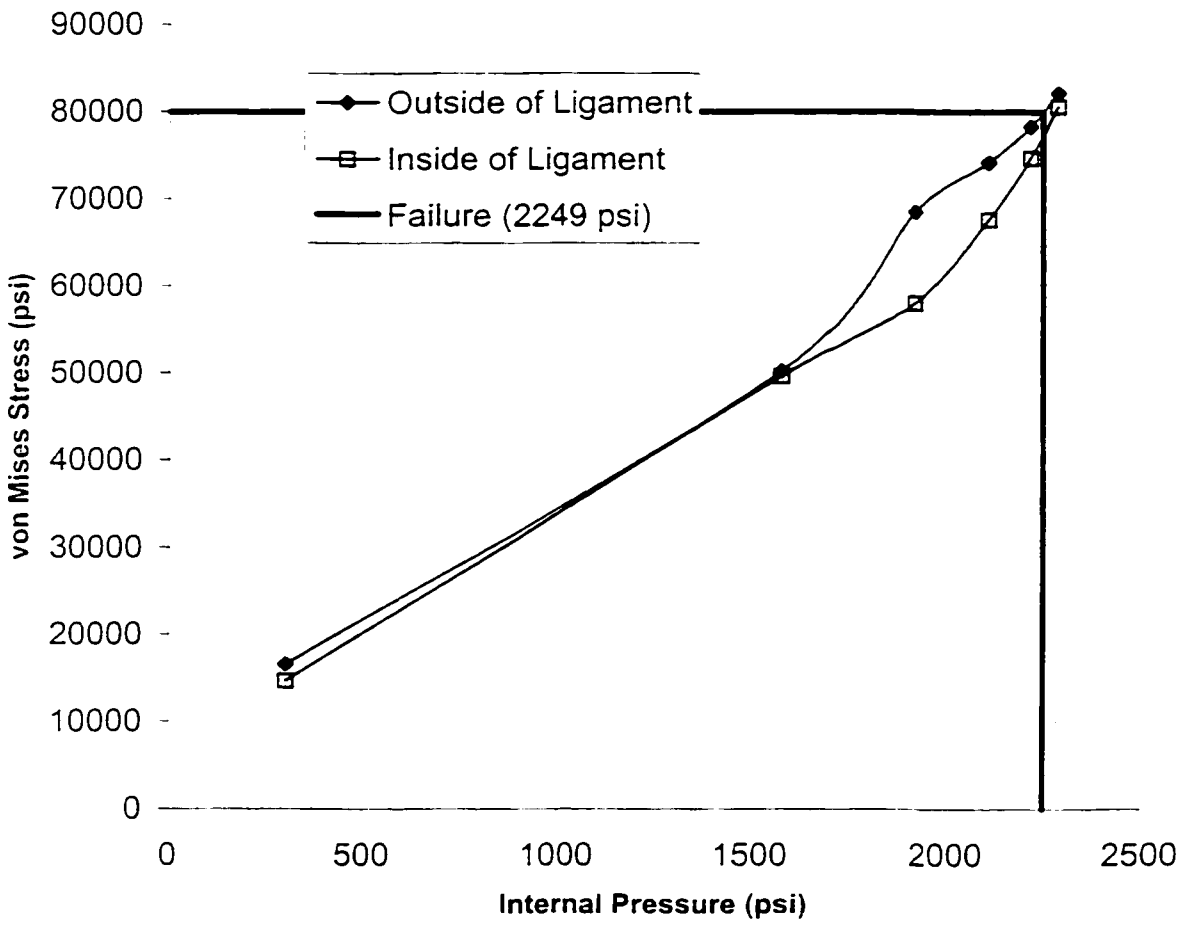


Figure 3.4.10: Axisymmetric groove 65% WT deep
- von Mises stress at the deepest point in the defect

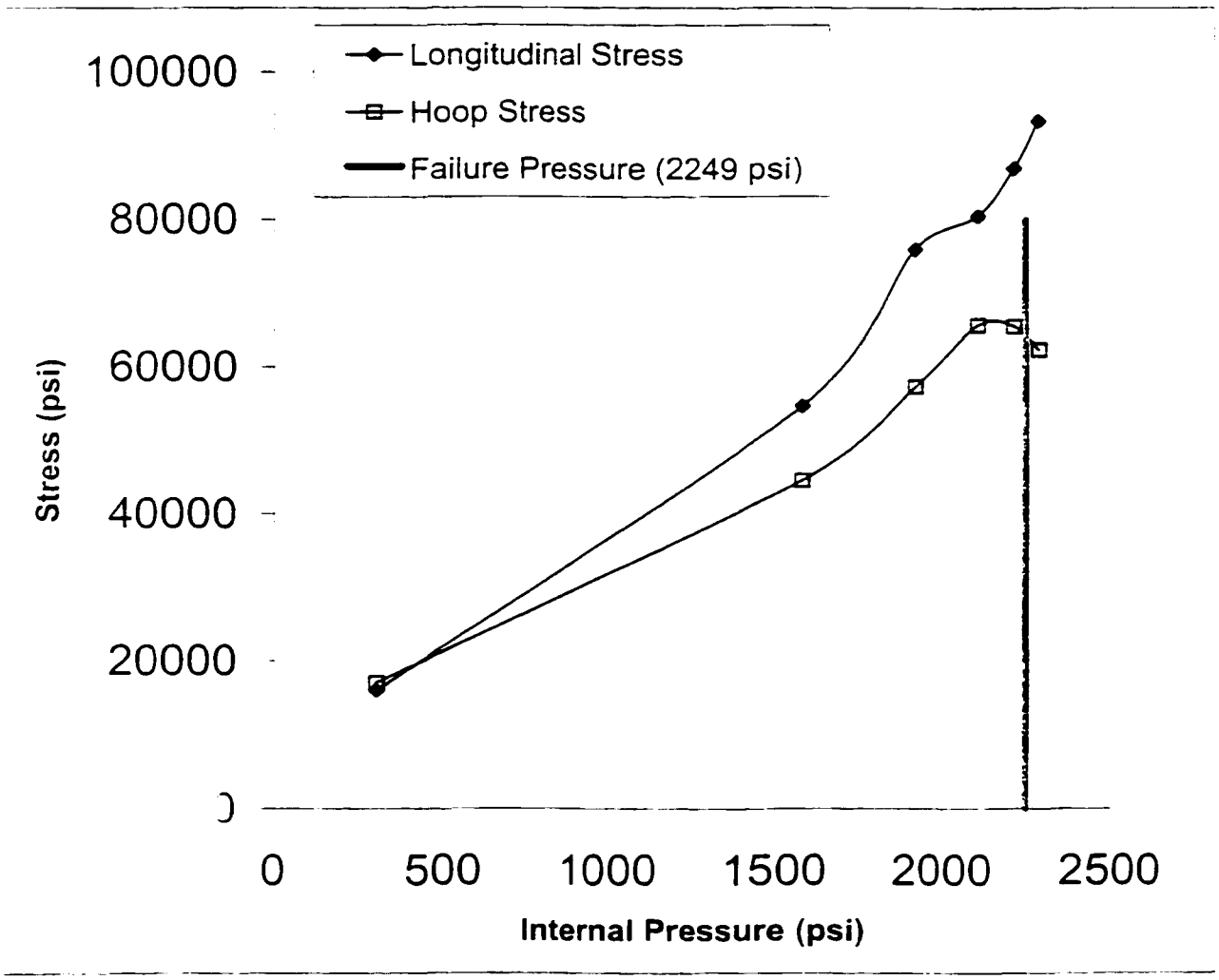


Figure 3.4.11: Axisymmetric groove 65% WT deep
- Hoop and longitudinal stresses at the deepest point

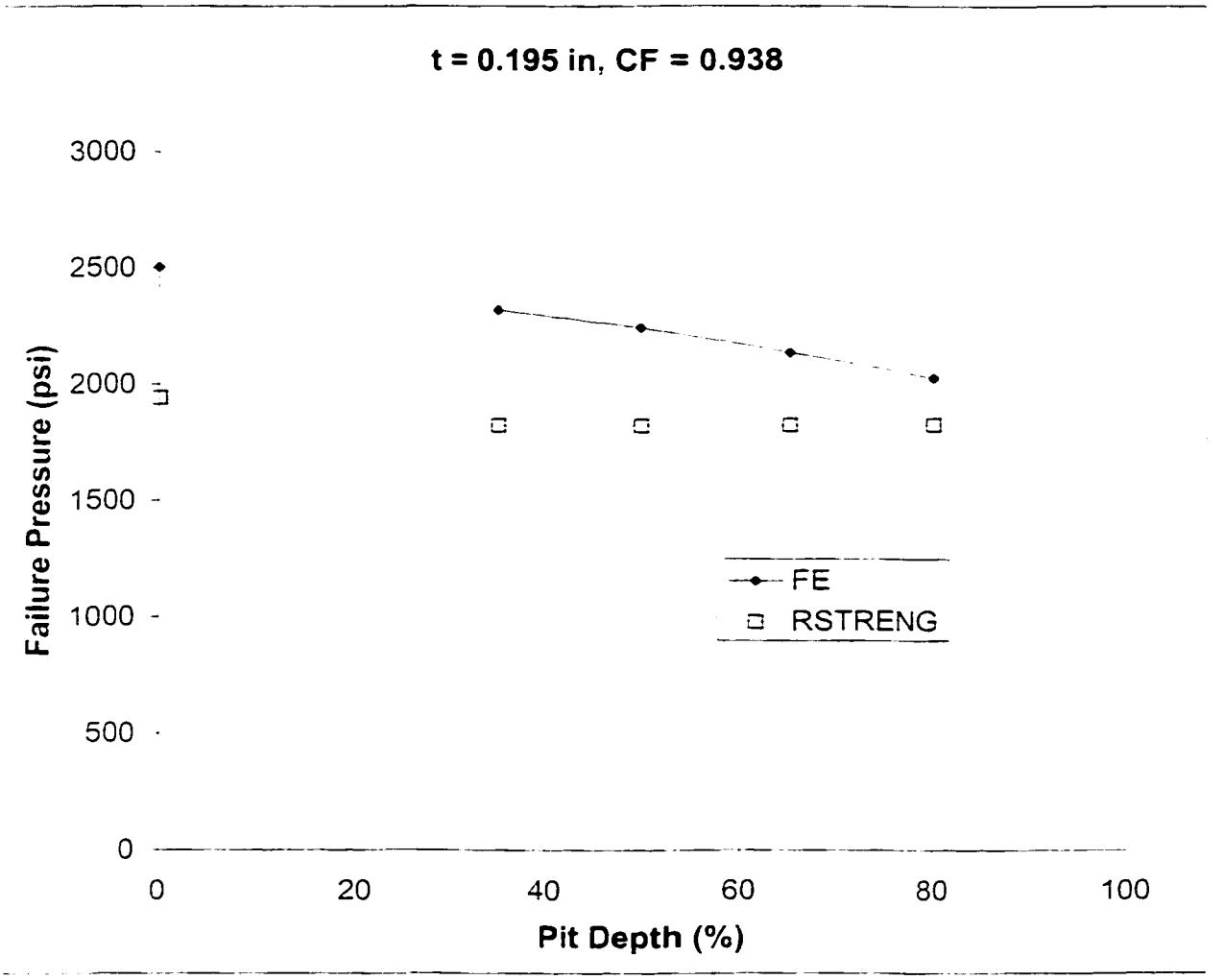


Figure 3.4.12: Single pit failure pressure as a function of % Depth
Corrosion factor = 0.938

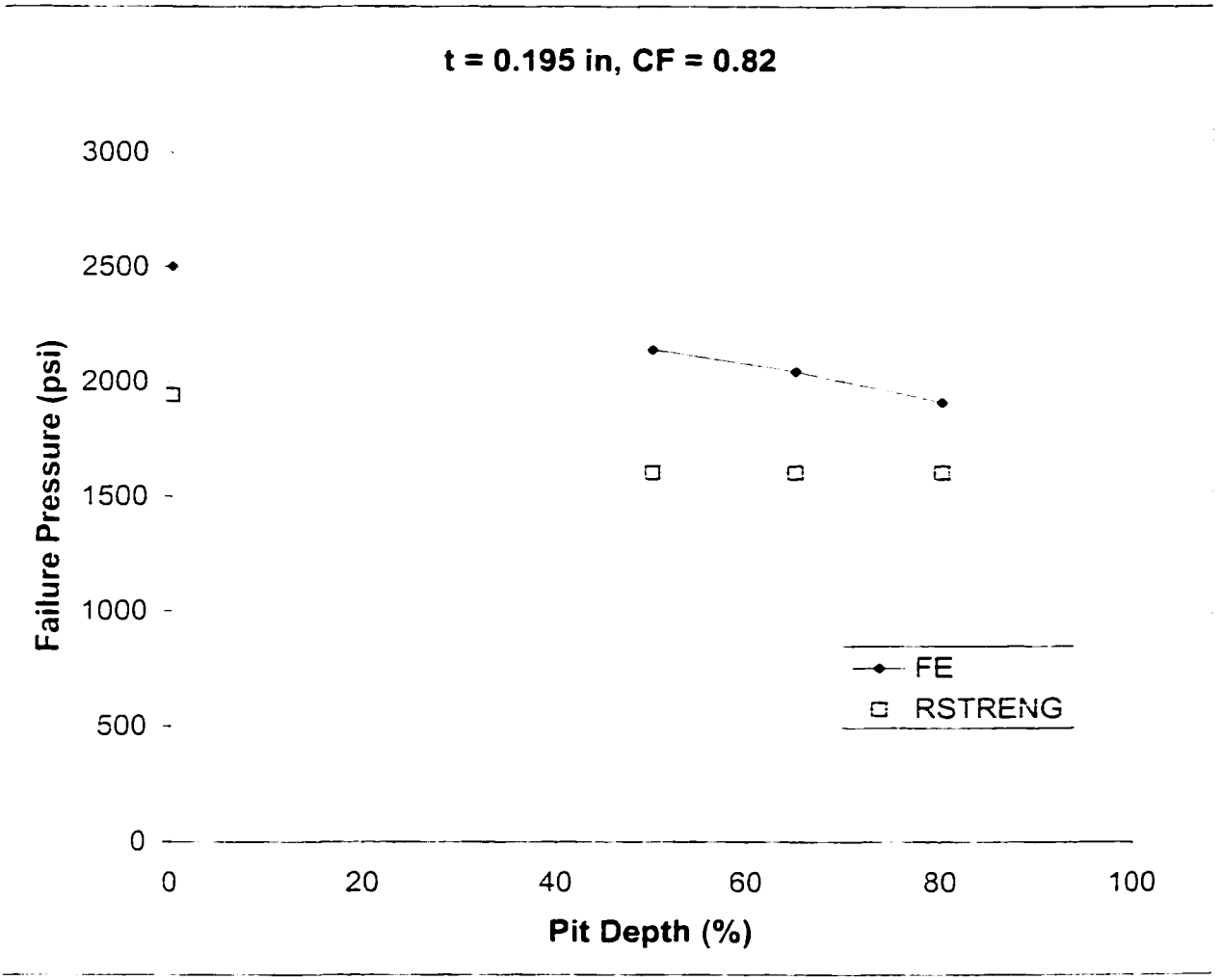


Figure 3.4.13: Single pit failure pressure as a function of % Depth
Corrosion factor = 0.82

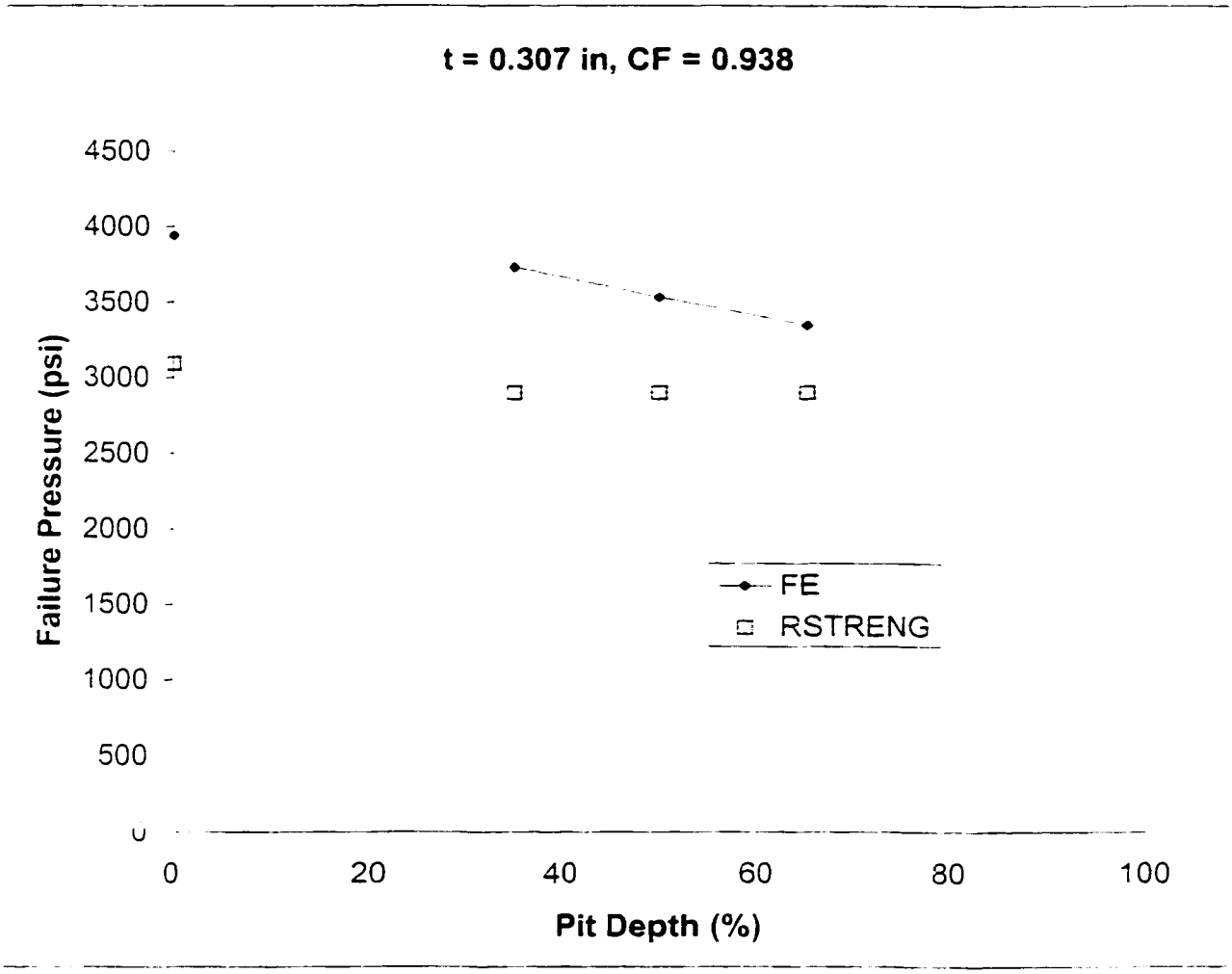
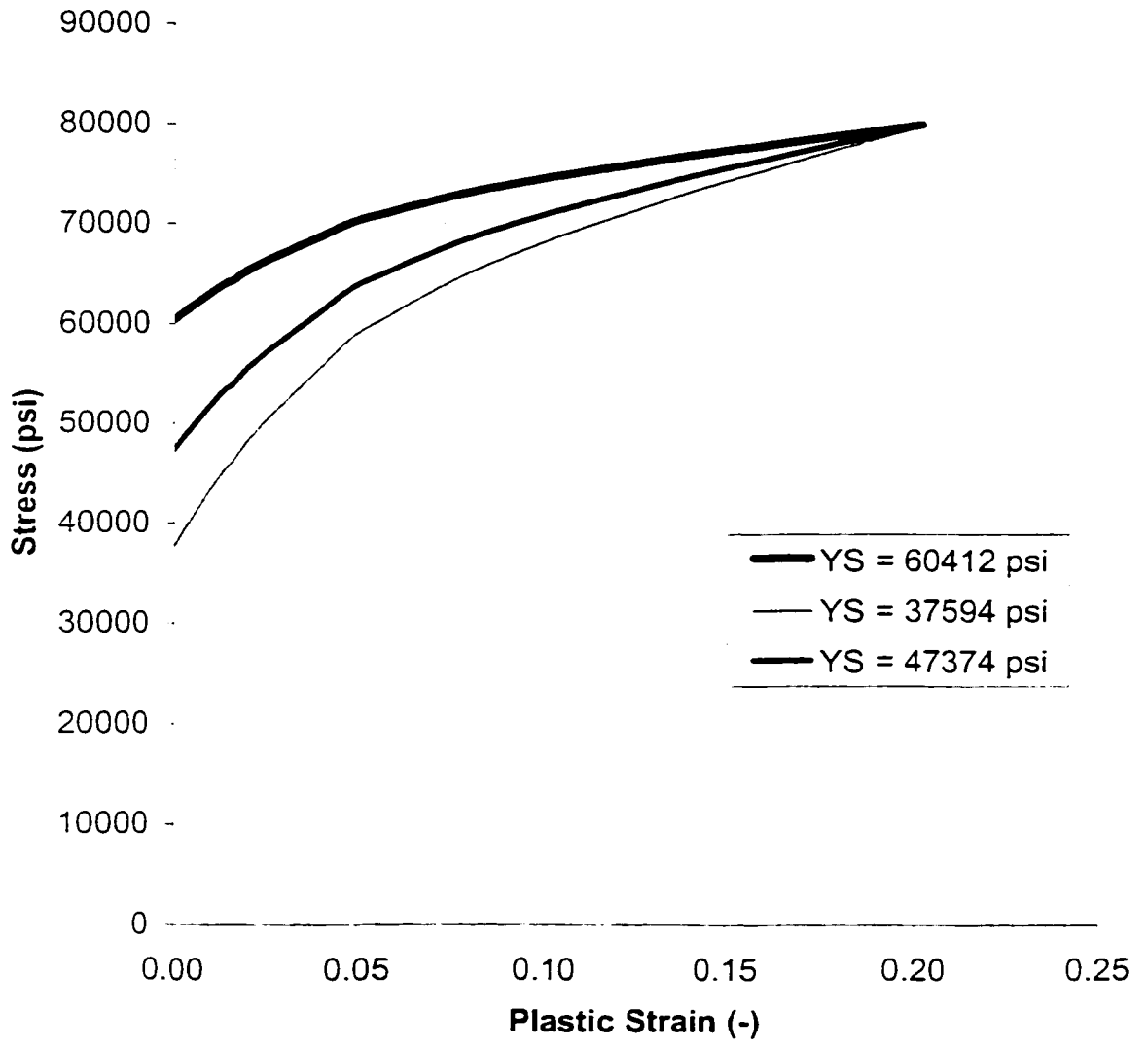
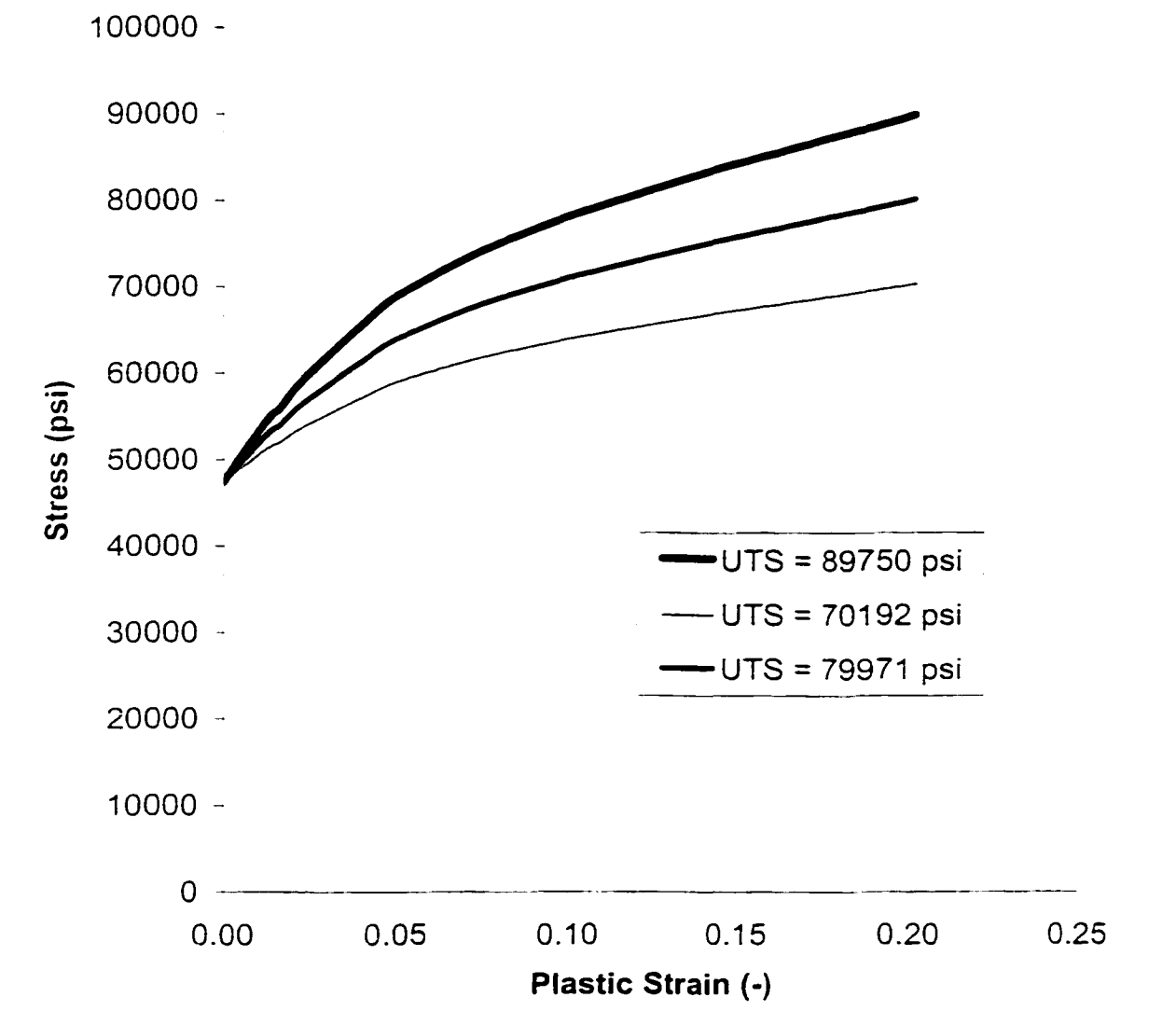


Figure 3.4.14: Single pit failure pressure as a function of % Depth
Corrosion factor = 0.938, thick-walled pipe



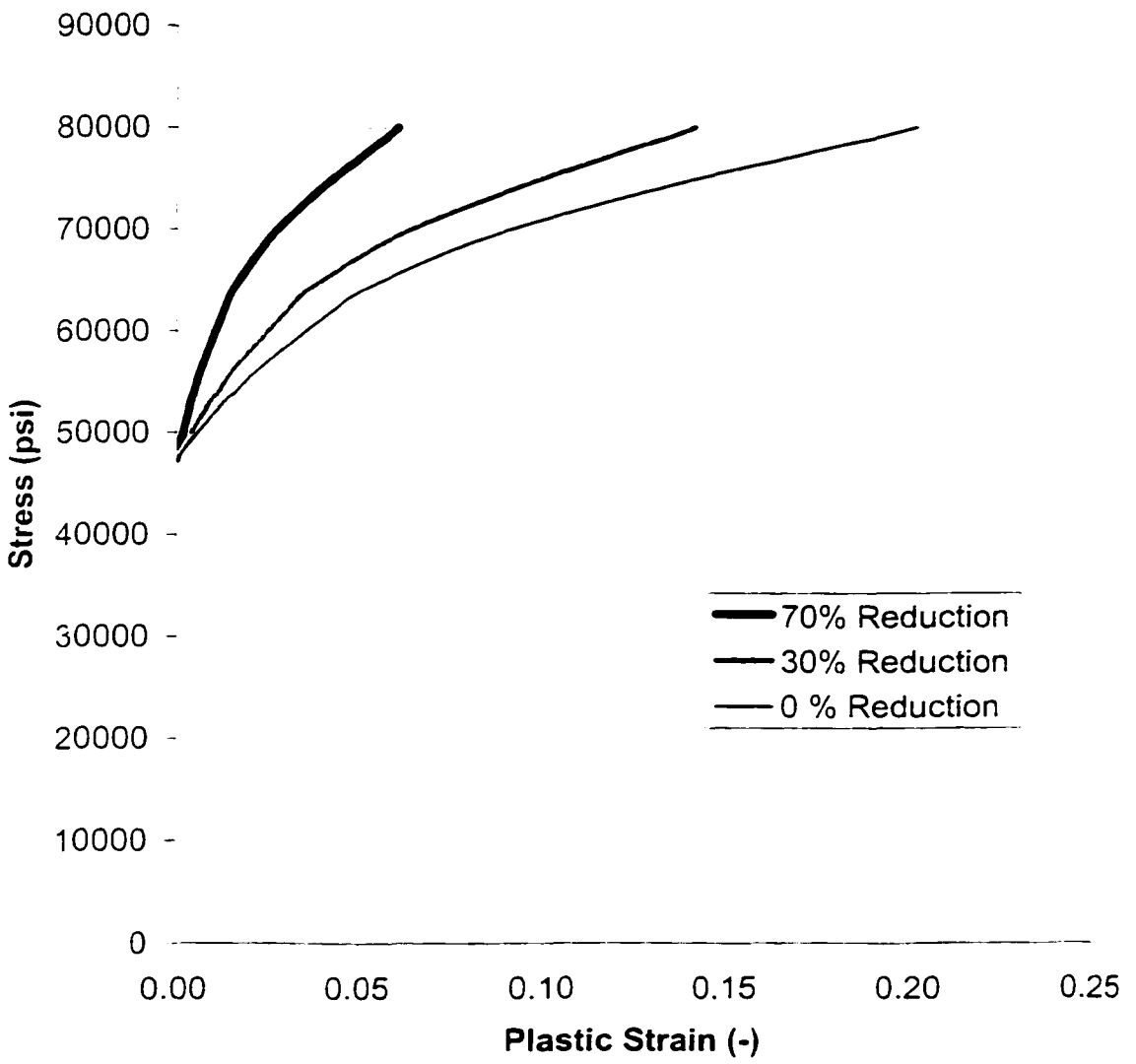
True Stress @ UTS = 79971 psi
Plastic Strain @ UTS = 0.2

Figure 3.4.15 Stress-strain curves with varying material yield strength



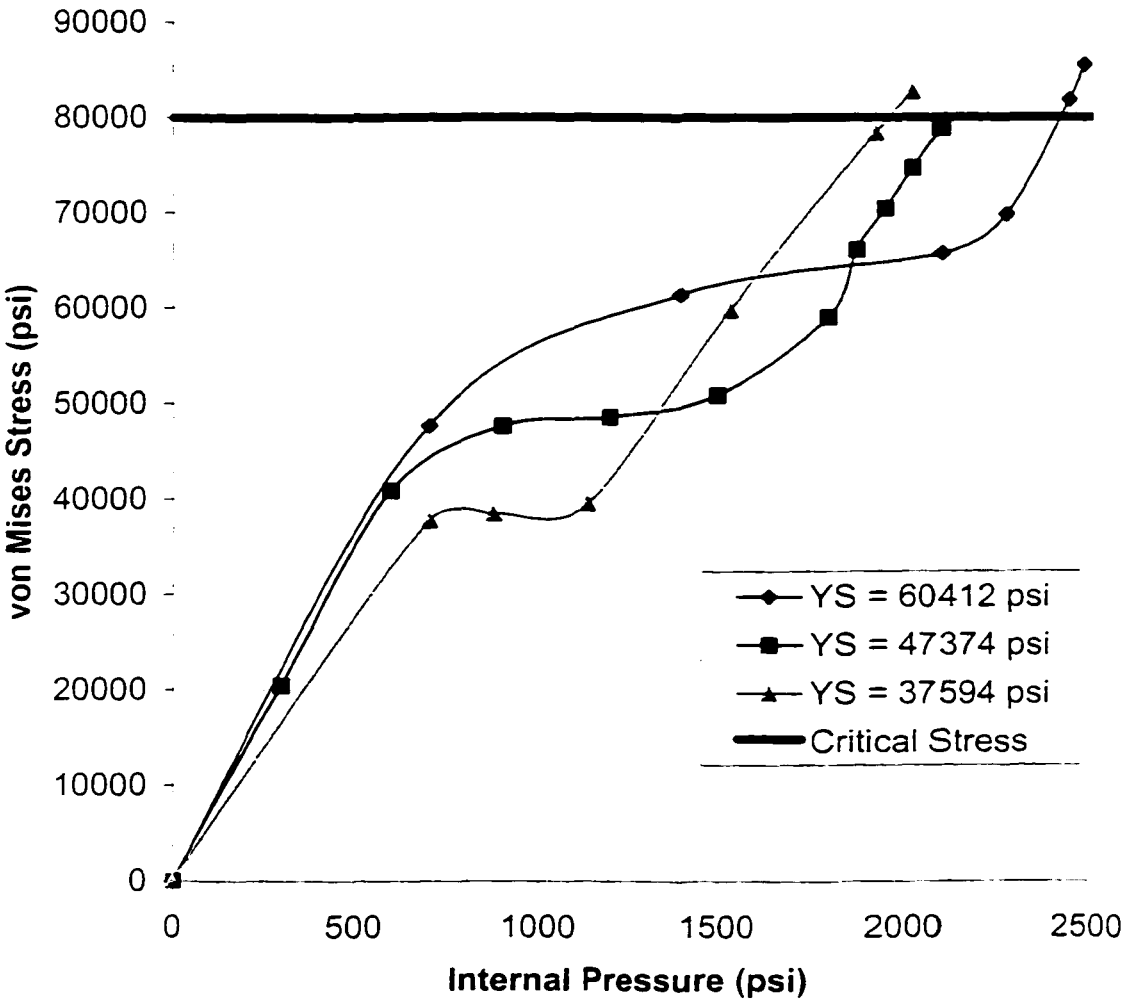
Yield Stress = 47374 psi
Plastic Strain @ UTS = 0.2

Figure 3.4.16: Stress-strain curves with varying stress at necking



Yield Stress = 47374 psi
True Stress @ UTS = 79971 psi

Figure 3.4.17: Stress-strain curves with varying strain at necking



True Stress @ UTS = 79971 psi
Plastic Strain @ UTS = 0.2

Figure 3.4.18: von Mises stress as a function of internal pressure with varying material yield stress. Single spherical pit, 65% depth

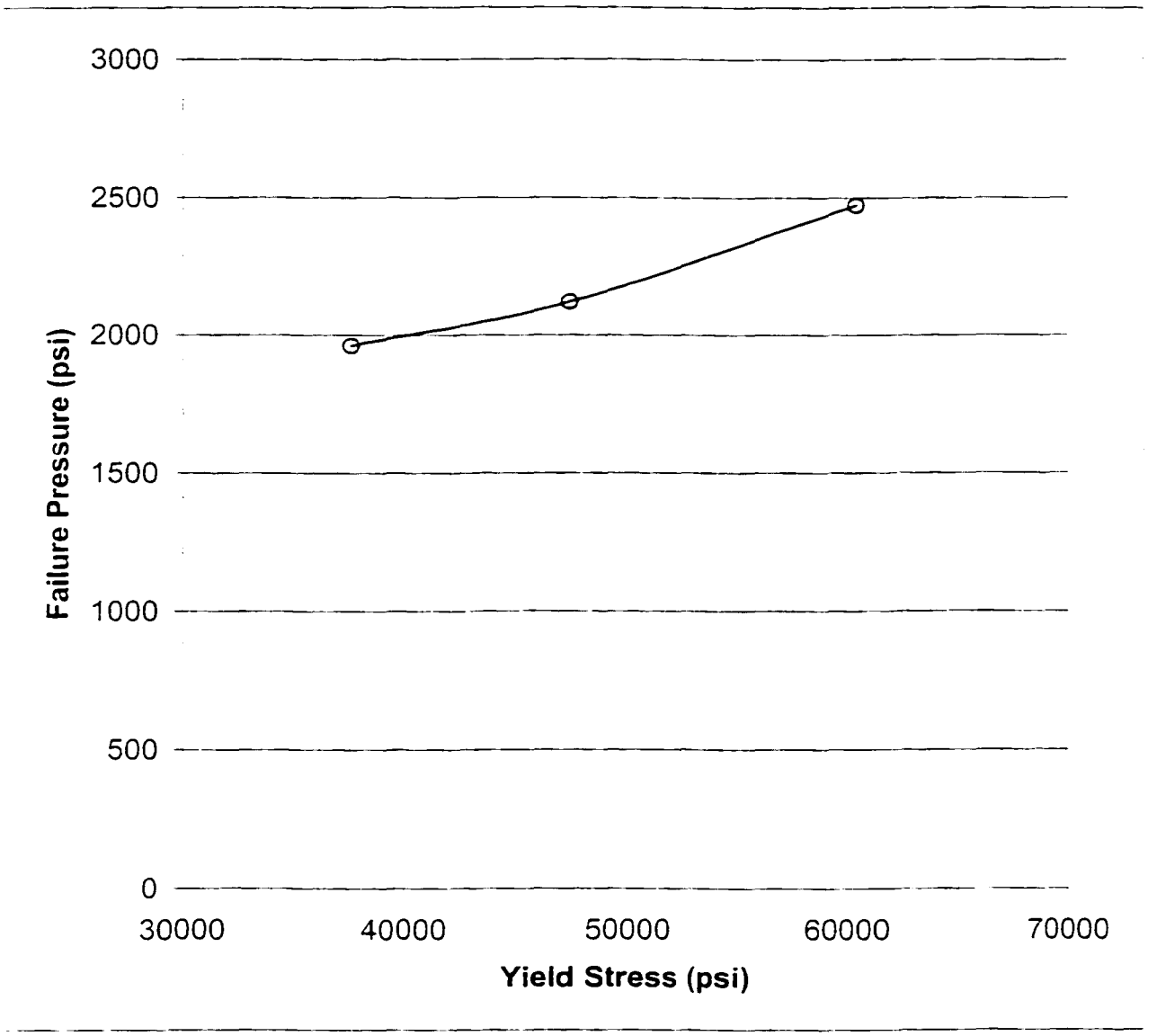
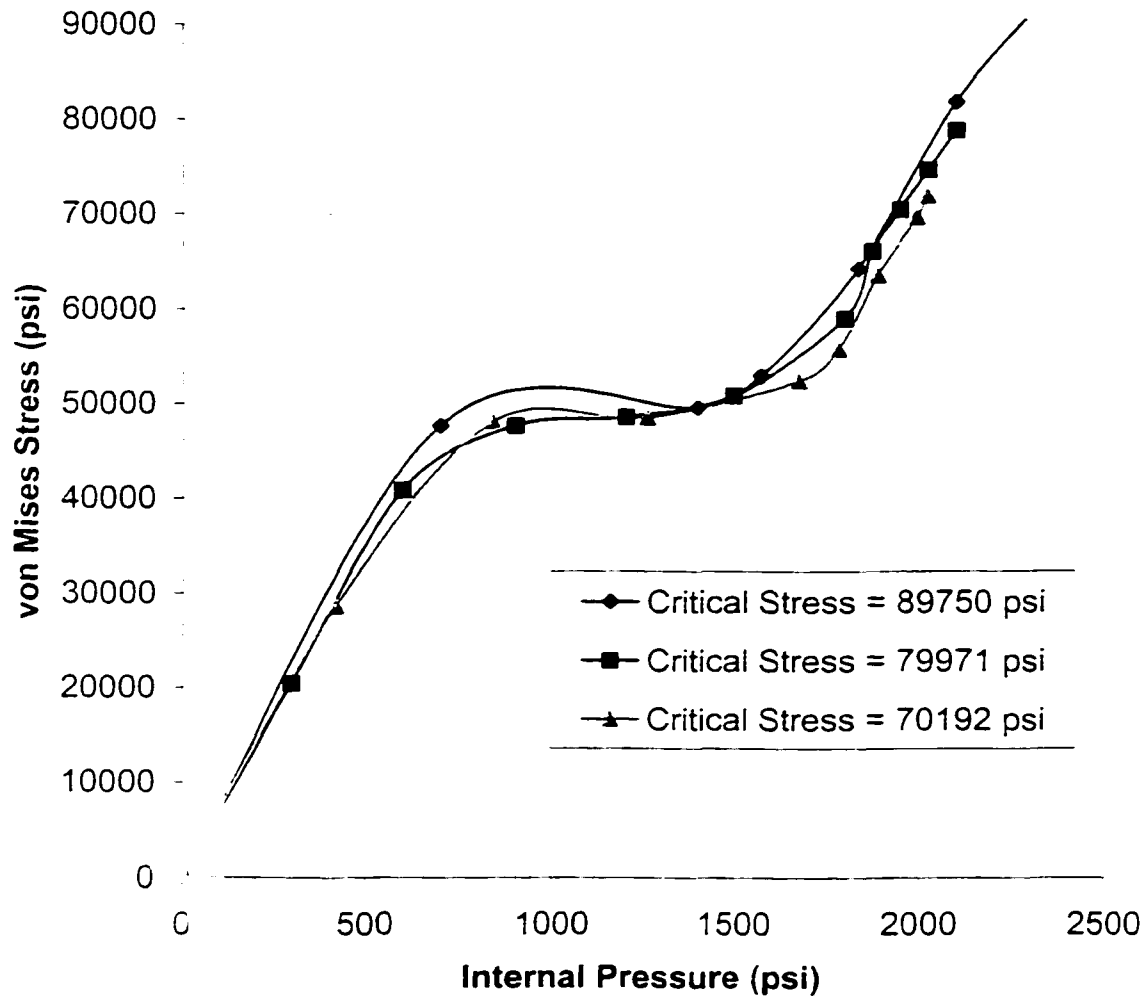


Figure 3.4.19: Failure pressure as a function of yield stress
Single spherical pit, 65% depth



Plastic Strain @ UTS = 0.2
Yield Stress = 47374 psi

Figure 3.4.20: von Mises stress as a function of internal pressure
with varying material Critical Stress.
Single spherical pit, 65% depth

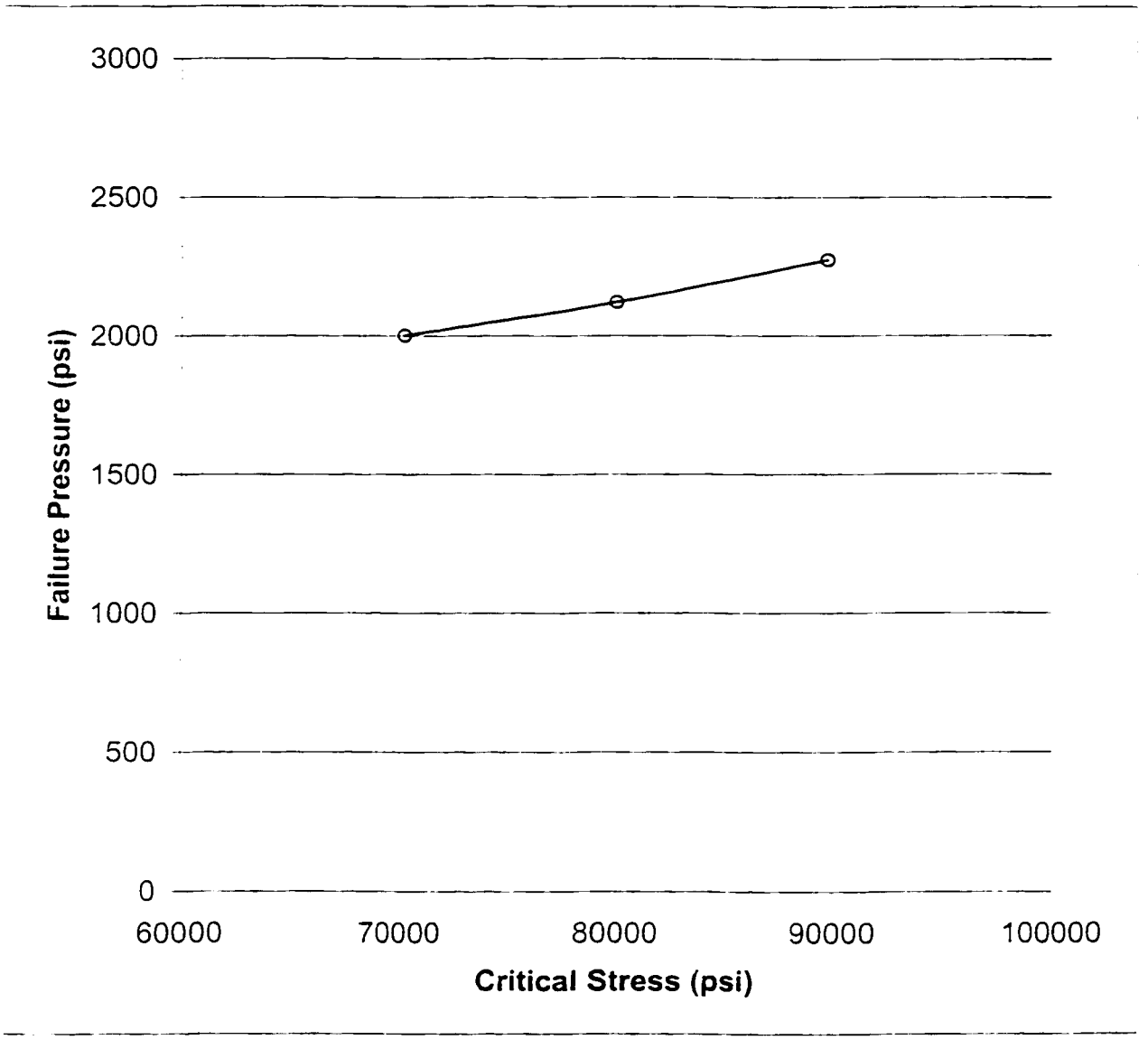
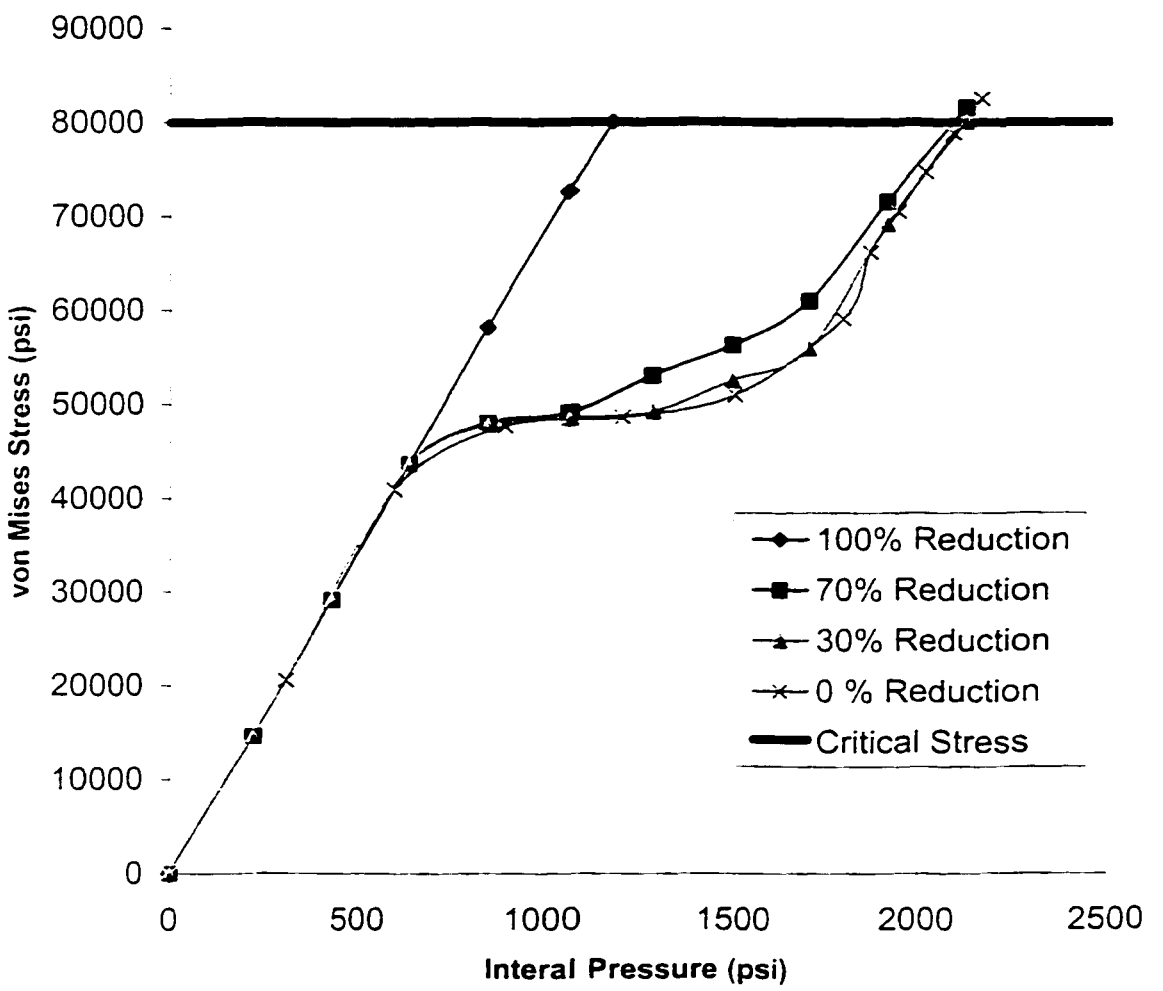


Figure 3.4.21: Failure pressure as a function of Critical Stress
Single spherical pit. 65% depth



Yield Stress = 47374 psi
True Stress @ UTS = 79971 psi

Figure 3.4.22: von Mises stress as a function of internal pressure with varying strain at the Critical Stress. Single spherical pit. 65% depth

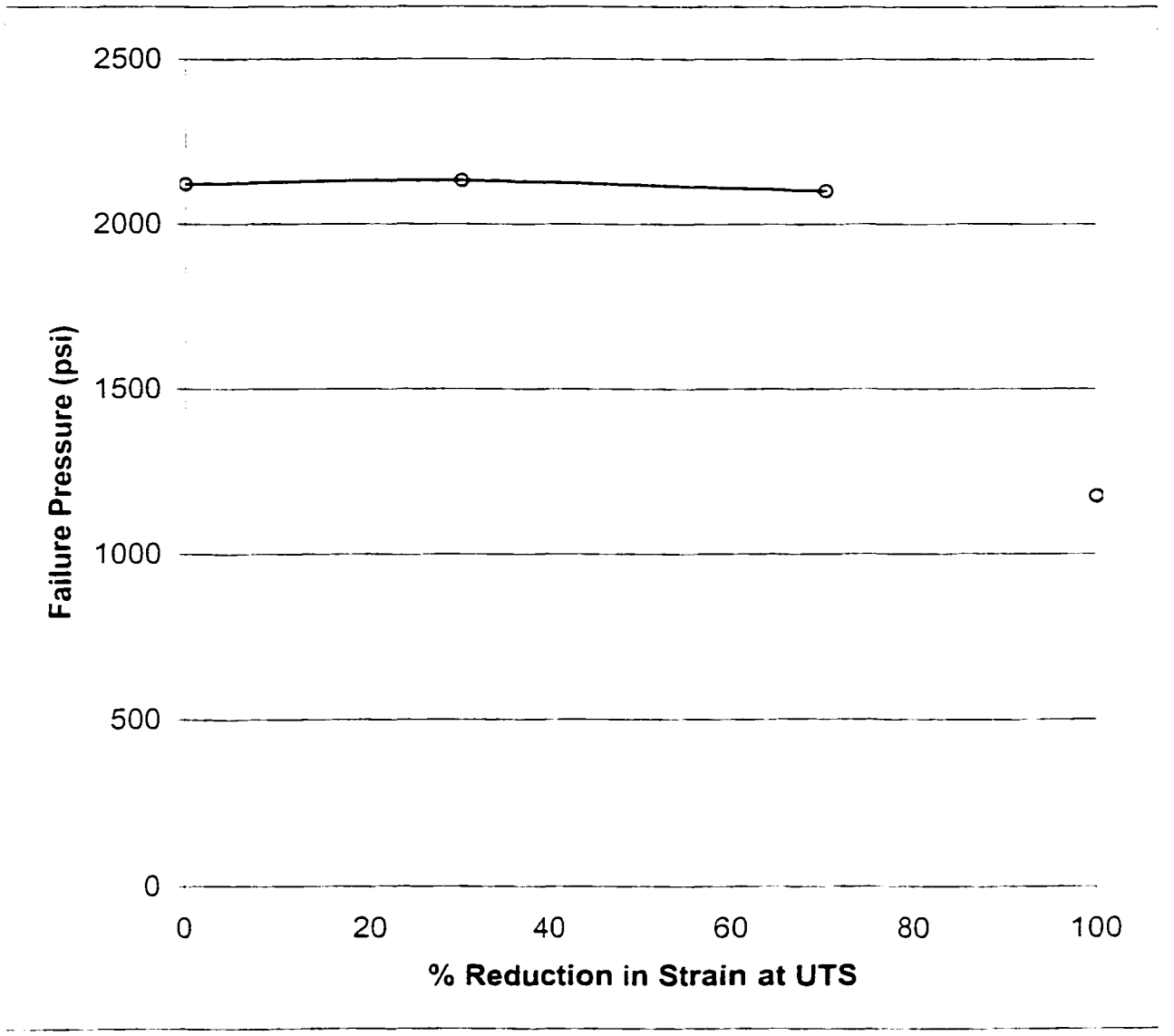


Figure 3.4.23: Failure pressure as a function of the strain at
the Critical Stress
Single spherical pit, 65% depth

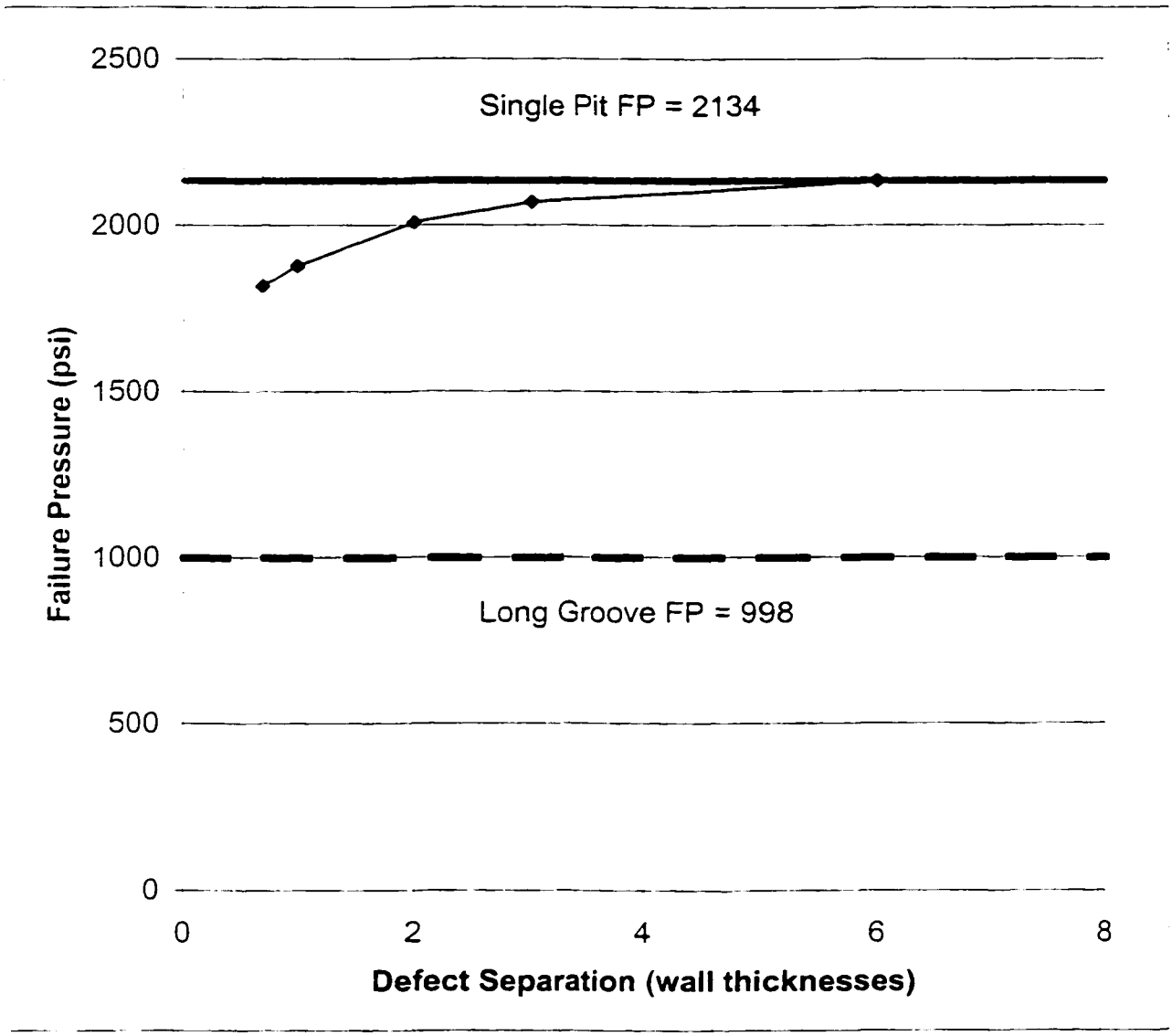


Figure 3.4.24: Failure pressure as a function of defect separation
65% Depth spherical corrosion pit

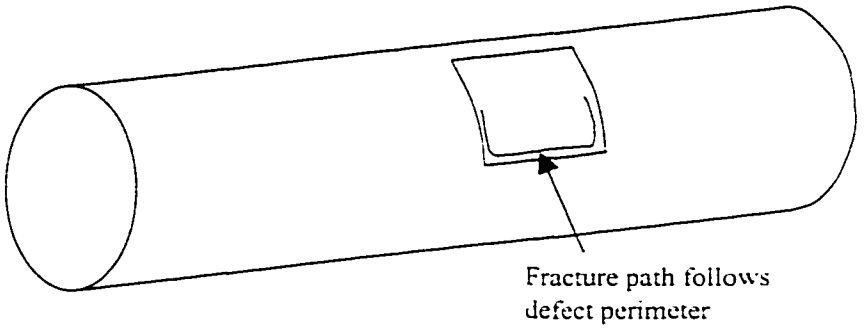


Figure 4.1.1a: Typical fracture path for a flat-bottomed defect

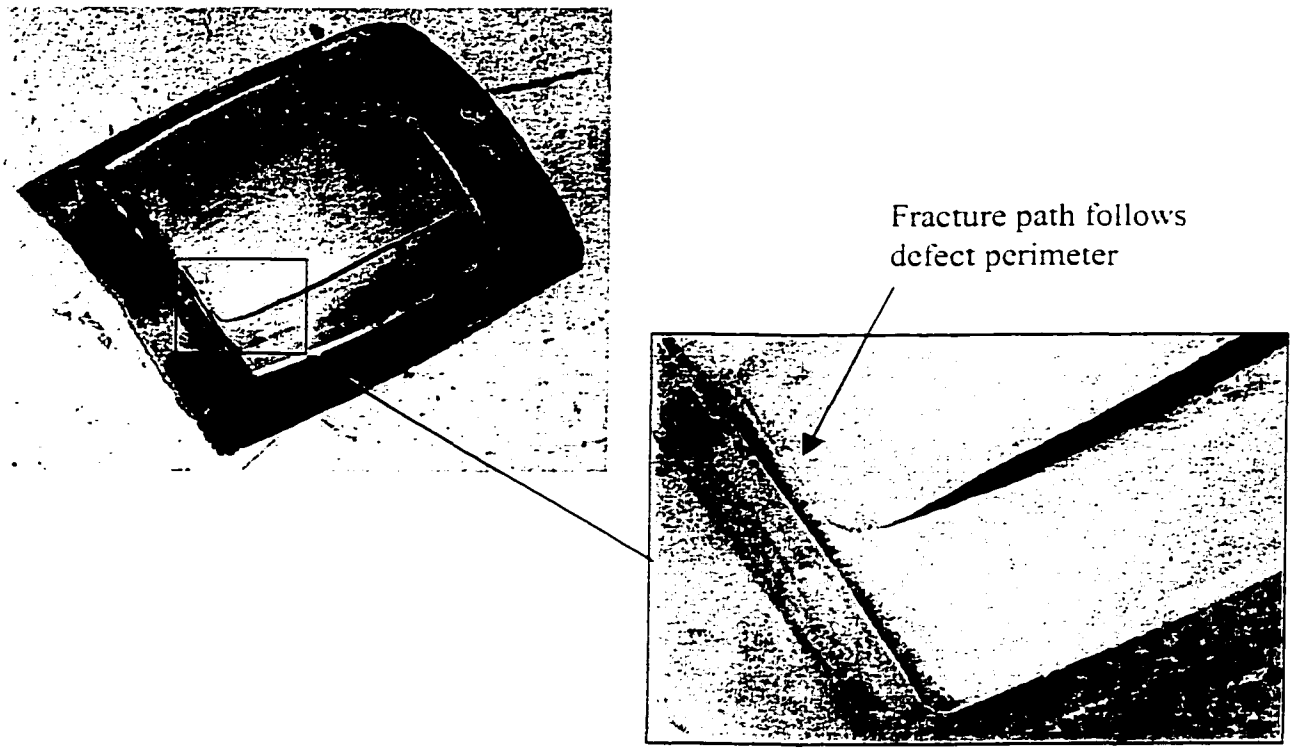


Figure 4.1.1b: Fracture path for a large flat-bottomed defect

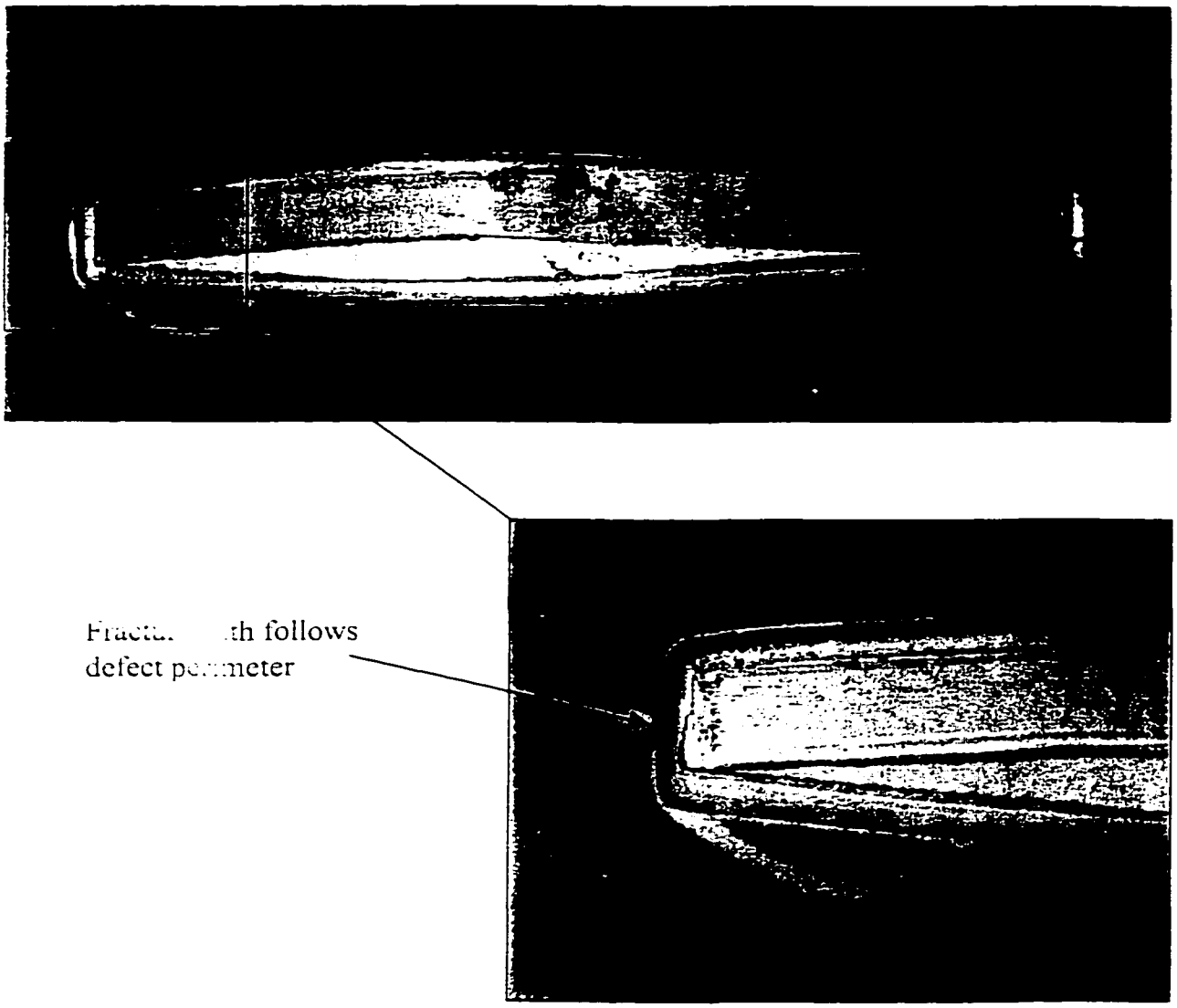


Figure 4.1.1c: Fracture path for a flat-bottomed defect with a small circumferential dimension

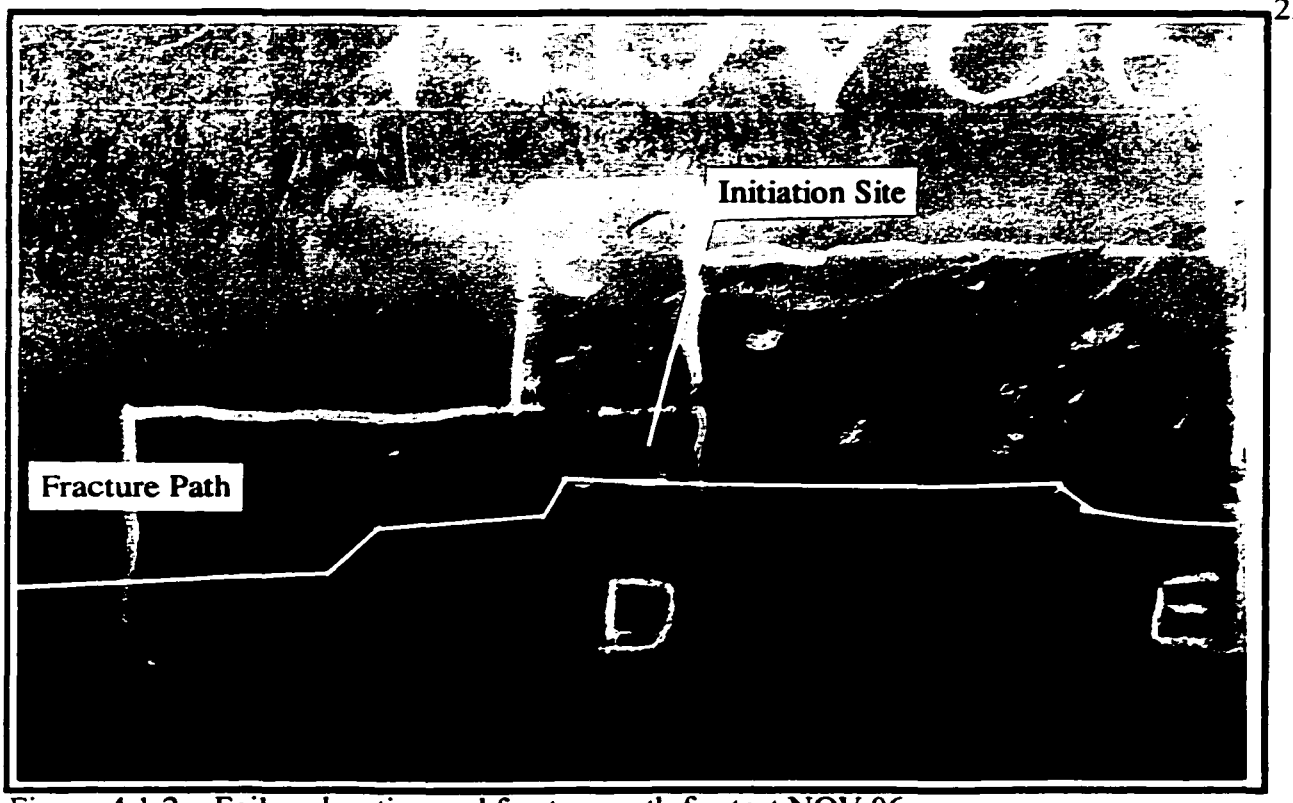


Figure 4.1.2a: Failure location and fracture path for test NOV 06

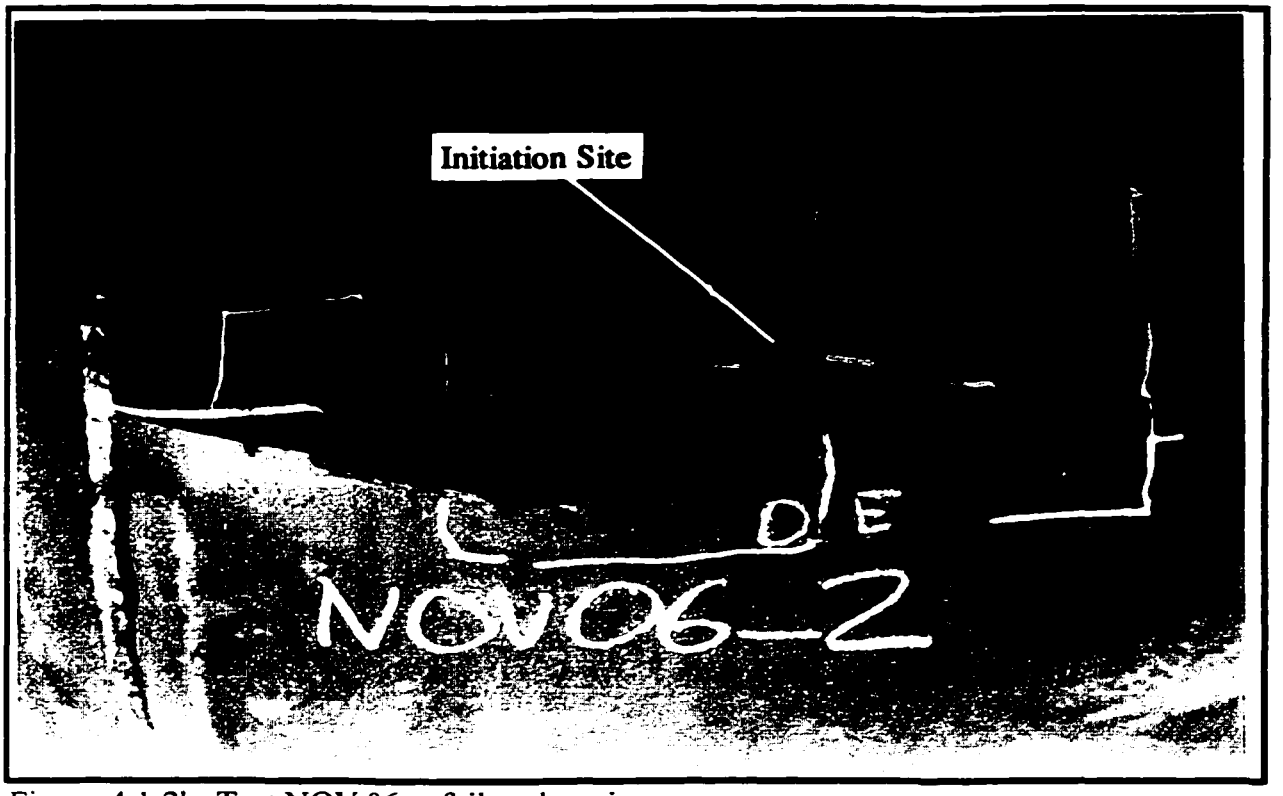


Figure 4.1.2b: Test NOV 06 at failure location

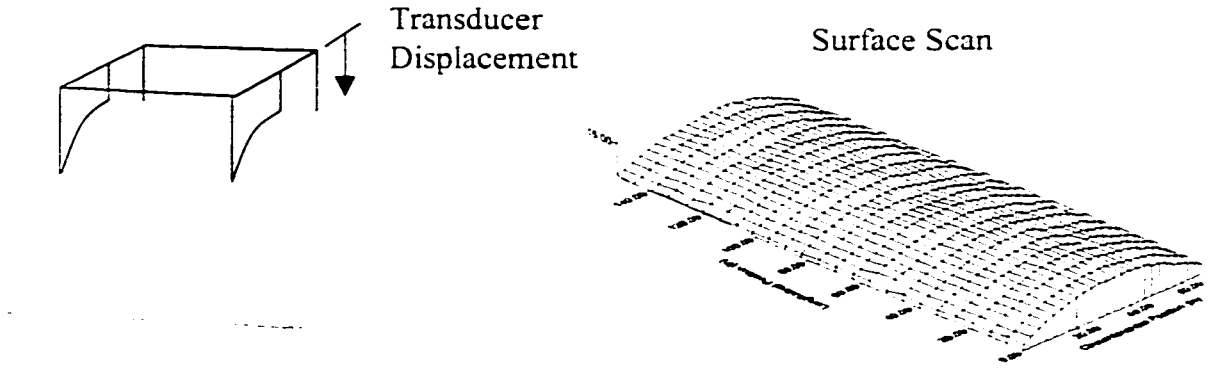


Figure 4.2.1 Surface scanning from a flat plane

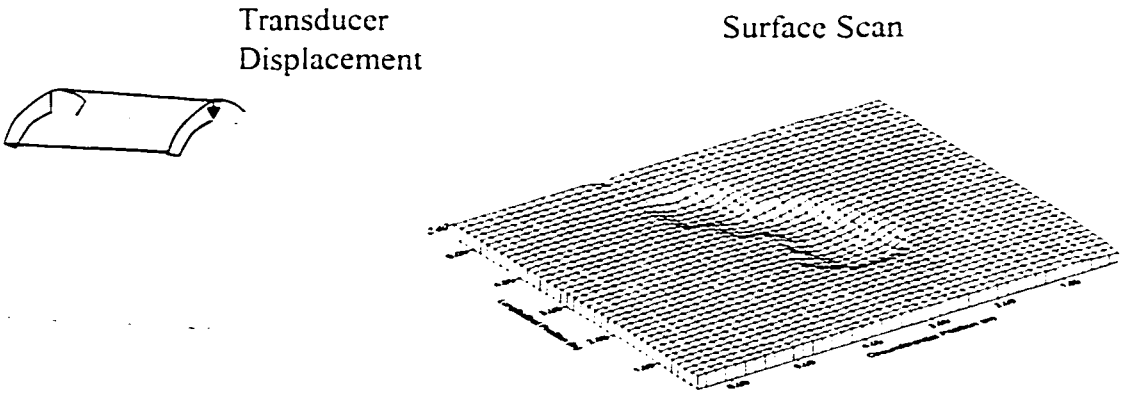


Figure 4.2.2 Surface scanning from a cylindrical plane

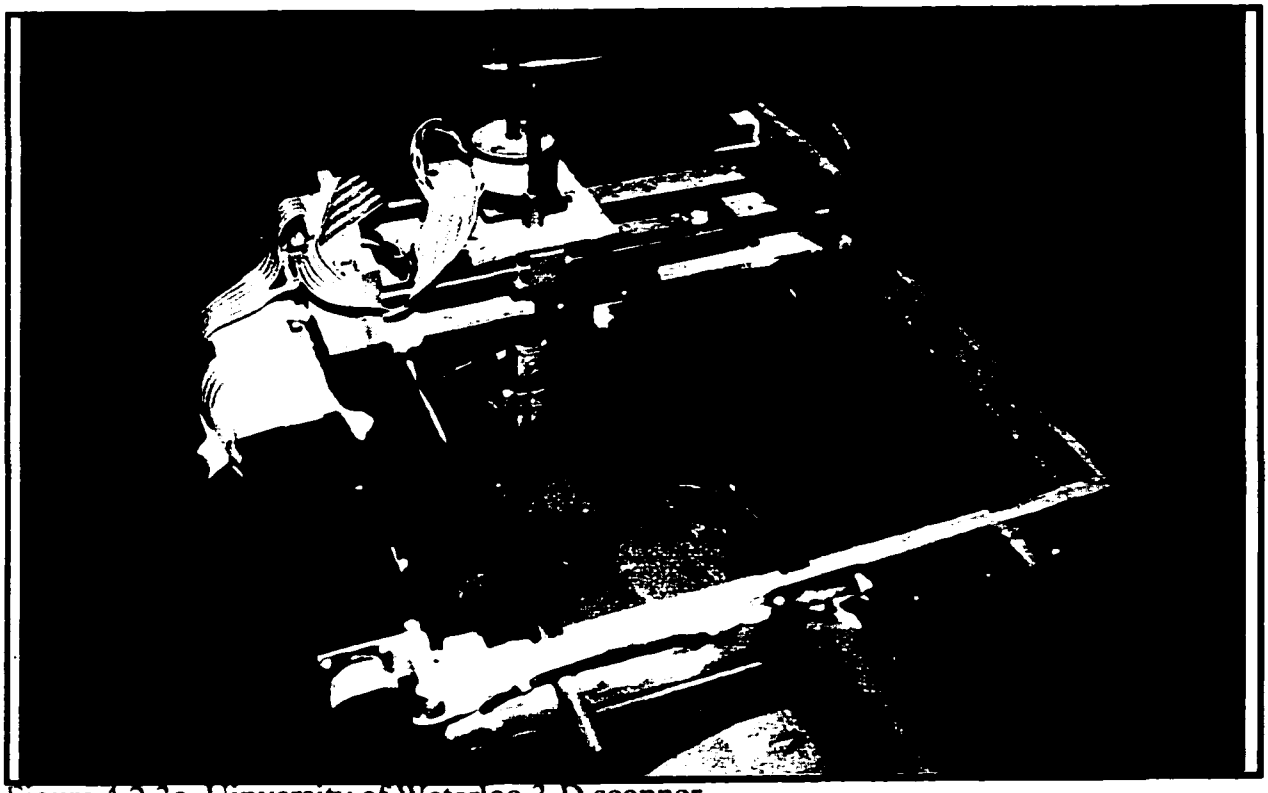


Figure 4.2.3a University of Waterloo 3-D scanner



Figure 4.2.3b University of Waterloo 3-D scanner and data system

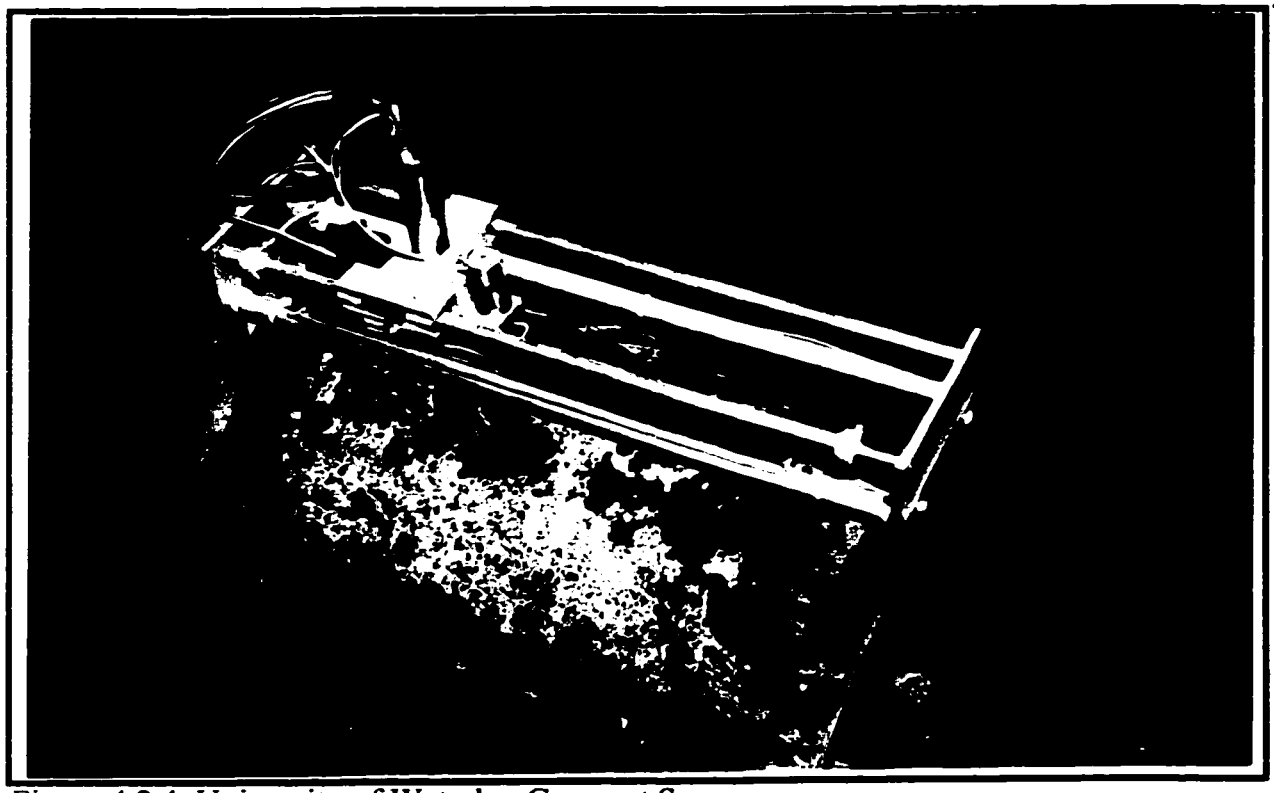


Figure 4.2.4 University of Waterloo Compact Scanner

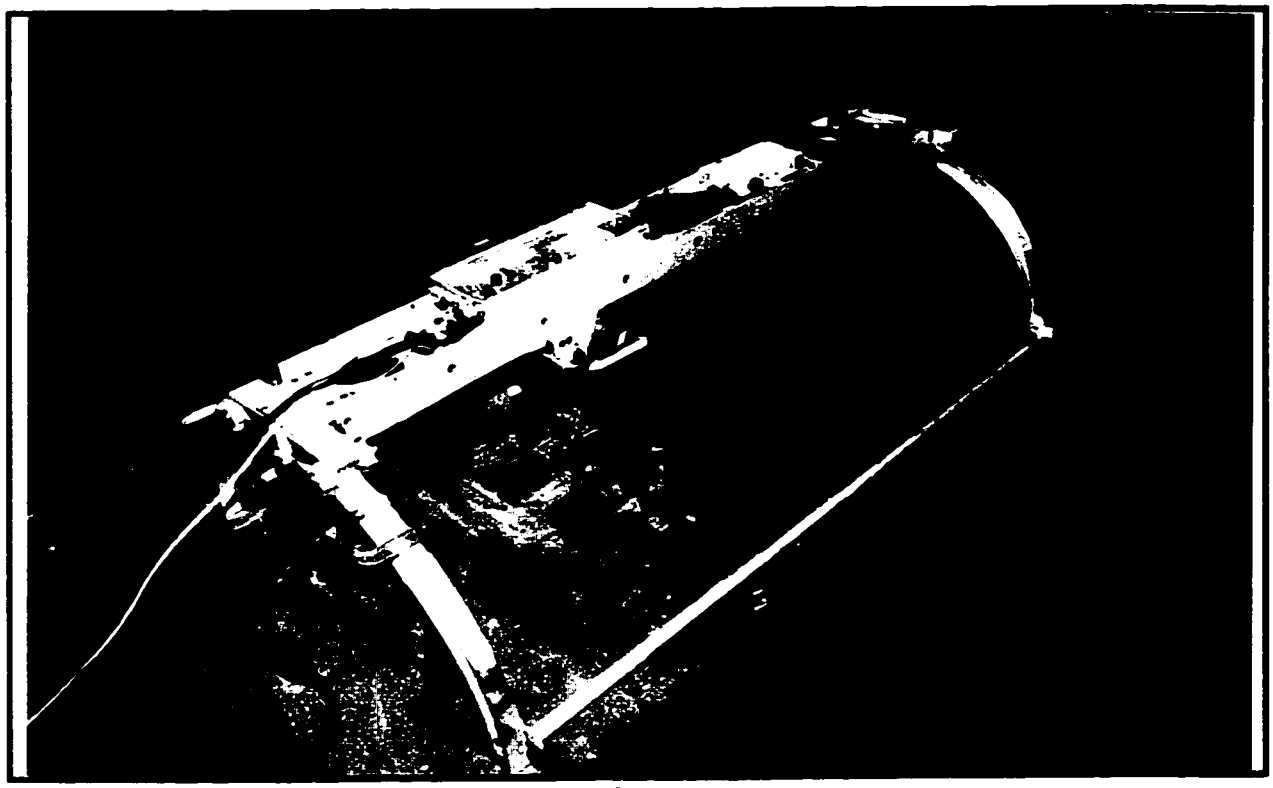


Figure 4.2.5 University of Waterloo Long Scanner

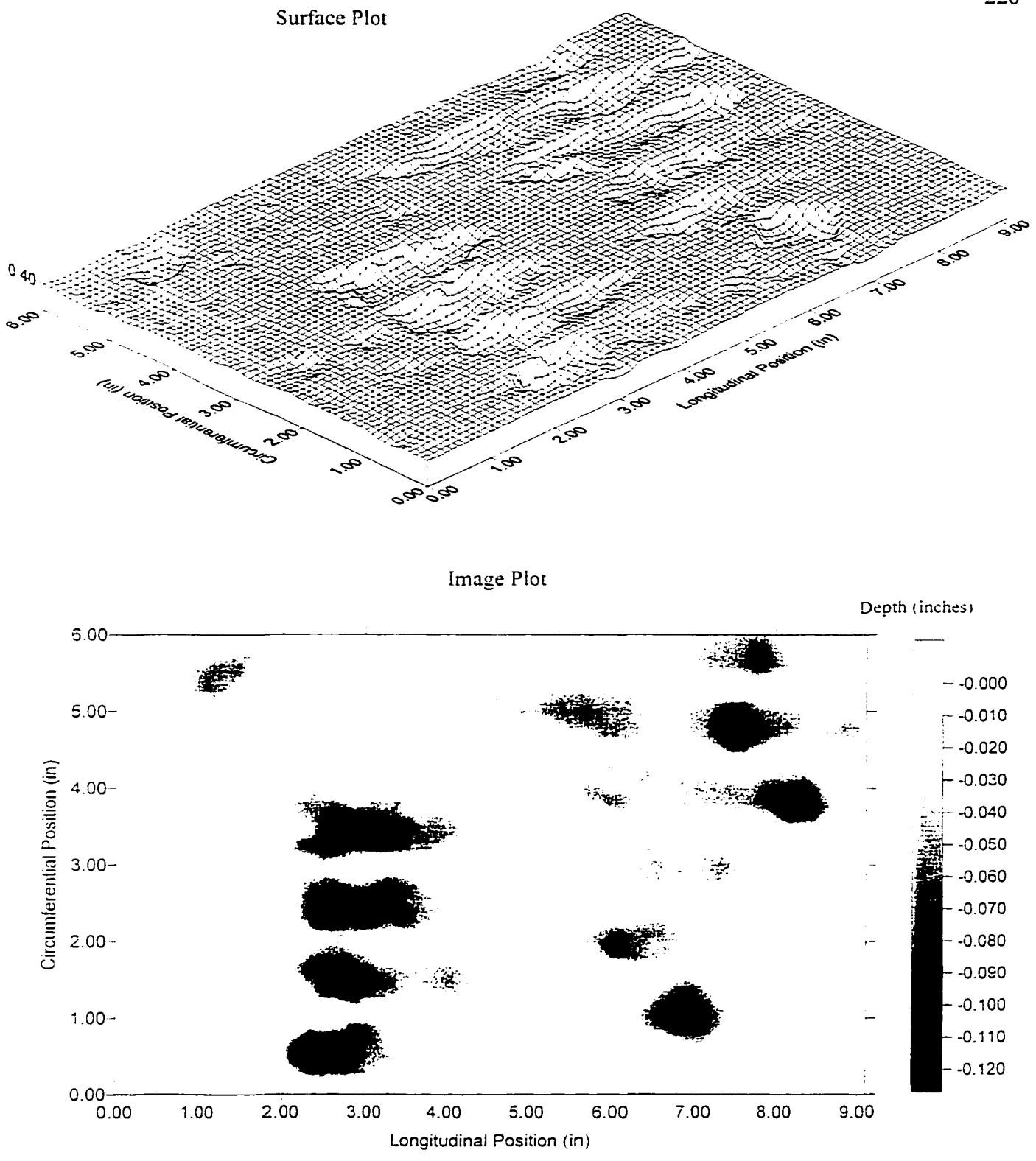
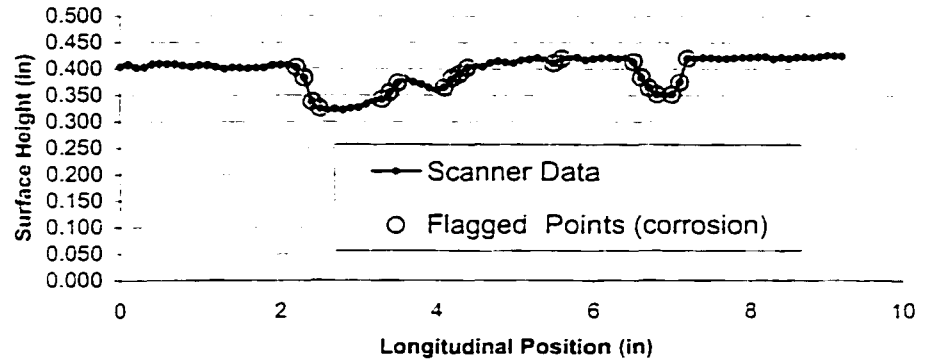
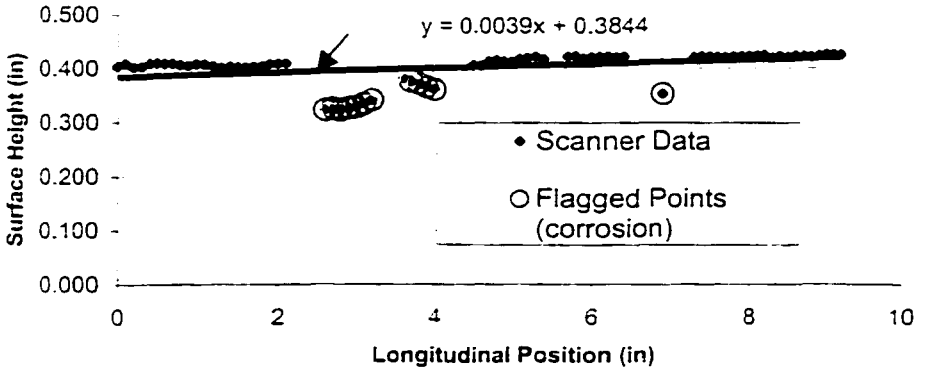


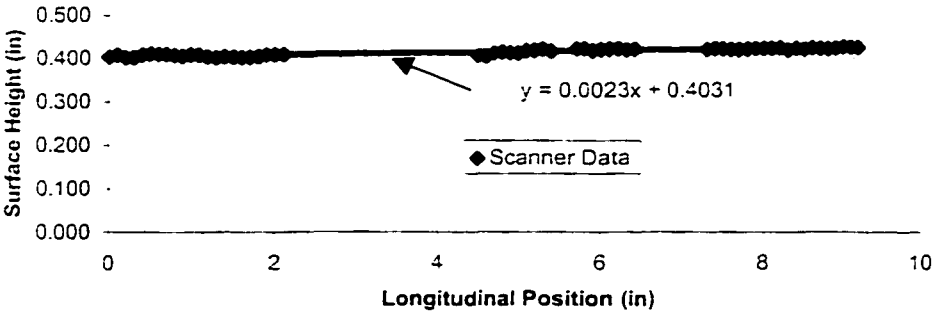
Figure 4.2.6 3-D Scanner suface and image plots for a complex corrosion defect (TCP01-AB)



A - Corrosion ID based on the longitudinal slope



B - Corrosion ID based on the distance from the linear regression



C - Longitudinal fit to the uncorroded surface

Figure 4.2.7 Transformation of a longitudinal line of scanned data

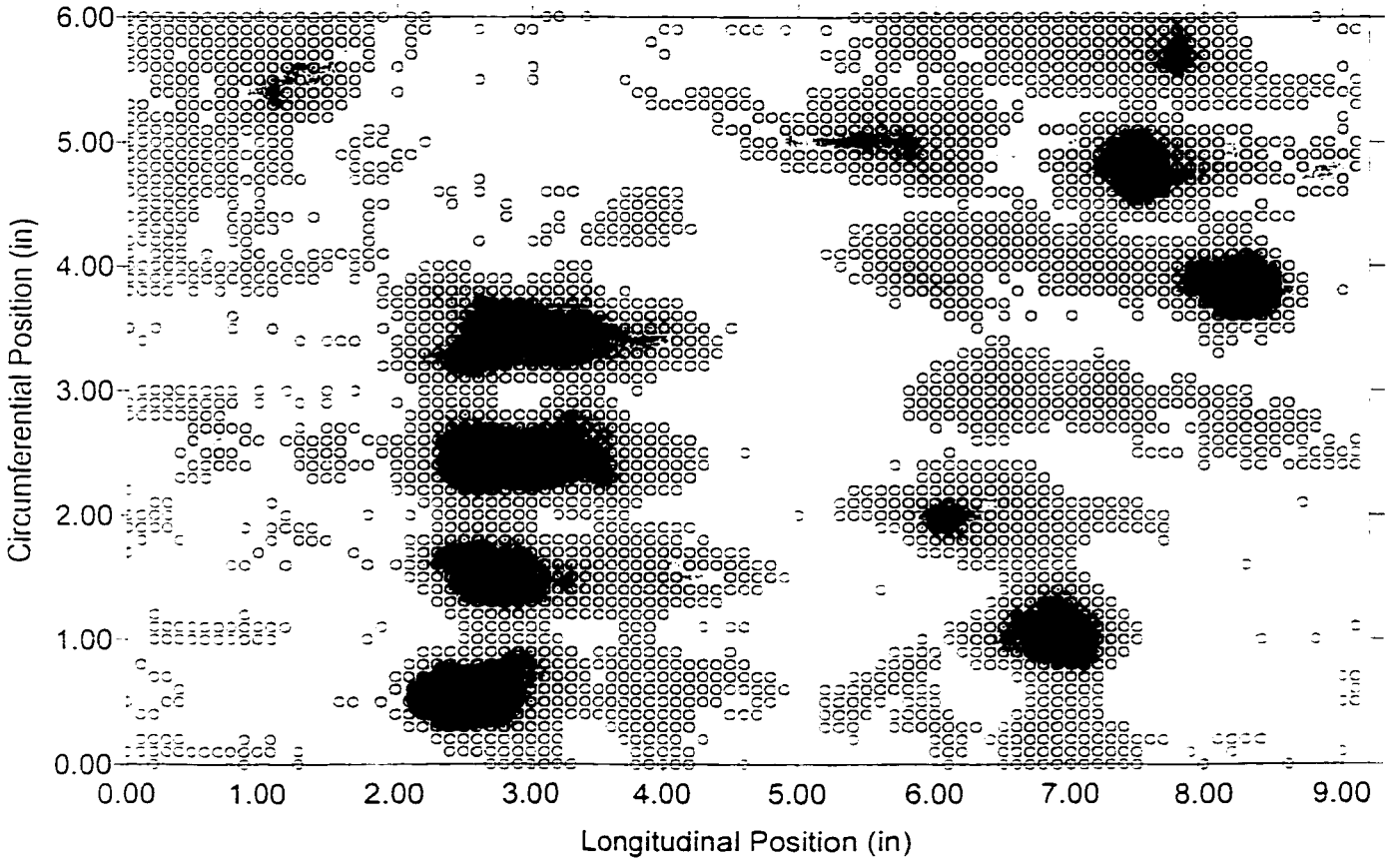
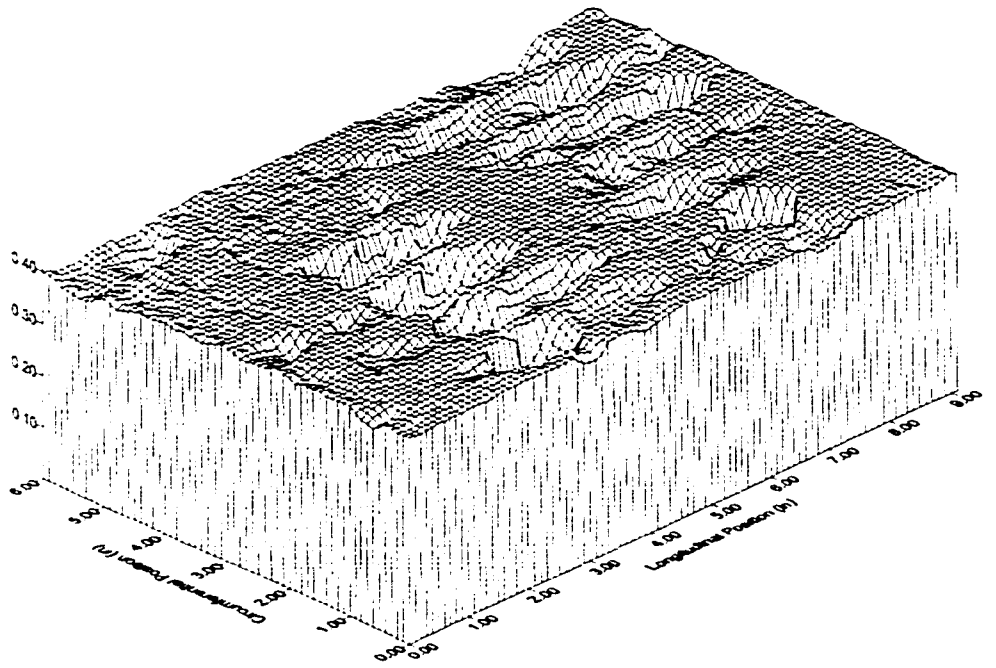
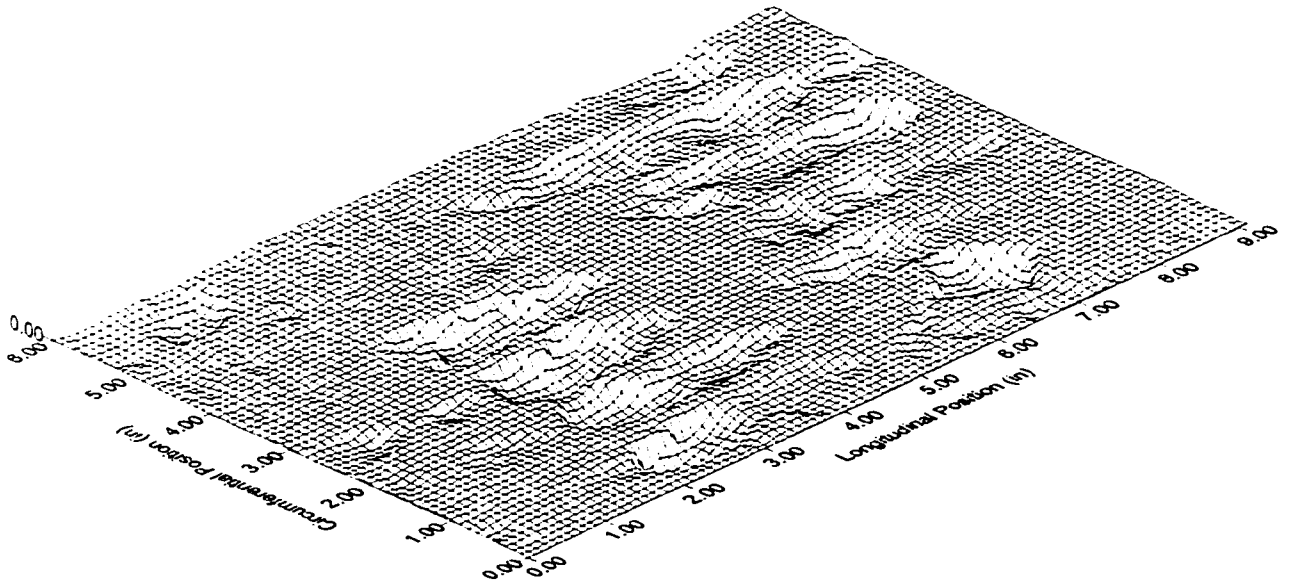


Figure 4.2.8 Scanner image with corrosion defects identified by the program (circles)

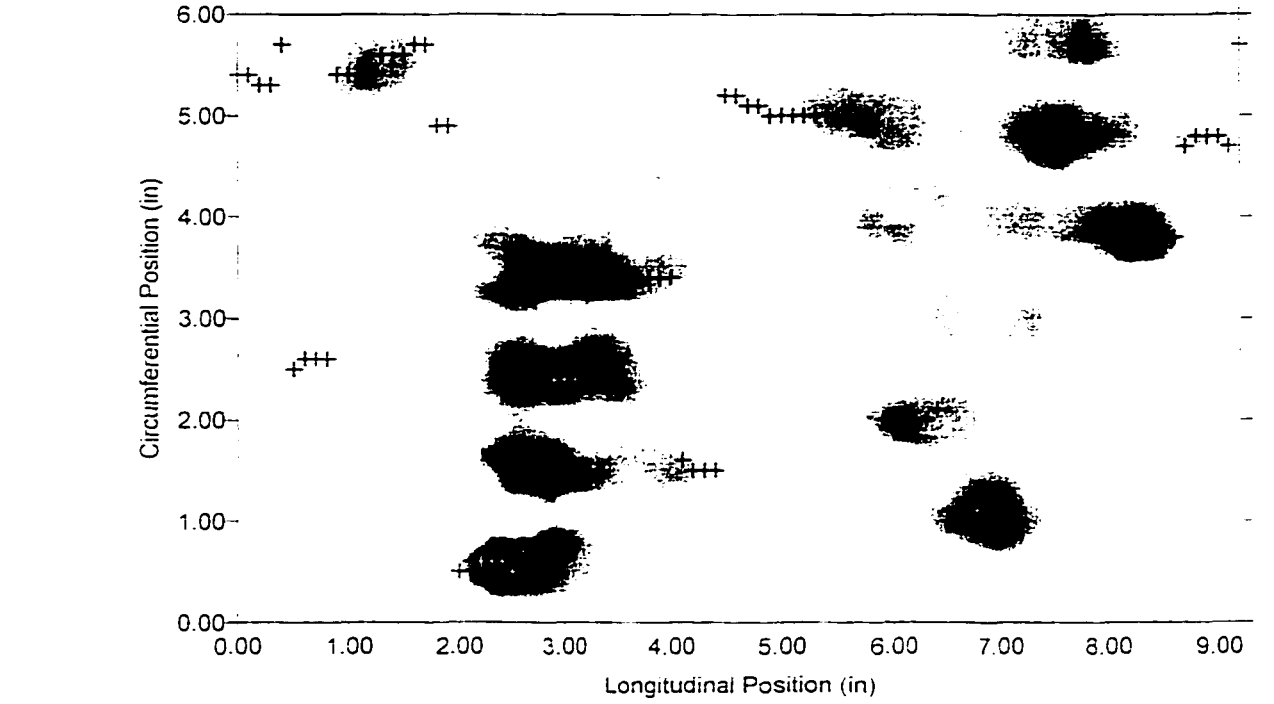


Original Scanner Surface Data



Transformed Scanner Surface Data

Figure 4.2.9 Original and transformed scanned surface data



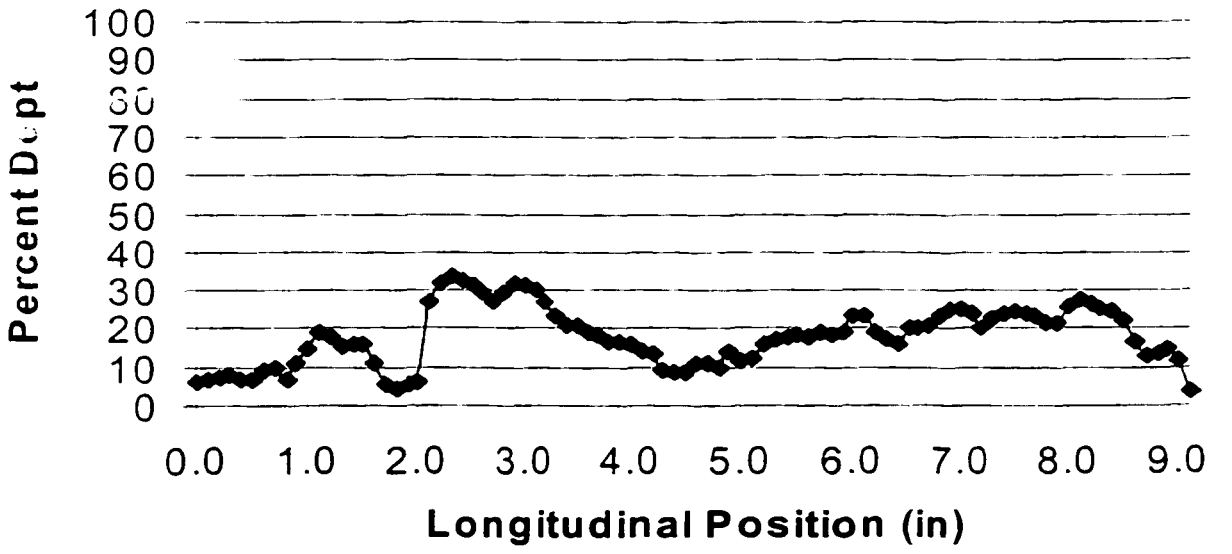
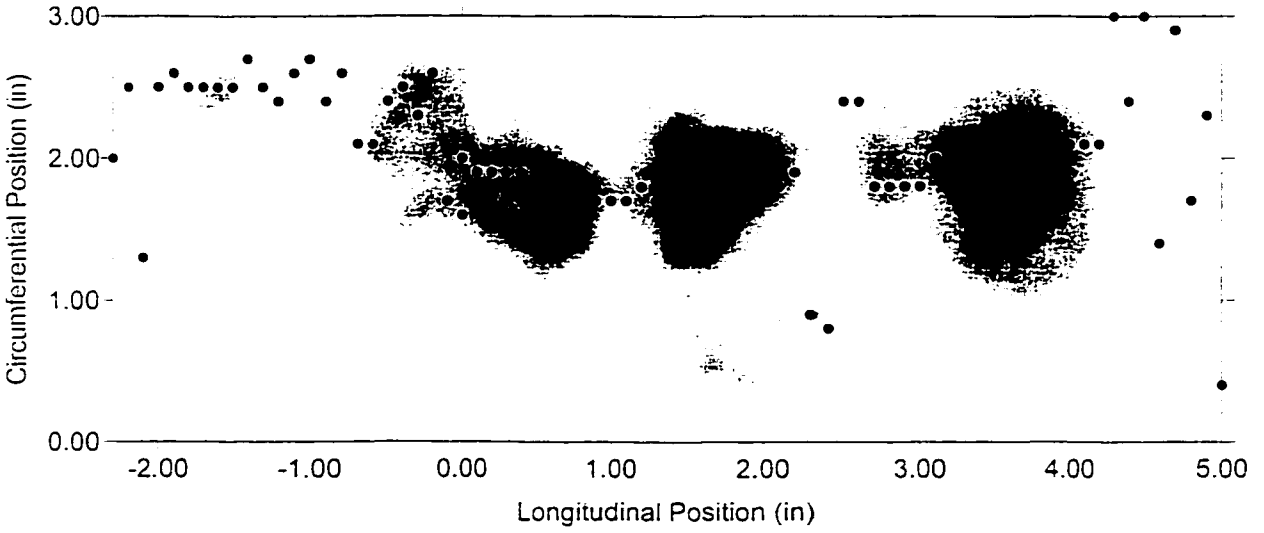


Figure 4.2.10 Scanner image of the corrosion defect with the deepest point on each circumferential line identified (crosses) using the projection method.



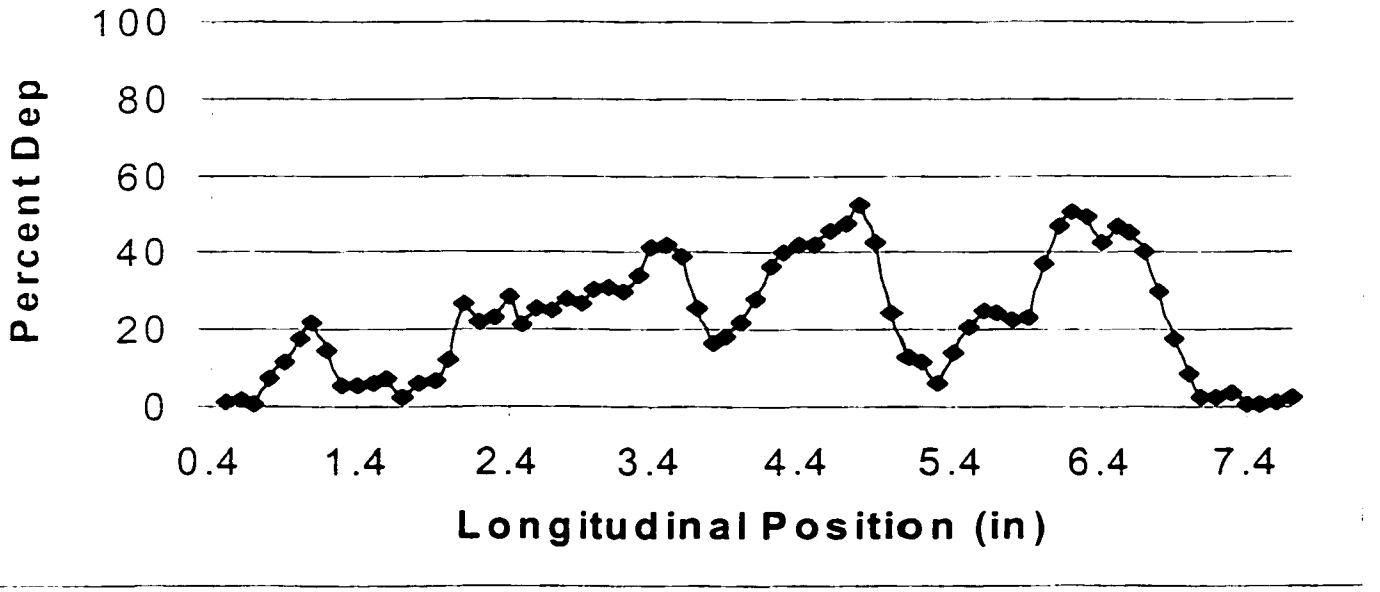


Figure 4.2.11 Projection method applied to a simply shaped corrosion defect

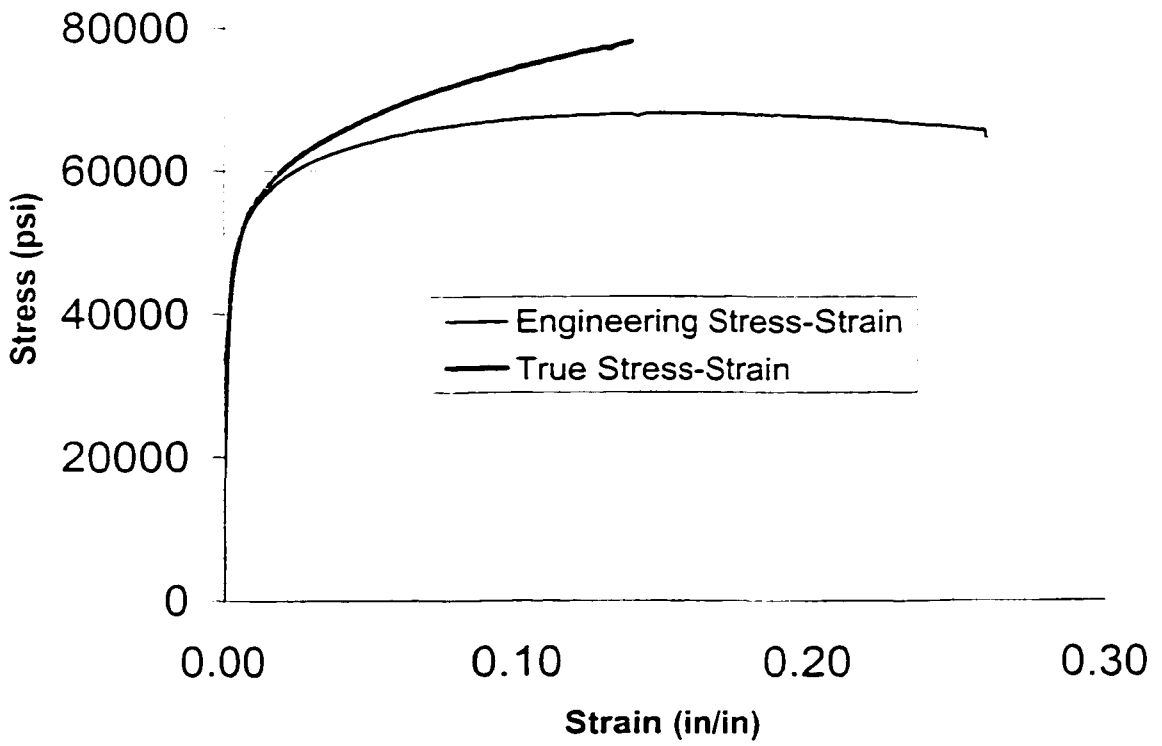


Figure 4.2.12 Typical Engineering and true stress-strain curves

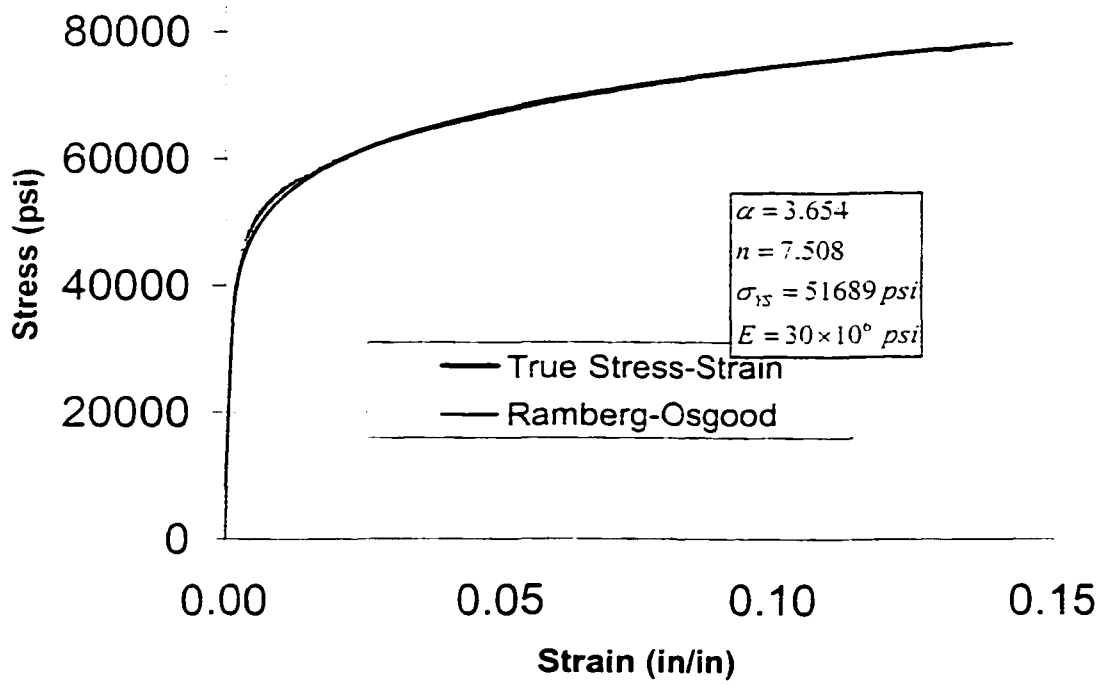


Figure 4.2.13 True stress-strain curve and corresponding Ramberg-Osgood curve fit

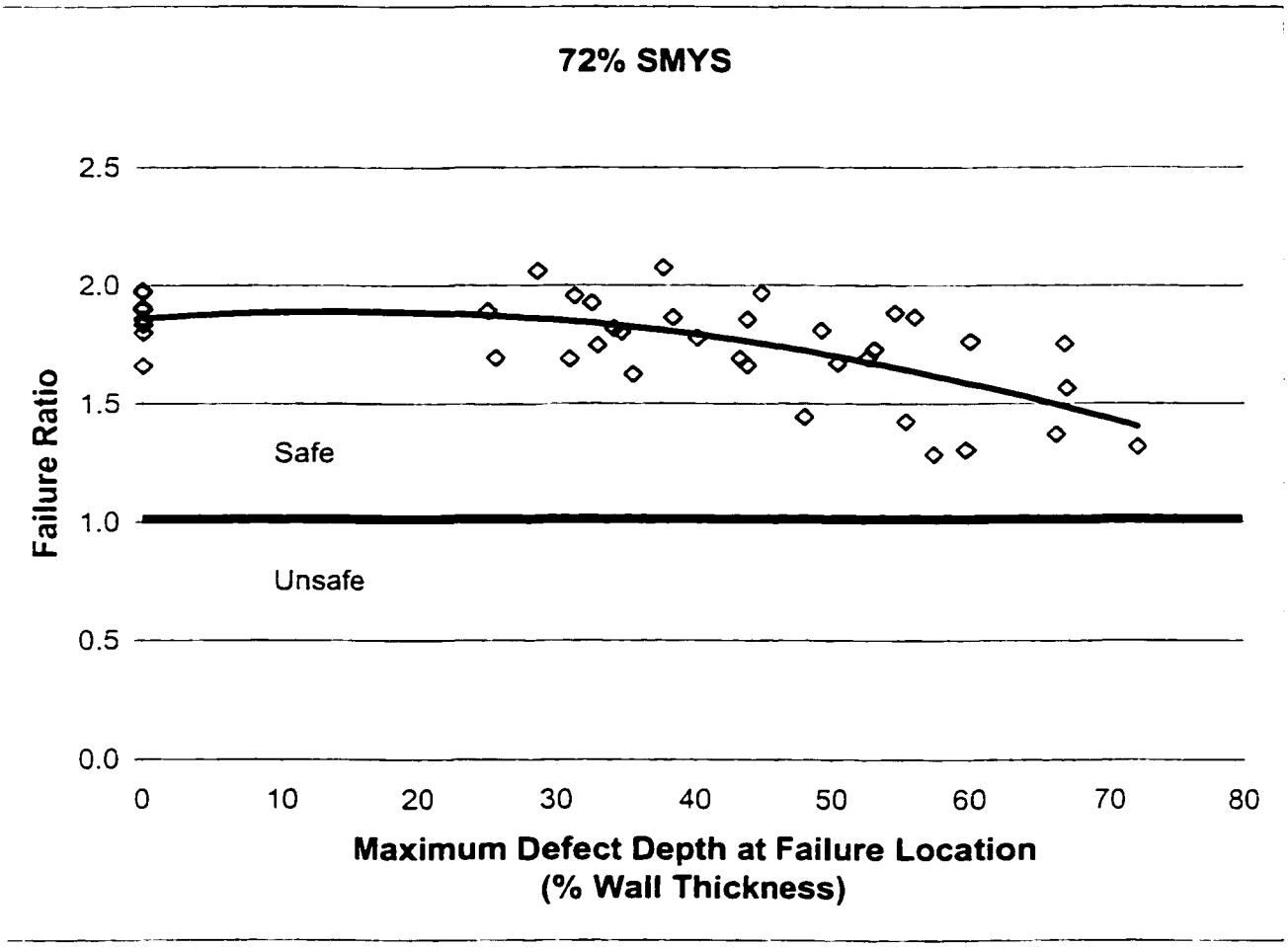


Figure 4.3.1 Failure ratio for pipe sections from the experimental database operating at 72% SMYS

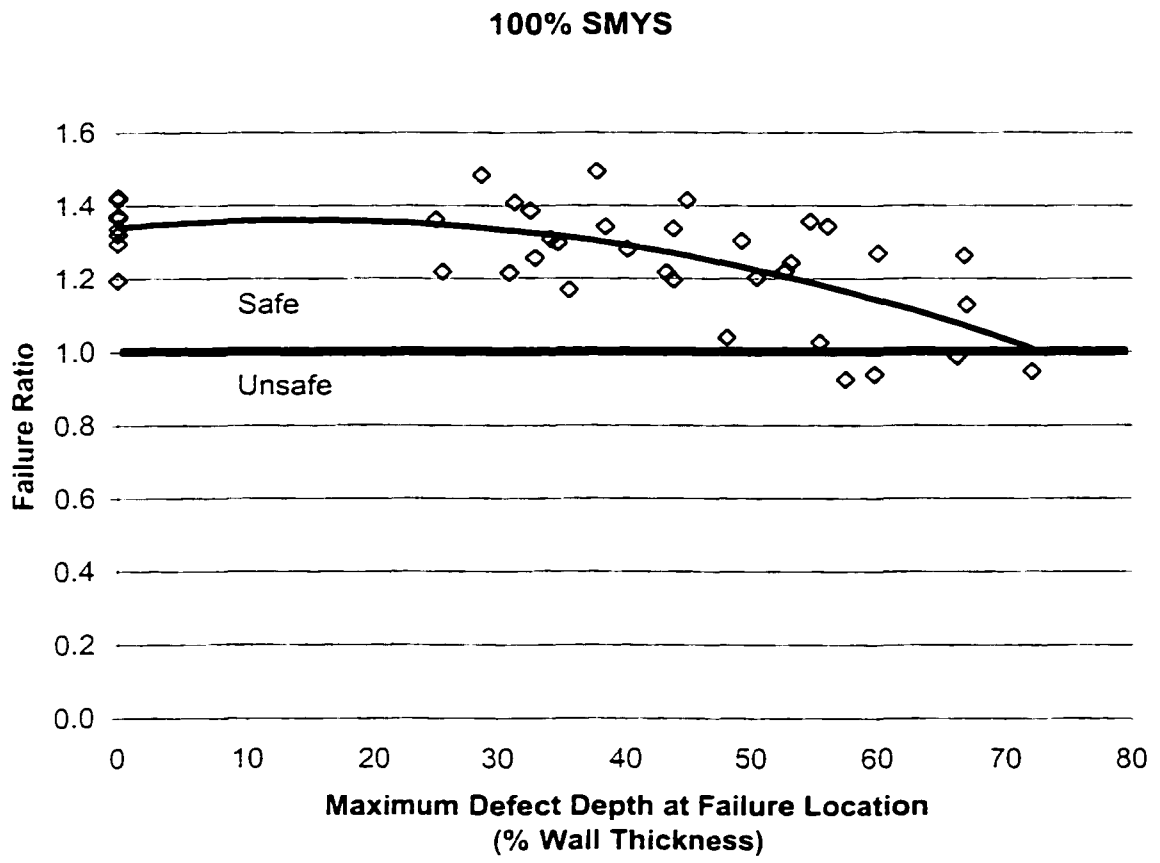


Figure 4.3.2 Failure ratio for pipe sections from the experimental database operating at 100% SMYS

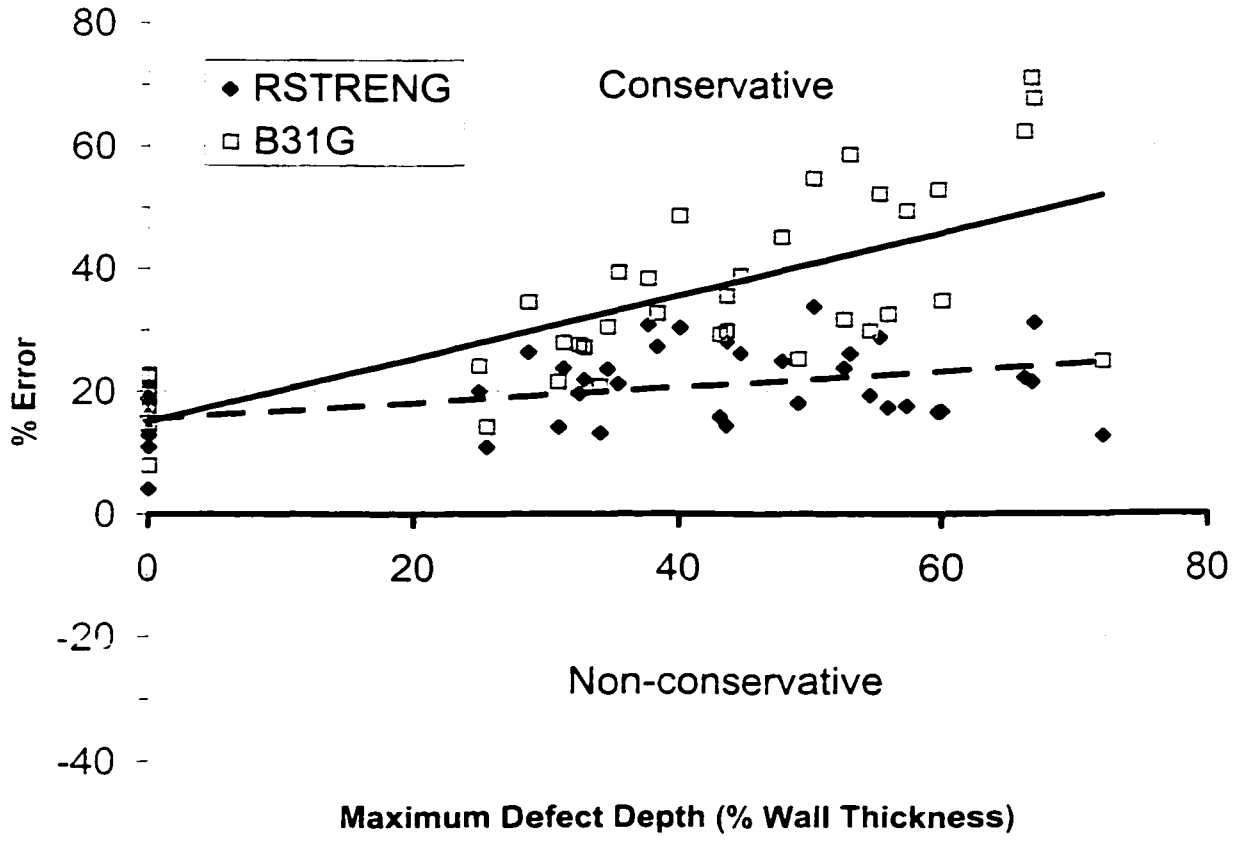


Figure 4.4.1 B31G and RSTRENG failure pressure preditions for the experimental database - % Error

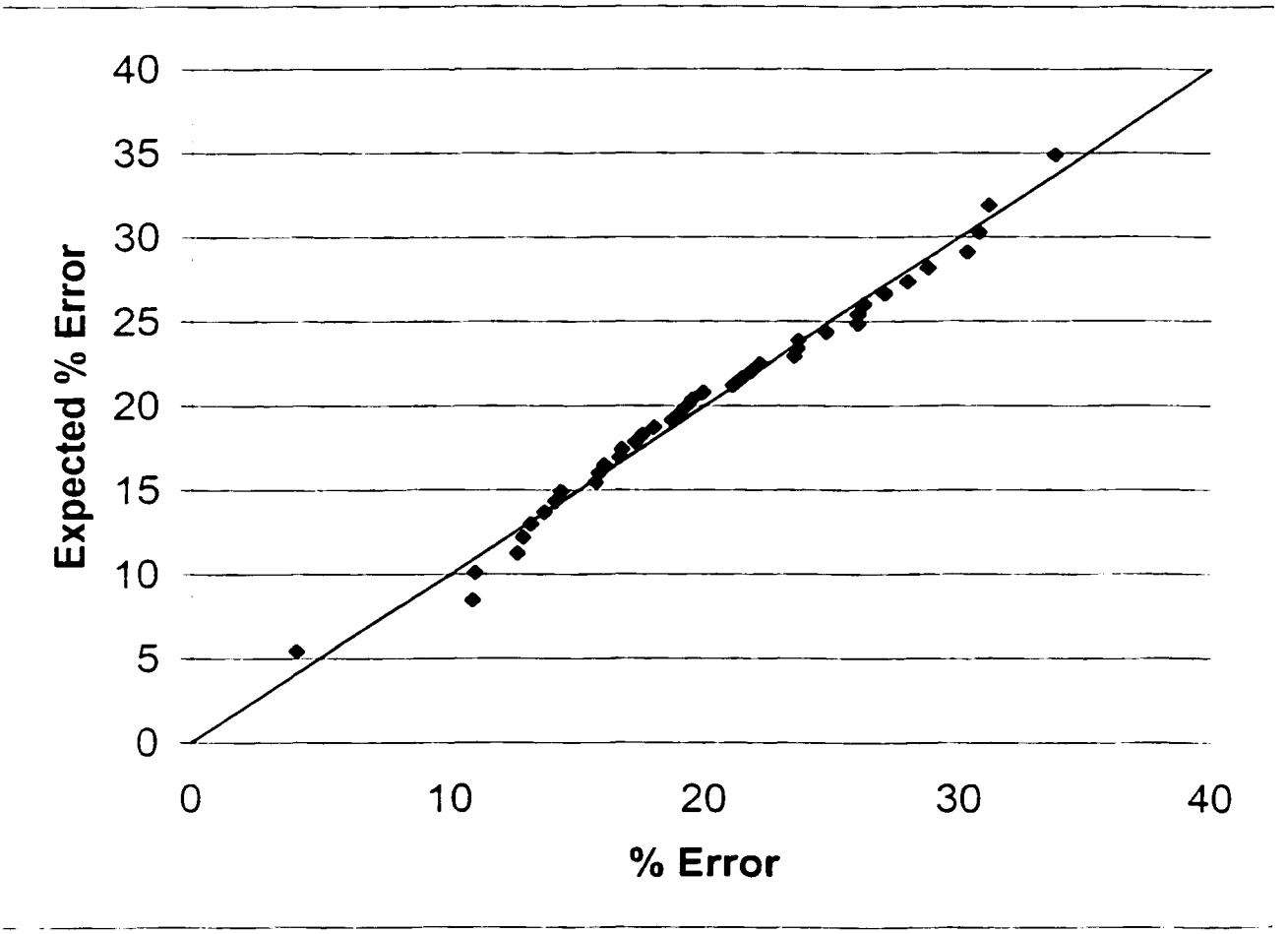


Figure 4.4.2 Normal probability plot for the % error in the RSTRENG predictions

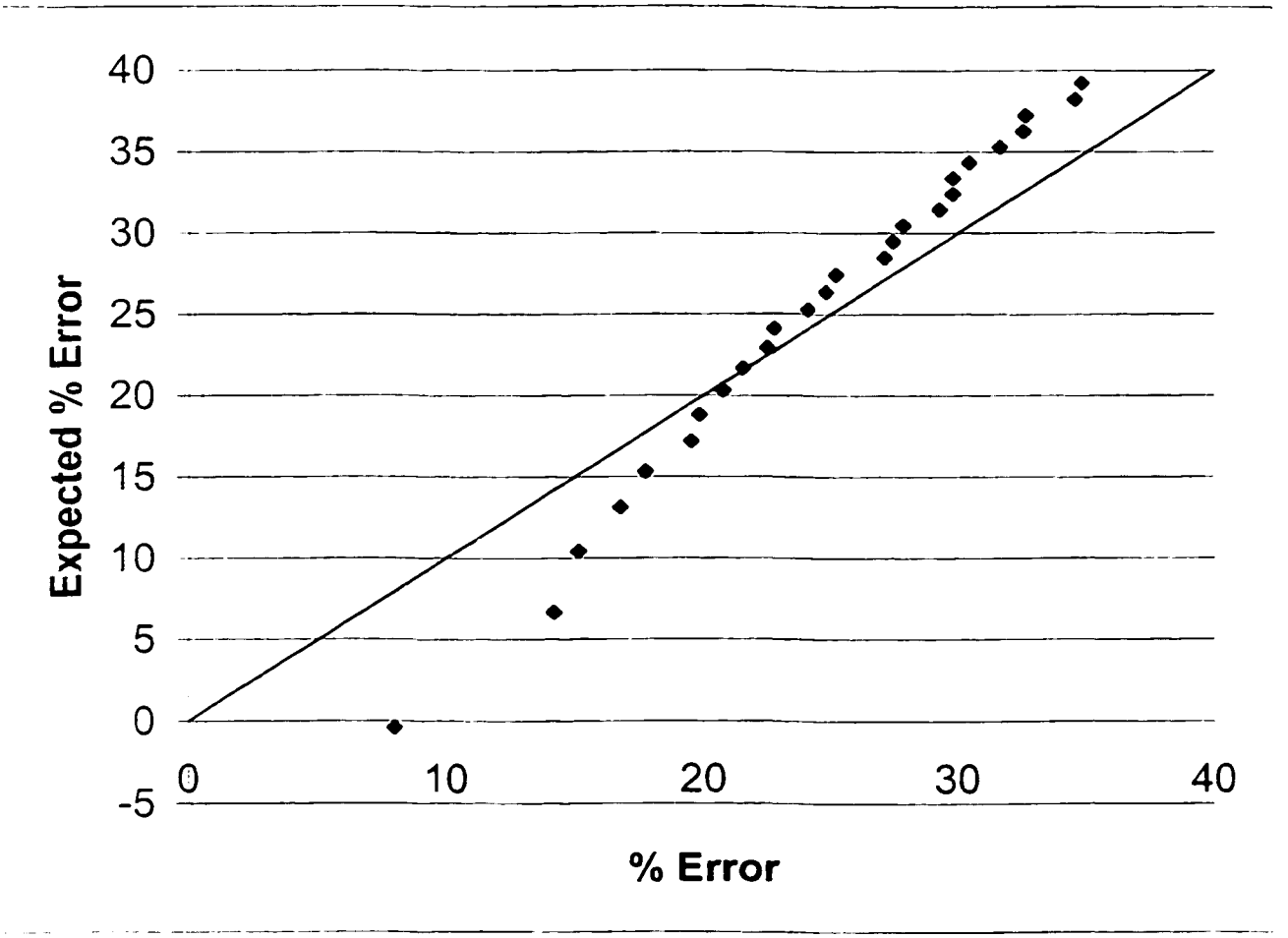


Figure 4.4.3 Normal probability plot for the % error in the B31G predictions

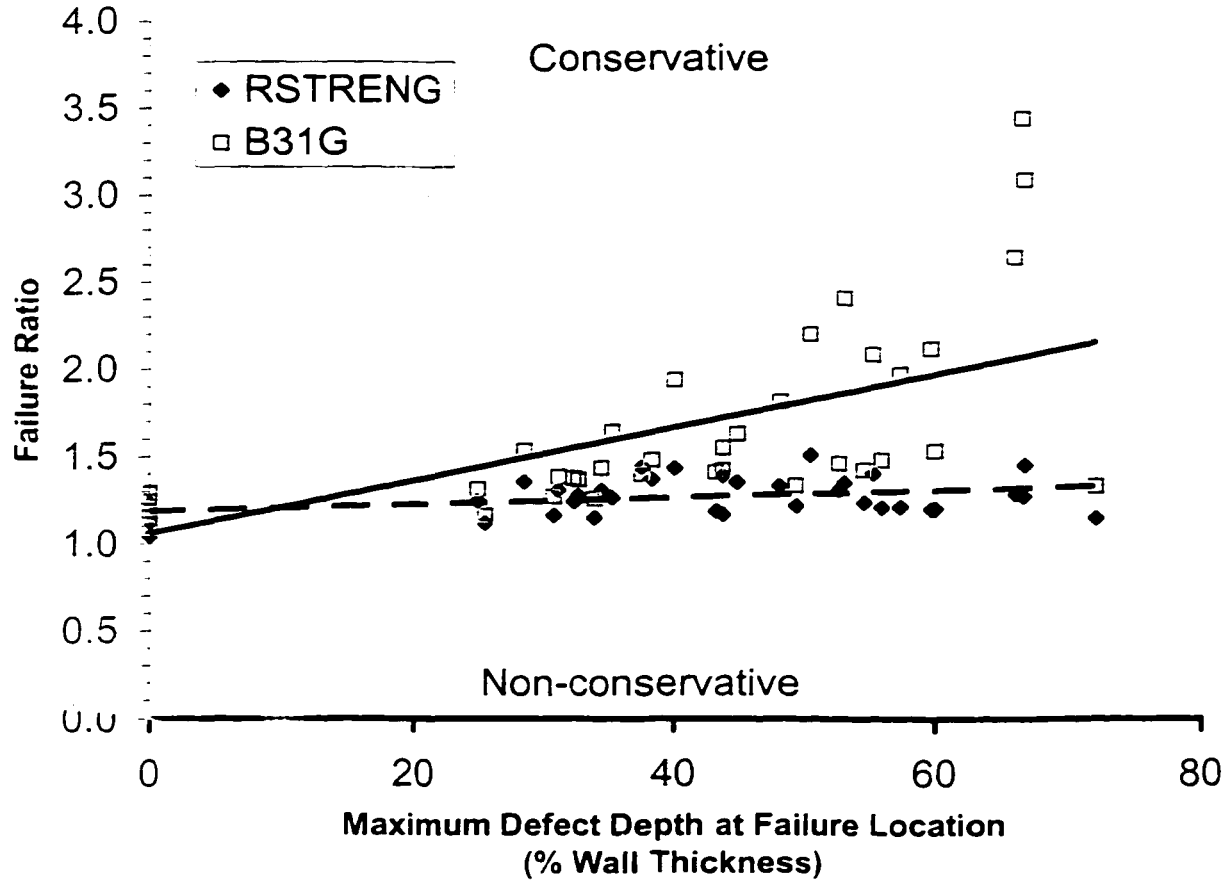


Figure 4.4.4 B31G and RSTRENG failure pressure preditions
for the experimental database - Failure ratio

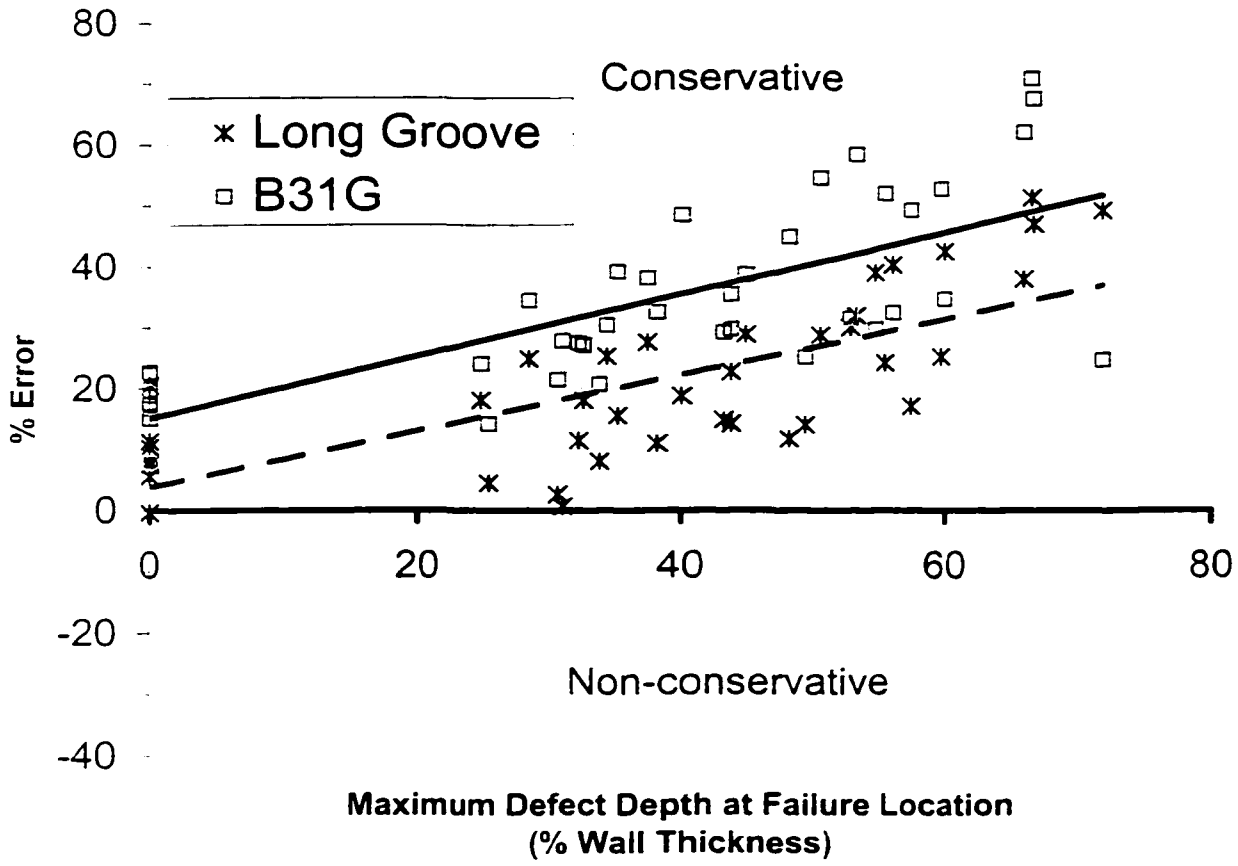


Figure 4.4.5 B31G and Long Groove failure pressure preditions for the experimental database - % Error

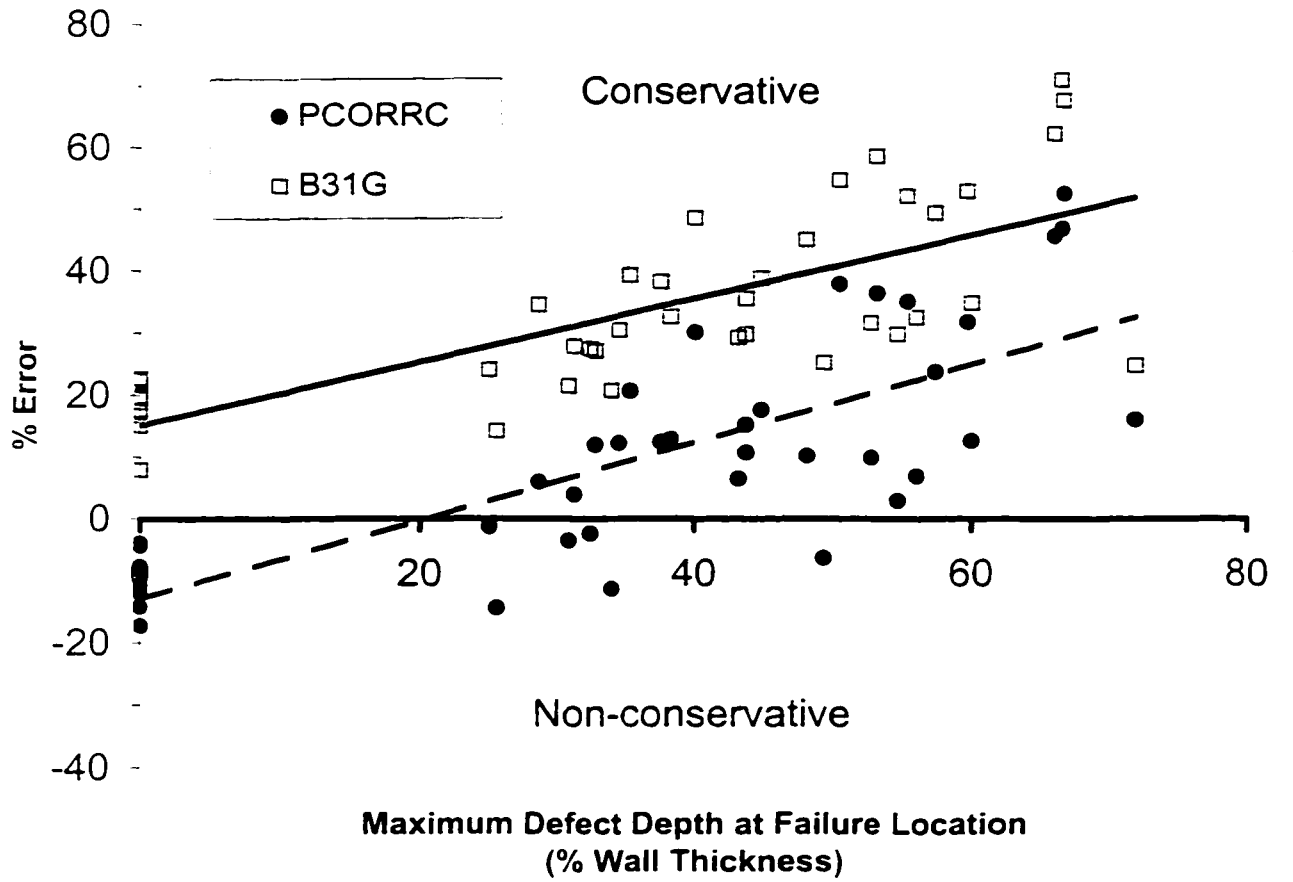


Figure 4.4.6 PCORRC and B31G failure pressure preditions
for the experimental database - % Error

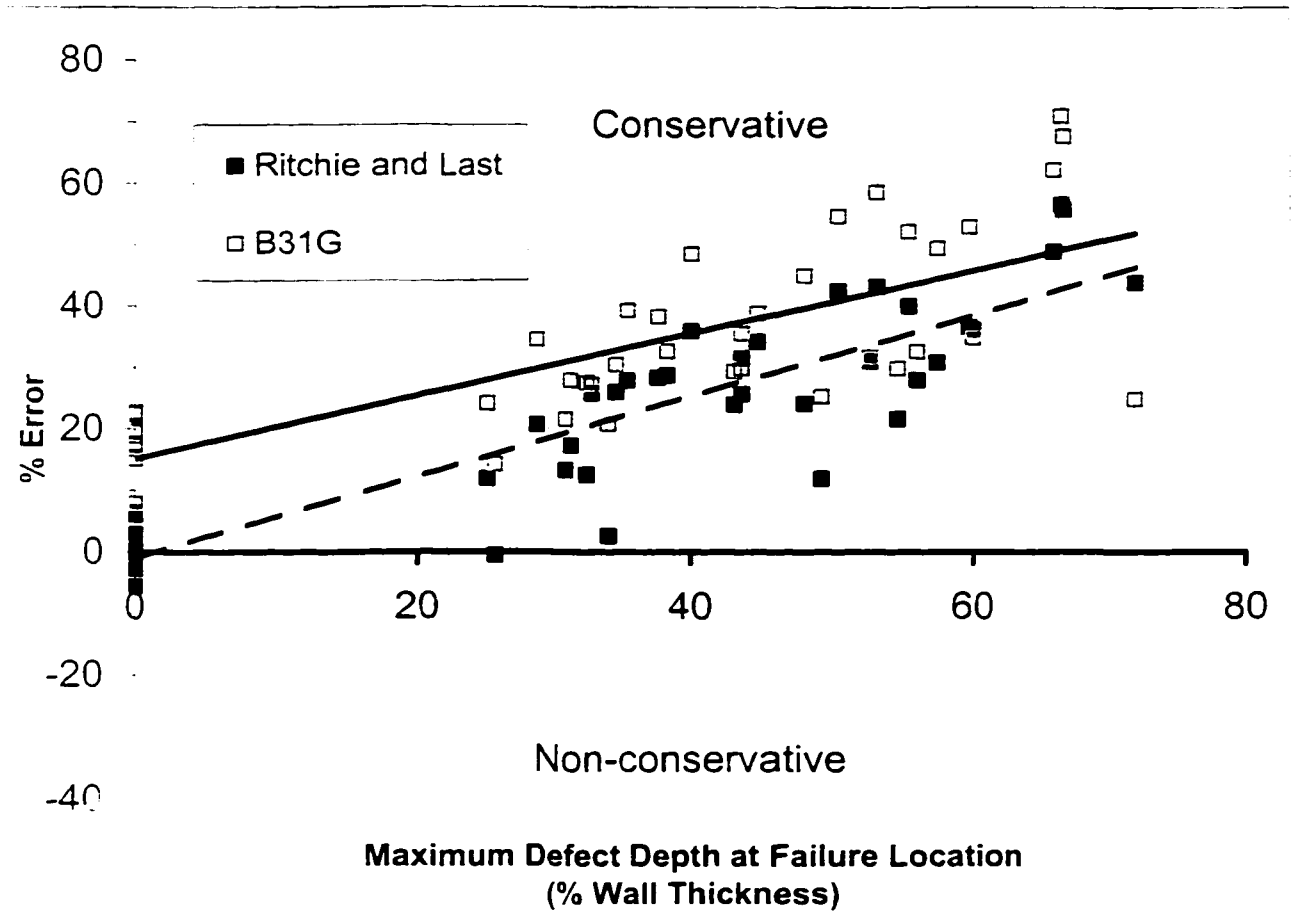


Figure 4.4.7 Ritchie and Last and B31G failure pressure preditions for the experimental database - % Error

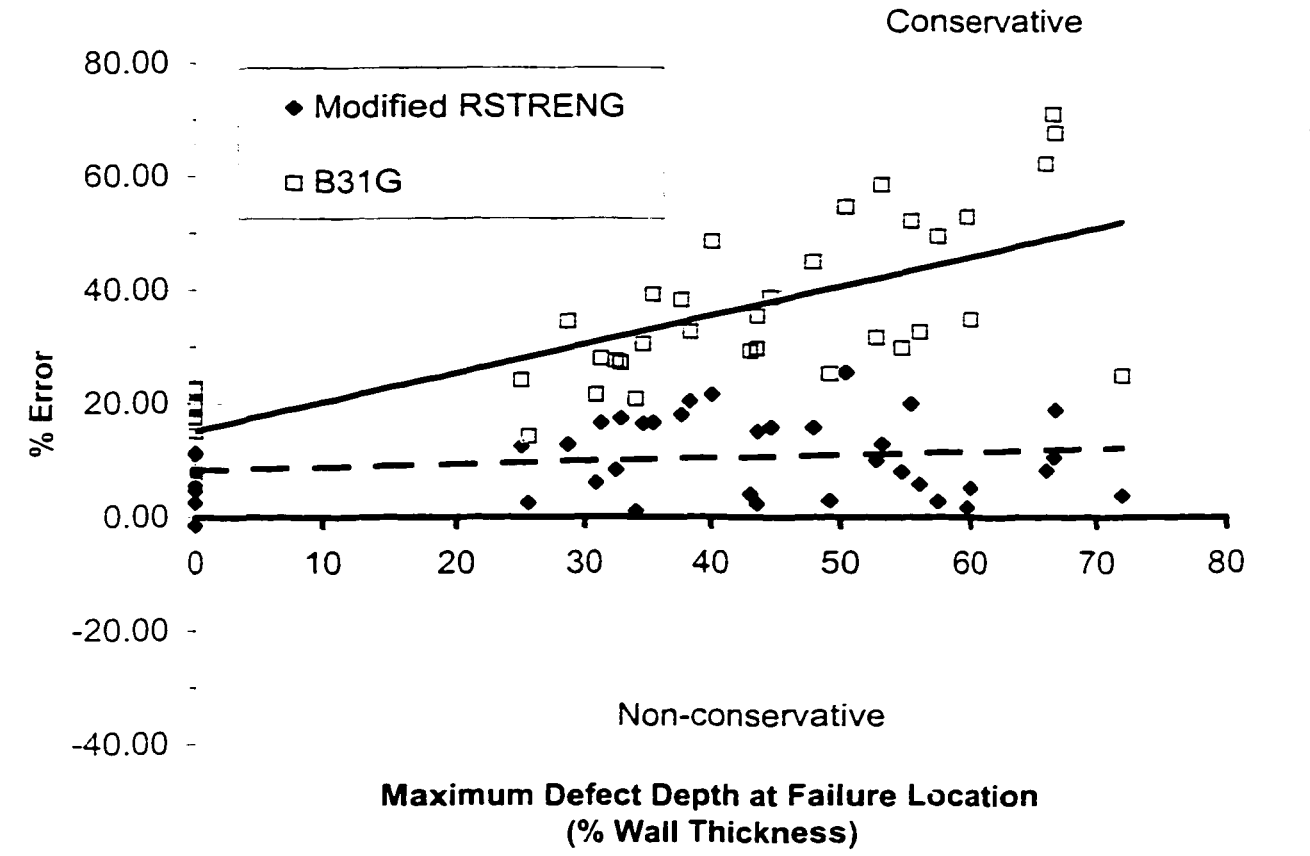


Figure 4.4.8 Modified RSTRENG and B31G failure pressure preditions for the experimental database - % Error

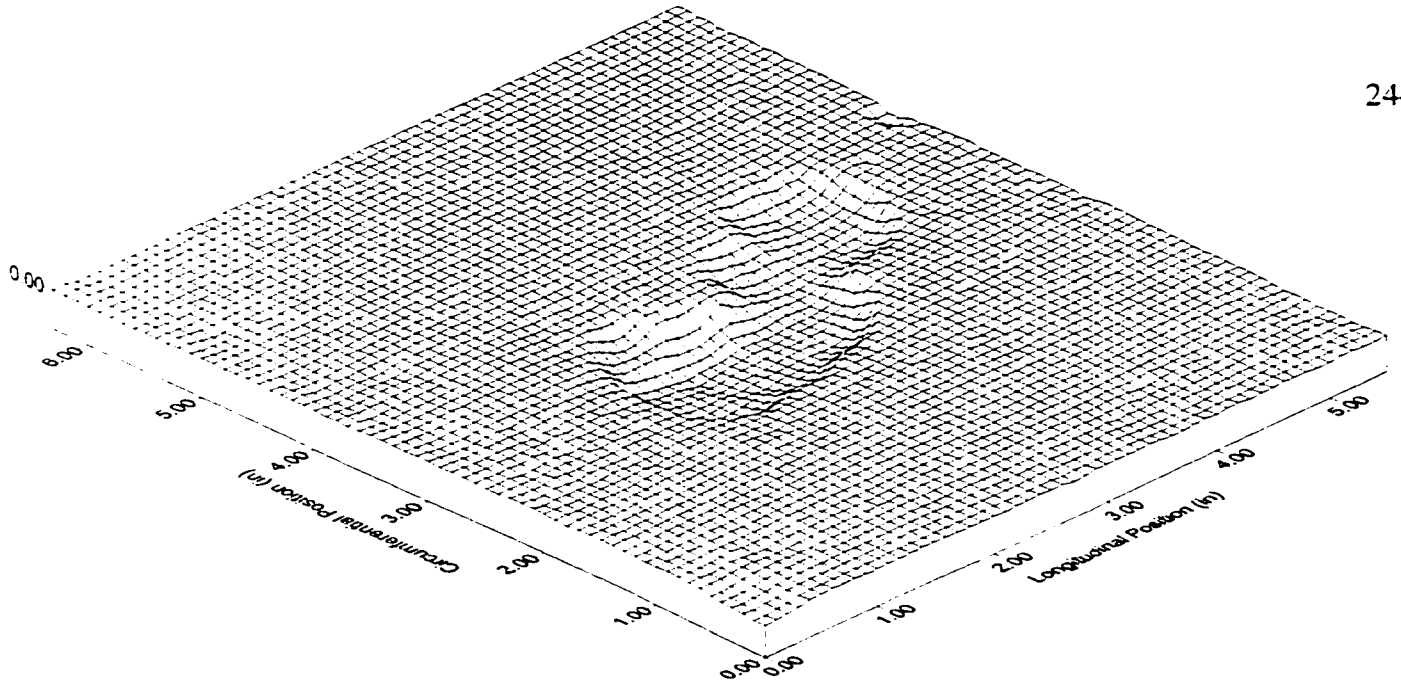


Figure 4.5.1a Scanned surface data

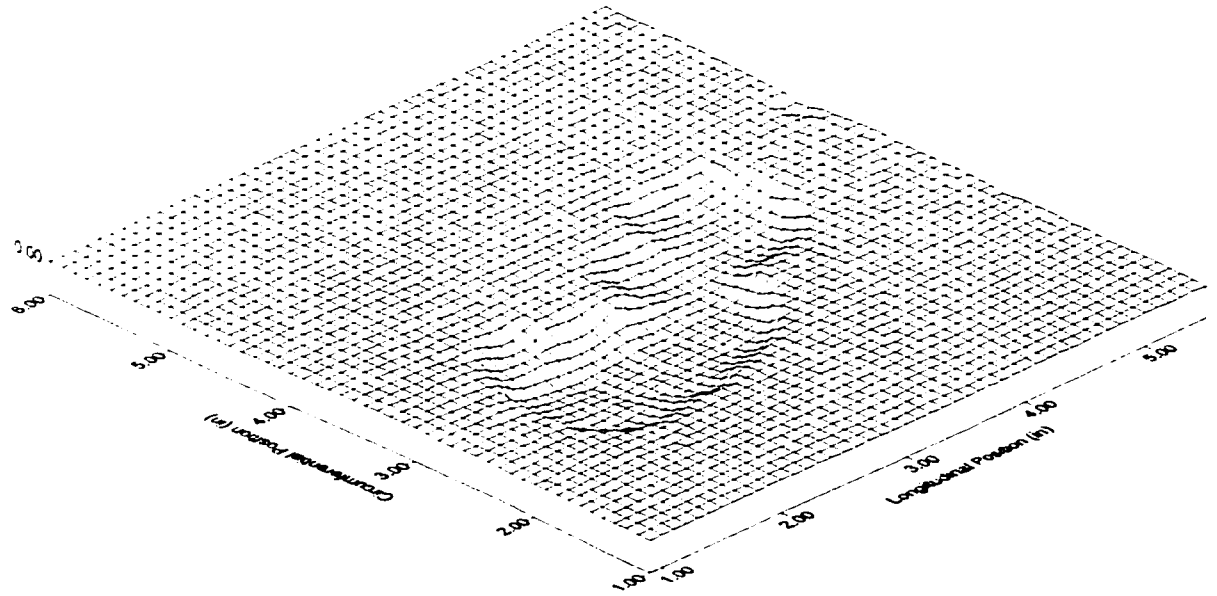


Figure 4.5.1b Surface grid file data

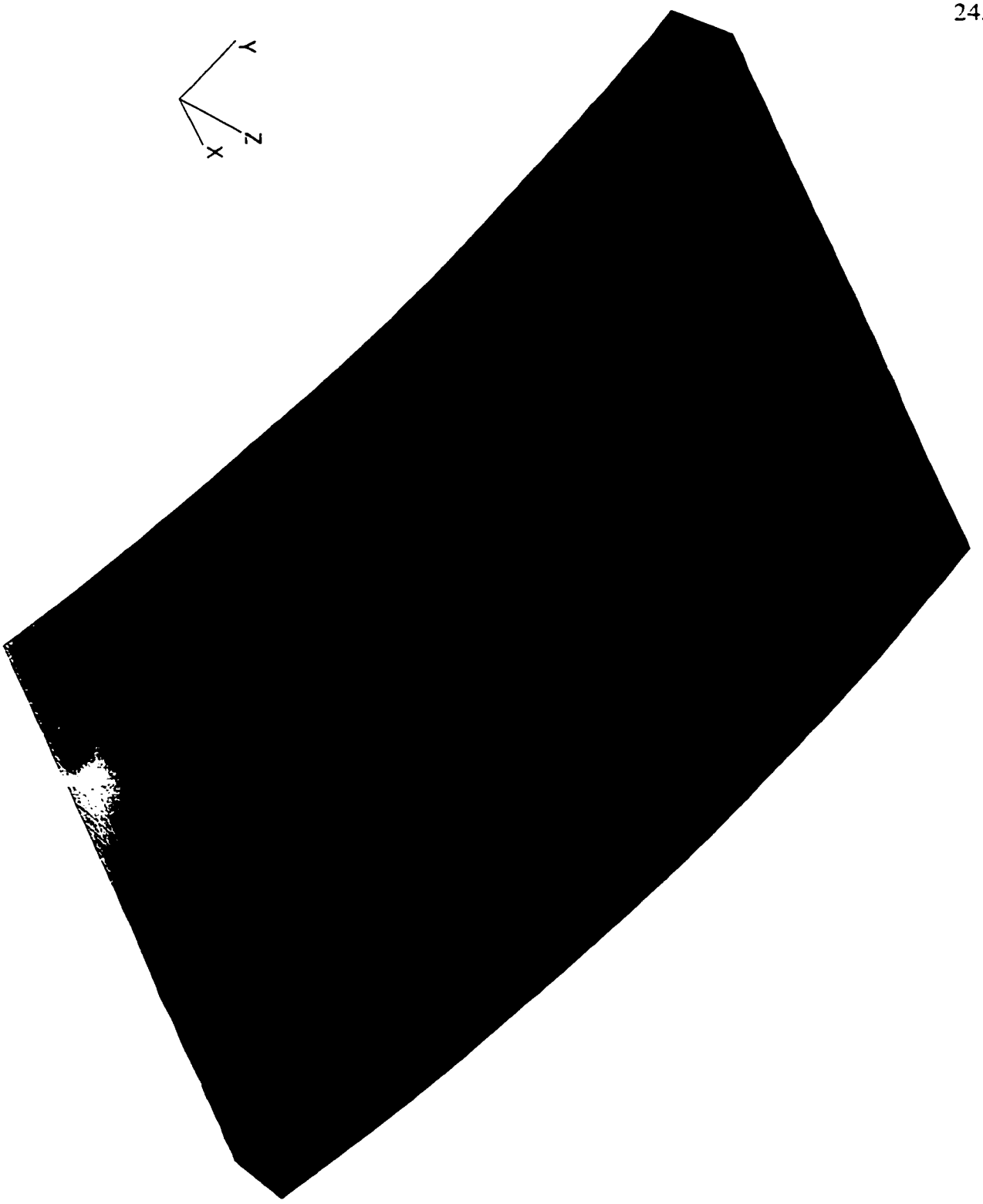


Figure 4.5.1c Local finite element mesh at the defect

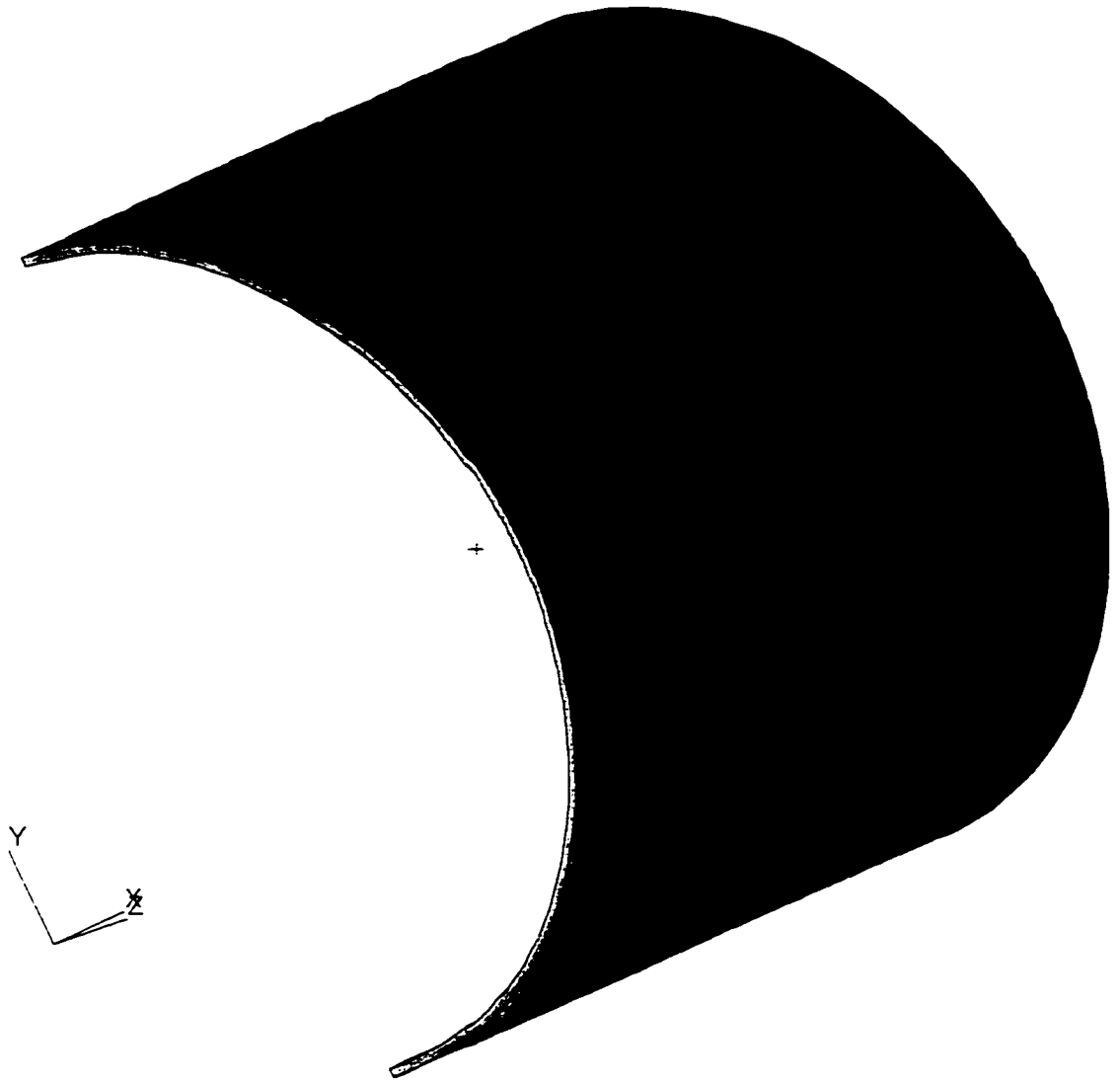


Figure 4.5.1d Global finite element mesh showing model extent

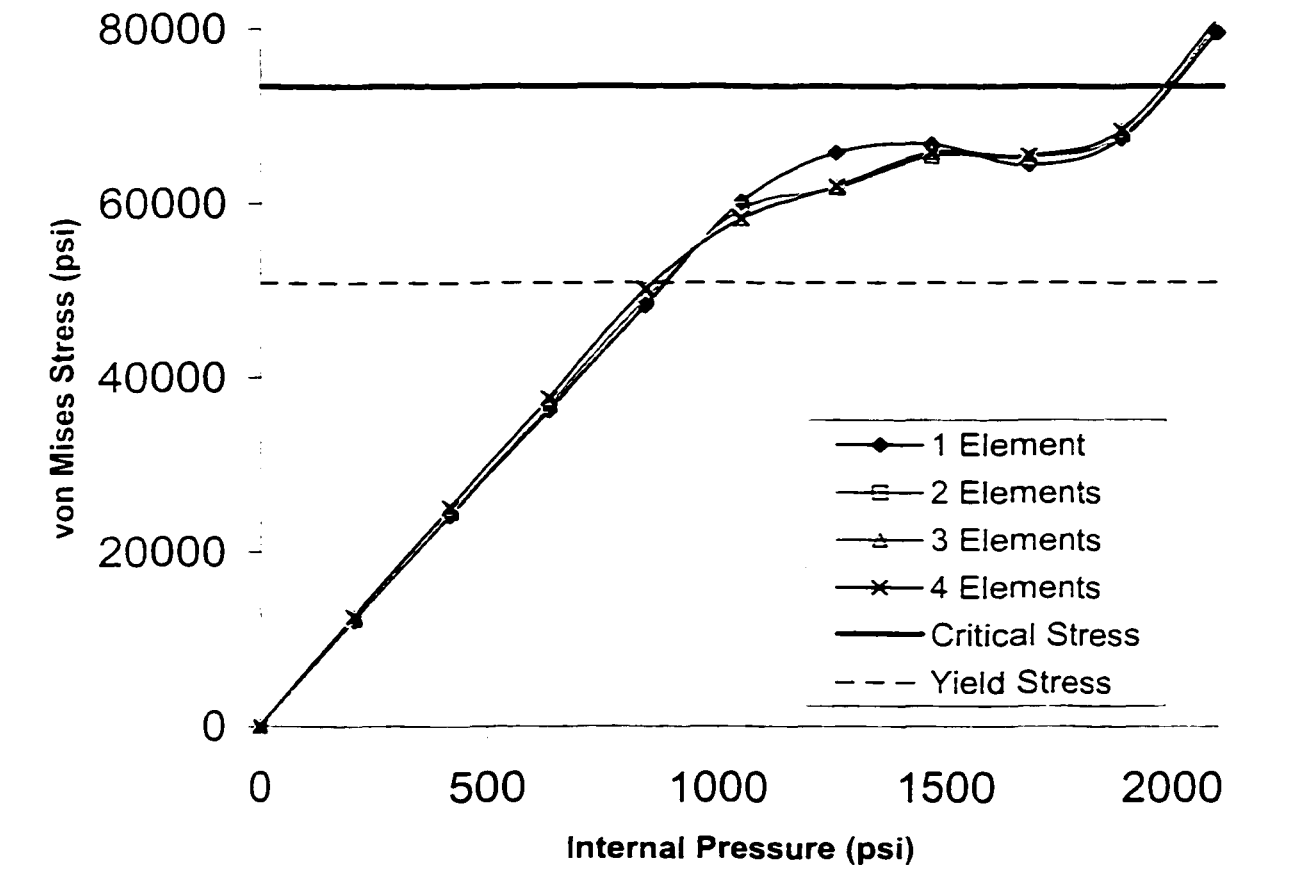


Figure 4.5.2 von Mises stress history for a varying number of elements through the thickness

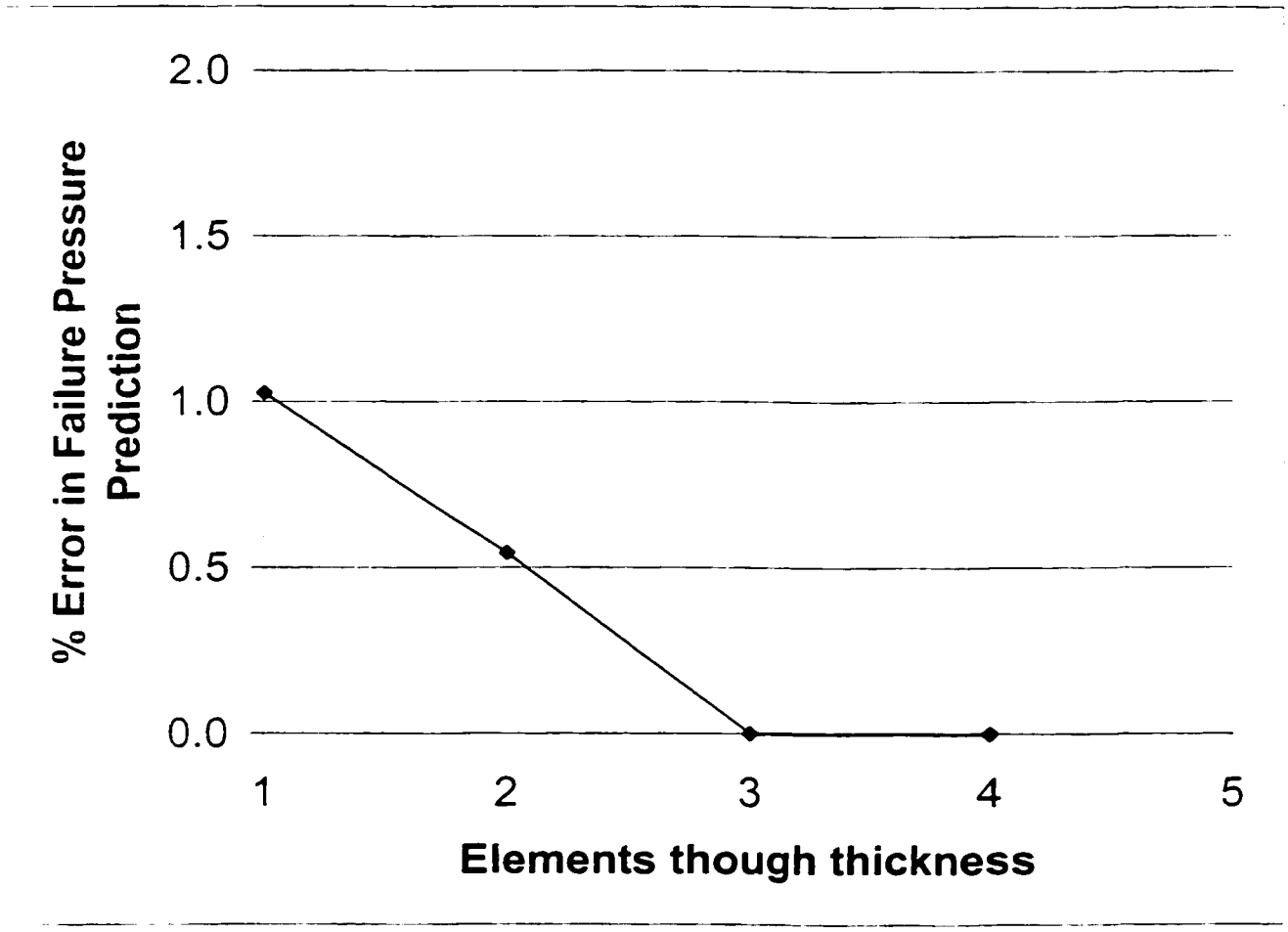


Figure 4.5.3 Percent error in the failure prediction as a function of the number of elements through the thickness

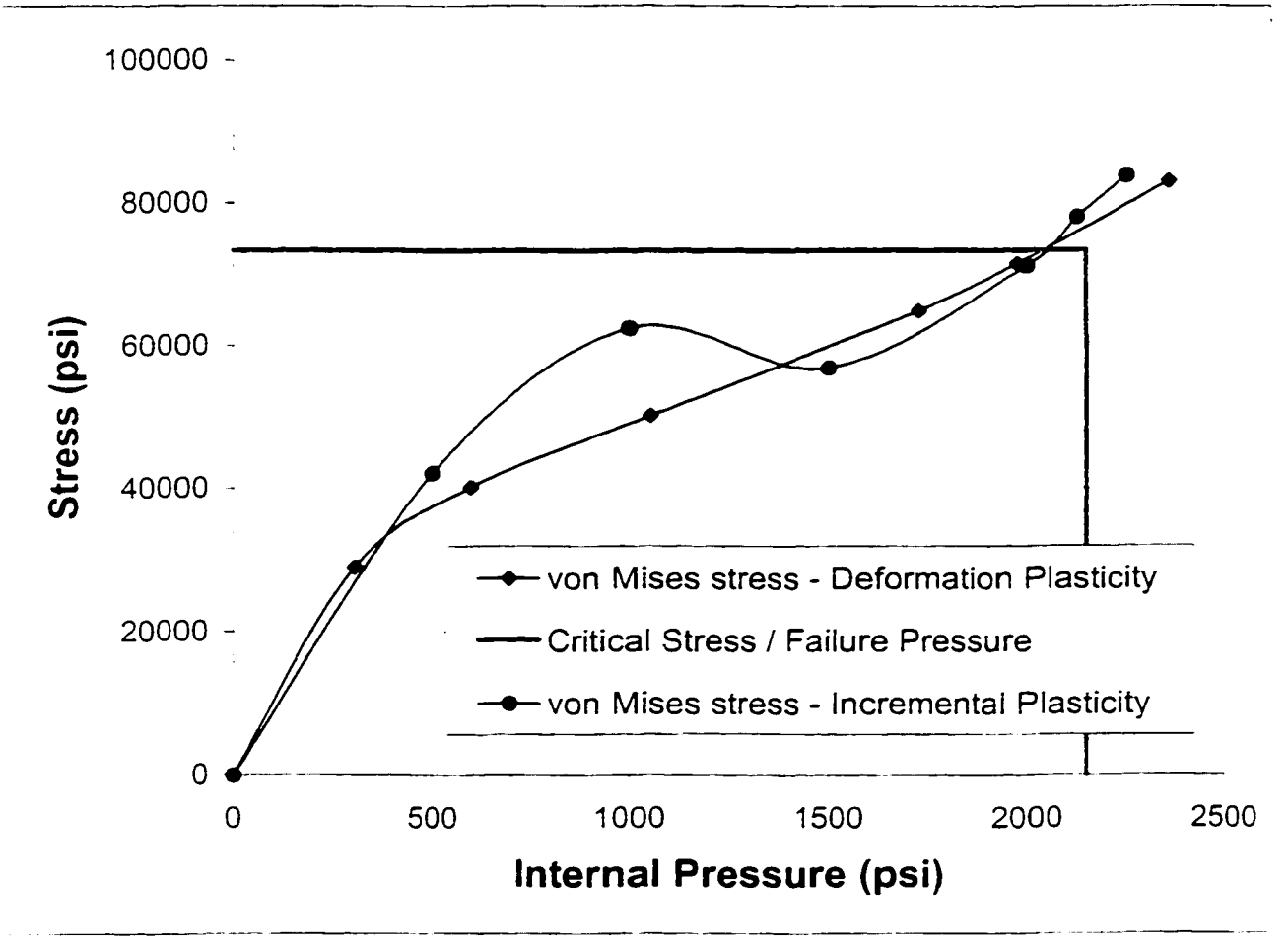


Figure 4.5.4 Analysis of defect BCG-08E using incremental and deformation plasticity material models

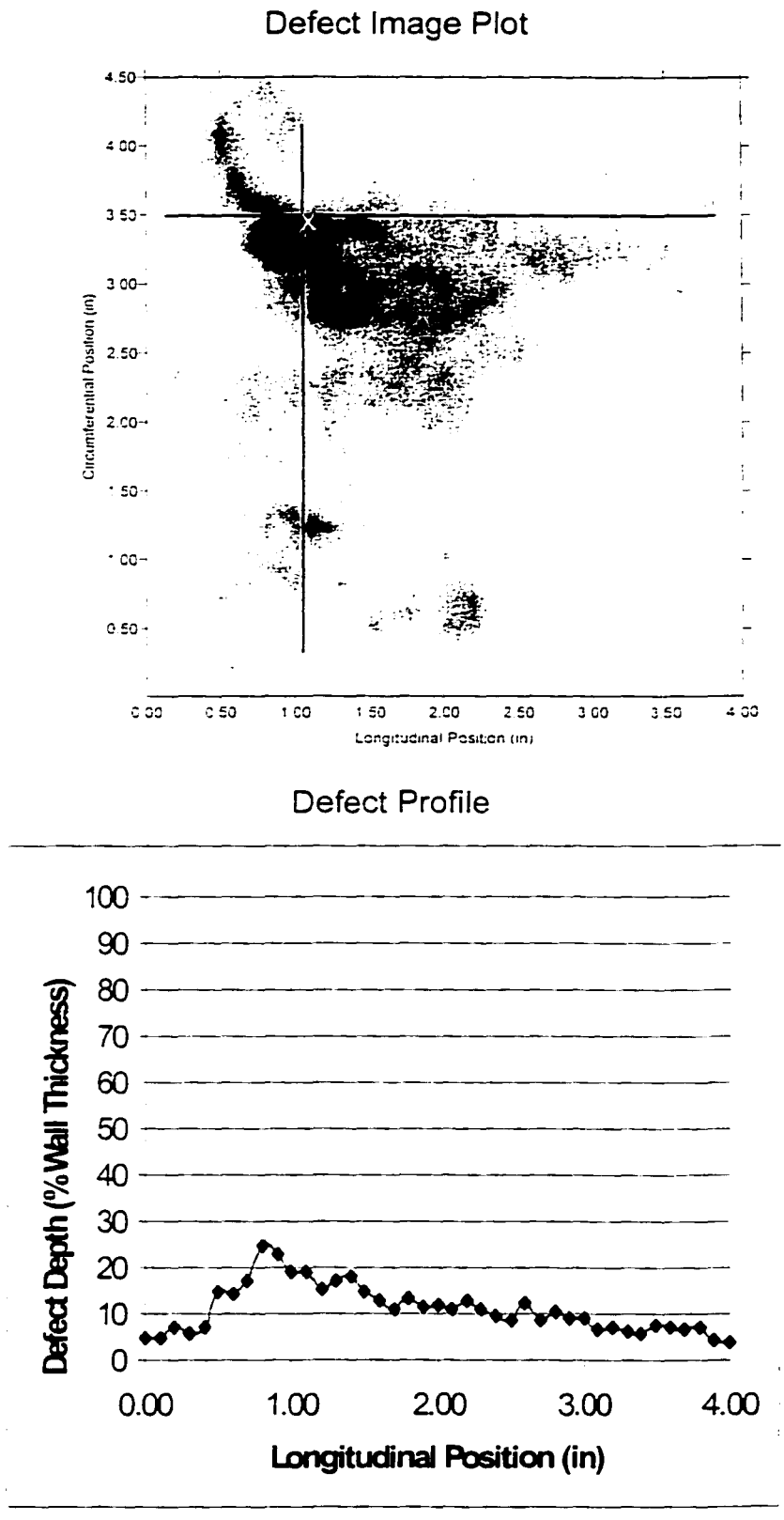
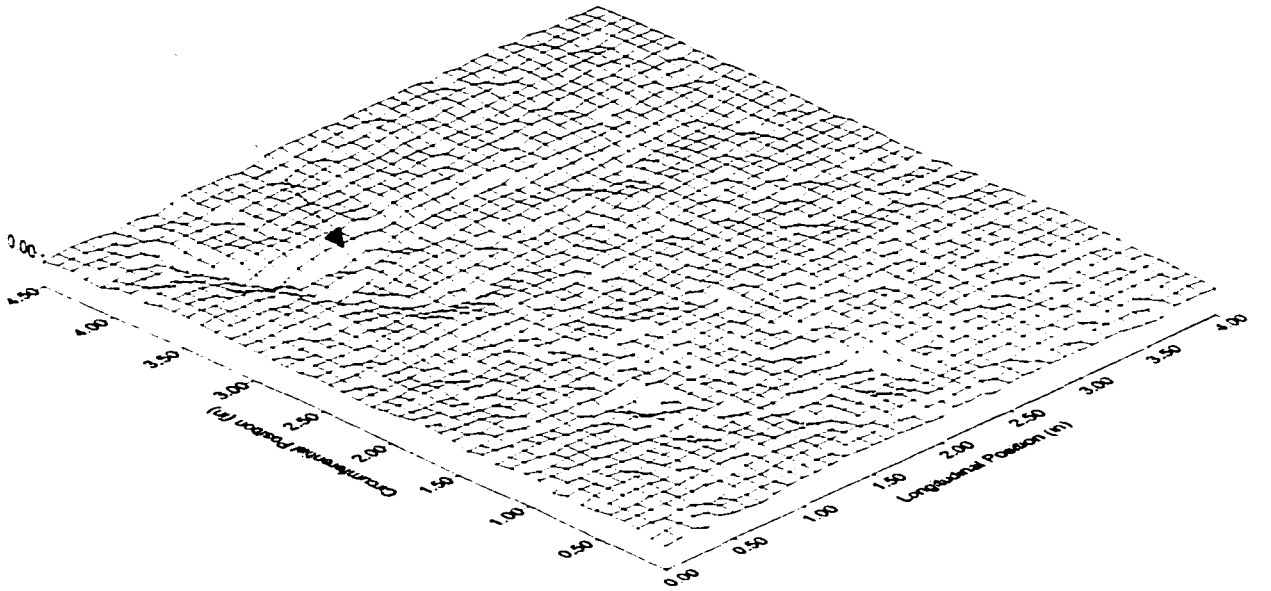
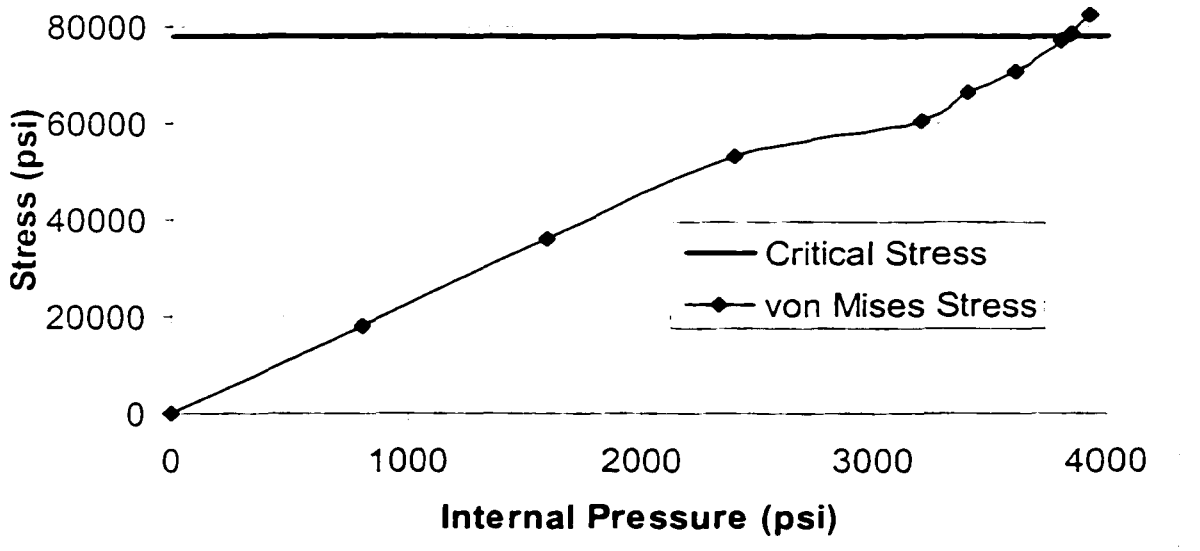


Figure 4.5.5a Burst test SOL02

Actual/Predicted Failure Location

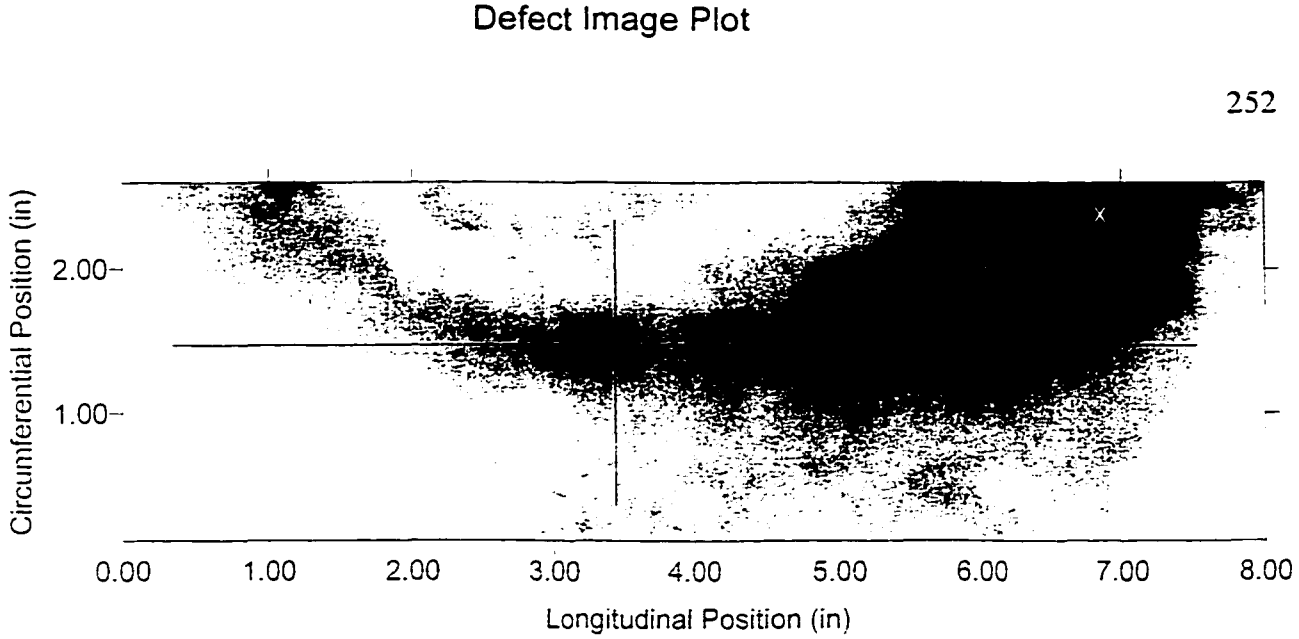


von Mises Stress vs. Internal Pressure at the Failure Location



Predicted Failure Pressure = 3832 psi
Actual Failure Pressure = 3535 psi

Figure 4.5.5b Burst test SOL02



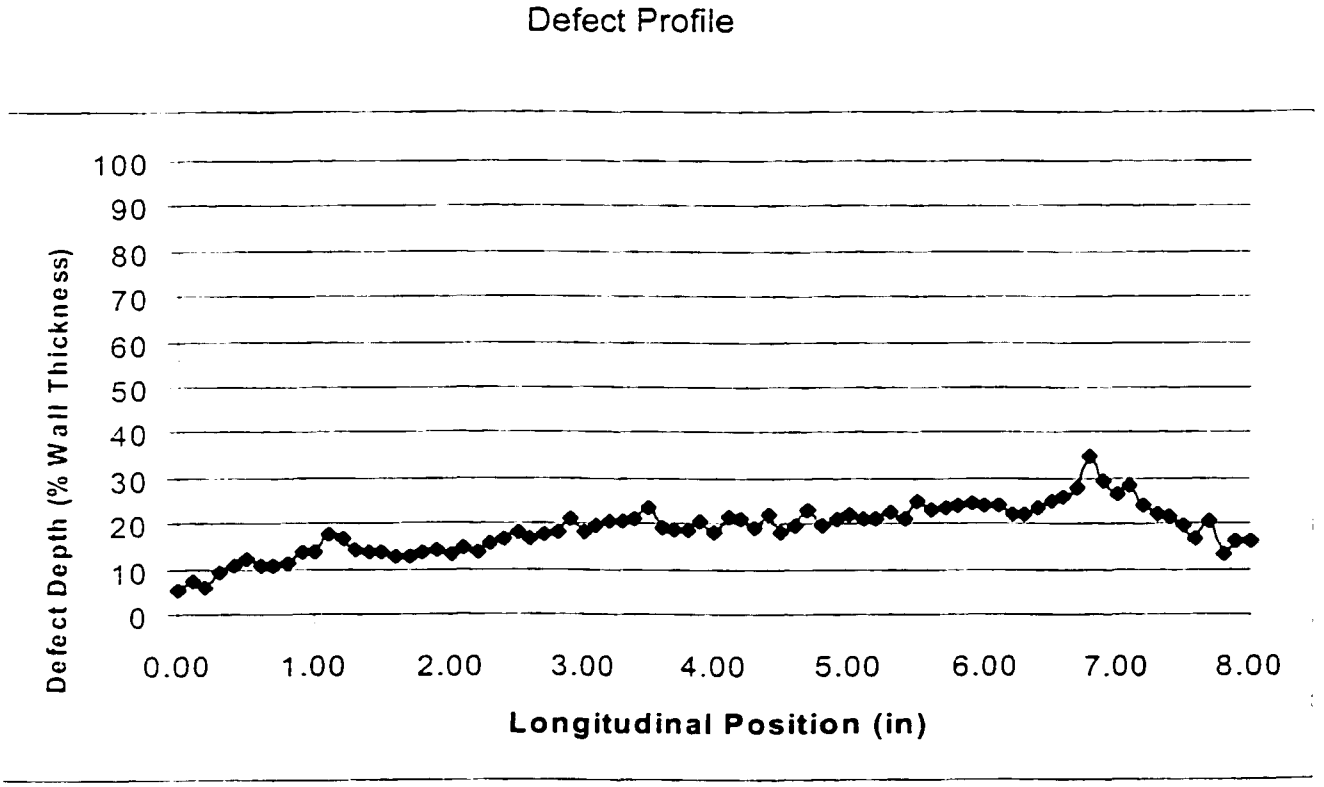
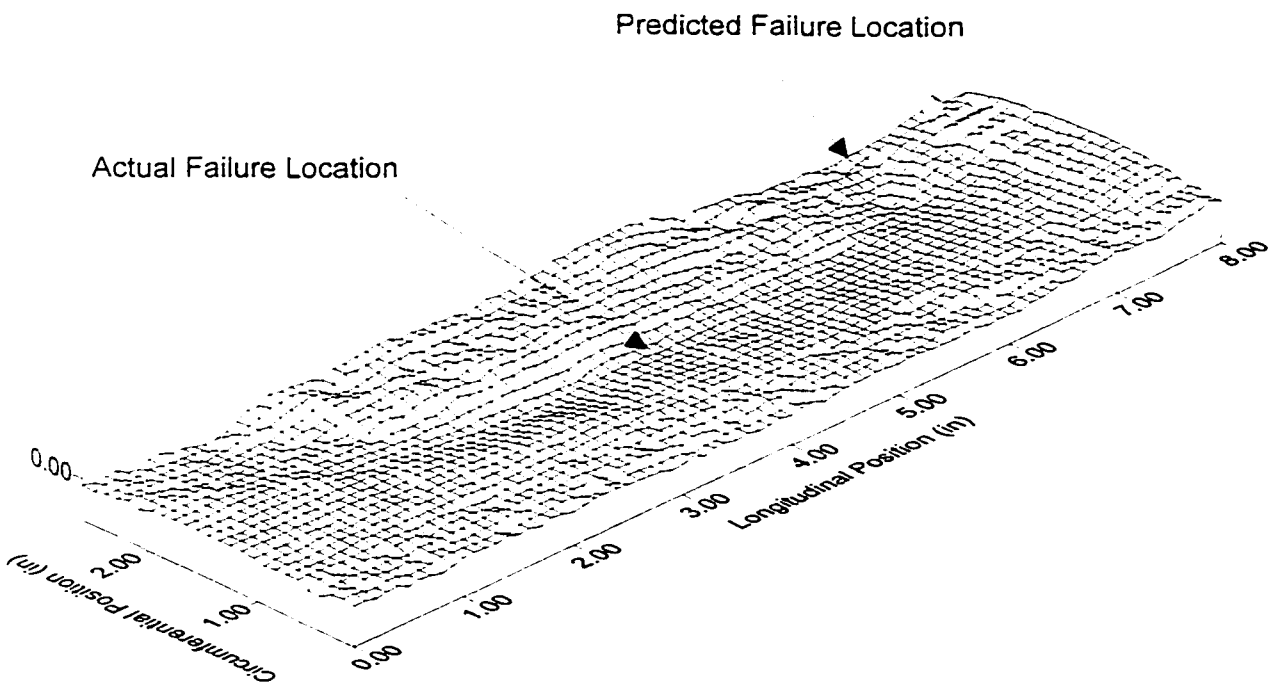
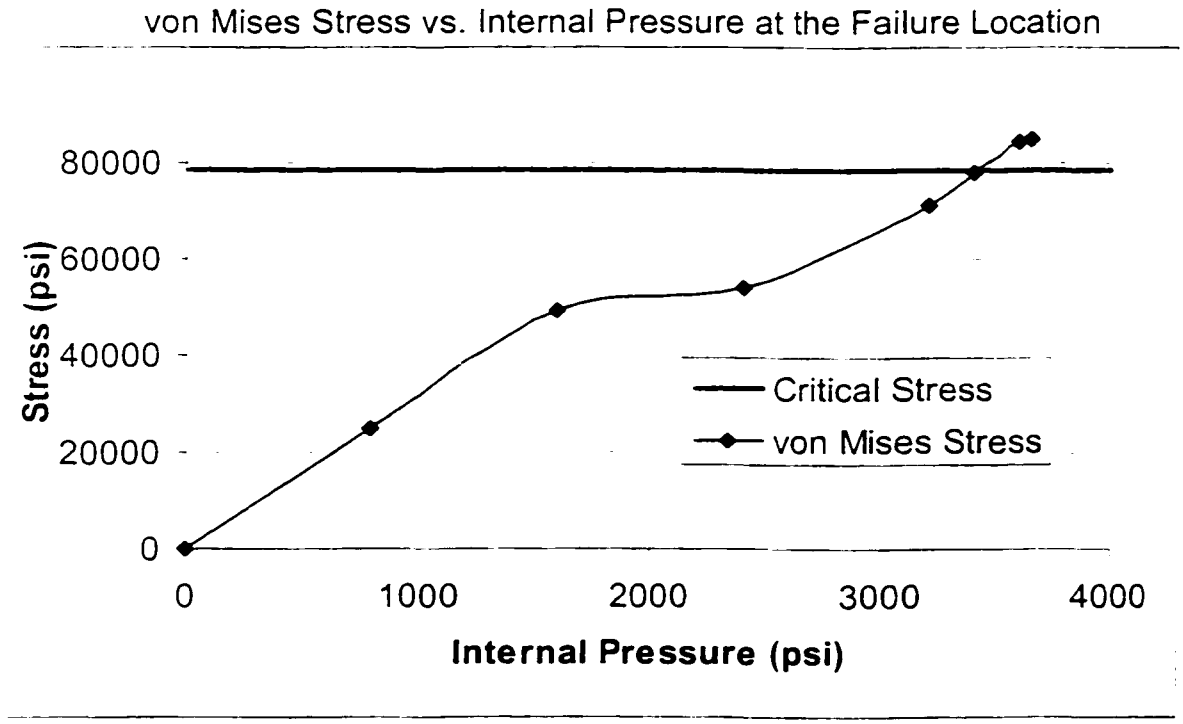


Figure 4.5.6a Burst test SOL04





Predicted Failure Pressure = 3419 psi
Actual Failure Pressure = 3351 psi

Figure 4.5.6b Burst test SOL04

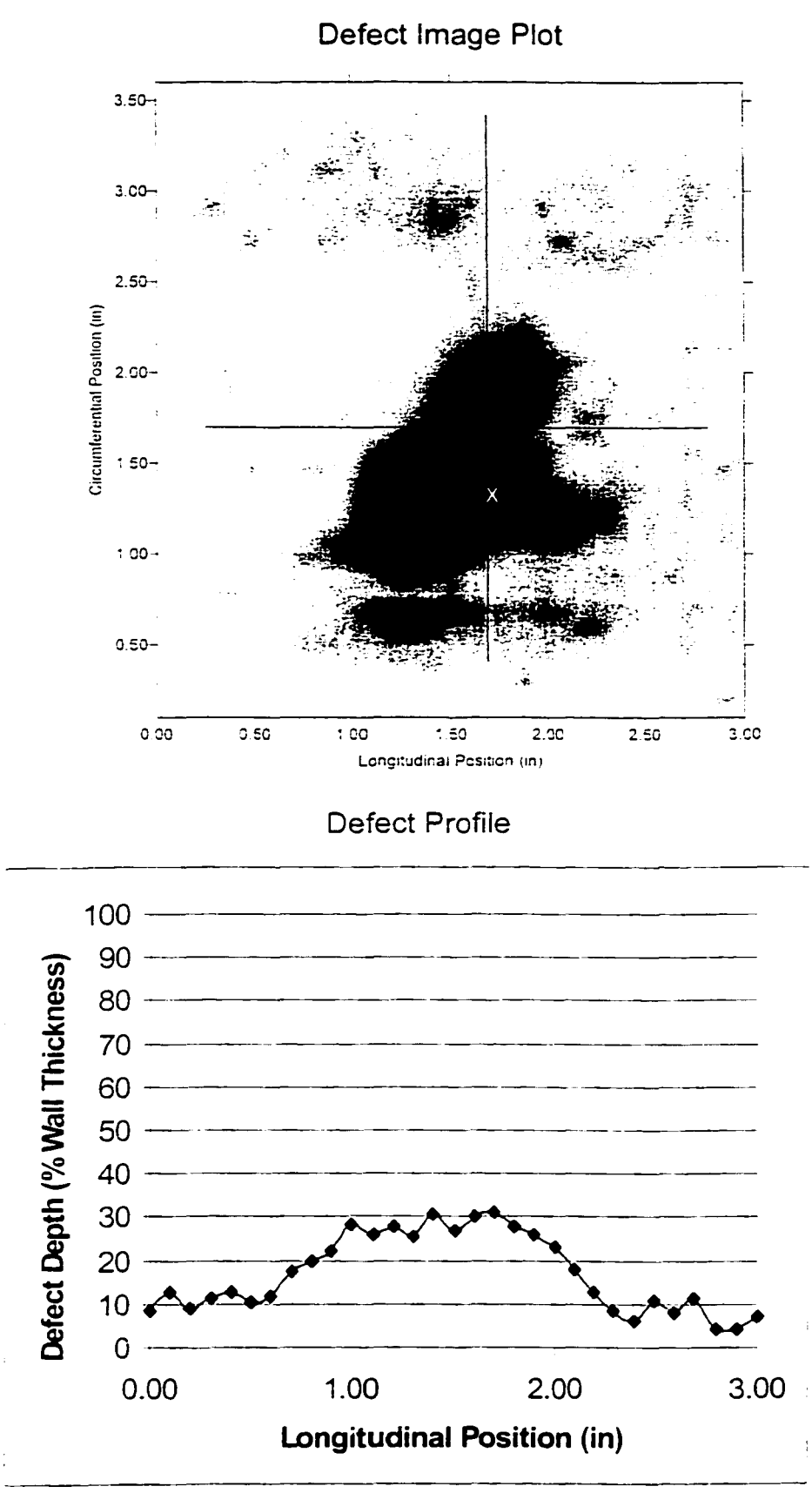
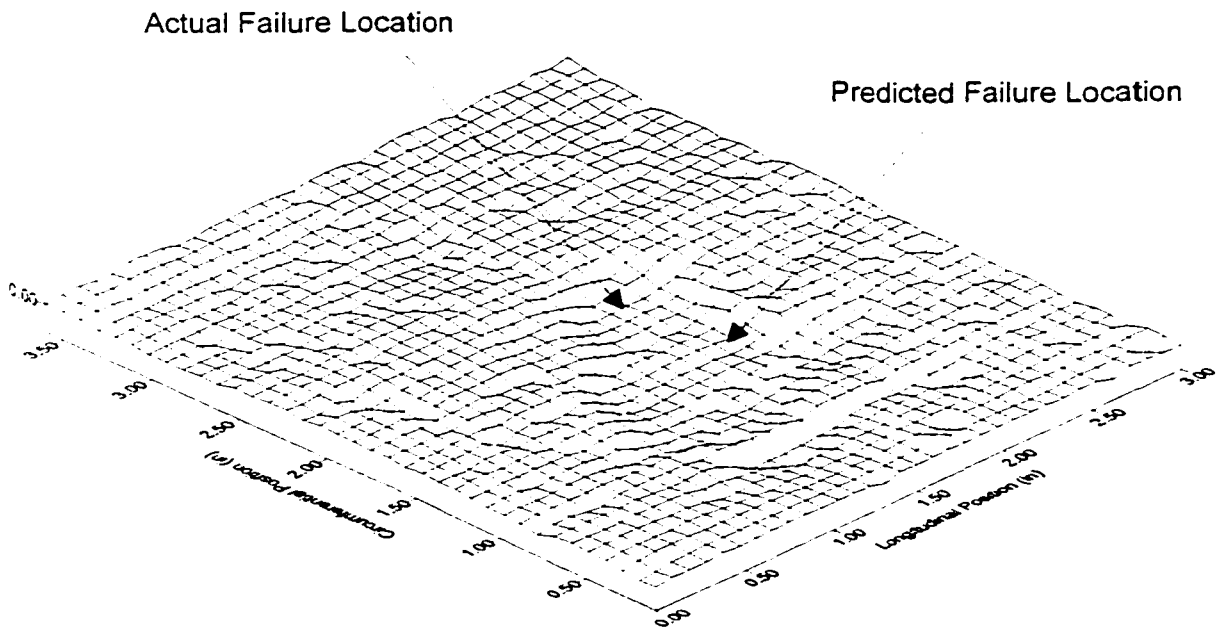


Figure 4.5.7a Burst test SOL06



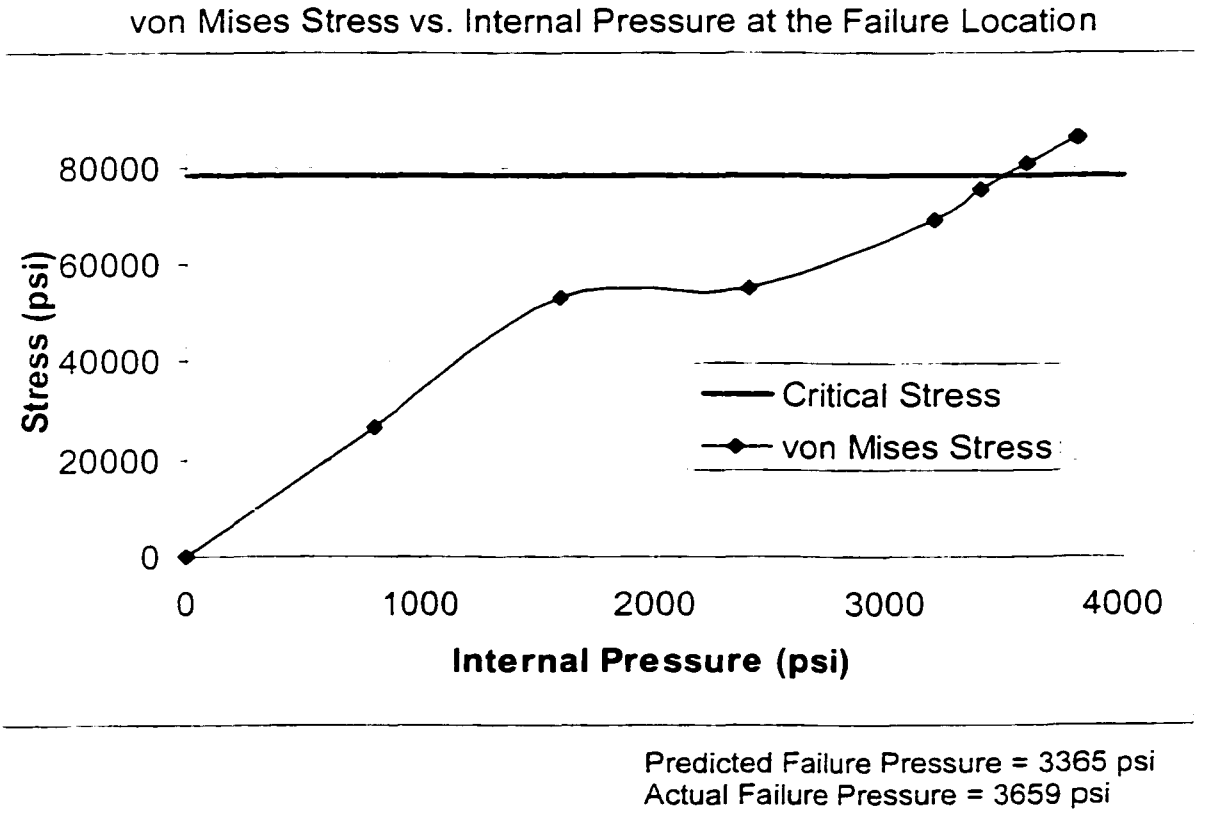
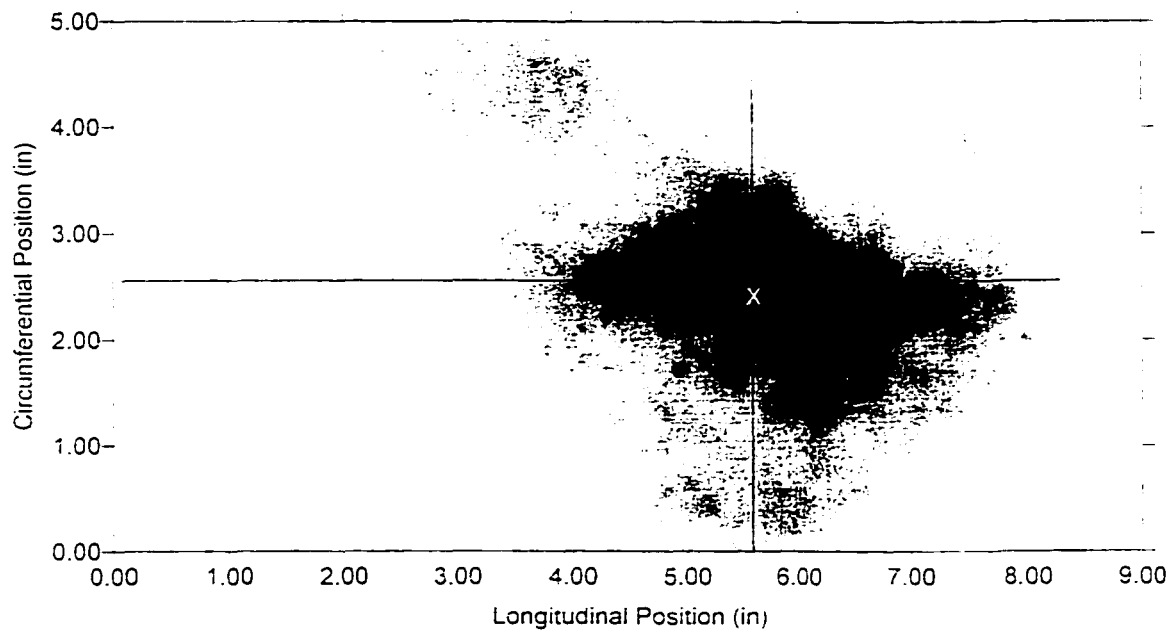


Figure 4.5.7b Burst test SOL06



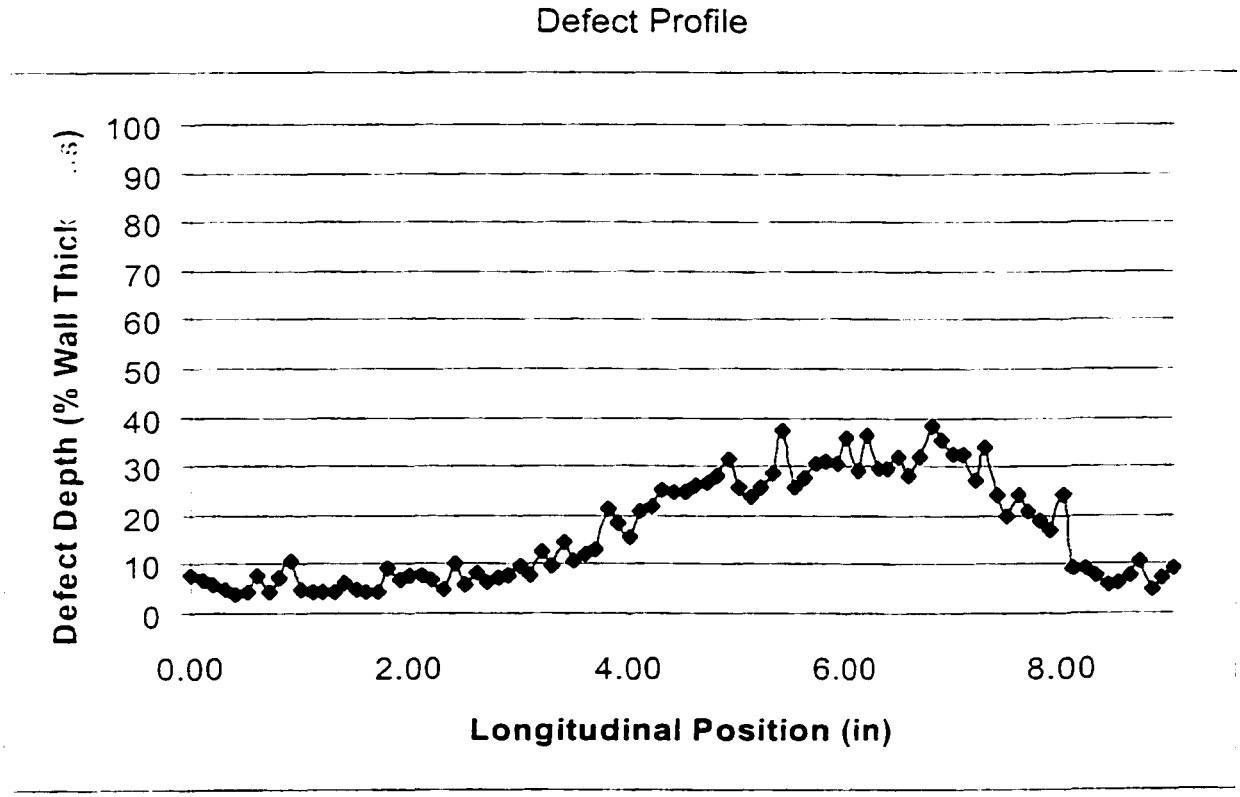


Figure 4.5.8a Burst test SOL10

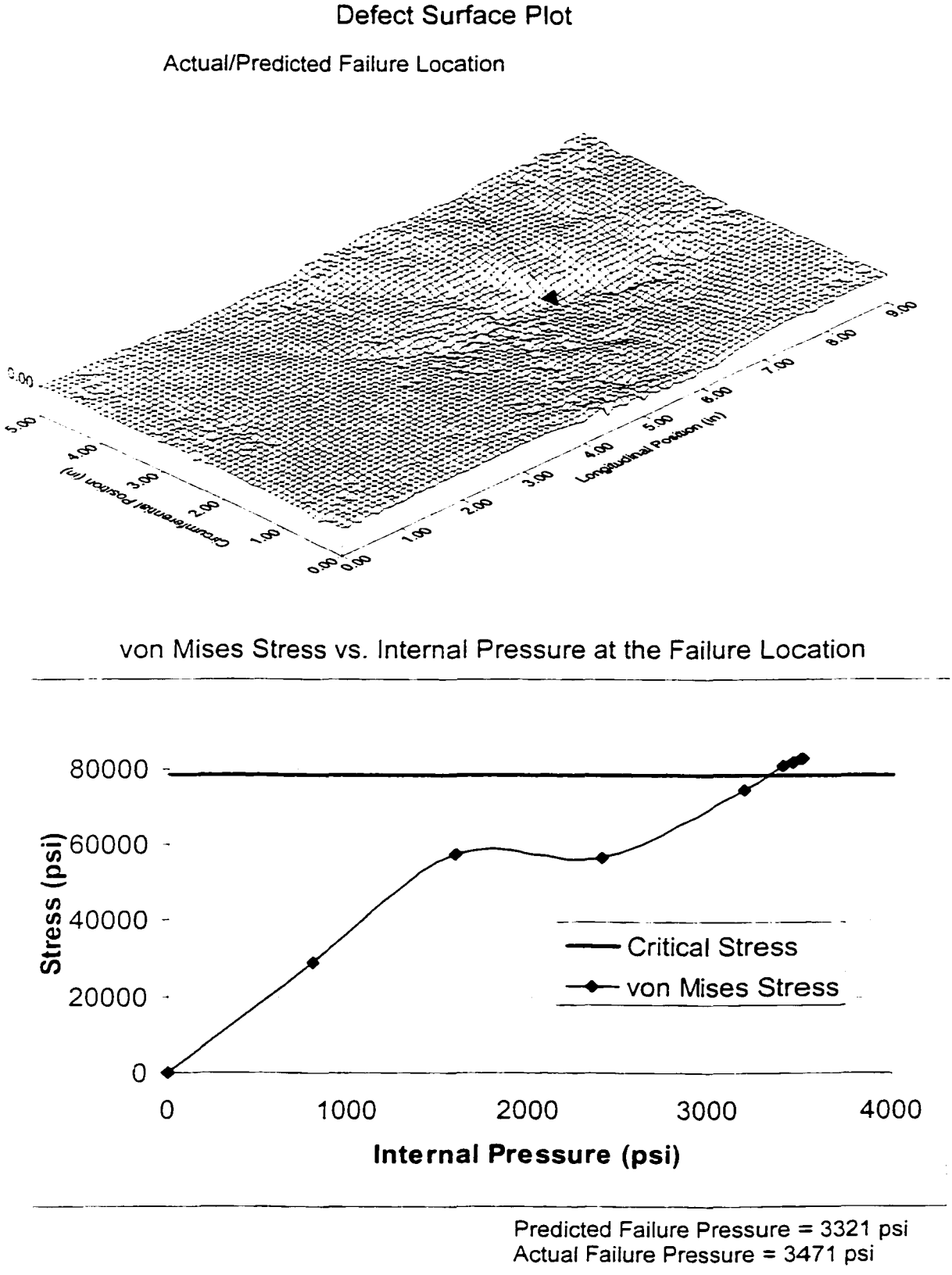
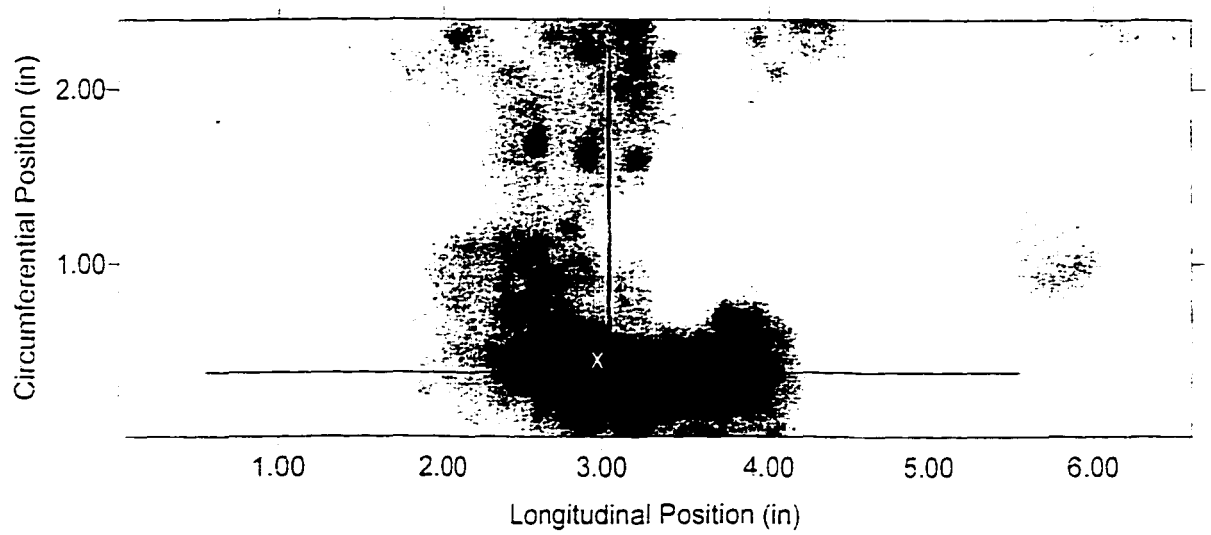


Figure 4.5.8b Burst test SOL10



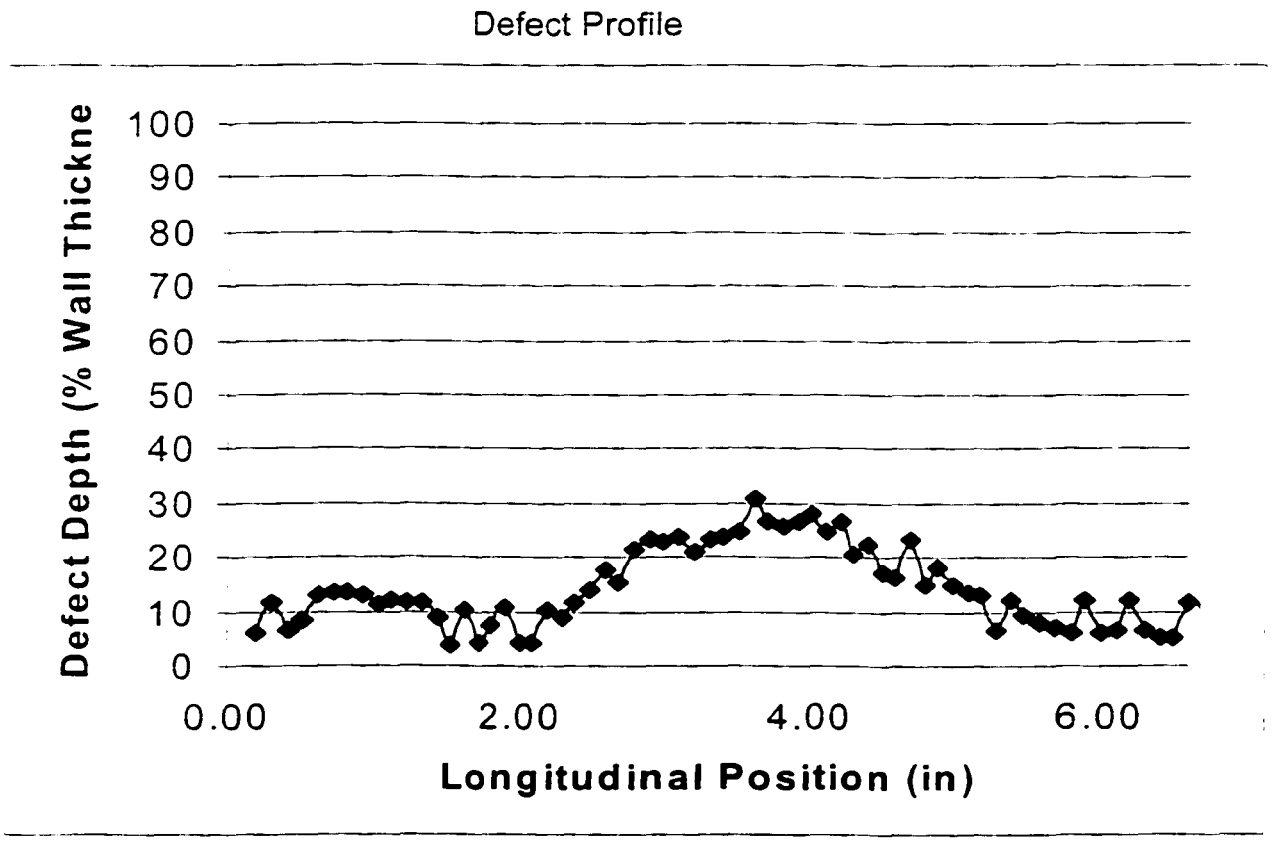


Figure 4.5.9a Burst test SOL11

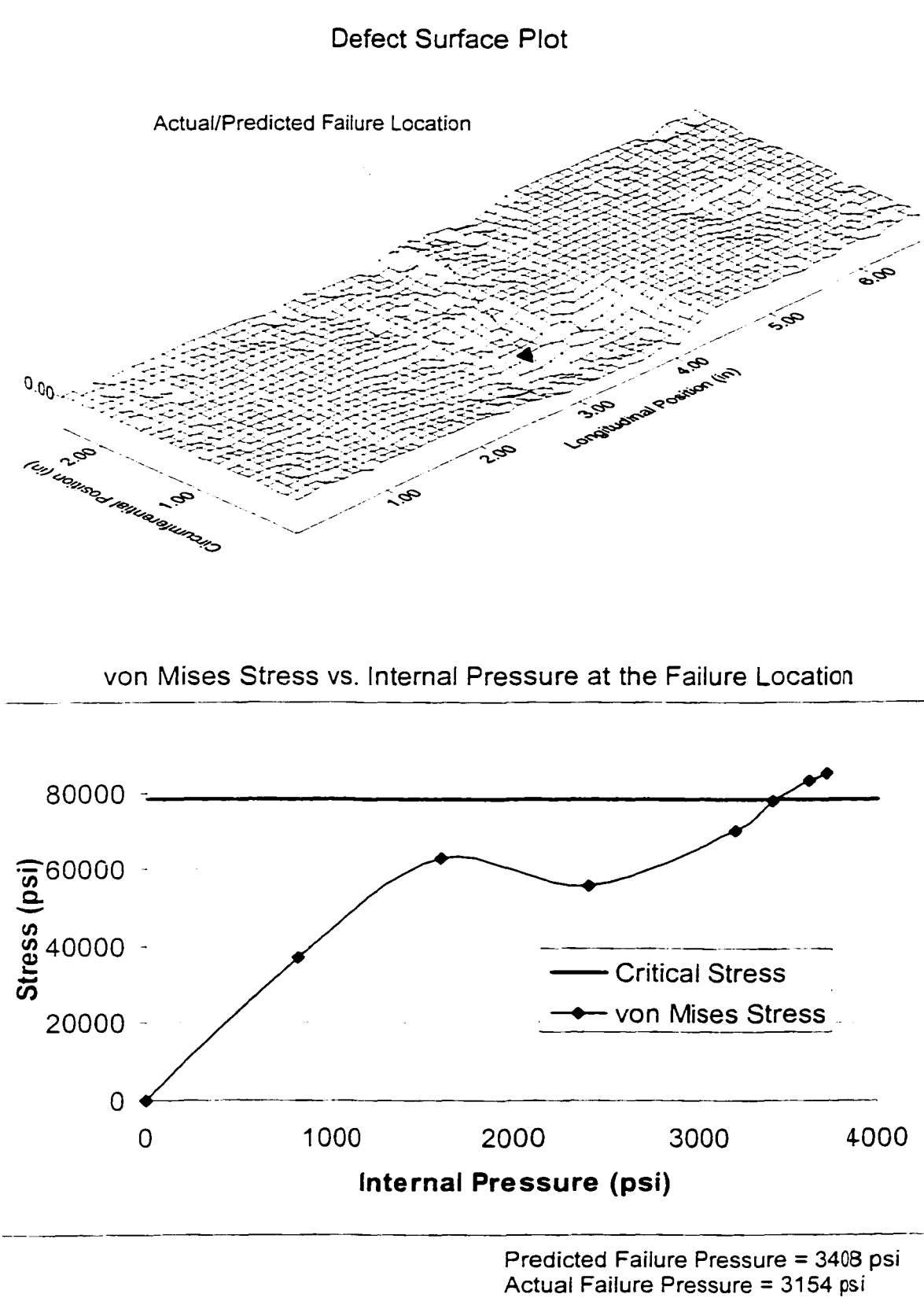
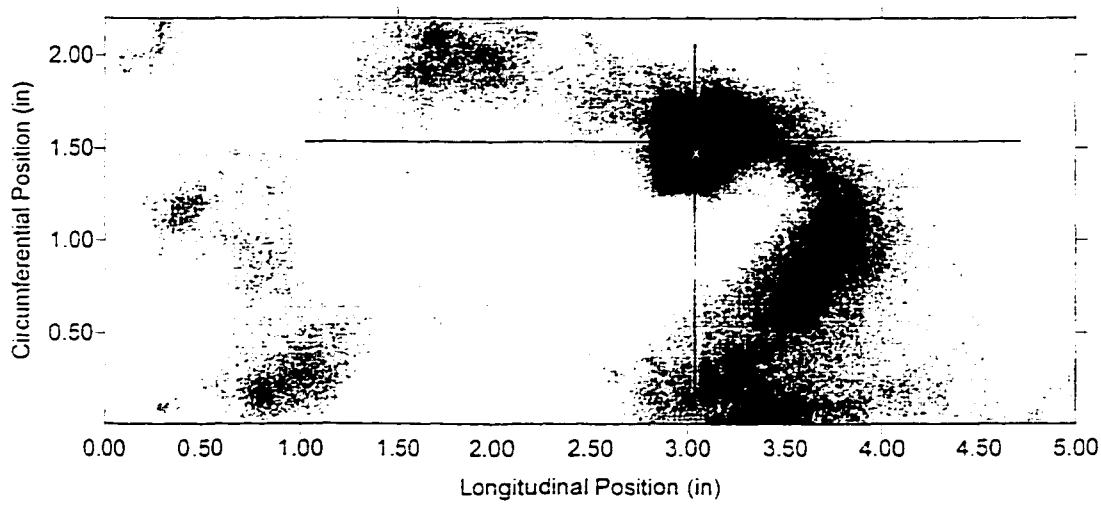


Figure 4.5.9b Burst test SOL11



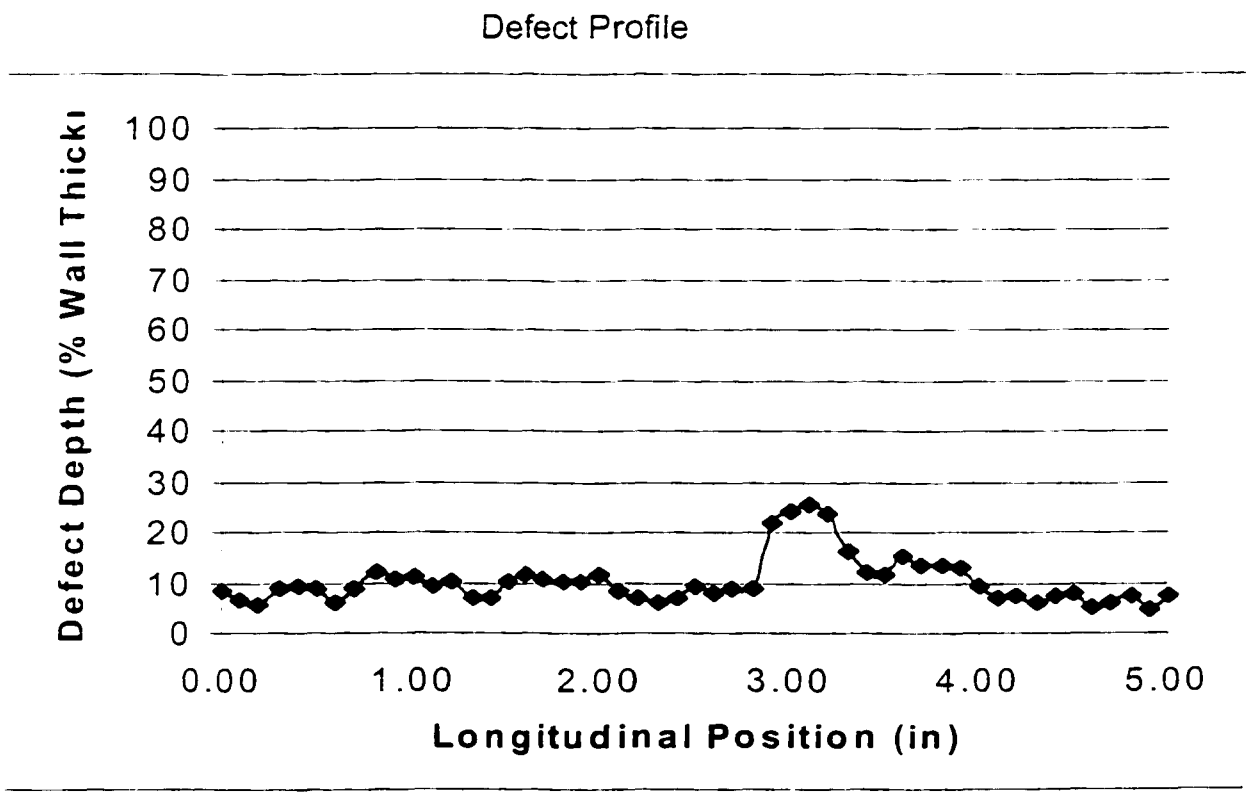


Figure 4.5.10a Burst test SOL12

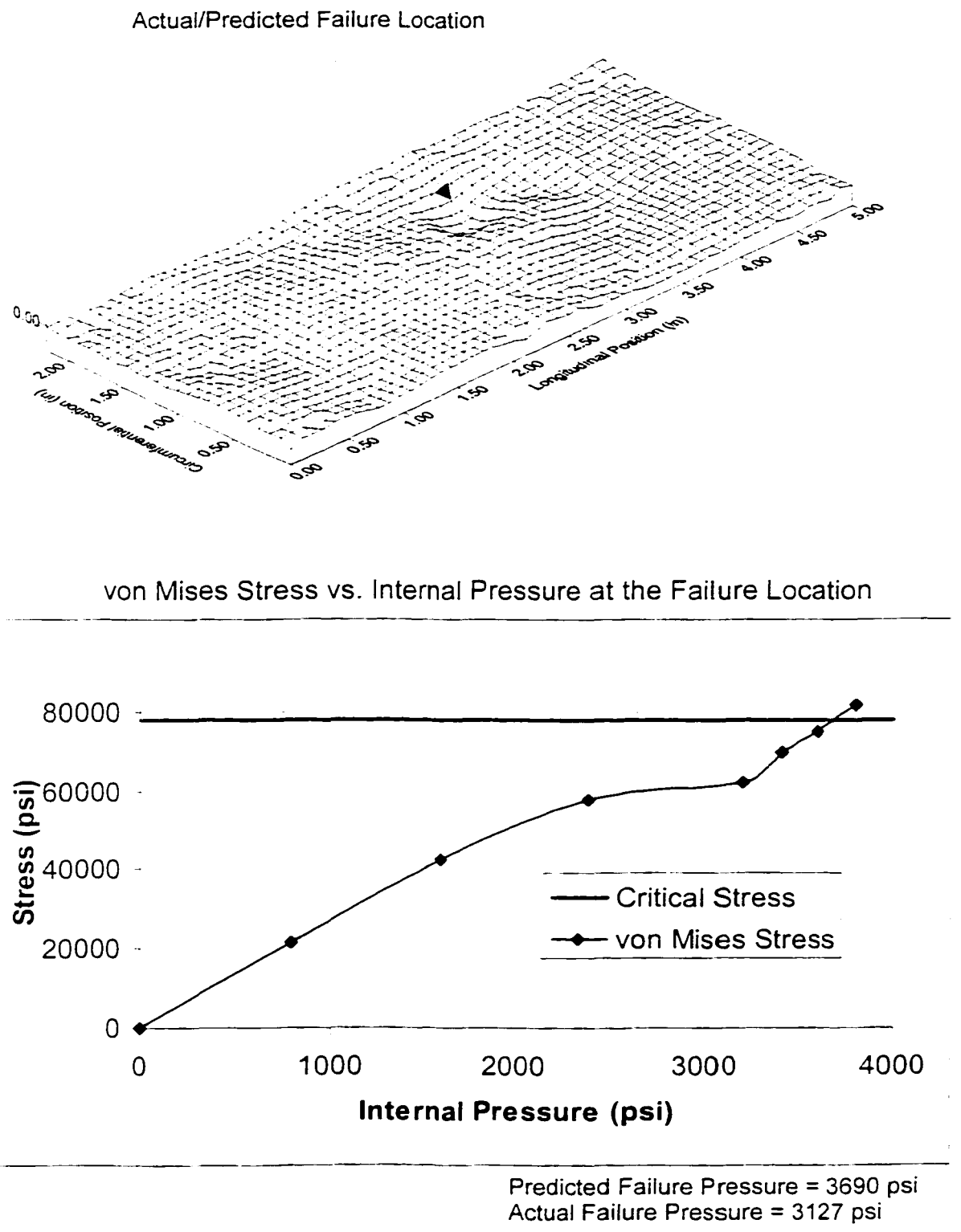


Figure 4.5.10b Burst test SOL12

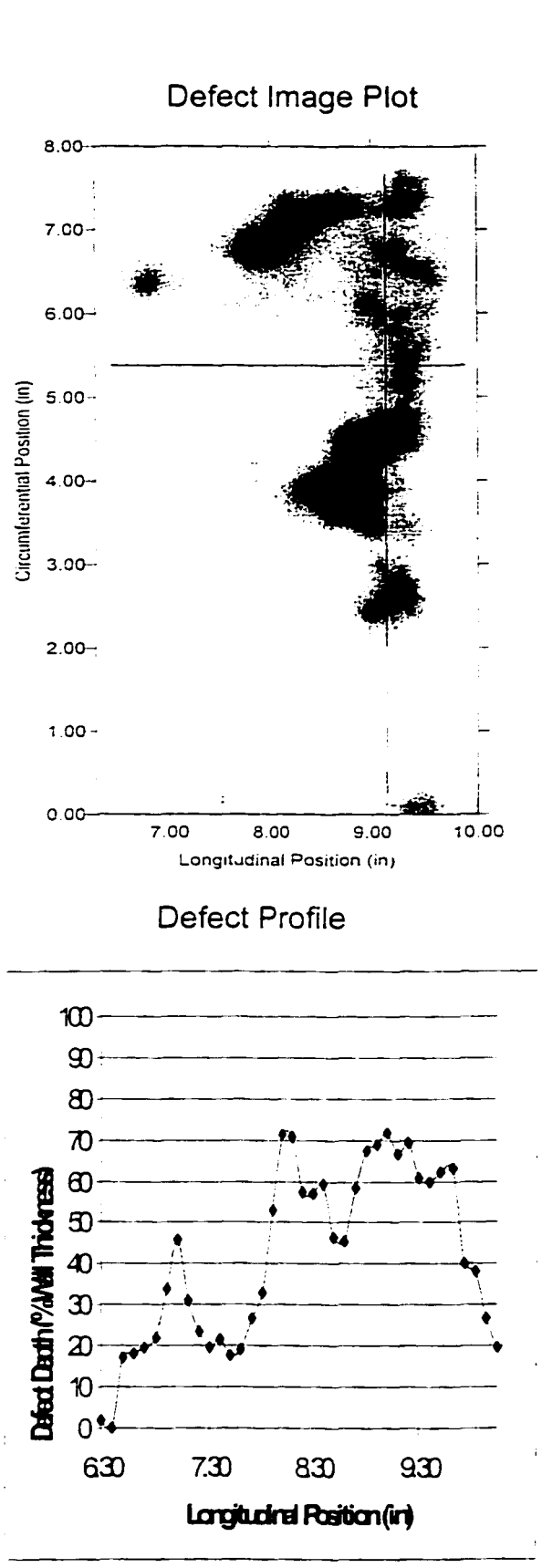
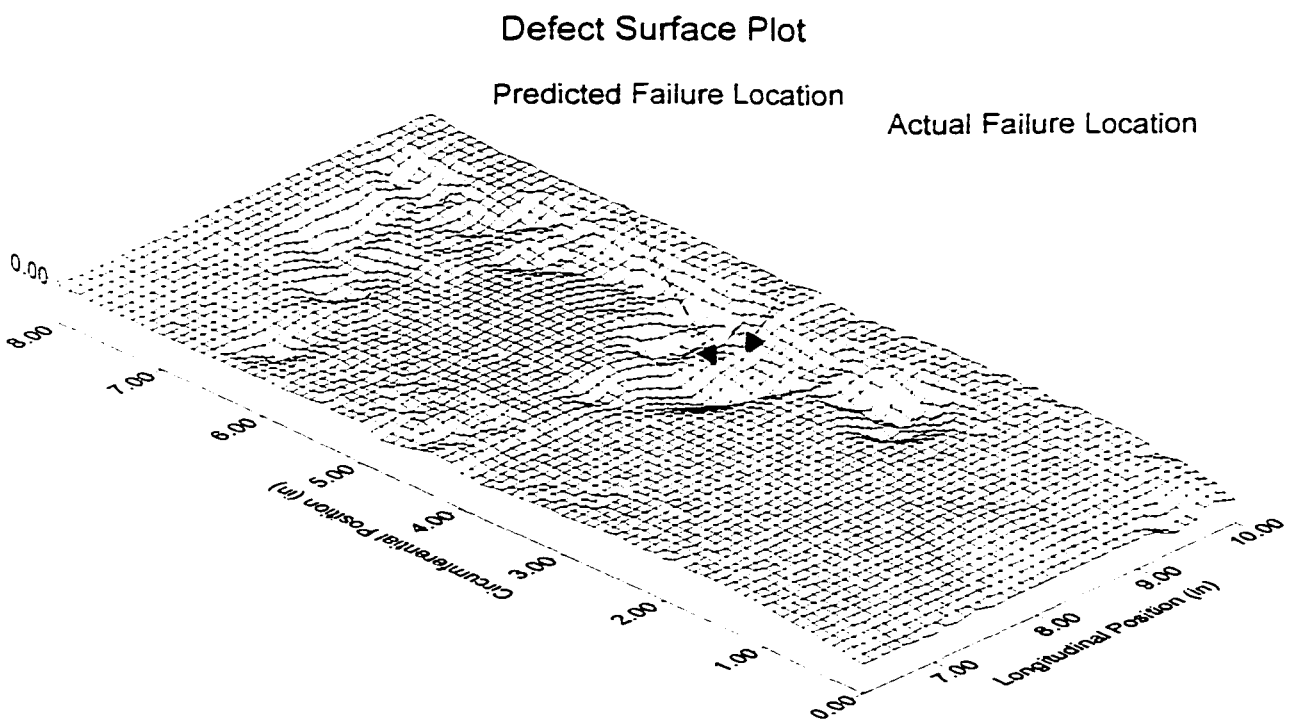
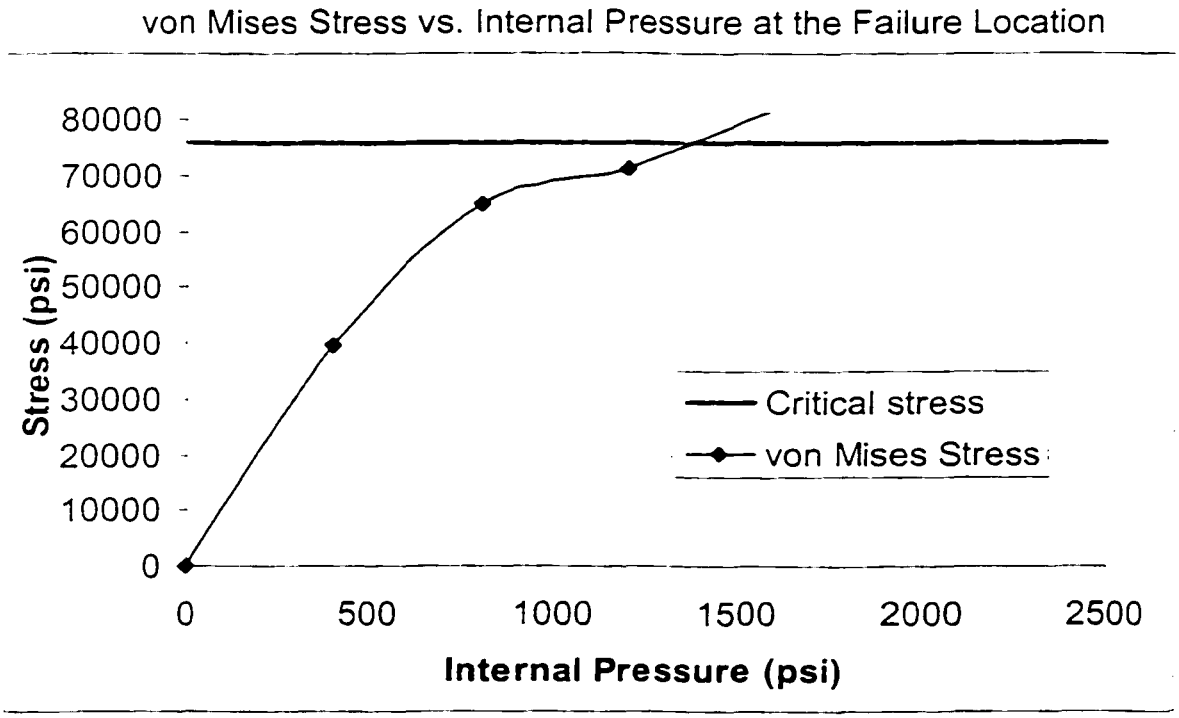


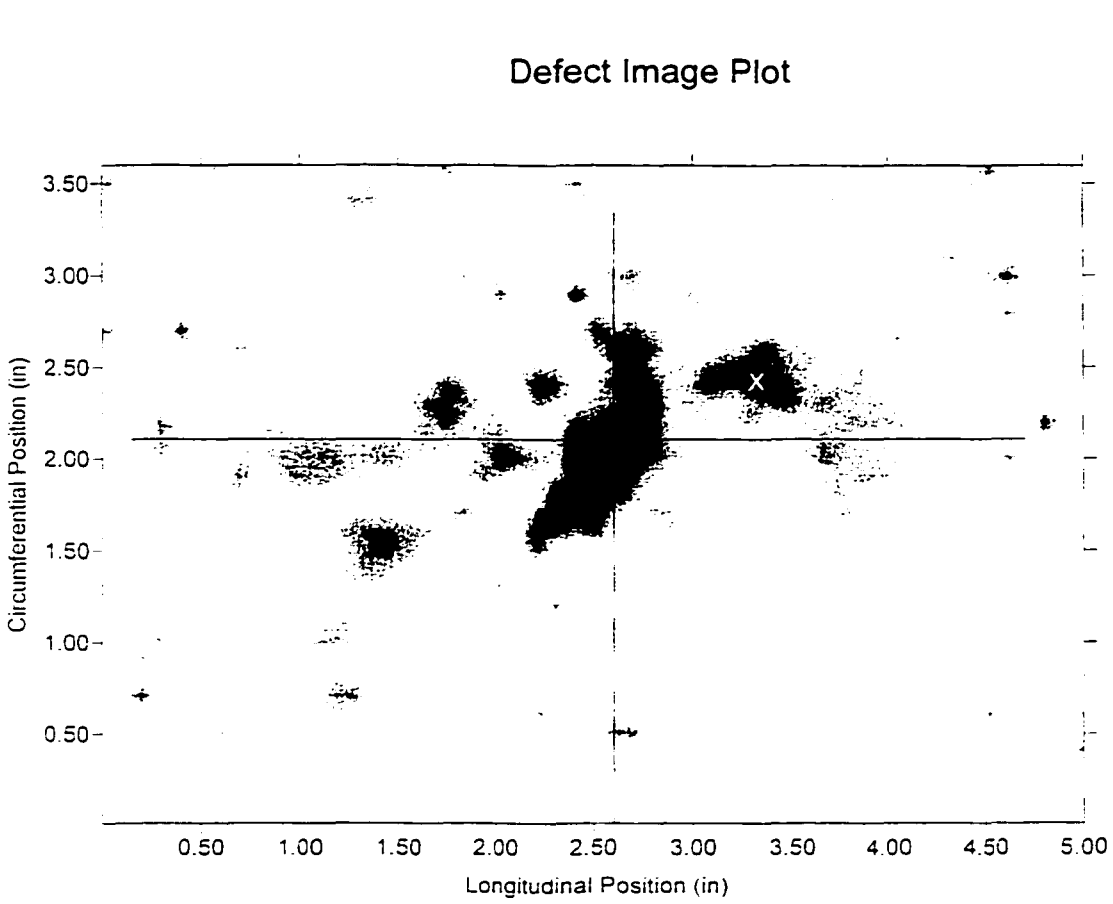
Figure 4.5.11a Burst test ESS01





Predicted Failure Pressure = 1370 psi
Actual Failure Pressure = 1412 psi

Figure 4.5.11b Burst test ESS01



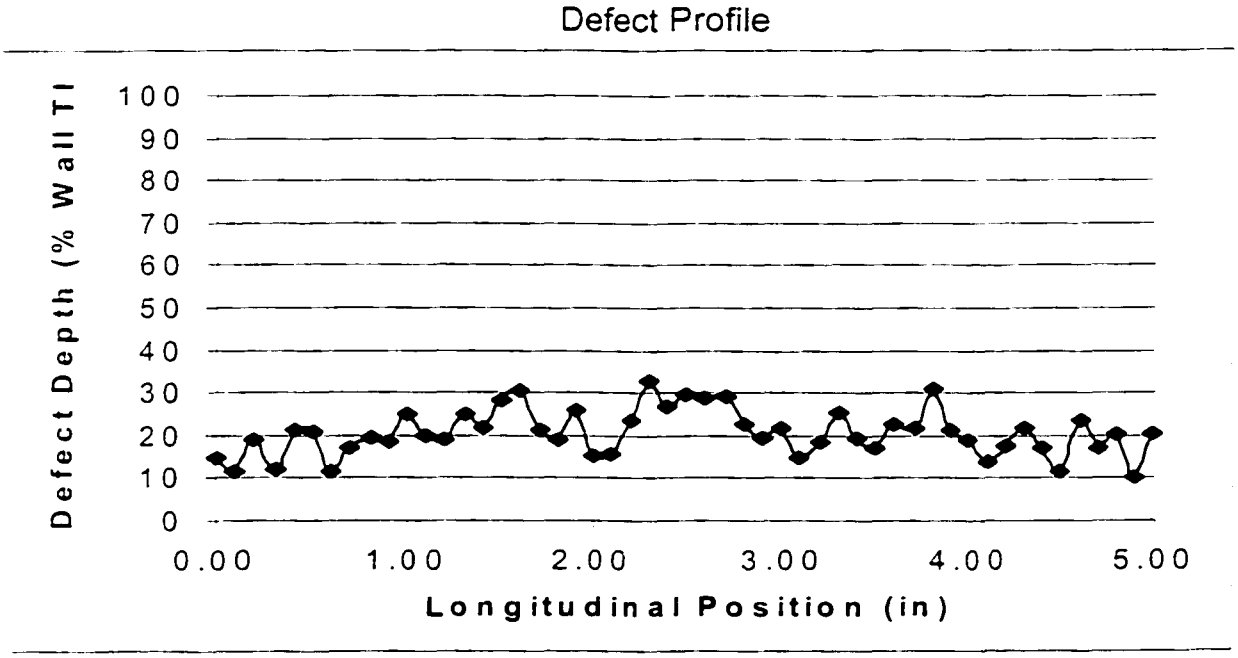


Figure 4.5.12a Burst test NOR02-4A

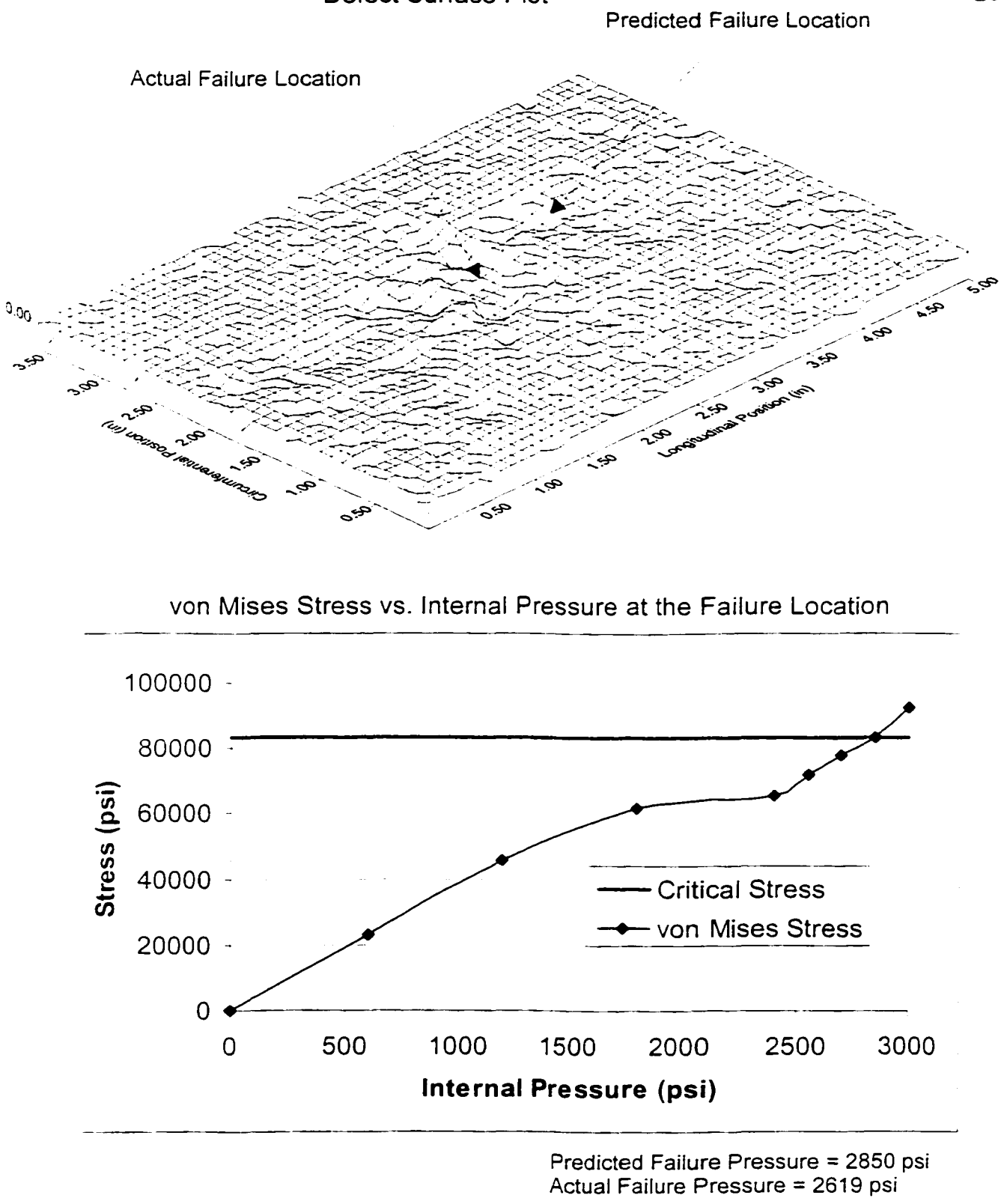


Figure 4.5.12b Burst test NOR02-4A

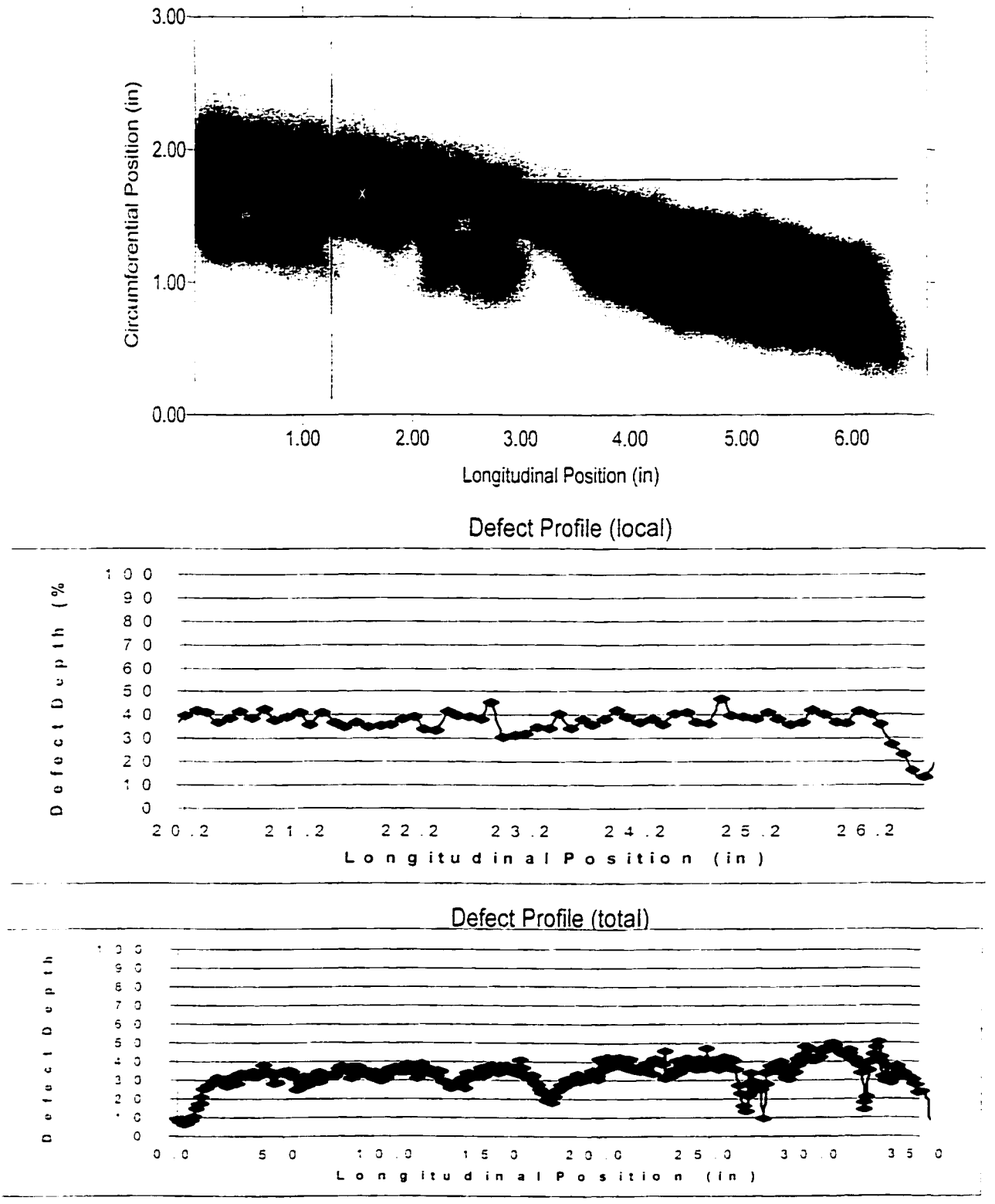


Figure 4.5.13a Burst test RLK0i

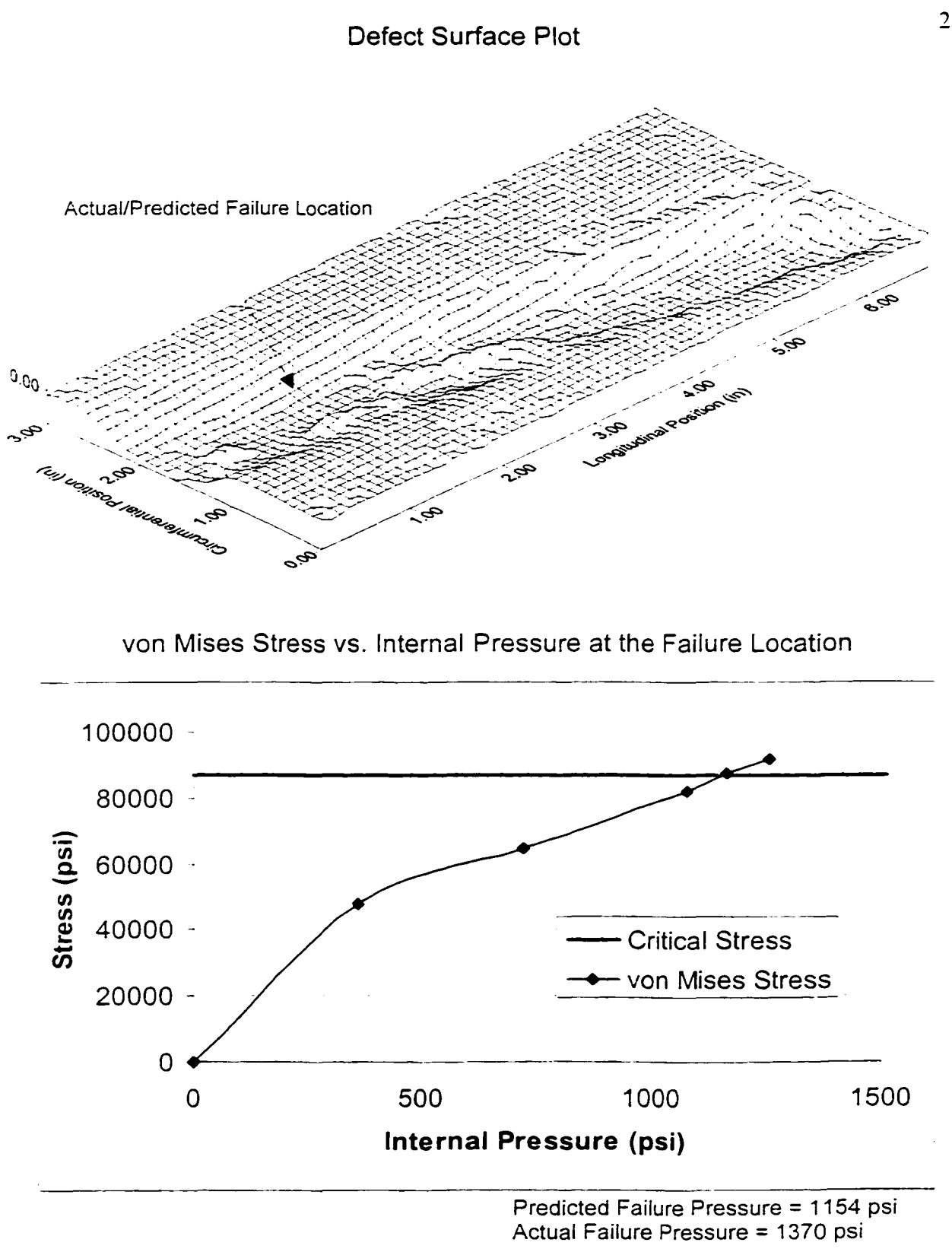
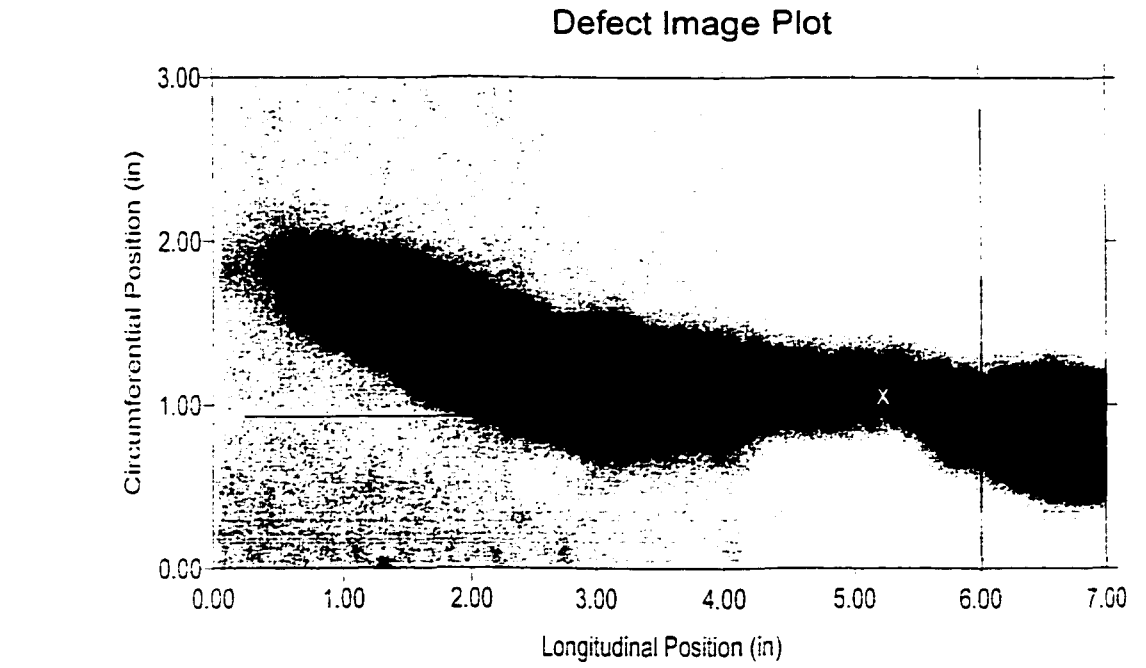
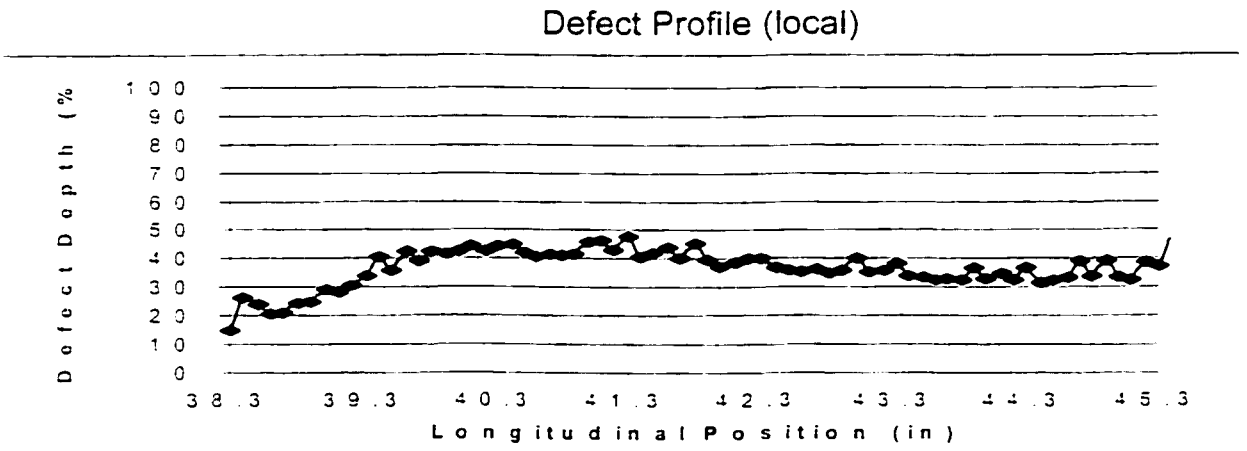


Figure 4.5.13b Burst test RLK01





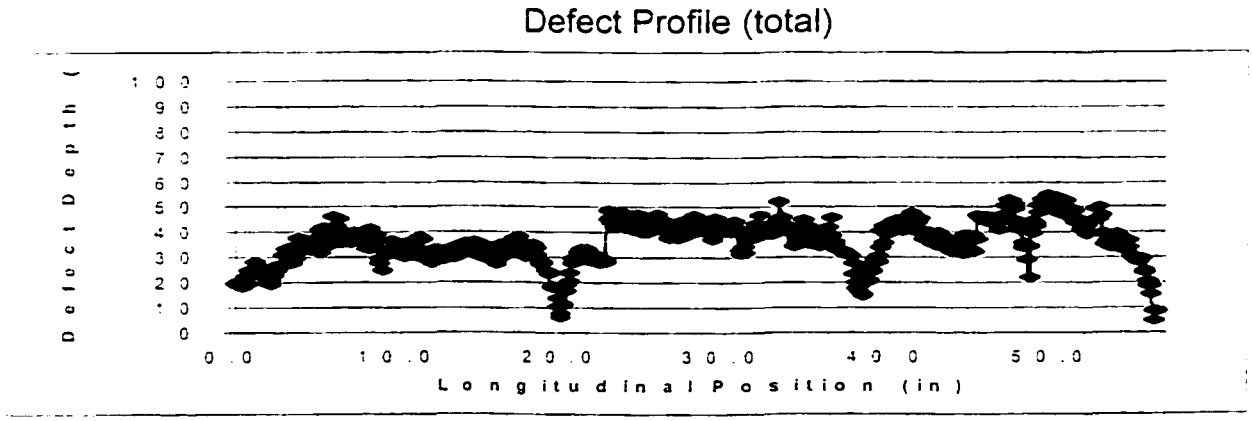
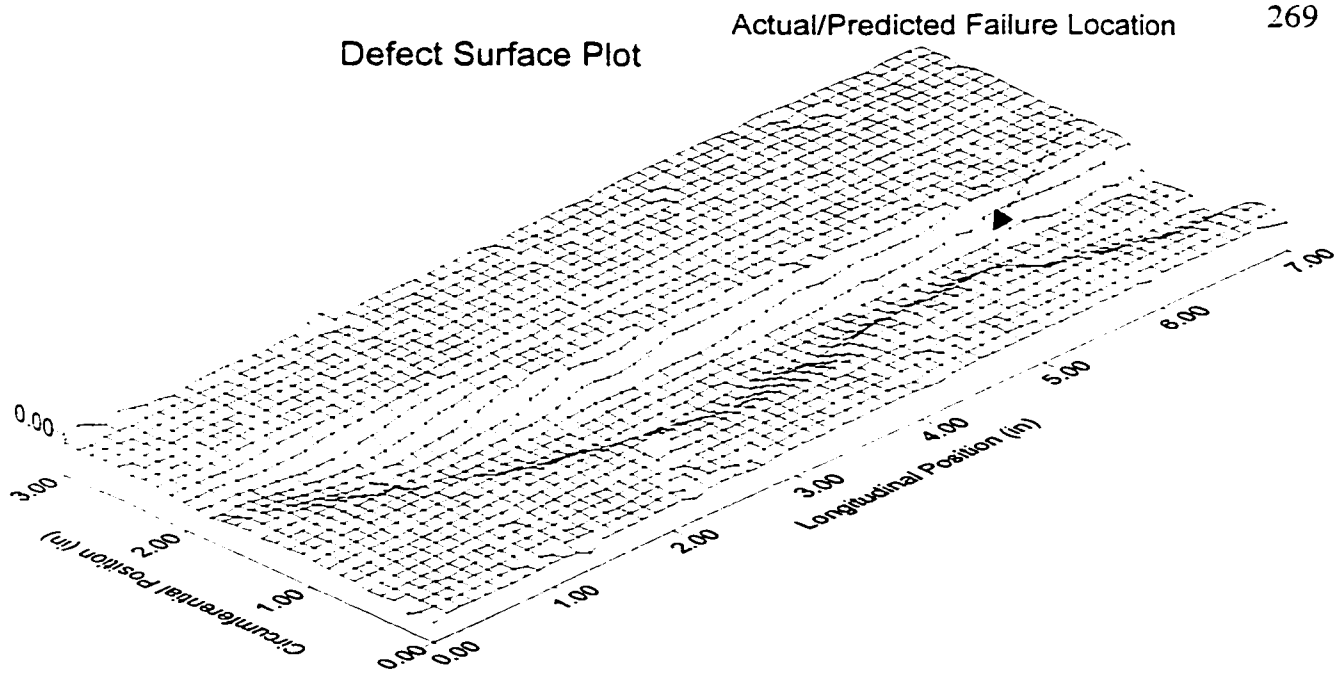
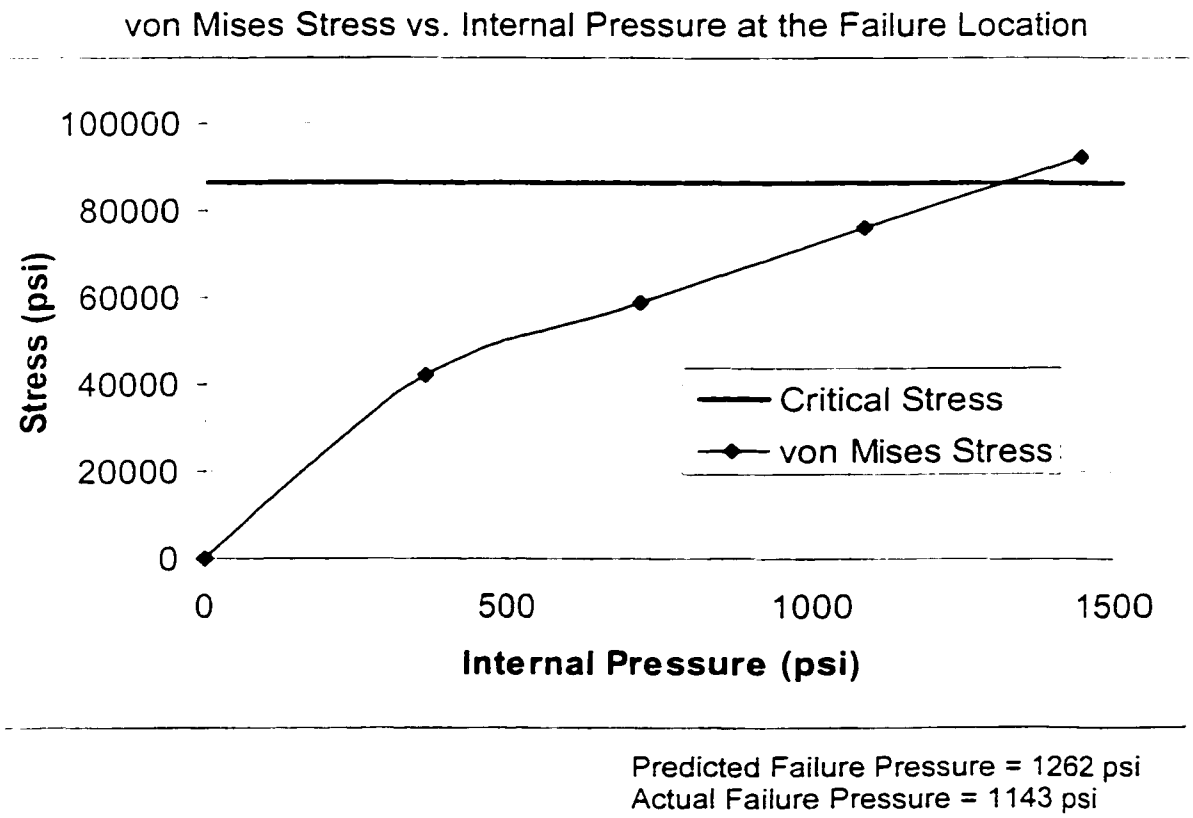


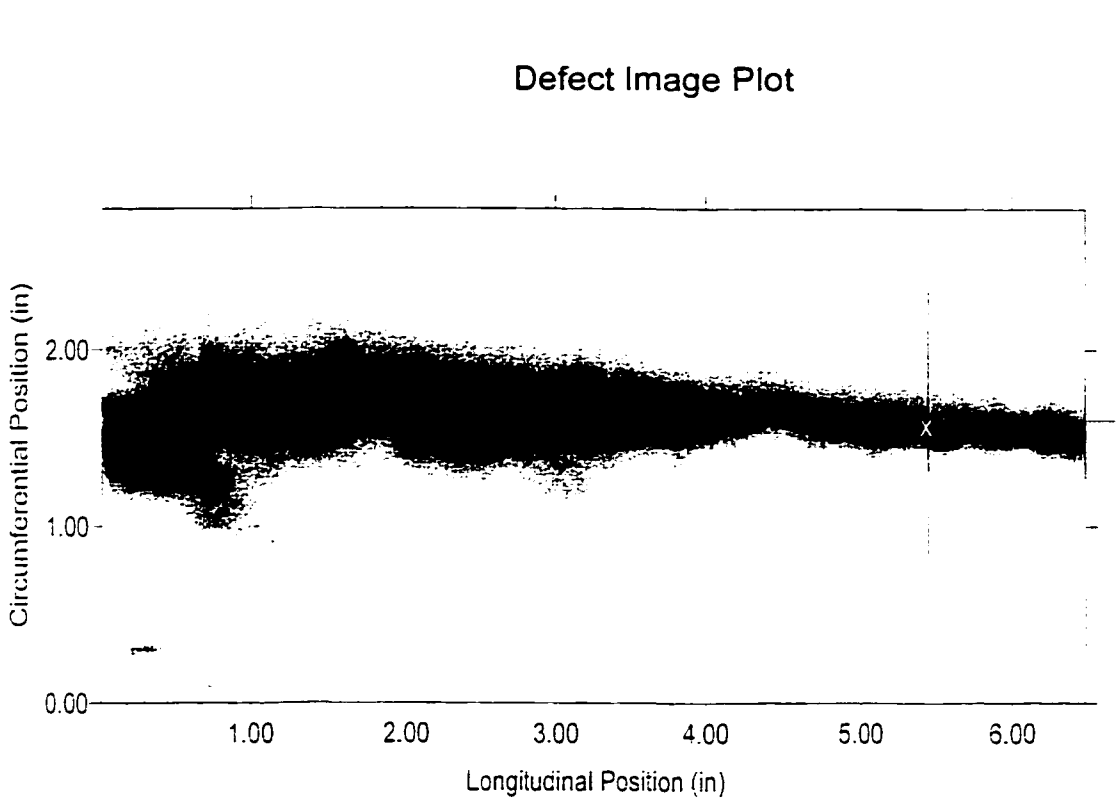
Figure 4.5.14a Burst test RLK02

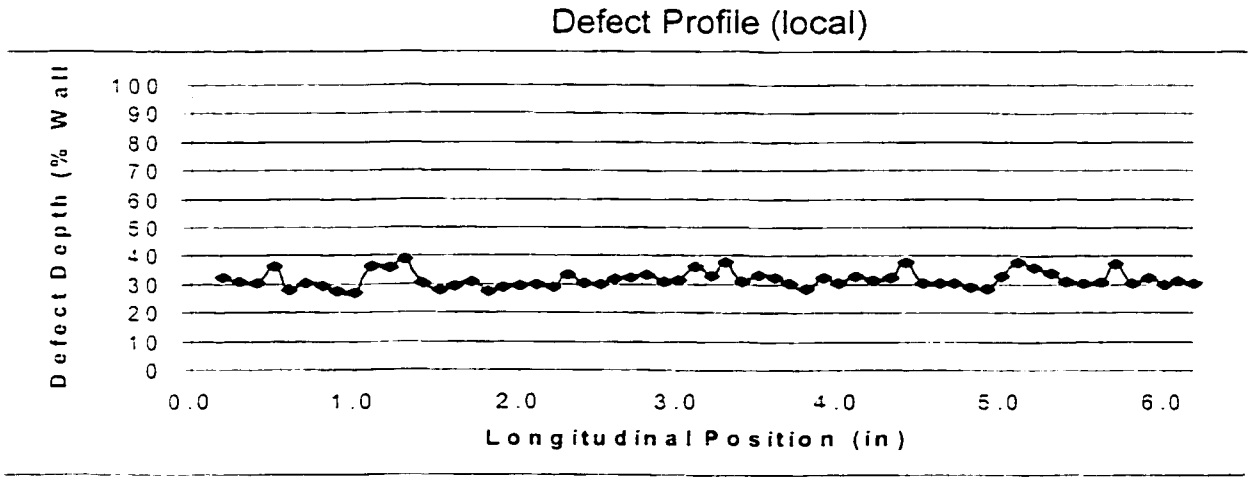




Predicted Failure Pressure = 1262 psi
Actual Failure Pressure = 1143 psi

Figure 4.5.14b Burst test RLK02





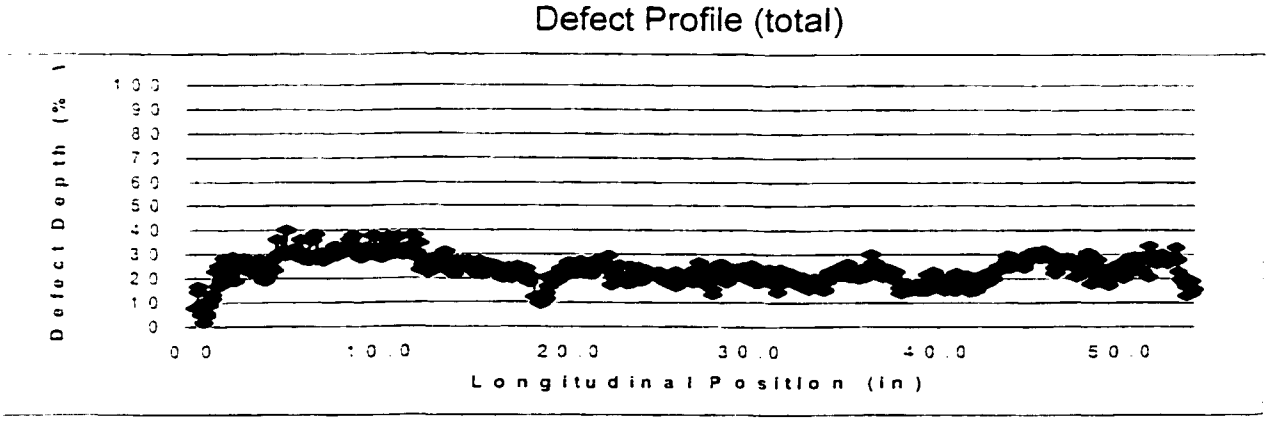


Figure 4.5.15a Burst test RLK03

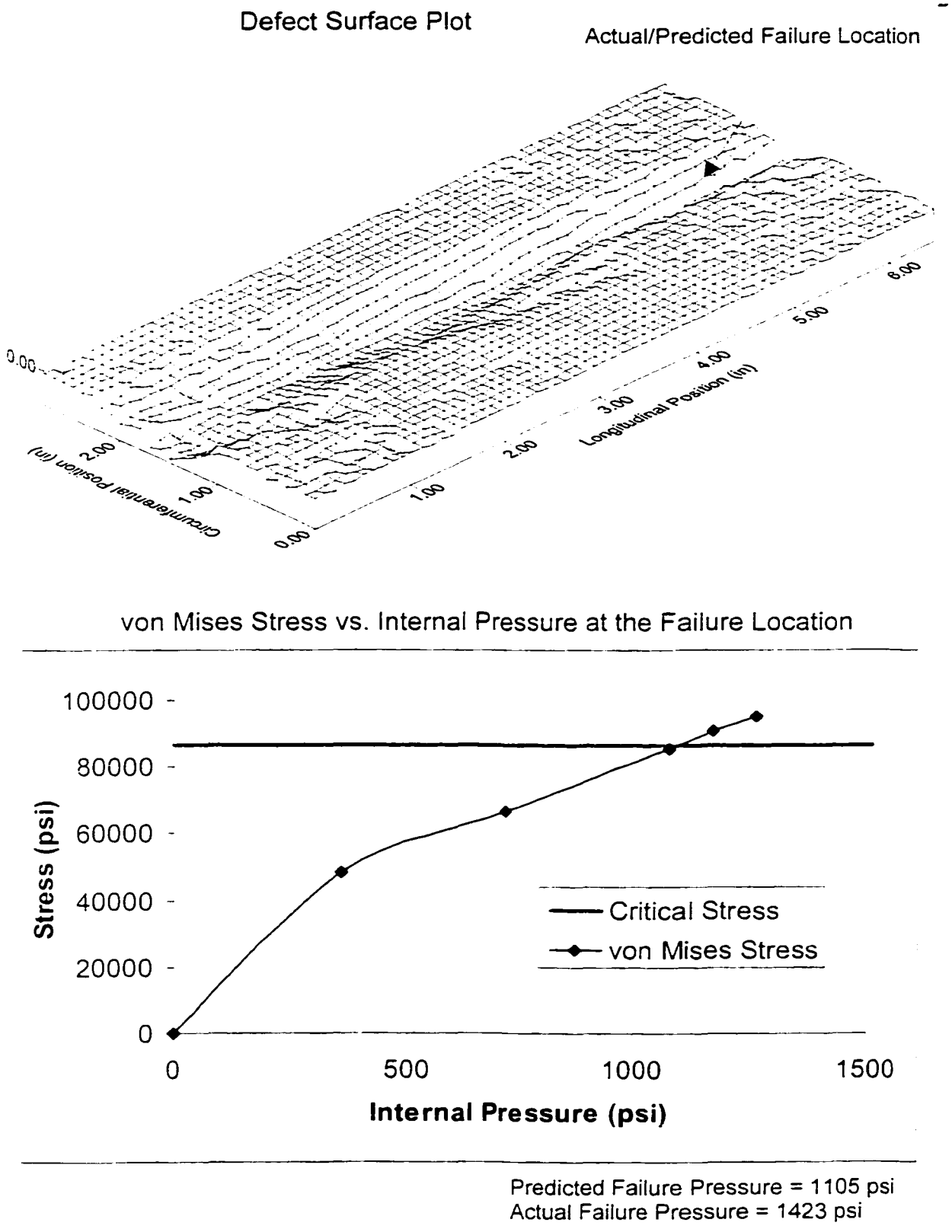


Figure 4.5.15b Burst test RLK03

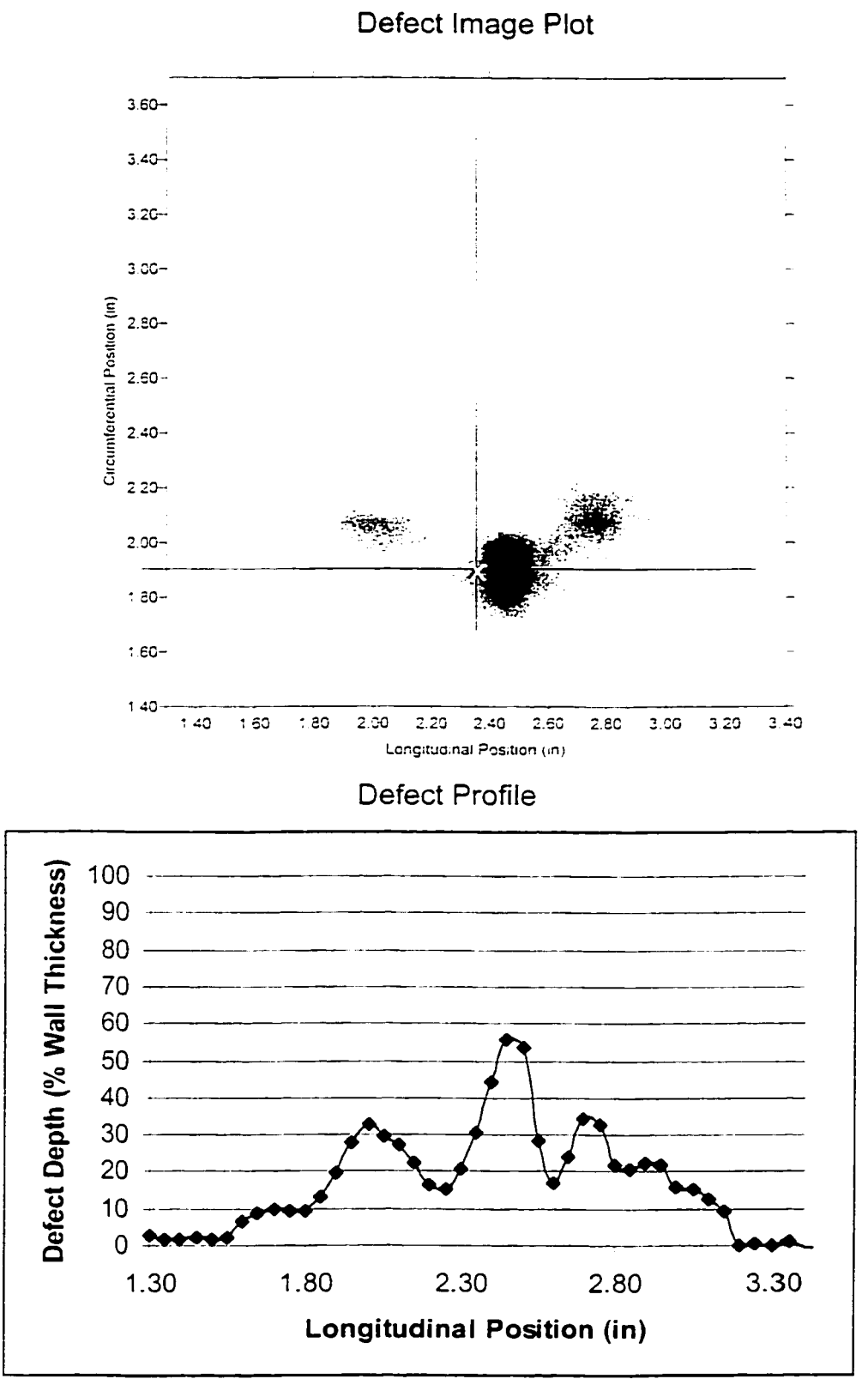
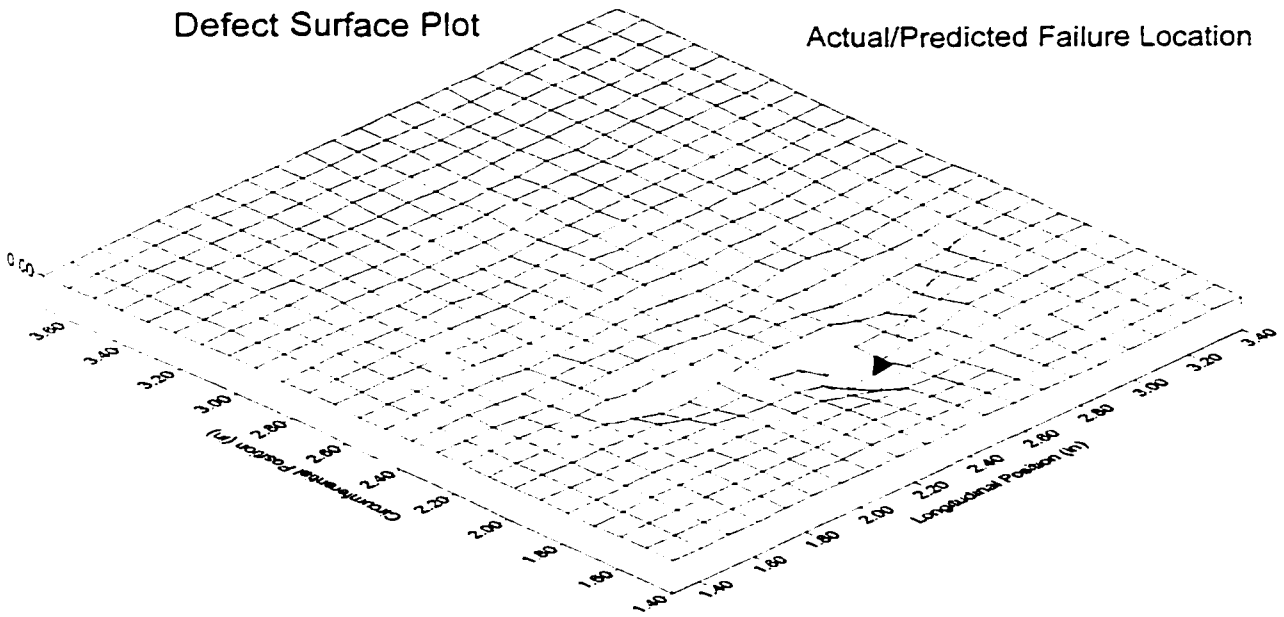


Figure 4.5.16a Burst test BCG02-B



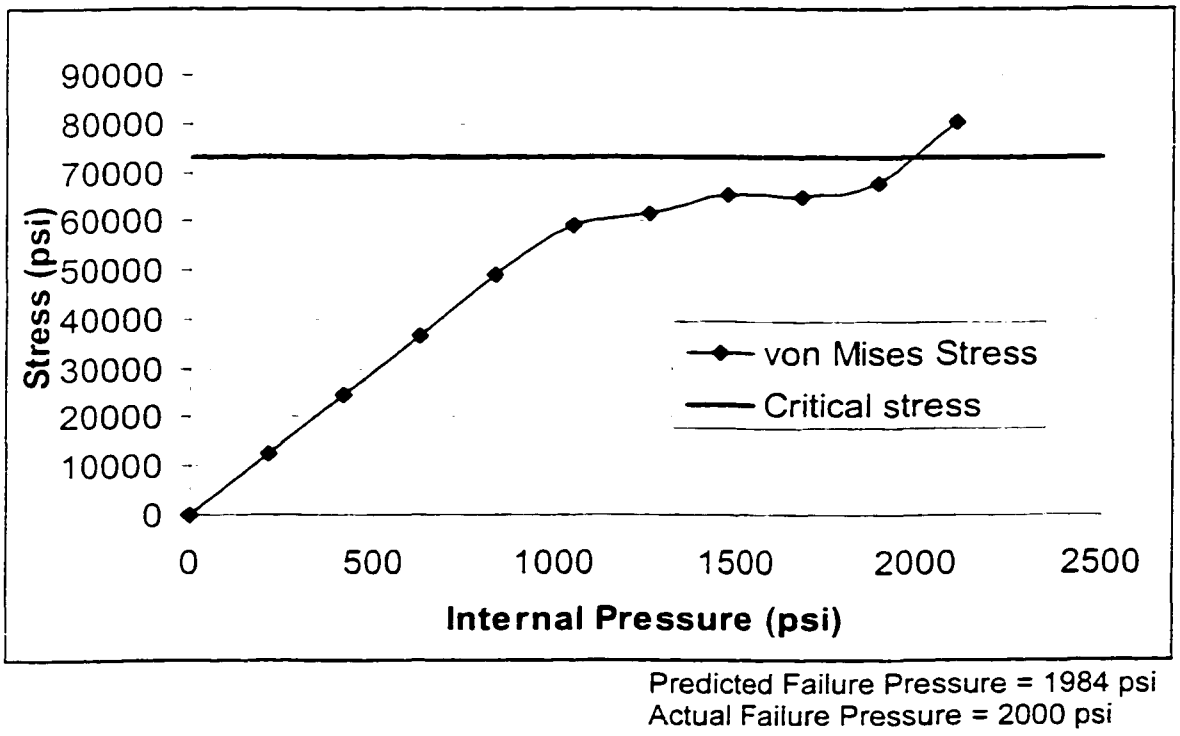
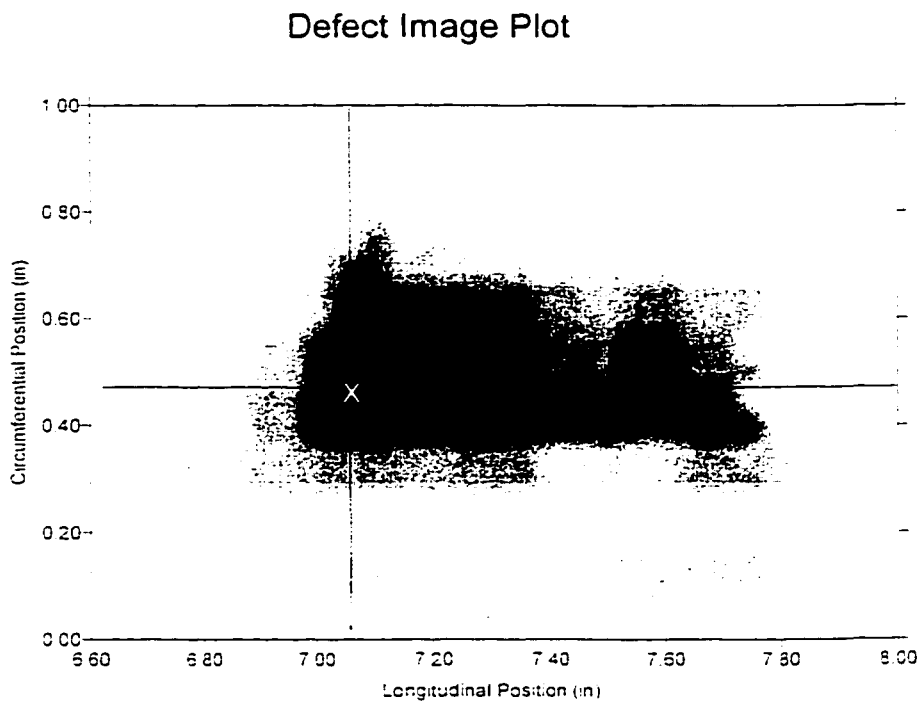


Figure 4.5.16b Burst test BCG02-B



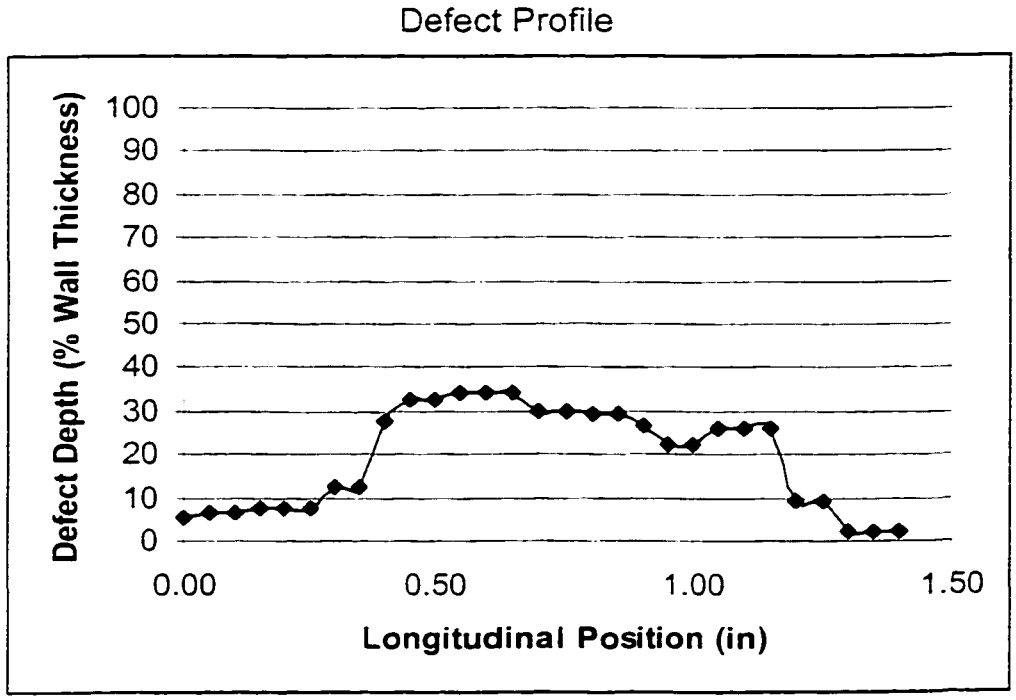
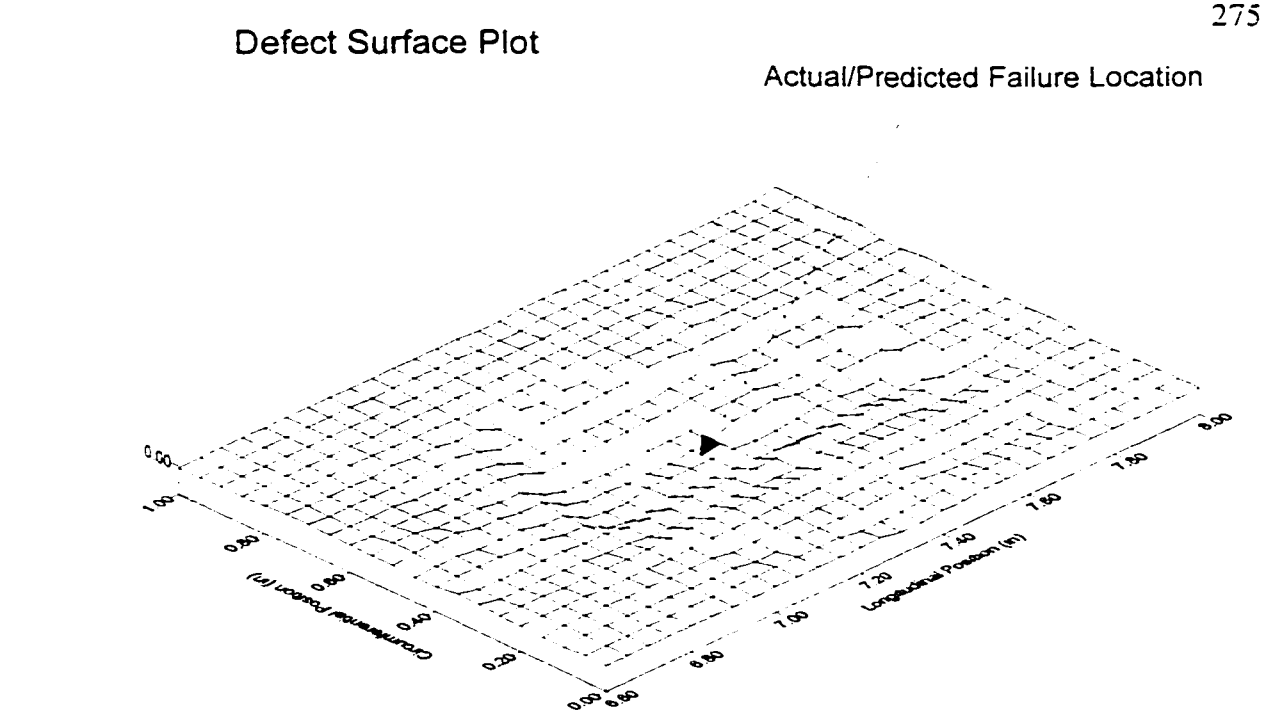
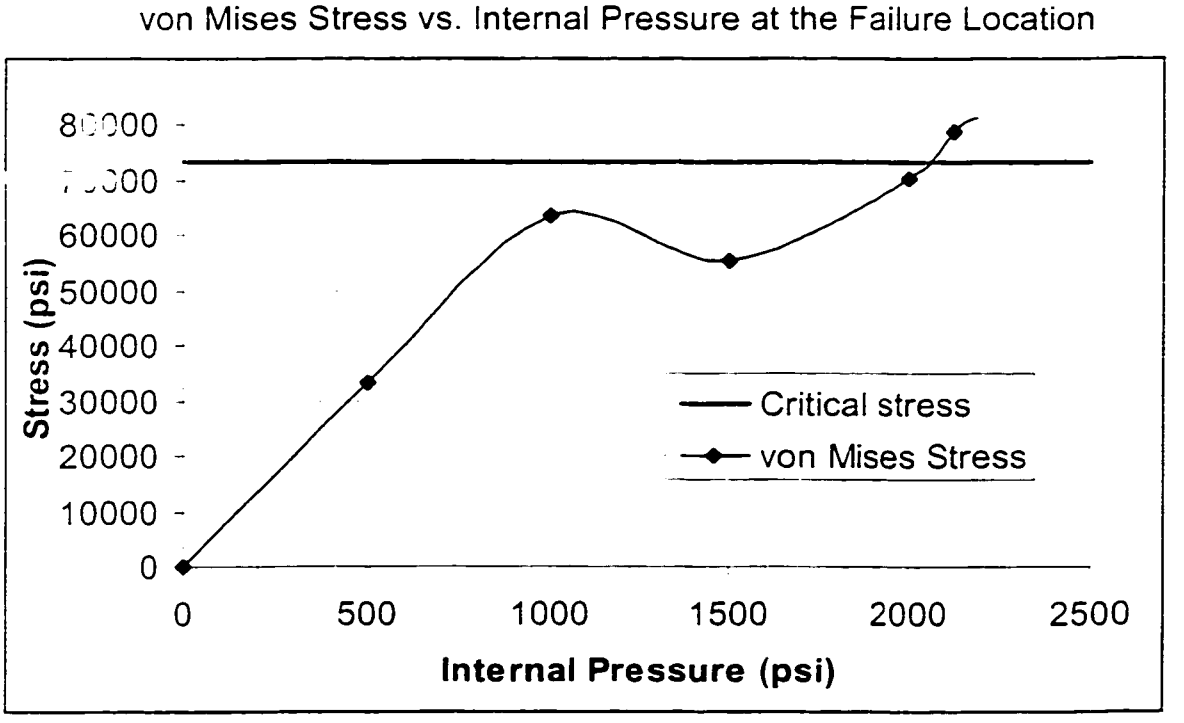


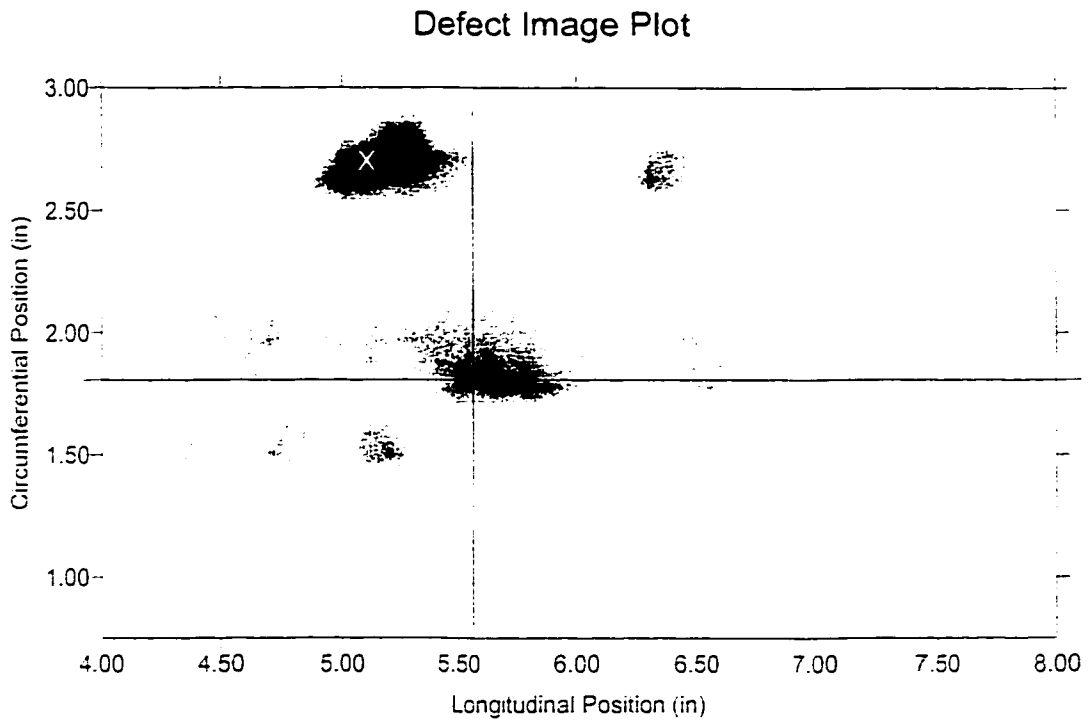
Figure 4.5.17a Burst test BCG03-D





Predicted Failure Pressure = 2050 psi
Actual Failure Pressure = 1988 psi

Figure 4.5.17b Burst test BCG03-D



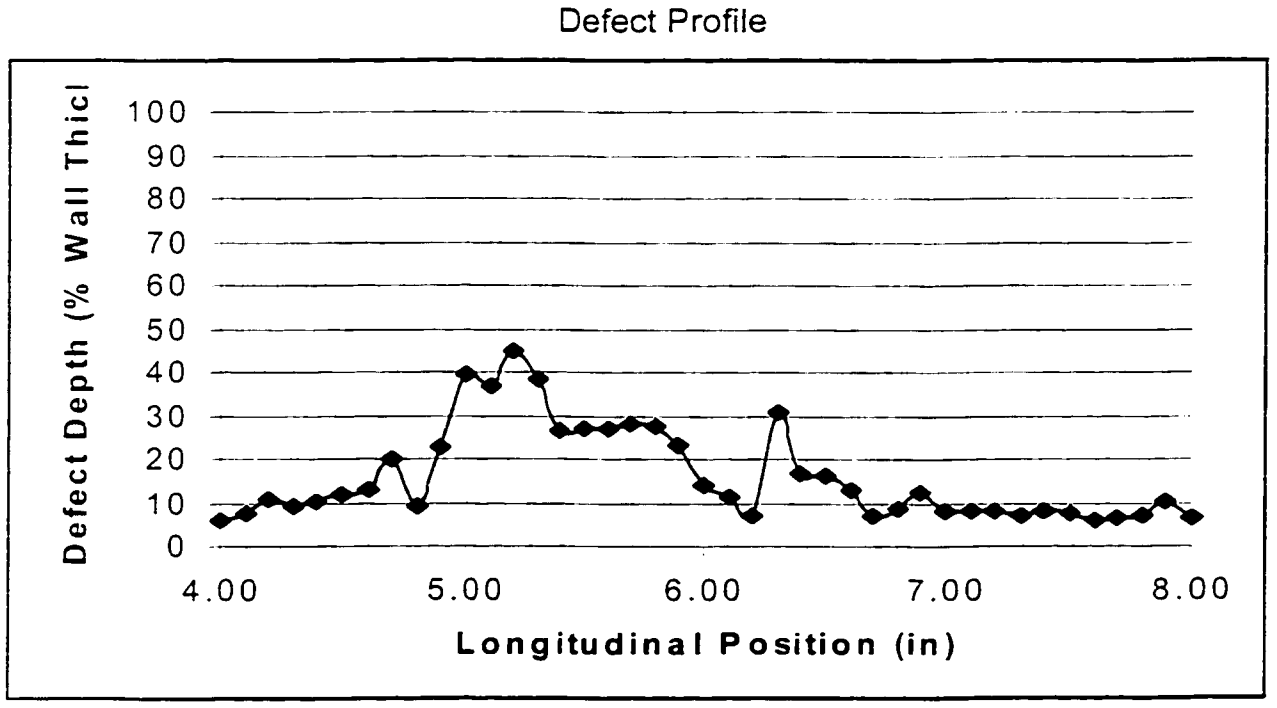
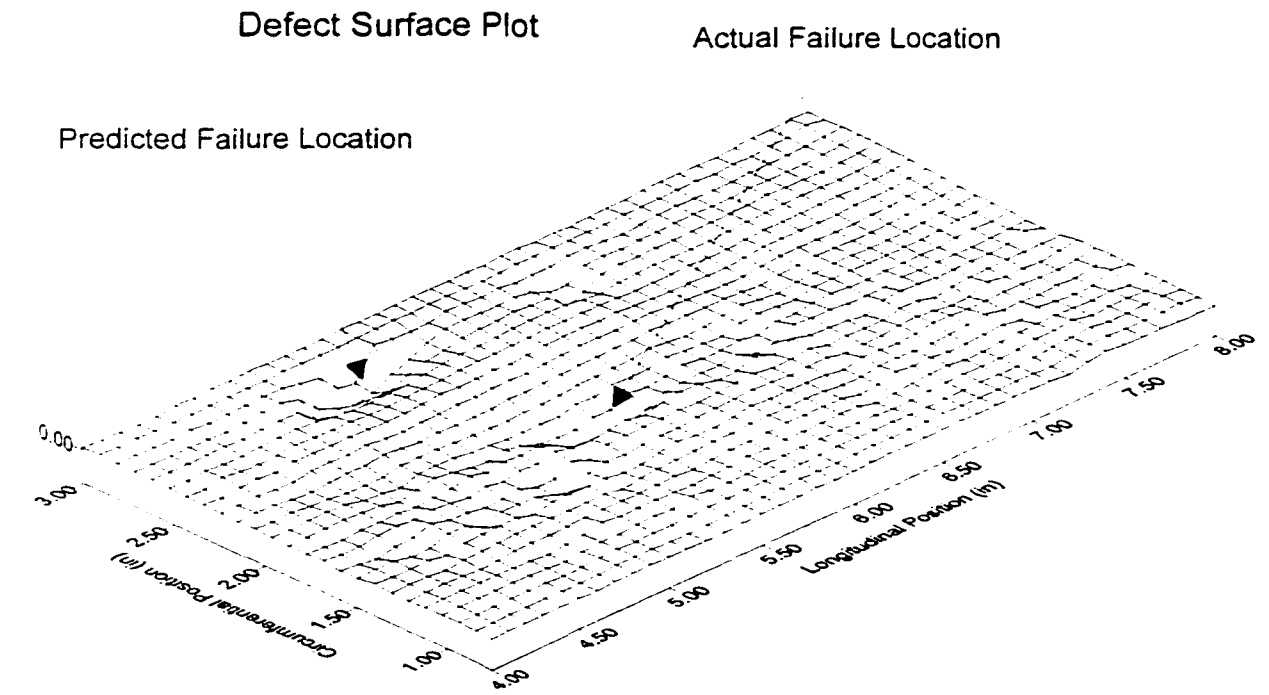
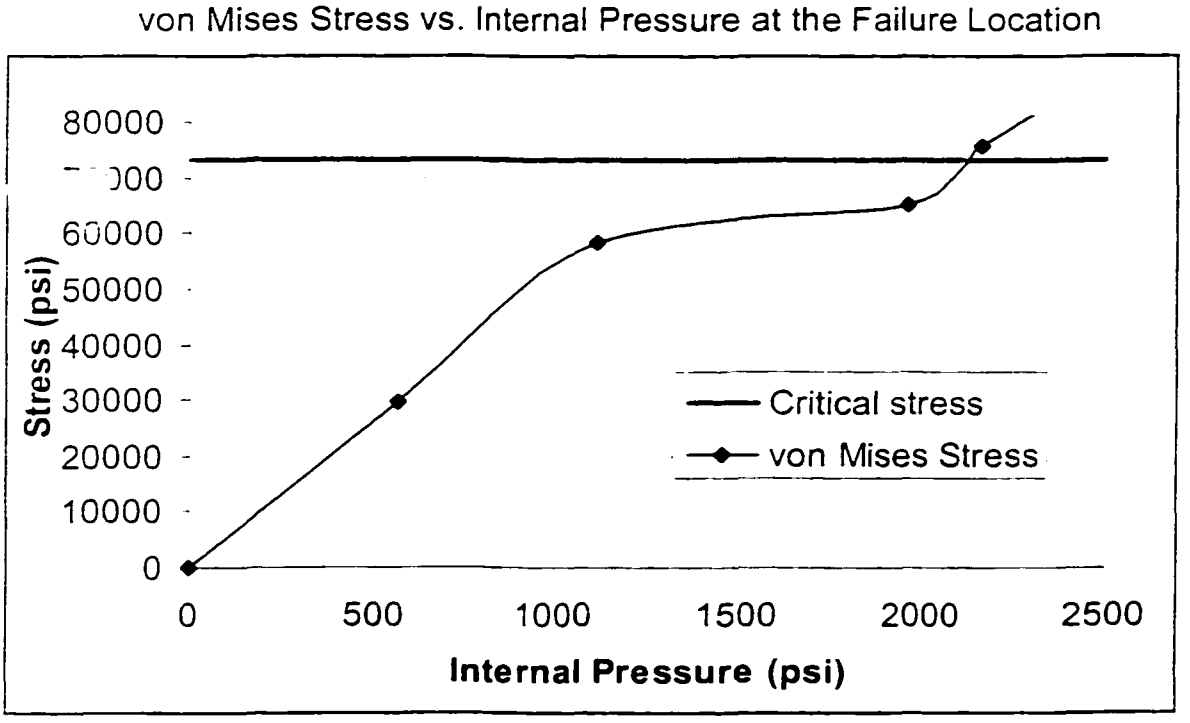


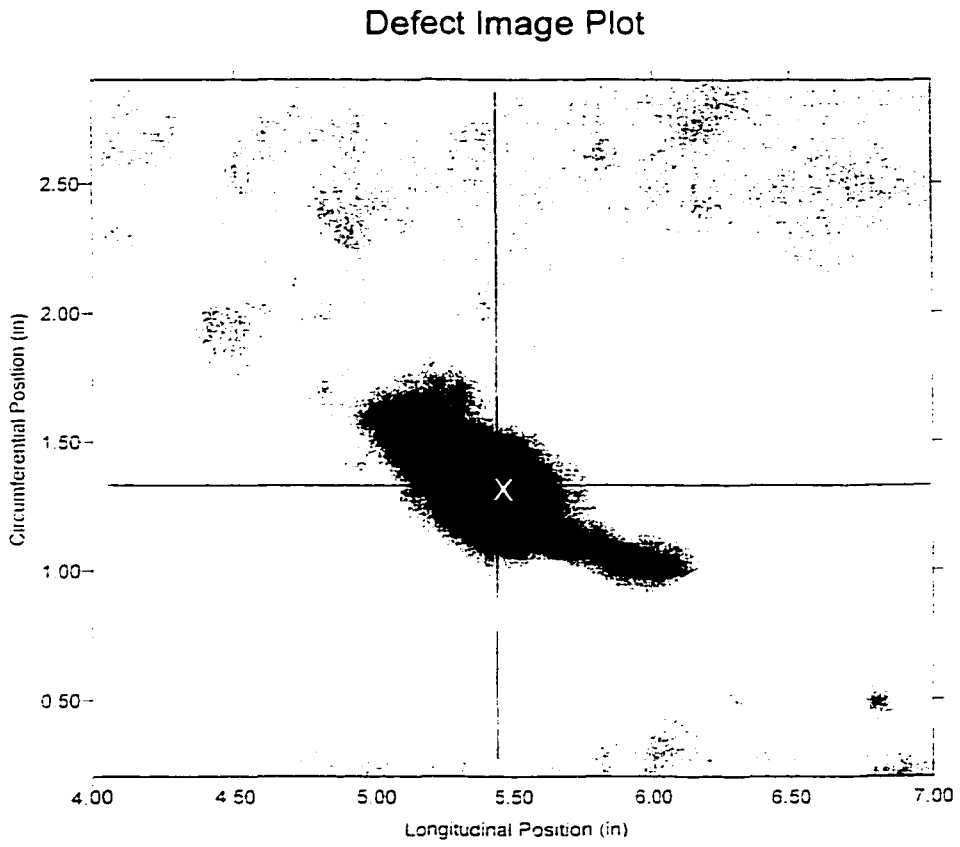
Figure 4.5.18a Burst test BCG04-A





Predicted Failure Pressure = 2120 psi
Actual Failure Pressure = 2201 psi

Figure 4.5.18b Burst test BCG04-A



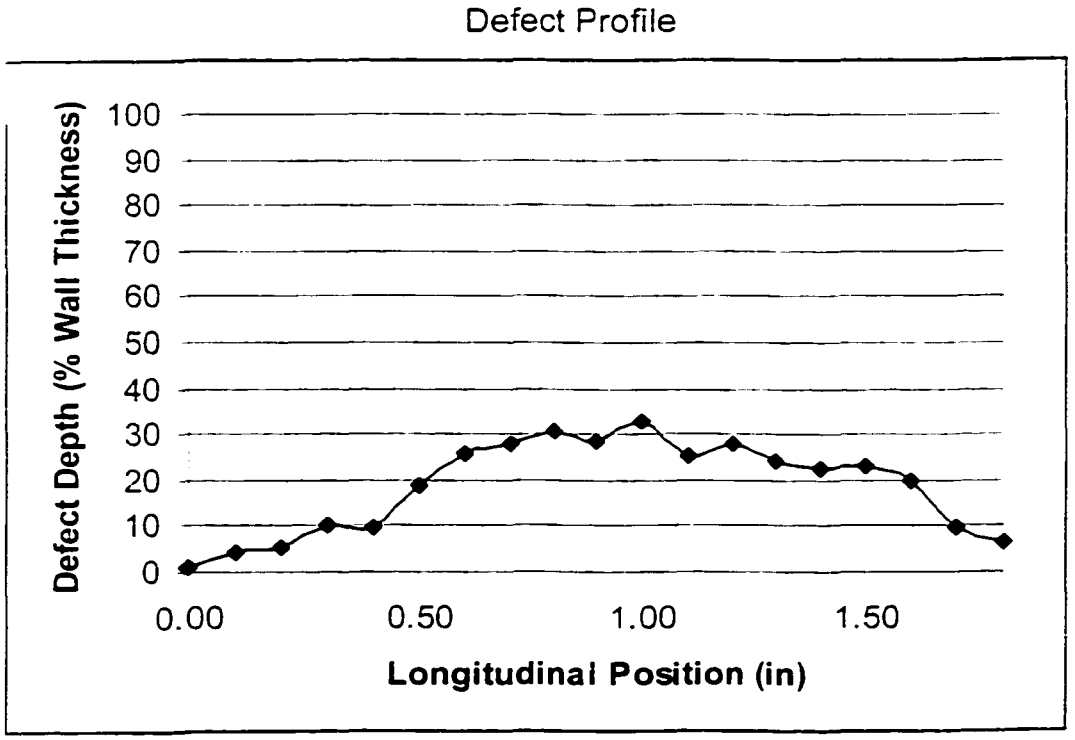
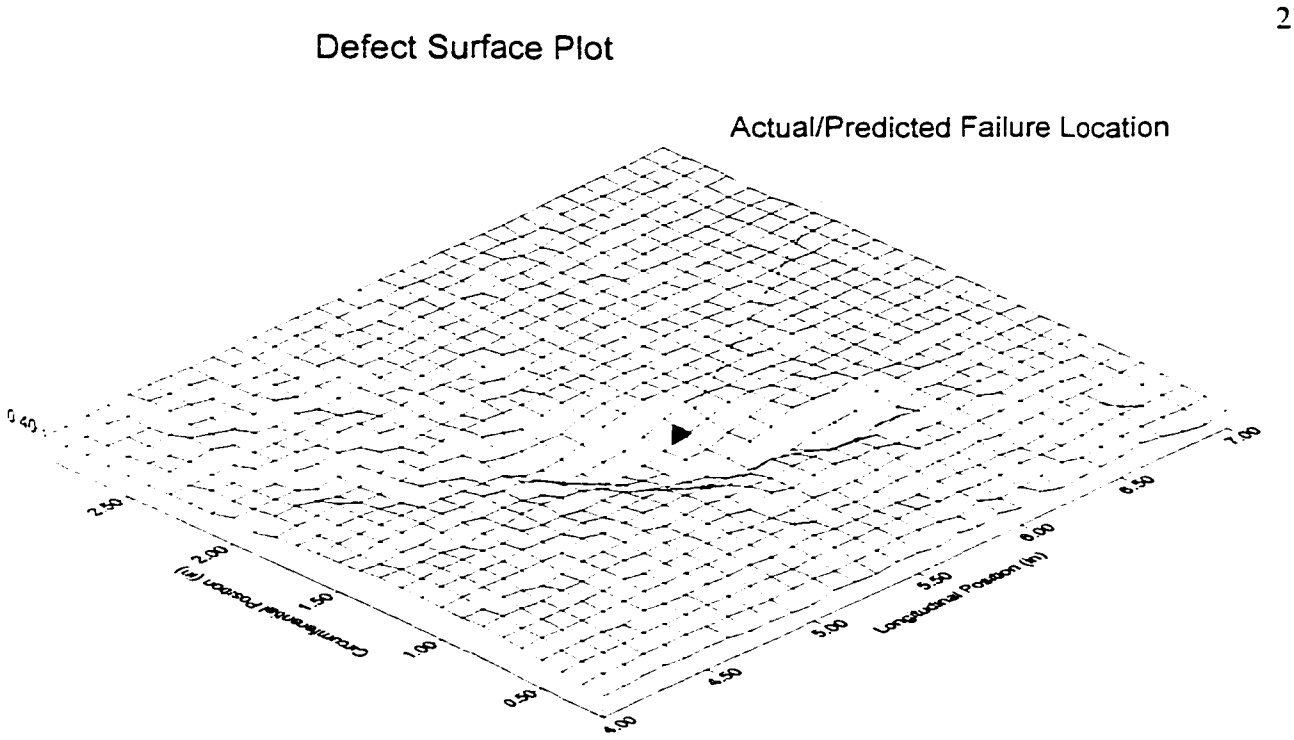
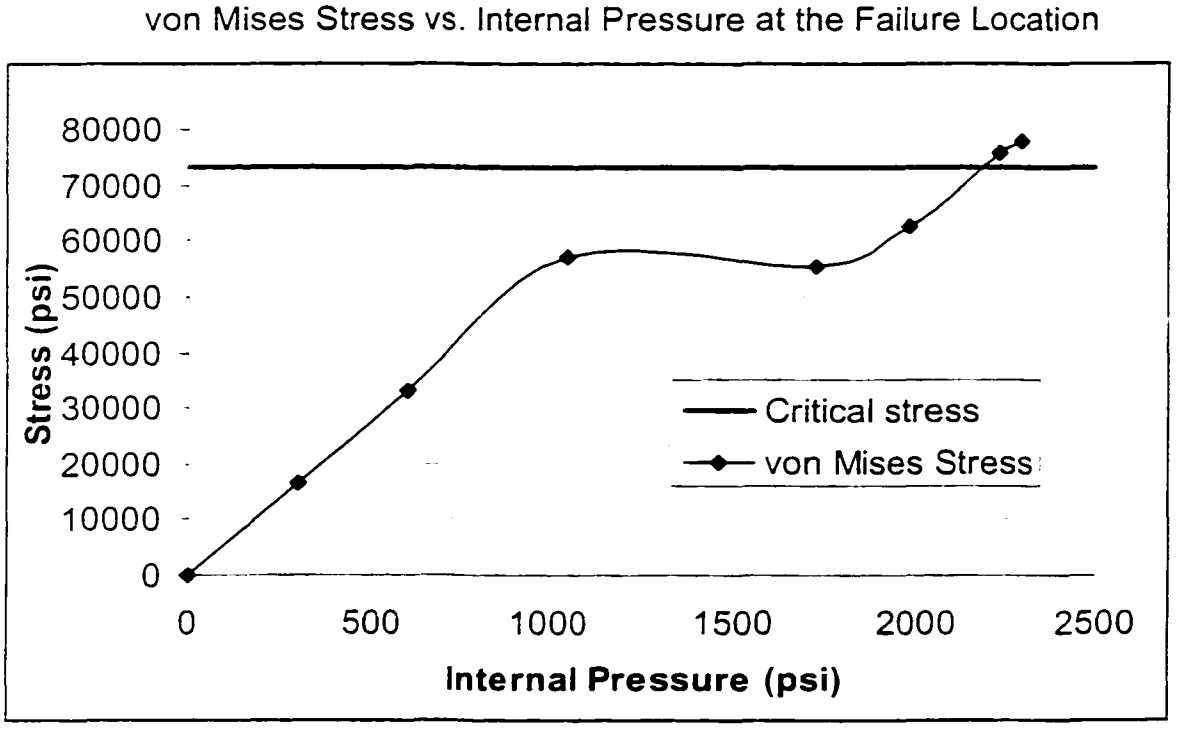


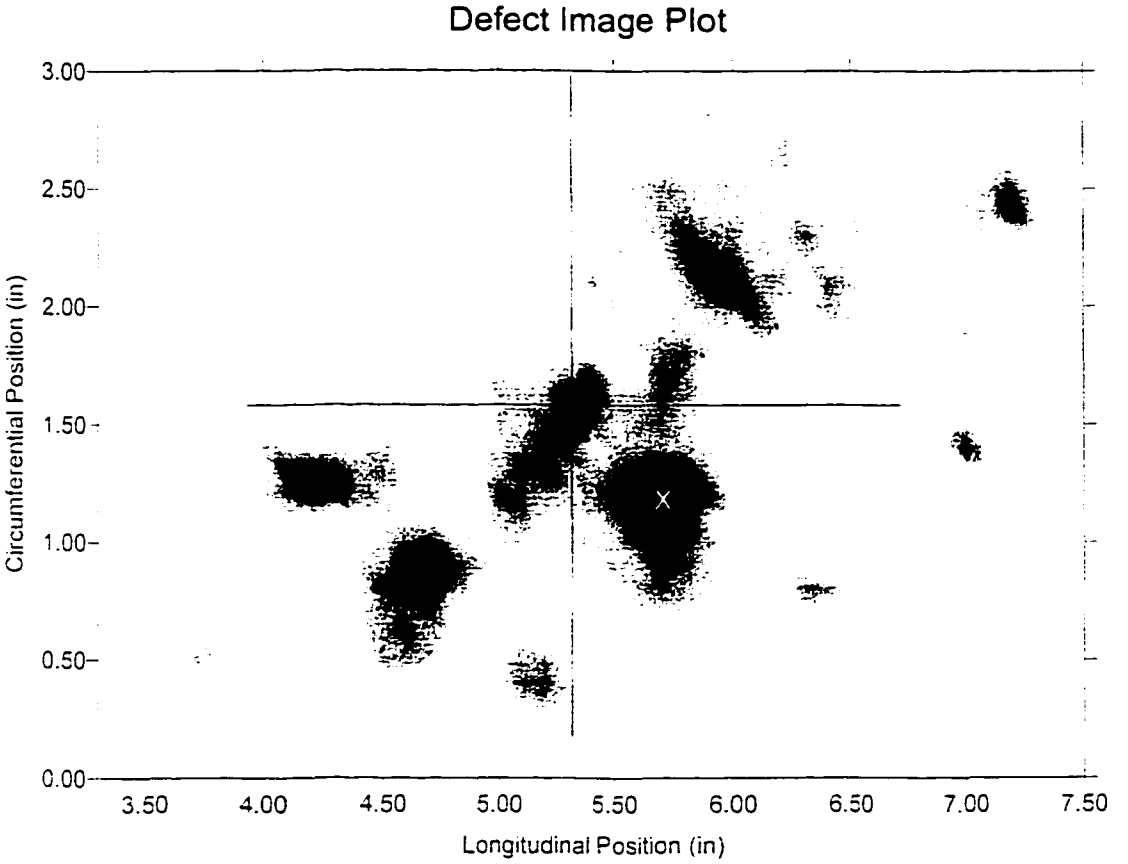
Figure 4.5.19a Burst test BCG05-C





Predicted Failure Pressure = 2183 psi
Actual Failure Pressure = 2174 psi

Figure 4.5.19b Burst test BCG05-C



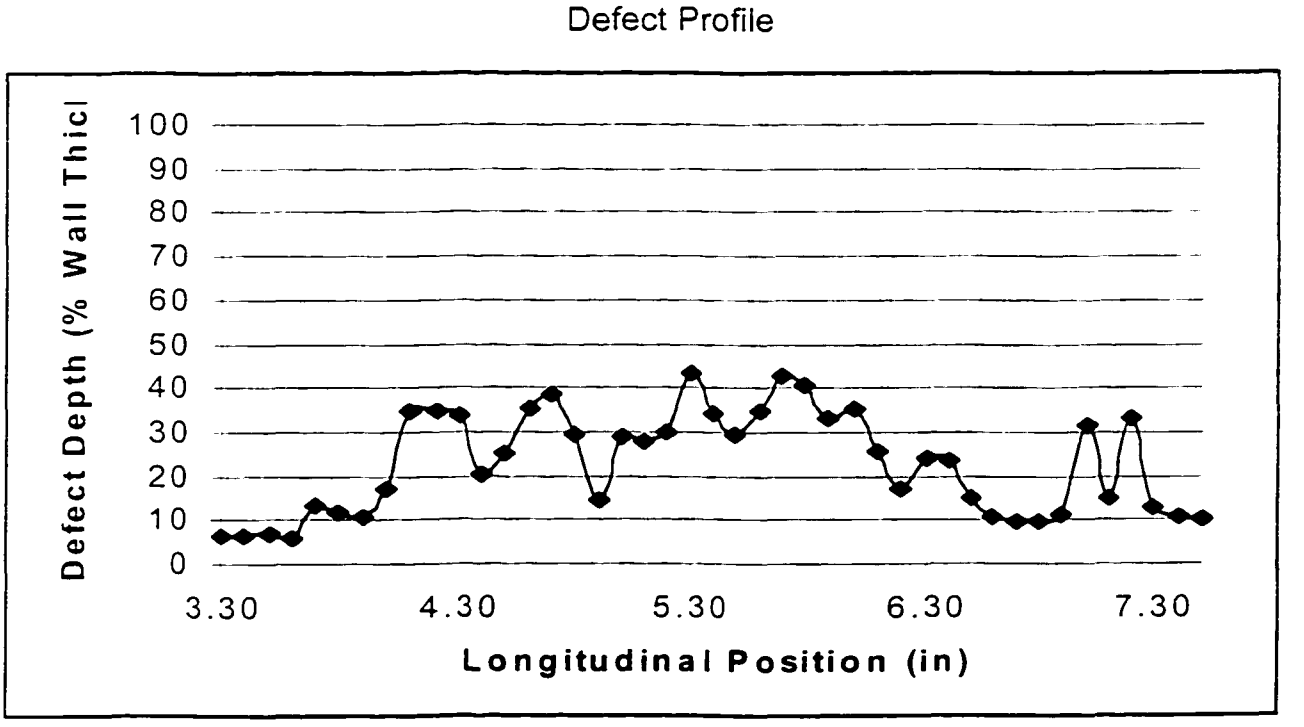
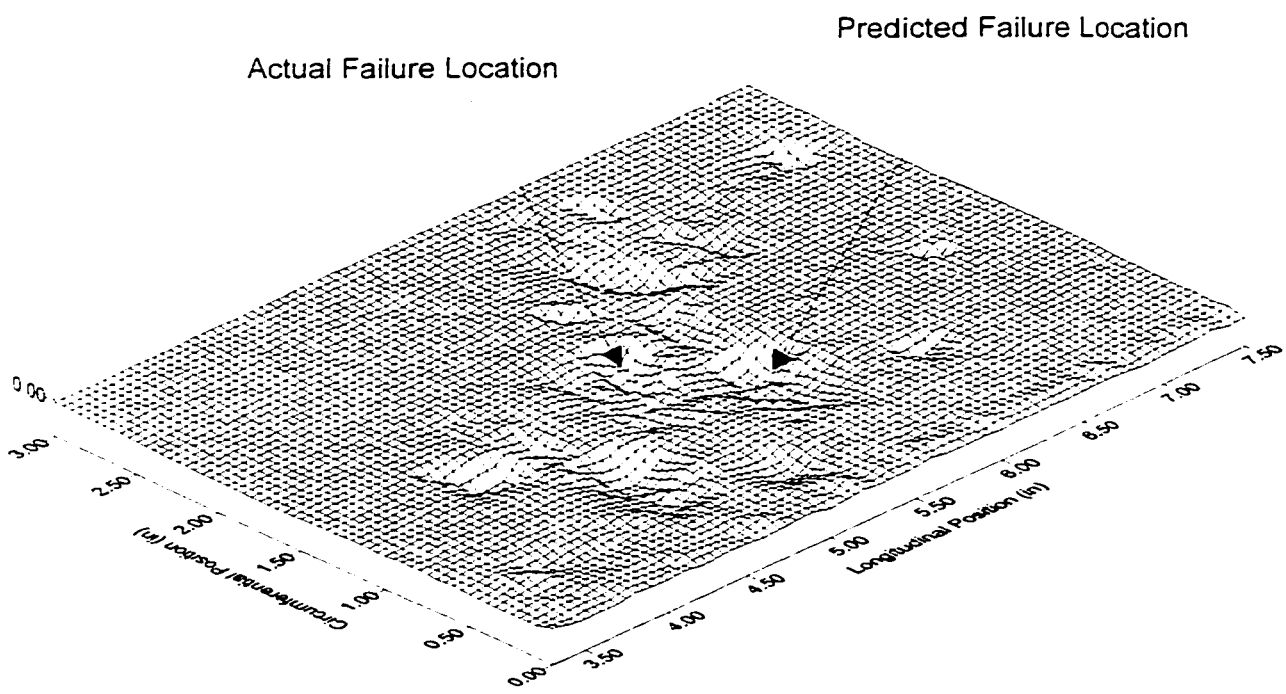
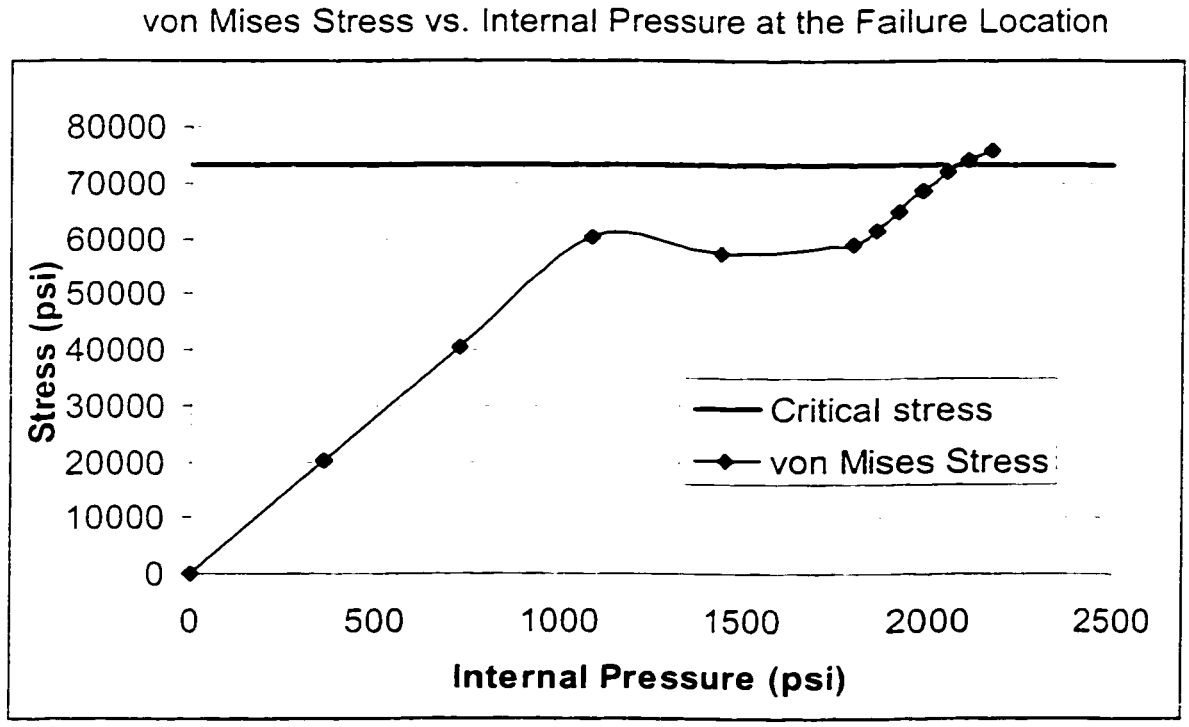


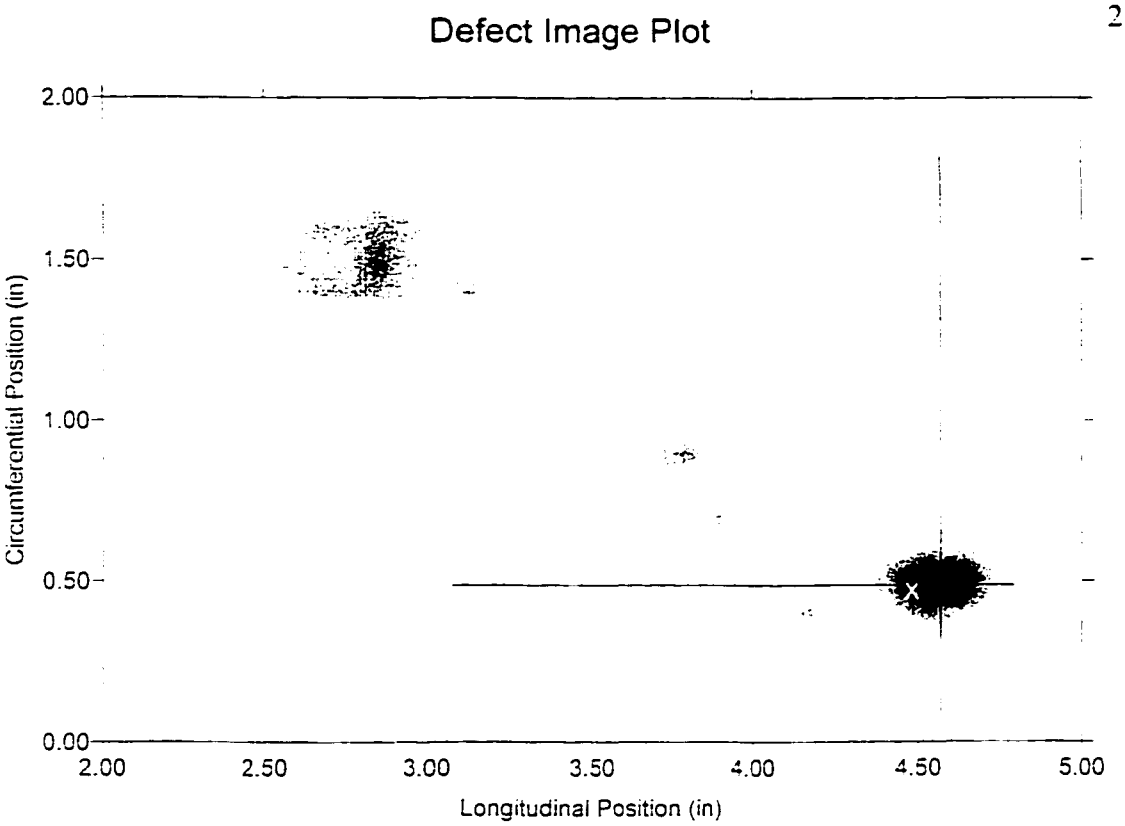
Figure 4.5.20a Burst test BCG06-A





Predicted Failure Pressure = 2078 psi
Actual Failure Pressure = 1936 psi

Figure 4.5.20b Burst test BCG06-A



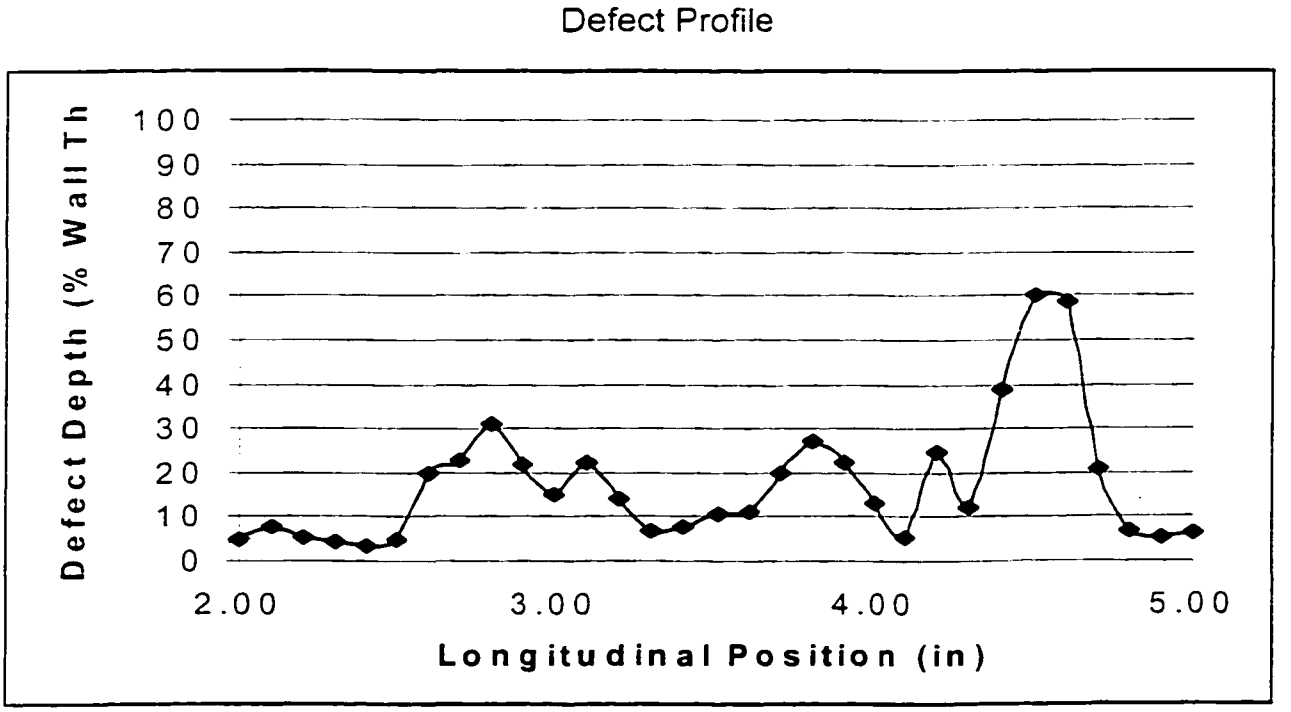
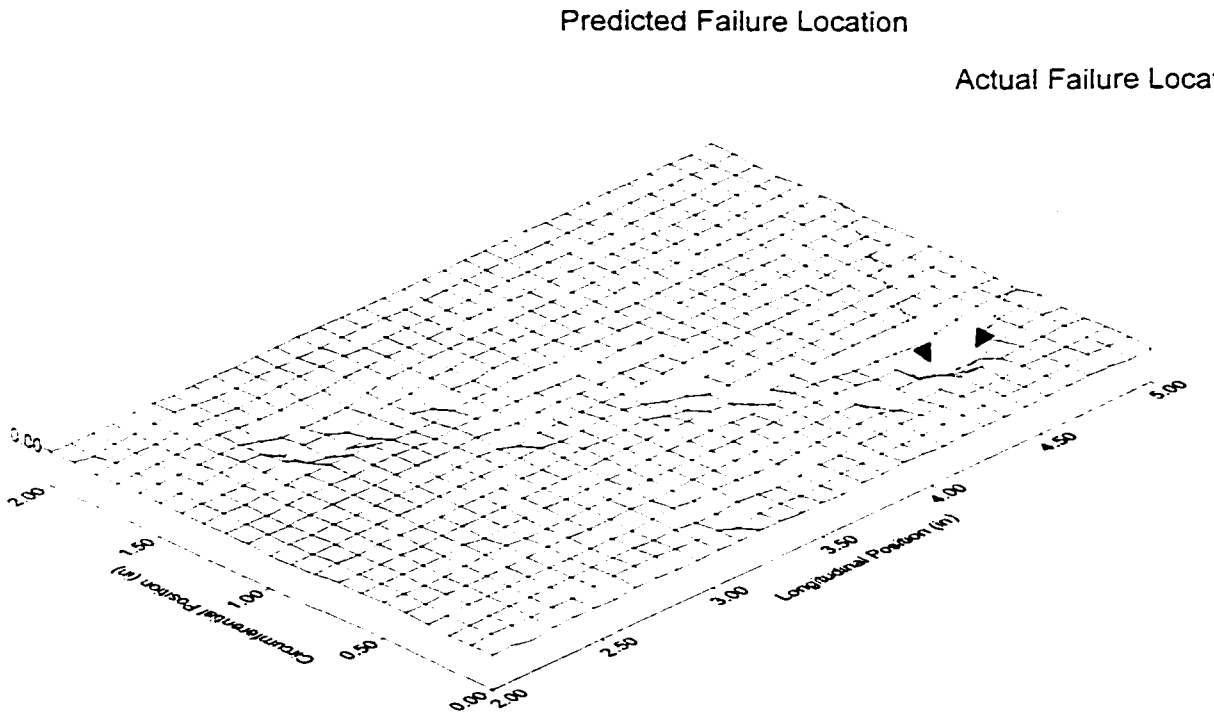
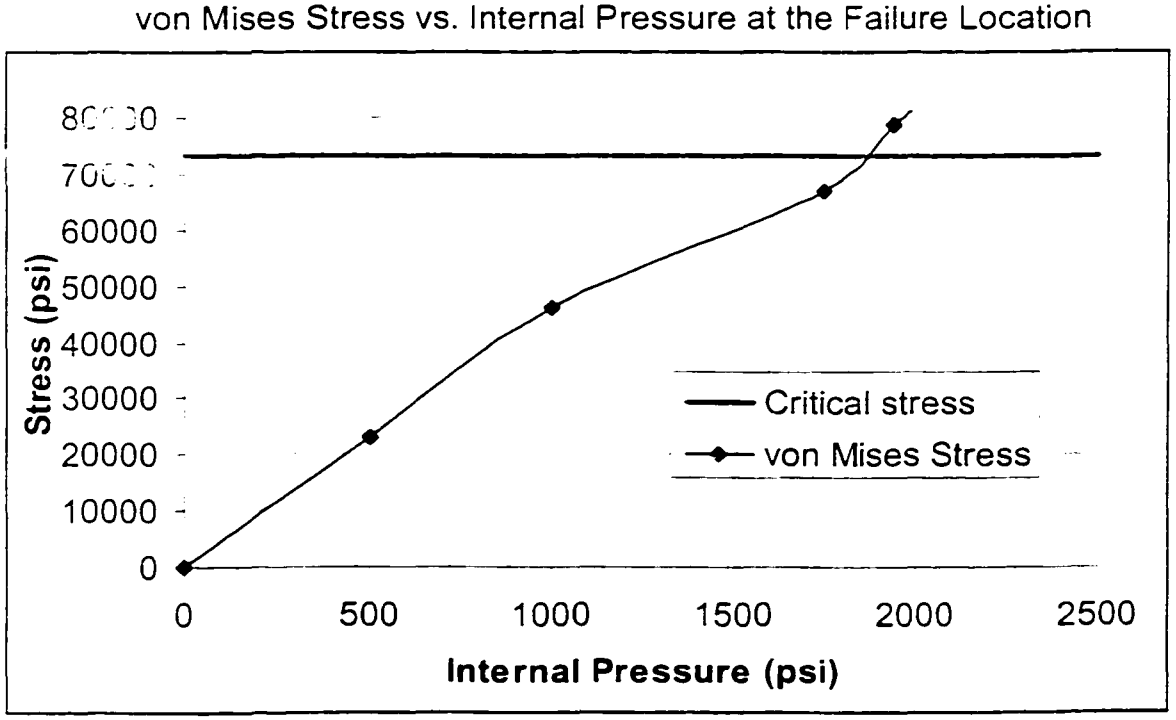


Figure 4.5.21a Burst test BCG07-C





Predicted Failure Pressure = 1849 psi
Actual Failure Pressure = 1838 psi

Figure 4.5.21b Burst test BCG07-C

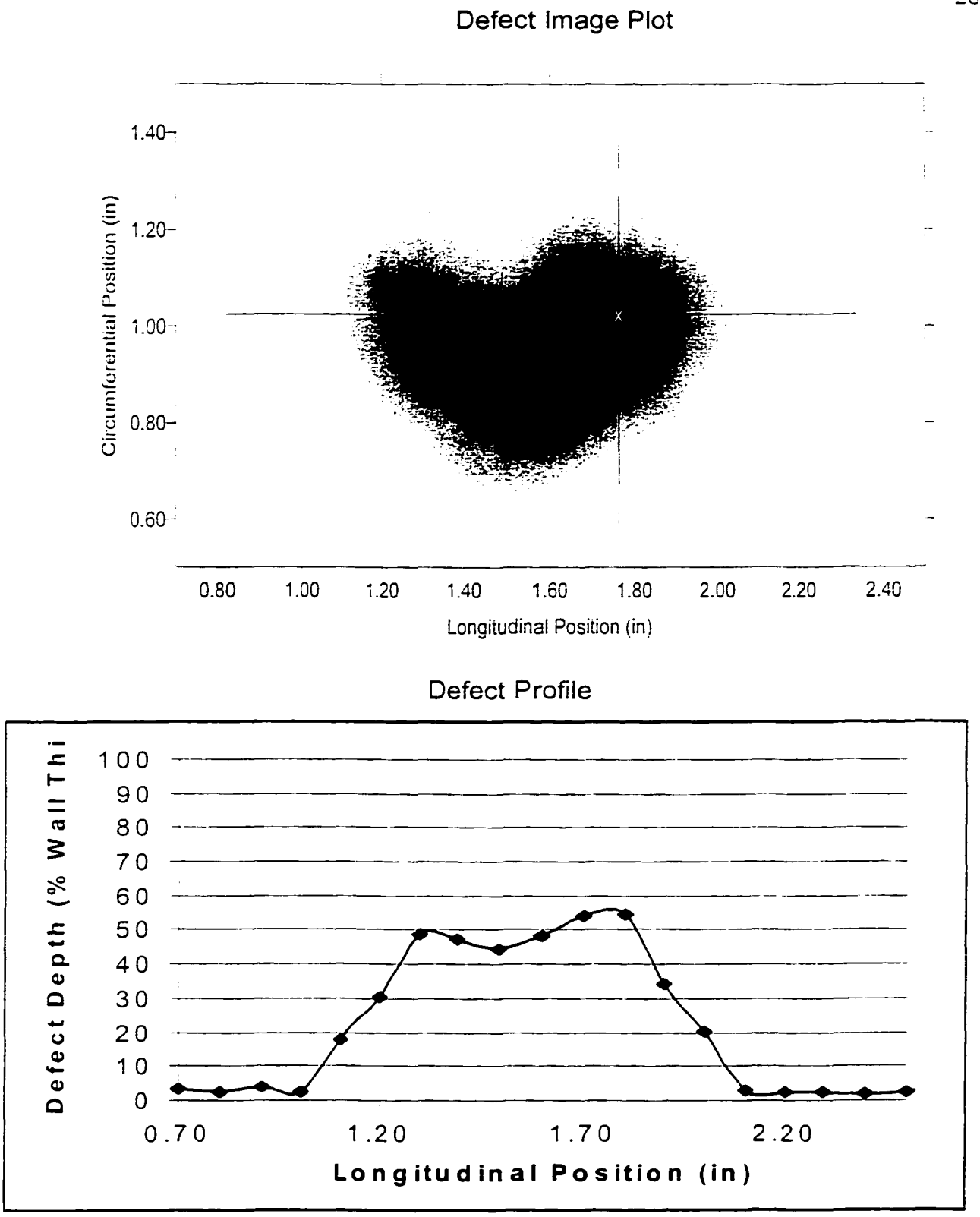
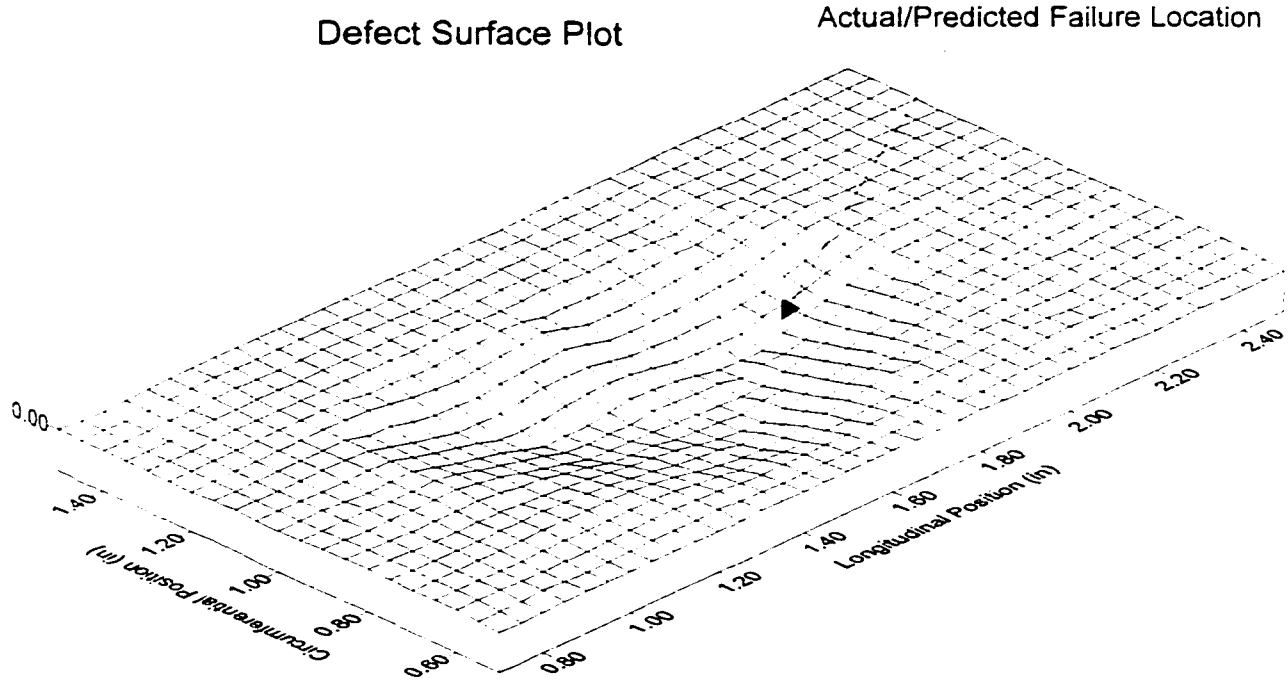
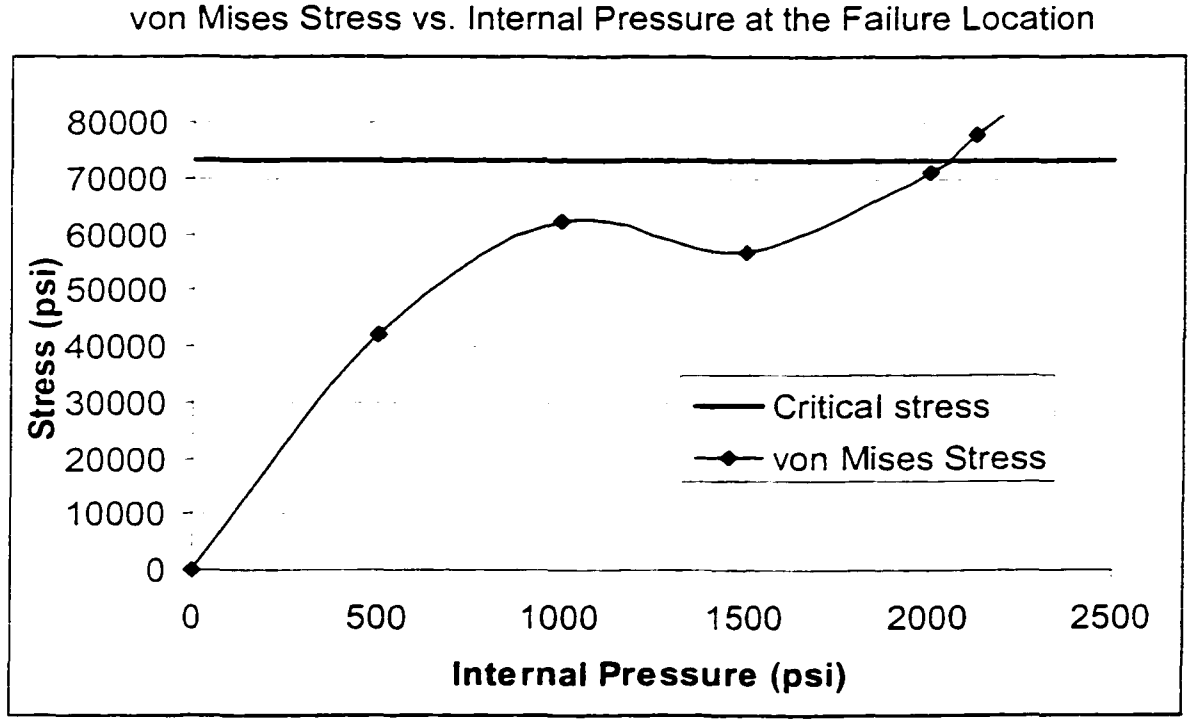


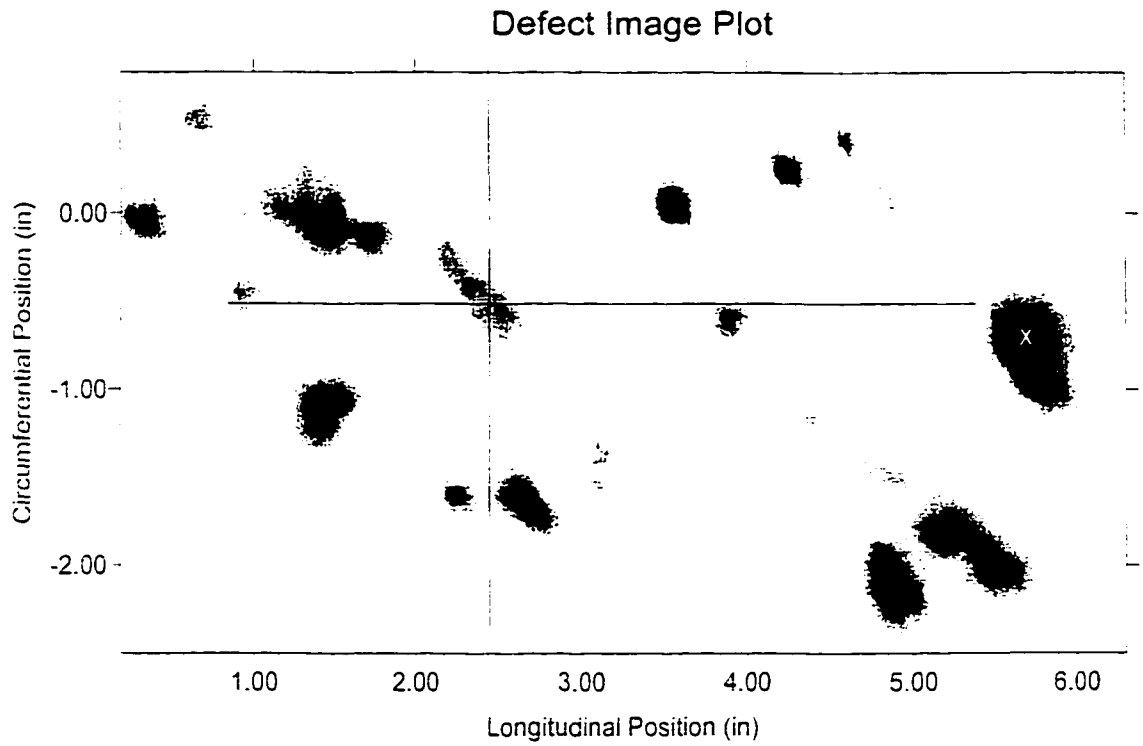
Figure 4.5.22a Burst test BCG08-E





Predicted Failure Pressure = 2040 psi
Actual Failure Pressure = 2147 psi

Figure 4.5.22b Burst test BCG08-E



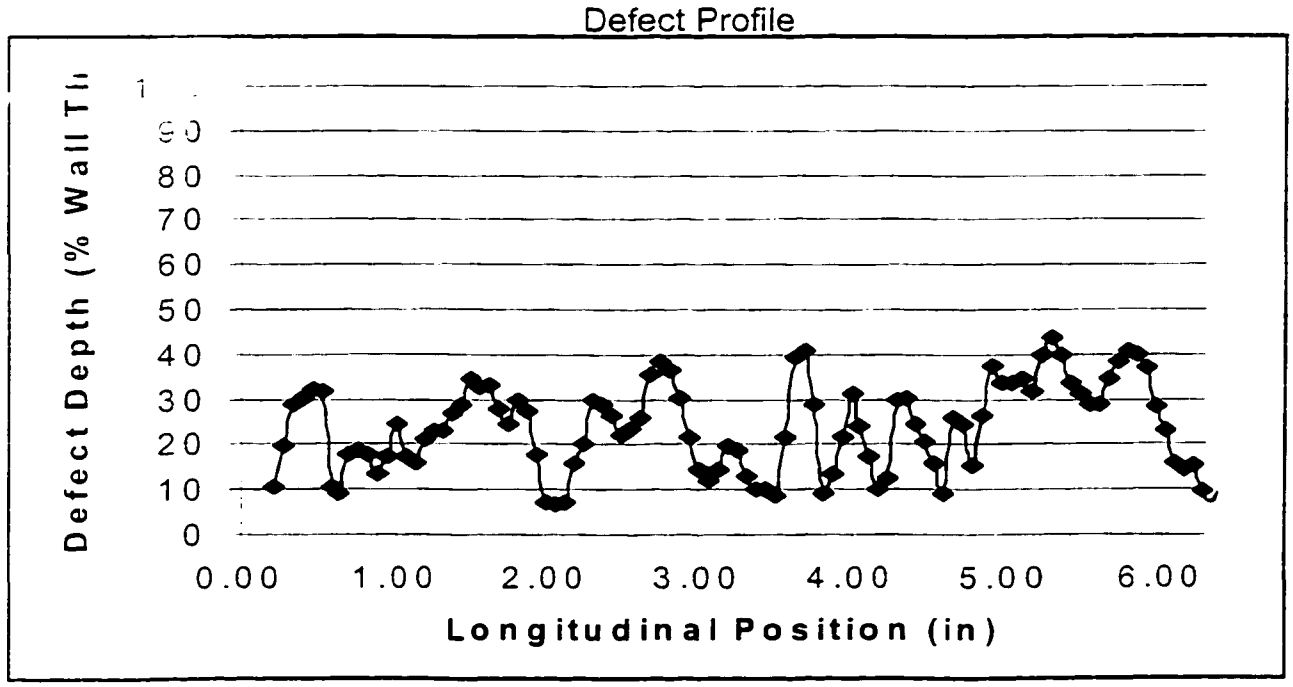
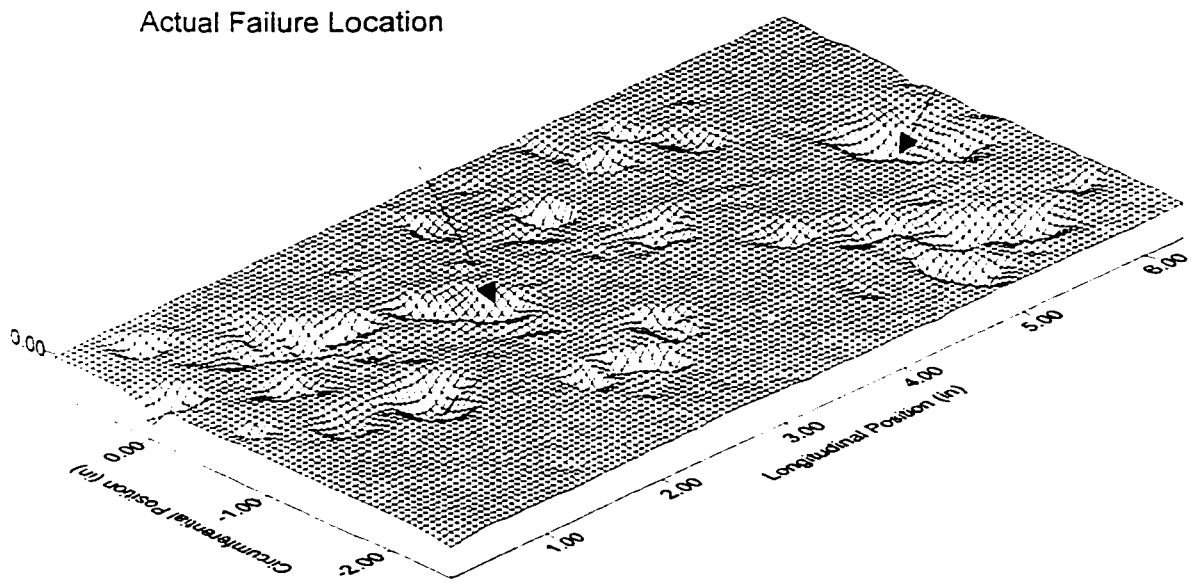
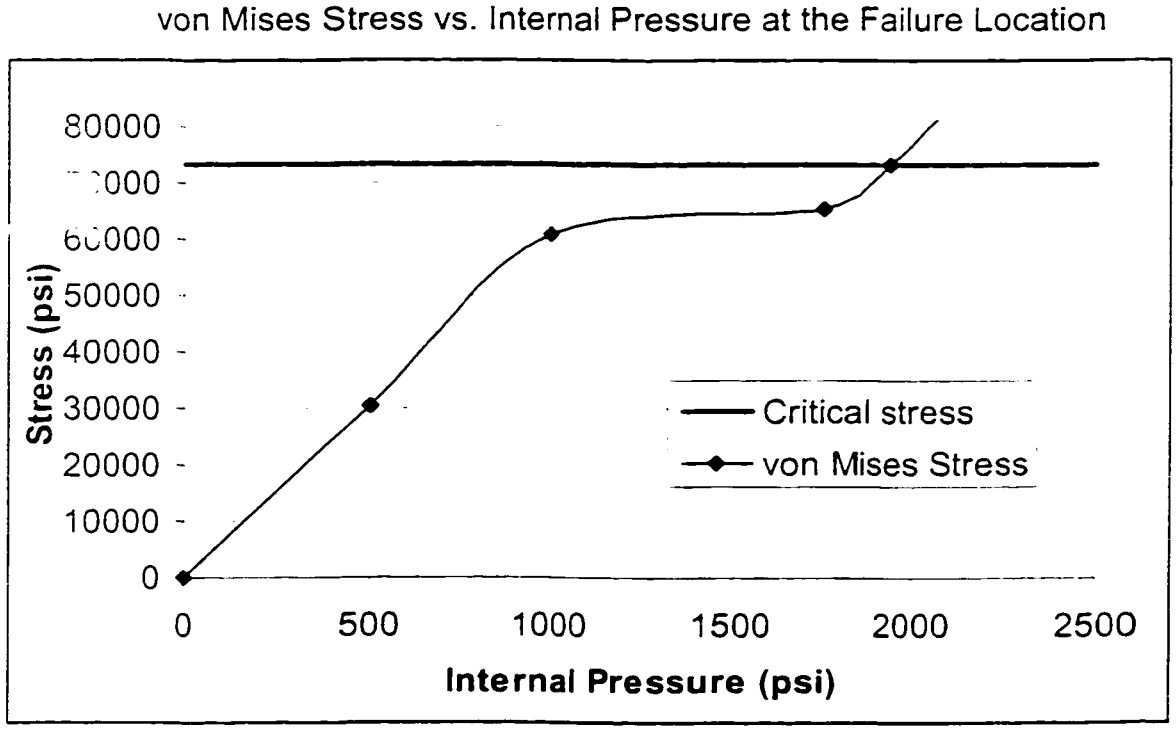


Figure 4.5.23a Burst test BCG09-F

Defect Surface Plot

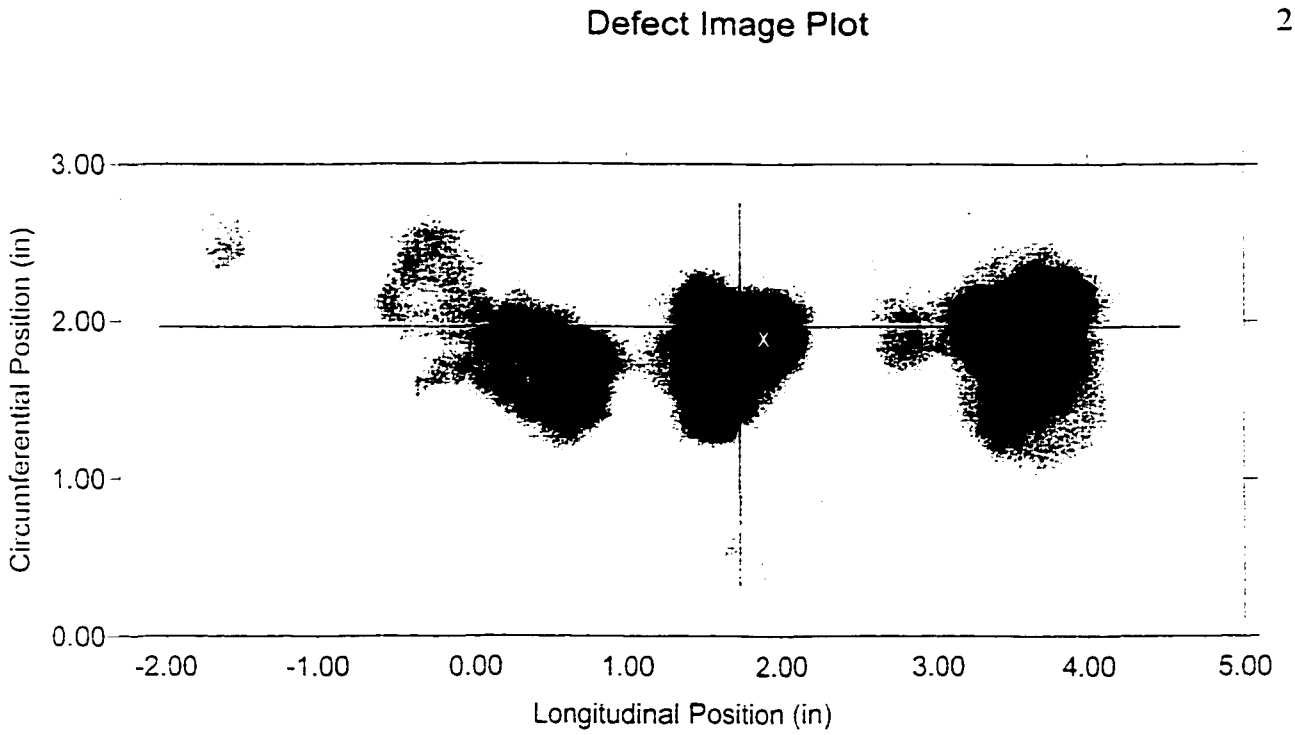
Predicted Failure Location 287





Predicted Failure Pressure = 1939 psi
Actual Failure Pressure = 1831 psi

Figure 4.5.23b Burst test BCG09-F



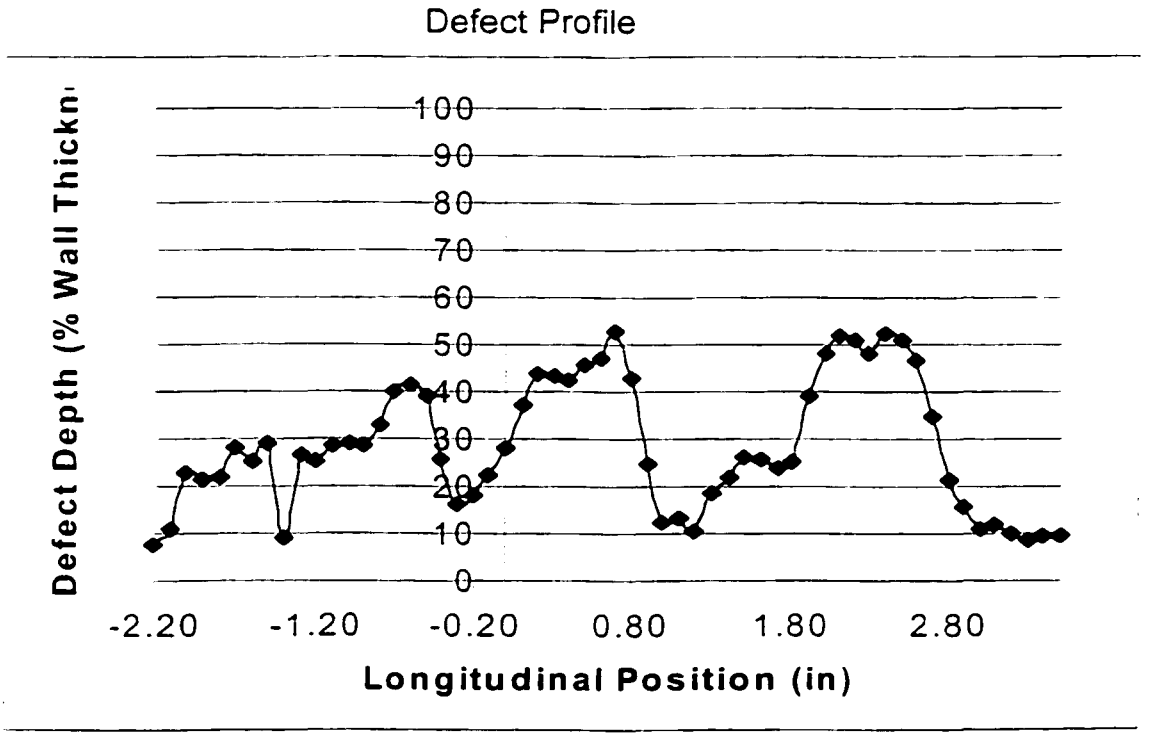
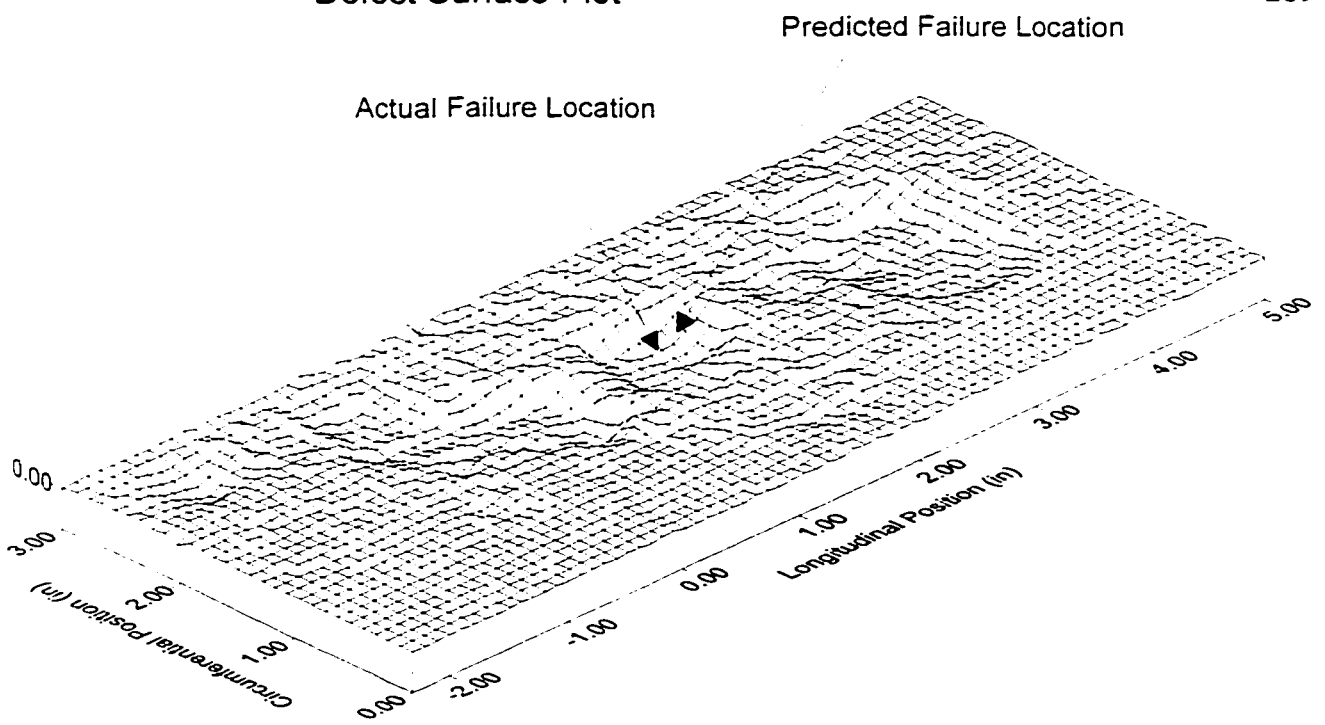
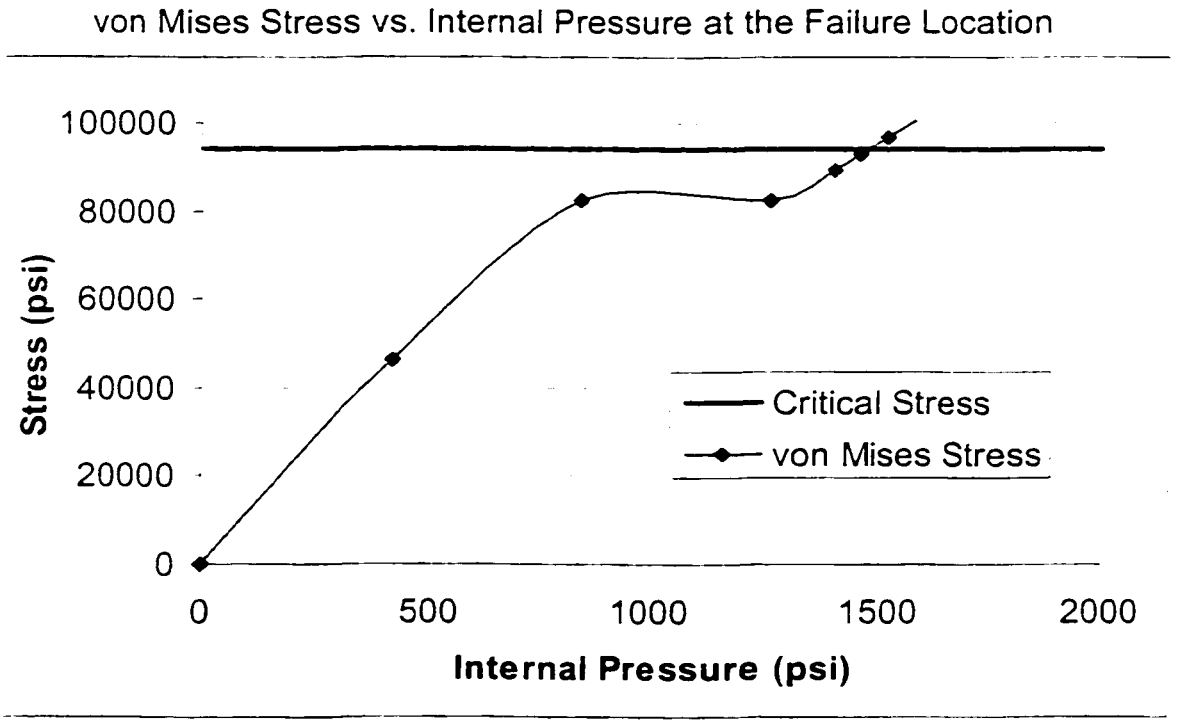


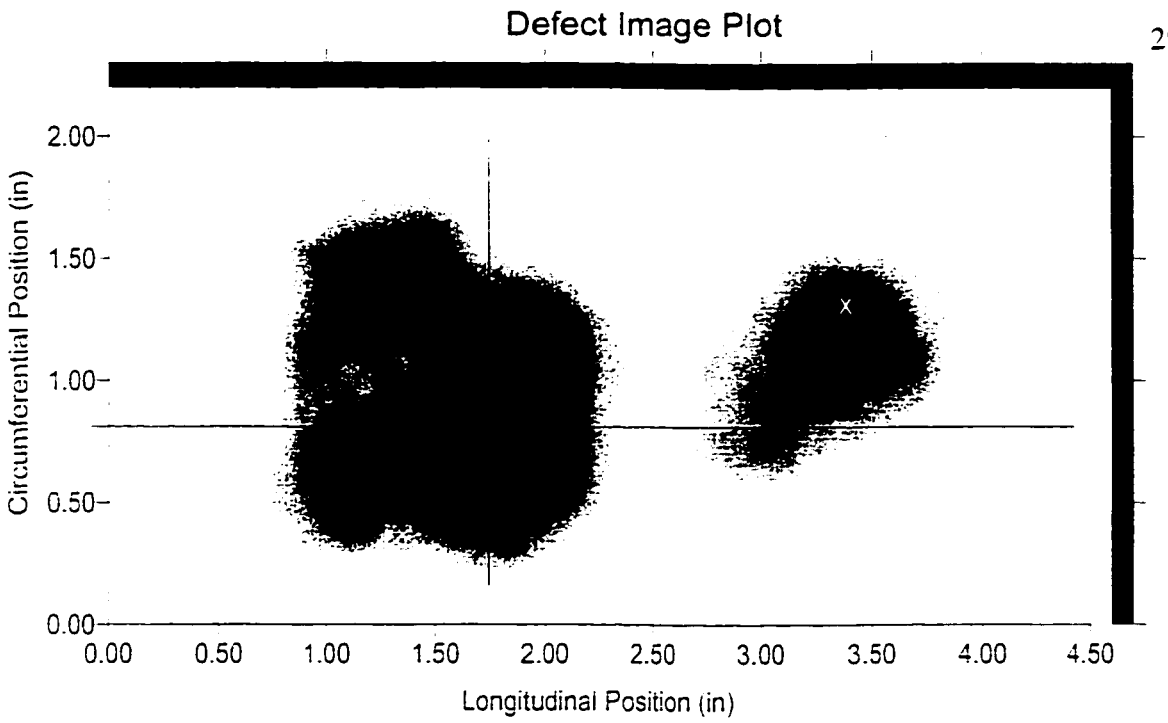
Figure 4.5.24a Burst test NOV01-XY





Predicted Failure Pressure = 1476 psi
Actual Failure Pressure = 1556 psi

Figure 4.5.24b Burst test NOV01-XY



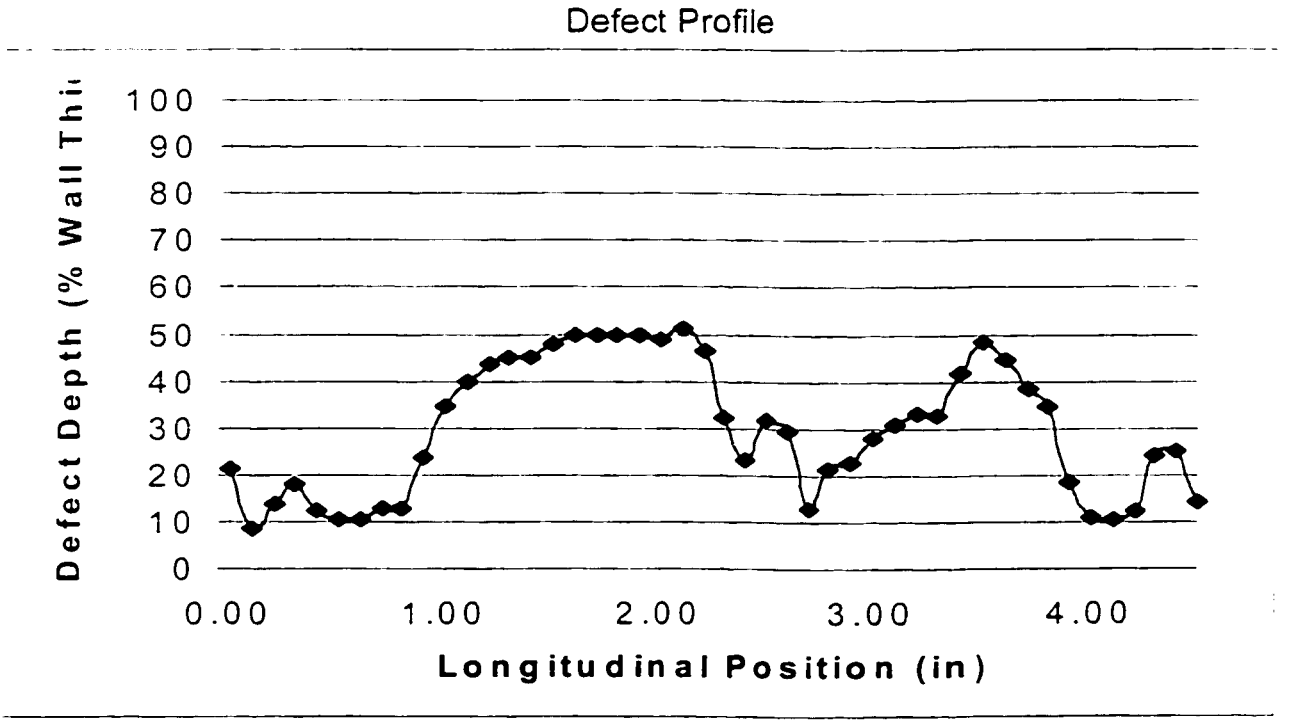
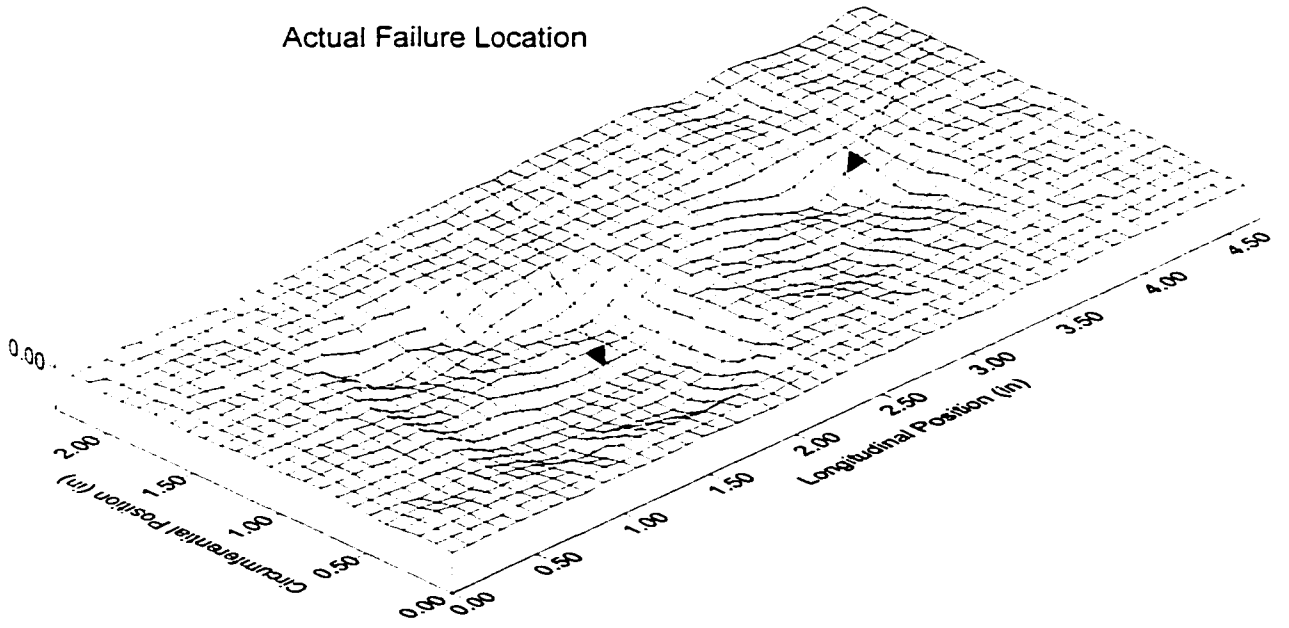
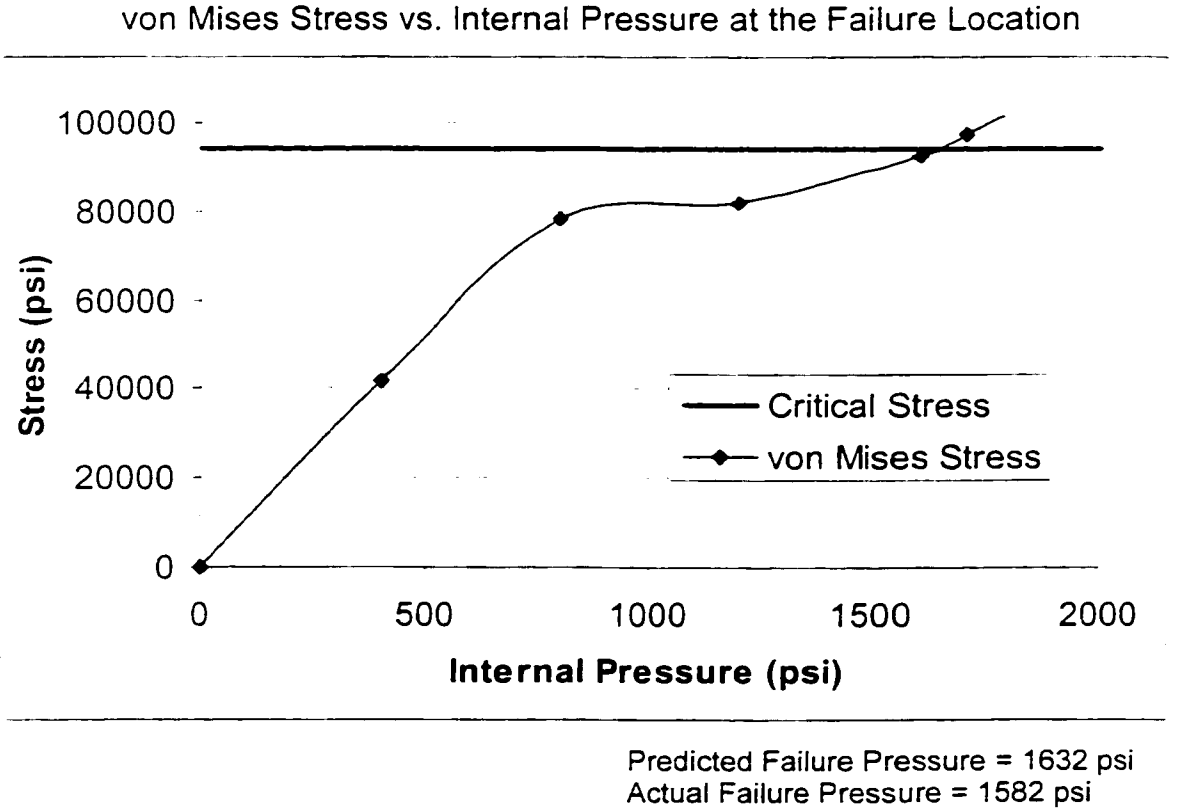


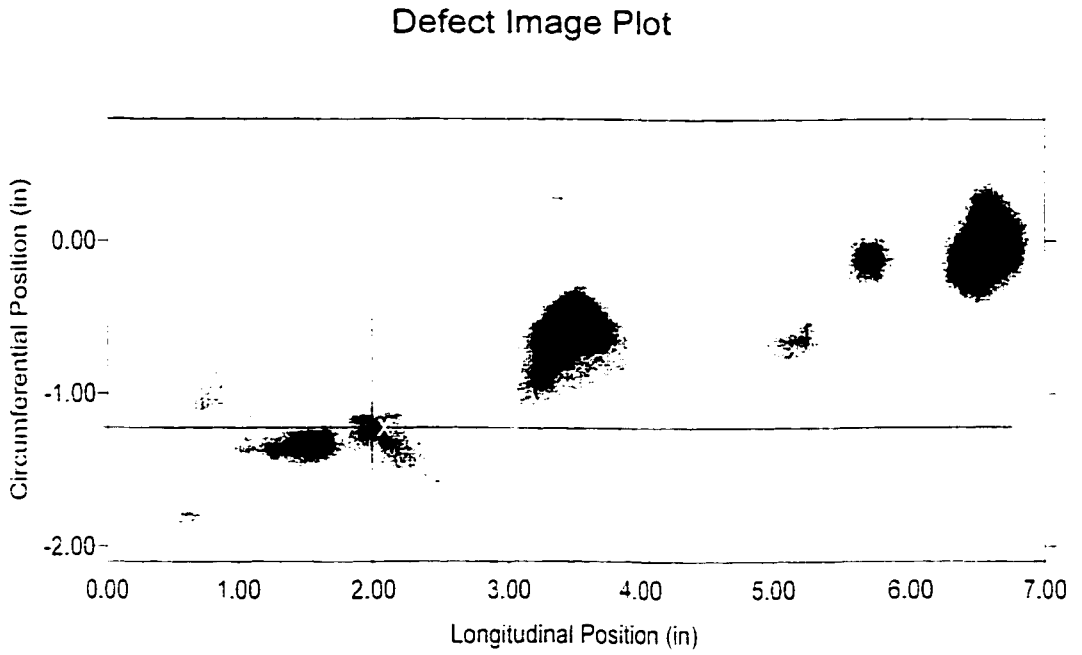
Figure 4.5.25a Burst test NOV04-J





Predicted Failure Pressure = 1632 psi
Actual Failure Pressure = 1582 psi

Figure 4.5.25b Burst test NOV04-J



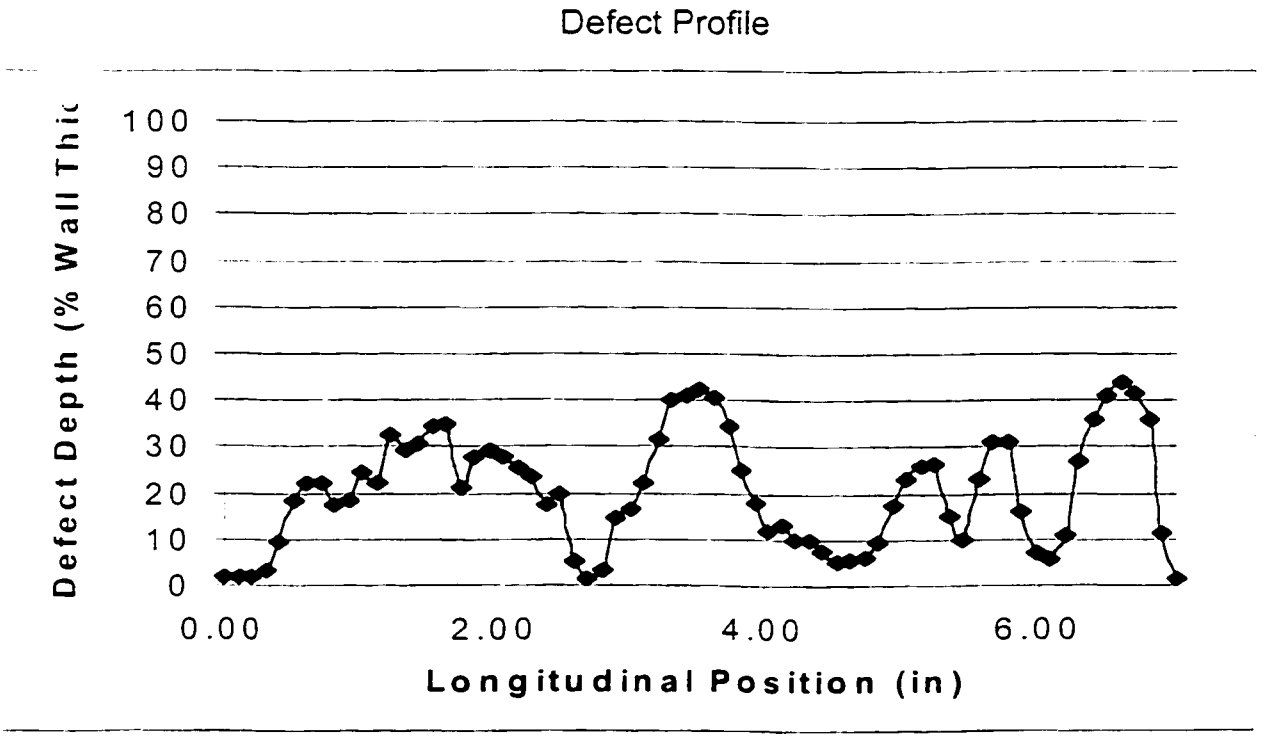
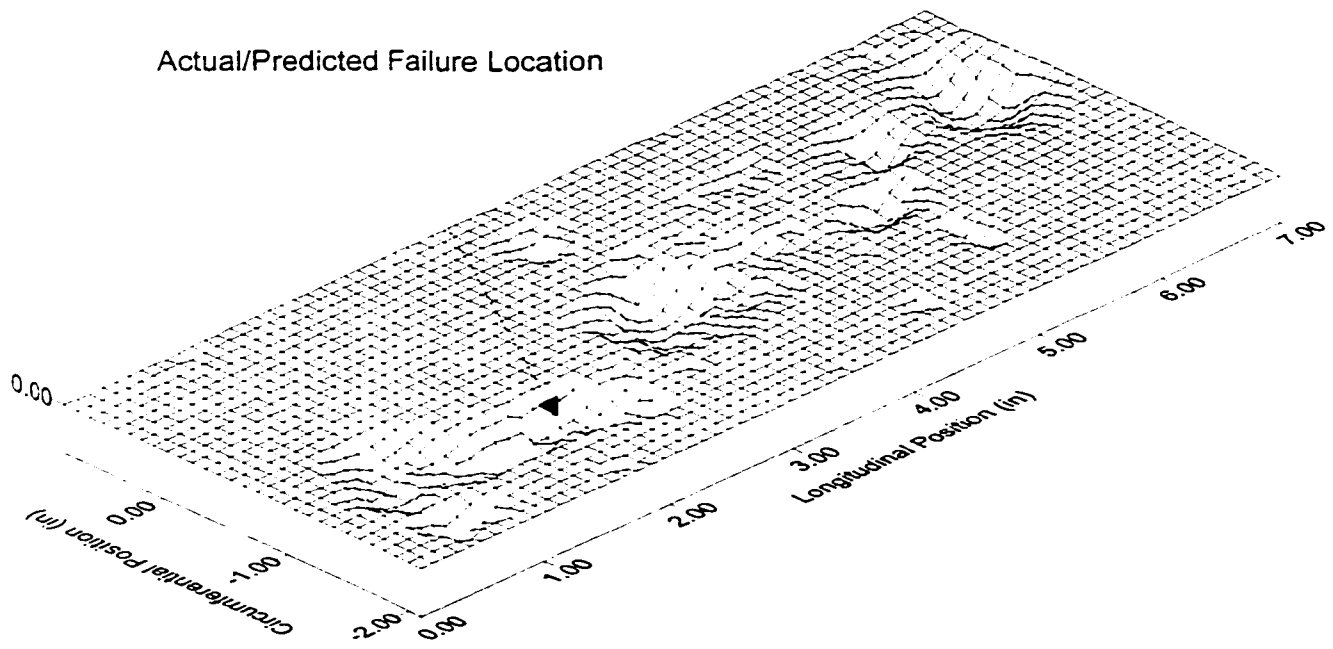
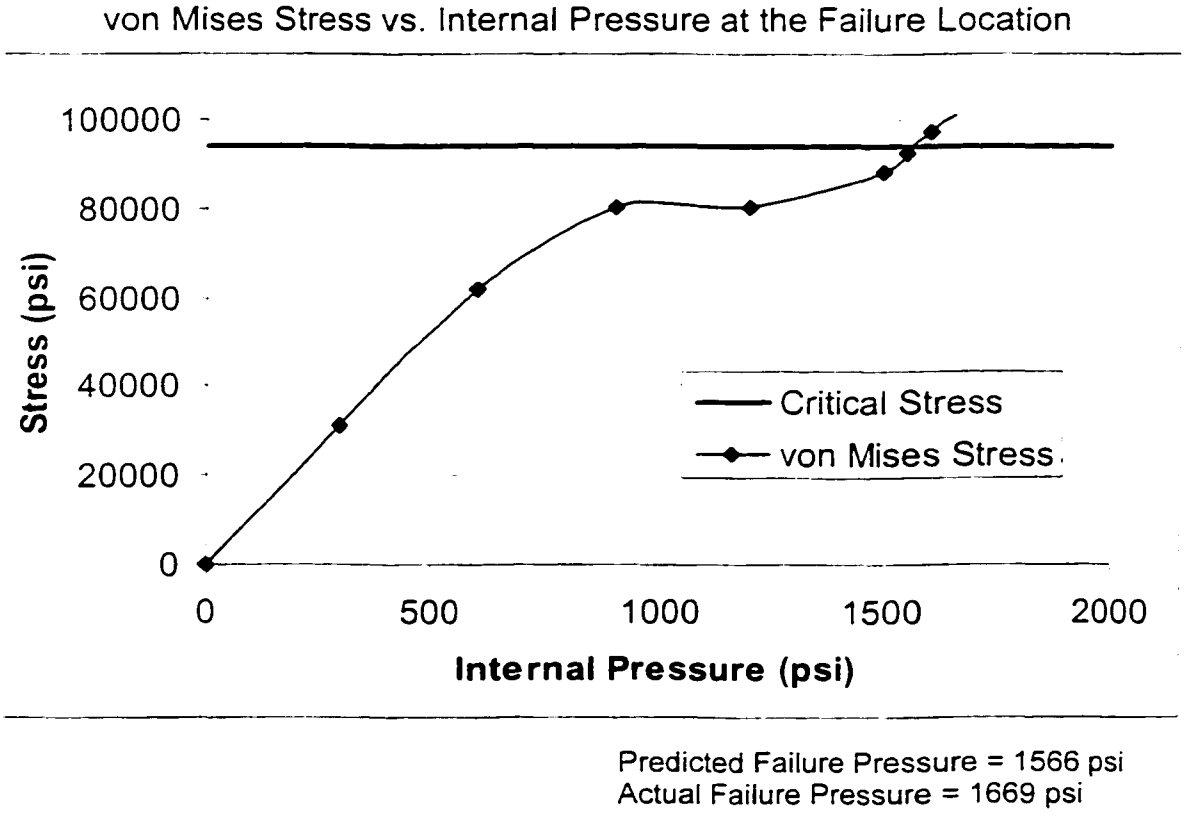


Figure 4.5.26a Burst test NOV06-D





Predicted Failure Pressure = 1566 psi
Actual Failure Pressure = 1669 psi

Figure 4.5.26b Burst test NOV06-D

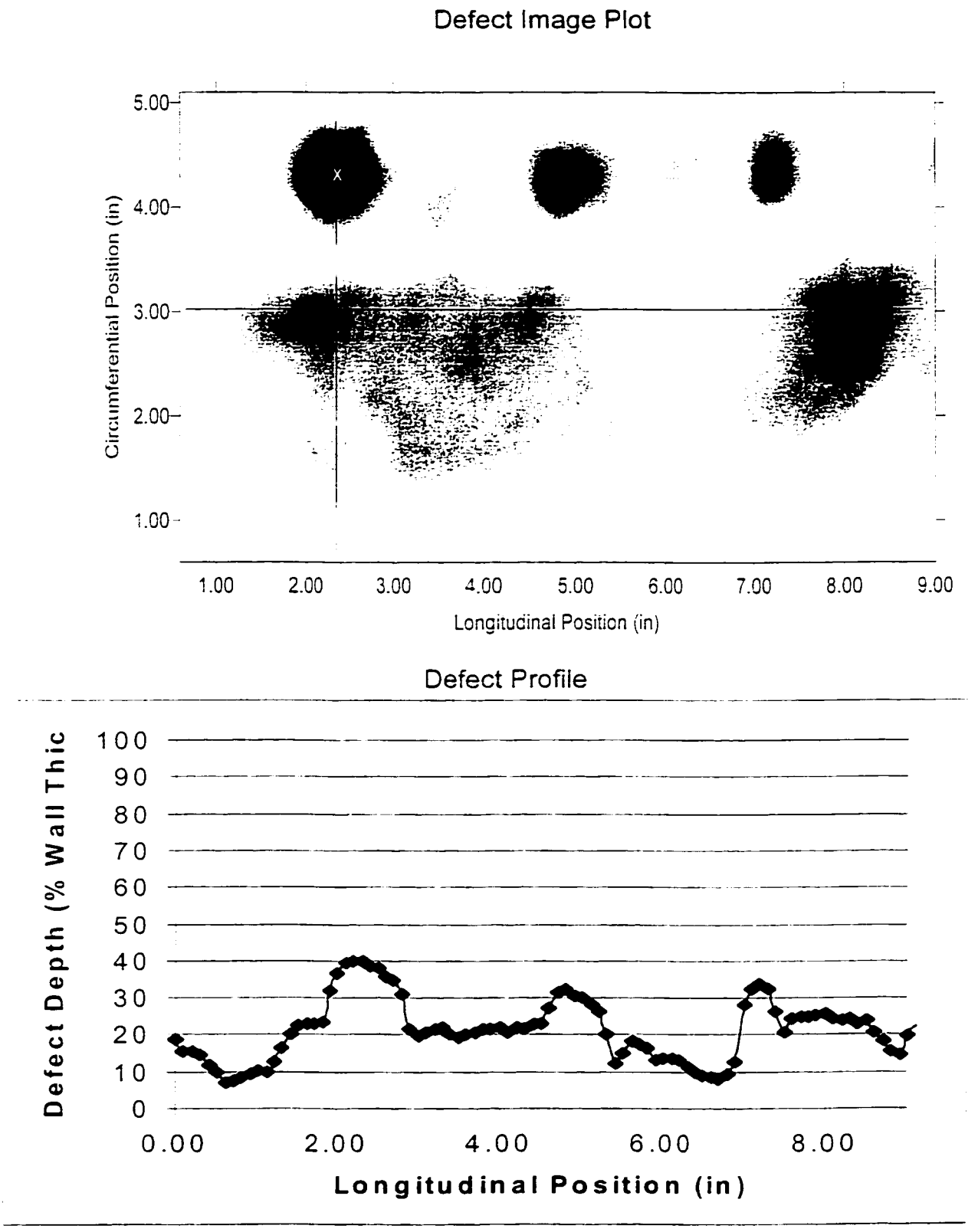
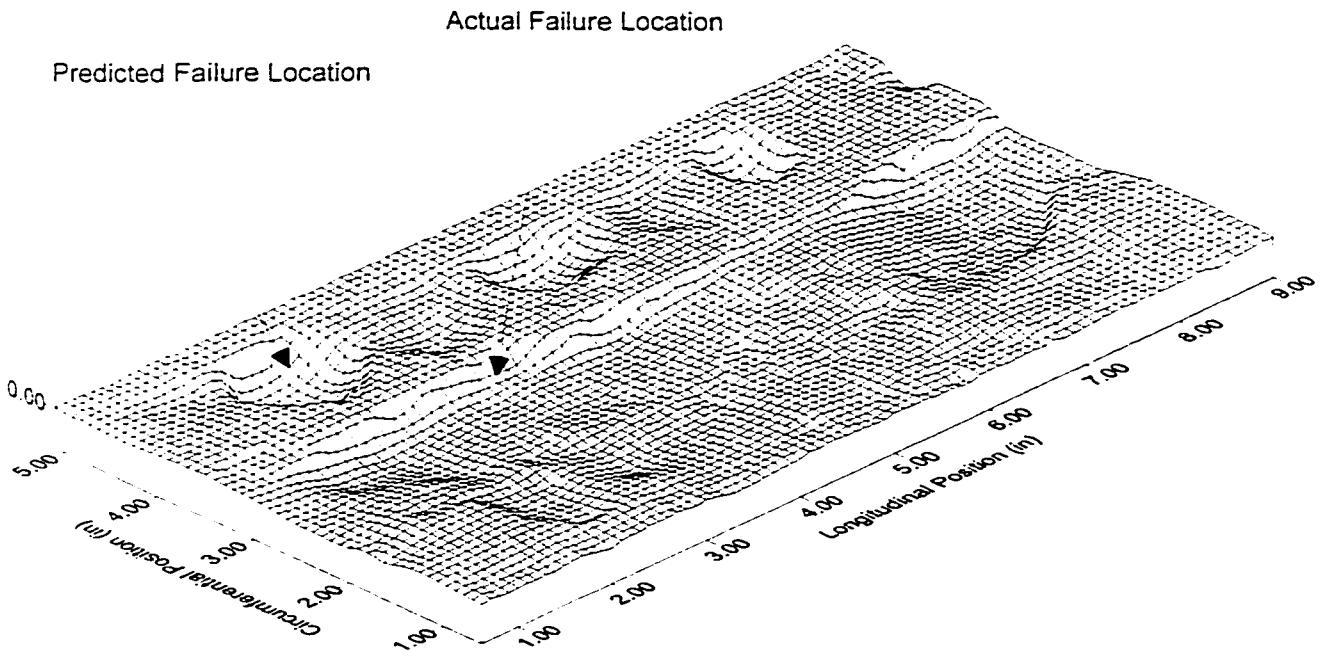
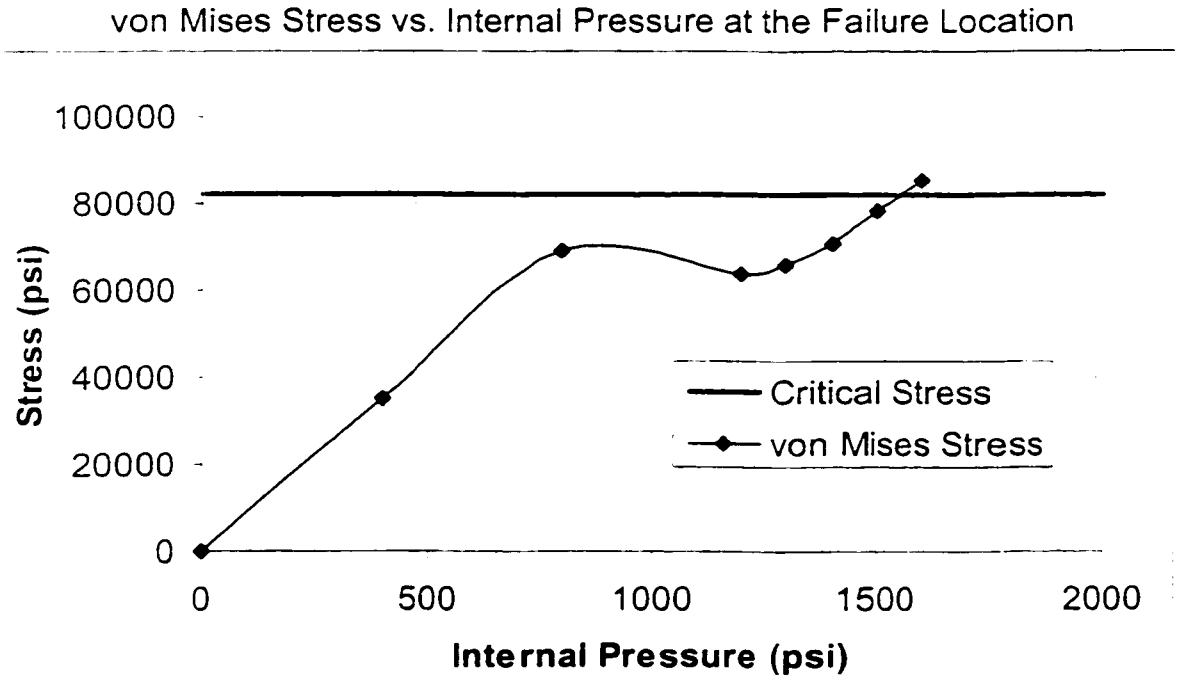


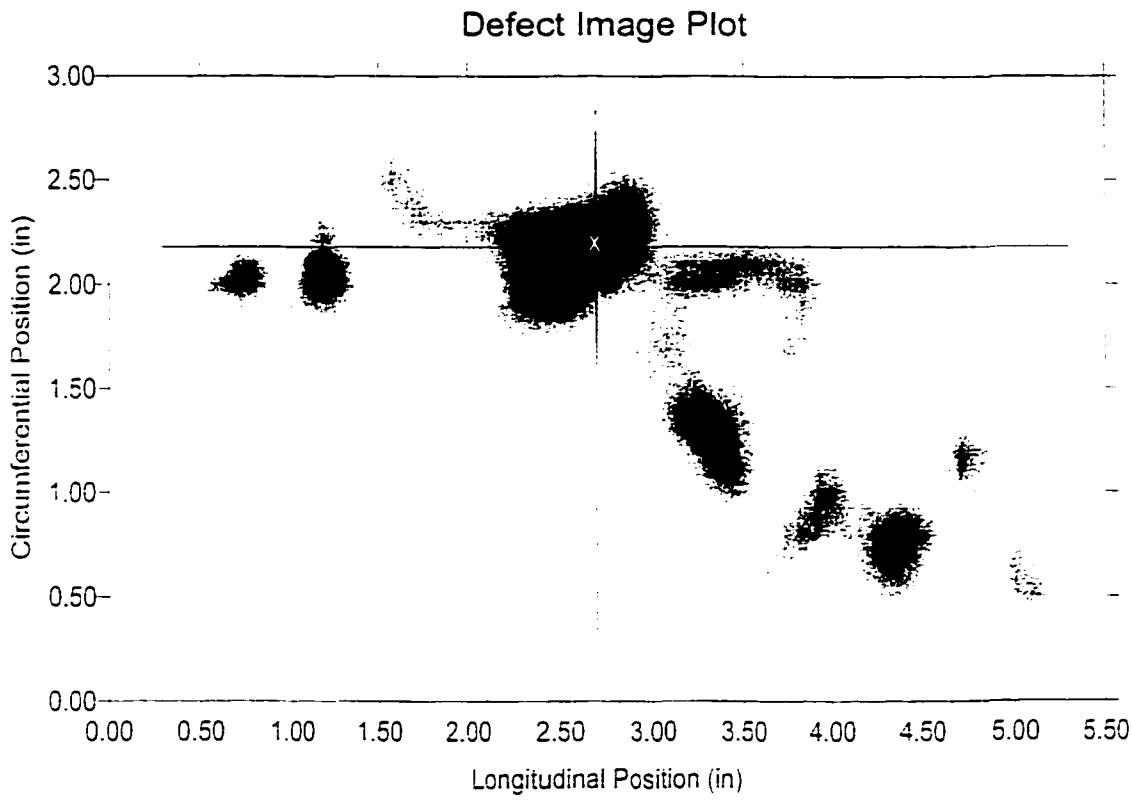
Figure 4.5.27a Burst test TCP01-C





Predicted Failure Pressure = 1555 psi
Actual Failure Pressure = 1567 psi

Figure 4.5.27b Burst test TCP01-C



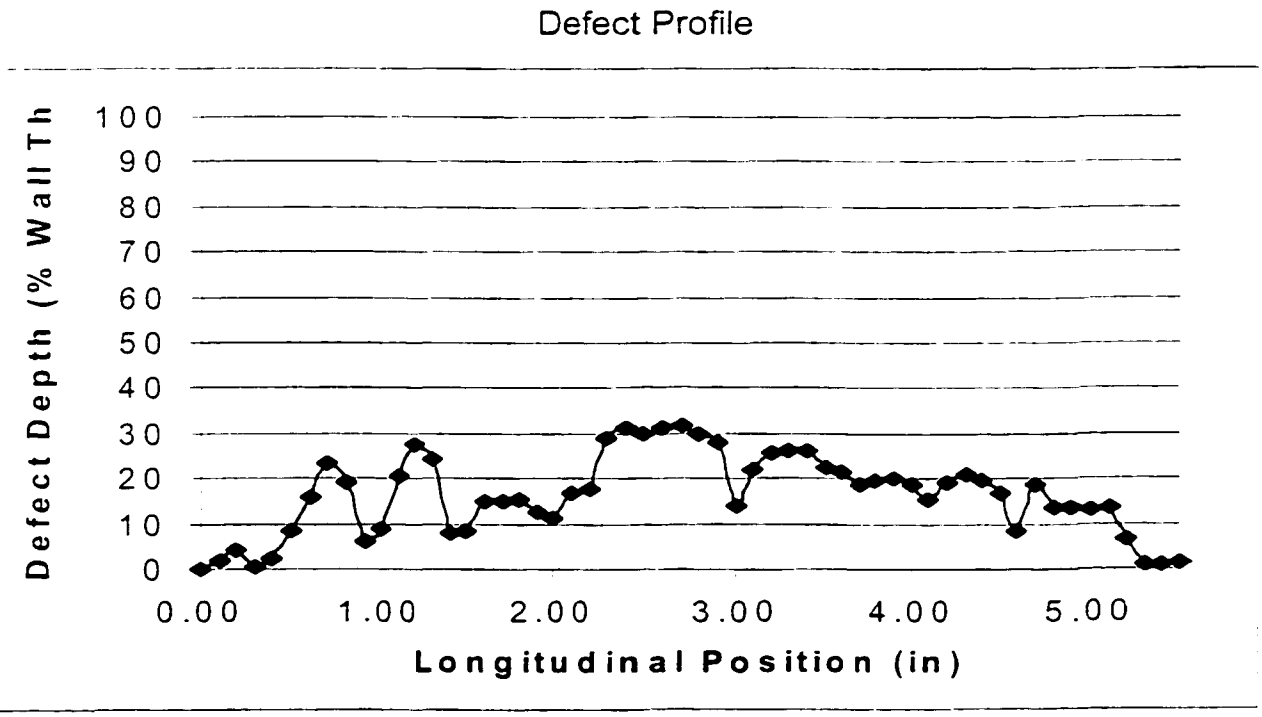


Figure 4.5.28a Burst test TCP02-G

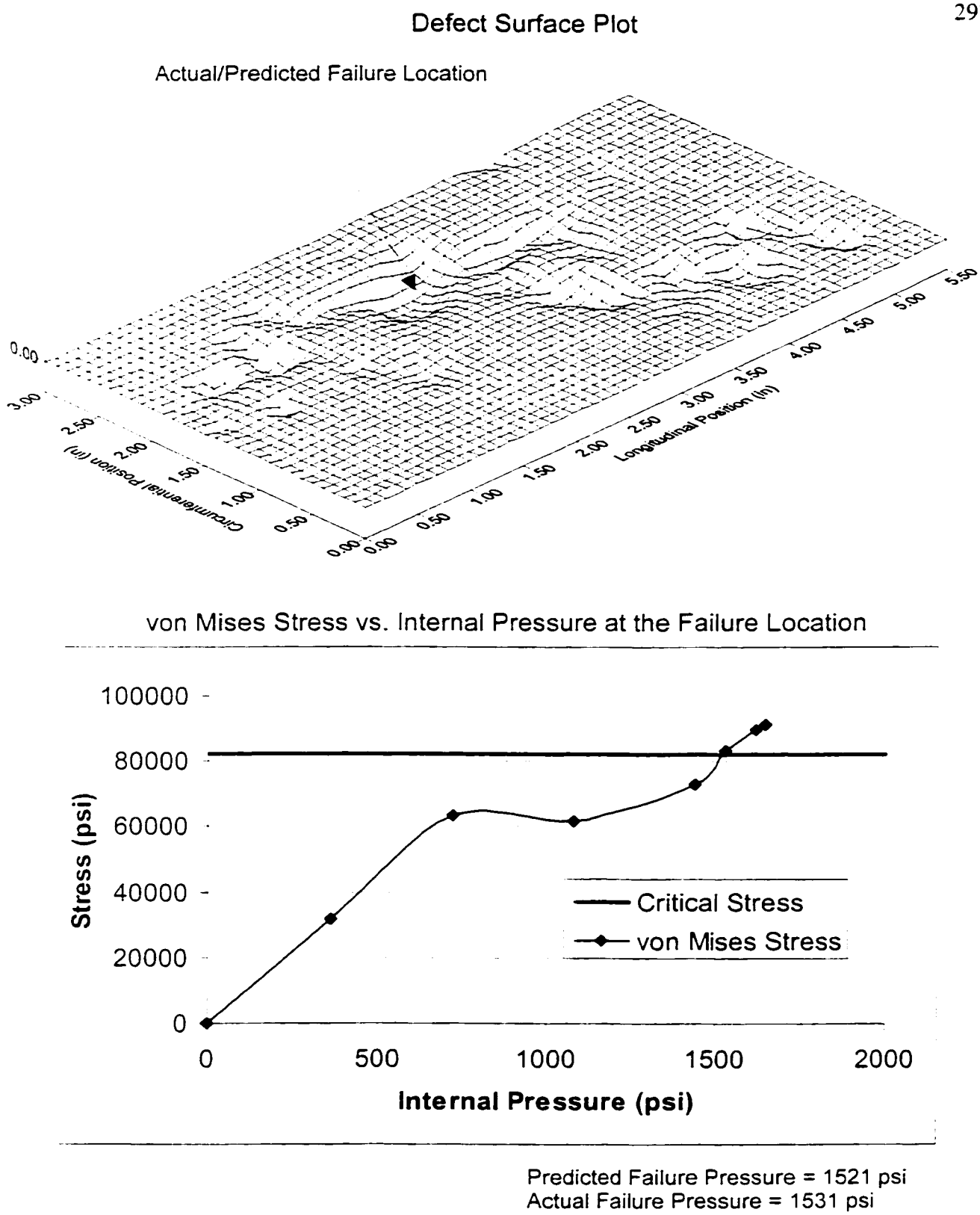


Figure 4.5.28b Burst test TCP02-G

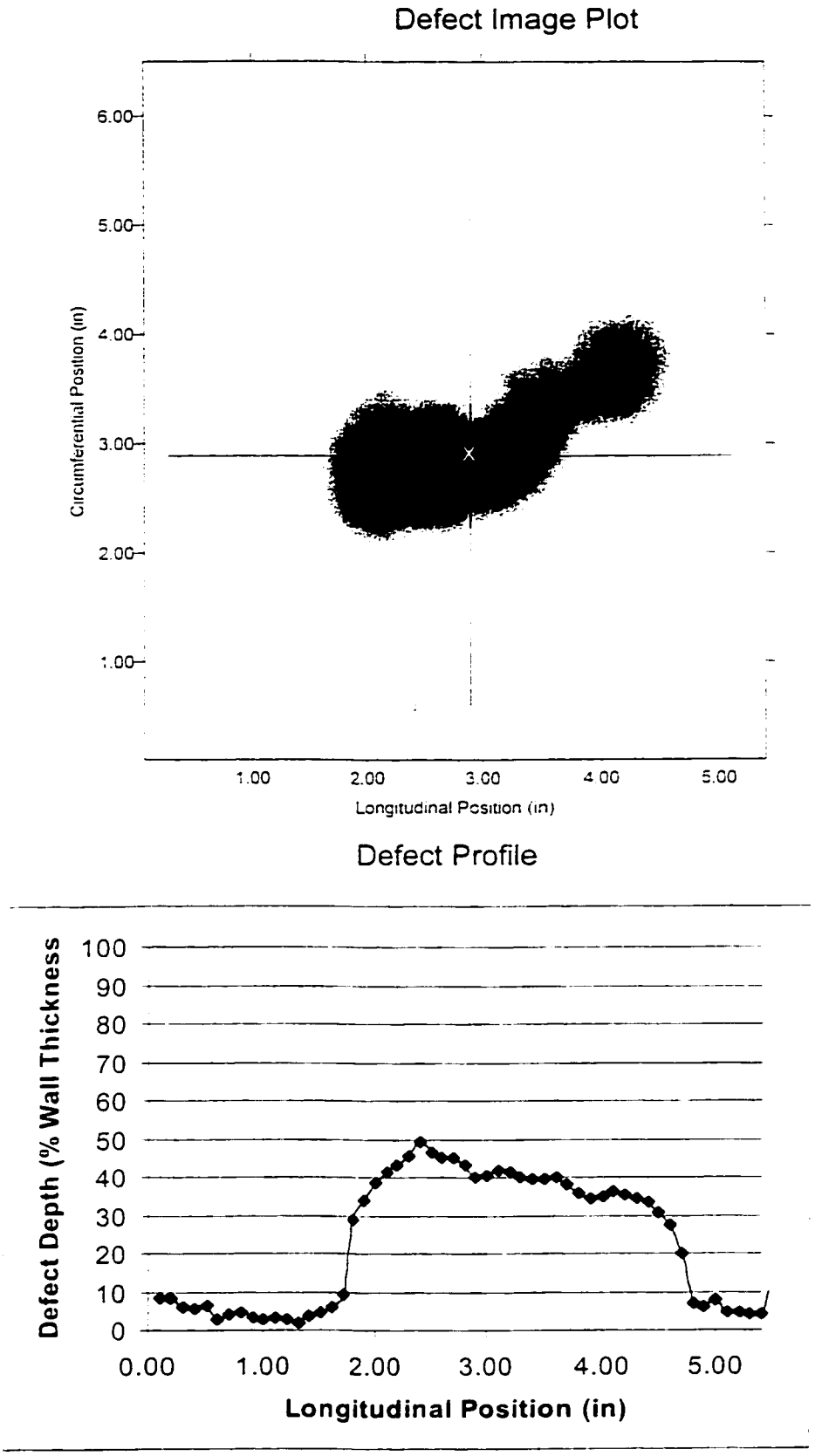


Figure 4.5.29a Burst test TCP03-C

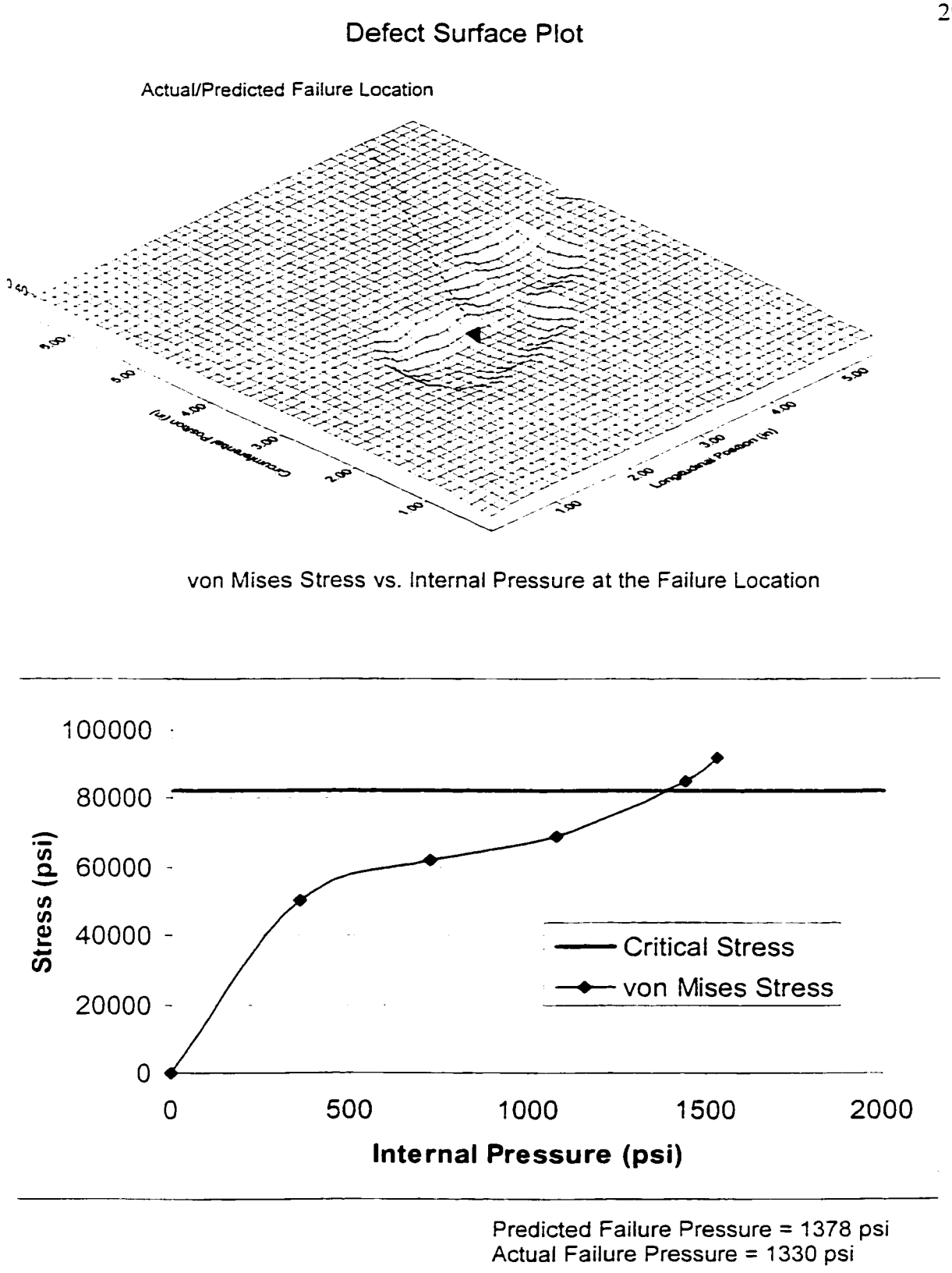


Figure 4.5.29b Burst test TCP03-C

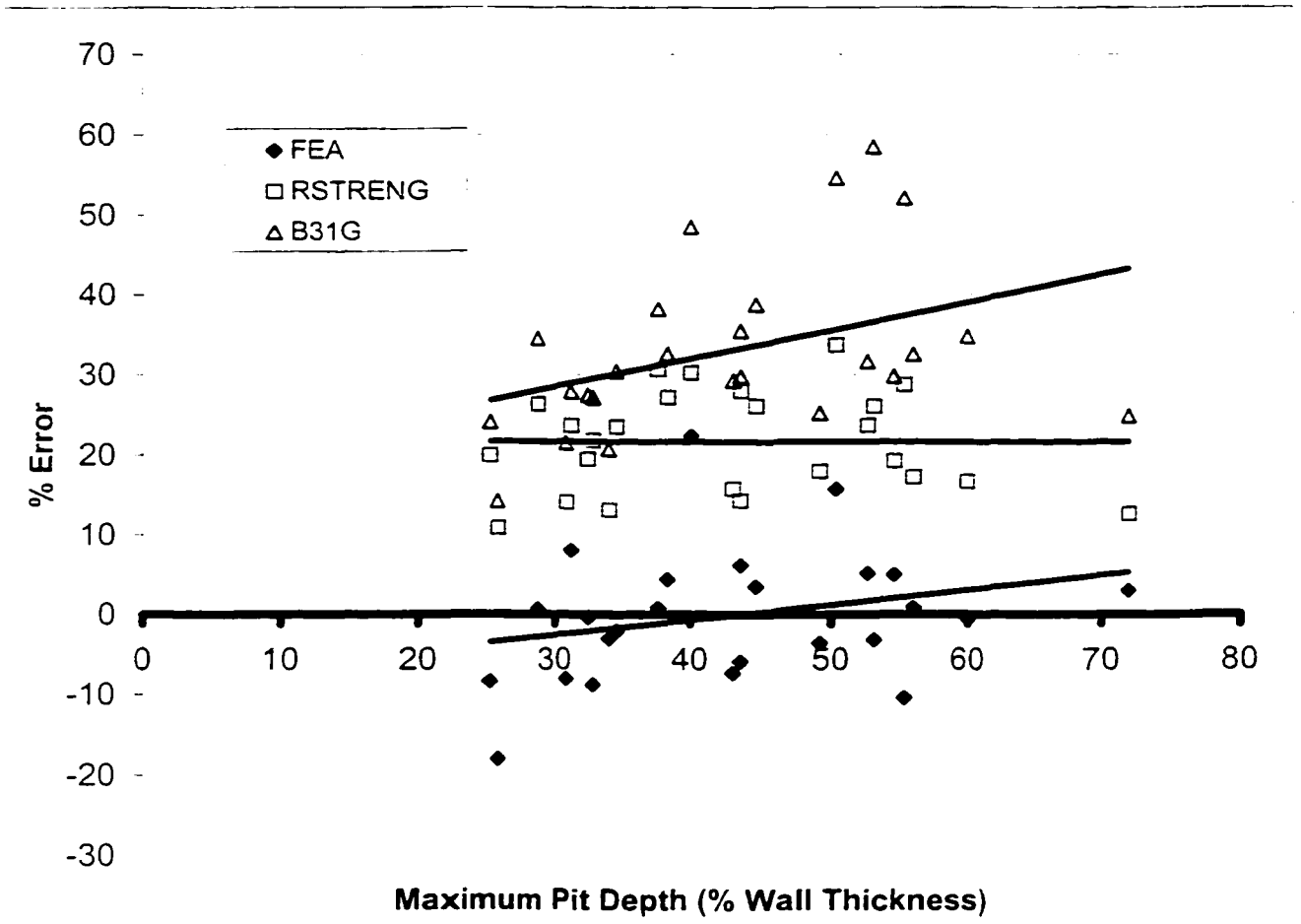


Figure 4.5.30 Error in the Finite Element predictions, with the RSTRENG and B31G results

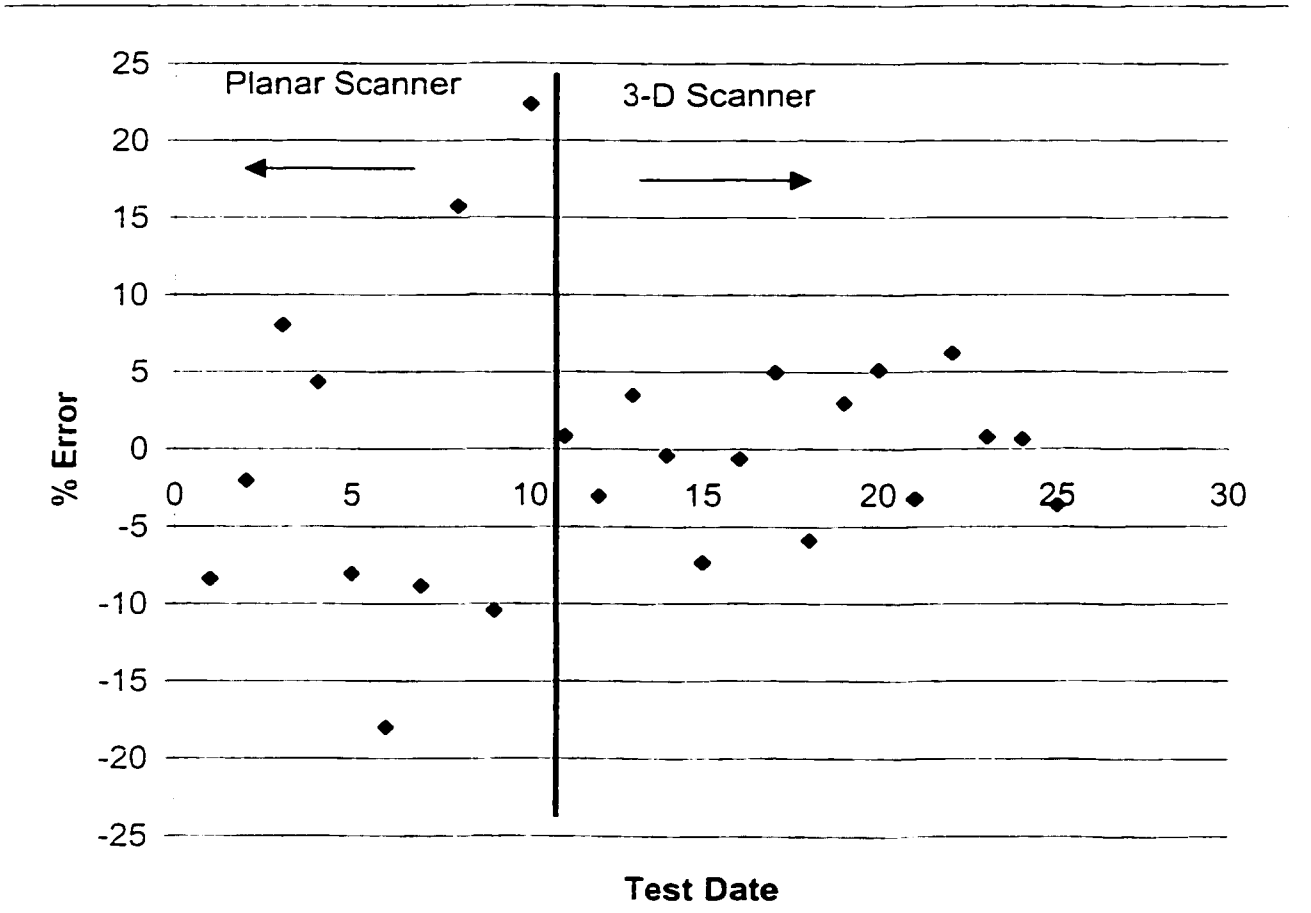


Figure 4.5.31 Error in the Finite Element predictions plotted as a function of time

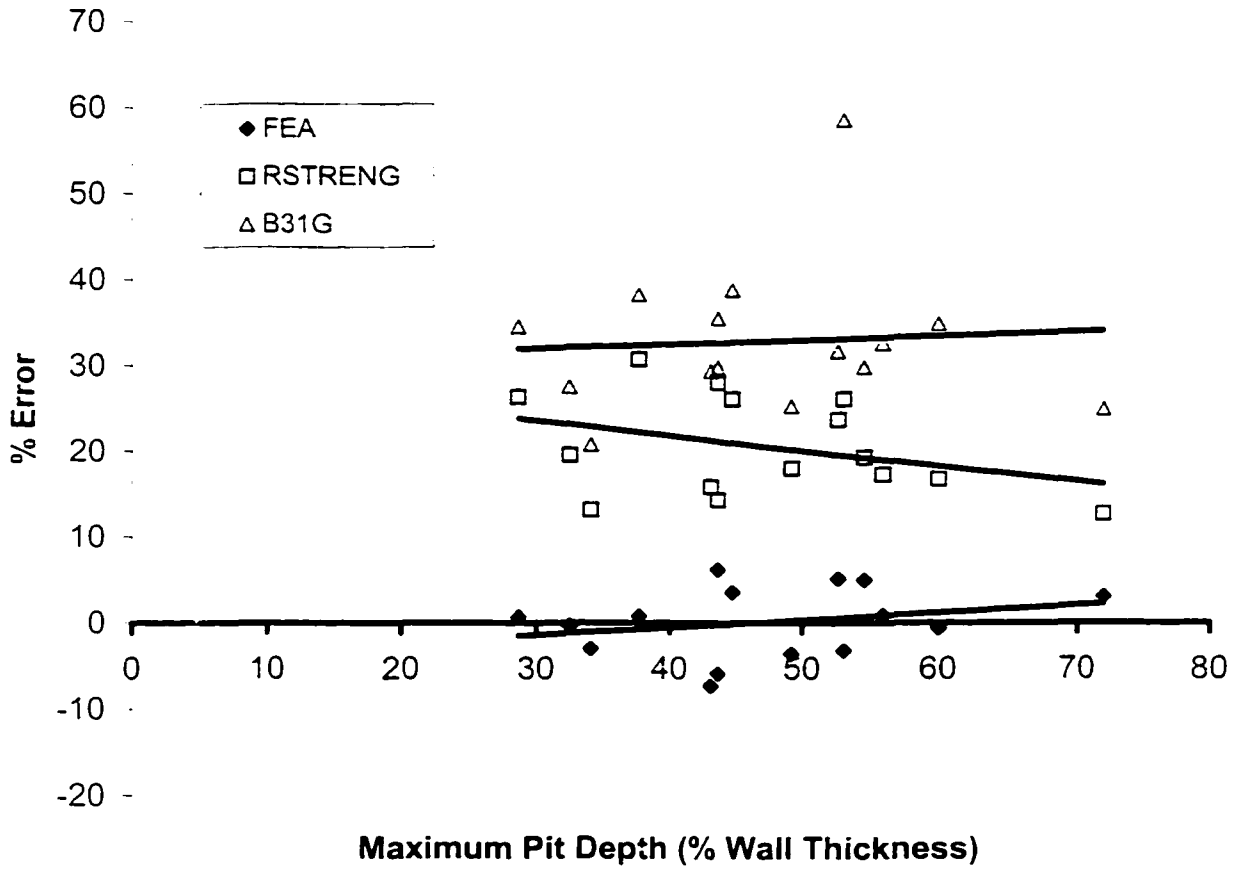


Figure 4.5.32 Error in the Finite Element predictions for defects mapped with the 3-D scanner

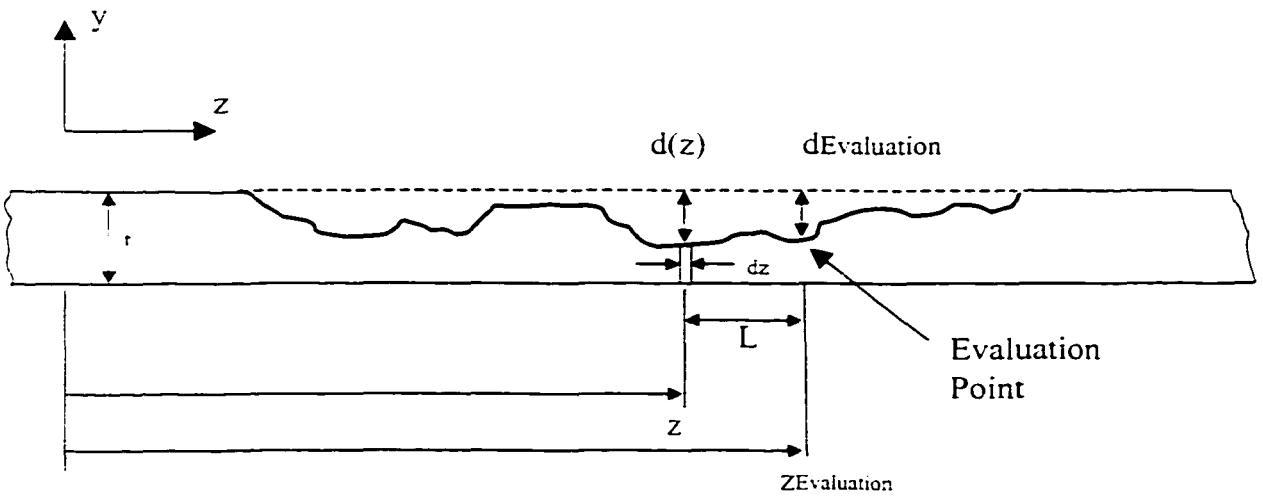


Figure 5.1.1 Corrosion evaluation parameters

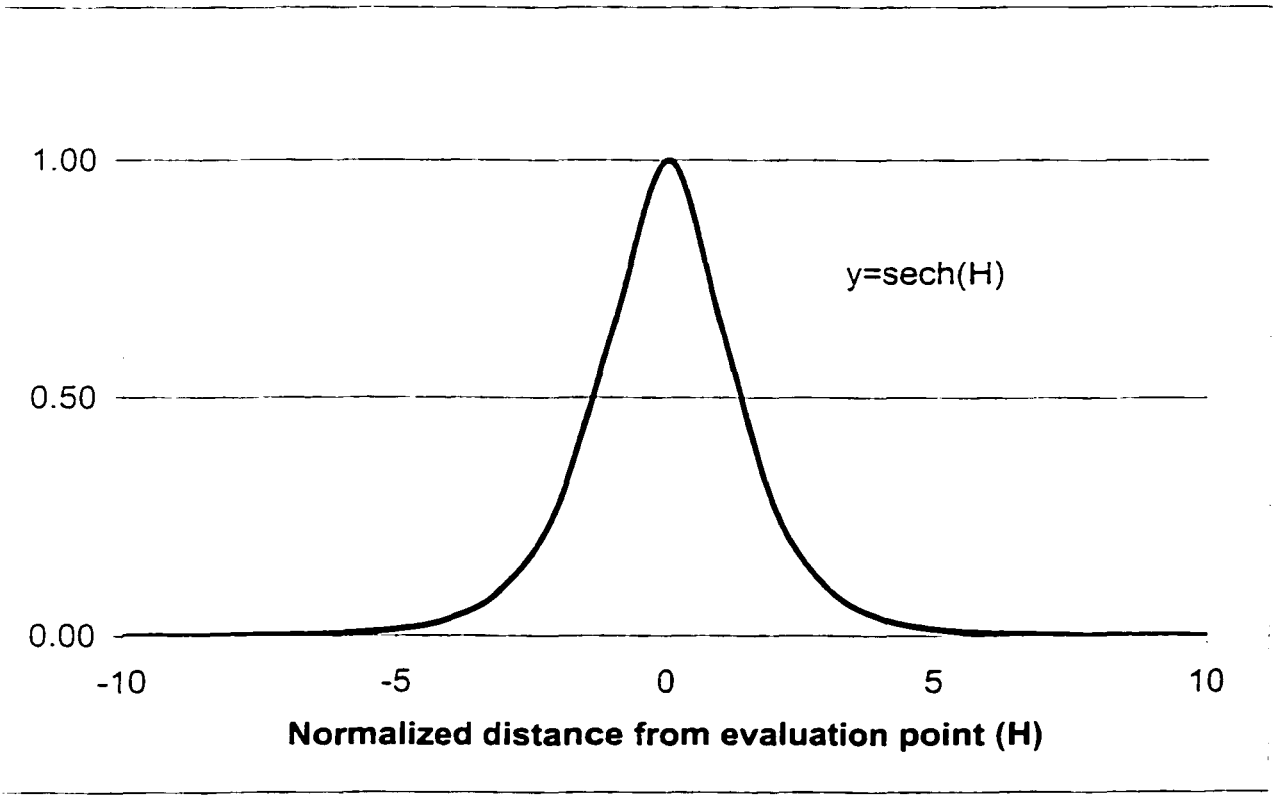


Figure 5.1.2 The hyperbolic secant function

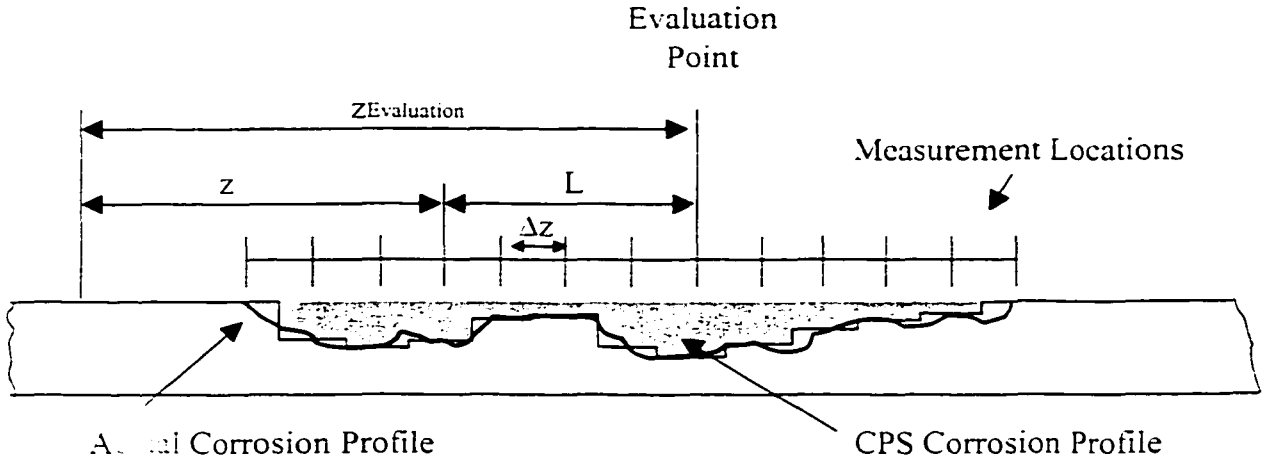


Figure 5.1.3 Actual and CPS Corrosion Profiles

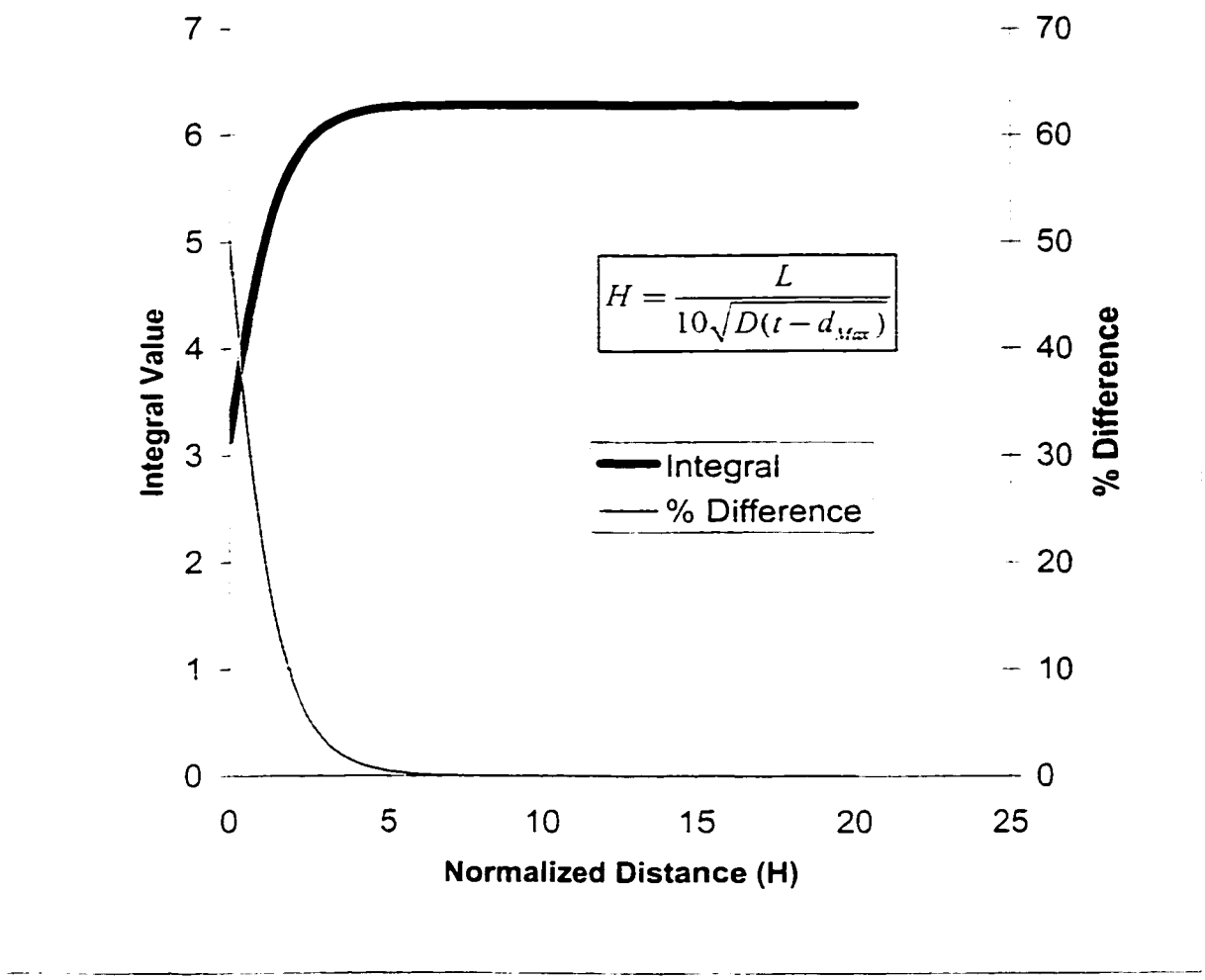
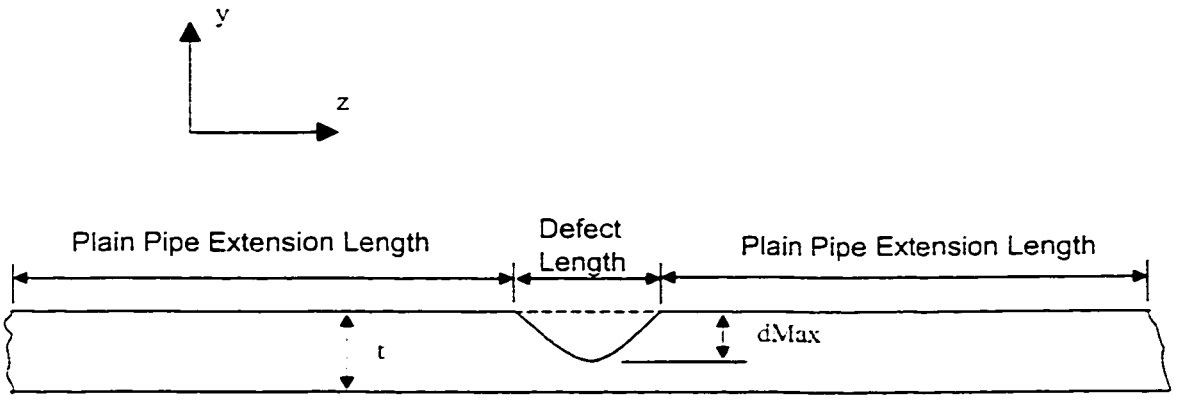


Figure 5.1.4 Integral of the hyperbolic secant function



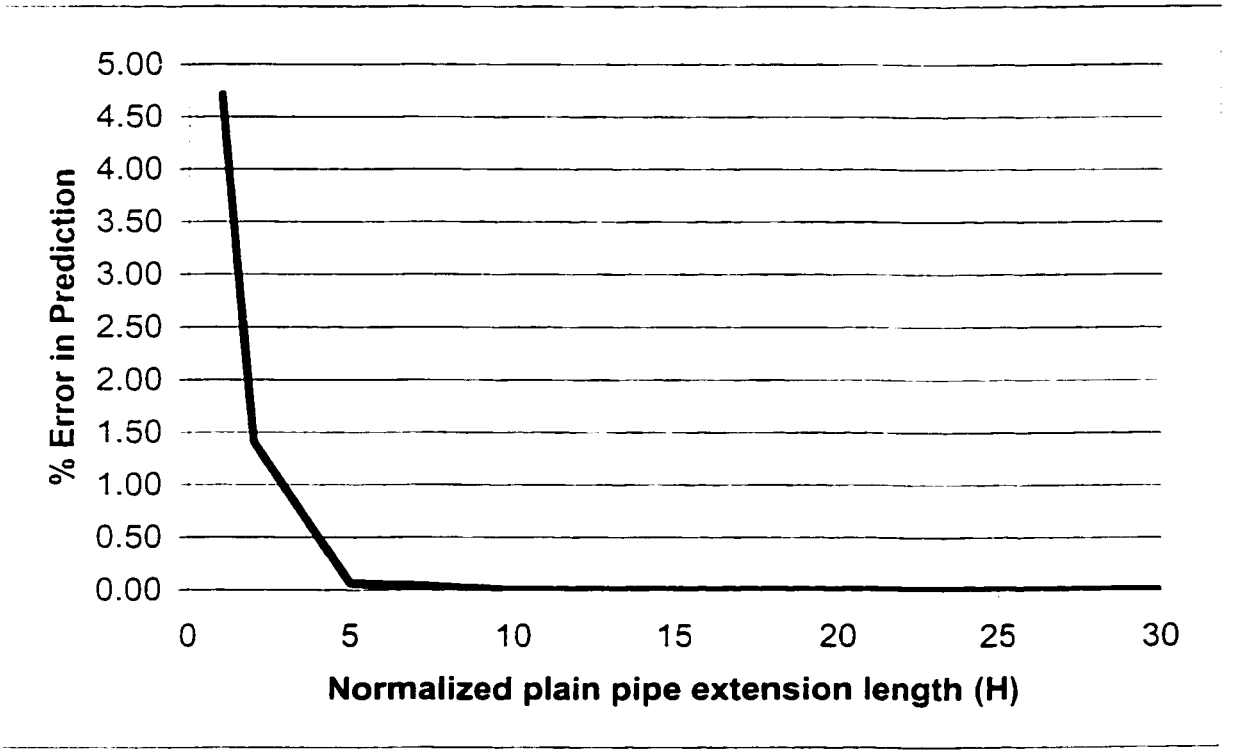


Figure 5.1.5 Percent error in failure pressure prediction versus plain pipe extension length (expressed as a normalized length) - 65% depth, 0.80" length single pit

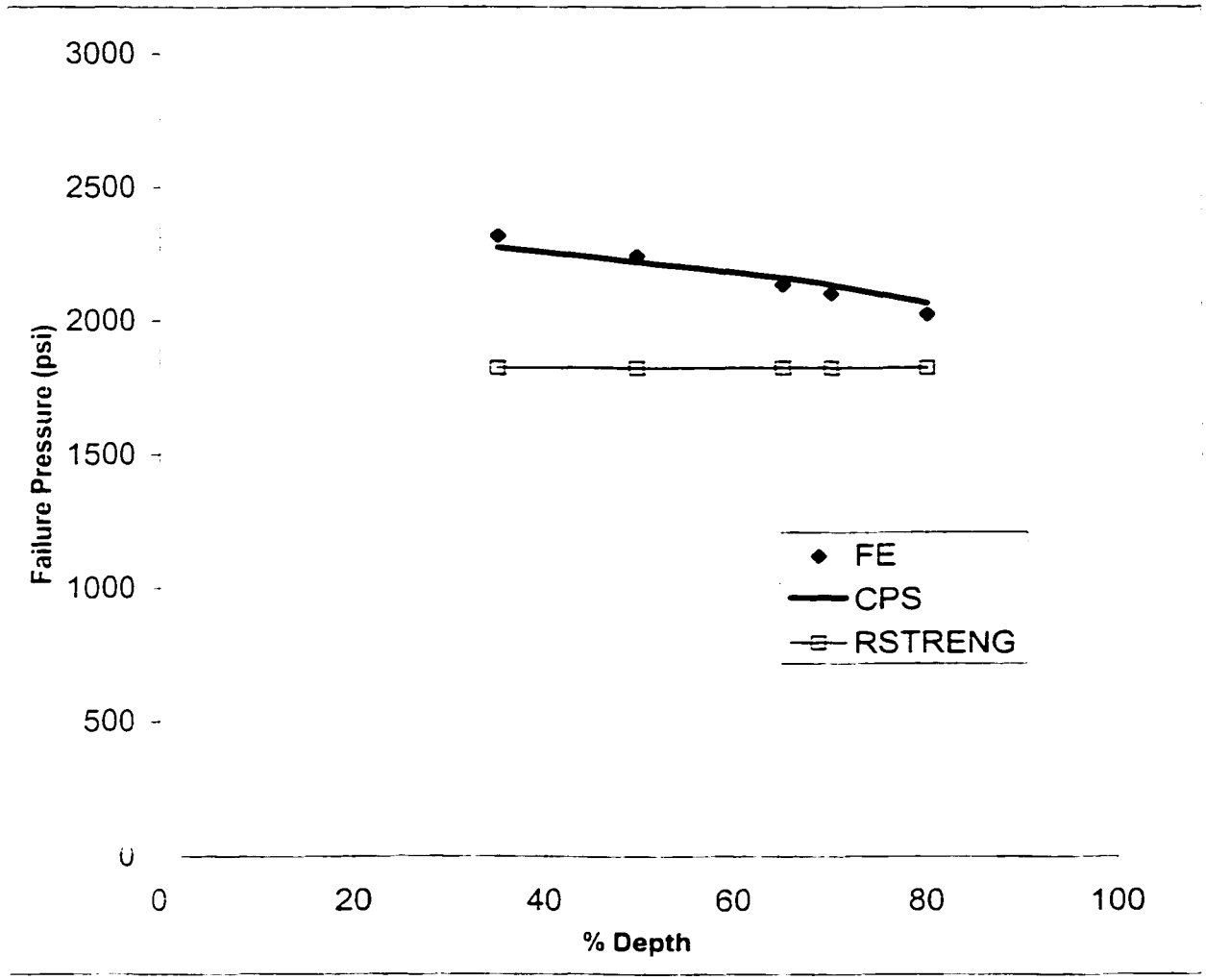


Figure 5.1.6 Failure pressure as a function of % Depth
Single pits. WT=0.195"
Constant Corrosion factor = 0.938

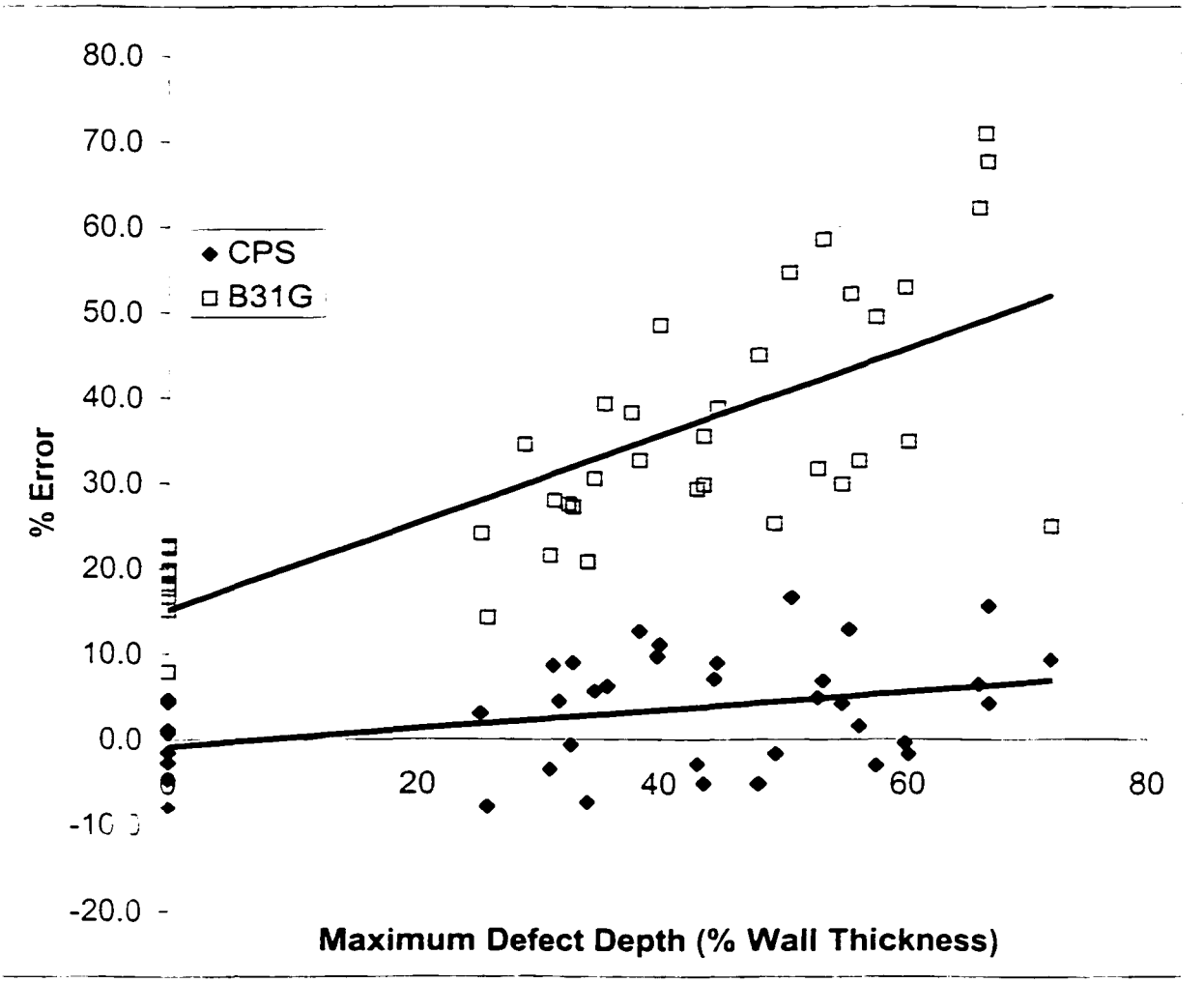


Figure 5.1.7 Error in failure pressure prediction for the weighted depth difference method (Calculated using the CPS program)

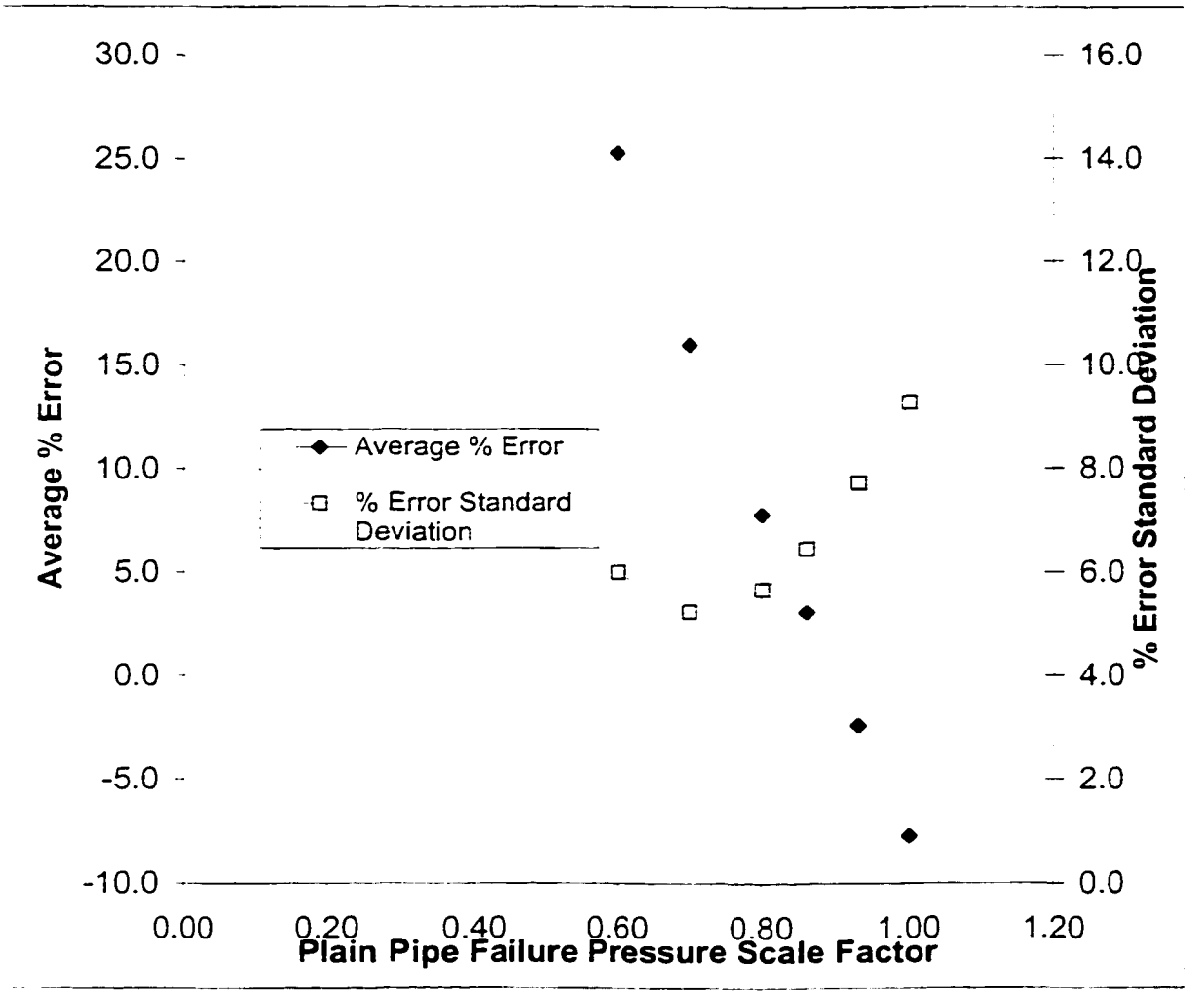


Figure 5.1.8 Variation in % error and standard deviation for different values of the plain pipe failure pressure scale factor

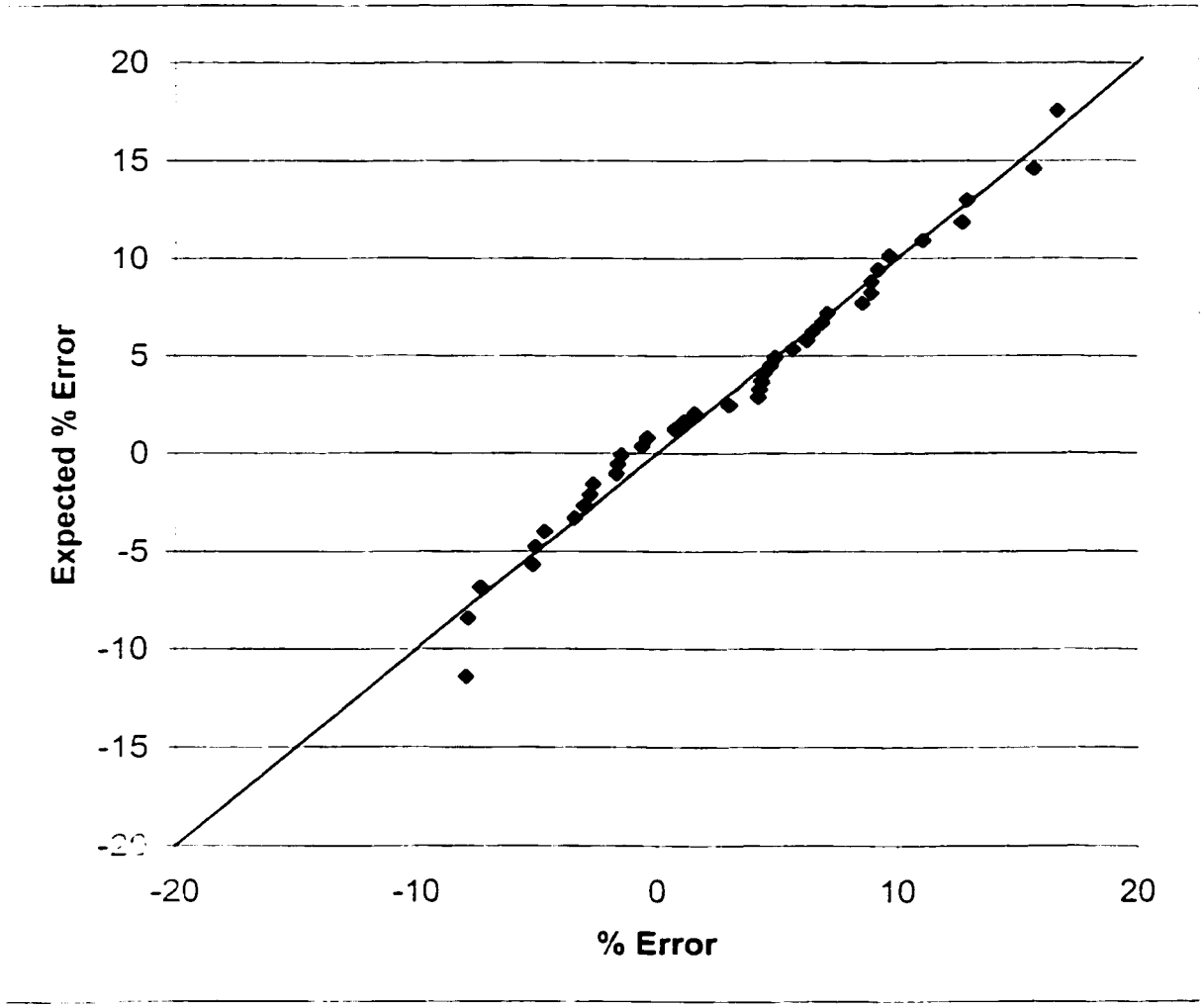


Figure 5.1.9 Normal probability plot for the % error in the CPS predicted failure pressures

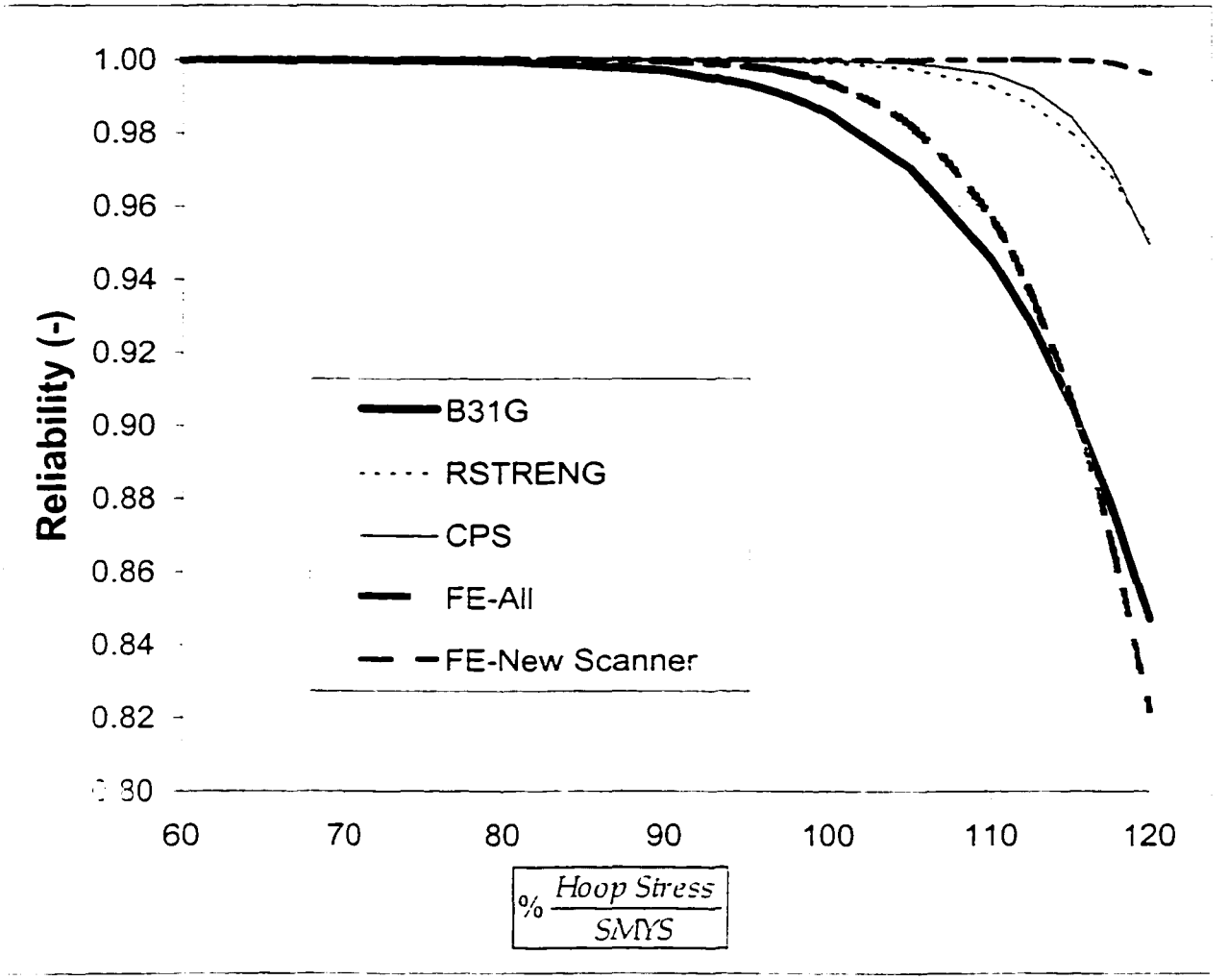


Figure 5.2.1 Defect reliability as a function of operating pressure
For defect BCG 02

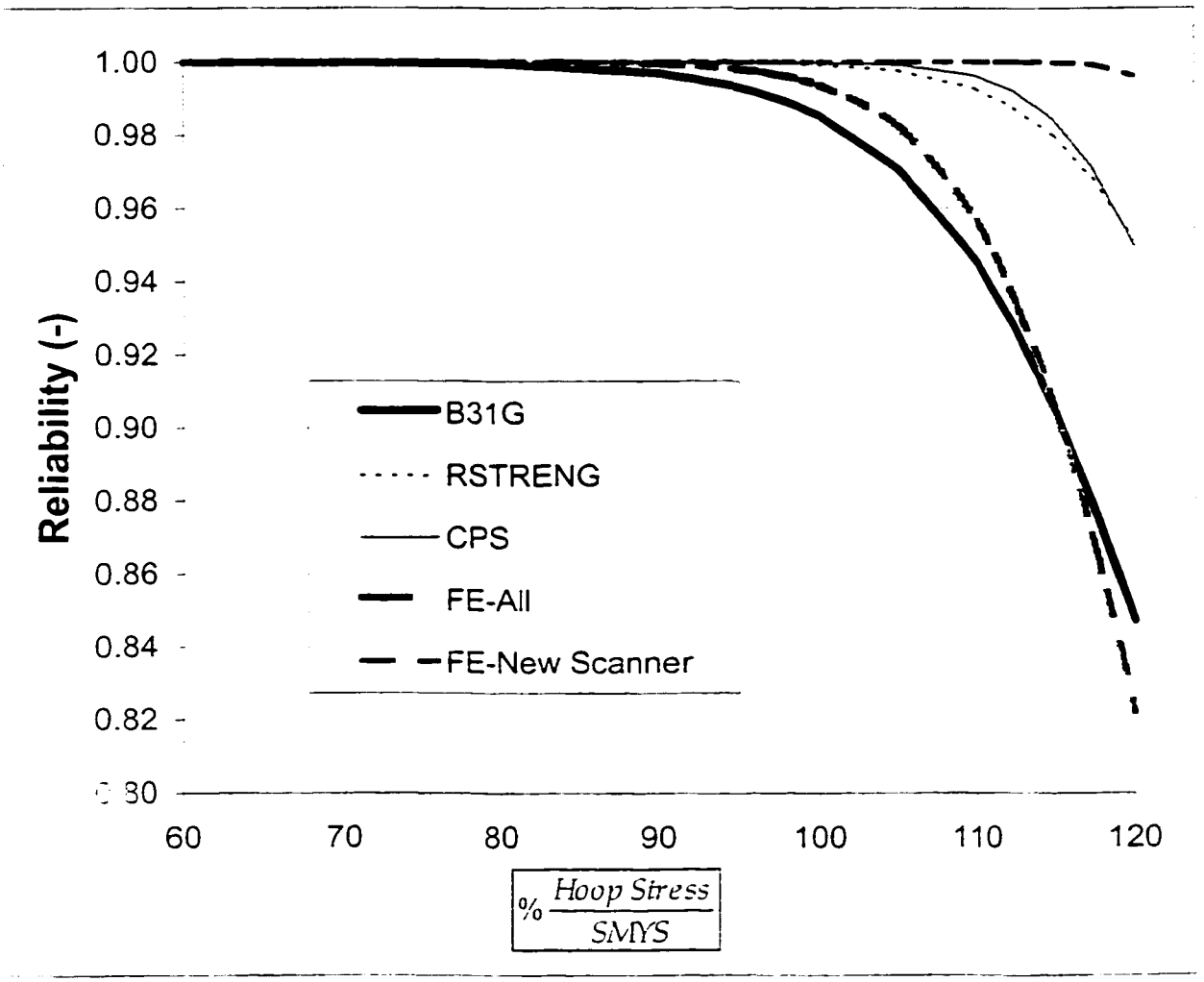


Figure 5.2.1 Defect reliability as a function of operating pressure
For defect BCG 02

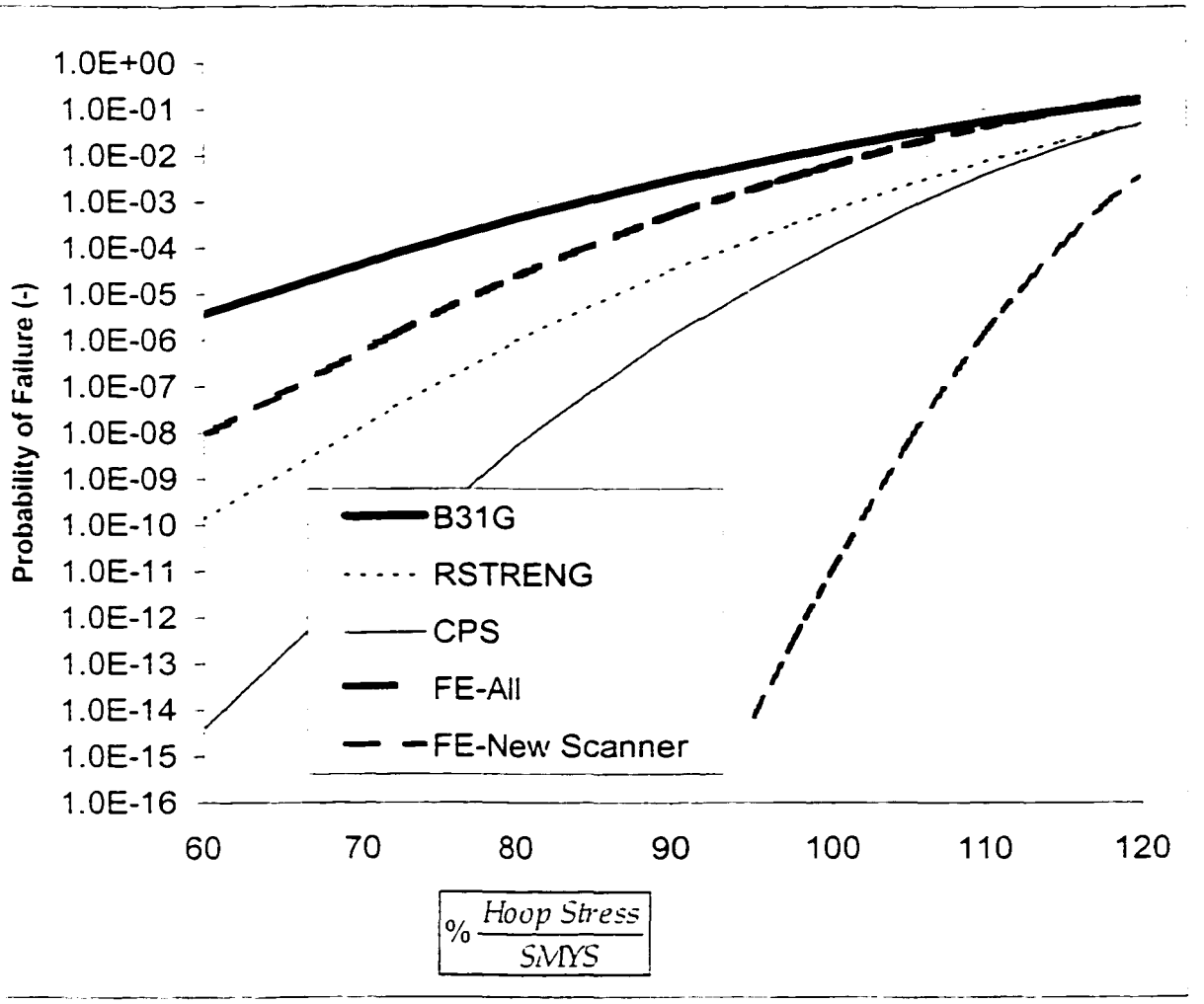


Figure 5.2.2 Probability of failure as a function of operting pressure
For defect BCG 02

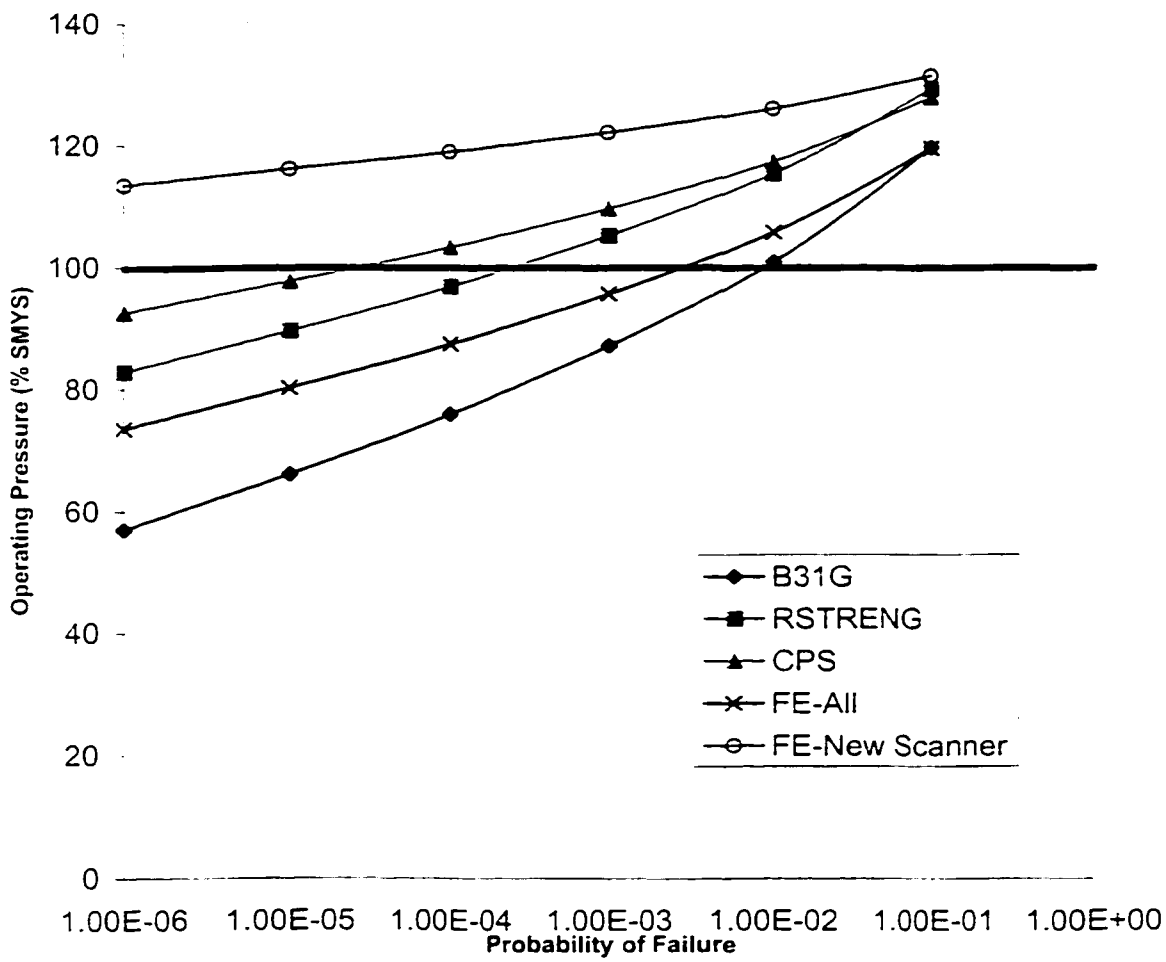


Figure 5.2.3 Operating pressure as a function of probability of failure
For defect BCG 02

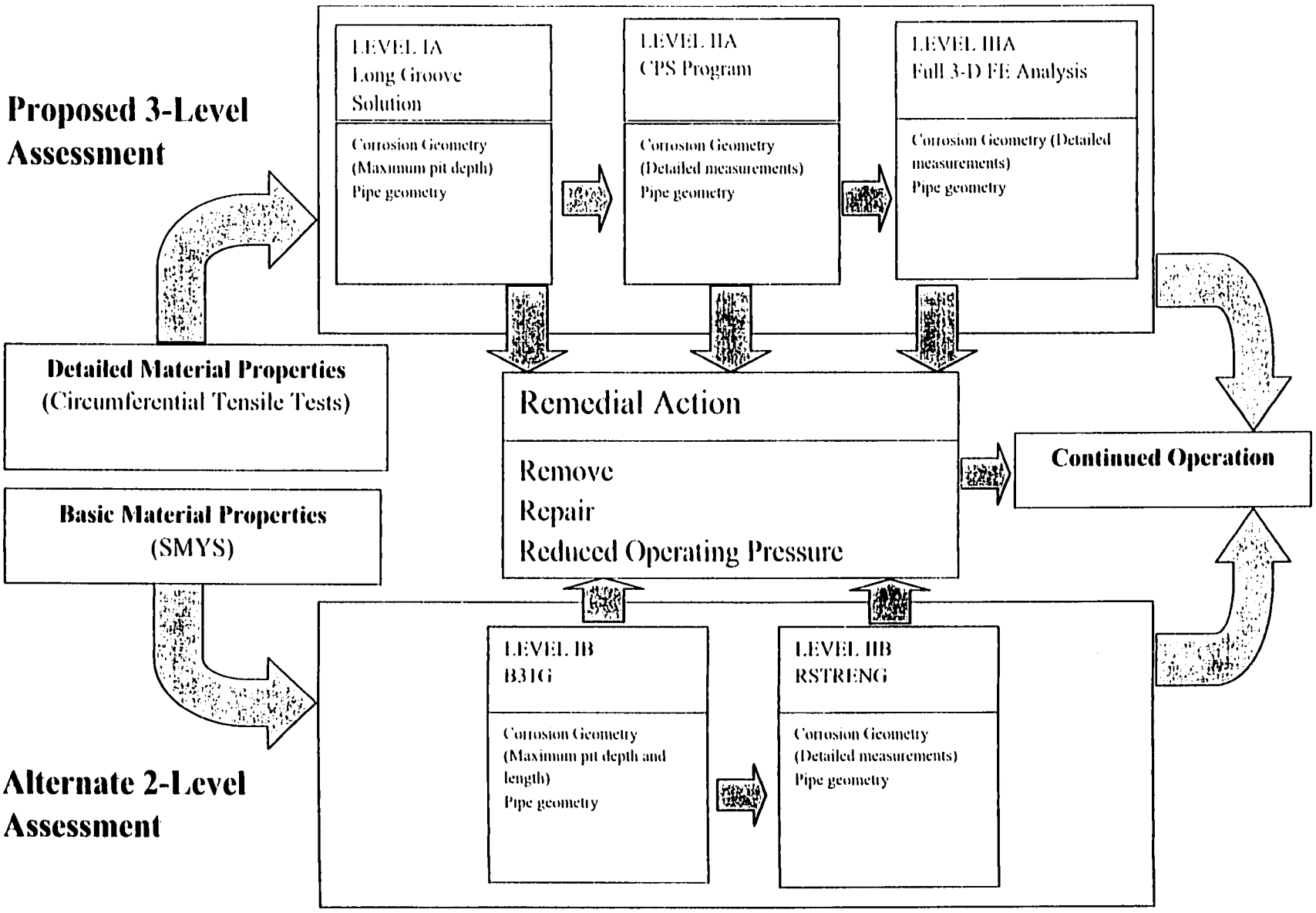


Figure 6.2.1 Three-level assessment procedure

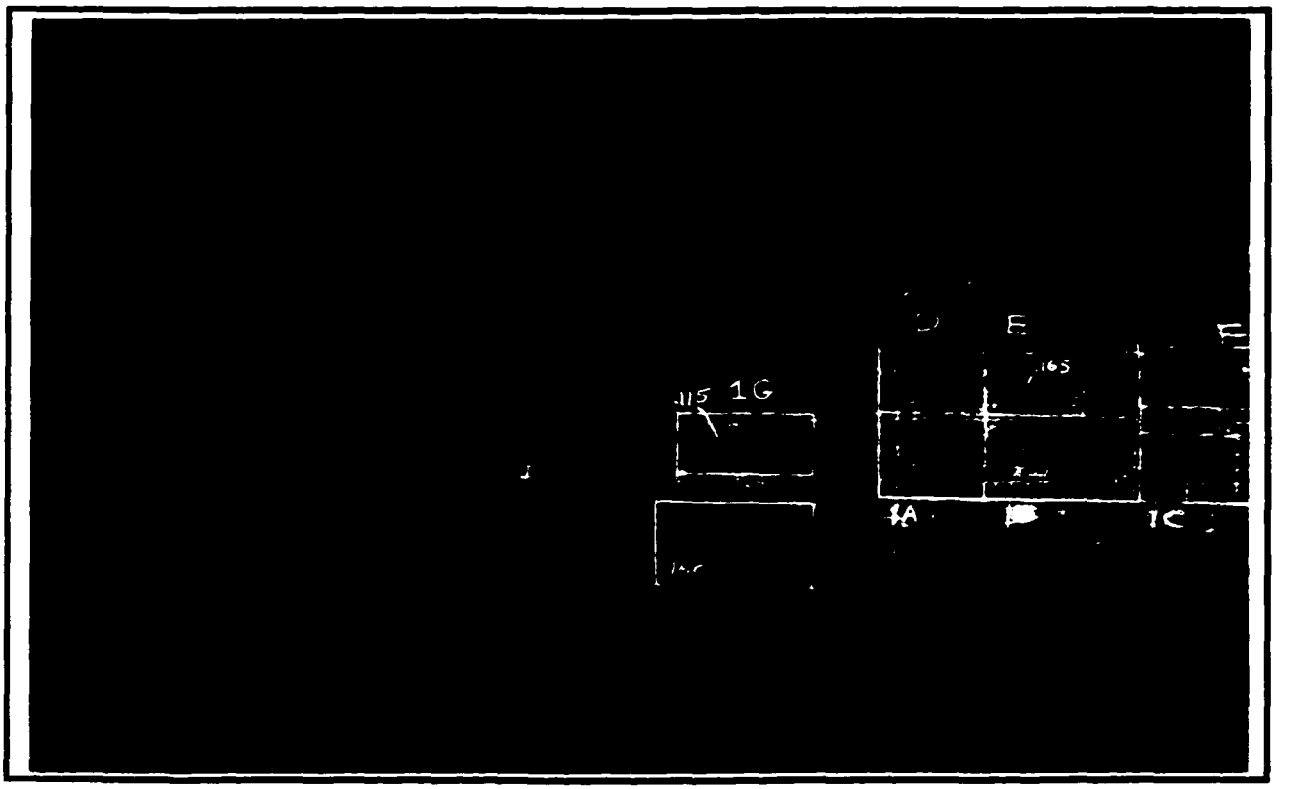


Figure 6.5.1 Pipe section TCP02 – corrosion defects

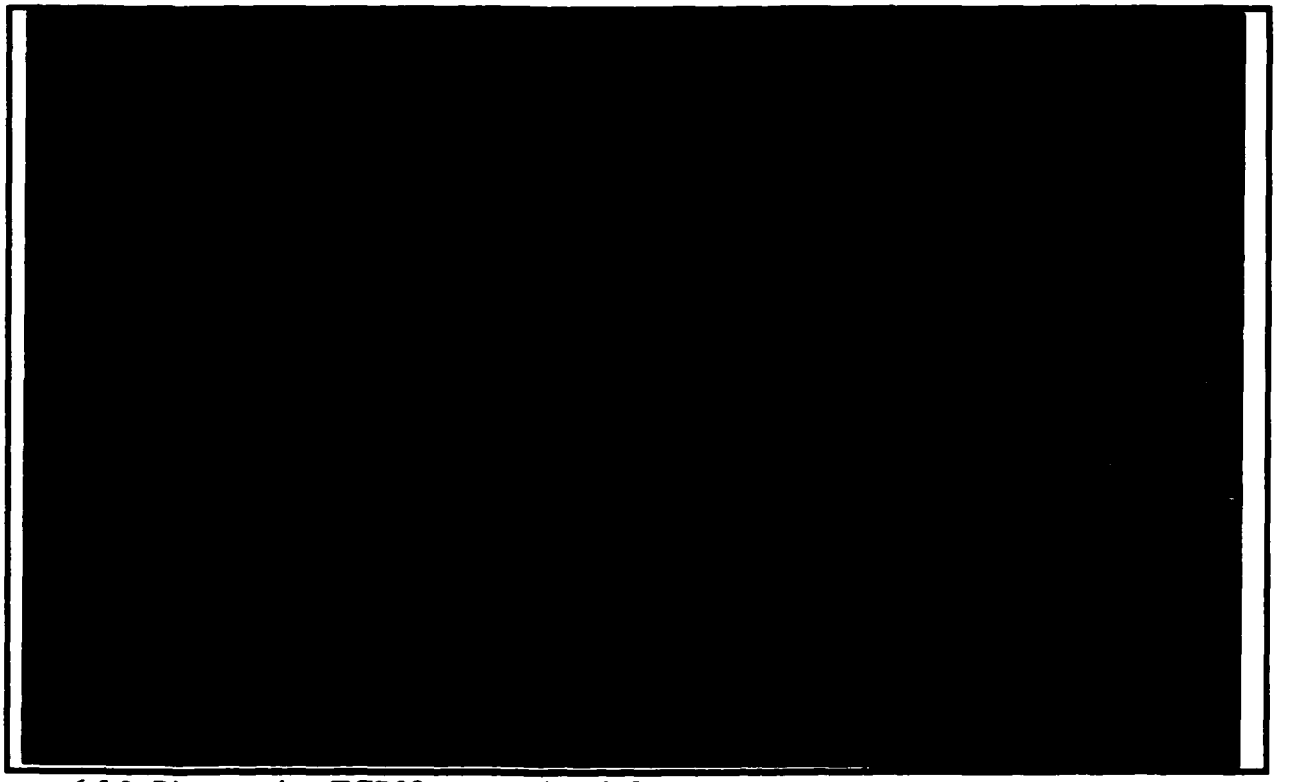


Figure 6.5.2 Pipe section TCP02 – corrosion defects

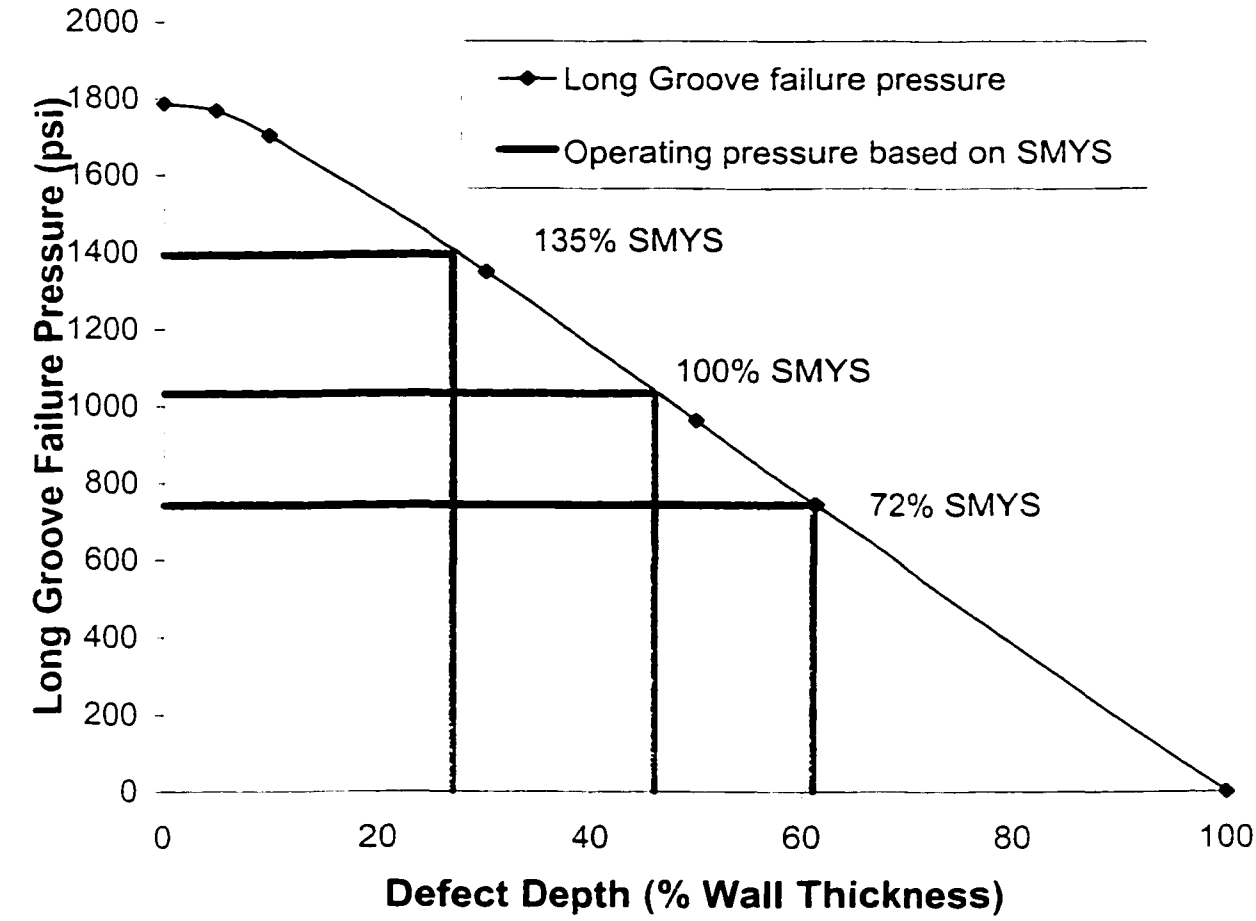


Figure 6.5.3 Long Groove solution failure pressure as a function of defect depth - allowable defect depths for selected operating pressures (based on the SMYS) are indicated.

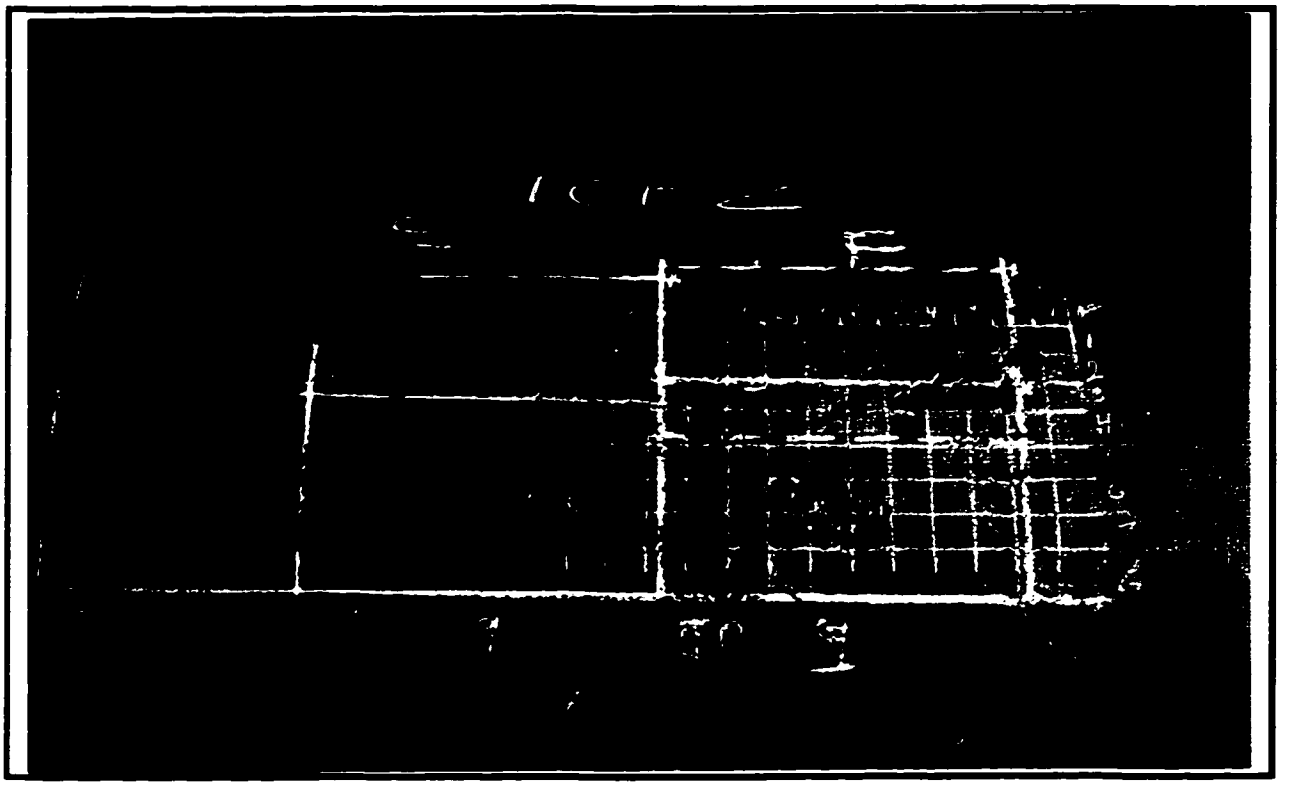


Figure 6.5.4 Pipe section TCP02 – defect TCP02-1A-1F

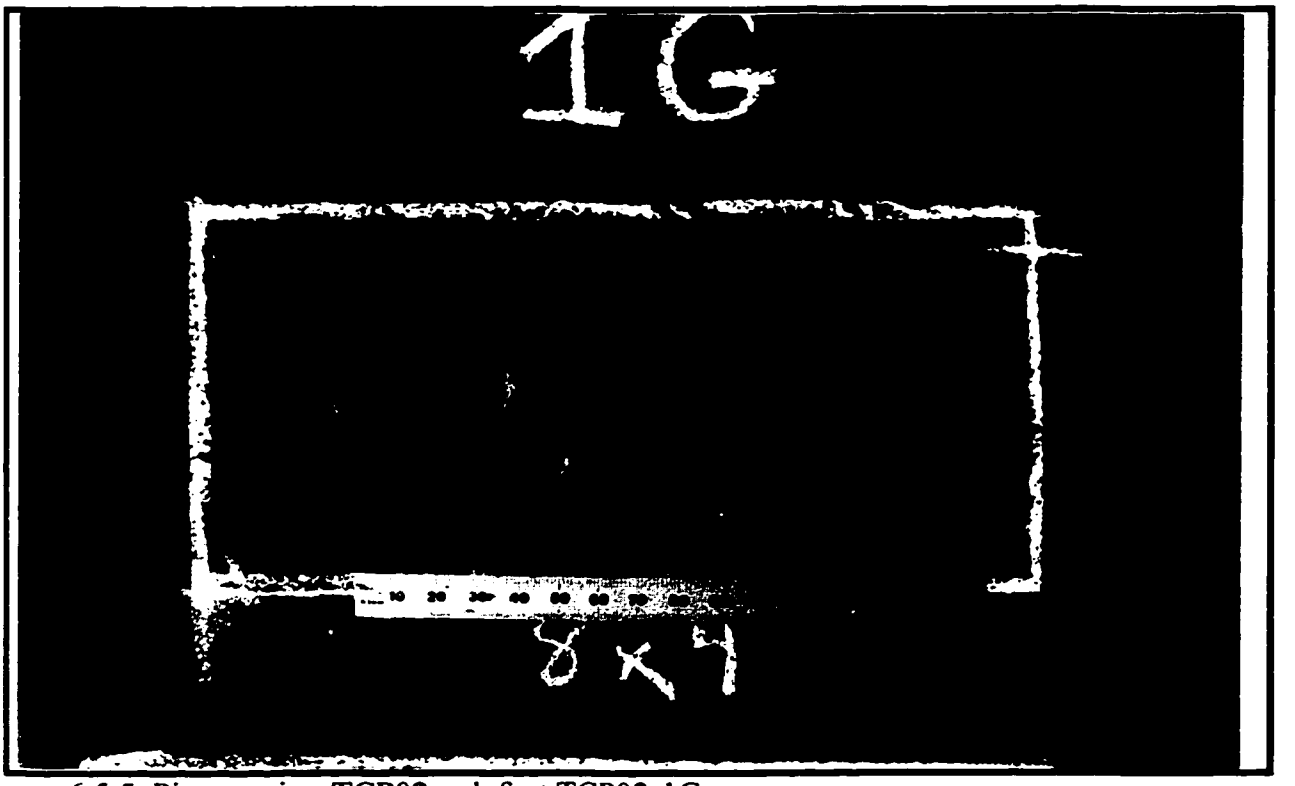


Figure 6.5.5 Pipe section TCP02 – defect TCP02-1G

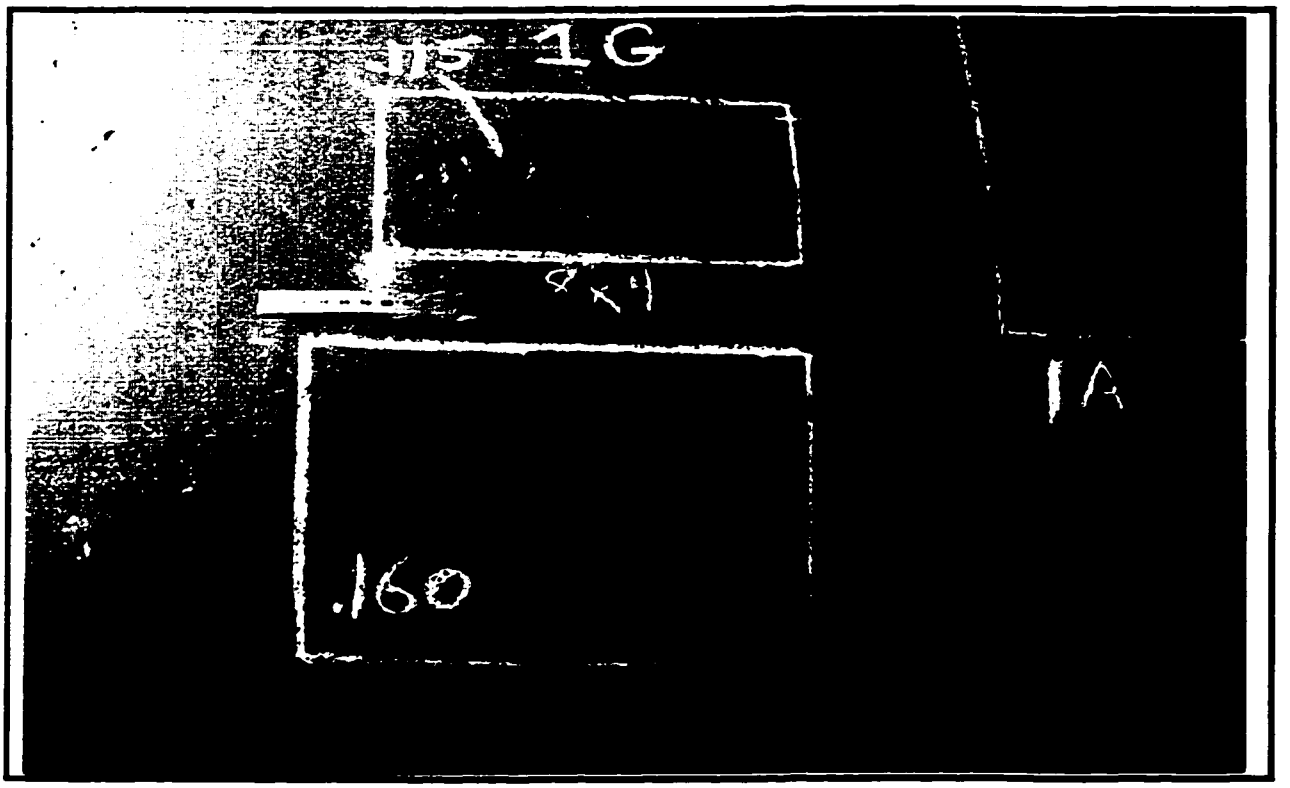


Figure 6.5.6 Pipe section TCP02 – defects TCP02-1G and TCP02-1H

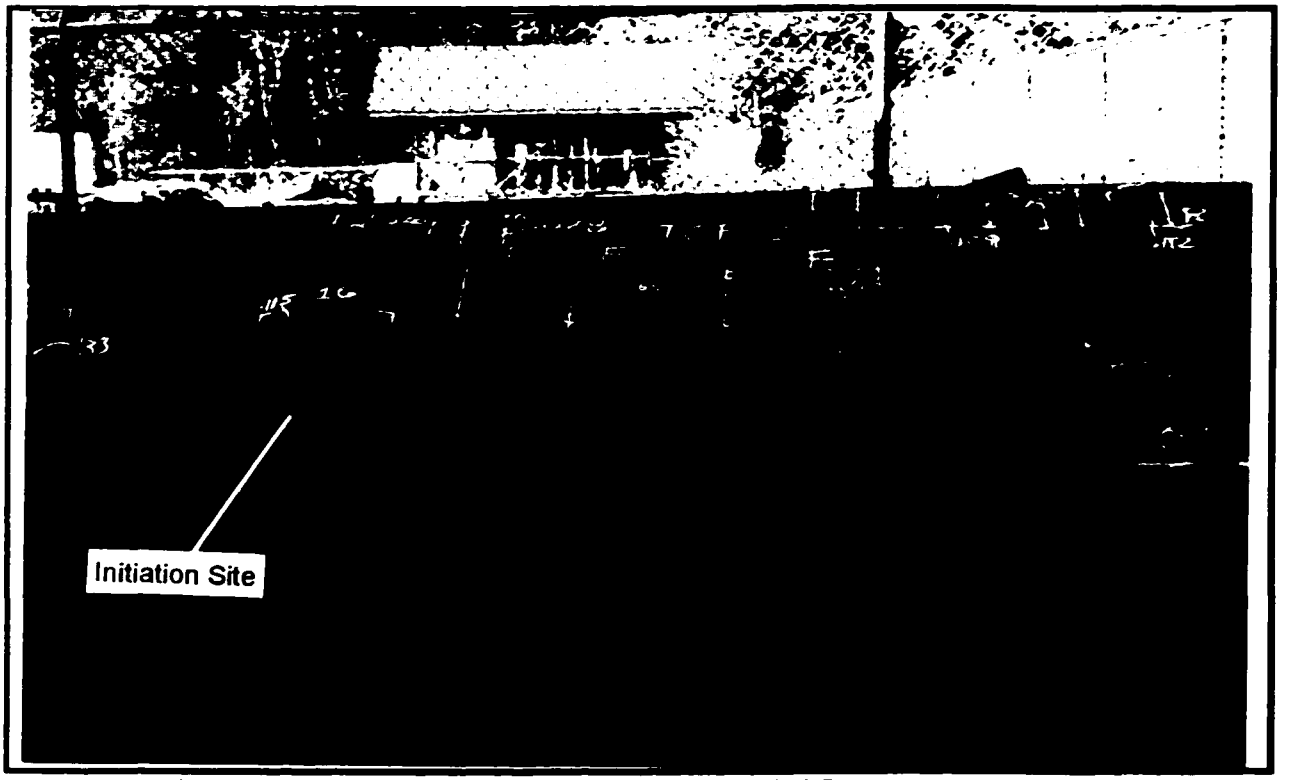


Figure 6.5.7 Pipe section TCP02 – failure at defect TCP02-1G

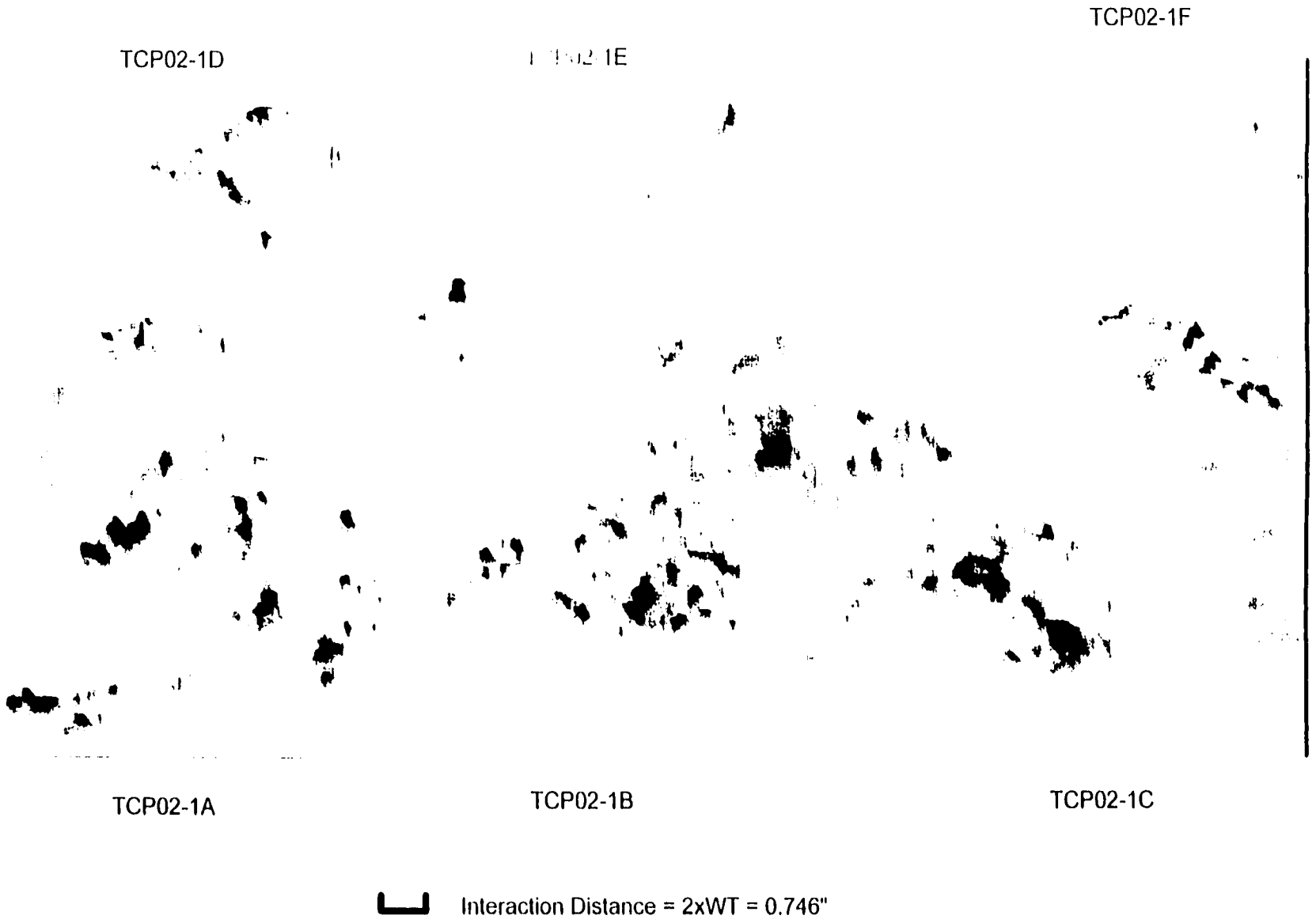


Figure 6.5.8 TCP02-1A-1F Scanner image plot

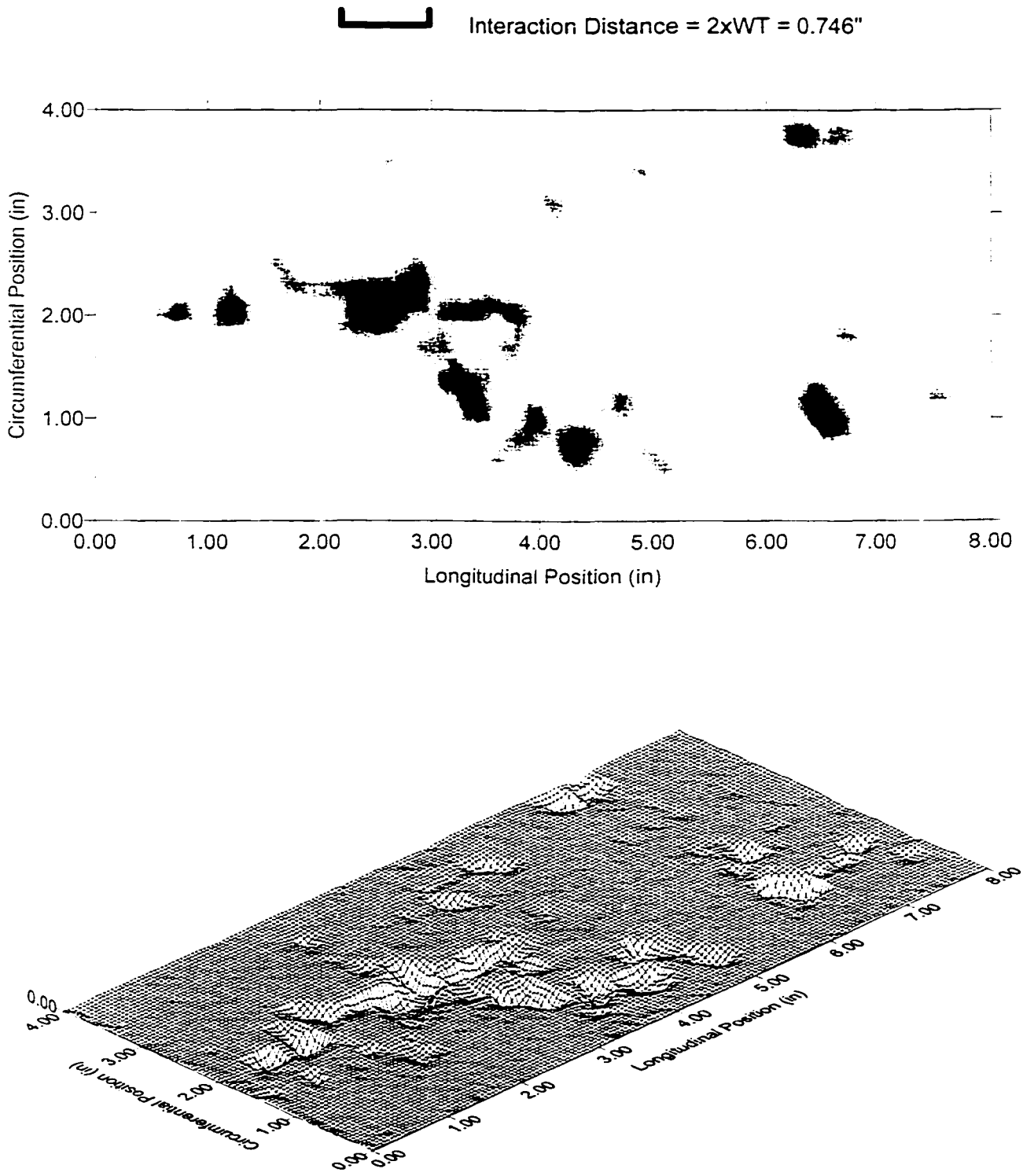
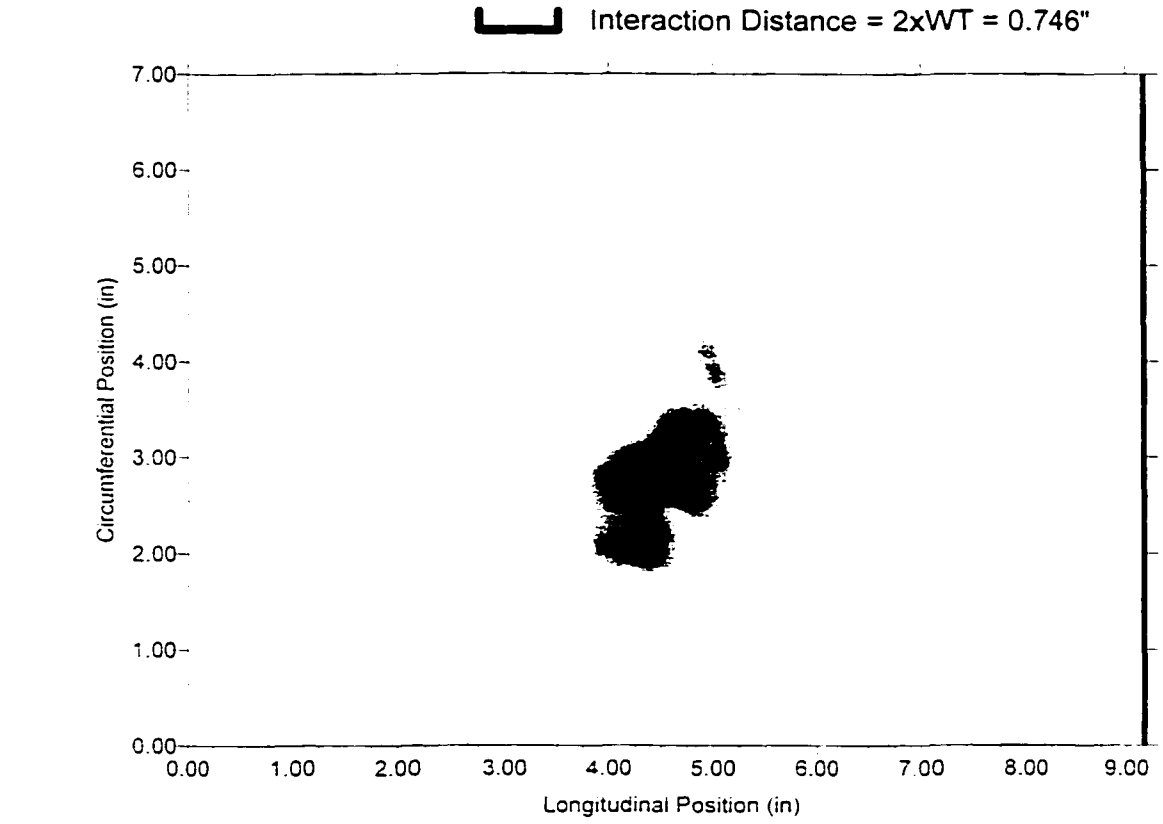


Figure 6.5.9 TCP02-1G Scanner image and surface plots



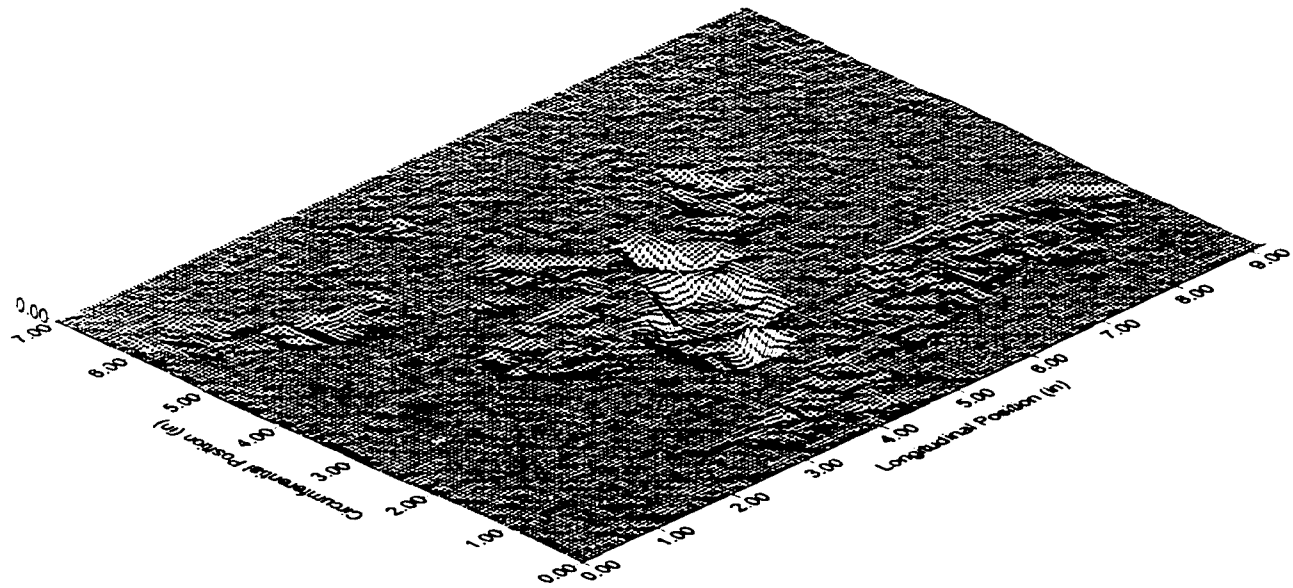


Figure 6.5.10 TCP02-1H Scanner image and surface plots

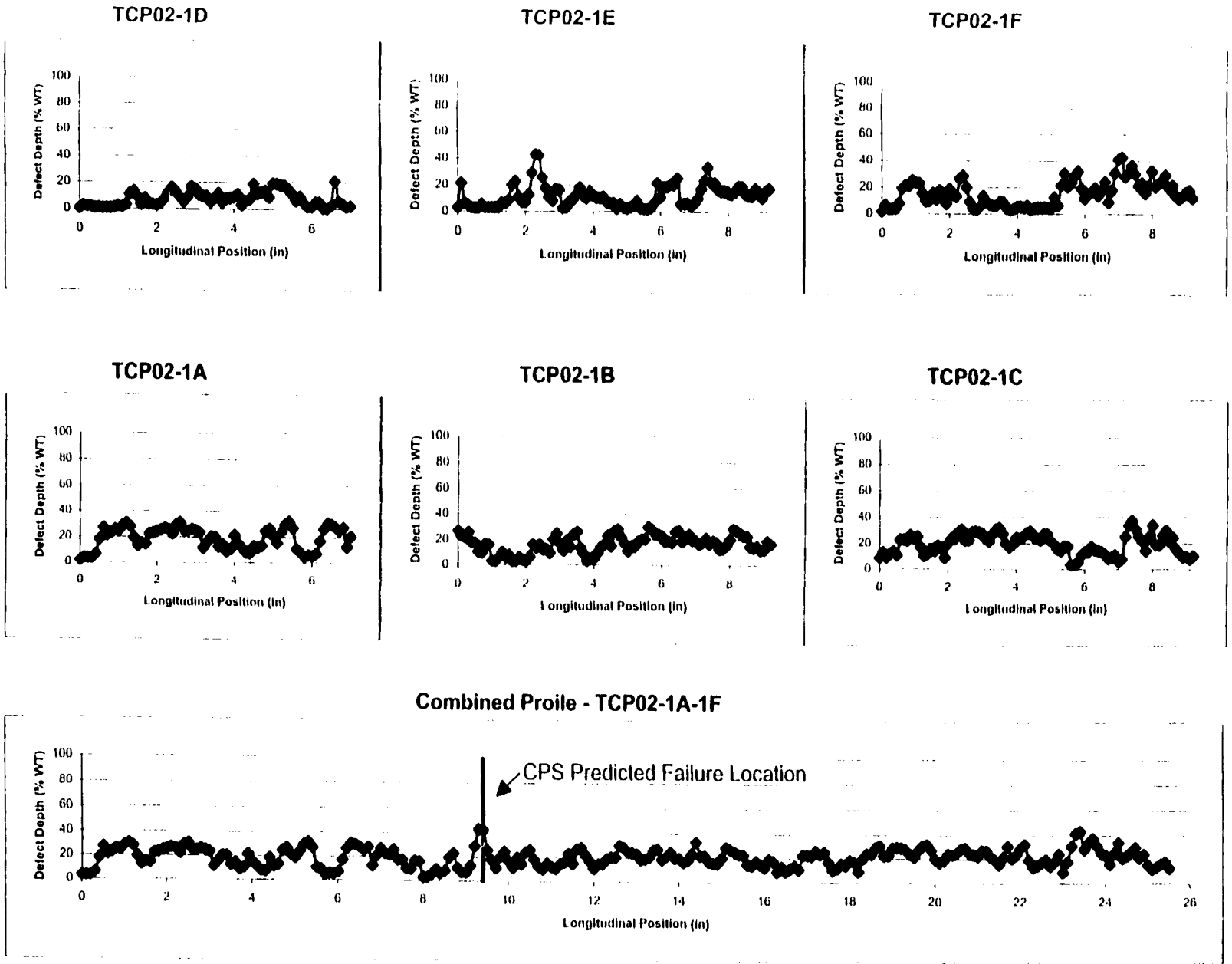
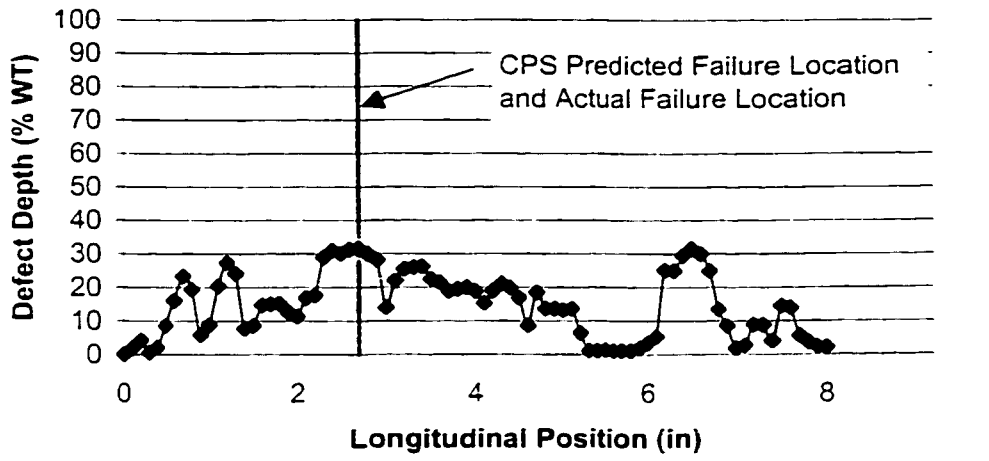
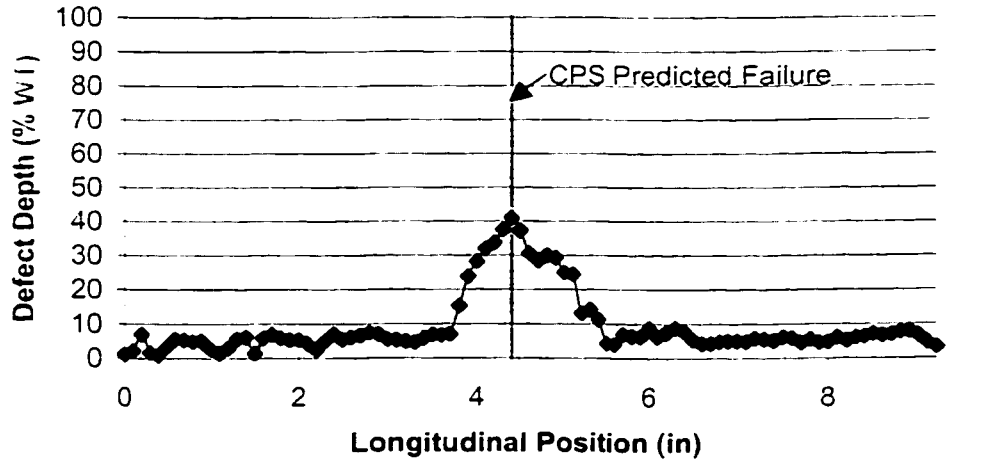


Figure 6.5.11 Individual and combined defect profiles for defect TCP02-1A-1F



Defect TCP02-1G

Figure 6.5.12 Defect profile for defect TCP02-1G



Defect TCP02-1H

Figure 6.5.13 Defect profile for defect TCP02-1H